REPORT DOCUMENTATION PAGE

Form Approved OMB NO. 0704-0188

1. REPORT DATE (DD-MM-YYYY)	2. REPORT TYPE	3. DATES COVERED (From - To)
14-09-2021	Final Report	25-Sep-2020 - 24-Sep-2021

4. TITLE AND SUBTITLE
Final Report: Twenty Second International Symposium on Molten Salts and Ionic Liquids

5a. CONTRACT NUMBER
W911NF-20-1-0342

5b. GRANT NUMBER

5c. PROGRAM ELEMENT NUMBER
611102

6. AUTHORS

5d. PROJECT NUMBER
611102
611102

5e. TASK NUMBER

5f. WORK UNIT NUMBER

7. PERFORMING ORGANIZATION NAMES AND ADDRESSES
The Electrochemical Society
65 South Main Street
Building D
Pennington, NJ 08534 -2839

8. PERFORMING ORGANIZATION REPORT NUMBER

9. SPONSORING/MONITORING AGENCY NAME(S) AND ADDRESS (ES)
U.S. Army Research Office
P.O. Box 12211
Research Triangle Park, NC 27709-2211

10. SPONSOR/MONITOR'S ACRONYM(S)
ARO

11. SPONSOR/MONITOR'S REPORT NUMBER(S)
77198-CH-CF.1

12. DISTRIBUTION AVAILIBILITY STATEMENT
Approved for public release; distribution is unlimited.

13. SUPPLEMENTARY NOTES
The views, opinions and/or findings contained in this report are those of the author(s) and should not contrued as an official Department of the Army position, policy or decision, unless so designated by other documentation.

14. ABSTRACT

15. SUBJECT TERMS

16. SECURITY CLASSIFICATION OF:			17. LIMITATION OF ABSTRACT	15. NUMBER OF PAGES	19a. NAME OF RESPONSIBLE PERSON
a. REPORT	b. ABSTRACT	c. THIS PAGE			William Reichert
UU	UU	UU	UU		19b. TELEPHONE NUMBER 251-460-7430

RPPR Final Report
as of 15-Sep-2021

Agency Code: 21XD

Proposal Number: 77198CHCF **Agreement Number: W911NF-20-1-0342**
INVESTIGATOR(S):

Name: William Matthew Reichert
Email: reichert@southalabama.edu
Phone Number: 2514607430
Principal: Y

Organization: **The Electrochemical Society**
Address: 65 South Main Street, Pennington, NJ 085342839
Country: USA
DUNS Number: 067386755 EIN: 131771269
Report Date: 24-Sep-2021 Date Received: 14-Sep-2021
Final Report for Period Beginning 25-Sep-2020 and Ending 24-Sep-2021
Title: Twenty Second International Symposium on Molten Salts and Ionic Liquids
Begin Performance Period: 25-Sep-2020 **End Performance Period:** 24-Sep-2021
Report Term: 0-Other
Submitted By: Kellie Gilbert Email: development@electrochem.org
Phone: (609) 737-1902101
Distribution Statement: 1-Approved for public release; distribution is unlimited.

STEM Degrees: **STEM Participants:**

Major Goals: The Twenty Second International Symposium on Molten Salts and Ionic Liquids is part of the 238th International Meeting (PRiME 2020) of the Electrochemical Society which was supposed to be held in Honolulu, HI, USA, October 4-9, 2020, but due to travel restrictions the meeting was held virtually. For nearly four decades it has served as the premiere forum for the interchange of ideas between molten salt and ionic liquids researchers from around the world. The Molten Salts and Ionic Liquids symposium was initiated in 1976, and has generally been held every other year in conjunction with The Electrochemical Society international meetings; however, twice in its history the symposium has been held at three-year intervals. Using recent history as an indicator, we expect roughly 100 presentations (oral and posters) representing investigators from 18 countries. We expect the oral and poster presentations will originate from among a diverse collection of international scholars, including USA, Japan, France, Germany, China, Canada, Norway, Belgium, United Kingdom, Italy, South Korea, Russia, and Ukraine. At the Twentieth International Symposium on Molten Salts and Ionic Liquids (MSIL 20) in Honolulu, HI, (October 02-07, 2016) researchers from over 10 different countries contributed nearly 70 oral presentations and over 30 poster presentations. In addition to the body of work discussed at the symposiums, publication of the symposium proceedings summarizes and expands on each presentation. The volume is published by The Electrochemical Society through its definitive proceedings series on numerous topics. The Electrochemical Society requests that a minimum of 80% of symposium presentations be included in the volume before publication is allowed; therefore, the volume provides a comprehensive overview of each published symposium. The Symposium on Molten Salts and its proceedings showcase the state-of-the-art in molten salt research, which spans a wide range of scientific basic research. The sampling of topics below illustrates the diversity of the most recent past symposium.

The symposium covers a wide range of topics of importance to the United States Army, including power and energy (e.g., battery and fuel cells), rare earth and nuclear chemistry (e.g. radioisotopes and nuclear reprocessing), separations (e.g., selective extractions and biphasic systems), extractive metallurgy (e.g., electrolytic deoxidation), electrodeposition (e.g. deposition of alloys, characterization of electroactive species), reactions (e.g. catalysis, synthesis, oligomerization, and polymerization), solute and solvent properties (e.g. structural investigations, melting behavior, and stability of molten salts), new molten salts and ionic liquids (e.g. liquid clathrates, binary and ternary melts, and task specific ionic liquids), and bio-materials and systems (e.g,, biological reactions, bio-catalysis, and bio-nanocomposites). Molten salts and ionic liquids offer the potential for unique solvent environments for biological reactions and biocatalysis. The high ionic strength and non-complexing nature of many of these systems provide unique opportunity for novel biological reactions.

Accomplishments: Due to the Covid-19 Global Pandemic, for the first time in its history, MSIL22 (as well as the entire PRiME2020 Conference) was held virtually. Regardless of the new format, MSIL22 was overwhelmingly

successful, featuring 80 oral and 40 poster presentations, representing investigators from more than 15 countries across 4 continents. The Max Bredig Award associated with the symposium was granted to Dr. Sheng Dai, from Oak Ridge National Laboratory.

Training Opportunities: Nothing to Report

Results Dissemination: A Proceedings (ECS vol 98-10) of ECS Transactions was published based on this meeting that included 47 peer-reviewed conference papers. A Special Issue of the Journal of the Electrochemical Society was also published featuring 50 peer-reviewed manuscripts. The Call for papers, Proceedings Preface & Table of Contents, and Preface for the Special Issue are attached.

Honors and Awards: The Max Bredig Award associated with the MSIL22 symposium was granted to Dr. Sheng Dai, from Oak Ridge National Laboratory.

Protocol Activity Status:

Technology Transfer: Nothing to Report

PARTICIPANTS:

Participant Type: PD/PI
Participant: William Reichert
Person Months Worked: 2.00
Project Contribution:
National Academy Member: N

Funding Support:

Partners

,

I certify that the information in the report is complete and accurate:
Signature: Kellie Gilbert
Signature Date: 9/14/21 7:36PM

TO: Dr. Robert A. Mantz, Program Manager

FROM: Dr. W. Matthew Reichert, Asst. Prof. of Chemistry, University of South Alabama

RE: Final Report on "Twenty Second International Symposium on Molten Salts and Ionic Liquids" (ARO Grant W911NF2010342)

DATE: September 8, 2021

Summary

The 22st International Symposium on Molten Salts and Ionic Liquids was held as part of a joint meeting of the 238th National Electrochemical Society (ECS) PRiME Meeting (held virtually). Funds were requested and awarded from the Army Research Office (ARO) in the amount of $30,000 to supplement travel expenses for speakers to the 22st International Symposium on Molten Salts and Ionic Liquids. These funds were specifically directed to support the registration fees for all symposium participants since no travel was allowed due to the global pandemic.

Relevance to ARO

The Symposium on Molten Salts and Ionic Liquids covers a wide range of topics of importance to the United States Army, including electrochemical power (e.g., battery and fuel cells), solid state materials (e.g., corrosion resistant alloys and semiconductors), molten salt promoted corrosion phenomena (e.g., high temperature turbine corrosion), separations (e.g., toxic gas sensing and removal), nuclear fuel reprocessing, and bio-materials and systems (e.g,, biological reactions, bio-catalysis, and bio-nanocomposites). Molten salts and ionic liquids offer the potential for unique solvent environments for biological reactions and biocatalysis. The high ionic strength and non-complexing nature of many of these systems provide unique opportunity for novel biological reactions and bio-based materials. The guiding philosophy for the symposia at the National Electrochemical Society meetings, including the Symposium on Molten Salts and Ionic Liquids, is based on the stated objectives of The Electrochemical Society which are to advance the theory and practice of electrochemistry, solid state sciences, and allied subjects; to encourage the research and dissemination of knowledge in these fields; and to promote the education of fundamental and applied scientists and engineers in these fields.

Accomplishments

Due to the Covid 19 Global Pandemic, for the first time in its history MSIL22 (as well as the entire PRiME2020 Conference) was held virtually . Regardless of the new format, MSIL22 was overwhelmingly successful, featuring 80 oral and 40 poster presentations, representing investigators from more than 15 countries across 4 continents. The Max Bredig Award associated with the symposium was granted to Dr Sheng Dai, from Oak Ridge National Laboratory. A Proceedings (ECS vol 98-10) of ECS Transactions was published based on this meeting that included 47 peer-reviewed conference papers. Also a Special Issue of the Journal of the Electrochemical Society was published featuring 50 peer-reviewed manuscripts (copies of the Proceedings, Special Issue were sent to the ARO in Durham, NC). The Call for papers, Proceedings Preface & Table of Contents, and Preface for the Special Issue are attached.

CALL FOR PAPERS

Molten Salts and Ionic Liquids 22

This symposium will provide an international and interdisciplinary forum to present the latest research on systems involving molten salts and ionic liquids. Papers on basic and applied research in all areas of chemistry, engineering, electrochemical systems, and physics related to molten salts and ionic liquids are solicited. The topics will include but are not restricted to: 1) Power & Energy Applications (e.g. batteries, fuel cells, semiconductors, photovoltaics, and phase change energy storage); 2) Rare Earth and Nuclear chemistry (e.g. lanthanides, actinides, radioisotopes, nuclear reprocessing); 3) Electrodeposition (e.g. deposition of alloys, characterization of electroactive species, and surface characterization); 4) Reactions (e.g. catalysis, synthesis, oligomerizations, and polymerizations); 5) Separations (e.g. selective extractions and biphasic systems); 6) Solute and Solvent Properties (e.g. structural investigations, thermal properties, dynamics, and stability of ionic liquids and molten salts); 7) Biomass applications (e.g. dissolution, modification, and/or reactions utilizing biomass), 8) Materials (e.g. polymer blends, additive manufacturing, active coatings, and corrosion studies); 9) New ionic liquids and molten salt mixtures (e.g. liquid clathrates, binary and ternary melts, and task specific ionic liquids); 10) Deep eutectic solvents (e.g., synthesis, properties, and applications). In addition, papers are encouraged for a special session to honor the 2020 recipient of the Max Bredig Award, Prof. Sheng Dai.

Keynote lectures will be presented by invited speakers. A poster session will be planned. Student participation is highly encouraged, and it is anticipated that some funds will be available for student and young scientist support.

An issue of ECS Transactions will be published "AT" the meeting. All authors will need to submit their manuscripts by June 26, 2020. All manuscripts will be submitted online, and must be in either MS Word or PDF format. Authors are encouraged to use the official ECS Transaction template.

Abstracts should be submitted electronically to the ECS Headquarters Office using the Online Abstracts Submission website. A template is available on the website. Suggestions and inquiries should be sent to the Symposium Organizers:

D. P. Durkin, United States Naval Academy, email: durkin@usna.edu
P. C. Trulove, United States Naval Academy, email: trulove@usna.edu
W. M. Reichert, University of South Alabama, email: reichert@southalabama.edu
R. A. Mantz; Army Research Office, email: robert.a.mantz.civ@mail.mil
H. C. De Long, Army Research Office, email: hugh.c.delong.civ@mail.mil
M. Mizuhata, Kobe University, email mizuhata@kobe-u.ac.jp
Mikito Ueda, Hokkaido University, email: mikito@eng.hokudai.ac.jp.
A. Bund, TU Ilmenau, email: Andreas.Bund@tu-ilmenau.de
A. Ispas, TU Ilmenau, email: Adriana.Ispas@tu-ilmenau.de
V. Di Noto, University of Padova, email: vito.dinoto@unipd.it

Molten Salts and Ionic Liquids 22

Editors:

D. P. Durkin

P. C. Truelove

A. Bund

A. Ispas

V. Di Noto

W. M. Reichert

R. A. Mantz

H. C. De Long

M. Mizuhata

M. Ueda

Sponsoring Divisions:

Electrodeposition

Energy Technology

Industrial Electrochemistry and Electrochemical Engineering

Physical and Analytical Electrochemistry

The Electrochemical Society of Japan

Published by

The Electrochemical Society

65 South Main Street, Building D

Pennington, NJ 08534-2839, USA

tel 609 737 1902

fax 609 737 2743

www.electrochem.org

ecstransactions™

Vol. 98, No. 10

Published by:

The Electrochemical Society
65 South Main Street
Pennington, New Jersey 08534-2839, USA

Telephone 609.737.1902
Fax 609.737.2743
e-mail: ecs@electrochem.org
Web: www.electrochem.org

ISSN 1938-6737 (online)
ISSN 1938-5862 (print)

ISBN 978-1-60768-905-8 (PDF)

Printed in the United States of America.

Preface

The papers included in this issue of *ECS Transactions* were originally scheduled to be presented in the symposium "Molten Salts and Ionic Liquids 22," held during PRiME 2020 in Honolulu, Hawaii, from October 4-9, 2020. Due to the COVID-19 pandemic, the meeting is now virtual. As with previous years, the symposium owes it success to strong international participation, with researchers and scientists from over 10 countries presenting their contributions to the field.

The symposium topics include a well-distributed mix of fundamental property exploration and unique applications of molten salts and ionic liquids. The symposium includes nearly 100 presentations, encapsulating 47 conference manuscripts on topics ranging from power and energy, rare earth and nuclear chemistry, electrodeposition, reactions and separations, solute and solvent properties, biomass applications, new ionic liquids, molten salt mixtures, and deep eutectics.

The co-organizers for this symposium were Paul C. Trulove, United States Naval Academy; Andreas Bund, Technische Universitat-Ilmenau; Adriana Ispas, Technische Universitat-Ilmenau; Vito di Noto, University of Padova; W. Matthew Reichert, University of South Alabama; Robert A. Mantz, Army Research Office; Hugh C. De Long, Army Research Office; Minoru Mizuhata, Kobe University; and Mikito Ueda, Hokkaido University. Without their help, the symposium would not have been a success.

The Molten Salts and Ionic Liquids symposium would not exist without the financial support it receives from both internal and external sources. The Physical and Analytical Electrochemistry Division, Energy Technology Division, and Electrodeposition Division of The Electrochemical Society, along with Sumimoto Metal Mining Company and Biologic, provided funds to host this year's symposium. In addition, the U.S. Army Research Office provided significant funding to support international and young investigators.

We are proud to honor the 2020 recipient of the Max Bredig Award, Sheng Dai, of the Oak Ridge National Laboratory. Sheng Dai obtained his BS (1984) and MS (1986) in chemistry at Zhejiang University, Hangzhou, China, and his PhD (1990) in chemistry at the University of Tennessee, Knoxville. He is currently a group leader in the Chemical Sciences Division of the Oak Ridge National Laboratory (ORNL), professor of chemistry at the University of Tennessee, Knoxville, and serves as a director for the Energy Frontier Research Center for Fluid Interface Reactions, Structures, and Transport. He was honored with the UT-Battelle Corporate Fellow in 2011, the highest designation a researcher can receive at ORNL. Dai's current research interests include ionic liquids, porous materials, and their applications for separation sciences and energy storage, as well as catalysis by nanomaterials. Because of his research, he has received various awards, including the 2019 ACS Award in Separation Science and Technology, 2018 International Mesostructured Materials Association Award, 2016 Battelle Distinguished Inventor Award, and six R&D100 Awards (2011, 2012, two in 2014, 2015, and 2016). He is also a fellow of the Material Research Society and fellow of the American Association for the Advancement of Science. In his award address, Prof. Dai will discuss his career investigating the fundamental principles underpinning ionic media through tailored interactions for energy-related applications.

Dr. David P Durkin
Lead Organizer, MSIL 22
United States Naval Academy
September 3, 2020

***ECS Transactions*, Volume 98, Issue 10**
Molten Salts and Ionic Liquids 22

Table of Contents

Chapter 4
L02 – Power & Energy Applications

Chapter 5
L02 – Materials from Ionic Liquids Session in Recognition of Prof. Sheng Dai

Chapter 6
L02 – Solute and Solvent Properties

Chapter 7
L02 – Electrodeposition

Chapter 8
L02 – Monday Poster Session

Chapter 9
L02 – Tuesday Poster Session

Preface—JES 2021 Focus Issue on Progress in Molten Salts and Ionic Liquids

David P. Durkin,[a, *, z] Robert A. Mantz,[b,*] Paul C. Trulove [a, **]

[a.] U.S. Naval Academy, Annapolis, Maryland 21402-5026, USA

[b.] Army Research Office, Durham, North Carolina 27703, USA

[z.] Email: durkin@usna.edu, 410 293-6601

[*] ECS Member
[**] ECS Fellow

Molten salts and ionic liquids have been associated with The Electrochemical Society for nearly 45 years. Over this time, the Society has published a Proceedings on the International Symposium every two years, the most recent being the 22nd Volume. Interest in the field has expanded considerably with recent symposia presenting a full week's worth of papers and posters across a diverse spectrum of molten salts and ionic liquids research. The objectives of this Focus Issue are to expose the broader society to the research going on within the molten salts and ionic liquids community beyond that which is presented in our symposia, and to inspire future collaboration. The topics covered include a diversity of fundamental property explorations as well as unique applications of molten salts and ionic liquids. These include but weren't limited to power and energy, sensors, rare earth and nuclear chemistry, electrodeposition, reactions, solute and solvent properties, deep eutectics, and the latest in new ionic liquids and molten salt mixtures.

This Focus Issue is dedicated to Prof. Austen Angell, a pioneer in our field, a long-standing member of the Electrochemical Society, and the 2010 Bredig Award winner who passed away in the Spring of 2021. His groundbreaking work on supercooled liquids, polymer and non-aqueous electrolytes, and ionic liquids (the subject of his last paper) has profoundly impacted our understanding and has left an indelible mark for generations of scientists to follow. In his repose, we wish Austen fair winds and following seas.

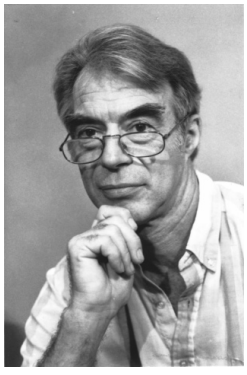

Molten Salts and Ionic Liquids 22

Editors:

D. P. Durkin

P. C. Truelove

A. Bund

A. Ispas

V. Di Noto

W. M. Reichert

R. A. Mantz

H. C. De Long

M. Mizuhata

M. Ueda

Sponsoring Divisions:

Electrodeposition

Energy Technology

Industrial Electrochemistry and Electrochemical Engineering

Physical and Analytical Electrochemistry

The Electrochemical Society of Japan

Published by

The Electrochemical Society

65 South Main Street, Building D

Pennington, NJ 08534-2839, USA

tel 609 737 1902

fax 609 737 2743

www.electrochem.org

ecstransactions™

Vol. 98, No. 10

Published by:

The Electrochemical Society
65 South Main Street
Pennington, New Jersey 08534-2839, USA

Telephone 609.737.1902
Fax 609.737.2743
e-mail: ecs@electrochem.org
Web: www.electrochem.org

ISSN 1938-6737 (online)
ISSN 1938-5862 (print)

ISBN 978-1-60768-905-8 (PDF)

Printed in the United States of America.

Preface

The papers included in this issue of *ECS Transactions* were originally scheduled to be presented in the symposium "Molten Salts and Ionic Liquids 22," held during PRiME 2020 in Honolulu, Hawaii, from October 4-9, 2020. Due to the COVID-19 pandemic, the meeting is now virtual. As with previous years, the symposium owes it success to strong international participation, with researchers and scientists from over 10 countries presenting their contributions to the field.

The symposium topics include a well-distributed mix of fundamental property exploration and unique applications of molten salts and ionic liquids. The symposium includes nearly 100 presentations, encapsulating 47 conference manuscripts on topics ranging from power and energy, rare earth and nuclear chemistry, electrodeposition, reactions and separations, solute and solvent properties, biomass applications, new ionic liquids, molten salt mixtures, and deep eutectics.

The co-organizers for this symposium were Paul C. Trulove, United States Naval Academy; Andreas Bund, Technische Universitat-Ilmenau; Adriana Ispas, Technische Universitat-Ilmenau; Vito di Noto, University of Padova; W. Matthew Reichert, University of South Alabama; Robert A. Mantz, Army Research Office; Hugh C. De Long, Army Research Office; Minoru Mizuhata, Kobe University; and Mikito Ueda, Hokkaido University. Without their help, the symposium would not have been a success.

The Molten Salts and Ionic Liquids symposium would not exist without the financial support it receives from both internal and external sources. The Physical and Analytical Electrochemistry Division, Energy Technology Division, and Electrodeposition Division of The Electrochemical Society, along with Sumimoto Metal Mining Company and Biologic, provided funds to host this year's symposium. In addition, the U.S. Army Research Office provided significant funding to support international and young investigators.

We are proud to honor the 2020 recipient of the Max Bredig Award, Sheng Dai, of the Oak Ridge National Laboratory. Sheng Dai obtained his BS (1984) and MS (1986) in chemistry at Zhejiang University, Hangzhou, China, and his PhD (1990) in chemistry at the University of Tennessee, Knoxville. He is currently a group leader in the Chemical Sciences Division of the Oak Ridge National Laboratory (ORNL), professor of chemistry at the University of Tennessee, Knoxville, and serves as a director for the Energy Frontier Research Center for Fluid Interface Reactions, Structures, and Transport. He was honored with the UT-Battelle Corporate Fellow in 2011, the highest designation a researcher can receive at ORNL. Dai's current research interests include ionic liquids, porous materials, and their applications for separation sciences and energy storage, as well as catalysis by nanomaterials. Because of his research, he has received various awards, including the 2019 ACS Award in Separation Science and Technology, 2018 International Mesostructured Materials Association Award, 2016 Battelle Distinguished Inventor Award, and six R&D100 Awards (2011, 2012, two in 2014, 2015, and 2016). He is also a fellow of the Material Research Society and fellow of the American Association for the Advancement of Science. In his award address, Prof. Dai will discuss his career investigating the fundamental principles underpinning ionic media through tailored interactions for energy-related applications.

Dr. David P Durkin
Lead Organizer, MSIL 22
United States Naval Academy
September 3, 2020

***ECS Transactions*, Volume 98, Issue 10**
Molten Salts and Ionic Liquids 22

Table of Contents

Chapter 4
L02 – Power & Energy Applications

Chapter 5
L02 – Materials from Ionic Liquids Session in Recognition of Prof. Sheng Dai

Chapter 6
L02 – Solute and Solvent Properties

Chapter 7
L02 – Electrodeposition

Chapter 8
L02 – Monday Poster Session

Chapter 9
L02 – Tuesday Poster Session

Facts about ECS

The Electrochemical Society (ECS) is an international, nonprofit, scientific, educational organization advancing the theory and practice of electrochemistry and solid state science and technology, and allied subjects. The Society was founded in Philadelphia in 1902 and incorporated in 1930. There are currently over 8,000 members from around the globe representing 13 technical division and 23 geographical sections and a growing student membership program with over 100 student chapters. The Society is also supported by more than 2,000 corporations, government agencies, and academic institutions through institutional membership, corporate programs, and subscriptions.

The technical activities of the Society are carried on by divisions. Sections of the Society host symposia, programs, and events focused on their respective geographic regions. Major international meetings of the Society are held in the spring and fall of each year. At these meetings, the divisions and partnered organizations hold general sessions and sponsor symposia on specialized subjects.

The Society has an active publications program that includes the following:

Journal of The Electrochemical Society — (JES) is the flagship journal of The Electrochemical Society and the oldest peer-reviewed journal in its field. Since its founding in 1902, JES has evolved into one of the most highly cited and prestigious journals in electrochemistry and materials science with a cited half-life of greater than 10 years.

ECS Journal of Solid State Science and Technology — (JSS) is a peer-reviewed journal covering fundamental and applied areas of solid state science and technology, including experimental and theoretical aspects of the chemistry, and physics of materials and devices.

ECS Transactions (ECST) — is the official conference proceedings publication of The Electrochemistry Society — a high-quality venue for authors and an excellent resource for researchers. ECST offers the full-text content of proceedings from ECS meetings and ECS sponsored conferences.

The Electrochemical Society Interface — Interface is an authoritative yet accessible publication for those in the field of solid state and electrochemical science and technology. Published quarterly, this full-color magazine contains technical articles about the latest developments in the field, and presents news and information about the Society.

ECS Books Series — ECS books and monographs provide authoritative, detailed accounts of specific topics in electrochemistry and solid state science and technology. These titles are sponsored by ECS and published in cooperation with noted publishers such as John A. Wiley & Sons.

For more information on these publications and other Society activities, visit the ECS website:

www.electrochem.org

Chapter 2

L02 – Physical and Analytical Electrochemistry Division Max Bredig Award Address in Molten Salt and Ionic Liquid Chemistry

ECS Transactions, 98 (10) 3-8 (2020)
10.1149/09810.0003ecst ©The Electrochemical Society

The Ionic Melting Pot: My Research in Molten Salts and Ionic Liquids

Sheng Dai[a,b]

[a] Chemical Sciences Division, Oak Ridge National Laboratory, Oak Ridge, TN 37831, USA
[b] Department of Chemistry, University of Tennessee, Knoxville, Tennessee 37996, USA

Molten salts and ionic liquids are a unique class of solvents that offer many advantages, such as negligible vapor pressures, wide liquidus ranges, good thermal stability, and tunable solubilities of both organic and inorganic species. This presentation will provide an overview of my research in the following five areas related to molten salts and ionic liquids: (1) speciation and thermodynamics of actinides and fission products in molten salts, (2) metal-ion extraction based on ionic liquids, (3) gas separation through functionalized ionic liquids, (3) synthesis of functional materials (e.g, carbon, porous materials) using molten salts and ionic liquids as reaction media, (4) electrolytes based on task-specific ionic liquids, and (5) emerging porous ionic liquids. The overall goal of my research is to investigate fundamental principles underpinning ionic media through tailored interactions for energy-related applications.

Introduction to Molten Salts & Ionic Liquids

My journey with molten salts and ionic liquids began during my work as a postdoctoral research associate jointly supervised by Gleb Mamontov at the University of Tennessee, Knoxville (UTK) and Jack P. Young at Oak Ridge National Laboratory (ORNL). This was in 1990, just after I had obtained my PhD in physical organic chemistry (on radical cations) under Ffrancon Williams at UTK. Both Gleb and Jack were extraordinary mentors; I owe much of my success in researching molten salts and ionic liquids to them. Gleb played an instrumental role in developing chloroaluminate and fluorochloroaluminate molten salts for refractive metal deposition and molten-salt batteries and received the Max Bredig Award in 1994 at the 9th Symposium on Molten Salts, which I was fortunate to attend. Jack developed the windowless spectroscopic technique that is still widely used in spectroscopic analysis of molten fluorides.

My postdoc work focused on the development of Raman fiber-optic instrumentation for the molten salt systems used by the Dow Chemical Company for sensing magnesium production. Afterwards (1994), I was hired as a staff member at ORNL by Mac Toth, who is another outstanding individual, a great experimentalist, and an expert on actinides and fission products in molten salts and has had a great impact on my career as an independent researcher. The following provides a summary of my work on molten salts and ionic liquids since I began my independent research career.

Research in Molten Salts & Ionic Liquids

High-Temperature Molten Salts

When I began my research, actinide chemistry in molten salts had been investigated. However, there was still a knowledge gap on the speciation of uranium compounds in such systems. Through high-temperature spectroscopic measurement, I was successful in identifying uranium oxychloride species (1). I used a high-temperature titration method involving CCl_4 to convert the uranium oxychloride species into the corresponding chloride species and thus established the existence of oxychloride species in molten KCl-$MgCl_2$. The high-temperature chemistry derived from that investigation was important in the development of pyrochemical processes involving actinide species. In the same period, I became interested in understanding the fundamental basis for the solubilities of actinide oxides in molten salts. This interest prompted me to elucidate the solubilities of actinide oxides through the integrated use of thermodynamic analysis and spectroscopic measurement (2). The thermodynamic driving force for dissolution of actinide species in high-temperature molten salts was elucidated through the Flood-Forland-Grjotheim cycle. The atomistic importance of the second coordination shell in molten salts was revealed through this study (2, 3). Because of a shift in the focus of research funding, my research in molten salts stopped around 2000, which was difficult because I had devoted a decade of my life to that area of research.

Rather interestingly, there is a recent resurgence in interest in molten salts, which is driven by the need for development of the next generation of molten salt nuclear reactors. After a 15-year hiatus, I resumed my research in molten salts in two areas: (a) synthesis of functional materials in molten salts and (b) X-ray and neutron scattering spectroscopic characterization methodologies for actinides and fission products in molten salts. In the first area, Xianbo Jin conducted research in my group during a 2-year (2015-2016) sabbatical from Wuhan University, during which he worked on the electrochemical graphitization of carbons in molten salts. We successfully developed a unique electrochemical graphitization method for synthesis of graphite from amorphous carbon materials (4). This new methodology can reduce graphitization temperatures considerably. In addition, various amorphous carbons, including hard carbons, can be used as graphite precursors. More recently, we found that we can extend the technique used for electrochemical graphitization to the crystallization of other 2D materials (e.g., BN) (5).

Room-Temperature Ionic Liquids (RTILs)

My interest in ionic liquids (ILs) started when I joined Gleb's group in 1990 even though my project was related to high-temperature molten salt systems. My first publication on ionic liquids is about a spectroscopic investigation of the uranium (IV) chloride complex species in $AlCl_3$-ethyl-methyl-imidazolium chloride in 1994, which demonstrated the strong solvation environment that can distort the symmetric environment via static interaction (6). As I recall, the field of ionic liquids started attracting great interest from diverse fields of chemistry in 1998, which was considerably popularized by the publication of a *C&EN* article by Freemantle (7) and a paper by Robin D. Rogers (8), who is the winner of the Max Bredig Award in 2018. My own research in ionic liquids can be divided into three categories: metal and gas separations, materials syntheses, and electrochemical processes.

Separation Chemistry Based on RTILs**:** My interest in actinide and fission products in high-temperature molten salts prompted me to investigate ILs as a unique class of solvents for the separation of metal ions (especially fission products) (9, 10). Initially, I was interested in the extension of my high-temperature research to RTILs to demonstrate that the second-shell coordination observed in high-temperature molten salts was also valid in ILs. Inspired by the strong effect of solvation on metal ion dissolution in RTILs, I started my investigation of RTILs as solvents for extraction of metal ions with crown ether extractants (10-14). The history of this research relevant to nuclear fuel cycles and metal ion separations was recently summarized in a review paper (15). The extraction of metal ions based on hydrophobic RTILs is still a very active research field in hydrometallurgy in the area of recovery of critical materials. In addition to my interest in metal-ion separations with ILs, I started developing RTILs for gas separations (16-19). More recently, my group (20-22) and the Brennecke group (23) initiated the use of anion-functionalized superbasic RTILs for carbon capture. This new class of RTILs can uptake CO_2 via a reversible 1:1 binding and can be used to capture carbon dioxide directly from the air because of strong basicity.

Ionothermal Synthesis and Ionic-Liquid Materials: In the middle 1990s, I became interested in synthesis of porous inorganic materials for separation and catalysis. It occurred to me that I could merge two fields of research (porous materials and ionic liquids) through the use of RTILs as a new reaction medium for synthesis of advanced materials. Nowadays, the use of ILs in the synthesis of inorganic materials has become an important research topic in materials chemistry (24). My paper that reported the first use of RTILs for making porous silicas, published in 2000 (25), was highlighted in *C&EN* (February 14, 2000, issue of page 79) and in *Chemistry and Industry* (April 3, 2000, issue of page 259). Another key advance brought about by this research was the discovery that aerogel materials can be derived from a non-supercritical process through the use of ILs.

My discovery of using RTILs to make porous carbon came serendipitously. In a review of thermogravimetric analysis of RTILs with Huimin Luo, the high char yield for RTILs containing nitrile groups prompted me to think that we can use ILs as a nonpolymer carbon precursor (26-28). This ionothermal synthesis of carbons represents a new direction in tailoring both functionality and pore structure for carbon materials. The functional carbon alloys derived by ionothermal synthesis have been widely applied in electrocatalysis, heterogeneous catalysis, energy storage, and gas storage.

In 2007, I read a very thought-provoking paper (29) by Stuart James, in which he and his coworkers proposed a concept for porous liquids. Initially, I asked my postdocs to attempt to make porous liquids by dissolving some palladium organometallic cavities in RTILs. However, that approach was unsuccessful and shelved. Then, I serendipitously came across a paper (30) by Giannelis on liquification of nanoparticles. My work on hollow silicas and carbons (31) immediately led me to think that we may be able to make porous ionic liquids by liquifying hollow silica and carbon nanospheres based on the strategy developed by Giannelis for solid nanospheres. With hard work of my postdoc (Jinshui Zhang), we have developed a new class of materials: porous liquids consisting of permanently empty liquid cavities. The porous liquid materials can be transformational media for future energy-related applications in carbon capture by taking advantage of the matrices as a separation medium and the cavities as free space to accelerate gas transport

in the dense liquid state (32). The porous liquids were synthesized by surface engineering hollow nanostructures with suitable ionic corona and canopy species. They constitute a totally new class of materials that destroys the fallacy that the porosity is unique to solid materials. The porous liquids can be readily integrated into commercially available membrane systems without requiring additional equipment. The porous liquid–based membrane technology combines individual advantages of traditional liquid membranes (high selectivity) and solid porous membranes (high permeability) and have great potential in replacing current CO_2 capture technologies based on solvent absorption and polymeric membrane separation for large-scale industrial applications.

Application of RTILs for Electrochemical Processes**:** My contribution in the application of RTILs in electrochemical processes entails three areas: proton-conducting media, battery electrolytes, and advanced electrodeposition systems. In the area of proton-conducting media, I developed a new strategy for synthesizing highly conductive protic RTILs based on dendrimer architectures (33). I used the same strategy to make highly stable superbase-based protic RTILs (34) that feature ultralow vapor pressure and unique oxygen solubility for electrocatalysis. In the area of battery electrolytes, My research group demonstrated RTILs for lithium-sulfur batteries (35) and synthesized new mixture electrolytes based on sulfones and RTILs (36). More recently, my group successfully developed ambient-pressure electrolytes for Li-SO_2 batteries based on ionic liquids. That work, which was based on a suggestion made by Yongsheng Hu, who was a visitor to my group in 2013 (37), opens up a new avenue for searching high-capacity batteries for military applications. In the area of advanced electrodeposition systems, my group was the first in synthesizing RTILs whose cations consist of metal complexes (38). The idea for synthesizing ILs whose cations containing metal ions (including lithium ions complexed by crown ethers) was originally proposed as media for gas separation and energy storage (39). This synthesis strategy is very versatile and can lead to highly functional task-specific RTILs tailored for electrochemical processes. This strategy was recently utilized in making new types of Al-based RTILs that can be used in high-rate electrodeposition of Al (40, 41). The deposition technology won an R&D 100 Award in 2014 jointly with Chuck Hussey, who is the winner of the Max Bredig Award in 2014.

Acknowledgments

I would like to thank my parents (Xiuqiu Dai and Cuihua Chen), my children (David, Thomas, and Ashley), and especially my wife (Huimin Luo) for their understanding and unwavering support. My award is really a celebration of the hard work and dedication of my past and present students, postdocs, and staff members in my group at both ORNL and UTK. I would like to thank the US Department of Energy, Office of Science, Office of Basic Energy Sciences, Chemical Sciences, Geosciences, and Biosciences Division, the US Department of Energy, Office of Science, Office of Basic Energy Sciences, Materials Sciences and Engineering Division, the US Department of Energy, Office of Nuclear Energy, Energy Frontier Research Center funded by the U.S. Department of Energy (DOE), Office of Science, Office of Basic Energy Sciences, and the Critical Materials Institute, an Energy Innovation Hub funded by the U.S. Department of Energy, Office of Energy Efficiency and Renewable Energy, Advanced Manufacturing Office for supporting the various aspects of my research in molten salts & ionic liquids over years.

References

1. S. Dai, L. M. Toth, G. D. Delcul and D. H. Metcalf, *Inorg. Chem.*, **34**, 412 (1995).
2. S. Dai, L. M. Toth, G. D. DelCul and D. H. Metcalf, *J. Phys. Chem.*, **100**, 220 (1996).
3. S. Dai, L. M. Toth, G. D. Delcul and D. H. Metcalf, *Chem. Phys.*, **200**, 271 (1995).
4. J. J. Peng, N. Q. Chen, R. He, Z. Y. Wang, S. Dai and X. B. Jin, *Angew. Chem.-Int. Edit.*, **56**, 1751 (2017).
5. P. Bagri, B. P. Thapaliya, Z. Z. Yang, W. Jiang, D. Sulejmanovic, H. M. Luo and S. Dai, *Chem. Commun.*, **56**, 2783 (2020).
6. S. Dai, L. M. Toth, G. D. Del Cul and D. H. Metcalf, in *Molten Salts IX*, C. L. Hussey, D. S. Newman, G. Mamantov and Y. Ito Editors, p. 308, Electrochemical Society: Pennington, NJ (1994).
7. M. Freemantle, *Chem. Eng. News*, **76**, 32 (1998).
8. J. G. Huddleston, H. D. Willauer, R. P. Swatloski, A. E. Visser and R. D. Rogers, *Chem. Commun.*, 1765 (1998).
9. S. Dai, Y. S. Shin, L. M. Toth and C. E. Barnes, *Inorg. Chem.*, **36**, 4900 (1997).
10. S. Dai, Y. H. Ju and C. E. Barnes, *J. Chem. Soc.-Dalton Trans.*, 1201 (1999).
11. H. M. Luo, S. Dai, P. V. Bonnesen, A. C. Buchanan, J. D. Holbrey, N. J. Bridges and R. D. Rogers, *Anal. Chem.,* **76**, 3078 (2004).
12. H. M. Luo, S. Dai and P. V. Bonnesen, *Anal. Chem.*, **76**, 2773 (2004).
13. H. Luo, S. Dai, P. V. Bonnesen, T. J. Haverlock, B. A. Moyer and A. C. Buchanan, *Solvent Extr. Ion Exch.*, **24**, 19 (2006).
14. X. Q. Sun, J. R. Bell, H. M. Luo and S. Dai, *Dalton Trans.*, **40**, 8019 (2011).
15. X. Q. Sun, H. M. Luo and S. Dai, *Chem. Rev.*, **112**, 2100 (2012).
16. C. D. Liang, C. Y. Yuan, R. J. Warmack, C. E. Barnes and S. Dai, *Anal. Chem.*, **74**, 2172 (2002).
17. M. R. Ally, J. Braunstein, R. E. Baltus, S. Dai, D. W. DePaoli and J. M. Simonson, *Ind. Eng. Chem. Res.*, **43**, 1296 (2004).
18. R. E. Baltus, R. M. Counce, B. H. Culbertson, H. M. Luo, D. W. DePaoli, S. Dai and D. C. Duckworth, *Sep. Sci. Technol.*, **40**, 525 (2005).
19. R. E. Baltus, B. H. Culbertson, S. Dai, H. M. Luo and D. W. DePaoli, *J. Phys. Chem. B*, **108**, 721 (2004).
20. C. M. Wang, H. M. Luo, D. E. Jiang, H. R. Li and S. Dai, *Angew. Chem.-Int. Edit.*, **49**, 5978 (2010).
21. C. M. Wang, X. Y. Luo, H. M. Luo, D. E. Jiang, H. R. Li and S. Dai, *Angew. Chem.-Int. Edit.*, **50**, 4918 (2011).
22. C. M. Wang, G. K. Cui, X. Y. Luo, Y. J. Xu, H. R. Li and S. Dai, *J. Am. Chem. Soc.*, **133**, 11916 (2011).
23. B. Gurkan, B. F. Goodrich, E. M. Mindrup, L. E. Ficke, M. Massel, S. Seo, T. P. Senftle, H. Wu, M. F. Glaser, J. K. Shah, E. J. Maginn, J. F. Brennecke and W. F. Schneider, *J. Phys. Chem. Lett.*, **1**, 3494 (2010).
24. Z. Ma, J. H. Yu and S. Dai, *Adv. Mater.*, **22**, 261 (2010).
25. S. Dai, Y. H. Ju, H. J. Gao, J. S. Lin, S. J. Pennycook and C. E. Barnes, *Chem. Commun.*, 243 (2000).
26. J. S. Lee, X. Q. Wang, H. M. Luo, G. A. Baker and S. Dai, *J. Am. Chem. Soc.*, **131**, 4596 (2009).
27. X. Q. Wang and S. Dai, *Angew. Chem.-Int. Edit.*, **49**, 6664 (2010).

28. J. S. Lee, X. Q. Wang, H. M. Luo and S. Dai, *Adv. Mater.*, **22**, 1004 (2010).
29. N. O'Reilly, N. Giri and S. L. James, *Chem.-Eur. J.*, **13**, 3020 (2007).
30. A. B. Bourlinos, R. Herrera, N. Chalkias, D. D. Jiang, Q. Zhang, L. A. Archer and E. P. Giannelis, *Adv. Mater.*, **17**, 234 (2005).
31. Z. A. Qiao, Q. S. Huo, M. F. Chi, G. M. Veith, A. J. Binder and S. Dai, *Adv. Mater.*, **24**, 6017 (2012).
32. J. Zhang, S.-H. Chai, Z.-A. Qiao, S. M. Mahurin, J. Chen, Y. Fang, S. Wan, K. Nelson, P. Zhang and S. Dai, *Angew. Chem.-Int. Edit.*, **54**, 932 (2015).
33. J. F. Huang, H. M. Luo, C. D. Liang, I. W. Sun, G. A. Baker and S. Dai, *J. Am. Chem. Soc.*, **127**, 12784 (2005).
34. H. M. Luo, G. A. Baker, J. S. Lee, R. M. Pagni and S. Dai, *J. Phys. Chem. B*, **113**, 4181 (2009).
35. X.-G. Sun, X. Wang, R. T. Mayes and S. Dai, *ChemSusChem*, **5**, 2079 (2012).
36. C. Liao, B. Guo, X.-G. Sun and S. Dai, *ChemSusChem*, **8**, 353 (2015).
37. H. B. Xing, C. Liao, Q. W. Yang, G. M. Veith, B. K. Guo, X. G. Sun, Q. L. Ren, Y. S. Hu and S. Dai, *Angew. Chem.-Int. Edit.*, **53**, 2099 (2014).
38. J. F. Huang, H. M. Luo and S. Dai, *J. Electrochem. Soc.*, **153**, J9 (2006).
39. H. Luo and S. Dai, in *Molten Salt XIV*, T. R. A. Mantz, H. C. De Long, G. R. Stafford, R. Hagiwara, and D. A. Costa Editors, p. 340, Electrochemical Society: Pennington, NJ (2004).
40. Y. Fang, K. Yoshii, X. Jiang, X.-G. Sun, T. Tsuda, N. Mehio and S. Dai, *Electrochimica Acta*, **160**, 82 (2015).
41. Y. X. Fang, X. G. Jiang, X. G. Sun and S. Dai, *Chem. Commun.*, **51**, 13286 (2015).

Chapter 3

L02 – Rare Earth and Nuclear Chemistry

ECS Transactions, 98 (10) 11-17 (2020)
10.1149/09810.0011ecst ©The Electrochemical Society

Process Engineering Challenges for the Development of Electrolytic Reduction of Uranium Oxide in Molten LiCl-Li_2O

Jarom Chamberlain[a], Adam Burak[b], and M. F. Simpson[a]

[a]Department of Materials Science & Engineering, University of Utah, Salt Lake City, Utah, 84112, USA
[b]Department of Nuclear Engineering and Radiological Sciences, University of Michigan, Ann Arbor, Michigan, 48109, USA

Electrolytic uranium oxide reduction has the potential to be used for recycling spent fuel to a range of nuclear reactors from commercial light water reactors to advanced nuclear reactors—including molten salt reactors and sodium cooled reactors. However, several process engineering-related problems have been identified that need to be addressed to support efficient, cost-effective commercial implementation. Two keys are cathode product purity and cell current efficiency. High product purity relies upon the effective removal of LiCl-Li_2O from the cathode basket and reduced uranium. Removal of the salt from the basket can be achieved via high speed spinning at 650°C. But entrained Li_2O will remain and should be minimized during the reduction process. Methods for removing hydroxide impurities from the salt are reported that improve cell-current efficiency. The extent of this reduction can be determined via three distinct techniques (thermogravimetric analysis, elemental oxygen analysis, and bromine dissolution) and is key in helping determine the efficiency of the electrochemical cell.

Introduction

After the reduction of oxide spent nuclear fuel to metals, various pyrochemical processes can be used to fabricate fuels suitable for metallic fueled or molten salt fueled reactors. Options include electrorefining in molten LiCl-KCl to make U metal-based fuel or oxidation to chloride or fluoride salts for a molten salt reactor (MSR). For this paper, the direct electrolytic reduction (DER) process that will be considered is the electrolytic reduction of uranium oxide in a cathode basket immersed in molten LiCl – 1 wt% Li_2O at 650 °C. The possible cathode reactions were reported by Herrmann et al. in equations 1-3 [1].

$$UO_2 + 4e^- \rightarrow U + 2O^{2-} \quad [1]$$
$$2Li_2O + 4e^- \rightarrow 4Li + 2O^{2-} \quad [2]$$
$$4Li + UO_2 \rightarrow U + 2Li_2O \quad [3]$$

Platinum metal is used as the anode. The reduction of uranium oxide is achieved by a controlled current with oxygen gas evolution at the anode surface according to reaction 4.

$$O^{2-} \rightarrow 2e^{-} + \frac{1}{2}O_{2(g)} \quad [4]$$

To advance the technology for recycling spent oxide fuels to make fast reactor fuel, several challenges with DER need to be addressed in order to support efficient, cost-effective large-scale implementation. This paper focuses on issues related to the cathode—including cathode product purity and reduction efficiency.

Cathode Product Purity

Salt adhered to the cathode needs to be removed before the cathode product is transferred to the next processing step such as electrorefining or oxidation in MSR fuel salt. In either of these processes, UCl_3, $PuCl_3$, and other actinides would be present in the salt. The adhered or held up salt on the cathode basket from the DER process will contain at least 1 wt% Li_2O, possibly higher due to generation of Li_2O in the cathode basket. Li_2O added to molten chloride salt can cause precipitation of actinides and rare earth fission products as oxides/oxychlorides [2]. Centrifugal salt removal (CSR) has been demonstrated to be effective at removing adhered salt from DER cathode baskets [3].

CSR can be done by suspending the cathode basket within a furnace with a stirrer or a motor. While at a temperature above the salt melting point (650°C), the cathode basket can be rotated in an empty crucible to remove adhered salt. Figure 1 shows photographs of a DER cathode basket before and after CSR [3]. In order to facilitate mass transfer of salt of held up Li_2O, the basket can also be transferred into a molten salt bath of pure LiCl and rotated as a rinse step if needed, followed by additional rotation in an empty crucible. A functional range of rotation rates was shown to be 250 to 2000 RPM [3].

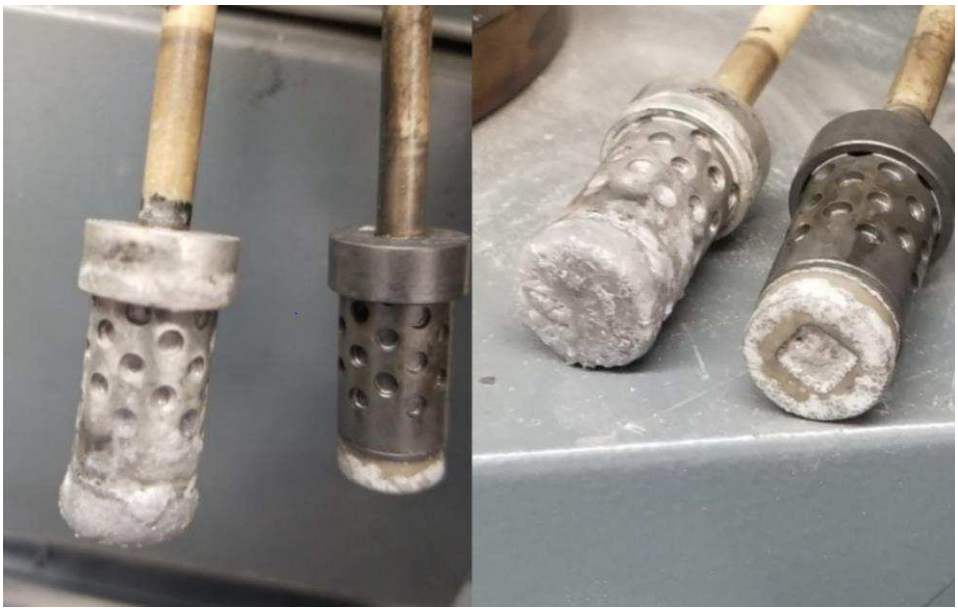

Figure 1. Photographs of baskets used for DER experiments before (left) and after (right) CSR [3].

Evidence was reported that during the reduction process, Li_2O can become entrained in the metallic uranium particles and resists removal via CSR [3]. It was reported that one factor that affects the amount of Li_2O holdup is whether the DER process occurs via reaction 1 (electrolytic) or reaction 3 (metallothermic). During a series of DER experiments, the electrical lead for the cathode was adjusted as shown in Figure 2 to either expose or isolate the urania material. It is inferred that during the experiments with the urania material isolated from the electrical lead, the predominant reduction mechanism was reaction 3 (metallothermic), which showed an increased value of entrained Li_2O.

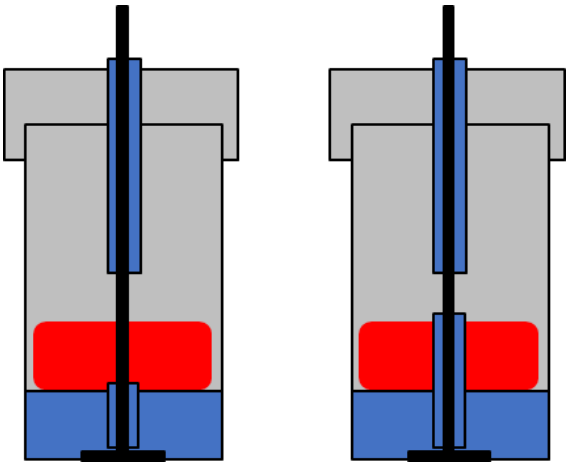

Color	Material/Component
Blue	MgO
Red	UO_2
Gray	Basket (316 S.S.)
Black	Electrical Lead (316 S.S.)

Figure 2. Two possible cathode basket orientations. The basket on the left would support an electrolytic reduction, as the basket on the right would support a chemical reduction.

The reduction potentials of Li^+ and uranium oxide are within about 0.1 V of each other, and so selectively controlling only one species to be reduced is difficult [4]. There are some possibilities that would allow an increase in the electrolytic reduction (reaction 1) for the UO_2. Increasing the area of contact between the current collector and the UO_2 should promote the kinetics of direct UO_2 reduction. Running in controlled potential mode with a precisely calibrated reference electrode can be used to favor direct UO_2 reduction. Figures 3 and 4 show the difference in cathode potential response for the two cathode lead configurations shown in Figure 2. Figure 3 shows the response when the lead wire is in contact with the UO_2. Figure 4 shows the response when the lead wire is not in contact with the UO_2. The potentials are characteristic of direct UO_2 reduction and Li reduction, respectively. But these experiments were run using a small basket containing one gram of UO_2. The resistance in a production-scale system may make it impossible to control the process based on precise potential control.

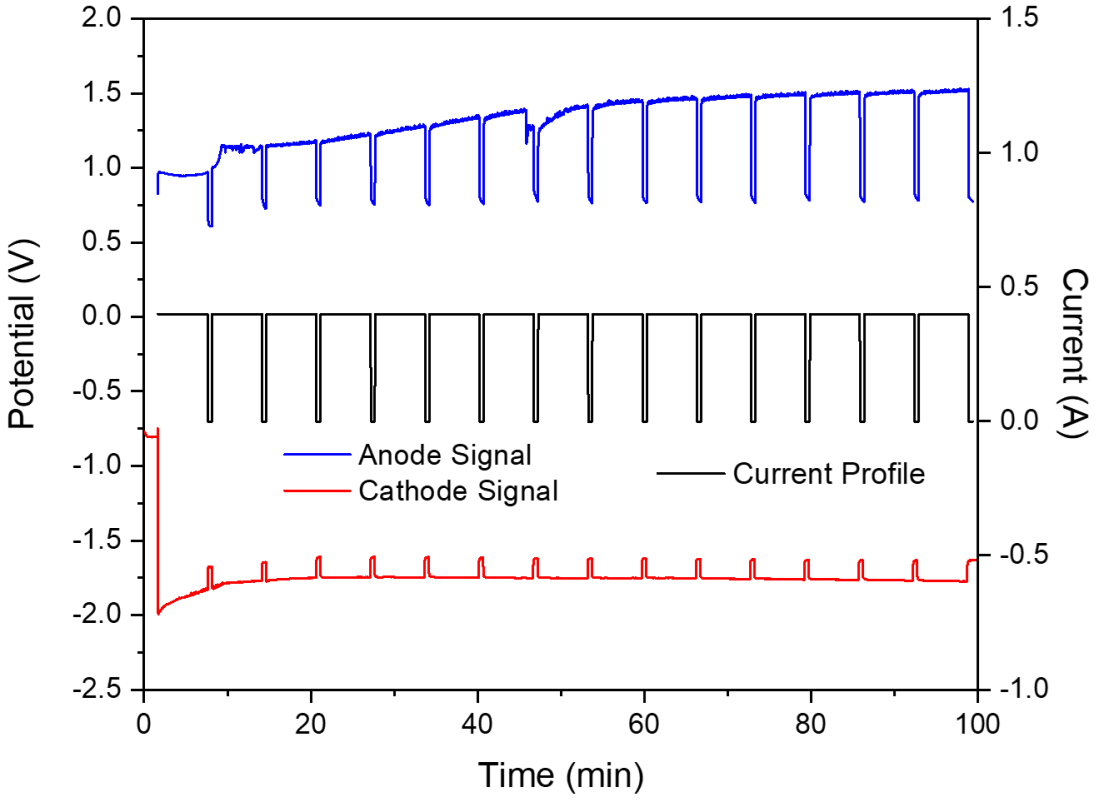

Figure 3. Current and potentials during DER experiment with the cathode lead in contact with UO_2 [3].

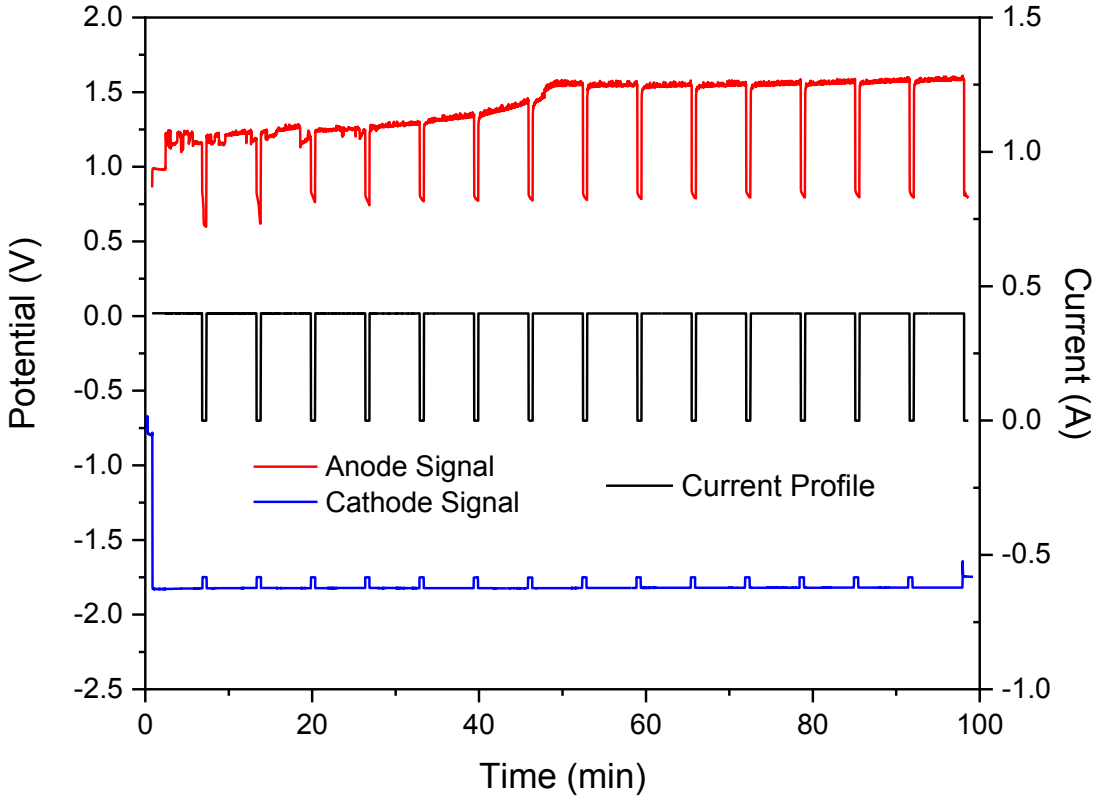

Figure 4. Current and potentials during DER experiment with the cathode lead electrically isolated from UO_2 [3].

Cell Efficiency

Cyclic voltammetry scans have shown that an impurity that is causing a non-productive current flow during DER is LiOH [5]. During DER, non-productive currents, caused by impurities, decrease the overall electrochemical cell efficiency through reactions that compete with the electrolytical reduction of UO_2 (reaction 1). Proposed electrochemical reactions involving LiOH in molten LiCl are in equations 5-7 [5].

$$LiOH + e^- = LiO^- + \frac{1}{2}H_2 \quad [5]$$

$$LiCl + LiO^- = Li_2O + Cl^- \quad [6]$$

$$Cl^- = \frac{1}{2}Cl_2 + e^- \quad [7]$$

Reduction of LiOH in a potential range from -1 to -1.75 V vs. Ni/NiO as per equation 5 has been observed with CV scans [10]. In comparison, the UO_2 reduction potential was recorded by Herrmann [6] to be -1.55 V. Thus, LiOH reduction (equation 5) should precede with UO2 reduction (equation 1). By way of illustration, the total amp-hours to reduce 0.5 wt% hydroxide in

500 kg of molten salt, can be compared to the total amp-hours to reduce the 50 kg of UO_2 at the cathode. Assuming the hydroxide reduction occurs according to equation 5, a total of 3,940 amp-hours would be needed to reduce all hydroxide present. Assuming UO_2 reduction occurs according to equation 1, a total of 22,522 amp-hours would be needed to reduce all UO_2 at the cathode. The non-productive current flow generated from the impurity LiOH thus could result in a 14.8% increase in total amp-hours need to fully reduce a batch of UO_2.

Two options for LiOH removal are electrolytic reduction and metallothermic reduction. But the electrolytic reduction step is what effectively reduces cell efficiency as discussed above. Alternatively, lithium metal can be added to chemically reduce LiOH to Li_2O and H_2. It is well established that lithium is partly soluble in LiCl [7]. Thus, additions of Li can be made to the salt with cyclic voltammetry (CV) used to determine the residual LiOH contamination [5]. A drawback of this approach is that lithium may attack the platinum anode, and result in the formation of lithium platinate [8], so care must be taken to avoid adding too much Li to the salt. Excess Li can be removed by immersing a cathode basket containing UO_2 into the salt and allowing reaction 3 to happen [1].

The measured extent of reduction is key to evaluating the cell efficiency for any given DER run. The determination of the extent of reduction has been determined via three different techniques—Thermo Gravimetric Analysis (TGA), elemental oxygen analysis (example: LECO TCH600), and a bromine dissolution method [9]. TGA is the simplest method in which a sample is heated to 950 °C in an oxygen-rich environment. All reduced uranium metal is converted to U_3O_8. The TGA measures the weight gained from this process. This allows for a calculation of the ratio of the original sample of uranium oxide to uranium metal.

Alternatively, the extent of reduction can be determined using a LECO elemental oxygen analyzer. In combination with a carbon crucible, combustion reactions at elevated temperatures convert all uranium into U_3O_8. All of the oxygen in the sample is converted to CO_2 which is then analyzed by the machine. The LECO can then determine the weight percentage of oxygen from the original sample. This allows for a calculation of how much uranium oxide was reduced in the sample, and then the resulting ratio of uranium oxide to uranium metal can be determined.

A comparison between the TGA and LECO elemental compositional analyzer methods to determine the extent of reduction in post DER samples has been reported [10]. Samples of known urania compounds (UO_2, U_3O_8, and U) were all tested via TGA, and elemental oxygen analysis via a LECO analyzer. Both methods recorded results that were comparable to one another and to the theoretical O/U for each urania compound (see Table 1). Additionally, a sample from a DER was tested via both methods, with only a 0.8% discrepancy in reduction extent between the two.

Table 1. Tested urania compounds with their theoretical O/U ratio as well the O/U ratio as determined by TGA and the LECO method.

	U	UO_2	U_3O_8
Theoretical O/U	0	2	2.666
O/U via TGA	-0.012*	1.87*	2.56
O/U via LECO	0.0024	2.085*	2.79*

*values were averaged from multiple tests

Summary

Process engineering challenges that the DER process faces include minimizing holdup of Li_2O in the cathode product and maximizing the current efficiency. When transferring reduced uranium from DER to the next processing step involving molten salts with dissolved actinides, it is important to remove all Li_2O. CSR can be implemented to remove adhered salt (LiCl-Li_2O) from the cathode basket. However, process optimization is needed to minimize buildup of entrained Li_2O in the reduced cathode product. Entrained Li_2O within the cathode product can be reduced by shifting the reaction towards direct electrolytic reduction of UO_2 rather than indirect via first reducing Li_2O. It is possible to control the reduction mechanism by adjusting the cathode vessel lead wire orientation. Mitigation of hydroxide contamination within the molten salt in the DER cell can help to maximize cell efficiency. CV scans can be used to check the hydroxide levels before an ER, and then with the addition of lithium metal, the hydroxide can be removed. Additionally, the extent of reduction post-DER can be done with the use of a TGA and a LECO to help determine the DER cell efficiency.

References

1. S. D. Herrmann, S.X. Li, M. F. Simpson, and S. Phongikarron, *Sep. Sci. Technol.,* **10**, 1965-1983 (2006).
2. G.S. Picard, Y.E. Mottot, and B.L. Tremillon, *J. Electrochem. Soc.,* **86**, 189, (1986).
3. A. J. Burak, *Study of Lithium Oxide Entrainment in Reduced Uranium Particles Formed from Electrolytic Reduction of UO_2 in Molten Lithium Chloride-Lithium Oxide Salt* (Doctoral Dissertation), (2019).
4. S. D. Herrmann, Shelly Li, and M. F. Simpson, *J. Nucl. Sci. Technol.,* **44**(3), 361-367 (2007).
5. M. Gonzalez, A. Burak, S. Guo, M. F. Simpson, *J. Nucl. Mat.,* **510**, 513-523 (2018).
6. S. D. Herrmann, Shelly Li, and M. F. Simpson, *J. Nucl. Sci. Technol.,* **44**(3), 361-367 (2007).
7. A.S. Dworkin, H.R. Bronstein, and M.A. Bredig, *J. Phys. Chem.,* **66** (3), 572-573, (1962)
8. M. Iizuka, Y. Sakamura, and Tadashi Inoue, *J. Nucl. Mat.,* **359**, 102-113 (2006).
9. G.F. Brunzie, T.R. Johnson, and R.K. Steunenberg, *J. Anal. Chem.,* **33** (8), 1005-1006, (1961).
10. A.J. Burak, J.L. Chamberlain, and M.F. Simpson, *J. Nucl. Mat.,* **529**, (2020).

ECS Transactions, 98 (10) 19-25 (2020)
10.1149/09810.0019ecst ©The Electrochemical Society

Methods of Redox Control and Measurement in Molten NaCl-$CaCl_2$-UCl_3

Matthew L. Newton, D. Ethan Hamilton, Michael F. Simpson

Department of Materials Science and Engineering, University of Utah, Salt Lake City, Utah 84112, USA

One problematic issue with molten salt reactors (MSRs) is the tendency for the salt's redox potential to increase with irradiation, causing greater corrosivity. U and Zr were identified as redox buffer candidates in a NaCl-$CaCl_2$-UCl_3 salt. Uranium and zirconium are attractive redox buffers since they should not reduce the redox potential below sustainable operating conditions for MSRs. Redox potentials—represented by open circuit potential (OCP)—were measured at a tungsten working electrode *vs.* a Ag/AgCl reference electrode housed in a mullite tube. Continuous OCP measurements were taken at 600°C, while $NiCl_2$ was added to the molten salt to replicate irradiation effects on redox potential. OCP rose by 0.23 V with the addition of 0.1 wt% $NiCl_2$. A zirconium rod was then submerged in the salt, causing an OCP drop of -0.63 V over a 100 min period. The potential drop for a U rod was -0.5 V over 160 min.

Introduction

The U.S. Department of Energy is currently supporting the design and planned construction of the Versatile Test Reactor (VTR), which will be capable of irradiating materials in a fast neutron field. VTR experiments are currently being designed and developed to study fast neutron irradiation effects on nuclear fuels, materials, and functional components. A molten salt irradiation experiment is planned to utilize the VTR to study the chemical changes and speciation in molten chloride or fluoride salts. Fast Neutron irradiation presents unique problems with structural materials, salt composition, and salt chemistry that are not present under normal conditions. If MSRs are going to be a reliable and viable source of energy, the behavior of these irradiated materials must be properly understood and controlled. The University of Utah, in collaboration with the University of Michigan, Virginia Commonwealth University, University of Idaho, and TerraPower LLC, is developing a molten salt irradiation experiment vehicle for the VTR that will feature a molten salt loop equipped with a number of sensors. Notably, the reference electrode will be included to measure the salt's open circuit potential (OCP) during each irradiation cycle. The OCP will measure the electrical potential difference between a W working electrode and the Ag/AgCl reference electrode. In order to perform experiments with active redox control, this project includes work to study redox buffer options compatible with a molten salt mixture consisting principally of NaCl-UCl_3. In early development, $CaCl_2$ has been included in the salt to lower the melting point while keeping the UCl_3 concentration relatively low.

Previously reported experiments with molten salt fuels have shown that the redox potentials of the salts increase with irradiation due to the fission of UCl_3. The fission of each UCl_3 molecule is predicted to release excess Cl or Cl_2 based on the formation of fission products that are bonded with an average of less than 3 Cl atoms. Consequently, the salt becomes progressively more corrosive to the reactor and reactor loop's metal components [1]. Therefore, the practicality of any MSR depends on proper control of the system's redox potential. Redox control, which can be monitored by the U^{4+}/U^{3+} ratio, can be achieved by implementing one or more of three methods—gas phase control, major metal control, and dissolved salt control [2]. Because of the VTR experiment's closed system, the non-passive addition of chemicals will not be possible. The reactor must, therefore, integrate a passive redox buffer into the system design. We opted to study insoluble metals as redox buffers and present results of experiments with U and Zr in this paper.

The Molten Salt Reactor Experiment (MSRE) employed the addition of Be metal for redox control in its fuel salt that consisted of $LiF\text{-}BeF_2\text{-}UF_4\text{-}UF_3$ [3]. The base salt $LiF\text{-}BeF_2$, often referred to as FLiBe, was used in the MSRE in a ratio of 2 parts LiF to one-part BeF_2 while U made up 0.9 wt% of the total salt [4]. In this experiment, researchers addressed the problem of continuously increasing redox potential due to salt irradiation by dissolving Be metal into the salt [5]. Oxidizing species in the salt convert U^{3+} to U^{4+}. By this method, researchers kept the total UF_3 concentration of the salt at roughly one percent of the total uranium [6]. Be metal was used to reduce U^{4+} back to U^{3+} by the following reaction.

$$Be^{\circ} + 2UF_4 = BeF_2 + 2UF_3. \quad [1]$$

The oxidizing components of the salt are thermodynamically more likely to oxidize U^{3+} to U^{4+} than to oxidize the reactor's structural components [3]. Thus, by controlling the U^{3+}/ U^{4+} ratio, the system's redox potential can be controlled to prevent corrosion.

Conversely, our study focuses on chloride-based salts, which have been identified as optimal for advanced fast reactors [7]. A new approach to redox control in these salts is needed. A $NaCl\text{-}CaCl_2$ base salt with 50 mol% each was chosen for this study due to the low melting point and the high actinide solubility it provides. While the melting points of NaCl (Alfa Aesar, 99%) and $CaCl_2$ (Alfa Aeser, 99%) are 801°C and 772°C respectively, an eutectic point at around 50 mol% allows for a melting point just over 500°C. These values were supported by thermogravimetric analysis (TGA) results that showed the melting point for the prepared, dehydrated eutectic salt to be 500°C.

The salt used in redox control experiments in this study was a $NaCl\text{-}CaCl_2\text{-}UCl_3$ with 5 wt.% UCl_3 added to the equimolar $NaCl\text{-}CaCl_2$ eutectic base. This ternary salt retains the low melting point of the binary base salt and is easily synthesized from the original salt using a high-temperature oxidation reaction.

Uranium Salt Synthesis

$NaCl\text{-}CaCl_2\text{-}UCl_3$ salt was prepared for electrochemical experiments by introducing uranium into a previously prepared and dehydrated $NaCl\text{-}CaCl_2$ eutectic salt. The NaCl-

$CaCl_2$ base salt is made by combining the two salts in a 50 mol% ratio. The salt was first heated to 200°C under vacuum and allowed to sit for one hour. It was then heated to 400°C while under vacuum to remove residual water. The vacuum was stopped, and the temperature was raised to 550°C. Then a custom mixture of 5% HCl gas (balance Ar) supplied by Praxair was diluted 10:1 with UHP Ar (Airgas, 99.999%) using a mass flow controller (MKS, GM100A). This 0.5% HCl gas mixture was bubbled through the molten salt. The HCl gas is intended to remove any oxides or hydroxides that remain in the molten salt. Either iron(II) chloride or iron(III) chloride can be used to form UCl_3 from U metal via one of the following two reactions.

$$U_{(m)} + 1.5\, FeCl_{2(salt)} \rightarrow UCl_{3(salt)} + 1.5\, Fe_{(m)} \quad [2]$$

$$U_{(m)} + FeCl_{3(salt)} \rightarrow UCl_{3(salt)} + Fe_{(m)} \quad [3]$$

Reaction 1 has a ΔG^o_{rxn} of -320.8 kJ/mole, and reaction 1 has a ΔG^o_{rxn} of -429.8 kJ/mole. While these reactions proceed far from standard conditions, thermodynamic data for $FeCl_2$, $FeCl_3$, and UCl_3 diluted in NaCl-$CaCl_2$ are not known to be available. Standard state properties, therefore, provide the best available data for predicting equilibrium behavior in this system. For the experiments reported in this paper, $FeCl_3$ was used for oxidize uranium. The uranium salt was synthesized by adding iron (III) chloride (Alfa Aesar, 98%) to the purified NaCl-$CaCl_2$. Sufficient $FeCl_3$ was weighed out to oxidize uranium metal to make a salt mixture with 5 wt% U as UCl_3. No measurements other than visual observation of the color and redox potential were made to ensure the oxidation state of the U in the salt. A 3% excess of iron (III) chloride was added to account for incomplete conversion and potential oxidant volatilization. After the addition of iron (III) chloride, a depleted uranium rod (International Bio-Analytical Industries) was immersed in the salt mixture at 600°C. After allowing the reaction to proceed overnight, a high-temperature Alnico magnet was placed below the crucible while it was tipped to allow molten salt to pour onto a stainless steel pan. The magnet appeared to be effective in retaining the metallic iron particles in the crucible, as they were not visible in the solidified salt product shown in Figure 1. In this experiment, $FeCl_3$ was added to NaCl-$CaCl_2$ at a concentration to make NaCl-$CaCl_2$-UCl_3 with 6.5 wt% U.

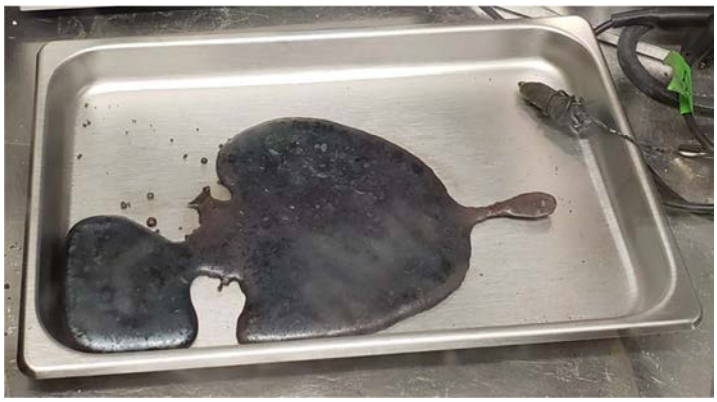

Figure 1. Image of salt batch after UCl_3 synthesis using NaCl-$CaCl_2$ and $FeCl_3$.

Redox Control Test Results

In the experiments run using U and Zr metal, redox potential was measured using open circuit potentiometry (OCP). The reference electrode was made from a 0.5-mm diameter Ag wire (Alfa Aesar, 99.9%) submerged in molten AgCl (Alfa Aesar, 99.99%) and encased in a thin mullite tube with one closed end, a 4-mm inner diameter, and a 6.35-mm outer diameter. This combination forms a thermodynamic reference electrode based on the equilibrium between Ag and AgCl. The working electrode was made from a 2-mm diameter W metal rod (Alfa Aesar, 99.95%). The experimental setup is pictured below in Figure 2. No current is passed between the two electrodes, allowing a potentiostat to measure the electrical potential difference between the fuel salt and the reference electrode. Since the working electrode's potential should be a function of the salt composition, the addition of an oxidizing agent ($NiCl_2$) should cause the OCP to increase based on the $Ni^{2+/}Ni$ redox couple. If a redox buffer metal is then submerged in the salt, the OCP of the salt should decrease.

Figure 2. Photograph of the redox buffer experiment.

The first metal/metal chloride redox buffer investigated was $Zr/ZrCl_4$. According to HSC Chemistry 9, $ZrCl_4$ has a theoretical reduction potential of -2.02 V *vs.* Cl^-/Cl_2 at 600°C. The reduction potentials for UCl_3 and $CrCl_2$ are -2.41 and -1.55 V, respectively. Zr metal should, thus, oxidize to $ZrCl_4$ and control the redox potential at a level that simultaneously prevents corrosion of Cr and other less stable components of possible structural materials, like stainless steel, while leaving UCl_3 unreduced from the salt.

A 6.2-mm diameter Zr rod (Alfa Aesar, 99%) was submerged in molten $NaCl\text{-}CaCl_2\text{-}UCl_3$ salt at 600°C to test Zr metals effectiveness as a redox buffer. The OCP of the $NaCl\text{-}CaCl_2\text{-}UCl_3$ salt with 5.17 wt.% U metal was measured at the tungsten working electrode *vs.* the Ag/AgCl reference electrode. $NiCl_2$ (Alfa Aesar, 98%), an oxidizing species, was added to the salt to simulate fission effect on redox potential. The OCP for this experiment is plotted versus time in Figure 3. The OCP of the salt, containing $NiCl_2$,

increased from -0.215 V to a new equilibrium of -0.0199 V. Once the equilibrium potential was reached, the Zr rod was lowered into the salt mixture. After submerging the Zr rod, the measured OCP dropped by -0.63 V over a 100-minute interval to a new equilibrium at -0.646 V.

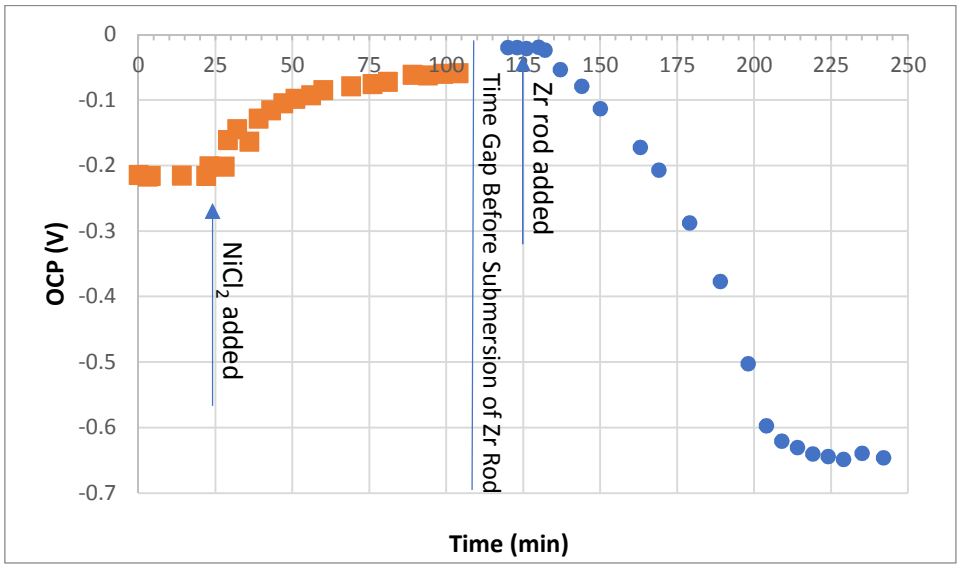

Figure 3. OCP *vs.* time for NaCl-CaCl-UCl_3 (5 wt% U) salt using W working electrode and Ag/AgCl reference electrode.

The same experiment was then repeated using U metal as the redox buffer. The OCP versus time for the U experiment is shown in Figure 4. $NiCl_2$ (Alfa Aesar, 99%) was again added to the salt at 600°C to a concentration of 0.01 wt.%. The OCP increased from -0.251 V to 0.19 V due to addition of $NiCl_2$. A depleted uranium rod was then immersed in the salt. Over the next 200 min, the molten salt system's redox potential dropped by -0.5 V before stabilizing around -0.3 V.

As mentioned before, U/UCl_3 has a standard reduction potential of -2.41 V *vs.* Cl^-/Cl_2. Therefore, it makes sense that UCl_3 would form preferentially over both UCl_4 and the $NiCl_2$ used to raise the redox potential of the system, which have calculated standard reduction potentials of -0.998 V and -0.976 V respectively. It is no surprise that the salt's redox potential would drop as the uranium rod reduces UCl_4 to UCl_3. It is interesting that although the standard reduction potential of U/UCl_3 is lower than that of $Zr/ZrCl_4$, the Zr rod appeared to be a better redox buffer than the U rod. This may be attributed to kinetics/mass transport factors. The interfacial contact area of the rods with the molten were not the same for the two experiments. The Zr rod provided an interfacial area of approximately 700-mm^2 whereas the U rod was limited to around 600-mm^2.

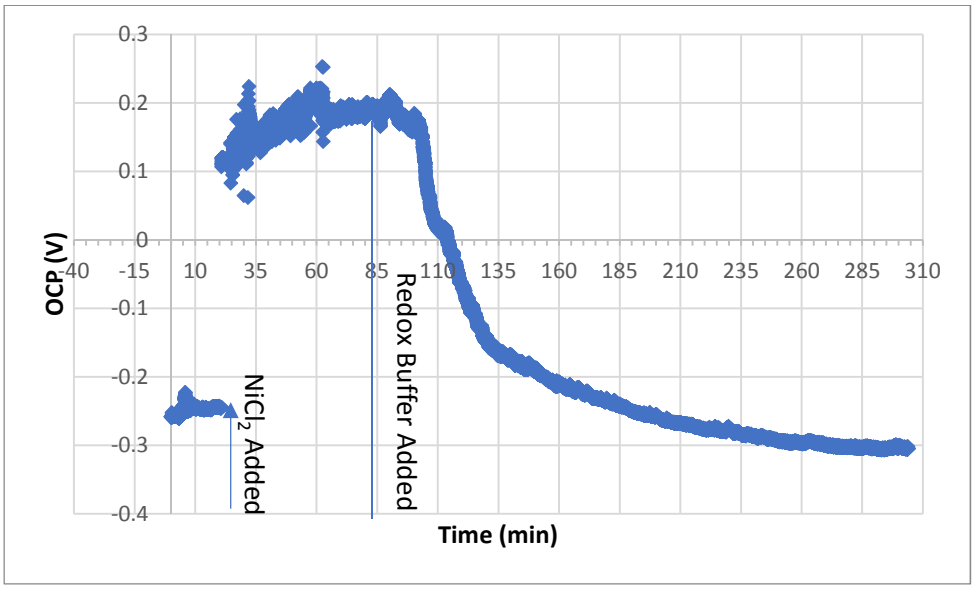

Figure 4. OCP *vs.* time for NaCl-CaCl-UCl_3 (5 wt% U) salt using W working electrode and Ag/AgCl reference electrode.

Conclusions

Synthesis of UCl_3 in a NaCl-$CaCl_2$ eutectic salt via oxidation of U metal was shown to be a simple and effective method to synthesize simulant fuel salt for studying chemistry of chloride salts for use as molten salt reactor fuel. It can be done at a relatively low temperature (600°C) using iron(III) chloride and a solid uranium metal rod. The resulting Fe metal particles can be separated from the salt magnetically. The redox potential of NaCl-$CaCl_2$-UCl_3 can be buffered by both Zr and U metal rods immersed in the salt. In a time-frame of less than 3 hours, the redox potential of the molten salt mixture in contact with the metal equilibrates at a value significantly lower than its initial value before adding an oxidizing compound such as $NiCl_2$. Further study is needed to understand the limiting rate processes for dissolution of U and Zr into the fuel salt to assess their applicability to use in chloride salt fueled MSRs.

Acknowledgments

Financial support for this project was provided by Idaho National Laboratory under the Versatile Test Reactor program. Valuable leadership and consultation were provided by Joel McDufee from Oak Ridge National Laboratory. Supathorn Phongikaroon and Dimitris Killinger from Virginia Commonwealth University and Xiaodong Sun and Adam Burak from University of Michigan have made essential technical contributions to the project.

References

1. D. A. Petti, G. R. Smolik, Michael F. Simpson, John P. Sharpe, R. A. Anderl, S. Fukada, Y. Hatano, M. Hara, Y. Oya, T. Terai, D.-K. Sze, and S. Tanaka, *Fusion Eng. Des.,* **81**, (2006).
2. D. Olander, *J. Nucl. Mater*., **300**, (2002).
3. GA, Clement Wong, and Brad Merrill. "Relevant MSRE and MSR Experience." (2004).
4. Paul N. Haubenreich, J. R. Engel, J. Nucl. Technol., **136**, (1970).
5. Jinsuo Zhang, Charles W. Forsberg, Michael F. Simpson, Shaoqiang Guo, Stephen T. Lam, Raluca O. Scarlat, Francesco Carotti, Kevin J. Chan, Preet M. Singh, William Doniger, Kumar Sridharan, James R. Keiser, *Corros. Sci.*, **144**, (2018).
6. P. N. Haubenreich, J. R. Engel, C. H. Gabbard, R. H. Guymon, B. E. Prince, MSRE Design and Operations Report, Part V-A, ORNL-TM-2111, (1969).
7. Holcomb, D. E., G. F. Flanagan, B. W. Patton, J. C. Gehin, R. L. Howard, and T. J. Harrison, Fast spectrum molten salt reactor options., *ORNL/TM-2011/105* (2011).

ECS Transactions, 98 (10) 27-32 (2020)
10.1149/09810.0027ecst ©The Electrochemical Society

Selective Permeation of Neodymium Through an Alloy Diaphragm in Molten Chloride Systems

T. Oishi[a], M. Yaguchi[a], Y. Katasho[a], and T. Nohira[b]

[a] National Institute of Advanced Industrial Science and Technology (AIST), Tsukuba, Ibaraki 305-8569, Japan
[b] Kyoto University, Uji, Kyoto 611-0011, Japan

As part of an ongoing study of a new recycling process for Nd-Fe-B permanent magnets, selective permeation of Nd through an RE-Ni (RE=Nd and Dy) alloy diaphragm was investigated in LiCl-KCl eutectic melts containing $NdCl_3$ and $DyCl_3$ or $LaCl_3$ at 450 °C. Selective permeation of Nd was achieved by controlling the potential of the alloy diaphragm, which functions as a bipolar electrode. Interestingly, EDX analysis revealed that the molar ratio of Nd/Dy in the alloy diaphragm was less than 0.05, which is two orders of magnitude lower than that of the permeated amount. These results suggest that the transportation rate of Nd atoms in the alloy diaphragm was extremely high compared to that of Dy. In order to obtain further insight into the transportation mechanism of RE atoms in the alloy diaphragm, STEM observations were also carried out. The results suggested that the transportation of RE atoms cannot be explained by simple grain boundary diffusion.

Introduction

Rare earth (RE) elements are widely used in industrial manufacturing because of their unique characteristics. Nd-Fe-B permanent magnets, which contain Nd, Dy and others in addition to Fe and B, are among the most important products containing RE elements. However, their resources, especially for heavy RE containing Dy, are scarce in the Earth's crust. On the other hand, the recycling ratio of RE elements is low owing to their high recycling cost. On the basis of this background, a simple RE (RE=Dy and Nd) recycling process from Nd-Fe-B permanent magnets has been investigated in this study (Figure 1). The process entails the use of RE-IG (IG=Fe, Ni, Co) alloy diaphragms for the separation of REs in molten salts (1, 2). The RE-IG alloy diaphragm acts as a bipolar electrode and the RE ions permeate via three steps: (a) reduction of RE ions to form an alloy on the anolyte side of the diaphragm according to reaction [1], (b) transportation of RE atoms in the diaphragm, and (c) oxidation of RE atoms that dissolve into the catholyte as RE ions on the other side of the diaphragm according to reaction [2]. Because the reaction and transportation rates depend on the kinds of RE elements and electrolytic conditions, selective permeation of Dy and/or Nd is possible under appropriate conditions. Using this selective permeation phenomenon through the alloy diaphragms, Dy and Nd can be separately recovered from Nd-Fe-B permanent magnets only by molten salt electrolysis, as shown in Figure 1.

$$RE^{3+}(\text{anolyte}) + 3e^- = RE_{\text{ in the alloy}} \quad [1]$$

$$RE_{\text{ in the alloy}} = RE^{3+}(\text{catholyte}) + 3e^- \quad [2]$$

Recently, the present authors reported selective Dy permeation through an RE-Ni alloy diaphragm in molten LiCl-KCl eutectic melts containing $NdCl_3$ and $DyCl_3$ at 450 °C (3). However, in order to realize the recycling process shown in Figure 1, selective Nd permeation is also indispensable. Thus, in the present study, the selective permeation of Nd was examined using a similar experimental setup under different electrolytic conditions.

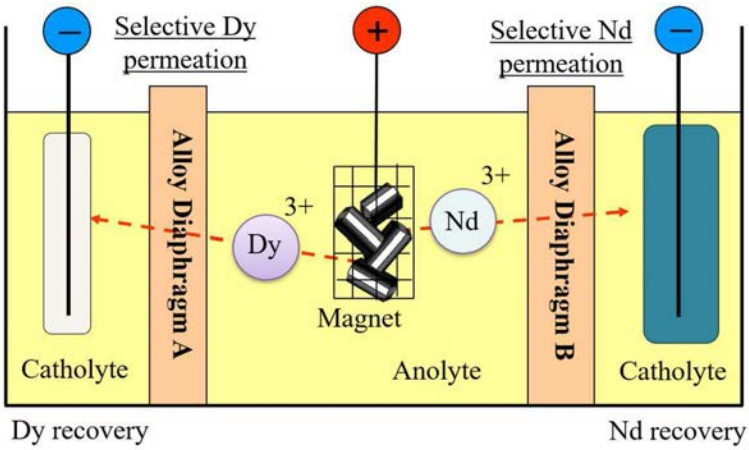

Figure 1. Schematics of the proposed recycling process (1) (modified from the original).

Experimental

Figure 2 illustrates the experimental setup, which basically corresponds to that described before (3). High-purity alumina was used for the electrolytic cell. A 0.1 mm-thick Ni film was employed as the starting material for the alloy diaphragm. The electrolyte was a LiCl–KCl eutectic melt (44:56 wt.%, Wako Pure Chemical, Co., Ltd.), which was dried under vacuum at 180 ºC for 3 days, and then melted under 1 atm of Ar at 450 ºC. Then, $NdCl_3$ and $DyCl_3$ (Kojundo Chemical Laboratory Co., Ltd.) were added to the anolyte so that each concentration was 0.50 mol%. In the catholyte, 0.5 mol% of $LaCl_3$ (Kojundo Chemical Laboratory Co., Ltd.) was added to prevent the dendric electrodeposition of RE metals on the cathode. An Ag^+/Ag reference electrode was used for both the anolyte and catholyte. The potential of the Ag^+/Ag electrodes was calibrated with reference to that of the Li^+/Li electrode, which was prepared by electrodepositing Li metal on a Mo wire. All the potentials in this paper are given with reference to the Li^+/Li potential. The counter electrode in the anolyte was a glassy carbon rod (3.0 mm in diameter) and that in the catholyte was a Ni plate (10 mm × 20 mm × 0.1 mm).

The permeation experiment was carried out by controlling the potential of each side of the diaphragm with two potentio-galvanostats (PGS–A and PGS–B), as shown in Figure 2. The potential of the anolyte side was controlled at +0.55 V by PGS–A, while that of the catholyte side was controlled at rest potential by PGS–B at the beginning of electrolysis. At this potential, alloy formation of $RENi_2$ (RE=Nd and Dy) is expected on the anolyte

side surface of the diaphragm. As the alloy formation proceeded from the anolyte side, the rest potential of the catholyte side of the diaphragm shifted in the negative direction, and stabilized at +0.70 V. At this potential, selective dealloying of Nd is expected because the stable alloy phases in Nd-Ni and Dy-Ni binary systems at this potential are $NdNi_3$ and $DyNi_2$, respectively. As a result, Nd can be dissolved from the $RENi_2$ phase according to reaction [3], while Dy remains in the alloy phase.

$$3NdNi_2 = Nd^{3+}(\text{catholyte}) + 2NdNi_3 + 3e^- \quad [3]$$

The electrolysis was occasionally suspended at predetermined times to retrieve a small amount of catholyte and change the Ni plate cathode. The obtained catholyte and Ni plate were dissolved in 0.2 M hydrochloric acid and 1 M nitric acid solutions, respectively. Then, the concentrations of Nd and Dy were measured by inductively coupled plasma atomic emission spectrometry (ICP–AES; Shimadzu, Co., Ltd., ICPE–9000). The cross-section of the diaphragm after electrolysis was analyzed using a scanning electron microscope equipped with an energy dispersive X-ray analyzer (SEM/EDX; Hitachi Hitech Co., Ltd., TM–4000 plus AZtecOne) and a scanning transmission electron microscope (STEM; Philips, Tecnai Osiris).

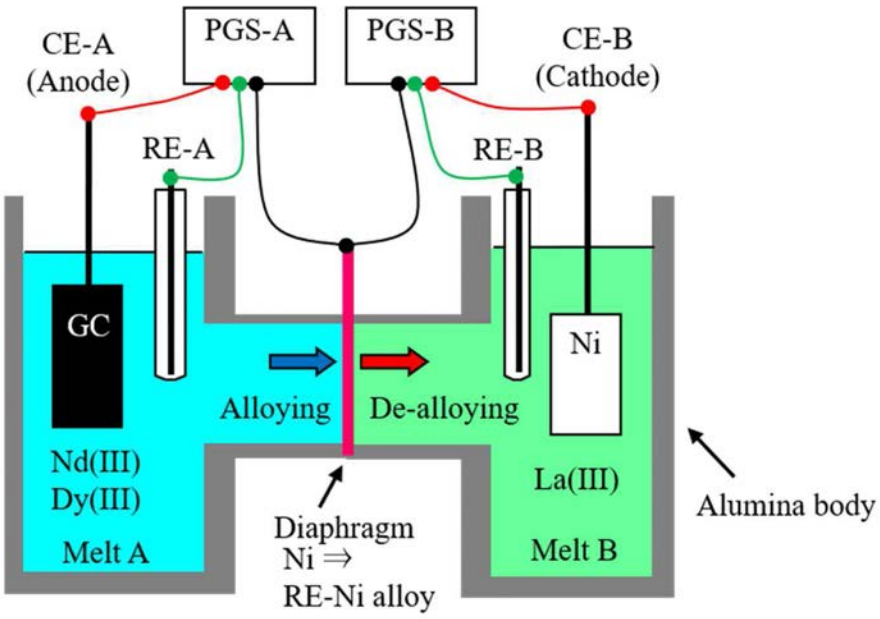

Figure 2. Schematic drawing of the experimental setup.

Results and discussion

Figure 3 shows the amount of permeated Nd and Dy through the alloy diaphragm plotted against the amount of charge measured by PGS-B, which corresponds to the charge used for reaction [2]. The figure indicates that Nd was selectively permeated through the alloy diaphragm. The molar ratio of Nd/Dy decreased with the amount of chage, yet remained ~6 even at the end of the electrolysis. The theoretical line was calculated from the amount of charge on the assumption that RE ions are dealloyed via a three-electron reaction (reaction [2]). Until the amount of charge reached 400 C, the sum of the permeated Nd and

Dy was close to the theoretical line, that is, the current efficiency during the dealloying step was close to unity. However, the sum of permeated Nd and Dy was higher than the theoretical value when the amount of charge was higher than 400 C. This may be attributed to the fact that some of the Nd dissolved as Nd^{2+} ions from the alloy diaphragm.

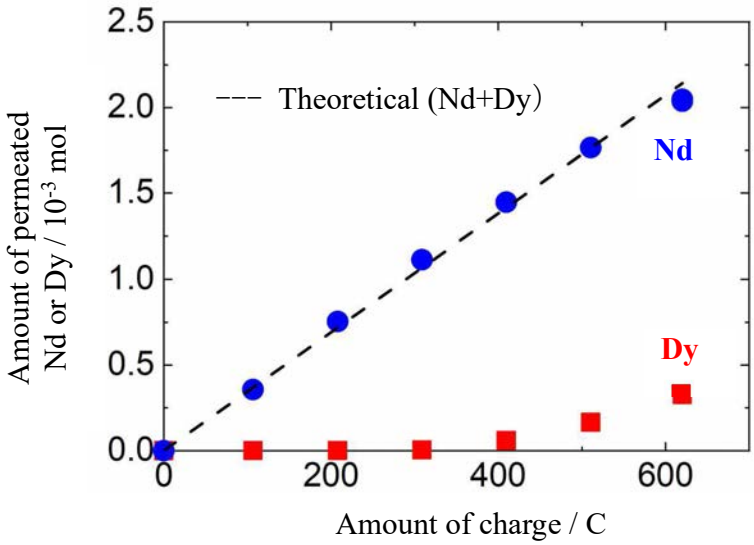

Figure 3. Amounts of permeated Nd and Dy plotted against the amount of charge.

Figure 4 shows the cross-sectional SEM image of the diaphragm after the permeation experiment. The diaphragm appeared to be nearly uniform. The results of the EDX analysis (Table I) indicate that the composition of the diaphragm was nearly homogeneous and that the molar ratio of Ni/RE was close to 2. This is consistent with the results of the XRD analysis (not shown here), which suggested diffraction patterns corresponding to the $RENi_2$ phase. Interestingly, the molar ratio of Nd/Dy was 0.06 or lower, even though Nd was selectively permeated through the diaphragm (Figure 3). These experimental results indicate that the transportation rate of Nd inside the alloy diaphragm was much higher than that of Dy during the permeation experiment.

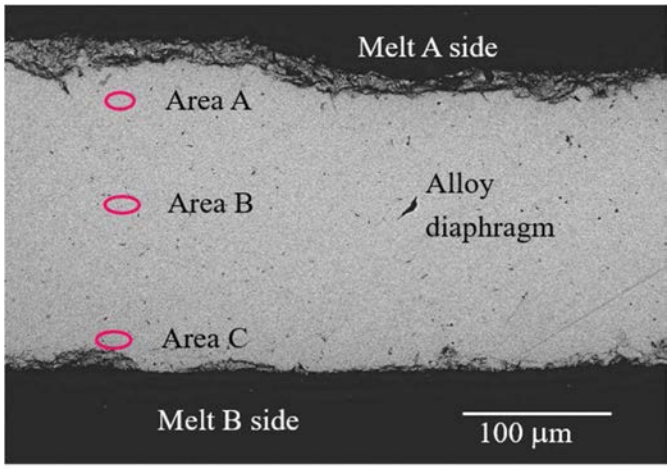

Figure 4. Cross-sectional SEM image of the alloy diaphragm after the permeation experiment.

Table I. Result of EDX analysis on the area shown in Figure 4.

Area	Composition / at%			Molar ratio	
	Ni	Dy	Nd	Ni/RE	Nd/Dy
A	67	31	2.0	2.0	0.06
B	67	31	1.9	2.0	0.06
C	67	32	1.6	2.0	0.05

In order to obtain further insight into the transportation of RE atoms in the alloy diaphragm, STEM observations were carried out. Figure 5 shows the cross-sectional STEM image of the alloy diaphragm, in which some bright lines were observed. Because the brightness of STEM observations usually changes depending on the composition, RE atoms are thought to be relatively concentrated in the bright part. If so, this part may function as a transportation path for RE atoms through the alloy diaphragm. However, the results of the EDX analysis (Table II), for which a several nm probe was used, indicate that the composition in the bright part was nearly the same as that of the other parts. These results suggest that the transportation of RE atoms in the alloy diaphragm cannot be explained by simple grain boundary diffusion. Consequently, further investigation is required to clarify the transportation mechanism of RE atoms in the alloy diaphragm.

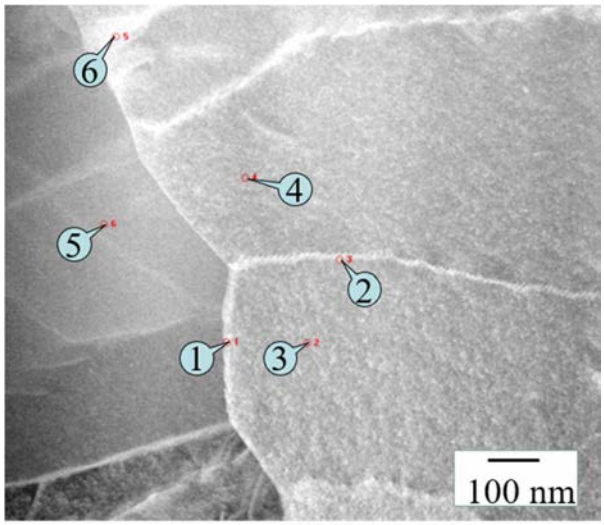

Figure 5. Cross-sectional STEM image of the alloy diaphragm after the permeation experiment.

Table II. Result of EDX analysis on the area shown in Figure 5.

Area	Composition / at%			Molar ratio	
	Ni	Dy	Nd	Ni/RE	Nd/Dy
1	67	29	2.3	2.1	0.08
2	63	30	2.1	2.0	0.07
3	66	29	2.1	2.1	0.07
4	65	30	2.2	2.0	0.07
5	32	31	2.1	1.9	0.07
6	66	29	2.8	2.0	0.10

Conclusions

Selective permeation of Nd through an RE-Ni alloy diaphragm was carried out in molten LiCl-KCl melts containing $NdCl_3$ and $DyCl_3$ or $LaCl_3$. The results were as follows:

1. Nd was selectively permeated through the diaphragm at an Nd/Dy molar ratio of approximately 6.
2. The Nd concentration in the alloy diaphragm was much lower than that of Dy, indicating that the transportation rate of Nd in the alloy diaphragm was much higher than that of Dy.
3. STEM observation and EDX analysis suggested that the transportation of RE atoms in the alloy diaphragm cannot be explained by simple grain boundary diffusion.

Acknowledgments

This work was partly supported by the New Energy and Industrial Technology Development Organization (NEDO) of Japan.

References

1. T. Oishi, H. Konishi, T. Nohira, M. Tanaka, and T Usui, *Kagaku Kogaku Ronbunshu*, **36**, 299–303 (2010).
2. T. Oishi, *Molten Salts (Yoyuen Oyobi Koon Kagaku)*, **63**, 78–83 (2020).
3. T. Oishi, M. Yaguchi, Y. Katasho, and T. Nohira, *Rare metal technology 2020*, 151–156 (2020).

ECS Transactions, 98 (10) 33-46 (2020)
10.1149/09810.0033ecst ©The Electrochemical Society

Rare Earth Silicide Formation on Si Electrode in LiCl-KCl Melt to Establish a Novel Used Salt Treatment Process

T. Murakami, Y. Sakamura, K. Uozumi, and M. Iizuka

Central Research Institute of Electric Power Industry, Yokosuka, Kanagawa 240-0196, JAPAN

After repeating the electrorefining of spent nuclear fuels, rare earth, alkaline earth and alkali fission products accumulate in the used LiCl-KCl melt. This paper proposes a novel used salt treatment process where dominant fission products, rare earths, are recovered electrochemically from the used melt in a form of their silicides and the silicides are then oxidized to be dissolved in a glass matrix as the waste form. The glass waste form stabilizing a higher concentration of fission products than the conventional waste form provides a reduction in volume of the waste form. The results of cyclic voltammetry using a Si electrode in LiCl-KCl melt containing a rare earth chloride ($LaCl_3$, $CeCl_3$, $PrCl_3$, $NdCl_3$, $SmCl_2$, $EuCl_2$ or $GdCl_3$) at 723 K indicated the corresponding lanthanide silicide formation. The rare earth silicides formed by potentiostatic electrolysis were analyzed by XRD and SEM-EDX. The obtained results confirmed a feasibility of rare earths recovery as silicides from the used LiCl-KCl melt, which was a key step of the proposed used salt treatment process.

Introduction

Pyroprocessing which uses chemical and electrochemical reactions in molten salts has been developed as one of the promising processes to recover actinides from spent nuclear fuels. The pyroprocessing has intrinsic advantages, for example, high stability against radiation, flexible applicability to various type of fuels, high proliferation resistance and so on. The high stability against radiation allows the pyroprocessing to process spent nuclear fuels in a shorter cooling period and to be applied in a scenario of the partitioning and transmutation. A reduction of an environmental burden for disposing the radioactive wastes is expected in the partitioning and transmutation scenario where fuels containing a higher concentration of minor actinides (MA : Np, Am and Cm) are irradiated in a fast reactor or accelerator driven system at a higher burn-up to transmute the long half-life nuclides, MA, to short half-life or stable nuclides (1, 2).

The main step of the pyroprocessing is electrorefining process where actinides are recovered from spent metallic state fuels separating from fission products (Figure 1): Actinides (An) in the spent fuels anodically dissolve into a LiCl-KCl melt leaving noble metal fission products as fuel residues,

$$An \rightarrow An^{3+} + 3e^- \qquad (An: U, Pu, MA) \qquad [1]$$

The dissolved actinides are deposited on two kinds of cathodes; an inert iron cathode for a selective U metal deposition (reaction 2) and a reactive liquid Cd cathode for a simultaneous recovery of all actinides (reaction 3),

$$U^{3+} + 3e^- \rightarrow U \quad [2]$$

$$An^{3+} + 3e^- \rightarrow An_{\text{in Cd}} \quad [3]$$

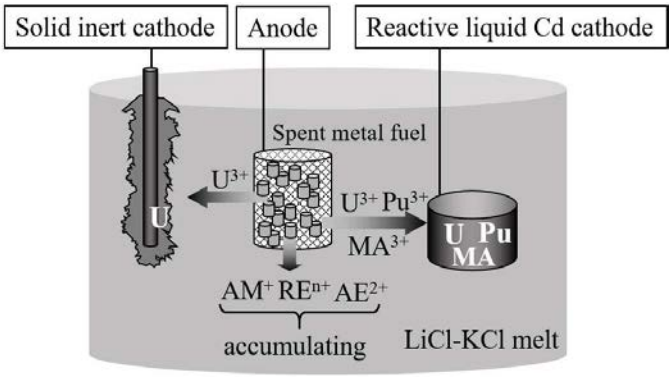

Figure 1. Schematic drawing of the concept of the electrorefining process of spent metal fuels. MA: minor actinides, RE: rare earth fission products, AE: alkaline earth fission products, AM: alkali fission products.

On the other hand, after repeating the electrorefining process, rare earth, alkali and alkaline earth fission products accumulate in the used LiCl-KCl melt. The accumulated fission products must be removed from the used melt to be stabilized in a waste form suitable for a geological disposal. A flowsheet of the conventional way for the removal and stabilization of the accumulated fission products is seen in Figure 2 (1, 3).

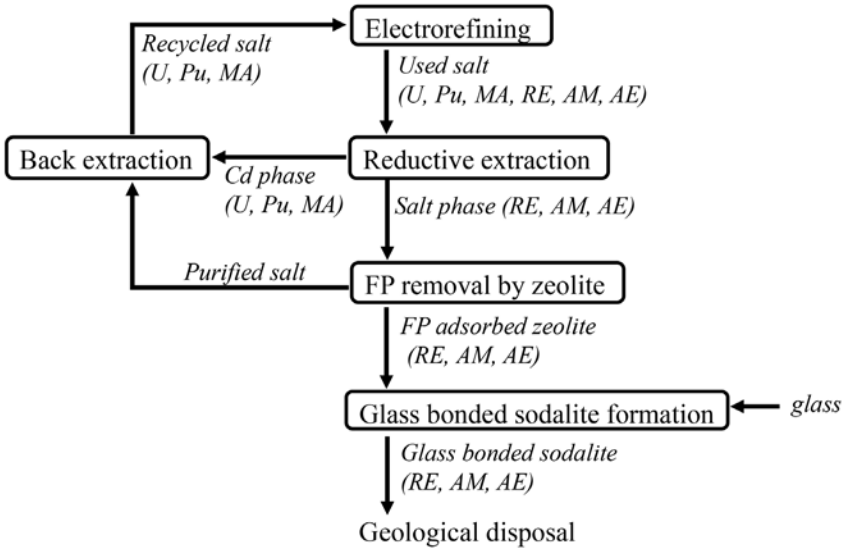

Figure 2. Flowsheet of the conventional used salt treatment process. MA: minor actinides, RE: rare earth fission products, AE: alkaline earth fission products, AM: alkali fission products.

The first step is called as a reductive extraction where actinide cations in the used melt are reduced to be recovered in a liquid Cd phase according to the following chemical reaction,

$$An^{3+} + 3Li_{\text{in Cd}} \rightarrow An_{\text{in Cd}} + 3Li^{+} \quad [4]$$

The remaining used melt containing the fission products are then treated by a zeolite, where the fission products are adsorbed and occluded in the structure of zeolite to be removed from the used melt. The zeolite is then mixed with a glass at high temperature, around 1100 K, to form a glass-bonded sodalite. The glass-bonded sodalite is a stable waste form, however, the achievable concentration of the fission products in the formed glass-bonded sodalite is limited to low values (1.6~4.3 wt%) (4, 5), causing a larger volume of the waste form.

It was reported that a homogeneous glass, in which the concentration of fission products was higher than in the glass-bonded sodalite, was produced (6, 7). Thus, in this paper, the authors propose a novel used salt treatment process utilizing the glass as the waste form. As mentioned in the following section in detail, in the proposed used salt treatment process, two steps are added to the conventional one, step I; electrochemical recovery of rare earth fission products as silicides from the used melt and step II; oxidation of the silicides to be dissolved in the glass matrix. For the purpose of investigating a feasibility of the proposed used salt treatment process, the behavior of electrochemical rare earth silicides formation on a Si substrate in molten chloride salts at step I is required to be clarified and the conditions for oxidizing the rare earth silicides to be stabilized in the glass matrix at step II must be optimized. The present study focused on the former challenge. Many researchers have studied on electrochemical formations of various kinds of silicides, Fe-Si, Ni-Si, Ca-Si, Mg-Si, Mo-Si, Zr-Si, Ti-Si, Li-Si, La-Si and so on, in molten chlorides, fluorides and their mixture salts (8-15). Concerning rare earth silicide formation, Kochetova et al. reported $LaSi_2$ formation by using the electrochemical co-deposition of La and Si on a Ni substrate in NaCl-NaF-LaF_3-K_2SiF_6 melt (12). However, as far as our knowledge, there have been no reports on rare earth silicides formation on a Si electrode in molten chloride salts, which is to be utilized in the step I of the proposed used salt treatment process. Therefore, in the present study, a basic behavior of a series of an individual lanthanide silicide (La-Si, Ce-Si, Pr-Si, Nd-Si, Sm-Si, Eu-Si and Gd-Si) formation on a Si electrode was investigated in the LiCl-KCl melt containing the corresponding lanthanide chloride at 723 K.

Novel used salt treatment process

It is difficult to stabilize chlorides in the glass waste form. Thus, as seen in the flowsheet of the novel used salt treatment process (Figure 3), the following two steps are added to the conventional one to convert fission products from chlorides to oxides which is a suitable chemical form to be stabilized in the glass matrix. Step I: In the used salt after the reductive extraction step, cations of rare earth (RE), which are dominant elements among the fission products, are reduced on a Si electrode to form rare earth silicides ($RESi_x$),

$$RE^{m+} + xSi + me^{-} \rightarrow RESi_x \qquad (m = 2 \text{ or } 3) \quad [5]$$

On the anode, chlorine gas is evolved (reaction 6) to be recycled as an oxidizing agent in the proprocessing,

$$2Cl^- \rightarrow Cl_2 + 2e^- \quad [6]$$

Step II: The rare earth silicides obtained at step I are then oxidized and dissolved into a glass matrix, for example a borosilicate glass. It is well known that in chloride melts, rare earths are recovered by alloying with the cathode material other than Si, for example Ni (16, 17), Cd (18-20) and so on. In the proposed process, Si is selected as the alloying material because Si is a main component of the glass matrix, resulting in that rare earths are not required to be separated from the formed alloy before step II. Since alkali and alkaline earth are hardly recovered as silicides with a high current efficiency in LiCl-KCl melt due to the competing reaction of Li silicide formation (21), the used salt after step I contains the remaining alkali and alkaline earth fission products. They are removed from the used salt and stabilized in a stable waste form in a similar manner to the conventional process: Alkali and alkaline earth fission products are adsorbed and occluded in the structure of zeolite and the zeolite is then mixed with a glass to form a glass-bonded sodalite.

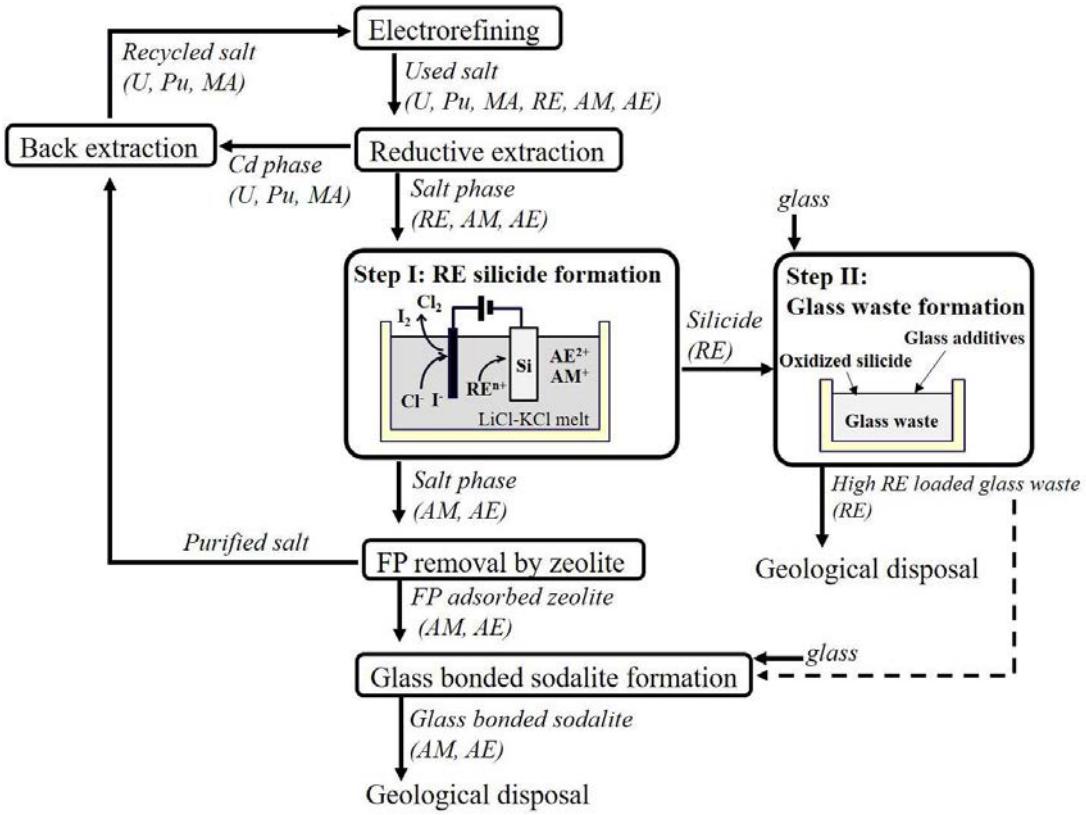

Figure 3. Flowsheet of the proposed novel used salt treatment process. MA: minor actinides, RE: rare earth fission products, AE: alkaline earth fission products, AM: alkali fission products.

Under the assumption that the concentration of rare earths would be ~10 wt% in the glass waste form, it is estimated that the volume of the waste form is reduced by ~7 % by adoption of the proposed used salt treatment process compared with the conventional one. In case that the glass waste produced at step II is served as the glass to be mixed with the zeolite to form the glass-bonded sodalite (the dotted line in Figure 3), the waste volume would be reduced by ~22 % (22). Further volume reduction would be expected by that

the oxidized rare earth silicides are stabilized as lanthanide borosilicate glass which is capable of containing 50~60 wt% of rare earth oxides (23). The proposed used salt treatment process would provide an additional advantage: Iodine fission product, which exists in the form of anion I^-, is separated from the used melt as iodine gas on the anode at step I,

$$2I^- \rightarrow I_2 + 2e^- \quad [7]$$

The separation of long half-life nuclides like iodine, ^{129}I, from the used melt could give a future potential of their transmutation into short half-life or stable nuclides (24).

Experimental

Figure 4 shows a schematic drawing of the experimental apparatus used in the present study. Experiments were carried out in a glove box filled with purified Ar atmosphere in which the concentrations of impurities, oxygen and moisture, were kept below 1 ppm. A eutectic LiCl-KCl (99.99 % purity, LiCl : KCl = 58.8 : 41.2 mol%, APL) was melted in an alumina crucible (60 mm diameter, SSA-S, Nikkato Co., Ltd.) and was used as an electrolyte at 723 K. One of the lanthanide chlorides among $LaCl_3$ (99.99 % purity, APL), $CeCl_3$ (99.99 % purity, APL), $PrCl_3$ (99.99 % purity, APL), $NdCl_3$ (99.99 % purity, APL) and $GdCl_3$ (99.9 % purity, APL) was added to the LiCl-KCl melt as the lanthanide ion source. Since the redox potentials for Sm^{3+}/Sm^{2+} and Eu^{3+}/Eu^{2+} are more positive than the anode potential at the electrorefining process, Sm and Eu exist as the divalent cation in the used salt. Since $SmCl_2$ and $EuCl_2$ were not commercially available, they were prepared according to reactions [8] or [9] by immersing Sm (99.9 % purity, The Nilaco Corp.) or Eu (99.9 % purity, The Nilaco Corp.) metal in a LiCl-KCl melt containing $SmCl_3$ (99.95 % purity, APL) or $EuCl_3$ (99.99 % purity, APL),

$$Sm + 2SmCl_3 \rightarrow 3SmCl_2 \quad [8]$$
$$Eu + 2EuCl_3 \rightarrow 3EuCl_2 \quad [9]$$

The prepared melts used in the present study were LiCl-KCl-0.70mol%$LaCl_3$, LiCl-KCl-1.2mol%$CeCl_3$, LiCl-KCl-0.71mol%$PrCl_3$, LiCl-KCl-2.2mol%$NdCl_3$, LiCl-KCl-0.22mol%$SmCl_2$, LiCl-KCl-0.24mol%$EuCl_2$ and LiCl-KCl-0.23mol%$GdCl_3$. The working electrode was a W wire (ϕ1 mm, 99.95 % purity, The Nilaco Corp.) electrode or a Si electrode. The Si electrode was composed of a Si wafer (n-type, <110>, 0.3~0.5 mm thickness, 0.2 Ωcm) wounded by a Ta wire (ϕ0.2 mm, 99.95 % purity, The Nilaco Corp.) as the lead (Figure 4(f)). Current density of the working electrode was calculated based on the initial electrode dimension and immersion depth in the melt. The counter electrode was a glassy carbon rod (ϕ3 mm) electrode. The reference electrode was Ag/AgCl electrode consisting of a Ag wire (ϕ1 mm, 99.99 % purity, The Nilaco Corp.) immersed in LiCl-KCl-AgCl (1.0 wt% AgCl, 99.9 % purity, APL) in a Pylex tube with a thin bottom to maintain an electrical contact with the electrolyte. The silicides layer formed by electrolysis was removed from the Si substrate and analyzed by X-ray diffraction (XRD). When the formed layer was thin, the Si electrode was analyzed by XRD without removing the layer. The cross section of the Si electrode after electrolysis was observed by scanning electron microscopy-energy dispersive spectroscopy (SEM-EDS).

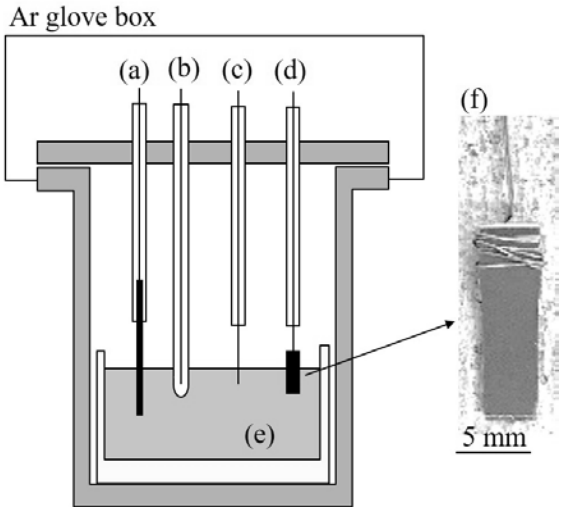

Figure 4. Experimental apparatus. (a) glassy carbon electrode, (b) Ag/AgCl reference electrode, (c) W wire electrode, (d) Si electrode (e) LiCl-KCl melt containing 0.70 mol% $LaCl_3$, 1.2 mol% $CeCl_3$, 0.71 mol% $PrCl_3$, 2.2 mol% $NdCl_3$, 0.22 mol% $SmCl_2$, 0.24 mol% $EuCl_2$ or 0.23 mol% $GdCl_3$ at 723 K and (f) Si wafer (n-type, <110>, 0.3~0.5 mm thickness, 0.02 Ωcm) for Si electrode.

Results and discussion

Cyclic voltammetry

For a comparison with the Si electrode, cyclic voltammetry was performed using the W electrode as summarized in Figure 5 (except for Figure 5(f2) where a glassy carbon rod was used as the working electrode to measure the reaction within the electrochemical window of the glassy carbon). A cathodic current increase and the corresponding anodic current are observed at around -2.0 V (vs. Ag/AgCl) in LiCl-KCl-$LaCl_3$, LiCl-KCl-$CeCl_3$, LiCl-KCl-$PrCl_3$, LiCl-KCl-$NdCl_3$ and LiCl-KCl-$GdCl_3$ melts as seen in Figure 5(a), (b), (c), (d) and (g), respectively. The cathodic and anodic current couple at around -2.0 V on the inert W electrode was ascribed to be the lanthanide (Ln : La, Ce, Pr, Nd, Gd) metal deposition and its dissolution, respectively (18-20, 25),

$$Ln^{3+} + 3e^- \rightarrow Ln \quad [10]$$
$$Ln \rightarrow Ln^{3+} + 3e^- \quad [11]$$

In Figure 5(d), a cathodic current increased gradually from around -1.7 V which was due to the reduction of Nd^{3+} to Nd^{2+} (25). In LiCl-KCl-$SmCl_2$ and LiCl-KCl-$EuCl_2$ melts, a sharp cathodic current and the corresponding anodic current were seen at around -2.4 V (Figures 5(e1) and (f1)), which corresponded to Li metal deposition and its dissolution, determining the cathodic limit of the LiCl-KCl melt as shown in cyclic voltammogram in Figure 5(h). Figures 5(e2) and (f2) show the cathodic and anodic current couples ascribed to the redox reactions, Sm^{3+}/Sm^{2+} and Eu^{3+}/Eu^{2+}, at around -0.8 V and 0.4 V, respectively (26, 27). These results confirmed that the inert cathode was not suitable to be used in the step I of the proposed used salt treatment process because of the following reasons: Neither Sm nor Eu was recovered from the melt and current efficiency for the recovery of Nd, of which amount was the largest among rare earth fission products, was low due to

the competing cathodic reaction ($Nd^{3+} + e^- \rightarrow Nd^{2+}$) and the re-dissolution reaction of the deposited Nd metal ($Nd + 2Nd^{3+} \rightarrow 3Nd^{2+}$).

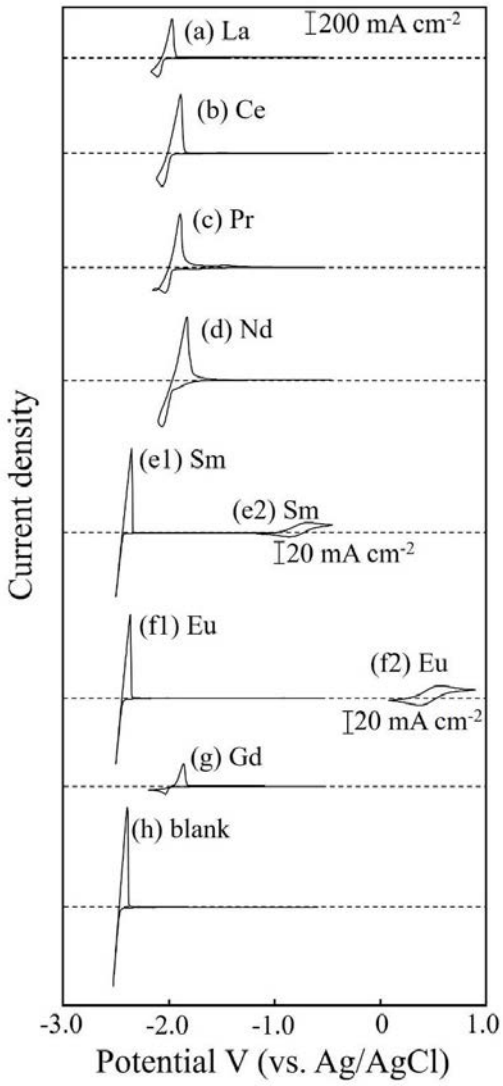

Figure 5. Cyclic voltammograms using a W electrode in (h) LiCl-KCl melt and in LiCl-KCl melt containing (a) 0.70 mol% $LaCl_3$, (b) 1.2 mol% $CeCl_3$, (c) 0.71 mol% $PrCl_3$, (d) 2.2 mol% $NdCl_3$, (e1) and (e2) 0.22 mol% $SmCl_2$, (f1) and (f2) 0.24 mol% $EuCl_2$ and (g) 0.23 mol% $GdCl_3$ at 723 K. Scan rate was 50 mV s^{-1}. Cyclic voltamograms (e2) and (f2) are magnified ten times as the scale indicates separately.

Figure 6 compares cyclic voltammograms using the Si electrode. In LiCl-KCl-$LaCl_3$ (Figure 6(a)), LiCl-KCl-$CeCl_3$ (Figure 6(b)), LiCl-KCl-$PrCl_3$ (Figure 6(c)), LiCl-KCl-$NdCl_3$ (Figure 6(d)) and LiCl-KCl-$GdCl_3$ (Figure 6(g)) melts, the cathodic current increasing from around -1.3 V and the corresponding broad anodic peak were observed. Since no cathodic and anodic currents were seen in the potential range from -1.7 V to -0.7 V in cyclic voltammograms using the W electrode (Figures 5(a), (b), (c), (d) and (g)), the cathodic current increase from around -1.3 V and the corresponding broad anodic peak were considered to be due to the lanthanide (La, Ce, Pr, Nd or Gd) ion reduction to form its silicide and the lanthanide dissolution from the silicide, respectively. A cathodic and anodic current couple observed at around -2.1 V in LiCl-KCl melt (Figure 6(h))

corresponded to lithium silicide formation and lithium dissolution from the silicide, respectively, according to the report (10),

$$Li^+ + xSi + e^- \rightarrow LiSi_x \quad [12]$$
$$LiSi_x \rightarrow Li^+ + xSi + e^- \quad [13]$$

In addition to the lithium silicide formation and lithium dissolution from the silicide at around -2.1 V, a cathodic peak with a shoulder was observed at around -1.7 V in LiCl-KCl-$SmCl_2$ melt (Figure 6(e)) and a cathodic current increased from around -1.9 V in LiCl-KCl-$EuCl_2$ melt (Figure 6(f)). These cathodic currents were not observed in the case of cyclic voltammetry using the W electrode (Figure 5(e1) and (f1)), suggesting that they were ascribed to the formation of Sm and Eu silicides. The corresponding anodic peaks for Sm and Eu dissolution from the silicides were observed at around -1.1 V and -0.8 V, respectively.

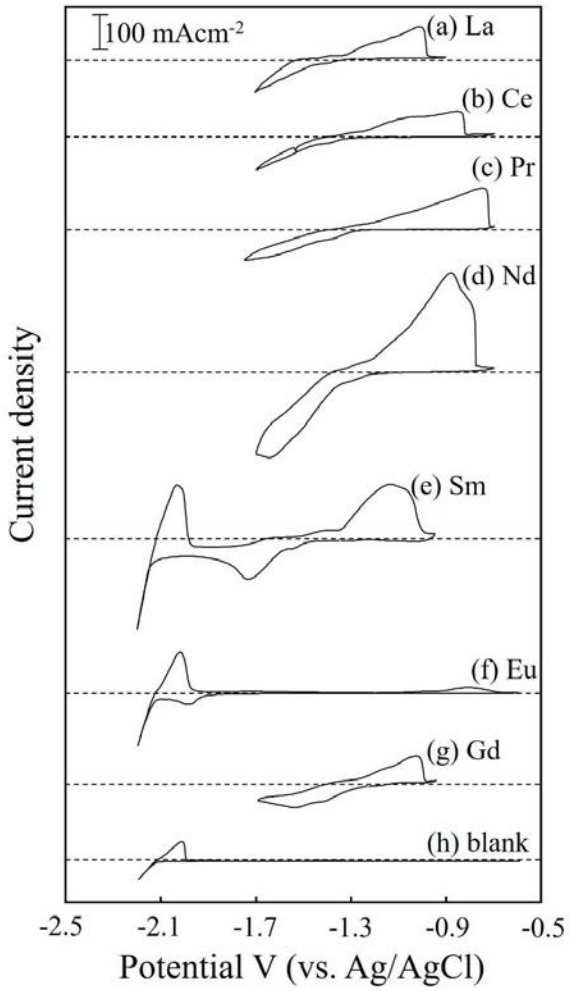

Figure 6. Cyclic voltammograms using a Si electrode in (h) LiCl-KCl melt and in LiCl-KCl melt containing (a) 0.70 mol% $LaCl_3$, (b) 1.2 mol% $CeCl_3$, (c) 0.71 mol% $PrCl_3$, (d) 2.2 mol% $NdCl_3$, (e) 0.22 mol% $SmCl_2$, (f) 0.24 mol% $EuCl_2$ and (g) 0.23 mol% $GdCl_3$ at 723 K. Scan rate was 50 mV s^{-1}.

Potentiostatic electrolysis

Potentiostatic electrolysis was performed using the Si electrode to prepare each silicide to be investigated by XRD and SEM-EDX. The experimental conditions, electrolysis potential determined based on the results of cyclic voltammetry, electrolysis time and passed electricity, are listed in Table I.

TABLE I. Conditions and results of potentiostatic electrolysis.

System	La-Si	Ce-Si	Pr-Si	Nd-Si	Sm-Si	Eu-Si	Gd-Si
Concentration of $LnCl_x$ in the melt (mol%)	0.70	1.2	0.71	2.2	0.22	0.24	0.23
Potentiostatic electrolysis at (V vs. Ag/AgCl)	-1.60	-1.60	-1.60	-1.50	-1.75	-2.05	-1.60
Passed electricity (C)	44.3	115.8	48.9	75.6	57.2	2.9	61.6
Electrolysis time (s)	5000	6000	4500	7000	14000	20000	12077
Si substrate weight before electrolysis (g)	0.066	0.104	0.114	0.019	0.057	0.063	0.091
Weight increase by electrolysis (g)	0.021	0.057	0.024	0.038	0.046	-*	0.032
Current efficiency (%)	98	102	101	100	103	-*	96
Formed silicide phase	$LaSi_2$	$CeSi_2$	$Pr_2Si_{3.6}$	$NdSi_2$	$SmSi_2$, Sm_3Si_5	$EuSi_2$	$GdSi_2$

*too small weight increase to calculate current efficiency.

Figure 7 shows a current change during potentiostatic electrolysis at -1.50 V in LiCl-KCl-$NdCl_3$ melt. The cathodic current density decreased gradually with electrolysis time. A similar trend was observed during potentiostatic electrolysis in the LiCl-KCl melt containing other lanthanide chlorides.

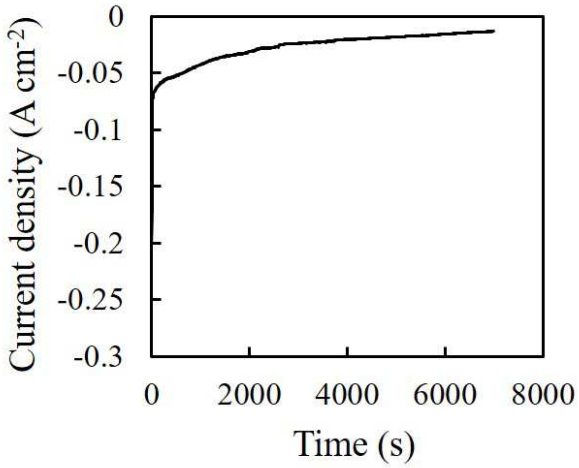

Figure 7. Current density change during potentiostatic electrolysis at -1.50 V using the Si electrode in LiCl-KCl-2.2mol%$NdCl_3$ melt at 723 K.

The Si electrode was washed by distilled water after the electrolysis to remove the adhered salt and then its weight increase by the electrolysis was measured. In the case of Eu silicide formation, although the color of the Si electrode was changed to gold after potentiostatic electrolysis at -2.05 V in LiCl-KCl-$EuCl_2$ melt suggesting a silicide

formation on the surface (Figure 8), the cathodic current density was quite small during the electrolysis and the passed electricity was too small to obtain a significant weight increase even after the long electrolysis time.

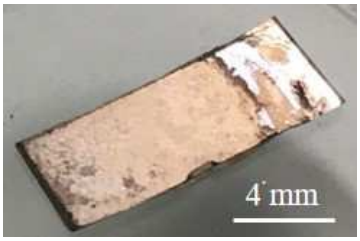

Figure 8. Photograph of the Si electrode after potentiostatic electrolysis at -2.05 V in LiCl-KCl-0.24 mol%$EuCl_2$ melt at 723 K.

A current efficiency for the lanthanide silicide formation (η) was calculated based on the weight increase (w) according to the following equation,

$$\eta\ (\%) = w / Q \times \mathrm{F} \times \mathrm{n} / \mathrm{M} \times 100 \qquad [14]$$

where Q, F, n and M is passed electricity, Faraday constant, electron number of the lanthanide silicide formation reaction (n = 3 for La, Ce, Pr, Nd and Gd silicides, n = 2 for Sm silicide) and atomic weight of the lanthanide, respectively. The calculated values, η, are summarized in Table I. The current efficiency was confirmed to be close to 100 %, as expected from the obtained results in cyclic voltammetry (Figure 5 and 6) showing that no cathodic reactions other than the lanthanide silicide formation proceeded at the potential for the potentiostatic electrolysis.

The Si electrode after the electrolysis was analyzed by XRD (Figure 9). The silicide phases confirmed to be formed in the present experimental condition are summarized in Table I. Two Sm silicide phases, $SmSi_2$ and Sm_3Si_5, were formed by potentiostatic electrolysis at -1.75 V, suggesting the cathodic peak with a shoulder found at around -1.7 V in cyclic voltammogram (Figure 6(e)) would be a superposition of two different cathodic peaks for $SmSi_2$ and Sm_3Si_5 formations. Among several alloy phases existing in each binary lanthanide-silicon system, the obtained silicide phases were the ones having a highest concentration of silicon (a highest and a second highest for Sm silicide), and $LaSi_2$, $CeSi_2$, $Pr_2Si_{3.6}$, $NdSi_2$ and $GdSi_2$ are the phase having a composition range while $SmSi_2$, Sm_3Si_5 and $EuSi_2$ are stoichiometric (28-31). Based on the results, it was confirmed that the silicide formation reactions indicated in cyclic voltammograms in Figure 6 were expressed as the following reactions,

$$Ln^{3+} + 2Si + 3e^- \rightarrow LnSi_2 \qquad \text{Ln: La, Ce, Nd, Gd} \qquad [15]$$
$$Pr^{3+} + 1.8Si + 3e^- \rightarrow 1/2Pr_2Si_{3.6} \qquad [16]$$
$$Sm^{2+} + 2Si + 2e^- \rightarrow SmSi_2 \qquad [17]$$
$$Sm^{2+} + 2SmSi_2 + Si + 2e^- \rightarrow Sm_3Si_5 \qquad [18]$$
$$Eu^{2+} + 2Si + 2e^- \rightarrow EuSi_2 \qquad [19]$$

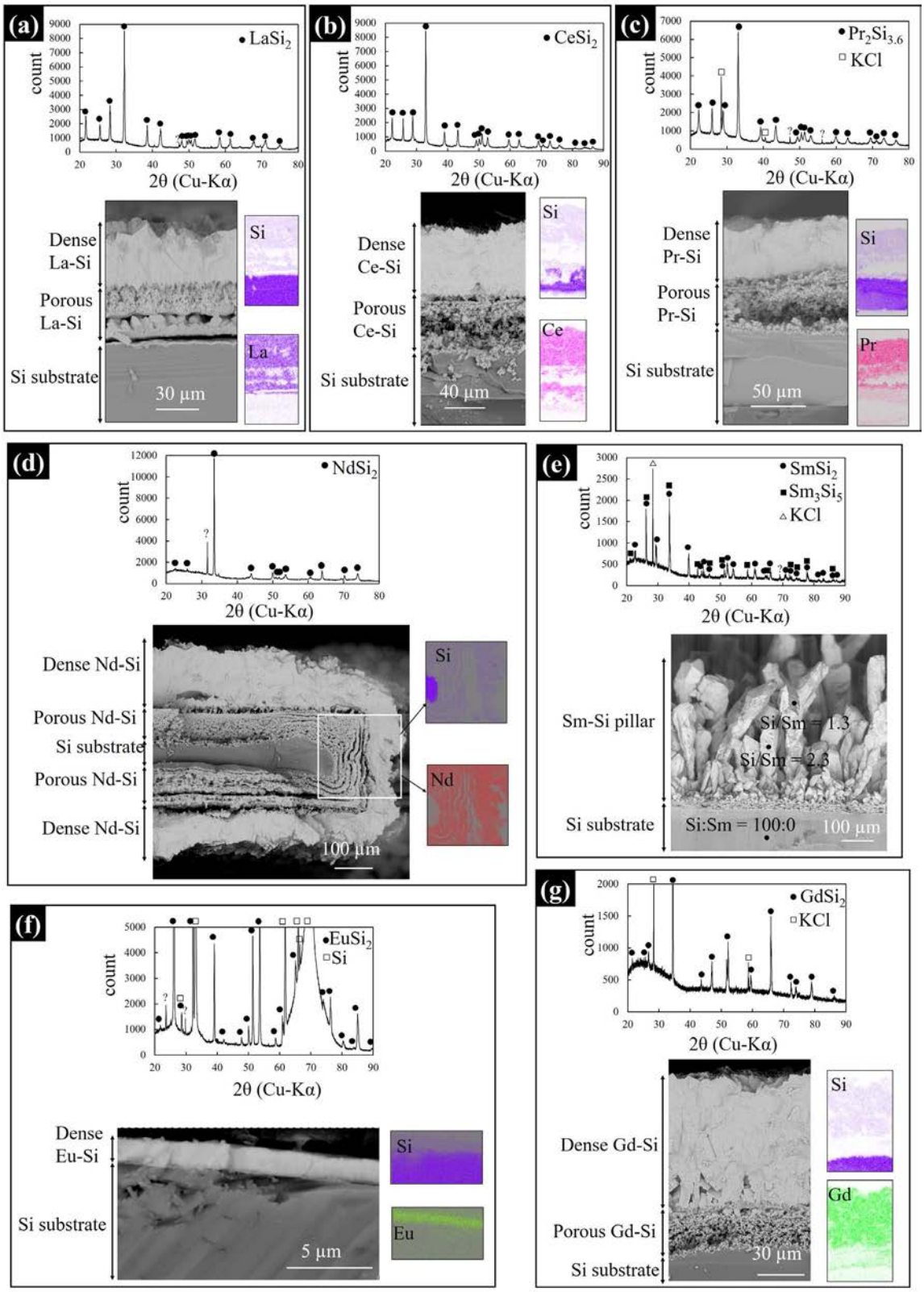

Figure 9. XRD patterns of the Si electrode and SEM-EDX analysis results of the cross section of the Si electrode after potentiostatic electrolysis in LiCl-KCl melt containing (a) 0.70 mol% $LaCl_3$, (b) 1.2 mol% $CeCl_3$, (c) 0.71 mol% $PrCl_3$, (d) 2.2 mol% $NdCl_3$, (e) 0.22 mol% $SmCl_2$, (f) 0.24 mol% $EuCl_2$ and (g) 0.23 mol% $GdCl_3$ at 723 K. SEM images (d) and (e) are reprinted from (32) with a permission of Atomic Energy Society of Japan.

Figure 9 also shows SEM images and EDX analysis results of the cross section of the Si electrodes after electrolysis. It was found that a pillar shaped Sm silicide ($SmSi_2$ and Sm_3Si_5) grew perpendicularly to the Si substrate and a dense and thin Eu silicide, $EuSi_2$, layer (~ 1.5 μm thickness) covered the Si substrate as seen in Figure 9(e) and (f), respectively. A similar morphology was observed among the silicides having a composition range, $LaSi_2$, $CeSi_2$, $Pr_2Si_{3.6}$, $NdSi_2$ and $GdSi_2$; a porous lanthanide silicide layer between a remaining Si substrate and a dense lanthanide silicide layer. Furthermore, as indicating the initial thickness of the Si substrate in Figure 10, it was noticed that the dense and porous layers appeared to grow outside and inside the Si substrate, respectively. This morphology might be formed by that Si would diffuse to outside the Si substrate to form the silicides leaving voids inside the Si substrate due to a faster diffusion rate of Si than the lanthanides in the silicides.

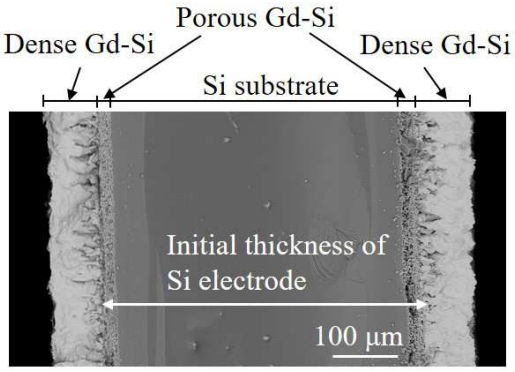

Figure 10. SEM image of the cross section of the Si electrode after potentiostatic electrolysis at -1.60 V in LiCl-KCl-0.23 mol%$GdCl_3$ melt at 723 K.

Conclusion

Fission products are stabilized in a waste form suitable for a geological disposal through pyroprocessing of spent nuclear fuels. For the purpose of reducing a volume of the waste form compared with the conventional process, a noble used salt treatment process was proposed, where rare earths, dominant among fission products, were electrochemically recovered from the used salt in a form of their silicids and the silicides were then oxidized to be dissolved in a glass matrix as a stable waste form, while the rest of fission products, alkalis and alkaline earths, were stabilized in a glass-bonded sodalite.

To investigate a basic behavior of a series of individual lanthanide silicide (La-Si, Ce-Si, Pr-Si, Nd-Si, Sm-Si, Eu-Si and Gd-Si) formation, cyclic voltammetry and potentiostatic electrolysis were performed using a Si electrode in LiCl-KCl melts containing the corresponding lanthanide chloride at 723 K. It was confirmed that all of the lanthanides studied here were recovered from the melt in the form of the silicides ($LaSi_2$, $CeSi_2$, $Pr_2Si_{3.6}$, $NdSi_2$, $SmSi_2$, Sm_3Si_5, $EuSi_2$ and $GdSi_2$). The current efficiency for forming silicides ($LaSi_2$, $CeSi_2$, $Pr_2Si_{3.6}$, $NdSi_2$, ($SmSi_2$ and Sm_3Si_5) and $GdSi_2$) was calculated to be as high as ~100 %. Various morphologies of silicides were found to be formed electrochemically on the Si substrate; a dense silicide layer outside the Si substrate and a porous silicide layer inside the substrate concerning the lanthanide silicides having a composition range ($LaSi_2$, $CeSi_2$, $Pr_2Si_{3.6}$, $NdSi_2$ and $GdSi_2$), a pillar

shaped Sm silicide ($SmSi_2$, Sm_3Si_5) growing perpendicularly to the Si substrate and a dense and thin $EuSi_2$ layer covering the Si substrate. The obtained results in this study confirmed a feasibility of the key step composing of the proposed used salt treatment process; rare earths recovery as silicides from the spent molten chloride salt.

Acknowledgments

Parts of the results were obtained in the project "Development of highly flexible technology for recovery and transmutation of minor actinide" entrusted to Central Research Institute of Electric Power Industry by the Ministry of Education, Culture, Sports, Science and Technology (MEXT).

References

1. M. Iizuka, T. Koyama, Y. Sakamura, K. Uozumi, K. Fujihata, T. Kato, T. Murakami, T. Hijikata, T. Tsukada, and J.-P. Glatz, Proceedings of Global 2013, Salt Lake City, U.S., September 30 - October 3, 2013, Paper No. 7987.
2. T. Mukaiyama, T. Takizuka, M. Mizumoto, Y. Ikeda, T. Ogawa, A. Hasegawa, H. Takada, and H. Takano, *Prog. Nucl. Energ*., **38**, 107 (2001).
3. K. Uozumi, K. Fujihata, and T. Tsukada, Nucl. Technol., **203**, 261 (2018).
4. Japan Atomic Energy Agency, Feasibility Study on Commercialized Fast Reactor Cycle Systems Technical Study Report of Phase II –(2) Nuclear Fuel Cycle Systems–, JAEA-Research 2006-043 (2006) (in Japanese).
5. T. Tsukada, M. Iizuka, T. Ogata, and K. Kinoshita, Final report on "Development and Improvement of Electrometallurgical Process" entrusted to Central Research Institute of Electric Power Industry (CRIEPI) by the Ministry of Education, Culture, Sports, Science and Technology (MEXT) (2007) (in Japanese).
6. T. Advocat, P. Jollivet, J.L. Crovisier, and M. del Nero, *J. Nucl. Mater*., **298**, 55 (2001).
7. K. Uruga, T. Tsukada, and T. Usami, *J. Nucl. Sci. Technol.*, **57**, 433 (2020).
8. T. Ueda, T. Goto, and Y. Ito, *J. Surf. Finish. Soc. Jpn*., **46**, 1173 (1995) (in Japanese).
9. V. V. Malyshev, N. N. Uskova, and V. I. Shapoval, *Powder Metall. Met. Ceram*., **36**, 289 (1997).
10. K. Amezawa, N. Yamamoto, Y. Tomii, and Y. Ito, *J. Electrochem. Soc*., **145**, 1986 (1998).
11. Y. Hu, X. Wang, J. Xiao, J. Hou, S. Jiao, and H. Zhu, *J. Electrochem. Soc*., **160**, D81 (2013).
12. S. A. Kochetova, A. D. Pisanenko, and S. V. Devyatkin, *ECS Transactions*, **64**(4), 523 (2014).
13. Y. Sakanaka, T. Goto, and K. Hachiya, *J. Electrochem. Soc*., **162**, D186 (2015).
14. S. A. Kochetova, R. N. Savchuk, A. D. Pisanenko, and S. V. Devyatkin, *ECS Transactions*, **75**(15), 437 (2016).
15. O. Takeda, S. Yamanaka, M. Hoshi, H. Zhu, and Y. Sato, *J. Electrochem. Soc*., **164**, D517 (2017).
16. H. Konishi, T. Nohira and Y. Ito, *Electrochem. Solid. State Lett*., **5**, B37 (2002).

17. T. Nohira, H. Kambara, K. Amezawa and Y. Ito, *J. Electrochem. Soc*., **152**, C183 (2005).
18. J.-H. Sim, Y.-S. Kim, S.-W. Paek, S.-H. Kim, and S.-J. Lee, *Int. J. Electrochem. Sci*., **13**, 2842 (2018).
19. Y. Castrillejo, M.R. Bermejo, P. D. Arocas, A. M. Martinez, and E. Barrado, *J. Electroanal. Chem*., **579**, 343 (2005).
20. Y. Castrillejo, R. Bermejo, A. M. Martinez, E. Barrado and P. D. Arocas, *J. Nucl. Mater*., **360**, 32 (2007).
21. Y. Sakamura and T. Murakami, Abstract of The 51st Symposium on Molten Salt Chemistry, Hokkaido, Japan, 24-25 October, 2019, paper No. 2A09 (in Japanese).
22. K. Uozumi, K. Kinoshita, and M. Iizuka, Abstract of 2020 Fall Meeting of the Atomic Energy Society of Japan, 16-18 September, 2020, paper No. 1F10 (in Japanese).
23. B. J. Riley, D. A. Pierce, J. V. Crum, B. D. Williams, M. M.V. Snyder, and J. A. Peterson, *Prog. Nucl. Energ*., **104**, 102 (2018).
24. M. Iizuka, T. Nohira, K. Tada, T. Murakami and H. Kofuji, Proceedings of Global 2019, Seattle, U.S., September 22-27, 2019, pp. 673.
25. H. Yamana, B. G. Park, O. Shirai, T. Fujii, A. Uehara and H. Moriyama, *J. Alloy. Compd*., **408-412**, 66 (2006).
26. G. Cordoba and C. Caravaca, J. Electroanal. Chem., **572**, 145 (2004).
27. M. R. Bermejo, F. de la Rosa, E. Barrado and Y. Castrillejo, *J. Electroanal. Chem*., **603**, 81 (2007).
28. T. B. Massalski (Ed.), Binary Phase Diagram, American Society for Metals, Metals Park, Ohio, (1986).
29. F. Wetzer, Y. Prots, W. Schnelle, K. Hiebl and Y. Grin, *J. Solid State Chem*., **177**, 2115 (2004).
30. D. V. Averyanov, A. M. Tokmachev, C. G. Karateeva, I. A. Karateev, E. F. Lobanovich, G. V. Prutskov, O. E. Parfenov, A. N. Taldenkov, A. L. Vasiliev and V. G. Strchak, *Sci. Rep*. **6**, 25980; doi: 10.1038/srep25980 (2016).
31. M. V. Bulanova, P. N. Zheltov, K. A. Meleshevich, P. A. Saltykov, G. Effenberg and J.-C. Tedenac, *J. Alloy. Compd*., **329**, 214 (2001).
32. M. Iizuka, T. Murakami, Y. Sakamura and T. Nohira, Abstract of 2019 Fall Meeting of the Atomic Energy Society of Japan, Toyama, Japan, 11-13 September, 2019, paper No. 2I18 (in Japanese).

ECS Transactions, 98 (10) 47-52 (2020)
10.1149/09810.0047ecst ©The Electrochemical Society

Electrochemical Technique to Monitor the Concentration of Oxide in Molten FLiNaK Salt

Suhee Choi, Andrew R. Strianese, and Michael F. Simpson

Department of Materials Science & Engineering, University of Utah, Salt Lake City, Utah 84112, USA

The effect of oxide concentration in molten FLiNaK (LiF-NaF-KF) salt on square wave voltammetry (SWV) oxidation peak heights using tungsten working electrodes was determined and compared to the results of acid-base titration of solid salt samples. SWV oxidation current was observed to be more sensitive than that of cyclic voltammetry (CV), possibly due to the elimination of non-faradaic current. The in-situ measurements of the O^{2-} concentrations in the molten salt using SWV showed good agreement with the results obtained from the acid-base titration method.

Introduction

Molten fluoride salts have attracted interest as fuel and/or coolant for several different molten salt reactor (MSR) designs(1). Fluoride salts have many advantageous properties for these applications, such as low viscosity, low vapor pressure, high heat capacity, and high solubility for actinides(2). However, impurities such as oxide ions are generally believed to increase the corrosivity of the salt (3-5). Therefore, sensors that measure oxide concentration in real-time would be advantageous to determine when the salt needs to be purified.

Electrochemical methods have been used for the investigation of electro-active species in molten salts because they have advantages such as quick response and compatibility with the harsh conditions found in a molten salt coolant of fuel for a nuclear reactor. This makes these methods suitable for real-time oxide concentration monitoring. SWV has been shown to respond to O^{2-} concentration in LiCl-Li_2O(6), O^{2-} concentration in LiF-NaF-Li_2O(7), and Pu^{3+} concentration in LiCl-KCl(8). Massot investigated the concentration of oxide in LiF-NaF eutectic by CV, SWV, and chronopotentiometry using an inert, gold working electrode and reported that SWV is far more appropriate because the observed signal is a well-defined oxidation peak. In addition, Choi proved that the oxidation of the O^{2-} in LiCl-Li_2O is diffusion-controlled(6).

In this work, we focused on measuring the concentration of oxide by adding Li_2O in the FLiNaK salt using two electrochemical methods: cyclic voltammetry (CV) and square wave voltammetry (SWV). This work is novel from that published by Massot in that we report the use of a non-inert tungsten working electrode. Moreover, after the electrochemical tests, the salts were analyzed for the concentration of oxygen by titration in order to compare with electrochemical results. We observed an oxidation peak

corresponding to tungsten oxidation using CV. Then SWV was used to correlate the oxidation peak height to oxide concentrations ranging from 0.1 to 2.0 wt.% Li_2O.

Experimental

Tungsten (Alfa Aesar, dia. 1 mm) and molybdenum (Alfa Aesar, dia. 2 mm) rods were used as the working electrode (WE) and counter electrode, respectively. A platinum wire (Alfa Aesar, dia. 0.5 mm) was used as the reference electrode. The electrodes were mechanically polished with sandpaper (grits 220, 600, and 2000) prior to use. All potential data were reported relative to the Pt quasi-reference electrode.

LiF (98.5%), NaF (99%), KF (99%), NaOH (98%), and Li_2O (99.5%) were purchased from Alfa Aesar. H_2SO_4 (98%) and phenolphthalein solution (0.5wt.% in ethanol: water (1:1)) were purchased from J.T.Baker and Sigma Aldrich, respectively. LiF-NaF-KF salt was mixed using the mole ratio of 46.5-11.5-42 mol%. This salt mixture will be referred to using the common FLiNaK abbreviation in this paper.

Figure 1 shows the picture of the experimental system used for electrochemical measurement. All the experiments were carried out in a glove box (Inert Technologies) under Ar atmosphere. The O_2 and H_2O levels were maintained to be less than 1 ppm. We used a vertical translator to precisely control the depth of the immersed WE surface area. The CV and SWV were performed using a Gamry Reference 600+ potentiostat. A nominal mass of 40 g of the FLiNaK salt mixture was measured in a nickel crucible (Alfa Aesar, 99.67%) and then loaded into a Thermolyne furnace (Kerr Auto Electro-Melt). All tests were run at 600°C. The pre-treatment of the LiF-NaF-KF mixture included holds for at least 12 hours at 300°C and 3 hours at 150°C before running the electrochemical measurements. Li_2O was added to the FLiNaK and held at least 2 hours for dissolution and equilibration.

Solid salt samples were taken for analysis via acid-base titration using the back-titration method. These samples were collected by quickly immersing a room temperature all-thread stainless steel rod into the molten salt and then quickly removing it. The samples were pried from the all-thread rod and collected into a pan where the total mass was measured. The 0.3 g of samples were then dissolved in 10 mL of 1.0 M H_2SO_4, and the O^{2-} in the samples reacted with H^+ in the H_2SO_4. The samples were titrated for the concentration of the remaining H^+ using 0.25 M NaOH solution to calculate the concentration of oxides in the samples. Each sample was titrated three times to calculate average concentration.

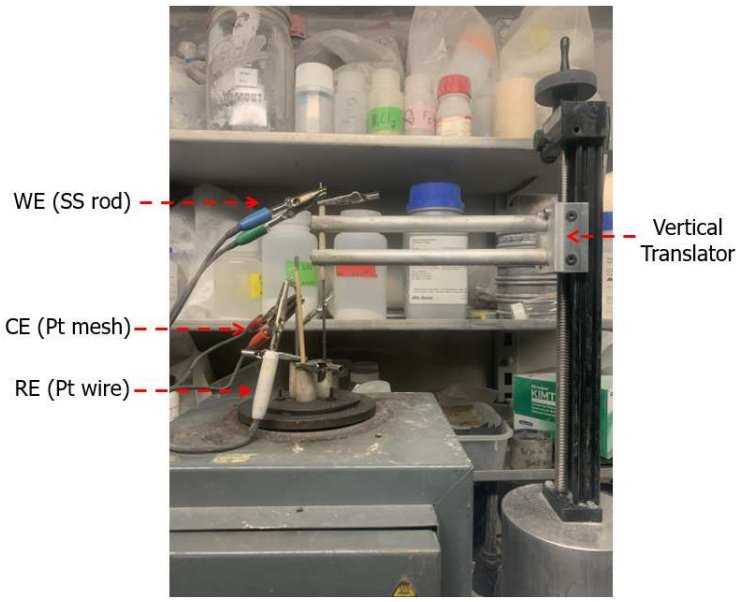

Figure 1. Photograph of the experimental system for electrochemical experiments in FLiNaK salt

Results and Discussion

CV was used to identify the potentials at which various oxidation and reduction processes occurred. Oxide ions are known to oxidize most metals under anodic polarization, with platinum being a notable exception. It was initially hypothesized that such metal oxidation could be quantified via CV. Before and after the addition of oxide ions in the melt as Li_2O, CV was performed using a tungsten working electrode at 600°C. The results are shown in Fig. 2. Note that a Pt quasi-reference electrode was used, so the potentials were shifted as a result of the change of the salt's redox potential or equilibrium potential at the Pt reference electrode. Three oxidation peaks were observed in the CV shown in Fig. 2 taken after addition of Li_2O with the following hypothesized associations: (i) tungsten oxidation via reaction with O^{2-} (from 1.35 V to 1.68 V), (ii) W oxidation via reaction with Cl^- followed by dissolution (from 1.75 V to 2.25 V), and (iii) F^- oxidation to F_2 (from 2.4 V).

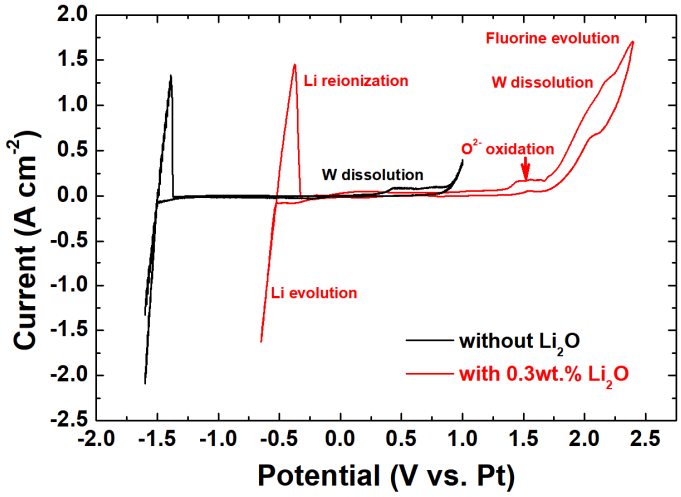

Figure 2. CV of the FLiNaK salt with/without 0.3 wt.% Li_2O at 600°C. The scan rate is 0.2 V/s.

Incremental additions of lithium oxide were made to the salt up to 2.0 wt.%. After each addition, the salt was stirred and allowed to equilibrate for at least 2 hours before running a CV. As can be seen in Fig. 3, the potential of oxidation peaks was positively shifted by adding Li_2O, and the current of oxidation peaks increased with the addition of Li_2O. This result is consistent with Shen's report(9).

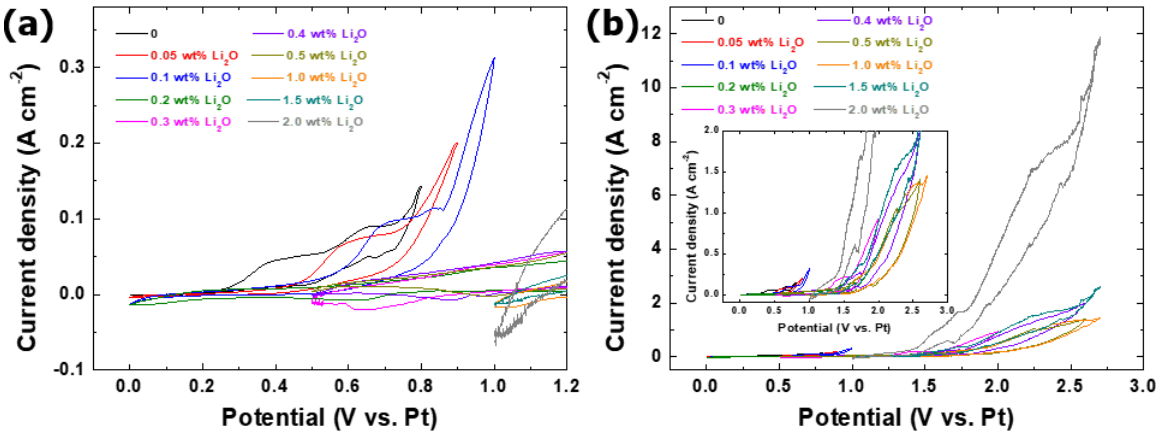

Figure 3. CV of the FLiNaK-Li_2O system at 0.2 V/s at T=600°C for various oxide ions concentrations. (a) The concentrations of Li_2O: 0, 0.05, and 0.1 wt.% and (b) the concentrations of Li_2O: from 0.05 wt.% to 2.0 wt.%. Inset graph shows an enlarged current range -0.1 A cm^{-2} to 2 A cm^{-2}.

Figure 4 shows the SWV results from the same set of salt mixtures with the tungsten working electrode. In the SWV tests, 10 Hz of frequency was used for measuring the oxidation peak. SWV and CV show the same tendency of increasing oxidation current with increasing Li_2O concentration. However, the SWV technique shows the oxidation peaks of more clearly.

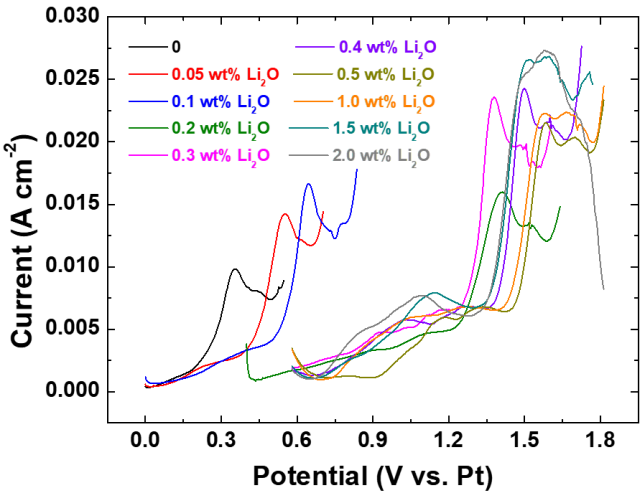

Figure 4. SWV at various Li_2O concentrations (0.05 ~ 2.0 wt.%). SWV parameters: frequency 10 Hz, amplitude 20 mV, step height 20 mV

In Fig. 5, the SWV peak current densities of O^{2-} and the concentration of O^{2-} as measured by titration are plotted versus the as weighed concentration of O^{2-}. The peak current density of O^{2-} increases with increasing O^{2-} concentration. The SWV peak current

density versus O^{2-} concentration shows an excellent fit to a linear function as shown in Fig 5(a). The O^{2-} concentration determined by titration does increase with increasing concentration of added Li_2O, but the relationship appears to be non-linear with a plateau effect above about 1 wt.% Li_2O. There is also less sensitivity in the titration response than the SWV response below 0.3 wt.%. This indicates that SWV has a larger range of O^{2-} concentrations that it is useful for analysis than titration. SWV, of course, also has the benefit of being capable of real-time, in-situ measurement.

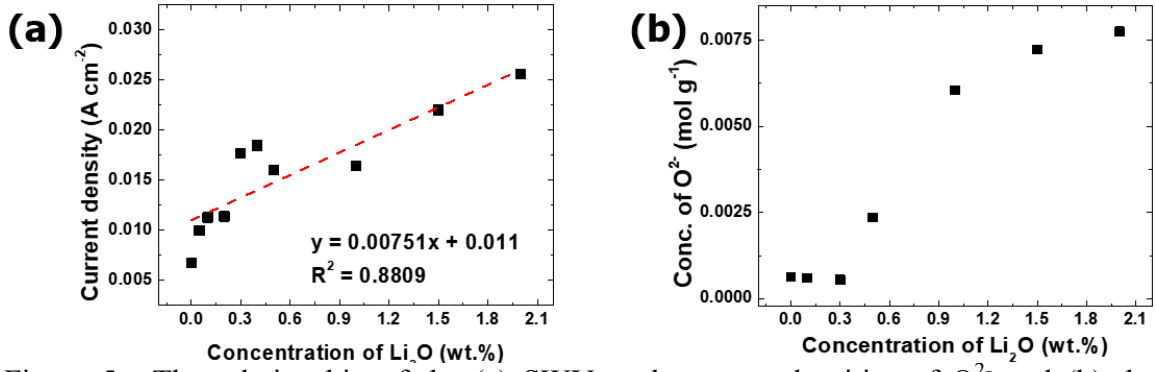

Figure 5. The relationship of the (a) SWV peak current densities of O^{2-} and (b) the concentration of O^{2-} by titration versus Li_2O concentration obtained in the FLiNaK system.

Summary

In this work, the electrochemical behavior of O^{2-} ions was investigated in the FLiNaK salt using CV and SWV and compared the results using the acid-base titration. Then, the use of square wave voltammetry on a tungsten electrode for free oxide titration was assessed in the FLiNaK melt. The linear equation $i_p = 0.0075[O^{2-}]$ of peak current density and O^{2-} concentration was established. In comparison, acid titrations yielded a non-linear correlation with O^{2-} concentration. Thus, we recommend in-situ SWV with a tungsten working electrode as a superior method to measure the concentration of O^{2-} in molten FLiNaK over a range of 0.3 to 2.0 wt.% (Li_2O equivalent).

Acknowledgments

We gratefully acknowledge the College of Mines and Earth Science and College of Engineering of the University of Utah for providing the resources needed for this project.

References

1. D. E. Holcomb and S. M. Cetiner. Oak Ridge National Laboratory, 2010.
2. R. O. Scarlat and P. F. Peterson, *Nucl. Instrum. Methods Phys. Res. A*, **733**, 57 (2014).
3. S. H. Cho, S. B. Park, J. H. Lee, J. M. Hur, and H. S. Lee, *J. Nucl. Mater.*, **412**, 157 (2011).

4. S.-H. Cho, J.-M. Hur, C.-S. Seo, J.-S. Yoon, and S.-W. Park, *J. Alloys. Compd.*, **468**, 263 (2009).
5. K. Sridharan and T. R. Allen, in *Molten Salts Chemistry,* F. Lantelme and H. Groult, eds., p. 241-267, Elsevier, Oxford, (2013).
6. E.-Y. Choi, I.-K. Choi, J.-M. Hur, D.-S. Kang, H.-S. Shin, and S. M. Jeong, *Electrochem. Solid-State Lett.*, **15** (3), E11 (2011).
7. L. Massot, L. Cassayre, P. Chamelot, and P. Taxil, *J. Electroanal. Chem.*, **606** (1), 17 (2007).
8. M. Iizuka, T. Inoue, O. Shirai, T. Iwai, and Y. Arai, *J. Nucl. Mater.*, **297** (1), 43 (2001).
9. M. Shen, H. Peng, M. Ge, Y. Zuo, and L. Xie, *J. Electroanal. Chem.*, **748**, 34 (2015).

ECS Transactions, 98 (10) 53-59 (2020)
10.1149/09810.0053ecst ©The Electrochemical Society

Electrochemical Reduction Behavior of Boron in Molten LiCl–KCl–KBF_4

Y. Katasho and T. Oishi

National Institute of Advanced Industrial Science and Technology (AIST), Tsukuba, Ibaraki, 305-8569, Japan

Although the electrochemical behavior of Nd and Dy in Ne-Fe-B magnets has been investigated, the behavior of B in molten salt has not been clarified yet. Herein, the electrochemical reduction behavior of B(III) is investigated in molten LiCl–KCl–KBF_4 at 723 K. A comparison of the cyclic voltammograms for Ni, Mo, and Ag electrodes suggests that Ni–B compounds were formed on the Ni electrode, and that the reduction of B(III) to B(0) occurred on the Ni, Mo, and Ag electrodes. Ni_2B was confirmed to form on the Ni electrode by potentiostatic electrolysis at 1.3 V vs. Li^+/Li. Granular deposits were observed on the same electrode. An Ag substrate was also electrolyzed at 1.3 V. Granular deposits were observed. However, in both cases, the presence of elemental B was not confirmed yet at this time.

Introduction

Consumption and demand of Nd-Fe-B magnets, also called neodymium magnets, is increasing every year. However, because rare earth elements such as Dy, used in Nd-Fe-B magnets to improve their thermal durability, have sparse mineral resources, it is necessary to develop recycling technologies for Ne-Fe-B magnets. The authors have been developing a technique to separately recover Nd and Dy from Ne-Fe-B magnets using alloy diaphragms and molten salt (1).

Although the electrochemical behavior of Nd and Dy has been intensively investigated, the Ne-Fe-B magnet contains B and Fe as well, and the behavior of B in molten salt has not been clarified yet. Behavior of boron in a molten salt has been investigated mainly for obtaining elemental boron. Cooper studied the behavior of boron in the KF/KCl-KBF_4–B_2O_3 molten salt from 923 to 1273 K (2). Polyakova *et al.* studied the electrochemical behavior of boron in LiF–NaF–KF from 823 to 923 K (3). Recently, Wang *et al.* investigated the behavior of B(III) in NaCl–KCl–KBF_4 at 1023 K and confirmed that a three-electron reaction occurs on the Mo electrode (4). They also reported the diffusion coefficient of B(III) in the system and the formation of spheroidal aggregate boron. Majumdar investigated the behavior of boron in KCl–KF–KBF_4 at 1133 K in a large-scale melt (total salt mixture was 2.5–3.5 kg) and reported the deposition of boron powder comprising spherical particles on a mild steel plate electrode (5). However, the electrochemical behavior of B(III) in the LiCl–KCl melt has not yet been reported.

In this study, we investigated the behavior of B in LiCl–KCl eutectic melts at 723 K. The LiCl–KCl eutectic melt was chosen because a high separation ratio of Nd and Dy was obtained in our previous studies (6).

Experimental

A schematic of the experimental apparatus is shown in Figure 1. The experiments were conducted in LiCl–KCl (44:56 wt%) eutectic melts at 723 K in a glove box with an electric furnace filled with a dry Ar atmosphere (Yamato Corp., Japan). First, 300 g of LiCl–KCl (LiCl: >99%, KCl: >99.5%, Fujifilm Wako Pure Chemical Co., Japan) in a graphite crucible (inner diameter: 700 mm, inner height: 135 mm, Toyo Tanso Corp., Japan) was vacuum dried at 473 K for more than 24 h before elevating the temperature. As working electrodes, Ni, Mo, and Ag wire (diameter 1.0 mm, Ni: >99%, Mo: >99.95%, Ag: >99.99%, Nilaco Corp., Japan) electrodes were used for cyclic voltammetry. Ni and Ag plate electrodes (size: 5 mm × 15 mm × 0.1 mm(t), Ni: >99%, Ag: >99.98%, Nilaco Corp., Japan) were used for electrodeposition. A glassy carbon rod (diameter 3 mm, Tokai Carbon Co. Ltd., Japan) was used as the counter electrode. An Ag^+/Ag electrode was used as the reference electrode, which was prepared by immersing an Ag wire in a LiCl−KCl melt containing 1 mol% of AgCl (AgCl: >99.5%, Fujifilm Wako Pure Chemical Co., Japan) set in a Pyrex glass tube. The potential of the reference electrode was calibrated using the Li^+/Li potential obtained by performing open circuit potential measurements on the Mo wire electrode immediately after electrodepositing the Li metal. All the potentials are described in reference to this Li^+/Li potential.

Electrochemical measurements and electrolysis were conducted using an electrochemical measurement system (HZ-Pro, Hokuto Denko Corp., Japan). The temperature of the electric furnace was controlled by a thermostat connected to a chromel-alumel thermocouple installed in a vertical furnace, and the temperature of the molten salt was monitored by another thermocouple immersed in the molten salt.

Cyclic voltammetry was conducted at KBF_4 concentrations of 0, 0.5, and 2.0 mol%. Potentiostatic and galvanostatic electrolysis was conducted at a KBF_4 concentration of 2.0 mol% using the Ni and Ag plate electrodes, the surface area of which immersed in the molten salt was ~1 cm^2. After the electrolysis, the plate electrodes were rinsed with distilled water and then characterized by scanning electron microscopy (SEM), energy-dispersive X-ray spectroscopy (EDX) (TM4000Plus, Hitachi High-Tech Corp., Japan), and X-ray diffraction (XRD) (D2 Phaser, Bruker AXS, Germany). One of the samples was weighed and dissolved in aqua regia using a microwave dissolution machine (Ethos Easy, Milestone Co., Ltd., Italy). Then, the resulting solution was analyzed by inductively coupled plasma atomic emission spectrometry (ICP-AES) (ICPE-9000, Shimazu Corp., Japan).

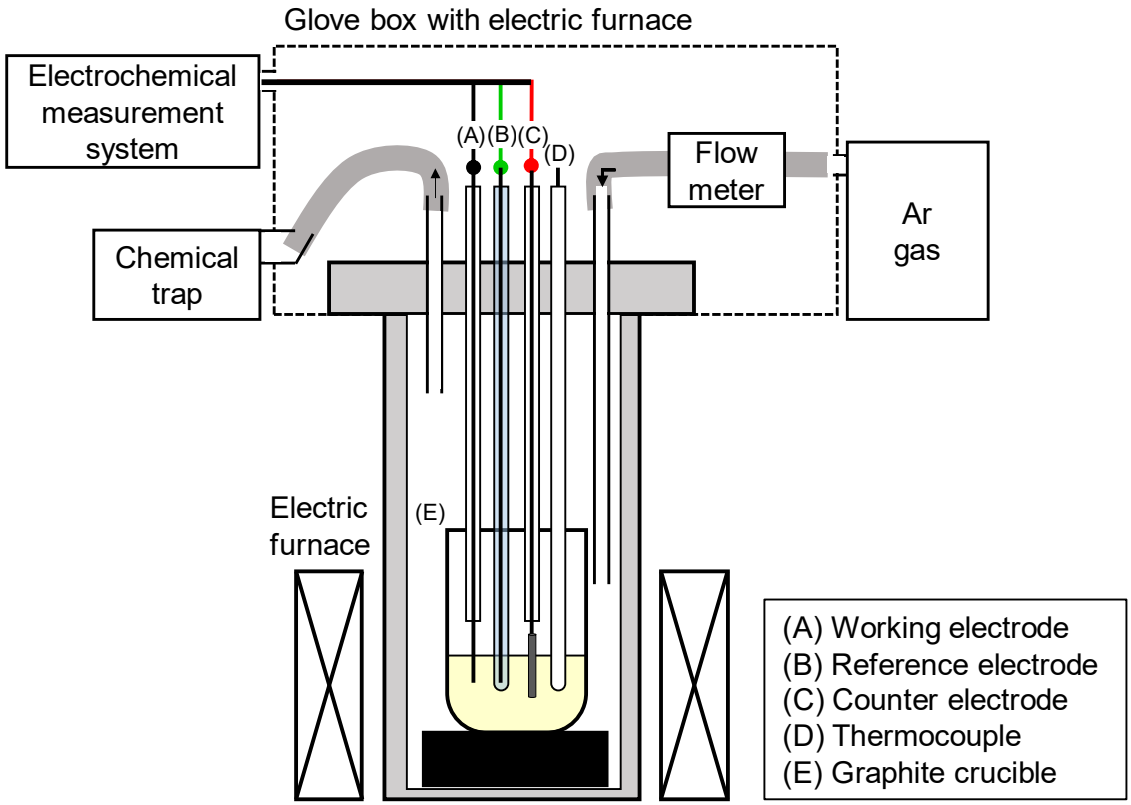

Figure 1. Schematic of the experimental apparatus.

Results and Discussion

Cyclic Voltammetry

Cyclic voltammograms (CVs) obtained by Ni, Mo, and Ag electrodes are shown in Figure 2(a), (b), and (c), respectively. Peaks "b" and "c" at approximately 0 V correspond to Li metal deposition and dissolution, respectively. For the Ni electrode, a cathodic current was observed at approximately 1.2 V ("a" in the figure). This peak corresponds to the reduction of B(III) to B(0). In addition to current peak "a", a small current peak "e" appeared at 1.8 V, which seems to correspond to the formation of Ni–B compounds. Except for peak "e", essentially the same results were obtained for both the Mo and Ag electrodes. In all cases, the peak current at approximately 1.2 V increased with the concentration of KBF_4 (shown as "a" in the figures).

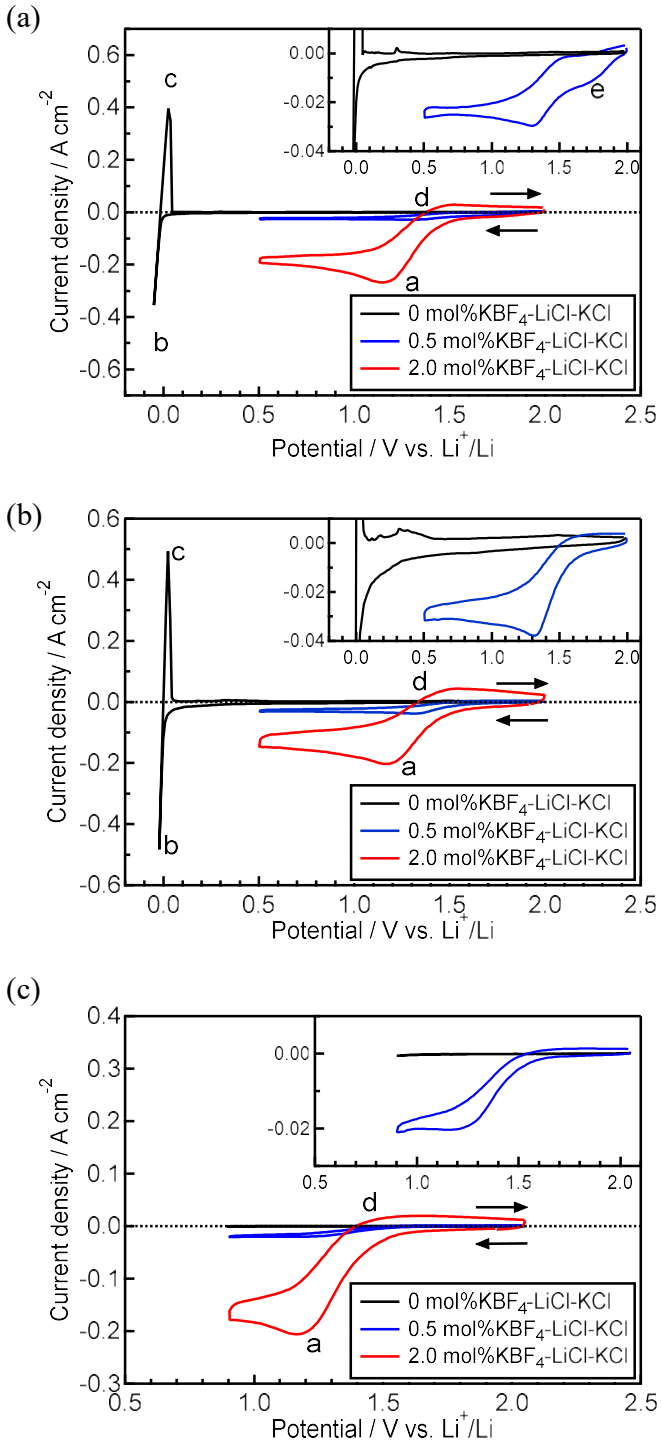

Figure 2. Cyclic voltammograms for (a) Ni, (b) Mo, and (c) Ag electrodes in a LiCl–KCl–KBF_4 melt at 723 K. Scan rate: 100 mV s^{-1}. Inset figures show the magnified portion of the graphs at 0 and 0.5 mol% KBF_4.

Characterization of Products Prepared by Potentiostatic and Galvanostatic Electrolysis

Figure 3 shows a microscopy image and an SEM image of the deposits on the Ni plate electrode obtained by potentiostatic electrolysis at 1.3 V, Q = −50 C. Granules of diameter 1–10 μm were observed. XRD measurements showed that the diffraction peaks of deposits coincided with those of Ni, Ni_2B, and $NiCl_2$. A peak corresponding to B was measured by EDX for the deposited granules. Note that EDX does not provide accurate data for light elements such as B. To determine the current efficiency, galvanostatic electrolysis at −9.8 mA/cm^2, Q = −50 C was conducted. The entire sample was dissolved in aqua regia using a microwave dissolution machine, and the obtained solution was measured by ICP-AES. From the amount of B in the sample, the current efficiency was evaluated to be 96.2%, assuming that all boron atoms are reduced via a three-electron reaction.

Next, potentiostatic electrolysis was conducted at 1.3 V, Q = −10 C using the Ag plate. Ag was selected as the substrate because the Ag–B phase diagram does not have any alloys of Ag and B (7). Figure 4 shows a microscopy image and an SEM image of the deposits on the Ag plate electrode after the potentiostatic electrolysis. Granules with a diameter of approximately 1 μm were observed. From the XRD results, clear diffraction peaks corresponding to metallic Ag were confirmed. Other peaks were also detected, but they did not correspond to elemental B. Similar to the Ni electrode, a peak corresponding to B was observed by EDX. Further analysis and experiments are needed to clarify the chemical composition and valency of B in the deposit using other techniques such as X-ray photoelectron spectroscopy.

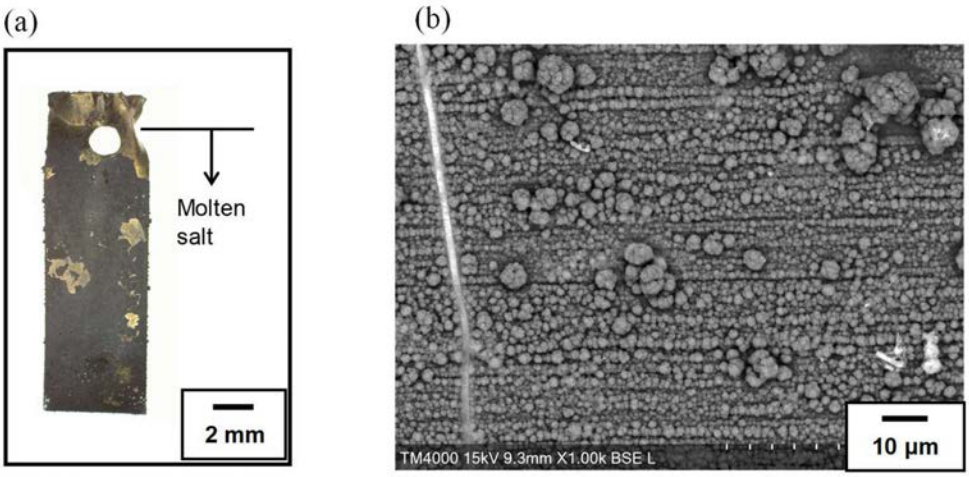

Figure 3. (a) A microscopy and (b) an SEM image of the electrodeposits obtained on the Ni plate electrode by potentiostatic electrolysis at 1.3 V vs. Li^+/Li, Q = −50 C in a LiCl–KCl–KBF_4 at 723 K.

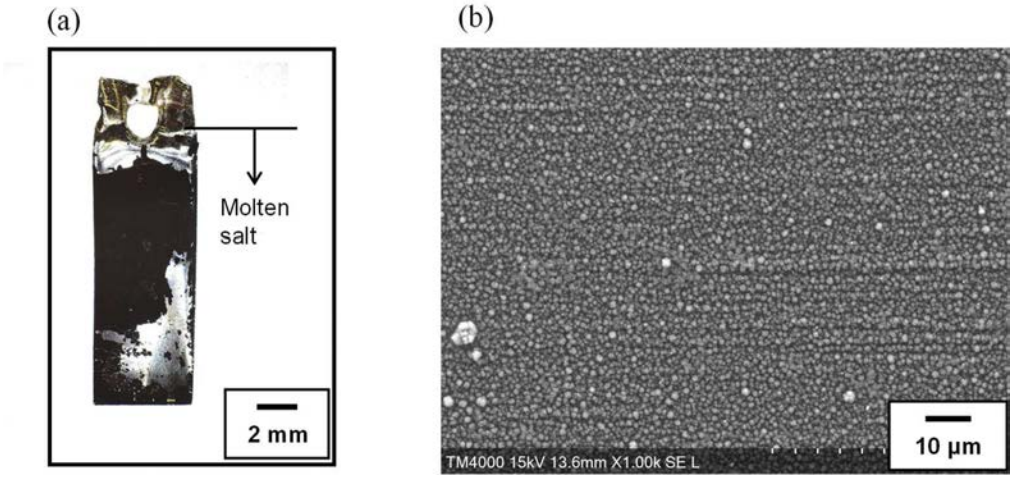

Figure 4. (a) A microscopy and (b) an SEM image of the electrodeposits obtained on the Ag plate electrode by potentiostatic electrolysis at 1.3 V vs. Li^+/Li, Q = −10 C in a LiCl–KCl–KBF_4 at 723 K.

Conclusion

Electrochemical reduction behavior of B(III) was investigated in molten LiCl–KCl–KBF_4 at 723 K. A comparison of cyclic voltammograms for Ni, Mo, and Ag electrodes suggested the formation of Ni–B compounds in addition to the reduction of B(III) to B(0) on the Ni electrode. Formation of Ni_2B was confirmed by XRD analysis of the Ni electrode after potentiostatic electrolysis at 1.3 V. Ag was selected as the substrate because the phase diagram did not have any alloys of Ag and B. Potentiostatic electrolysis was conducted at 1.3 V for the Ag plate electrode. In both cases, granular deposits, supposed to comprise amorphous B, on the substrates were observed by SEM. However, the chemical composition and valency of B in the deposit were not confirmed. Thus, further analysis and experiments are needed to clarify the behavior of B.

Acknowledgement

This work was partly supported by the New Energy and Industrial Technology Development Organization (NEDO) of Japan.

References

1. T. Oishi, H. Konishi, T. Nohira, M. Tanaka, and T Usui, *Kagaku Kogaku Ronbunshu*, **36**, 299 (2010).
2. H. S. Cooper, *US Pat*, 2, 369, 214 (1945).
3. L. P. Polyakova, G. A. Bukatova, E. G. Polyakov, E. Christensen, J. H. von Barner, and N. J. Bjerrum, *J. Electrochem. Soc.*, **10**, 3178 (1996).
4. Q. Wang, Y. L. Wang, H. J. Liu, and C. L. Zeng, *RSC Adv.*, **6**(61), 55953 (2016).

5. S. Majumdar, *J. Electrochem. Soc.*, **167**, 062507 (2020).
6. T. Oishi, M. Yaguchi, Y. Katasho and T. Nohira, *Rare metal technology 2020*, 151 (2020).
7. K. Shobu, *Calphad*, **33**(2), 279 (2009) and its website <https://sites.google.com/site/catcalcphase/metal/b/b-ag> (Access 2020/08/03)

Chapter 4

L02 – Power & Energy Applications

ECS Transactions, 98 (10) 63-71 (2020)
10.1149/09810.0063ecst ©The Electrochemical Society

Electrical Conductivity of Ceria-based Oxides/ Alkali Carbonate Eutectics Nanocomposites

Minoru Mizuhata[a,b], Hiroshi Kubo[a], Yudai Ichikawa[a],
Hideshi Maki[a,c], and Matsui Masaki[a]

[a] Department of Chemical Science and Engineering, Graduate School of Engineering, Kobe University, Kobe 657-8501, Japan
[b] Faculty of Chemistry, Jagiellonian University ul. Gronostajowa 2, 30-387 Kraków, Poland
[c] Environment Management Center, Kobe University, Kobe 657-8501, Japan

Thermal properties and the electrical conductivity for the SDC / ternary carbonate coexisting system was measured and the influence of the solid phase was discussed. In the ceria-based oxide/carbonate coexistence system, the melting enthalpy of carbonate disappeared when the liquid phase volume fraction was less than 45 vol%, and the melting point decreased due to the influence of the solid phase. The activation energy of conductivity increases in the region where the apparent average thickness is approximately 0.5 nm or less, the carbonate is significantly affected by the solid phase in a very narrow range, and the ceria-based oxide causes ion migration in the interface layer. It became clear that it did not inhibit. From these results, it was clarified that the low temperature characteristics are remarkably improved although the influence of the solid phase on the ionic conduction is limited.

Introduction

At present, the problems of global warming and depletion of fossil fuels have become major problems on a global scale. There is a need for a highly efficient power generation device that does not emit greenhouse gases such as carbon dioxide. In particular, there is an advantage that high-temperature fuel cells such as solid oxide fuel cells (SOFC) and molten carbonate fuel cells (MCFC) operate at high temperatures, so they are highly efficient and do not require expensive precious metal catalysts such as platinum as electrode materials (1). However, operation at high temperature leads to deterioration of the cell and is not suitable for long-term use. Therefore, in order to reduce the corrosion and improve the durability of the materials in the cell equipment, numerous research for the eutectic molten salt composite with fine powder at lower temperature operations have been carried out. Yttria-stabilized zirconia (YSZ) has been used as the electrolyte material for conventional SOFCs, but the operating temperature must be 1273 K or higher to obtain sufficient electrical conductivity when YSZ is used as the electrolyte. So, trivalent Sm and Gd-doped ceria-based oxides (SDC or GDC) are of interest. It is known that ceria has oxygen ion conductivity by doping with trivalent ions like zirconia, and has sufficient oxygen ion conductivity even in the intermediate temperature range of 773-973 K. However, Ce^{4+} is easily reduced to Ce^{3+} under H_2 atmosphere and shows electron conductance (2). Furthermore, it is known that the open circuit voltage is reduced and the

electrolyte is reduced and expanded due to electron conduction, and it is difficult to use it as a single electrolyte at a sufficiently high temperature.

In recent years, a ceria-based oxide/carbonate composite electrolyte obtained by adding a carbonate having an electron-insulating property to a ceria-based oxide has attracted attention. In such a composite electrolyte, the molten carbonate is used in a state of being impregnated with the oxide, and an interface layer is formed between the solid oxide and the carbonate due to the interaction between the solid and the liquid. This interface layer is considered to play an important role in improving the electrical conductivity, and it is considered that a behavior of carbonate different from that of bulk (3-6). H^+, O^{2-}, and CO_3^{2-} are considered as the ionic species for ionic conduction in the ceria-based oxide/carbonate composite electrolyte, which shows high ionic conduction in the medium temperature range (673-1023 K). Among these ionic species, H^+ and O^{2-} are considered to have ion conduction paths in the interface layer, and the mechanism of ion conduction called the Swing model or "gear" mechanism was proposed(7-9). Although these ionic conduction mechanisms are rational to explain the improvement of ionic conduction, little detailed research has been done on the state of carbonate at the interface. Therefore, further studies are needed on the behavior of carbonates on solid surfaces and how the interactions contribute to ionic conduction at intermediate temperatures. Therefore, the behavior of carbonates existing in the vicinity of solids has been investigated using a ceria-based oxide having a large specific surface area synthesized by the Pechini method, which is one of the complex polymerization methods, in the solid phase (10, 11). We have been using Sm-doped CeO_2 (SDC), which is a ceria-based oxide doped with CeO_2 and Sm at a ratio up to 20 mol%, and a composite material using a eutectic salt of alkali-metal carbonates. As a result of thermophysical property measurement and electric conductivity measurement, it has been reported that the molten carbonate is affected by the solid phase, the enthalpy of fusion disappears, and contributes to the electric conductivity at lower temperature (12). In this study, CeO_2 and SDC nanoparticles prepared by the Pechini method (11) were used as the ceria-based oxide, and eutectic salts of Li_2CO_3, Na_2CO_3, and K_2CO_3 (LNK) were used as the carbonate. We measured thermal properties and the electrical conductivity for the SDC / ternary carbonate coexisting system and discussed the influence of the solid phase.

Experimental

Samples

Preparation of nanoparticles of CeO_2 and SDC. Cerium nitrate hexahydrate ($Ce(NO_3)_3 \cdot 6H_2O$ (Nacalai Tesque, Inc.) and samarium nitrate hexahydrate ($Sm(NO_3)_3 \cdot 6H_2O$ manufactured by Nacalai Tesque, Inc.) were dissolved in deionized distilled water, and a predetermined amount of citric acid (Nacalai Tesque, Inc.) aqueous solution and ethylene glycol (Nacalai Tesque, Inc.) was added as written in Ref.11 (11). An organic precursor was obtained by heating at 333 K for 12 hours and then at 573 K for 12 hours. Further, the precursor was calcined under air atmosphere at 673 K for 4 hours and vacuum dried at 473 K for 3 hours to obtain CeO_2 and SDC10 and SDC20 with Sm ratio of 10 and 20 mol %. The obtained oxide sample was stored in a glove box under an argon atmosphere.

Preparation of LNK eutectic carbonate. Lithium carbonate (Li_2CO_3: Nacalai Tesque Co., Ltd.), sodium carbonate (Na_2CO_3 : Kishida Chemical Co., Ltd.) and potassium carbonate (K_2CO_3: Nacalai Tesque Co., Ltd.) were used. It was dried for 48 hours under

CO_2 atmosphere at 473 K, respectively and kept in a glove box under an argon atmosphere. These carbonates were mixed so that the eutectic composition was Li_2CO_3:Na_2CO_3:K_2CO_3=32:35:33 in weight ratio, corresponded to $(Li_{0.435}Na_{0.315}K_{0.25})_2CO_3$, and this carbonate is abbreviated as LNK hereinafter. Table 1 shows the physical properties of LNK. The eutectic point is 670 K and Density is 2.32 gcm^{-1} (13).

Preparation of samples for measurement of ac impedance. LNK was mixed with CeO_2 or SDC using an agate mortar under an argon atmosphere so as to have a predetermined liquid phase volume fraction, to obtain LNK-CeO_2 or LNK-SDCs. The liquid volume fraction; φ, was calculated by the following equation.

$$\varphi = \frac{w_{salt} / d_{salt}}{w_{salt} / d_{salt} + w_{solid}/d_{solid}} \quad [1]$$

where w_{salt}, d_{salt}, w_{solid} and d_{solid} in the above equation are the weight and density of the carbonate melt, the weight and density of the solid phase, respectively. The mixed sample was pressure-formed at 60 MPa for 30 minutes, heated at 773 K in a carbon dioxide atmosphere for 1 hour, and the solid phase was impregnated with carbonate to prepare a tablet-shaped sample (12).

Evaluation of solid phase samples

SEM shape observation. A field emission scanning electron microscopy (FE-SEM) was used for surface observation of the prepared CeO_2 and SDC using JSM-6335F (JEOL Ltd). The accelerating voltage of the electron beam at the time of measurement was set to 15 kV, and in order to prevent the sample surface from being charged up, a carbon coater (Meiwa Shoji CC-40FM) was applied to the sample surface before observation.

Specific surface area. To measure the specific surface area of the prepared sample, a high-speed specific surface area/pore distribution measuring device (NOVA-2200e Quantachrome, Inc., USA) was used, and nitrogen adsorption/desorption isotherm was measured at 77 K in a relative pressure range of 0.05-0.1. As a pretreatment of the sample, it was dried in vacuum at 473 K for 5 hours. The specific surface area was determined by the BET method as an analytical method.

XRD measurement. X-ray diffraction measurement was performed on the prepared CeO_2 and SDC by the following method. For the measurement, X-ray diffraction measurement was performed using a fully automatic multipurpose horizontal X-ray diffractometer (Rigaku Smart Lab). The apparatus was set up with a tube voltage of 45 kV, a tube current of 200 mA, and the X-ray source was a CuKα1 (λ = 1.541Å) wire for the concentrated method. The measurement conditions were θ = 10 - 100°, scan speed; 2.0°/min, and scan step; 0.01°.

Evaluation of carbonate/ceria-based oxide coexisting system

Differential Thermogravimetric Analysis (TG-DTA). Using Thermo Plus Evo TG 8120 manufactured by Rigaku Corporation, thermal analysis was performed using α-Al_2O_3 as a Ref 12 [12]. The measurement conditions were temperature range 373-773 K, heating

rate 5 K/min, CO_2 atmosphere, and DTA range 100 μV.

AC impedance measurement. The electrical conductivity of the sample was measured by the AC impedance method. Figure 1 shows a schematic diagram of the electrochemical measurement device. A Hewlett Packard 4284A precision LCR meter was used for the measurement of the prepared tablet-shaped sample, and the electrode was an Au-Pd electrode (diameter: 10 mm, Au:Pd =90:10) was used. The measurement conditions were CO_2 flow (0.1 MPa, 50 ml/min), frequency range 25 Hz-1 MHz, temperature range 573-773 K, and applied voltage 0.6 V. In addition, the ionic conductivity was measured during heating process, and the data was analyzed using impedance analysis software (ZView Version 3.1c).

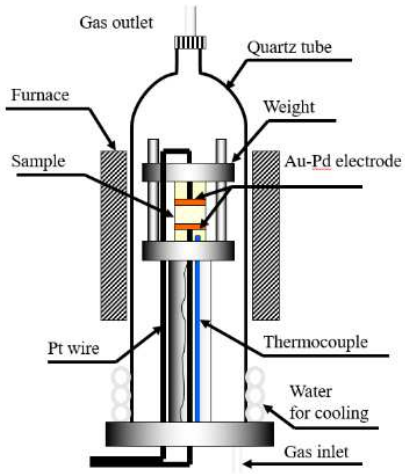

Figure 1. Apparatus for electric conductivity measurement.

Results and Discussion

Evaluation of fabricated CeO_2 and SDC

SEM observation. Figure 2 shows SEM images of CeO_2, SDC10, and SDC20. From these SEM images, it was confirmed that the particle size of both CeO_2 and SDC was about several tens nm, and the shape and particle size were not affected by the solid solution of Sm^{3+}.

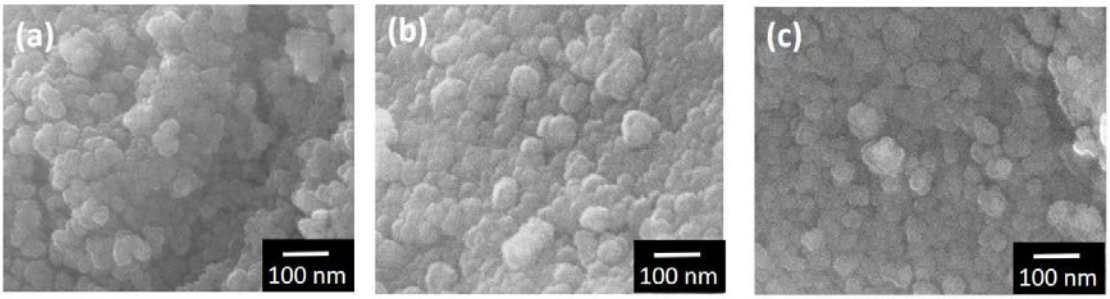

Figure 2. SEM images of CeO_2 and SDCs nanoparticles (a) CeO_2 (b) SDC10 (c) SDC20.

Evaluation of specific surface area by BET method. Table I shows the specific surface area obtained by the BET method. Similar to the shape, no proportional relationship was found between the solid solution of Sm^{3+} and the specific surface area, and it was confirmed that both CeO_2 and SDC have the same large specific surface area.

Table I. Specific surface area and density of powder sample.

Samples	Specific surface area/m^2g^{-1}	Density/gcm^3
CeO_2	90.1	7.09
SDC10	70.2	7.14
SDC20	63.1	6.96

XRD measurement. XRD measurement was performed to examine the crystal structures of the prepared CeO_2 and SDC. Fig. 3 (a) shows the XRD measurement results of each sample. The diffraction pattern assigned to CeO_2 indexed in ICDD PDF-4 database #34-0394 was confirmed for all the samples. Fig. 3(b) shows the magnified diffraction patterns assigned to the 111 plane of CeO_2, SDC10, and SDC20. In each diffraction pattern, it was confirmed that as the doping amount of Sm3+ increased, it shifted to the lower angle side. It is considered that this is because the ionic radius of Sm^{3+} was larger than that of Ce^{4+}, so that the interplanar spacing was widened, and it was confirmed that Sm^{3+} was properly doped.

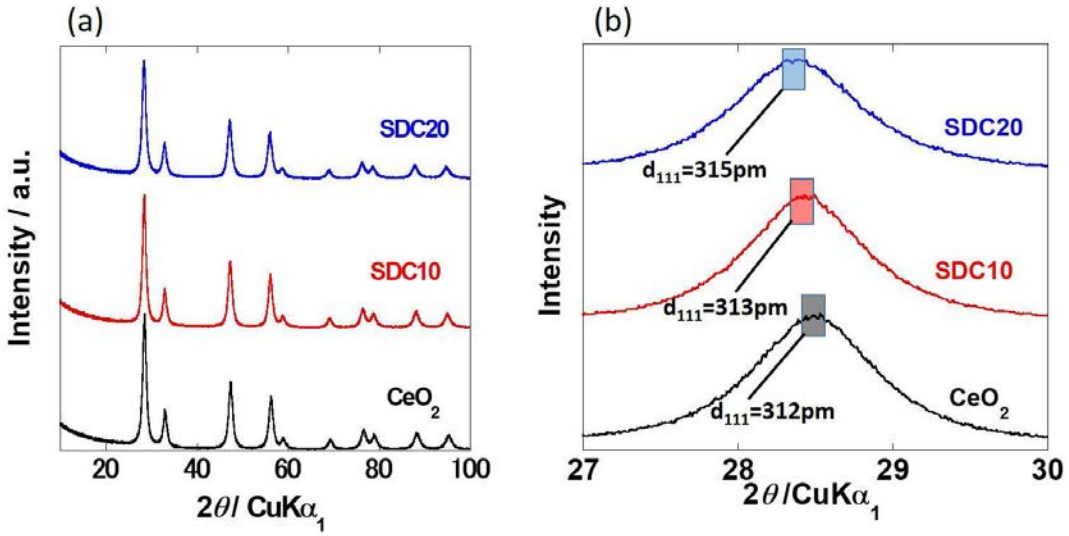

Figure 3. (a)XRD patterns and (b) detail profile for 111 of CeO_2 and SDCs nanoparticles.

Evaluation of LNK-CeO_2 and LNK-SDCs

Thermal analysis. In order to observe the phase transition of carbonate near the solid, thermal analysis measurement was performed in the ceria-based oxide/carbonate coexisting system. Figure 4 shows the DTA curve in the coexisting system of LNK and CeO_2, SDC10 and SDC20. In any system, the enthalpy change due to the melting of carbonate was not confirmed at the liquid phase volume fraction of 15-45 vol%, but appeared slightly at 55 vol%. Comparing with the past results of composite materials using eutectic salt of Li_2CO_3 and Na_2CO_3 in the liquid phase, enthalpy change due to melting

was confirmed even at liquid phase volume fraction of 35 vol% [12], and carbonate It is considered that the change from binary system to ternary system caused a change in the interaction between the solid phase and the liquid phase, resulting in a change in the liquid phase volume fraction where an endothermic peak appeared.

It is considered that the interaction between the solid phase and the liquid phase changed due to the change of the carbonate from the binary system to the ternary system, and the liquid phase volume fraction where the endothermic peak appeared changed. The eutectic point of LNK was found to be 671 K, and it was confirmed that the eutectic point was shifted to the low temperature side by the influence of the solid phase when mixed with CeO_2, SDC10, and SDC20. Also, at 45 and 55 vol% of LNK-SDC20, the ternary carbonate phase-separates into $LiKCO_3$, $LiNaCO_3$, etc., and each melts independently, resulting in a peak around 660 K and a peak of 690 K. It is considered that a slight change in enthalpy could be confirmed. From these results, it is considered that the larger the amount of Sm^{3+} doped, the easier the phase separation of carbonate, and the greater the influence on the thermal properties of carbonate.

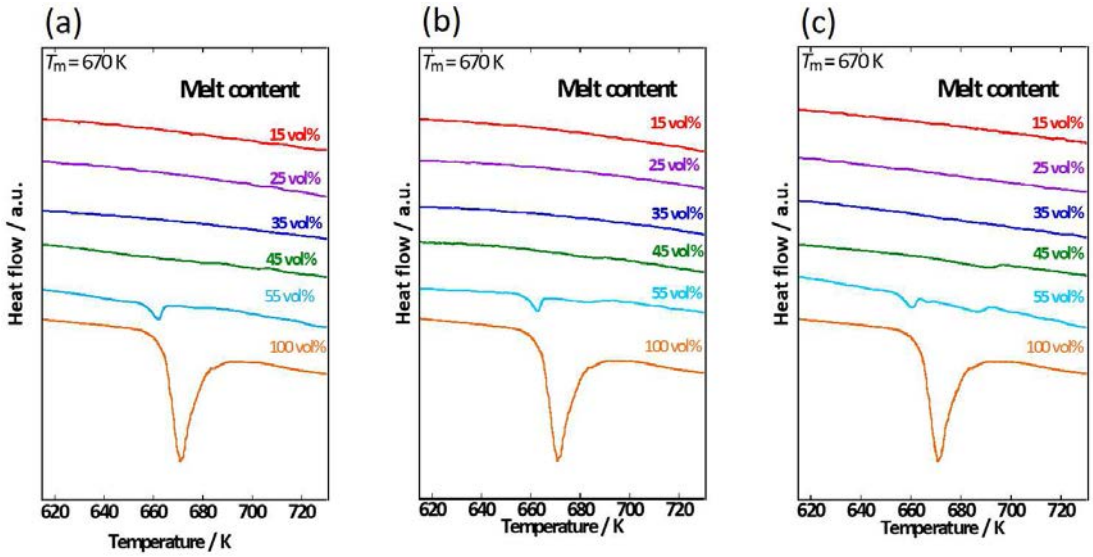

Figure 4. DTA curves of LNK coexisting with (a)CeO_2(90.1 m^2 g^{-1}), (b)SDC10 (70.2 m^2 g^{-1}), (c)SDC20 (63.1 m^2 g^{-1}) for each melt contents.

AC impedance measurement. Figure 5 shows the temperature dependence of ionic conductivity in the ceria-based oxide/carbonate coexisting system obtained from the results of AC impedance measurement. In LNK-CeO_2, only a few inflection points due to melting of the molten salt were observed in the samples with a liquid volume fraction of 35 vol% or less. At temperatures below the inflection point, the conductivity of 55 vol% is lower than the value of 25-45 vol%.This is because there is no inflection point in the 25 and 35 vol% sample, so it exists at the solid interface even below the eutectic point. This is because the carbonate that was used was in a molten state and the conductivity did not decrease even at low temperatures. In addition, inflection points associated with melting were observed in LNK-SDC10 at a liquid volume fraction of 15-55 vol% and in LNK-SDC20 at 45 and 55 vol%. In all systems, the inflection point associated with the melting of carbonate was confirmed at about 645 K, which was shifted to a temperature lower than

the melting point of the eutectic carbonate, similar to the measurement results of thermal analysis. It suggests that it was greatly influenced by the solid phase. In addition, in any of the samples with low liquid volume fraction, the temperature dependence of the electrical conductivity follows the VTF equation, and continuous bending is observed. This is considered to be bending due to the influence of free volume, such as the viscosity of the molten carbonate increasing due to the glass transition. Especially in the system of LNK-SDC20 composite, it was shown that the temperature dependence of VTF type with strong bending and the increase of T_0 were accompanied with the increase of the doping amount of Sm^{3+}.

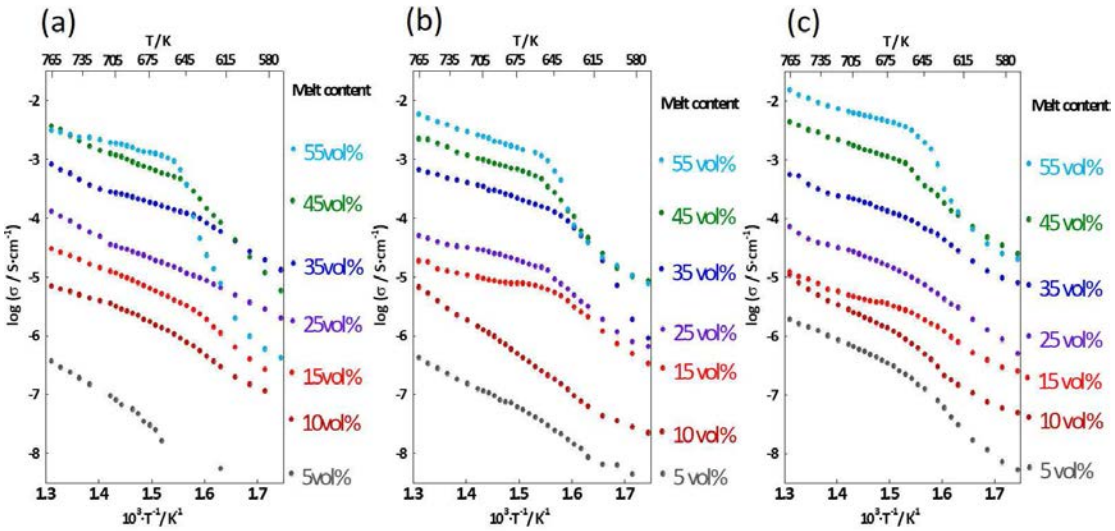

Figure 5. Temperature dependence of electrical conductivity for LNK coexisting with (a)CeO_2(90.1 m^2 g^{-1}), (b)SDC10 (70.2 m^2 g^{-1}), and (c)SDC20 (63.1 m^2 g^{-1}).

Apparent average thickness and activation energy. Introducing the apparent average thickness to estimate how far the effect of the solid phase will reach in the liquid phase. Apparent average thickness is defined as

[Apparent average thickness]
= [Total volume of liquid phase] / [Total surface area of solid phase] [2]

It has a dimension of length and represents the thickness of the liquid layer on the solid surface.The activation energy was calculated from the graph in Fig. 5 using the following VTF equation.

$$\log \sigma = AT^{-1/2} \exp[-B/(T-T_0)] \quad [3]$$

where T_0 is the glass transition point, and A and B are constants. Figure 6 shows a graph of the relationship between the apparent average thickness of the liquid phase and the activation energy of electrical conductivity; ΔE_a. The activation energy; ΔE_a, increased as the apparent average thickness decreased, and increased sharply in the region where the apparent mean thickness was about 0.5 nm or less. Therefore, it was revealed that carbonate was significantly affected by solids in a very narrow range, suggesting that the ceria-based oxide did not inhibit ion transfer in the interfacial layer.

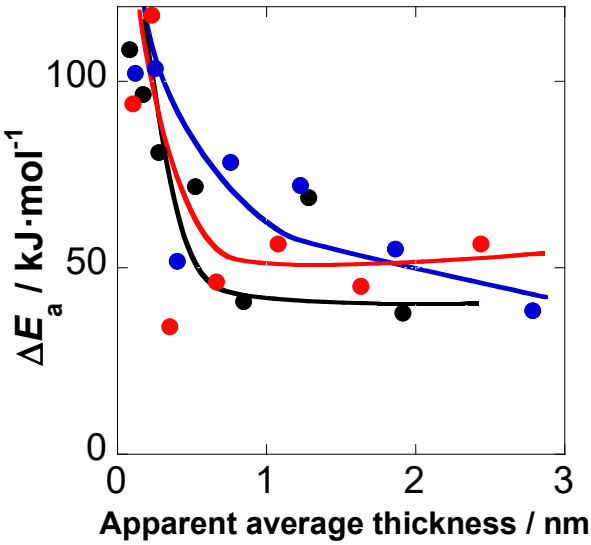

Figure 6. The variation of activation energy; ΔE_a, of the electrical conductivity with apparent average thickness for Ceria-based oxide / LNK composite systems.

Dependence of conductivity on liquid content. Fig. 7 shows changes in conductivity at various temperatures depending on the liquid volume fraction. At 673 K and 723 K, all carbonates were in a molten state, so that the conductivity increased as the amount of liquid phase increased in all these systems due to the increase in the number of carrier ions moving in the electrolyte. On the other hand, at the temperature below the eutectic point (623 K, 583 K), the maximum conductivity was confirmed. When the liquid phase volume fraction is high, a large amount of bulk carbonate is present, and in the region below the eutectic point, many parts are crystallized. Ionic conduction is difficult to occur in this region, and the ions melt even at low temperatures at the solid-liquid interface It is considered that the region moves in the state, and by increasing the solid phase, the region in the molten state is maintained toward lower temperate range, the conductivity increases, and the conductivity becomes maximum. In LNK-CeO_2, maximum values appeared at 623 K at 45 vol% and at 583 K at 35 vol%.

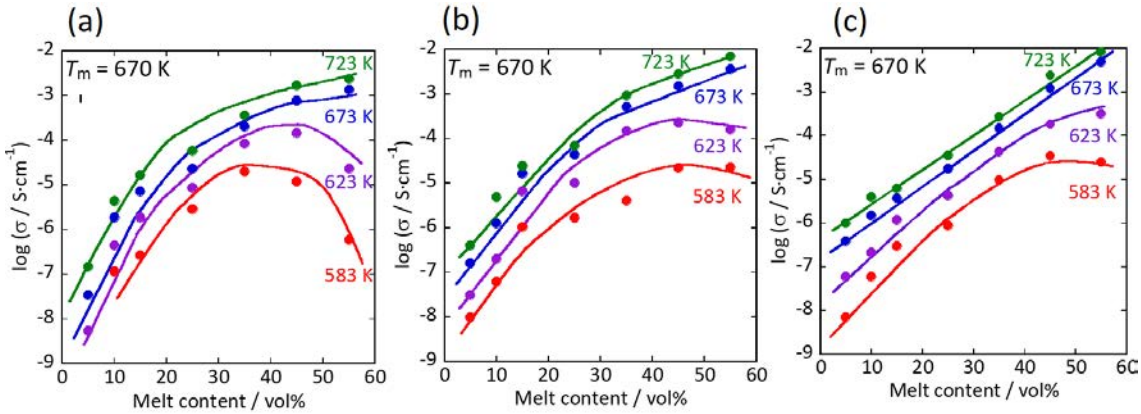

Figure 7. Variation of conductions for LNK coexisting with (a)CeO_2(90.1 m^2 g^{-1}), (b)SDC10 (70.2 m^2 g^{-1}), and (c)SDC20 (63.1 m^2 g^{-1}) at various temperatures.

It is considered that the conductivity was decreased because the number of carrier ions was decreased and the conduction path was interrupted when the solid phase was further increased. However, in LNK-SDC10 and LNK-SDC20, ions do not move easily even if the solid phase is increased due to the effect of the free volume of the molten carbonate due to the glass transition, the conductivity does not rise so much, and the maximum value like LNK-CeO[2]. It is believed that it did not appear clearly. In addition, since the position of the maximum value shifts to the larger liquid phase volume fraction as the Sm^{3+} content increases, it is suggested that the conductivity is affected by the Sm^{3+} content of the coexisting solid oxide.

Summary

Thermal properties and the electrical conductivity for the SDC / ternary carbonate coexisting system was measured and the influence of the solid phase was discussed. From the DTA measurement results, it was confirmed that in the ceria-based oxide/carbonate coexistence system, the melting enthalpy of carbonate disappeared when the liquid phase volume fraction was less than 45 vol%, and the melting point decreased due to the influence of the solid phase. From the results of AC impedance measurement, the inflection point due to melting was about 645 K in all systems, but there was a difference in the liquid phase volume fraction where the inflection point appeared, and there was a difference in the mutual interaction with carbonate due to Sm^{3+} doping. It was suggested that the action changed and that the higher the proportion of Sm^{3+}, the more the temperature dependence of VTF type was shown. In addition, the activation energy greatly increases in the region where the apparent average thickness is approximately 0.5 nm or less, the carbonate is significantly affected by the solid phase in a very narrow range, and the ceria-based oxide causes ion migration in the interface layer. It became clear that it did not inhibit From these results, it was clarified that the low temperature characteristics are remarkably improved although the influence of the solid phase on the ionic conduction is limited.

References

1. N. Laosiripojana and S. Assabumrungrat, *J. Power Sources*, **163**, 943 (2007).
2. D. J. L. Brett, A. Atkinson, N. P. Brandon, and S. J. Skinner, *Chem. Soc. Rev.*, **37**, 1568 (2008).
3. M. Mizuhata and S. Deki, *J. Rare Earths*, **23**, 1 (2005).
4. M. Mizuhata T. Ohta, and S. Deki, *Electrochemistry*, **77**, 721 (2009).
5. M. Mizuhata, T. Ohashi, and A. B. Bèlèkè, *Int. J. Hydrog. Energy*, **37**, 19407 (2012).
6. M. Mizuhata, K. Takeda, and H. Maki, *ECS Trans.*, **64(4)**, 45 (2014).
7. X. Wang, Y. Ma, S. Li, A.-H. Kashyout, B. Zhu, and M. Muhammed, *J. Power Sources*, **196**, 2754 (2011).
8. C. Qin and A. Gladney, *Comput. Theor. Chem.*, **999**, 179 (2012).
9. X. Lei, K. Haines, K. Huang, and C. Qin, *J. Power Sources*, **305**, 161 (2016)
10. L. Spiridigliozzi, M. Biesuz, G. Dell'Agli, E. Di Bartolomeo, F. Zurio, and V. M. Sglavo, *J. Mater Sci.*, **52**, 7479 (2017).
11. P. Ramos-Alvarez, M. E. Villafuerte-Castrejon, G. Gonzalez, M. Cassir, and C. Flores-Morales, J. A. Chavez-Carvayar, *J. Mater. Sci.*, **52**, 519 (2017).
12. M. Mizuhata, H. Kubo, H. Maki, and M. Matsui, *ECS Trans.*, **86(14)**, 101 (2018).
13. M. Kenisarin, *Renew. Sust. Energ. Rev.*,**14**, 955 (2010).

ECS Transactions, 98 (10) 73-87 (2020)
10.1149/09810.0073ecst ©The Electrochemical Society

A Comparative Study of Imidazolium-Based Ionic Liquid-Single-Walled Carbon Nanotube Composites with Enhanced Conductivity Properties for Supercapacitor Applications

Tirandai Hemraj-Benny[a], Sharon I. Lall-Ramnarine[a], Sophia N. Suarez[b], Domenec Paterno[b], Jasodra D. Ramdihal[a], Rawlric Sumner[a], Katelyn Urena[a], and James F. Wishart[c]

[a]Department of Chemistry, Queensborough Community College of the City University of New York, Bayside, New York 11364, USA
[b]Department of Physics, Brooklyn College of the City University of New York, Brooklyn, New York 11210, USA
[c]Chemistry Division, Brookhaven National Laboratory, Upton, New York 11973, USA

Mixtures of ionic liquids (ILs) containing single-walled carbon nanotubes (SWCNTs) were prepared and characterized to obtain electrolytes with optimized transport properties for use in energy storage devices such as supercapacitors. Imidazolium ILs bearing cations with side chains of different functionality, coupled with bis(trifluoromethylsulfonyl)amide (NTf_2^-) or bis(fluorosulfonyl)-amide (FSA^-) anions, were used in mixtures containing up to 5 wt% SWCNTs. At and above 2 wt% nanotube loading, the mixtures exhibited higher conductivities than the pure ILs, in spite of the extremely high viscosities. Loadings of 5 wt% produced very high conductivities, and studies of the temperature dependence indicated a change in the charge transport mechanism between 2 and 5 wt% loading. At 5 wt% loading, the highest conductivities (up to 540 mS/cm at 25 °C) were obtained for the ILs containing the NTf_2^- anion. These results can significantly contribute to the development of improved energy storage devices.

Introduction

Due to growing global environmental concerns, there are increasing demands for environmentally-friendly, efficient, renewable energy storage devices (1-3). Batteries, fuel cells, and supercapacitors are useful energy storage devices that function on the principle of electrochemical energy conversion (1). Supercapacitors have many improved properties over batteries and fuel cells, which include higher power density, shorter charge time, and longer life cycles, and thus they have various potential applications (1-5). Supercapacitors can be used as power supplies in small portable devices, and they can be used to provide energy in rural areas where costly electrical infrastructures are not available. Moreover, supercapacitors have great potential in electric and hybrid vehicles due to their high power density, which is required for short-term acceleration and recovery of energy during braking (1). Still, the main hindrance to more extensive usage of supercapacitors is their modest energy densities (~0.005 to ~10 W h/kg) (2, 6), which are accomplished through either their electric double layers or Faradaic reaction charge storage mechanisms. The energy density E is determined by the specific capacitance C and the maximum working voltage V through the relationship: $E = ½ CV^2$. Generally, C is related to the electrode and

electrolyte properties, while *V* depends on those of the electrolyte. Therefore, the choice of electrode-electrolyte combination is extremely important in the performance and potential applications of the resulting supercapacitor.

For optimal operation, supercapacitors require electrodes with high surface area, high conductivity, and suitable temperature and chemical stability (1, 3, 7). Carbon-based nanomaterials have been considered as promising electrodes for supercapacitors due to their unique high surface area, high conductivity and stability properties, and low cost (1, 4, 8, 9). Nevertheless, activated carbon and reduced graphene oxide electrodes have shown weak performance, respectively due to their irregular pore structure and lack of restacking ability during chemical processes, which prevents the availability of maximum surface area to the electrolyte ions, thereby limiting charge storage (1, 4, 10).

Carbon nanotubes can serve as more efficient electrodes in supercapacitors (10). A single-walled carbon nanotube (SWCNT) consists of a single graphene sheet seamlessly wrapped into a cylindrical tube (0.4 nm to 3 nm in diameter with lengths up to micrometers) which can be either metallic or semiconducting depending on its diameter and chirality (11). SWCNTs of various diameters are found in bundles held together by strong van der Waals forces in a 'spaghetti' network (10, 12). It is expected that electrical transport in such materials is dominated by the contained metallic nanotubes (13). In fact, the electrical conductivity of SWCNTs has been reported to range between 10^2 to 10^6 S/cm (14). Multi-walled carbon nanotubes (MWCNTs) are made of concentric cylinders placed around a common central core with outer diameters ranging from 5 to 100 nm and lengths of tens of microns (15, 16). In general, carbon nanotube electrodes in electrochemical devices have lower equivalent series resistance than activated carbon, and they have substantial capacitance (~15 to ~200 F/g) because electrolyte ions can easily penetrate the mesoporous network of the nanotubes where small separations of about one nanometer exist between the charge on carbon nanotube electrodes and the countercharge in the electrolytes (4, 8, 9, 15, 17). SWCNTs are considered to be superior to MWCNTs for energy storage applications due to their higher surface area (smaller diameter), and improved purity, structural integrity, and capacitance (180 and 102 F/g for SWCNT and MWCNT electrodes, respectively) (12, 15, 17, 18).

Optimized electrolytes for supercapacitors should have a wide potential window, high ionic conductivity, excellent electrochemical stability, small solvated ion radius, low equivalent series resistance, and low volatility and viscosity (19). Common supercapacitor electrolytes include aqueous solutions, organic solutions, and ionic liquids. Whereas the main limitation for aqueous electrolytes such as KOH and H_2SO_4 is their small potential window due to water decomposition (~ 1.2 V), the limitation for organic solvents such as acetonitrile lies in their high vapor pressure and flammability (2, 20, 21). Ionic liquids are optimal electrolytes for supercapacitors because of their low volatility, excellent thermal stability, and wide working voltage windows (22). However, they suffer from relatively low ionic conductivities, which directly affects their high-power output and energy density.

The combination of ILs with SWCNTs presents researchers with materials having the attributes of the individual components as well as the expanded range of applications due to their tunable softness and electroconducting and thermoconducting properties (23, 24). While there have been numerous molecular dynamics simulations studies on these systems (25), there is a lack of experimental data in the literature. Although there are variations in

the results, a common theme that has emerged is the local IL/SWCNT environment having a higher-density, layered ion arrangement at the interface (26). Generally, when a liquid is confined to a solid surface, the resulting molecular arrangement differs from the bulk due to the combination of the restrictions in mobility of the ions at the solid interface, and the Coulombic interactions that exist between them and the counterions of the neighboring liquid interface. Inside the SWCNT, these result in 'solid-like' or 'solvation layers' that can extend for several molecular diameters from the interface (27, 28). This ordering of the liquid into 'solvation layers' is characterized by an oscillatory molecular density profile and is a common feature for many liquids, including polymer melts and molecular liquids (27). As you move away from the interface, the packing density decreases (29). This was the case for hexylmethylimidazolium bis(trifluoromethylsulfonyl)amide (Hmim NTf_2) IL inside a (20,20) CNT (29), and ethylmethylimidazolium tetrafluoroborate (Emim BF_4) inside (*n*,*n*) SWCNTs (30). In addition to this is the bulk IL environment, which numerous studies have shown depends on the combination of anion and cation (31, 32). It should be noted that there are two interfaces – inside and outside the SWCNT and that the behavior of the IL at the interfaces can differ depending on its characteristics, as well as those of the SWCNT.

ILs with imidazolium cations ($Rmim^+$) exhibit attractive properties for energy storage applications such as relatively lower viscosities and higher conductivities than most ammonium and pyrrolidinium ILs, and electrochemical windows greater than 4 V (20, 21). Moreover, imidazolium ILs are excellent solvents for the dispersion of SWCNT bundles. Imidazolium ILs have a strong affinity towards the π-electronic SWCNT surfaces, thus disrupting π-π stacking interactions among SWCNTs and enabling the unraveling of the nanotube bundles (24, 33, 34). However, there are few studies that specifically investigate the relationship between increased ionic conductivity of imidazolium ILs upon the incorporation of single-walled carbon nanotubes, which leads to improved energy densities in supercapacitors. Recently, Kong et al. observed that the addition of SWCNTs to Emim BF_4 (electrochemical window 4.2 V) directly improved the ionic conductivity of the IL, and consequently increased the capacitance, energy density and cycling stability of a supercapacitor (35). Specifically, 0.5 wt% SWCNTs were dispersed in Emim BF_4 by a sonication method, and a 38 % increase in ionic conductivity of the pure IL to 26 mS cm^{-1} was observed. The IL-SWCNT mixture exhibited a higher energy density (35 Wh/kg) than the pure Emim BF_4 IL (30 Wh/kg) at a power density of 30 W/kg. While this reported 17% performance increase upon adding SWCNTs to an IL is modest, we undertook the present study in the belief that better results could be obtained at higher SWCNT loadings, and that the role of imidazolium cation functional groups in mediating IL-SWCNT interactions should be studied in order to optimize mixture performance.

In this work, we investigate the effect of cation and anion types, and SWCNT concentration, on the ion transport properties of the IL-SWCNT mixtures. It is well known that the ionic conductivities of pure ILs can be altered by varying the side chains on the imidazolium cation ring (36-38). In addition, various IL anions have different de-bundling effects on single-walled carbon nanotubes, which may alter the conductivity properties of SWCNT-IL mixtures differently (34). In addition to the limited fundamental experimental data available on IL-SWCNT mixtures, there is also a knowledge gap concerning the influence of varying the side chains of the imidazolium cation on the conductivity properties of IL-SWCNT composites. Therefore, for the first-time temperature-dependent electrochemical impedance spectroscopy (EIS) measurements were performed to

understand the electron transfer properties of composites containing varying concentrations of SWCNTs in combination with ILs composed of $Rmim^+$ cations bearing side chains with different functionalities, (R = butyl (B), allyl (A), and 2-methoxyethyl (EOM)), coupled with NTf_2^- or bis(fluorosulfonyl)amide (FSA^-) anions (Figure 1).

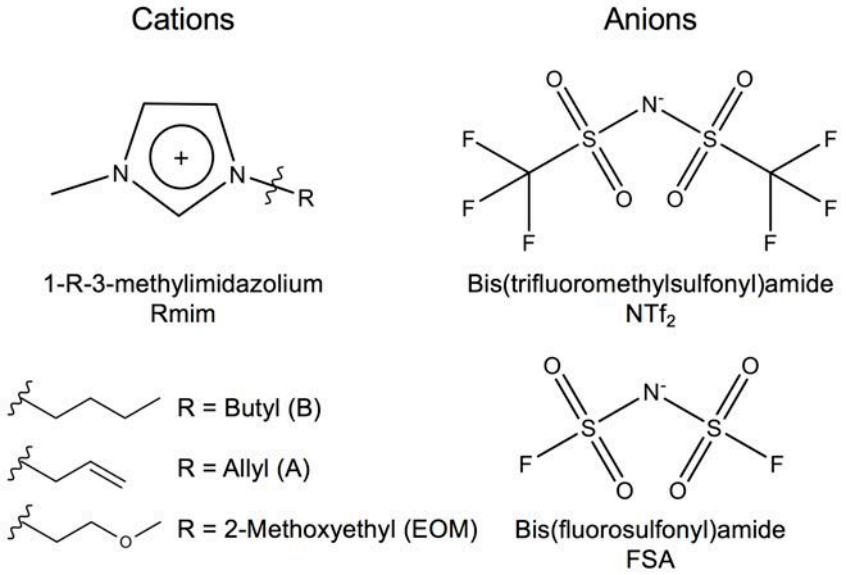

Figure 1. Structures of the ions used in this study.

The three functionalities were selected to vary the interionic interactions within the IL and the interactions between the IL cation and the SWCNT. $Bmim^+$ cation represents a standard 1-alkyl-3-methylimidazolium cation for baseline comparison, with an alkyl chain length short enough that the bulk IL is not divided into separate polar and non-polar domains (31) for better comparison to the other cations. $Amim^+$ cation includes a second unsaturated moiety in addition to the imidazolium cation head, to provide additional means of π-π interactions between the cation and the SWCNT. Ether-functionalized ILs containing cations such as $EOMmim^+$ are structured differently than their alkyl congeners because the ether group competes with the NTf_2^- or FSA^- anion for hydrogen bonding at the ring proton positions, with both intra- and intermolecular H-bonding modes (39-43). This difference in structure for the $EOMmim^+$ ILs may affect the way in which the cations interact with the SWCNT.

This study is one part of a series aimed at deciphering the IL-SWCNT interactions that govern the ion dynamics in these mixtures. Here we will focus almost exclusively on the ionic conductivity data, but our future publications will include temperature-dependent viscosity measurements as well as spectroscopic (Mid-IR and Raman) analyses.

Experimental

Materials. SWCNTs (CoMoCAT) (with a purity of > 95%, averaged diameter of 0.78 nm, median tube length of 1.5 μm, and specific surface area of 790 m^2/g) were obtained from Sigma Aldrich and were used without further purification. All chemicals used for the ionic liquid syntheses including 1-allyl-3-methylimidazolium chloride were of reagent grade, obtained from Sigma-Aldrich and used as received. ^1H and ^{13}C NMR spectra were recorded

on a Bruker 400 MHz NMR spectrometer. Water contents of the synthesized pure ionic liquid samples were ≤ 70 ppm, as determined using a Mettler Toledo DL39 Karl Fischer Coulometer.

Ionic Liquid Synthesis

1a. Synthesis of 1-butyl-3-methylimidazolium bromide (Bmim Br)
1-methylimidazole (19.87 g, 0.2419 mol) dissolved in 50 mL acetonitrile was reacted with 10% excess of 1-bromobutane (34.80 g, 0.0.2540 mol) dissolved in 50 mL acetonitrile in a round bottom flask fitted with a stir bar and reflux condenser. The reaction was initiated at room temperature and left to stir for 3 days at 60 °C. The reaction mixture was rotary evaporated and the resulting product was washed with ethyl acetate. The final product was a pale-yellow liquid (50.33 g, 95 %, molar mass: 219.12 g/mol). ^{1}H (400 MHz; D_2O) δ 0.94-0.98 (t, 3H), 1.32-1.41 (m, 2H), 1.86-1.93 (m, 2H), 3.94 (s, 3H), 4.23-4.27 (t, 2H), 7.48 (d, 1H), 7.54 (d, 1H), 8.77 (s, 1H); ^{13}C (101 MHz; D_2O) δ 12.71, 18.79, 31.30. 33.28, 49.32, 122.20, 123.45, 135.84.

2a. Synthesis of 1-(2-methoxyethyl)-3-methylimidazolium bromide (EOMmim Br)
1-methylimidazole (10.00 g, 0.1218 mol) dissolved in 25 mL acetonitrile was reacted with 10% excess of 2-bromoethylmethylether (18.62 g, 0.1218 mol) dissolved in 25 mL acetonitrile in a round bottom flask fitted with a stir bar and reflux condenser. The reaction was initiated at room temperature and left to stir for 5 days at 40 °C. The reaction mixture was rotary evaporated and the resulting product was washed with ethyl acetate. The final product was a pale-yellow liquid (24.52 g, 92 %, molar mass: 221.10 g/mol). ^{1}H (400 MHz; D_2O) δ 3.26 (s, 3H), 3.67-3.70 (t, 2H), 3.88 (s, 3H), 4.36-4.39 (t, 2H), 7.75 (d, 1H), 7.79 (d, 1H), 9.22 (s, 1H); ^{13}C (101 MHz; D_2O) δ 35.76, 48.58, 58.05, 69.56, 122.58, 123.42, 136.78.

Preparation of Bis(trifluoromethylsulfonyl)amide Ionic Liquids

1b. Synthesis of 1-butyl-3-methylimidazolium bis(trifluoromethylsulfonyl)amide (Bmim NTf_2):1-butyl-3-methylimidazolium bromide (40.11 g, 0.1830 mol) dissolved in 90 mL deionized water was reacted with one equivalent of lithium bis(trifluoromethylsulfonyl)amide (52.56 g, 0.1830 mol) dissolved in 60 mL deionized water in a round bottom flask containing a stir bar. The reaction mixture was left to stir at room temperature for 24 hours. The resulting ionic liquid was washed with deionized water until the wash tested negative for residual bromide with 50 mM aqueous silver nitrate. The product was rotary evaporated and dried in a high vacuum oven at 60 ˚C for several days. The final product was a pale yellow, viscous liquid (71.94 g, 94 %, molar mass: 419.475 g/mol, water content: 23 ppm). ^{1}H (400 MHz; DMSO-d_6) δ 0.89-0.93 (t, 3H), 1.24-1.30 (m, 2H), 1.74-1.81 (m, 2H), 3.85 (s, 3H), 4.15-4.18 (t, 2H), 7.48 (d, 1H), 7.54 (d, 1H), 8.77 (s, 1H); ^{13}C (101 MHz; DMSO-d_6) δ 13.10, 18.70, 31.30, 35.63, 48.47, 114.64, 117.84, 121.04, 122.18, 123.54, 124.34, 136.45.

2b. Synthesis of 1-(2-methoxyethyl)-3-methylimidazolium bis(trifluoromethylsulfonyl) amide (EOMmim NTf_2)
1-(2-methoxyethyl)-3-methylimidazolium bromide (16.71 g, 0.07558 mol) dissolved in 20 mL deionized water was reacted with one equivalent of lithium bis(trifluoromethyl-sulfonyl)amide (21.71 g, 0.07558 mol) dissolved in 25 mL deionized water in a round

bottom flask containing a stir bar. The reaction mixture was left to stir at room temperature for 24 hours. The resulting yellow ionic liquid was washed with deionized water until the wash tested negative for bromide with 50 mM aqueous silver nitrate. The product was rotary evaporated and dried in a high vacuum oven at 60 °C for several days. The final product was a pale-yellow viscous liquid (26.93 g, 85 %, molar mass: 421.33 g/mol, water content: 26 ppm). ^{1}H (400 MHz; DMSO-d_6) δ 3.08 (s, 3H), 3.67-3.70 (t, 2H), 3.88 (s, 3H), 4.37-4.39 (t, 2H), 7.49 (d, 1H), 8.00 (d, 1H), 9.24 (s, 1H), ^{13}C (101 MHz; DMSO-d_6) δ 36.2, 49.1,58.5, 60.2, 70.1, 114.6, 117.8, 121.0, 123.1, 123.9, 124.2, 137.3.

3b. Synthesis of 1-allyl-3-methylimidazolium bis(trifluoromethylsulfonyl)amide (Amim NTf_2)

1-allyl-3-methylimidazolium chloride (25.00 g, 0.1576 mol) dissolved in 30 mL deionized water was reacted with one equivalent of lithium bis(trifluoromethylsulfonyl)amide (45.26 g, 0.1576 mol) dissolved in 50 mL deionized water in a round bottom flask containing a stir bar. The reaction mixture was left to stir at room temperature for 24 hours. The resulting ionic liquid was washed with deionized water until the wash tested negative for residual chloride using 50 mM aqueous silver nitrate. The product was rotary evaporated and dried in a high vacuum oven at 70 ˚C for 48 hours. The final product was a very pale yellow, viscous liquid (59.79 g, 94%, molar mass: 403.31 g/mol, water content: 10 ppm). ^{1}H (400 MHz; DMSO-d_6) δ 3.85 (t,3H), 4.83-4.84 (d, 2H), 5.28-5.38 (m, 2H), 5.99-6.09 (m, 1H), 7.69 (d, 1H), 7.70 (d, 1H), 9.09 (1H, s), ^{13}C (101 MHz; DMSO-d_6) δ 35.77, 50.81, 114.70, 117.90, 120.13, 121.10, 122.34, 123.77, 124.29, 131.67, 136.64.

Preparation of Bis(fluorosulfonyl)amide Ionic Liquids

1c. Synthesis of 1-butyl-3-methylimidazolium bis(fluorosulfonyl)amide (Bmim FSA)

1-butyl-3-methylimidazolium bromide (20.00 g, 0.09127 mol) dissolved in 30 mL deionized water was reacted with one equivalent of lithium bis(fluorosulfonyl)amide (20.01 g, 0.09127 mol) dissolved in 30 mL deionized water in a round bottom flask containing a stir bar. The reaction mixture was left to stir at room temperature for 24 hours. The resulting pale-yellow ionic liquid was washed with deionized water until the wash tested negative for residual bromide with 50 mM aqueous silver nitrate. The product was rotary evaporated and dried in a high vacuum oven at 60 ˚C for several days. The final product was a pale yellow, viscous liquid (25.04 g, 86 %, molar mass: 319.36 g/mol, water content: 25 ppm). ^{1}H (400 MHz; DMSO-d_6) δ 0.89-0.93 (t, 3H), 1.24-1.30 (m, 2H), 1.74-1.81 (m, 2H), 3.85 (s, 3H), 4.14-4.18 (t, 2H), 7.68 (d, 1H), 7.75 (d, 1H), 9.10 (s, 1H); ^{13}C (101 MHz; DMSO-d_6) δ 13.18, 18.72, 31.30, 35.67, 48.47, 122.20, 123.56, 136.44.

2c. Synthesis of 1-(2-methoxyethyl)-3-methylimidazolium bis(fluorosulfonyl)amide (EOMmim FSA)

1-(2-methoxyethyl)-3-methylimidazolium bromide (26.31 g, 0.1190 mol) dissolved in 20 mL deionized water was reacted with one equivalent of potassium bis(fluorosulfonyl)amide (26.09 g, 0.1190 mol) dissolved in 30 mL deionized water in a round bottom flask containing a stir bar. The reaction mixture was left to stir at room temperature for 24 hours. The resulting yellow ionic liquid was washed with cold deionized water until the wash tested negative for bromide with 50 mM aqueous silver nitrate. The product was rotary evaporated and dried in a high vacuum oven at 60 °C for several days. The final product was a yellow, viscous liquid (19.24 g, 49 %, molar mass: 321.32 g/mol, water content: 70 ppm). ^{1}H (400 MHz; DMSO-d_6) δ 3.27 (s, 3H), 3.67-3.69 (t, 2H), 3.86

(s, 3H), 4.33-4.36 (t, 2H), 7.67-7.68 (d, 1H), 7.70-7.71(d, 1H), 9.07 (s, 1H), ^{13}C (101 MHz; DMSO-d_6) δ 35.73, 48.66, 58.04, 69.57, 122.61, 123.44, 136.80.

3c. Synthesis of 1-allyl-3-methylimidazolium bis(fluorosulfonyl)amide (Amim FSA)
1-allyl-3-methylimidazolium chloride (25 g, 0.1576 mol) dissolved in 30 mL deionized water was reacted with one equivalent of potassium bis(fluorosulfonyl)imide (34.55 g, 0.1576 mol) dissolved in 40 mL deionized water in a round bottom flask containing a stir bar. The reaction mixture was left to stir at room temperature for 24 hours. The resulting ionic liquid was washed with deionized water until the wash tested negative for chloride using 50 mM aqueous silver nitrate. The product was rotary evaporated and dried in a high vacuum oven at 70 ˚C for 48 hours. The final product was a very pale yellow, viscous liquid (40.20 g, 84%, molar mass: 303.30 g/mol, water content: 9 ppm). ^{1}H (400 MHz; DMSO-d_6) δ 3.86 (s, 3H), 4.82-4.83 (d, 2H), 5.28-5.38 (m, 2H), 6.00-6.08 (m, 1H), 7.67-7.69 (m, 2H), 9.08 (s, 1H), 13C (101 MHz; DMSO-d_6) δ 35.79, 50.86, 120.25, 122.33, 123.77, 131.60, 136.64.

Preparation of Ionic Liquid-Single-Walled Carbon Nanotube Mixtures

All mixtures were prepared in a low-moisture dry box under compressed air. Based on the density of each IL, mixtures were prepared with three mL of ionic liquid and 0.5, 2, or 5 wt% of SWCNTs. The mixtures were sonicated for 120-minute periods in sealed vials of the similar dimensions using a VWR Ultrasonic Cleaner Model 97043-992 water bath sonicator. The IL-SWCNT dispersions remained stable for several months. Sonication time of less than 120 minutes did not result in stable IL-SWCNT mixtures with improved conductivity values. A hand grinding method attempted using a mortar and pestle also did not result in consistently uniform IL-SWCNT combinations with improved conductivity values.

Characterization of Ionic Liquid-Single-Walled Carbon Nanotube Mixtures

Viscosities of pure ILs and IL-SWCNTs mixtures were measured with a Cambridge Applied Systems ViscoLab 4100 electromagnetic reciprocating piston viscometer that was temperature regulated by a Lauda RM-6 recirculating water bath.

Electrochemical Impedance Spectroscopy - Variable Temperature Ionic Conductivities:
IL-SWCNT samples were packed in a dry nitrogen atmosphere into an airtight 3 mL (Biologic Brand) two-electrode sample cell, leaving 50% of the cell volume available for thermal expansion. The cells were temperature controlled from 15 to 90 °C using a silicone oil bath. The electrochemical impedance measurements were done using a Solartron 1260 Impedance Analyzer coupled with a Solartron 1287 Electrochemical Interface. Experimental parameters utilized a frequency sweep from 25 Hz to 2.5 MHz using a resolution of 20 data points per decade, and the energization was set with an AC amplitude of 10 mV with no DC offset. The resulting Nyquist plot of reactance versus resistance was inspected to determine the real electrical resistance. Using the corresponding cell constants and the electrical resistance, conductivity was calculated and plotted versus temperature. The data shown and discussed are the averages of three sets of measurements.

Results and Discussion

Electrochemical impedance spectroscopy of the ionic liquid-single walled carbon nanotube (IL-SWCNT) mixtures was performed over a wide temperature range (15 to 85 °C; 288 to 358 K) in order to obtain information about the nature of the conductivity (σ) of each composite. Conductivity values were obtained from corresponding Nyquist plots. As shown in Tables I and II, the conductivity of the IL-SWCNTs composites depended on temperature, cation and anion types, and SWCNT concentration.

Due to the composite nature of the mixtures, the resulting conductivity is due to the bulk IL, IL-solid interface, and SWCNT contributions. The SWCNTs are comprised of metallic and semiconducting nanotubes, and their electrical conductivity results from the motions of both electrons and holes. In the IL, the ionic conductivity is due to the motions of both the cations and anions. The IL transport properties depend on the structure of the IL, as determined by the composition of the ions and their intermolecular interactions. In imidazolium ILs, in addition to hydrogen bonding and Coulombic interactions, there are Van der Waals, polarization, π−π, and dipole−dipole interactions between the ions (44). In the imidazolium ILs studied here, the side chain functionality varied from alkyl to allyl to ether and the associated anions varied in size and dynamical complexity (from FSA^- to NTf_2^-).

TABLE I. Viscosities and Temperature-Dependent Conductivities of NTf_2 Ionic Liquids and NTf_2 Ionic Liquid-Single-Walled Carbon Nanotube Mixtures.

Cation and SWCNT content	Viscosity cP, 25 °C	Conductivity (σ, mS/cm), at temperature (°C)							
		15	25	35	45	55	65	75	85
Bmim	50	3.9	5.0	6.3	8.0	10.1	12.8	16.2	20.5
Bmim + 2 wt% SWCNTs	*	19.2	25.1	42.9	52.6	60.0	66.6	75.7	89.1
Bmim + 5 wt% SWCNTs	*	268	277	287	298	309	322	335	350
Amim	34	6.8	8.4	10.5	13.0	16.2	20.1	25.0	31.0
Amim + 0.5 wt% SWCNTs	-	8.3	11.0	15.7	20.4	26.0	32.0	34.4	37.9
Amim + 2 wt% SWCNTs	*	17.3	24.3	33.9	44.6	54.0	65.4	76.1	90.5
Amim + 5 wt% SWCNTs	*	475	496	490	511	506	529	525	530
EOMmim	45	3.3	4.7	6.5	8.9	11.8	15.0	18.4	21.7
EOMMIM + 2 wt% SWCNTs	*	8.8	14.6	17.3	27.4	35.7	48.1	57.1	72.6
EOMmim + 5 wt% SWCNTs	*	-	540	556	578	594	610	635	657

* Viscosity higher than 10,000 cP.

TABLE II. Viscosities and Temperature-Dependent Conductivities of FSA Ionic Liquids and FSA Ionic Liquid-Single-Walled Carbon Nanotube Mixtures.

Cation and SWCNT content	Viscosity cP, 25 °C	Conductivity (σ, mS/cm), at temperature (°C)							
		15	25	35	45	55	65	75	85
Bmim	33	7.9	9.7	11.9	14.7	18.1	22.4	27.6	34.0
Bmim + 2 wt% SWCNTs	*	39.7	47.4	57.4	70.9	84.8	101	116	132
Bmim + 5 wt% SWCNTs	*	87.1	76.7	78.1	83.7	88.8	91.7	98.1	102
Amim	25	12.5	15.1	18.3	22.1	26.7	32.3	39.0	47.2
Amim + 0.5 wt% SWCNTs	-	14.3	18.7	23.5	29.9	32.5	39.7	47.6	53.0
Amim + 2 wt% SWCNTs	*	63.7	77.2	93.4	112	126	134	146	168
Amim + 5 wt% SWCNTs	*	404	382	406	417	432	453	465	480
EOMmim	30	-	8.0	10.8	14.7	18.2	22.9	27.7	32.7
EOMMIM + 2 wt% SWCNTs	*	-	30.1	33.4	43.4	62.7	130	163	228
EOMmim + 5 wt% SWCNTs	*	-	176	189	194	208	208	234	262

* Viscosity higher than 10,000 cP.

For liquid systems, the ionic conductivity can be qualitatively described by the Nernst-Einstein (NE) equation [1]. Here the ionic conductivity (σ) depends mainly on temperature (*T*), the number of available charge carriers (*c*), and the self-diffusion coefficient (*D*). Connecting the ionic conductivity to the viscosity (η) is accomplished by the self-diffusion coefficient (D) through the Stokes-Einstein (SE) relationship [2], Here q, k_B, and r represent the charge of the carrier, Boltzmann constant, and hydrodynamic radius, respectively. It should be understood that both equations were developed for applications to very dilute solutions and that in these solutions, the ions are depicted as hard non-interacting spheres, moving through a continuum of viscosity η. The ions are also expected to be single entities.

$$\sigma = \frac{Dq^2c}{k_BT} \quad [1]$$

$$D = \frac{k_BT}{4\pi r\eta} \quad [2]$$

Since the IL-SWCNT mixtures are not dilute nor purely ionic, the NE and SE relationships will be used sparingly in the discussions that follow.

Temperature and Nanotube Concentration Effects

As shown in Tables I and II, an increase in SWCNT concentration significantly increased σ, with the largest enhancement (up to 540 mS/cm at 25 °C) being observed for the 5 wt% composites, regardless of temperature, and anion and cation types. Figure 2 is a graph of the temperature-dependent conductivity values obtained for a representative IL-SWCNT system - pure EOMmim NTf_2 and the corresponding 2 and 5 wt% SWCNT composites. As shown, increased conductivity was observed as SWCNT concentration increased. From the NE equation, at a specific temperature an increase in charge carrier concentration will cause an increase in the conductivity. Conductivity increased with temperature in a similar fashion for the 0 and 2 wt% SWCNT samples, while it rose only slightly for 5 wt% SWCNT. Similar trends were observed with the other pure ILs and their corresponding SWCNT composites.

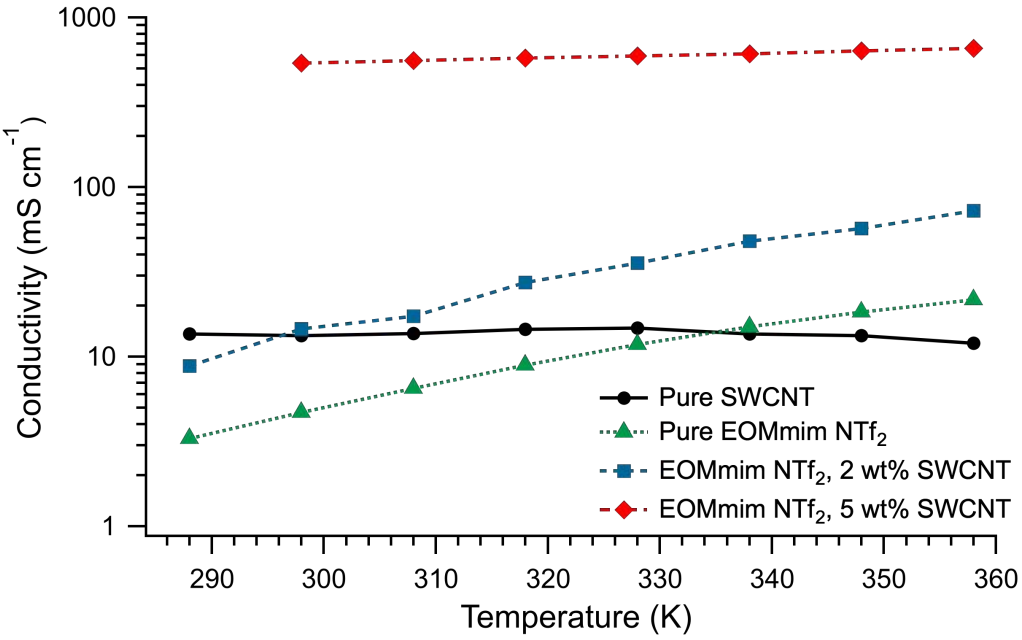

Figure 2. Temperature-dependent conductivities of pure EOMmim NTf_2 and its 2 and 5 wt% SWCNT mixtures, compared to pure SWCNT for reference, obtained from EIS Nyquist plots. Numerical values are given in Table I. Similar trends were observed with the other pure ILs and their corresponding mixtures.

From the NE and SE relationships, it is expected that an increase in conductivity results from a decrease in liquid solution viscosity. The viscosities of the pure ILs decrease with increasing temperature in a non-Arrhenius fashion typical of ILs. However, the addition of the SWCNTs significantly increased the viscosity of the composites to beyond the range of our instrumentation (>10,000 cP). Despite the dramatic increase in viscosity, the conductivities of the 0.5 and 2 wt% SWCNT mixtures are factors of 1.1-1.6 and 2.5-7 times larger than the conductivities of their respective pure ILs over the temperature ranges measured. In addition, the conductivities of the 0.5 and 2 wt% SWCNT mixtures have very similar, non-Arrhenius temperature dependences as those of their respective pure ILs. From this behavior we infer that the nanotubes contribute significantly to the conductivity of the mixtures in this concentration regime, but charge transport is still regulated by the dynamics of the ILs, which is linked to their viscosities.

In contrast, the conductivities for the 5 wt% SWCNT mixtures follow Arrhenius behavior with a much weaker temperature dependence than the lower-concentration mixtures and pure ILs. For comparison we include in Figure 2 our own measurements for pure SWCNTs, which were fairly constant over the entire temperature range. Generally, the temperature dependence of the electrical conductivity in semiconductors increases with increasing temperature. Although the measured values ranging from 12-14.8 mS/cm are very small compared to reported values (~ 10^2 to 10^6 S/cm) (14), it should be pointed out that in our measurements, the platinum probes of the BioLogic cell are immersed into the SWCNTs. Therefore, proper contact between the electrodes and the SWCNTs was lacking. Generally, in conductivity measurements on CNTs, a CNT sheet or sputtered wires of

CNTs onto a solid surface are used to ensure proper contact (45). Despite this, the data is useful in that it can be used as a representation of the temperature dependence of the conduction process in the nanotubes, which as shown in Figure 2, differs from that of the pure IL and even the 2 wt% mixture. However, it is quite similar to the 5 wt% EOMmim NTf_2/SWCNT mixture and those observed for the other IL-SWCNT mixtures as well, suggesting the conduction process of those mixtures is dominated by that of the SWCNTs.

To further illustrate the differences in conductivity mechanisms between lower and higher SWCNT loadings, we obtained activation energies for conductivity from Arrhenius fits of the variable-temperature conductivity data. Although some data sets clearly show curvature, linear Arrhenius fits were sufficient to indicate a clear difference between the behavior of all six IL-SWCNT combinations at 5 wt% loading versus lower loadings, as shown in Table III. The difference is that the activation energies are small for the 5 wt% loadings (1.3 to 5.7 kJ/mol) while for the 0.5 and 2 wt% loadings the activation energies are large and generally comparable to those of the corresponding pure ILs (11.5 to 25.6 kJ/mol). This is clear evidence for a conductivity mechanism at the 5 wt% loading level that is based on the charge transport properties of the nanotubes, and that the role of the IL in this regime is to suspend the nanotubes in a manner that facilitates nanotube-centered transport and makes good contact with the conductivity probe electrodes.

TABLE III. Activation Energies for the Conductivity of Pure Ionic Liquids and Ionic Liquid-Single-Walled Carbon Nanotube Mixtures.

Cations	Activation Energy, kJ/mol	
	NTf_2 anion	FSA anion
Bmim	23.5 ± 0.4	20.6 ± 0.3
Bmim + 2 wt% SWCNTs	18.3 ± 1.8	15.1 ± 0.2
Bmim + 5 wt% SWCNTs	3.2 ± 0.1	4.4 ± 0.2
Amim	21.1 ± 0.3	18.4 ± 0.3
Amim + 0.5 wt% SWCNTs	19.3 ± 1.2	15.9 ± 0.5
Amim + 2 wt% SWCNTs	20.0 ± 0.8	11.5 ± 0.6
Amim + 5 wt% SWCNTs	1.3 ± 0.2	3.3 ± 0.1
EOMmim	23.5 ± 0.6	20.9 ± 0.4
EOMmim + 2 wt% SWCNTs	25.6 ± 0.9	19.1 ± 0.6
EOMmim + 5 wt% SWCNTs	2.7 ± 0.1	5.7 ± 0.4

As discussed above, at lower SWCNT loadings (0.5 and 2 wt%), conductivities increase over those of the pure IL despite very large increases in viscosity. Given the very high intrinsic conductivity of the nanotubes, it is reasonable to assume that they make a large contribution to the conductivity mechanism, but the temperature dependences indicate that IL dynamics still regulates charge transport. This could be due to the Brownian fluctuations of the IL ions inducing field fluctuations and polarized charges in the nanotubes that inhibit longitudinal charge transport within the nanotubes. The result of this polarizing effect would be a distribution of regimes with varying ion dynamics throughout the mixture, which can contribute incoherently to the conductivity. We hypothesize that at the higher 5 wt% loading, fluctuations in the IL are reduced and it is behaving like a confined fluid where the dynamics are frozen out. We are looking at ways to test this hypothesis.

Cation and Anion Effects

As mentioned above, we selected three imidazolium cations and two sulfonylamide anions to investigate how changes in IL-nanotube interactions affect the conductivities of the composite systems. In fact, some clear patterns in the conductivity data are apparent, as shown in Figure 3. For SWCNT loadings up to 2 wt%, the conductivities of the composites track in opposite order with the viscosities of their constituent ILs, as they do in the pure ILs. Thus FSA^- anion-based IL composites have higher conductivities compared to the NTf_2^- analogues, because the viscosities of the FSA^- salts are lower and, as discussed above, IL dynamics play a role in charge transport in the regime up to 2 wt% SWCNT.

Between 2 and 5 wt% SWCNT the trend between the two anion families is reversed, with the NTf_2^- anion-based 5 wt% composites having greater conductivities compared to their FSA^- analogues (see Figure 3). In this regime, the activation energies indicate that IL dynamical properties such as viscosity are not a factor in the conductivity mechanism. Instead, we must look in the direction of structural differences in the IL-nanotube interactions, considering that the trifluoromethyl groups on the NTf_2^- anion may impose steric or packing factors on the interactions that are lacking in the FSA^- case, or that FSA may have a more polarizing effect on the nanotube, changing the energetic landscape of charge transport. In the future, these hypotheses can be tested by substituting other perfluoroalkylsulfonylamide anions or other types of anion families.

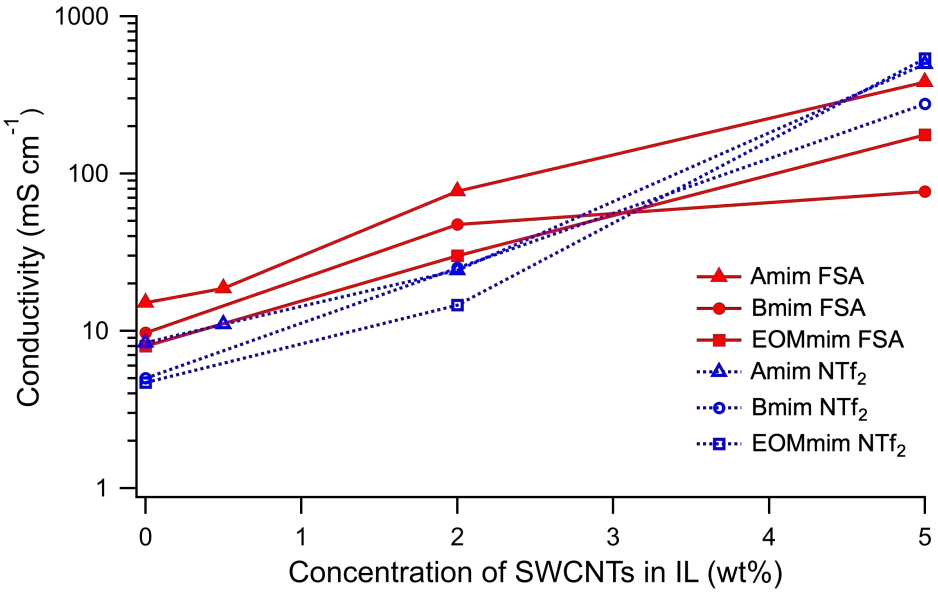

Figure 3. Conductivity of IL-SWCNT mixtures containing 0 - 5 wt% SWCNTs, at 25 °C.

Figure 3 also shows interesting patterns among the three chosen cations. At 2 wt% loading and below, the conductivity trends of the cations basically follow the viscosities of their respective ILs. However at 5 wt% loading, the $EOMmim^+$ and $Amim^+$ composites show higher conductivities than the $Bmim^+$ composites. The precise reasons for this may need to be elucidated by molecular dynamics calculations or interface-selective spectroscopy techniques. We have postulated that the allyl group of $Amim^+$ might provide additional interaction with the π-orbital system of the nanotube. In the case of $EOMmim^+$,

the ether group alters anion-cation hydrogen bonding interactions, with impacts on the structure of the IL phase (39-43). The $Bmim^+$ cation appears to be least effective in promoting conductivity at 5 wt% loading. Although the butyl chain is too short to induce polar/non-polar domain segregation in the bulk IL, it may have a steric or structural organizational effect on the IL-nanotube interaction that makes it less favorable in promoting conductivity. This idea can be tested by substituting shorter- ($Emim^+$) or longer-chain ($Hmim^+$, $Omim^+$) cations, which we will do in subsequent studies.

Conclusion

The temperature-dependent conductivity profiles of six IL-SWCNT composites were studied over a wide range of nanotube concentrations. Between 0 and 2 wt% SWCNT loading, the presence of nanotubes increased the conductivity by factors up to 7-fold, despite the fact that the viscosities of the IL-SWCNT composites were very high. Within this concentration range, the temperature dependences of the conductivities indicated that IL dynamics still regulates the enhanced charge transport. The performance of the composites was generally inversely related to the relative viscosities of the pure IL components.

The mechanism of conductivity was clearly different at 5 wt% SWCNT loading for all six ILs. This loading is higher than generally reported in other literature, and it provided some provocative results. Remarkably, conductivity values of 540, 496 and 382 mS cm^{-1} were obtained for 5 wt% SWCNT mixtures containing EOMmim NTf_2, Amim NTf_2, and Amim FSA, respectively. The activation energies for all six 5 wt% composites were much smaller than they were for the lower SWCNT loading regime, and comparable to the behavior of pure SWCNTs. It appears that the role of the IL in the 5 wt% regime is to suspend the nanotubes in a manner that facilitates nanotube-centered transport and makes good contact with the conductivity probe electrodes. Concurrent with the change in mechanism at 5 wt% loading, the ranking of conductivity as a function of anion flips, such that the composites with NTf_2^- anions have higher conductivities than their FSA^- congeners, the opposite of the lower loading regime where the lower viscosities of the FSA^- ILs benefit the conductivities of their composites. The reason for this inversion in ranking can be explored by substituting with other perfluoroalkylsulfonylamide anions (46) to elucidate the effects of anion structure on IL-SWCNT interactions.

Examining the effects of different functional groups on the IL cations provided interesting results. At low loadings, the effects of cation substitution on IL-SWCNT composite conductivity are traceable to their influence on the viscosities of the pure ILs. At 5 wt% loading, there is evidence that differential IL-SWCNT interactions depend on the identity of the functional group, in ways that could facilitate or possible inhibit charge transport. Interestingly, the aliphatic imidazolium cation $Bmim^+$ performed worse than $EOMmim^+$ and $Amim^+$, which has interesting implications for prior work that has mainly been focused on 1-alkyl-3-methylimidazolium ILs. This finding suggests that further investigation with shorter- ($Emim^+$) or longer-chain ($Hmim^+$, $Omim^+$) cations, as well as other types of ether-substituted imidazolium cations (41), is warranted. Future work will involve spectroscopic (Mid-IR and Raman) analyses on the IL-SWCNT mixtures to better understand the interaction between the ILs and the SWCNTs. In addition, the efficiency of these unique electrode-electrolyte mixtures in supercapacitors will be determined.

Acknowledgments

The authors thank the National Institutes of Health (NIH), Research Initiative for Minority Students (RIMS) Program (NIH 5R25GM065096) at the City University of New York for student internship support. The synthesis of the mixtures was supported by the Professional Staff Congress-City University of New York Grants (# 69297-00 47 and 50) and the CUNY Advanced Science Research Center Faculty Fellows Program 2018. The IL physical characterization work at BNL was supported by the U.S. Department of Energy, Office of Basic Energy Sciences, Division of Chemical Sciences, Geosciences, and Biosciences under contract DE-SC0012704. The ionic conductivity measurements performed at Brooklyn College/CUNY was supported by the National Science Foundation, Solid State and Materials Chemistry Program, Division of Materials Research, EAGER award #1841398.

References

1. Poonam, K. Sharma, A. Arora and S. K. Tripathi, *J. Energy Storage*, **21**, 801 (2019).
2. M. Winter and R. J. Brodd, *Chem. Rev.*, **104**, 4245 (2004).
3. A. Dive and S. Banerjee, *J. Electrochem. Energy Convers. Storage*, **15**, 011001 (2017).
4. Q. Cheng, J. Tang, J. Ma, H. Zhang, N. Shinya and L.-C. Qin, *Phys. Chem. Chem. Phys.*, **13**, 17615 (2011).
5. A. Burke, *J. Power Sources*, **91**, 37 (2000).
6. M. F. El-Kady, V. Strong, S. Dubin and R. B. Kaner, *Science*, **335**, 1326 (2012).
7. Y. Zhu, S. Murali, M. D. Stoller, K. J. Ganesh, W. Cai, P. J. Ferreira, A. Pirkle, R. M. Wallace, K. A. Cychosz, M. Thommes, D. Su, E. A. Stach and R. S. Ruoff, *Science*, **332**, 1537 (2011).
8. H. J. In, S. Kumar, Y. Shao-Horn and G. Barbastathis, *Appl. Phys. Lett.*, **88**, 083104 (2006).
9. P. Simon and Y. Gogotsi, *Nat. Mater.*, **7**, 845 (2008).
10. C. Liu and H.-M. Cheng, *J. Phys. D, Appl. Phys.*, **38**, R231 (2005).
11. J. N. Coleman, U. Khan, W. J. Blau and Y. K. Gun'ko, *Carbon*, **44**, 1624 (2006).
12. A. Chou, T. Böcking, R. Liu, N. K. Singh, G. Moran and J. J. Gooding, *J. Phys. Chem. C*, **112**, 14131 (2008).
13. M. Burghard, *Surf. Sci. Rep.*, **58**, 1 (2005).
14. Q. Cao, Q. Yu, D. W. Connell and G. Yu, *Clean Technol. Environ. Policy*, **15**, 871 (2013).
15. R. H. Baughman, A. A. Zakhidov and W. A. de Heer, *Science*, **297**, 787 (2002).
16. R. Saito, M. Fujita, G. Dresselhaus and M. S. Dresselhaus, *Appl. Phys. Lett.*, **60**, 2204 (1992).
17. K. H. An, W. S. Kim, Y. S. Park, J.-M. Moon, D. J. Bae, S. C. Lim, Y. S. Lee and Y. H. Lee, *Adv. Funct. Mater.*, **11**, 387 (2001).
18. A. Izadi-Najafabadi, S. Yasuda, K. Kobashi, T. Yamada, D. N. Futaba, H. Hatori, M. Yumura, S. Iijima and K. Hata, *Adv. Mater.*, **22**, E235 (2010).
19. W. S. Zhang, W. J. Xu, F. Zhang, Y. Z. Wang, J. Li, B. A. Wang and Y. Li, *J. Chin. Chem. Soc.*, **59**, 753 (2012).

20. S. Kazemiabnavi, Z. Zhang, K. Thornton and S. Banerjee, *J. Phys. Chem. B*, **120**, 5691 (2016).
21. S. Lall-Ramnarine, S. Suarez, N. Zmich, D. Ewko, S. Ramati, D. Cuffari, M. Sahin, Y. Adam, E. Rosario, D. Paterno and J. Wishart, *ECS Trans.*, **64**, 57 (2014).
22. G. A. Snook, P. Kao and A. S. Best, *J. Power Sources*, **196**, 1 (2011).
23. T. Fukushima, K. Asaka, A. Kosaka and T. Aida, *Angew. Chem. Int. Edit.*, **44**, 2410 (2005).
24. T. Fukushima, A. Kosaka, Y. Ishimura, T. Yamamoto, T. Takigawa, N. Ishii and T. Aida, *Science*, **300**, 2072 (2003).
25. R. Hayes, G. G. Warr and R. Atkin, *Chem. Rev.*, **115**, 6357 (2015).
26. J. L. Bañuelos, G. Feng, P. F. Fulvio, S. Li, G. Rother, S. Dai, P. T. Cummings and D. J. Wesolowski, *Chem. Mat.*, **26**, 1144 (2014).
27. J. N. Israelachvili, *Intermolecular and Surface Forces*, Academic Press: New York, (2011).
28. R. Hayes, G. G. Warr and R. Atkin, *Phys. Chem. Chem. Phys.*, **12**, 1709 (2010).
29. W. Shi and D. C. Sorescu, *J. Phys. Chem. B*, **114**, 15029 (2010).
30. Y. Shim and H. J. Kim, *ACS Nano*, **3**, 1693 (2009).
31. K. Shimizu, C. E. S. Bernardes and J. N. Canongia Lopes, *J. Phys. Chem. B*, **118**, 567 (2014).
32. A. A. Freitas, K. Shimizu and J. N. Canongia Lopes, *J. Chem. Eng. Data*, **59**, 3120 (2014).
33. J. Wang, H. Chu and Y. Li, *ACS Nano*, **2**, 2540 (2008).
34. N. Hameed, J. S. Church, N. V. Salim, T. L. Hanley, A. Amini and B. L. Fox, *RSC Adv.*, **3**, 20034 (2013).
35. C. Kong, W. Qian, C. Zheng, Y. Yu, C. Cui and F. Wei, *Chem. Commun.*, **49**, 10727 (2013).
36. S. Lall-Ramnarine, C. Rodriguez, R. Fernandez, N. Zmich, E. Fernandez, S. Dhiman and J. F. Wishart, *ECS Trans.*, **75**, 215 (2016).
37. H. Tokuda, K. Hayamizu, K. Ishii, M. A. B. H. Susan and M. Watanabe, *J. Phys. Chem. B*, **109**, 6103 (2005).
38. S. J. Zhang, N. Sun, X. Z. He, X. M. Lu and X. P. Zhang, *J. Phys. Chem. Ref. Data*, **35**, 1475 (2006).
39. K. Shimizu, C. E. S. Bernardes, A. Triolo and J. N. Canongia Lopes, *Phys. Chem. Chem. Phys.*, **15**, 16256 (2013).
40. A. Triolo, O. Russina, R. Caminiti, H. Shirota, H. Y. Lee, C. S. Santos, N. S. Murthy and E. W. Castner, *Chem. Commun.*, **48**, 4959 (2012).
41. S. I. Lall-Ramnarine, M. Zhao, C. Rodriguez, R. Fernandez, N. Zmich, E. D. Fernandez, S. B. Dhiman, E. W. Castner and J. F. Wishart, *J. Electrochem. Soc.*, **164**, H5247 (2017).
42. G. D. Smith, O. Borodin, L. Y. Li, H. Kim, Q. Liu, J. E. Bara, D. L. Gin and R. Nobel, *Phys. Chem. Chem. Phys.*, **10**, 6301 (2008).
43. H. J. Zeng, M. A. Johnson, J. D. Ramdihal, R. A. Sumner, C. Rodriguez, S. I. Lall-Ramnarine and J. F. Wishart, *J. Phys. Chem. A*, **123**, 8370 (2019).
44. S. Zhang, J. Zhang, Y. Zhang and Y. Deng, *Chem. Rev.*, **117**, 6755 (2017).
45. B. Earp, D. Dunn, J. Phillips, R. Agrawal, T. Ansell, P. Aceves, I. De Rosa, W. Xin and C. Luhrs, *Mater. Res. Bull.*, **131**, 110969 (2020).
46. M. Zhao, B. N. Wu, S. I. Lall-Ramnarine, J. D. Ramdihal, K. A. Papacostas, E. D. Fernandez, R. A. Sumner, C. J. Margulis, J. F. Wishart and E. W. Castner, *J. Chem. Phys.*, **151**, 074504 (2019).

ECS Transactions, 98 (10) 89-95 (2020)
10.1149/09810.0089ecst ©The Electrochemical Society

Basic Performance of Tubular Molten Carbonate-Type Direct Carbon Fuel Cells

A. Ido and M. Kawase

Central Research Institute of Electric Power Industry (CRIEPI),
2-6-1 Nagasaka, Yokosuka, Kanagawa 240-0196, Japan

Direct carbon fuel cells (DCFCs) are expected to be useful devices that effectively utilize carbon resources. We have proposed novel tubular molten carbonate-type direct carbon fuel cells (TMC-DCFCs). In this study, basic performance of TMC-DCFCs such as influence of the difference in the cathode gas and fuel on the cell performance was investigated. I-V measurements and continuous power generation tests were conducted at 1073 K. It was shown that cell performance of TMC-DCFCs was improved by increase of O_2/CO_2 concentration in the cathode gas. When using carbonized wood as carbon fuel, high power density over 160 mW/cm^2 was obtained as well as when using activated carbon. These results suggested that the change of the carbon/carbonate ratio is permissible to some extent and a small amount of ash hardly affects the cell performance.

Introduction

In order to realize a low carbon society, novel technologies for more effective utilization of carbon resources such as plant biomass and organic waste are needed. Direct carbon fuel cells (DCFCs) are fuel cells utilizing solid carbon directly as fuel. DCFCs as well as typical fuel cells are expected to achieve relatively high efficiency even on a small scale. Due to utilizing solid fuel, storage and transportation of fuel are easy. However, conventional DCFCs had two big problems such as the way to continuously supply solid fuel and low cell performance. Then, we have proposed novel tubular molten carbonate-type direct carbon fuel cells (TMC-DCFCs) to resolve those problems (1). It is relatively easy to continuously supply solid fuel when adopting tubular cells. Molten carbonate electrolyte is expected to have better durability against impurities compared with solid oxide electrolyte. When molten carbonate is used as electrolyte for DCFCs, each electrode reaction can be expressed as follows.

$$\text{Cathode: } O_2(g) + 2CO_2(g) + 4e^- = 2CO_3^{2-} \quad [1]$$

$$\text{Anode: } C(s) + 2CO_3^{2-} = 3CO_2(g) + 4e^- \quad [2]$$

$$: CO(g) + CO_3^{2-} = 2CO_2(g) + 2e^- \quad [3]$$

This study investigated basic performance of TMC-DCFCs such as influence of the difference in the cathode gas and fuel on the cell performance.

Experimental

Fabrication of TMC-DCFCs

We have already developed tubular molten carbonate-type fuel cells (TMCFCs) with comparatively high robustness and good durability against impurities (2,3), and the fabrication method of them were applied for TMC-DCFCs. Each cell component of TMC-DCFCs was almost same with typical MCFCs as shown in Table 1. Cathode was NiO-3%MgO, electrolyte matrix was $LiAlO_2$, anode was Ni-2%AlCr and they were formed by slurry coating methods. Electrolyte was 60%Li_2CO_3-40%Na_2CO_3 molten carbonate and impregnated into electrolyte matrix before the operation. Details of the fabrication method were reported in our previous paper (1). Figure 1 shows the fabricated cell used in this study.

TABLE I. Characteristics of cell components.

Cell component	Material	Thickness
Cathode	NiO-3%MgO	0.8 mm
Electrolyte matrix	α-$LiAlO_2$	1.4 mm
Anode	Ni-2%AlCr	1.1 mm

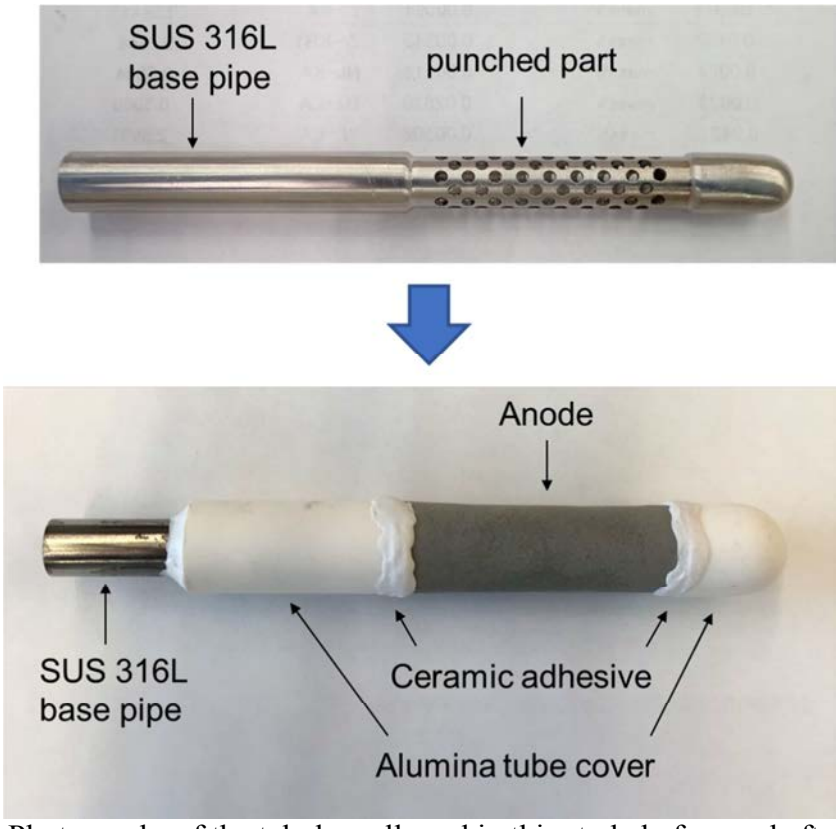

Figure 1. Photographs of the tubular cell used in this study before and after fabrication.

Fuel mixture and used carbon fuel

Activated carbon powder (Median diameter: 43 μm) or carbonized wood powder (Median diameter: 31 μm) was used as carbon fuel. Fuel mixture was composed of

carbon fuel and carbonate powder same with electrolyte in the weight ratio of 80/20. In this paper, we refer to the mixing ratio between fixed carbon and molten carbonate as "the carbon/carbonate ratio". Activated carbon was almost composed of fixed carbon, so the net carbon/carbonate ratio was about 80/20 when activated carbon was used as carbon fuel. On the other hand, carbonized wood was sawmill residues from conifer carbonized at 623 K and included 50.3 % of volatile matter, 46.3 % of fixed carbon and 3.4 % of ash. Therefore, the net carbon/carbonate ratio was 65/35 when carbonized wood was used as carbon fuel.

Equipment and condition

Figure 2 shows the experimental apparatus for the power generation test. A tubular cell was inserted into an alumina crucible filled with about 50 g of fuel mixture. The alumina crucible was set in a nickel alloy holder and heated in an electric furnace. The cathode gas was introduced inside the tubular cell and the anode gas was introduced from the bottom of the holder. The cathode gas was O_2/CO_2 (33/67 vol%) with a flow rate of 110 mL/min or $N_2/O_2/CO_2$ (55/15/30 vol%) with a flow rate of 260 mL/min. Both compositions corresponded to the stoichiometric ratio in the cathode reaction [1]. $N_2/O_2/CO_2$ (55/15/30 vol%) was equivalent to Air/CO_2 (70/30 vol%). Both flow rates meant 10 % of the cathode utilization when the current density was 100 mA/cm^2. The anode purge gas was N_2 (100 vol%) with a flow rate of 150 mL/min. I-V measurements and continuous power generation tests were conducted at 1073 K. During the I-V measurement the current density rose 10 mA/cm^2 per minute.

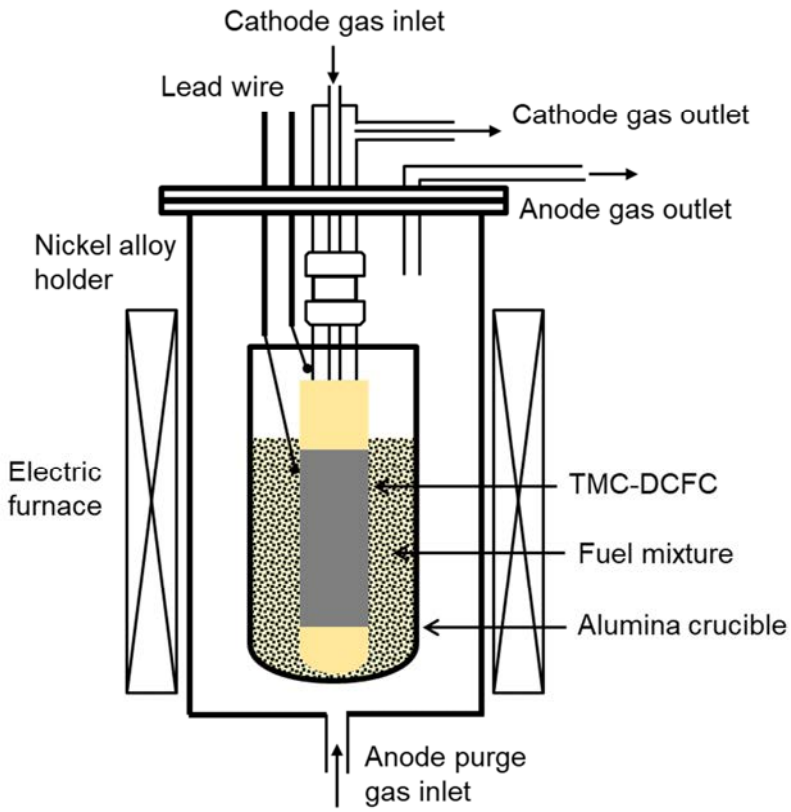

Figure 2. Experimental apparatus for the power generation test.

Results and Discussion

Influence of the cathode gas composition

I-V curves of the TMC-DCFC with each cathode gas composition are presented in Figure 3. Activated carbon was used as carbon fuel in these tests. These results show that the open circuit voltage (OCV), which is equivalent to the cell voltage of 0 mA/cm^2, was larger and the overvoltage, which is equivalent to the slope of the I-V curve, was smaller in O_2/CO_2 condition compared with those in $N_2/O_2/CO_2$ condition.

OCV in O_2/CO_2 condition was 49 mV larger than that in $N_2/O_2/CO_2$ condition. The OCV for the TMC-DCFCs is expressed as equation [4] or [5] from equations [1]-[3] by Nernst equation.

$$E = E^{\circ} + \frac{RT}{4F} \ln \frac{{p_{CO2(Ca)}}^2 p_{O2(Ca)}}{{p_{CO2(An)}}^3} \quad [4]$$

$$E = E^{\circ} + \frac{RT}{4F} \ln \frac{{p_{CO2(Ca)}}^2 p_{O2(Ca)} {p_{CO(An)}}^2}{{p_{CO2(An)}}^4} \quad [5]$$

where E is the OCV, E° is the theoretical electromotive force, R is the gas constant, T is the temperature and p is the partial pressure of each gas. From the equation [4] or [5], the theoretical OCV in O_2/CO_2 condition is 55 mV larger than that in $N_2/O_2/CO_2$ condition at 1073 K. This theoretical value is consistent with the experimental value well.

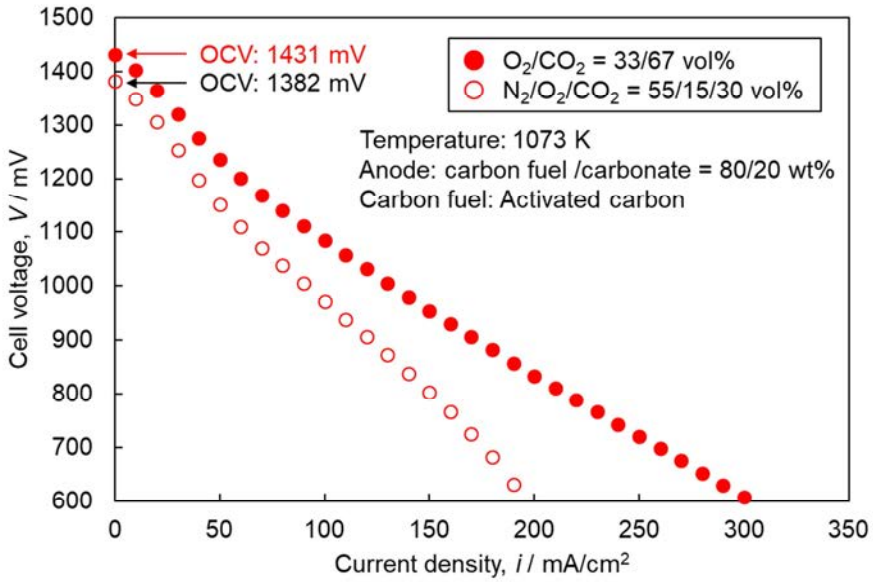

Figure 3. I-V curves of the TMC-DCFC with each cathode gas composition.

The overvoltage in O_2/CO_2 condition was smaller than that in $N_2/O_2/CO_2$ condition. The cell voltage of fuel cells can be expressed as follows.

$$V = E - E_{ne} - (R_{ir} + R_a + R_c) \times i \quad [6]$$

where V is the cell voltage, E_{ne} is the Nernst loss, R_{ir} is the internal resistance, R_a and R_c are the anode and cathode polarization resistance, and i is the current density. Since experimental conditions other than the cathode gas composition were same and the difference of the cathode Nernst loss was relatively small in this low cathode utilization, the difference of the overvoltage was considered to be mainly the cathode overvoltage. The cathode polarization resistance of MCFCs is expressed as follows (4).

$$R_c = a_{c1}\, p_{O2(ca)}^{-0.75} p_{CO2(ca)}^{0.5} + a_{c2}\, M_{CO2(ca)}^{-1.0} \quad [7]$$

where a_{c1} and a_{c2} are reaction parameters and M is the mole fraction, which is equal to the partial pressure at atmospheric pressure. This equation means that increase of O_2/CO_2 concentration in the cathode gas leads to decrease of the cathode polarization resistance.

These results show that the cell performance of TMC-DCFCs is improved by increase of O_2/CO_2 concentration in the cathode gas as with MCFCs (5).

Influence of the difference in carbon fuel

Figure 4 shows I-V curves of the TMC-DCFC with activated carbon and carbonized wood. Carbon/carbonate ratio was 80/20 for activated carbon and 65/35 for carbonized wood. The cathode gas composition was O_2/CO_2 (33/67 vol%). The difference of OCV was relatively small. Although the difference of the overvoltage increased as the current density increased until 100 mA/cm^2, it decreased after 100 mA/cm^2. These behaviors are considered to correspond to the change of OCV during I-V measurements. The current density was raised 10 mA/cm^2 per minute during the I-V measurement, so increase of the current density meant time passed. In addition, it is known that reverse Boudouard reaction [8] occurs and CO is generated in fuel mixture during power generation at 1073 K (1).

$$C(s) + CO_2(g) = 2CO(g) \quad (\Delta G_f = -17.5 \text{ kJ/mol at } 1073 \text{ K}) \quad [8]$$

Therefore, the gas composition around the anode gradually changes for a while after the current density changes. This transition is affected by the state of fuel mixture. Since the carbon/carbonate ratio when using carbonized wood was different from that when using activated carbon, transition of the gas composition around the anode between two conditions might be different. It led to the change of OCV during I-V measurement from equation [4] or [5]. On the other hand, the difference of the cell voltage was relatively small at the high current density. The gas composition around the anode would become same level as time passed. These results suggest that the difference of the electrode overvoltage is comparatively small between two conditions.

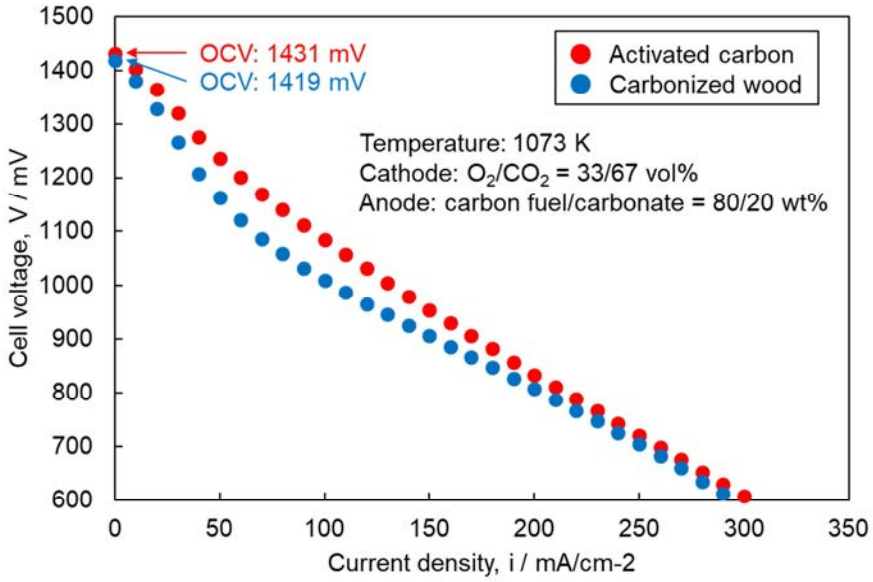

Figure 4. I-V curves of the TMC-DCFC with each carbon fuel.

Figure 5 shows cell voltage transient curves during continuous power generation tests for 120 min with each carbon fuel. The cathode gas composition was O_2/CO_2 (33/67 vol%) and the current density was 230 mA/cm^2. The cell voltages became stable about 60 min after the beginning of power generation. High power density over 160 mW/cm^2 was obtained when using carbonized wood as well as when using activated carbon. These results show that TMC-DCFCs can sufficiently use carbonized wood powder as fuel and a small amount of ash hardly affects the cell performance. In addition, the change of the carbon/carbonate ratio is considered to be permissible to some extent for TMC-DCFCs.

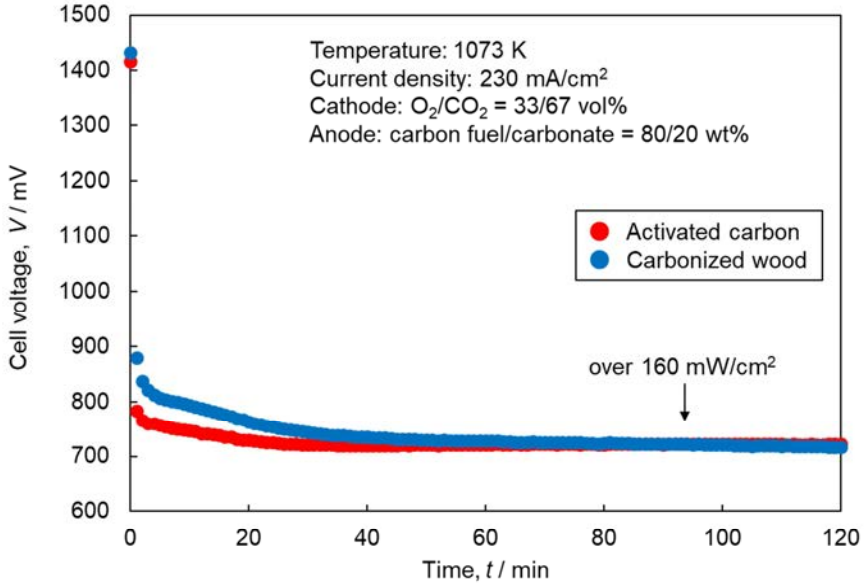

Figure 5. Cell voltage transient curves during continuous power generation tests.

On the other hand, it is presumed that some problems occur when the carbon/carbonate ratio is immoderate. When solid carbon is too much in the fuel mixture, the contact between the anode and solid carbon might be poor because molten carbonate has an effect on the contact between them. When molten carbonate is too much in the fuel mixture, the electrode flooding might occur. Both of them lead to decrease of Three phase boundary (TPB) on the anode and degradation of cell performance. A moderate carbon/carbonate ratio for TMC-DCFCs should be investigated furthermore to improve the cell performance and to achieve long-term operation.

Conclusions

Basic performance of TMC-DCFCs such as influence of the difference in the cathode gas and fuel on the cell performance was investigated. It was shown that the cell performance of TMC-DCFCs was improved by increase of O_2/CO_2 concentration in the cathode gas as with MCFCs. When using carbonized wood, high power density over 160 mW/cm^2 was obtained as well as when using activated carbon. TMC-DCFCs could sufficiently use carbonized wood powder as fuel. These results suggested that a small amount of ash hardly affects the cell performance and the change of the carbon/carbonate ratio was permissible to some extent.

References

1. A.Ido and M. Kawase, *J. Power Sources*, **449,** 227483 (2020).
2. M. Kawase, *J. Power Sources*, **285**, 260-265 (2015).
3. M. Kawase, *J. Power Sources*, **371**, 106-111 (2017).
4. H. Morita, M. Komoda, Y. Mugikura, Y. Izaki, T. Watanabe, Y. Masuda, and T. Matsuyama, *J. Power Sources*, **112**, 509-518 (2002).
5. H. Morita, Y. Mugikura, Y. Izaki, T. Watanabe, and T. Abe, *J. Electrochem. Soc.*, **145**(5), 1511-1517 (1998).

Chapter 5

L02 – Materials from Ionic Liquids Session in Recognition of Prof. Sheng Dai

ECS Transactions, 98 (10) 99-113 (2020)
10.1149/09810.0099ecst ©The Electrochemical Society

Developing Polyionic Biocomposite Materials through Natural Fiber Welding

David P. Durkin,[a] Christian E. Hoffman,[a] Tyler Cosby,[a] Ashlee Aiello,[a] Julia A. McFarland,[a] Hugh C. De Long,[b] Jeremiah W. Woodcock,[c] and Paul C. Trulove[a]

[a] Department of Chemistry, U. S. Naval Academy, Annapolis, MD, 21401, USA
[b] U. S. Army Research Office, Research Triangle Park, NC, 27709, USA
[c] Material Measurement Laboratory, Materials Science and Engineering Division, National Institute of Standards and Technology, Gaithersburg, MD, 20899, USA

This study presents our progress on using imidazolium-based polymerizable ionic liquids (Poly-ILs) in the NFW process to prepare polyionic biocomposites. Two novel Poly-ILs containing the 1-alkyl-3-vinylimidazolium cation and an alkylphosphonate anion were synthesized and subsequently characterized using NMR. Each Poly-IL was evaluated for its ability to (i) polymerize and (ii) solubilize a biopolymer (cellulose) matrix, and optimized parameters yielded polyionic biocomposite materials whose physicochemical properties were evaluated using ATR-FTIR, RAMAN, and SEM.

Introduction

Biomaterials (e.g., cotton, wood, silk) are abundant natural resources formed from biopolymers (e.g., cellulose, lignocellulose, silk proteins) that were the primary textile and manufacturing material until the introduction of synthetic polymers such as Bakelite and nylon (1,2). However, these natural biomaterials often have mechanical properties (e.g., strength, toughness) exceeding those of synthetic polymer materials such as Kevlar and steel (3-6). The superior mechanical properties are derived from the complex native structure of the material. Current industrial methods for processing biomaterials alters the innate morphology of the biomaterials and use toxic solvents such as carbon disulfide (7,8). The result of these processes are materials with degraded mechanical properties and the release of hazardous byproducts. Our previous research has focused on enhancing the chemical and physical properties of biopolymer materials, particularly cotton, using a patented and environmentally-friendly process termed Natural Fiber Welding (NFW), that enables the controlled manipulation of native biopolymer materials using ionic liquids (ILs) (9-11). This report discusses our progress towards creating fiber welded polyionic biocomposites using polymerizable ionic liquids (Poly-ILs) and evaluating the material's physicochemical properties.

Biomaterials have complex, highly ordered, structures that form during the natural synthesis process. The superior mechanical properties of biomaterials originate from this complex structure. Degrading any portion of the structure leads to the deterioration of mechanical properties. Using ILs, the NFW process enables controlled manipulation of biomaterials and their structure without significantly degrading their material properties (12). Ionic liquids (IL) are nonvolatile, low melting point salts (typically < 100 °C) (13,14). The low melting point of ILs is cause by weak-intermolecular interactions between the

cation and anion pair, as well as the inability for the pair to stack well in a crystalline structure (15). Altering the cation/anion combinations produces ILs with unique physical and chemical properties that can be exploited for a variety of applications including environmentally-friendly purifiers (16), lubricants (17), and solvents for biomaterials (7). Polymerizable ionic liquids (Poly-ILs) are ILs that contain an alkenyl functional group, such as a vinyl (-CH=CH_2) or allyl (-CH_2-CH=CH_2), in the cation or anion structure. These functional groups can undergo controlled radical chain growth polymerization with heat (i.e., thermal initiation), or UV irradiation (i.e., photoinitiation) using radical initiators (18,19).

Extensive research has been conducted on the use of ILs to solubilize biomaterials such as silk (20-22) and cotton (7,13,23,24). The manipulation of these natural materials to further enhance their mechanical properties has been accomplished using ILs in a process called Natural Fiber Welding (NFW) (9,10,12). The NFW process controls the dissolution of biopolymers through careful regulation of IL concentration, exposure time, and environmental conditions. Upon contacting a biomaterial substrate, the chaotropic cations and anions of the IL disrupt both the intra- and inter-molecular van der Waals forces between individual biopolymer chains. Disrupting these bonding forces enables the mobilization of the biopolymer. The degree of mobilization is dependent upon the interaction time between the biopolymer and IL and viscosity of the IL. Longer welding times and less viscous ILs enable a greater biopolymer mobilization. When the IL is removed from the biopolymer with a solvent (e.g., water, methanol, acetone), a process termed 'quenching', the van der Waals forces within and between biopolymer strands reform. The result of the NFW process is a redistributed biopolymer matrix that has enhanced physical and chemical properties (25). An alternative quenching process is possible when using Poly-ILs in the NFW process. Polymerizing Poly-ILs during NFW creates a cation or anion polymer chain that inhibits disruption of the van der Waals forces and limits further mobilization of the biopolymer. In-situ polymerization also retains the Poly-IL within the biopolymer matrix, potentially providing enhanced chemical properties, such as charged species mobilization.

Previous work in our group has successfully demonstrated the ability for certain Poly-ILs to act as NFW solvents while retaining their ability to polymerize (11,26). This prior work resulted in the synthesis of rudimentary polyionic biocomposites which required welding times of 3 hours and temperatures of 100 °C, conditions that are not optimal for timely and energy-efficient synthesis. Further work was also needed to exercise control over the polymerization process. The scope of the present work is focused on optimizing Poly-IL composition (cation and anion) to facilitate controlled polymerization, shorter welding times, and lower welding temperatures during the synthesis of polyionic biocomposites. This report outlines recent efforts using two novel Poly-ILs containing the 1-alkyl-3-vinylimidazolium cation and alkylphosphonate anions. The Poly-ILs were synthesized and characterized before being evaluated for their ability to polymerize and act as an NFW solvent. Poly-ILs that met both of these criteria were further investigated for their ability to prepare polyionic biocomposites. The structure and morphology of synthesized polyionic biocomposites were evaluated via SEM, RAMAN and ATR-FTIR, and initial methods are presented that can be used to further explore their material properties through TGA and EIS.

Experimental

Materials

The following chemicals were used as received: Cotton yarn (white, 100% cotton, mercerized, Coats Cotton), microcrystalline cellulose (MCC, Sigma), deuterium oxide (99.8%, Acros Organics); dimethyl sulfoxide (DMSO-d_6, 99.9%, Sigma Aldrich); acetonitrile (ACN, 99.8%, Sigma-Aldrich); 2-hydroxy-2-methylpropiophenone (HMPP, 97%, Sigma-Aldrich); methanol (99%, Pharmco-Aaper); 2,6-di-tert-butyl-4-methylphenol (BHT, 99%, Aldrich); azobisisobutyronitrile (AIBN, 98%, Sigma-Aldrich); potassium persulfate (99%, Sigma-Aldrich); sodium hydroxide pellets (98.8%, Fisher); chloroform-*d* (99.8%, Acros Organics); and tetrahydrofuran (THF, 99%, Sigma-Aldrich). Dimethyl phosphite (98%, Sigma-Aldrich); diethyl phosphite (98%, Sigma-Aldrich), and 1-vinylimidazole (99%, Aldrich) were distilled before conducting alkylation reactions. All aqueous solutions were prepared using ultrapure water (Barnstead E-pure filtration system) with resistivity of > 18 MΩ cm^{-1}.

Poly-IL Synthesis

The Poly-ILs highlighted in this study are show in in Figure 1. Each were synthesized via the alkylation of 1-vinylimidazole with a dialkylphosphite (Figure 1a) and their final structures (Figure 1b) were confirmed via NMR. For purposes of this report, the Poly-ILs will be abbreviated at follows: 1-ethyl-3-vinylimidazolium ethylphosphonate (EVIEPhos), 1-methyl-3-vinylimidazolium methylphosphonate (MVIMPhos).

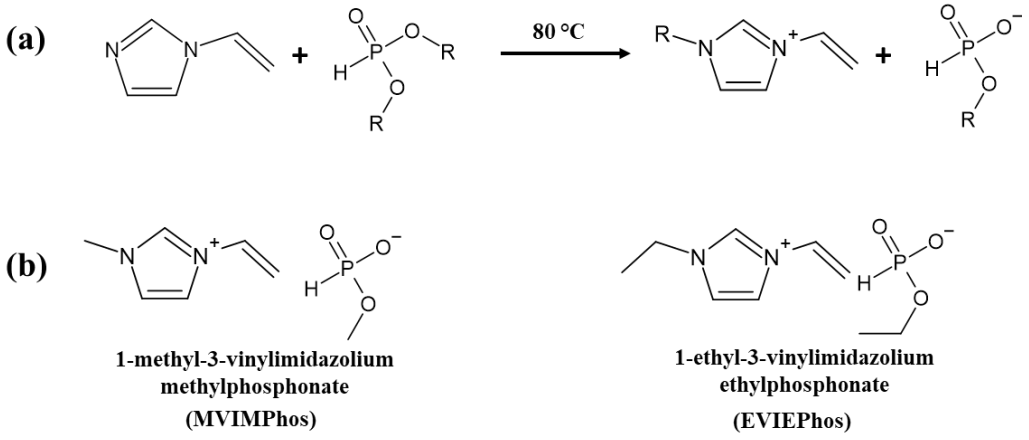

Figure 1. Showing the (a) general scheme for alkylation of 1-vinylimidazole with dialkylphosphite where R- represents one of the alkyl groups (-CH_3 or –CH_2CH_3) on the dialkylphosphite reactant to synthesize (b) the phosphonate-based Poly-ILs highlighted in this report.

1-vinylimidazole and dimethylphosphite (10 mole% excess of dimethylphosphite) were mixed in 50% (v/v) dry THF in accordance with procedures by Fukaya *et al.*(27). The solution was refluxed and stirred under N_2 for two days. Excess THF was removed under reduced pressure via rotary evaporation. The resulting MVIMPhos solution was transferred to a separatory funnel, rinsed with ethyl ether three times to remove any excess reactant, then dried under reduced pressure via rotary evaporation. The MVIMPhos was

placed on a vacuum line to dry for 7 days, then transferred into a dry N_2 atmosphere glovebox as an amber room-temperature liquid. EVIEPhos was synthesized in a similar manner (using 1-vinylimidazole:diethylphosphite), except the solution was refluxed under N_2 for 21 days because the diethylphosphite was less reactive than the dimethylphosphite. Each product was characterized using ^{1}H NMR in DMSO-d_6.

Ex-situ Polymerization of Poly-ILs

EVIEPhos and MVIMPhos were polymerized with a photoinitiator (HMPP) or with thermal initiators (AIBN or potassium persulfate) via radical chain growth polymerization. Solutions of EVIEPhos, and MVIMPhos with various mole% of HMPP were prepared in the glovebox and irradiated with a 120V/100W mercury vapor lamp (Evergreen Pet Supplies) from 3 min to 1 hr. This procedure was repeated for neat Poly-IL samples, Poly-IL solutions containing 3 wt% MCC, and samples that had undergone microwave NFW treatment. These polymerized products of neat Poly-ILs were dissolved in DMSO-d_6 and characterized using ^{1}H-NMR and Raman spectroscopy. For thermally initiated polymerizations, potassium persulfate was added to neat Poly-ILs while AIBN required a co-solvent to dissolve into solution. Both initiators were added in 1 mole% concentrations with respect to the Poly-IL. The solutions were initiated at temperatures between 60 °C to 100 °C for times ranging from 5 min to 1 hr. These polymerized products were characterized using ATR-FTIR spectroscopy. Raman spectroscopy was attempted, but unsuccessful because the polymerized samples emitted a large amount of fluorescence during analysis.

Poly-IL Welding Experiments

In the glovebox, cotton yarns were wetted with MVIMPhos at 92 °C for treatment times of 10, 20, and 30 min. This temperature was selected to match viscosity of 1-ethyl-3-methylimidazolium acetate, the most common NFW solvent used in our lab. Welding was quenched with a methanol rinse. The treated yarns were then rinsed in ultrapure water for 24 hr before drying in at 60 °C for 24 hr. After drying, the yarns were potted in epoxy, cross-sectioned using a microtome, and characterized using Raman spectroscopy. Similarly, in the glovebox neat EVIEPhos and a solution of EVIEPhos:1 mole% HMPP were heated to 90 °C for five min. Aliquots of each liquid were deposited onto cotton yarns arranged in parallel and perpendicular orientations. Treatment lasted for 60 min at 90 °C before welding was quenched via methanol rinse for the neat EVIEPhos treated yarns and UV irradiation (30 min) for the EVIEPhos:HMPP treated yarns. Yarns treated with neat EVIEPhos were then rinsed in ultrapure water for 24 hr before drying in a 60 °C oven for 24 hr. Following drying, neat EVIEPhos treated yarns were cross-sectioned, gold sputter coated, and analyzed via SEM.

Instrumental Methods

Nuclear Magnetic Resonance Spectroscopy (NMR). ^{1}H and ^{13}C NMR spectroscopy was conducted using a JEOL 400 MHz Spectrometer with JEOL Delta software. NMR spectroscopic analysis was utilized to monitor synthesis progress and assess the ultimate purity the Poly-ILs. In addition, NMR was used to evaluate the extent of polymerization of the Poly-ILs after initiation. To perform NMR measurements the neat and polymerized Poly-ILs were dissolved in either DMSO-d_6, $CDCl_3$, or D_2O.

Attenuated Total Reflection Fourier Transform Infrared Spectroscopy (ATR-FTIR). ATR-FTIR spectra were collected using a Thermo Scientific Nicolet iS50 FTIR spectrometer. Spectral analysis was conducted using Thermo Scientific's OMNIC software.

Raman Spectroscopy. Raman was conducted using a Renishaw inVia Qontor confocal Raman microscope with an excitation wavelength of 785 nm over the range 325 – 1500 cm^{-1}. The exposure time and laser power were adjusted to maximize the signal-to-noise level while preventing sample damage. Spectral mapping was accomplished using Renishaw's software in StreamLine Map mode. The spatial resolution under the measuring conditions was approximately 1.9 μm/pixel.

Scanning Electron Microscopy (SEM). SEM was performed using a Tescan Mira3. Imaging was conducted at 10 kV acceleration voltage. Unpolymerized fiber-welded samples were gold sputtered prior to analysis to prevent sample charging. Polyionic biocomposites did not require gold sputtering due to their ability to adequately conduct electrons during imaging.

Thermogravimetric Analysis (TGA). TGA (TA Q500) was used to evaluate the thermal stability of MVIMPhos in N_2 and in air. Samples were evaluated under conditions similar to the isothermal welding experiment (60°C for 60 min) and subsequent thermal initiation polymerization experiment (80°C, 90°C or 100°C for 120 min) as discussed in this report. The TGA data were analyzed using TA Universal Analysis software.

Results and Discussion

Evaluating the Structure, Polymerizability and Welding Potential of 1-alkyl-3-vinylimidazolium Alkylphosphonate Poly-ILs

Experiments with EVIEPhos (and MVIMPhos) were motivated from the results of several reports that demonstrated the ability for alkylphosphonate-based ILs to dissolve cellulose (27-29). In order for ILs to be useful in this study, they must be (i) polymerizable and (ii) able to fiber-weld natural biopolymer materials. Successful, reproducible polymerization was first achieved with EVIEPhos using the photoinitiator HMPP (1 mole% and 2 mole%) and irradiation via 120V/100W mercury vapor lamp. Generally, it was observed that as the mole% of photoinitiator increased, the hardness of the polymerizable product decreased forming viscous liquids vice hard plastics. EVIEPhos polymerization experiments also indicated that the degree of polymerization was influenced by the time of exposure to the UV source. At low (3 min) irradiation times, EVIEPhos solutions (at all HMPP concentrations) did not appear to polymerize appreciably; however, when irradiated for longer periods of time (30-60 min), the EVIEPhos polymerized into a solid material.

Next, we determined that EVIEPhos could dissolve cellulose. While this is not completely necessary to be considered as an NFW solvent (previous work in our lab has shown that some ILs that do not dissolve cellulose can still be used for NFW(11)) it is a simple screening method. Solutions of EVIEPhos:3 wt% MCC with HMPP (1 mole% with

respect to the EVIEPhos) were easily prepared, and when polymerized produced harder plastics (than products absent MCC) following 1 hr irradiation. The polymerized material had minimal deformation when exposed to pressure, but still demonstrated hygroscopic properties when exposed to the atmosphere outside of the glovebox. Our results suggest that MCC acted as a binder within the new polymer matrix, thereby producing harder materials.

NFW experiments conducted with EVIEPhos successfully produced welded substrates. Cotton yarns were treated with EVIEPhos at 90°C for 60 min in the N_2 atmosphere glovebox. After 60 min the yarns appeared swollen, indicating the EVIEPhos had sufficiently wetted the material. Additional swelling in areas not originally wetted with the Poly-IL indicated that the EVIEPhos had a low enough viscosity to wick along the yarns. Following quenching and reconstitution, the structure and morphology of the EVIEPhos-treated yarns were characterized with SEM (Figure 2).

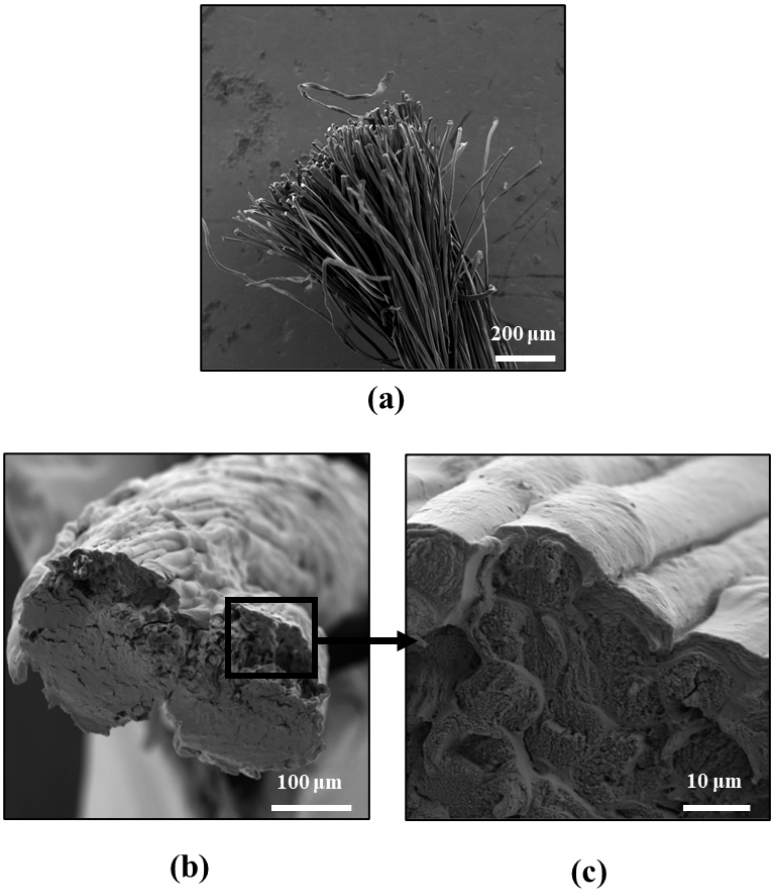

Figure 2. Scanning electron microscopy images of, (a) untreated cotton yarn, (b) low resolution and, (c) higher resolution images of cotton yarn fiber-welded with EVIEPhos.

The region at the top of Figure 2b illustrates the surface of the treated yarns. Individual fibers have consolidated on the surface of the yarns and there appears to be a coating of biopolymer material that conjoins the fibers. Further, the image depicts the region between the two yarns where the mobilized material had propagated and been reconstituted in a manner that welds the yarns together. Figure 2c shows the depth at which the EVIEPhos and mobilized material penetrated the yarn matrix. While the structure of the fibers has

been altered, there are clear veins of material that extend down from the surface and in-between the fibers located within the yarn. Additionally, the consolidated material on the surface is readily apparent, coating the exterior of individual fibers and linking adjacent fibers together. These images demonstrate the ability for EVIEPhos to adequately weld the surface of the cotton yarn substrates and permeate into the biopolymer matrix. These results, combined with the successful polymerization, make EVIEPhos a promising candidate for creating polyionic biocomposites.

Novel polyionic biocomposites were successfully prepared from cotton yarns and EVIEPhos. A solution of EVIEPhos:1 mol % HMPP photoinitiator was prepared and heated to 90 °C for 5 min to lower the viscosity of the solution. The EVIEPhos:HMPP solution was then applied to cotton yarns in parallel and perpendicular configurations for 60 min at 90 °C. After 60 min the treated yarns appeared swollen from the uptake of the Poly-IL solution. Observations also indicated the successful mobilization of the material as the two parallel yarns were now indistinguishable and appeared to form one yarn. Following polymerization of the EVIEPhos by irradiating the samples with a UV light for 30 min, the yarns appeared to consolidate further and decrease in diameter. These physical changes mirrored the observations of standard NFW experiments and were the first indications of a successful welding and polymerization sequence to form a polyionic biocomposite. The biocomposite's surface and cross-section were characterized using SEM (Figure 3).

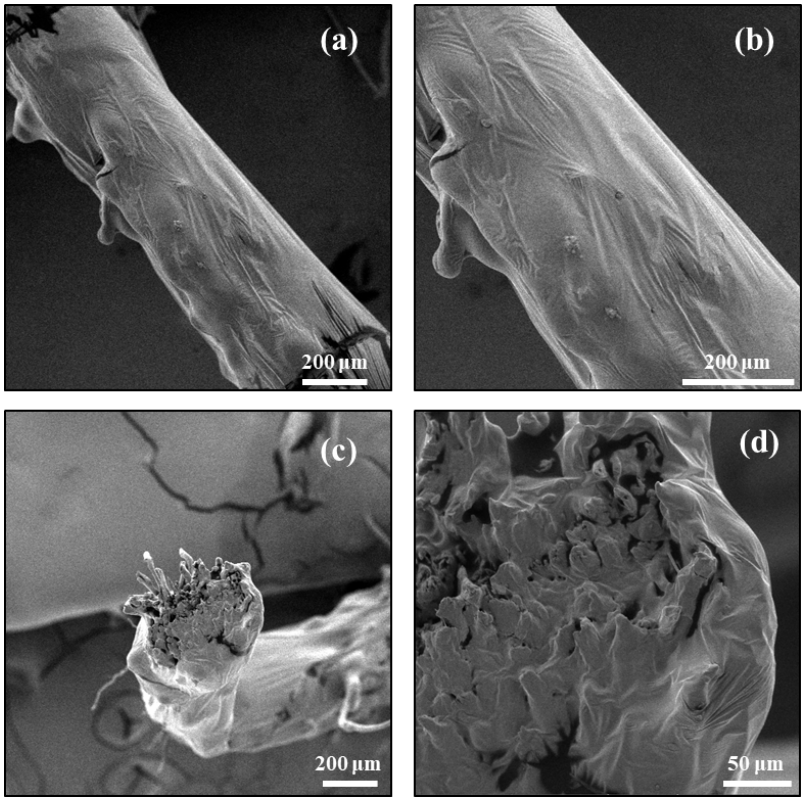

Figure 3. Scanning electron microscopy of a polyionic biocomposite synthesized with EVIEPhos showing (a) low-resolution surface image, (b) high-resolution surface image, (c) low-resolution cross-section image, (d) high-resolution cross-section image.

Figure 3a and 3b indicate a relatively smooth surface with small wrinkles scattered across the yarn. This surface feature resembles the shell of mobilized cotton present in substrates that have undergone extensive welding. However, this degree of welding is not present in the cotton substrates welded at the same temperature and time (see Figure 2). Comparison of Figure 2 and Figure 3 suggests that the surface features are the result of an EVIEPhos polymer coating on the surface of the welded yarn. The polymer coating appears more readily in Figure 3d, in which the edge of the cotton yarn is encompassed by the amorphous coating. These observations are unique to the EVIEPhos polyionic biocomposite. In Figure 2c, which illustrates welding quenched with the removal of EVIEPhos, the individual fibers are distinguishable on the surface of the yarn and around the edges of the cross section. This suggests that the surface features in Figure 3 are the result of the polymerization of the EVIEPhos on the surface of the welded yarn.

While EVIEPhos was successfully shown to synthesize polyionic biocomposites, experiments soon shifted to MVIMPhos due to our ability to produce MVIMPhos in larger quantities with additional purification steps in accordance with the literature (27). Polymerization of MVIMPhos was conducted via photo- and thermal-initiation using HMPP and potassium persulfate initiators, respectively. Solutions of MVIMPhos:1 mole% HMPP were initiated with a 120V/100W mercury vapor lamp for 30 min to produce a hard plastic. Following irradiation and cooling, the poly-MVIMPhos was characterized using ^{1}H NMR, Raman, and ATR-FTIR spectroscopies.

Differences between the ^{1}H NMR spectra (not shown) of the neat and polymerized MVIMPhos indicated successful polymerization. Analysis of the sharp C=C peak (ca. 1660 cm^{-1}) in the Raman spectrum (Figure 4) indicates the relative concentration of the vinyl group present in the MVIMPhos monomer. Comparison of the normalized Raman spectra demonstrates a substantial decrease in the concentration of the vinyl group after initiation.

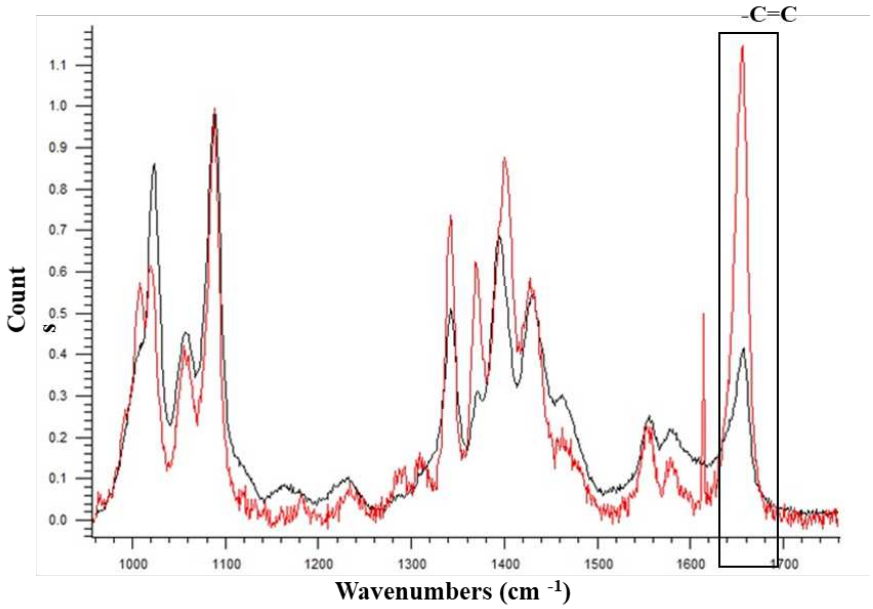

Figure 4. Raman spectra of 1 mole% HMPP:MVIMPhos pre-initiation (red) and after UV irradiation for 30 min (black).

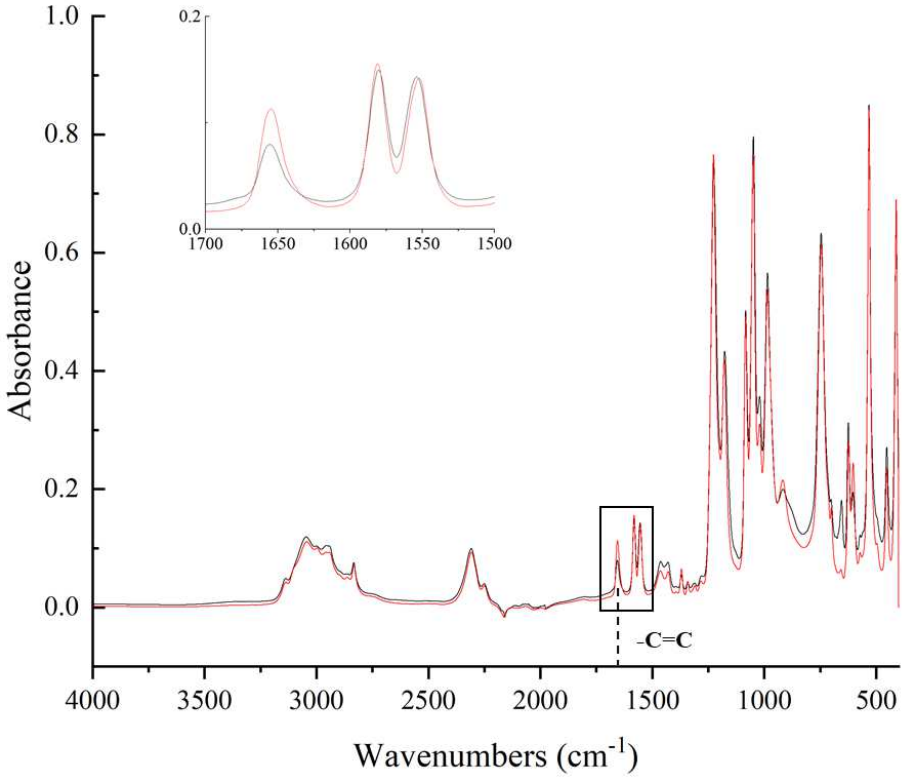

Figure 5. ATR-FTIR spectra of neat MVIMPhos (red) and poly-MVImMPhos (black) from 1 mole% HMPP:MVIMPhos after UV irradiation for 30 min. Spectra were peak normalized to the stretch at ca. 2830 cm^{-1} which is present in each sample with invariant intensity.

Results from the Raman spectra were supported by analysis of the C=C stretch (ca. 1655 cm^{-1}) in the ATR-FTIR spectra, shown in Figure 5. Comparison of the neat and polymerized MVIMPhos spectra indicate a decrease in the concentration of the vinyl group after polymerization. This decrease, along with the change in physical properties supports successful polymerization. However, the continued presence of the peak post-initiation also indicates the presence of residual MVIMPhos monomer, suggesting further optimization is needed for this polymerization route.

Polymerization was also conducted using solutions of MVIMPhos:1 mole% potassium persulfate, a thermal initiator. Potassium persulfate was chosen because it is an ionic compound that is soluble in the MVIMPhos. Solutions of MVIMPhos containing persulfate became substantially more viscous over a period of 24 hr, indicating polymerization could occur slowly at room temperature. The effect of temperature and time on the extent of polymerization was evaluated by polymerizing samples of MVIMPhos:1 mole% potassium persulfate solutions at 60 °C, 80 °C, and 100 °C for times ranging from 5 to 45 min. The resulting polymers were characterized using ATR-FTIR and are shown in Figure 6.

Similar to the analysis of Figure 5, the C=C stretching peak (ca. 1655 cm^{-1}) was used to determine the relative extent of polymerization. Each spectrum demonstrates a decrease in vinyl group concentration with an increase in polymerization time. Additionally, all of the ATR-FTIR spectra indicate the presence of residual MVIMPhos monomer, as the vinyl

peak persists even after being exposed to 100 °C for 45 min. The continued presence of the vinyl peak suggests a significant concentration of monomer remains after polymerization. Further, while the vinyl peak generally decreases with increase polymerization time, there appears to be a time at which the concentration change of the vinyl functional group is minimal. This result suggests that there is a time beyond which polymerization proceeds at a much slower rate.

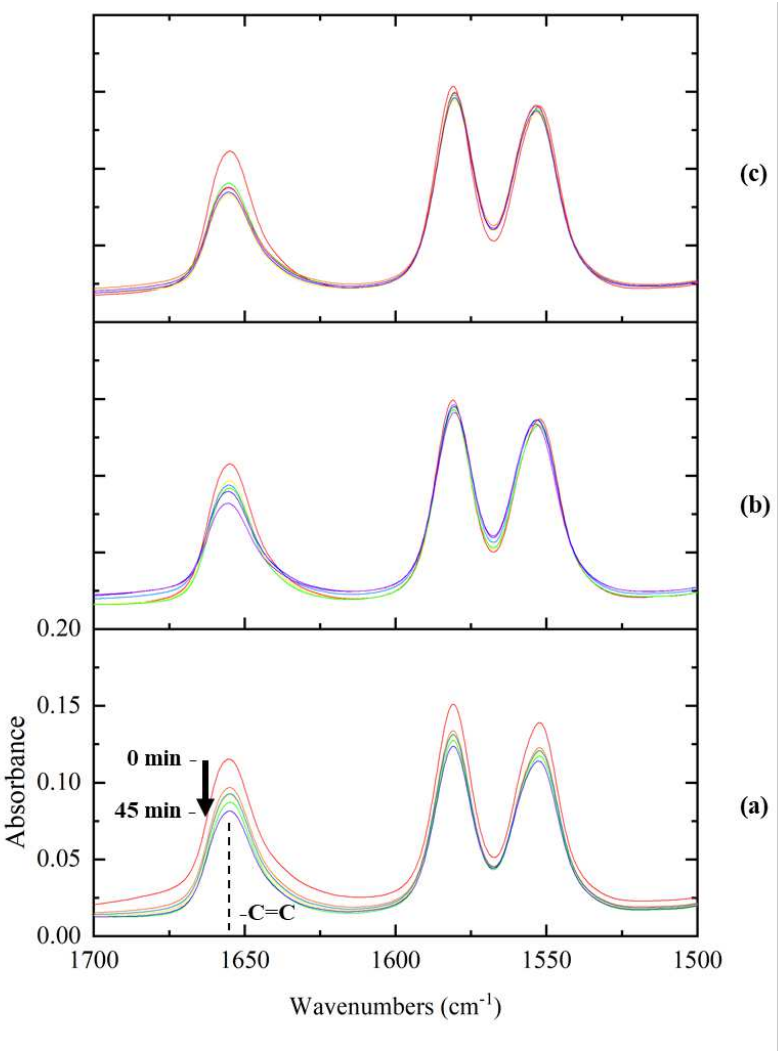

Figure 6. ATR-FTIR spectra of MVIMPhos containing 1 mole % potassium persulfate polymerized at (a) 60 °C, (b) 80 °C, and (c) 100 °C for times ranging from 0 min to 45 min (as indicated by the arrow in frame (a)). A similar reduction in the C=C stretch was observed in the spectra at each welding temperature. Spectra were peak normalized to the stretch at ca. 2830 cm^{-1} which is present in each sample with invariant intensity.

Successful welding was also achieved when cotton yarns were treated with MVIMPhos. Cotton yarns were treated with MVIMPhos at 92 °C for times ranging from 10 min to 30 min. After quenching and reconstituting with rinses of methanol and water, the treated yarns were potted in epoxy and cross sectioned. Characterization of the cross-sections using Raman spectroscopy produced spectral contour plots for each sample (Figure 7). The contour plots measure the relative intensity of a peak at 380 cm^{-1}, which decreases as the extent of welding increases, compared to a peak at 354 cm^{-1}, which remains unchanged during the welding process.

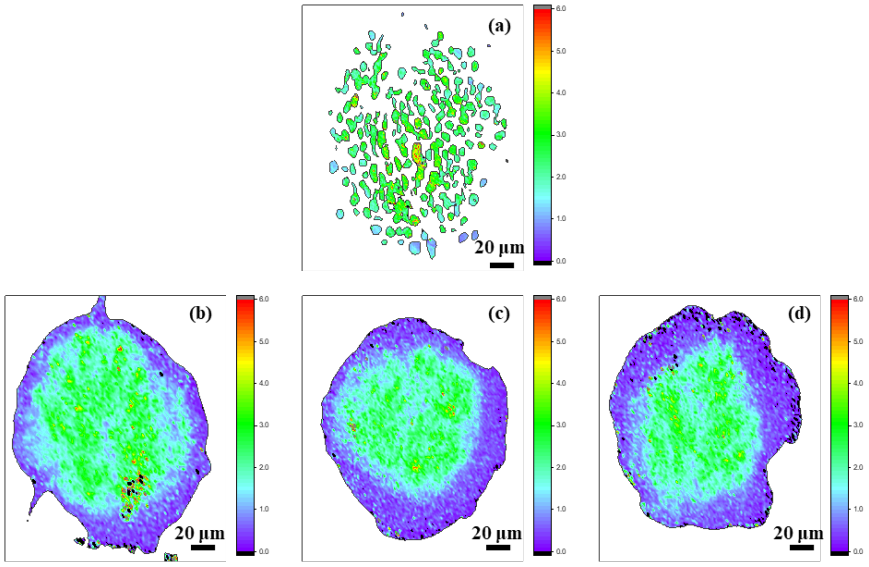

Figure 7. Cross-section contour plot of the intensity ratio between 380 cm^{-1} and 354 cm^{-1} peaks for cotton yarns welded with MVIMPhos at 92 °C at various times, (a) 0 min treatment (untreated control), (b) 10 min treatment time, (c) 20 min treatment time, and (d) 30 min treatment time.

In the Raman maps, individual fibers are distinguishable in the untreated cotton yarn (Figure 7a). Once the yarn has been treated with MVIMPhos, it undergoes considerable consolidation as seen in the Figures 7b, 7c, and 7d, similar to what was observed in SEM images of cotton welded with EVIEPhos (Figure 2). Present in each Raman map of the treated yarns is a 'violet ring' on the outermost edge of the yarn that increases with welding time. This violet ring represents the outer regions of the yarn that have undergone a transition from crystalline (the light-green colored core) to amorphous cellulose, as a result of biopolymer interactions with the MVIMPhos during fiber-welding. This effect clearly increases with welding time, as shown in Figure 7b-d. These contour plots support the successful welding of cotton substrates and demonstrated the potential for MVIMPhos to synthesize polyionic biocomposites.

Following the successful polymerization and welding experiments, MVIMPhos was used to synthesize polyionic biocomposites using the potassium persulfate thermal initiator. A thermal initiator was chosen in an effort to produce a more thorough and consistent polymerization throughout the biocomposite matrix, as previous experiments with photoinitiators had only achieved polymerization on the surface of the welded substrate. Polyionic biocomposites were synthesized by treating cotton yarns with a solution of MVIMPhos:1 mole% potassium persulfate at 60 °C for times ranging from 5 min to 60 min. The temperature was then increased to 100 °C for 19 hr to initiate polymerization. A lower welding temperature was selected to minimize the extent of polymerization occurring during the welding process. Extensive polymerization times were utilized to ensure sufficient polymerization of the material. After polymerization, the polyionic biocomposites were characterized using SEM (Figure 8). Due to the ability of the polymerized MVIMPhos to conduct electrons, a gold sputter coating was not required to obtain the SEM images. Each of the images in Figure 8 demonstrates material consolidation, as many of the fibers have coalesced into one welded bundle. In addition, a coating of polymerized MVIMPhos clearly covers each of the welded yarns. The fact that

the polymerized MVIMPhos did not significantly charge during analysis at 10kV supports the conclusion that the resulting polyionic biocomposites are conductive.

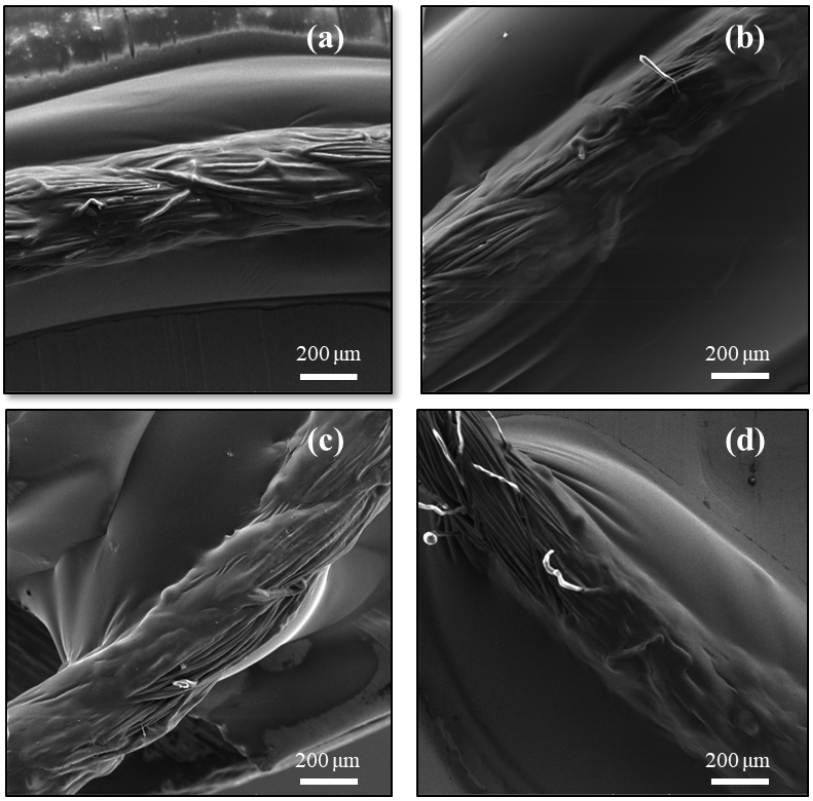

Figure 8. Scanning electron microscopy of polyionic biocomposites produced via welding with MVIMPhos:1 mole% potassium persulfate solution at 60 °C for (a) 5 min, (b) 15 min, (c) 45 min, and (d) 60 min. After welding, each sample was polymerized at 100 °C for 19 hr.

Optimizing Polymerization and Welding Parameters using Thermogravimetric Analysis

Due to the elevated temperatures and extended polymerization times used to synthesize the MVIMPhos-based polyionic biocomposites, TG analysis of neat MVIMPhos was conducted to investigate potential degradation of the Poly-IL (Figure 9). Samples of neat MVIMPhos were heated in an N_2 atmosphere at 60 °C for 60 min before the temperature was increased to either 80 °C, 90 °C, or 100 °C and held there for 2 hr.

Sample weight loss was observed to occur at a constant rate once the maximum thermal temperature was reached. The onset of the weight loss was indicated by the presence of a local maximum in the first derivative of the sample weight change (ca. 77 min). In an effort to determine whether the weight changes were more substantial than the evaporation of water from the sample, a comparison was conducted between the ratio of the rate of mass loss and ratio of the changes in the heat of vaporization of water (see Table I) (30). Analysis indicates that between 80 °C and 100 °C the change in heat of vaporization for water increases at a near constant value while the ratio of mass loss doubles between 80 °C to 90 °C and 90 °C to 100 °C. This suggests that more than just the evaporation of water contributes to sample weight loss at higher temperatures. Sample analysis was also done in air and showed higher rates of mass loss most likely due to air oxidation.

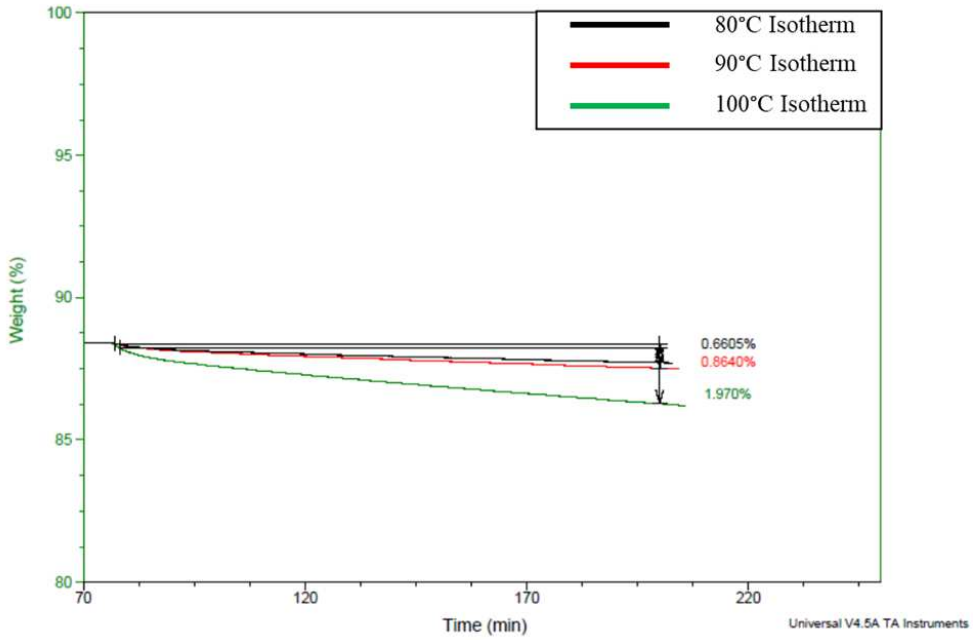

Figure 9. Thermogravimetric Analysis of MVIMPhos in N_2 at 80 °C, 90 °C, and 100 °C.

Table I. Summary of MVIMPhos TGA Data

Isothermal Temperature (°C)	Mass loss During Polymerization Isotherm (%)	Rate of Mass Loss During Polymerization Isotherm (%/min)	Heat of Vaporization (kJ/kg)	Ratio of the Rate of Mass Loss	Ratio of the Heat of Vaporization
100	1.97	0.016	417.50 (ca. 99.6 °C)	2.3	1.1
90	0.86	0.0070	377.06		
				1.3	1.1
80	0.66	0.0053	335.10		

These TGA data suggest that lower initiation temperatures would mitigate potential sample degradation over extended polymerization times. These results will be used to inform future experiments to design polyionic biocomposites while maintaining sample integrity. Additionally, fine-tuning synthesis parameters may lead to more energy efficient and timely synthesis processes.

Conclusion

In this study, two novel ILs containing the 1-alkyl-3-vinylimidazolium cation and alkylphosphonate anions are presented as viable NFW solvents and are used to create polyionic biocomposites. Polymerization experiments demonstrated the ability for EVIEPhos and MVIMPhos to can polymerize ex-situ using photo- and thermal initation. Increasing exposure time and/or the addition of 3 wt% MCC resulted in the successful formation of hard plastics using HMPP photoinitiator. Potassium persulfate was effective at various temperatures to polymerize MVIMPhos and extended polymerization times

>1hr. Following successful ex-situ polymerization, NFW experiments were conducted on cotton yarn substrates; MVIMPhos and EVIEPhos both show potential as welding solvents. Polyionic biocomposites were successfully prepared with both EVIEPhos and MVIMPhos using a HMPP photoinitiator and potassium persulfate thermal initiator. SEM images of the biocomposites demonstrated substantial welding and polymerization had occurred on the treated yarns. Further, imaging was conducted without sputter coating the biocomposites and did not result in charge buildup on the sample, indicating that the biocomposites were sufficiently conductive. TGA was shown to be an effective tool to help optimize design parameters, and EIS shows promise for elucidating the conductive properties of the composites.

Acknowledgments

This work was primarily funded by the Air Force Office of Scientific Research [MIPR# F4FGA08354G001]. We are grateful for the facilities support from the USNA Chemistry Department. Any opinions, findings, conclusions, or recommendations expressed herein are those of the authors and do not necessarily reflect the views of the U.S. Navy or U.S. Air Force.

References

[1] Society, A. C., The Bakelizer Commemorative Booklet. ACS: Washington D.C., 1993; pp 1-5.
[2] Hoff, G. P., *Ind. Eng. Chem.* **1940,** *32* (12), 1560-1564.
[3] Liu, X.; Zhang, K.-Q., In *Oligomerization of Chemical and Biological Compounds*, Lesieur, C., Ed. InTech: Rijeka, 2014; p Chapter 3.
[4] Byrom, D., *Biomaterials: Novel Materials from Biological Sources*. Stockton Press: New York, NY, 1991.
[5] Agnarsson, I.; Kunter, M.; Blackledge, T. A., *PLOS ONE* **2010,** *5* (9), e11234.
[6] Lenz, R. W., In *Biopolymers I. Advances in Polymer Science*, Springer, Berlin, Heidelberg: 1993; Vol. 107, pp 1-40.
[7] Swatlotski, R. P.; Spear, S. K.; Holbrey, J. D.; Rogers, R. D., *J. Am. Chem. Soc.* **2002,** *124* (18), 4974-4975.
[8] Hadadi, A.; Whittaker, J. W.; Verrill, D. E.; Hu, X.; Larini, L.; Salas-de la Cruz, D., *Biomacromolecules* **2018,** *19*, 3970-3982.
[9] Haverhals, L. M.; Reichert, W. M.; De Long, H. C.; Trulove, P. C., *Macromol. Mater. Eng.* **2010,** *295* (5), 425-430.
[10] Haverhals, L. M.; Sulpizio, H. M.; Fayos, Z. A.; Trulove, M. A.; Reichert, W. M.; Foley, M. P.; De Long, H. C.; Trulove, P. C., *Cellulose* **2012,** *19* (1), 13-22.
[11] Chung, R. T.; Park, S.; Yates, E. A.; Durkin, D. P.; De Long, H. C.; Trulove, P. C., *Electrochem. Soc. Trans.* **2018,** *86* (14), 249-255.
[12] Haverhals, L. M.; Foley, M. P.; Brown, E. K.; Fox, D. M.; De Long, H. C.; Trulove, P. C., In *Ionic Liquids: Science and Applications*, American Chemical Society: 2012; Vol. 1117, pp 145-166.
[13] Rogers, R. D.; Seddon, K. R., *Science* **2003,** *302* (5646), 792-793.
[14] Plechkova, N. V.; Seddon, K. R., *Chem. Soc. Rev.* **2008,** *37* (1), 123-150.
[15] Krossing, I.; Slattery, J. M.; Daguenet, C.; Dyson, P. J.; Oleinikova, A.; Weingartner, H., *J. Chem Soc. (A)* **2006,** *128* (41), 13427-13434.
[16] Nie, Y.; Li, C.; Sun, A.; Meng, H.; Wang, X., *Energy Fuels* **2006,** *20*, 2083-2087.

[17] M., S. A.; A., P. M.; S., P., *J. Phys. Chem. Lett.* **2014,** *5*, 4032-4037.
[18] Murakami, M.-a.; Kaneko, Y.; Kadokawa, J.-i., *Carbohydr. Polym.* **2007,** *69* (2), 378-381.
[19] Zhang, H.; Wu, J.; Zhang, J.; He, J., *Macromolecules* **2005,** *38* (20), 8272-8277.
[20] Trulove, P. C.; Reichert, W. M.; De Long, H. C.; Kline, S. R.; Rahatekar, S. S.; Gilman, J. W.; Muthukumar, M., *Electrochem. Soc. Trans.* **2008,** *16*, 129-139.
[21] Phillips, D. M.; Drummy, L. F.; Conrady, D. G.; Fox, D. M.; Naik, R. R.; Stone, M. O.; Trulove, P. C.; De Long, H. C.; Mantz, R. A., *J. Am. Chem. Soc.* **2004,** *126* (44), 14350-14351.
[22] Mantz, R. A.; Fox, D. M.; Green, J. M.; Fylstra, P. A.; De Long, H. C.; Trulove, P. C., *Z. Naturforsch., A: Phys. Sci.* **2007,** *62* (5-6), 275-280.
[23] Wang, H.; Gurau, G.; Rogers, R. D., *Chem. Soc. Rev.* **2012,** *41*, 1519-1537.
[24] Visser, A. E.; Bridges, N. J.; Rogers, R. D., *Ionic liquids: science and applications*. American Chemical Society: 2012; Vol. 1117, p 0.
[25] Haverhals, L. M.; Nevin, L. M.; Foley, M. P.; Brown, E. K.; De Long, H. C.; Trulove, P. C., *Chem. Commun.* **2012,** *48*, 6417-6419.
[26] Chung, R. T. *Development of Advanced Functional Biomaterials* United States Naval Academy: Annapolis, MD, 2019; p 66.
[27] Fukaya, Y.; Hayashi, K.; Wada, M.; Ohno, H., *Green Chem.* **2008,** *10* (1), 44-46.
[28] Xu, K.; Xiao, Y.; Cao, Y.; Peng, S.; Fan, M.; Wang, K., *Carbohydr. Polym.* **2019,** *209*, 382-388.
[29] Hirosawa, K.; Fujii, K.; Hashimoto, K.; Shibayama, M., *Macromolecules* **2017,** *50* (17), 6509-6517.
[30] Rumble, J. R., (Ed.), *CRC Handbook of Chemistry and Physics, 100th edition (Internet Version 2020)*. CRC Press/Taylor & Francis: Boca Raton, FL, 2020.

Chapter 6

L02 – Solute and Solvent Properties

ECS Transactions, 98 (10) 117-127 (2020)
10.1149/09810.0117ecst ©The Electrochemical Society

Charge Transport and Dynamics in Imidazolium Chloroaluminate Ionic Liquids

T. Cosby[a], D. P. Durkin[a], R. A. Mantz[b], and P.C. Trulove[a]

[a] Department of Chemistry, United States Naval Academy, Annapolis, MD, USA
[b] Army Research Office, Durham, NC, USA

Ion dynamics and charge transport in 1-alkyl-3-methylimidazolium chloroaluminate ionic liquids were investigated over broad temperature and frequency ranges by broadband dielectric spectroscopy and differential scanning calorimetry. The timescale of ion dynamics, as captured by the imaginary component of the complex dielectric modulus as well as the calorimetric glass transition temperature (T_g), is strongly composition-dependent, with the fastest dynamics, lowest T_g, and highest fragility observed for the Lewis acidic 67 mol% $AlCl_3$ + 1-ethyl-3-methylimidazolium chloride composition. The DC ionic conductivity scales directly by the ion dynamics for all compositions indicating the primary effect of ion speciation is an alteration of the underlying ion mobility. The fragility (m) of the 67 mol% $AlCl_3$ + 1-ethyl-3-methylimidazolium chloride ionic liquid, m=148, is among the highest reported fragilities for a glass-forming liquid.

Introduction

Chloroaluminates are a class of halometallate ionic liquids (ILs) formed by the reaction of aluminum chloride ($AlCl_3$) with a chloride salt (1–4). Physicochemical properties such as high ionic conductivities, low viscosities, tunable Lewis acidity/basicity, wide liquidus ranges, and electrochemical stability windows make chloroaluminates advantageous solvents for numerous technological applications including high energy density batteries, electrodeposition, and catalysis (5–12). Despite these advantages the investigation of structure-property relationships in chloroaluminates lags behind that of many other aprotic ILs due in large part to their reactivity with atmospheric moisture. Notably, the reported ionic conductivities of chloroaluminates are limited to temperatures at and above room temperature (8,13–15). The aim of this study is to extend the investigation of chloroaluminate transport properties over a broader range of compositions, chemical structures, and temperatures in order to elucidate the influence of these factors on charge transport and dynamics.

The unique properties of chloroaluminates are strongly influenced by the composition-dependent formation of complex chloroaluminate anions (16). The initial addition of $AlCl_3$ to a chloride salt results in the formation of tetrachloroaluminate ($AlCl_4^-$). This can yield a binary IL consisting of a single cation and a mixture of chloride and tetrachloroaluminate anions when the mole fraction of $AlCl_3$, χ_{AlCl_3}, is <0.5. The chloride anion imparts a Lewis basicity to the IL and therefore these compositions are referred to as 'basic melts'. When χ_{AlCl_3} is >0.5 the anions are a mixture of the tetrachloroaluminate and heptachlorodialuminate ($Al_2Cl_7^-$) species. The $Al_2Cl_7^-$ anion is a strong Lewis acid,

therefore these IL compositions are referred to as 'acidic melts'. In these systems, the elucidation of structure-property relationships requires a comprehensive approach in which the anion speciation, as well as the physicochemical properties and underlying ion dynamics, are investigated with systematically varying cation chemical structure, composition and temperature. By employing broadband dielectric spectroscopy (BDS) and differential scanning calorimetry (DSC) to investigate ion dynamics over a broad range of temperatures and timescales, the interplay of ion chemical structure, dynamics, and charge transport may be elucidated.

In this study, four chloroaluminate ILs based on 1-ethyl-3-methylimidazolium and 1-butyl-3-methylimidazolium cations with 40 and 67 mol% $AlCl_3$ were prepared and investigated. The chemical structures and abbreviations are provided in Figure 1. A detailed analysis of the DC ionic conductivity, ion dynamics, and calorimetric glass transition temperature (T_g) data reveal a glass-transition-assisted charge transport mechanism as found in other classes of aprotic ionic liquids (17,18). The rate of slowing of dynamics as temperature approaches the T_g, known as the fragility and calculated from Vogel-Fulcher-Tammann (VFT) fit parameters, is strongly dependent on both IL composition, due to anion speciation, as well as cation chemical structure.

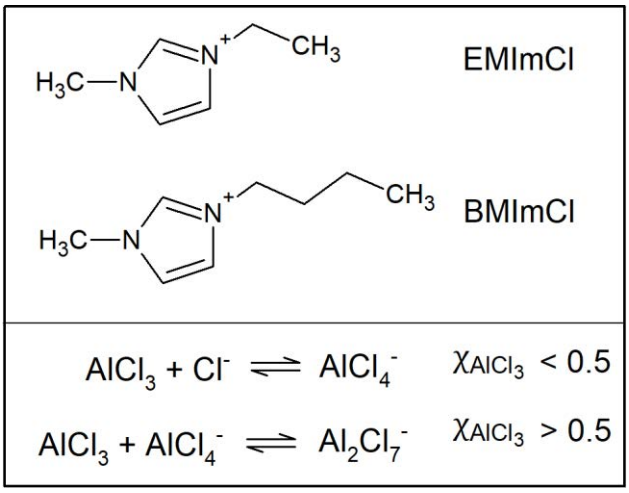

Figure 1. Chemical structures of the investigated chloroaluminate ionic liquids.

Experimental Methods

Ionic liquids were prepared by adding 1-alkyl-3-methyl-imidazolium chloride (alkyl = ethyl, butyl) to aluminum chloride and stirring at room temperature until a clear liquid was formed. The imidazolium chlorides were synthesized by gently refluxing 1-methylimidazole and ethylchloride/n-butylchloride in acetonitrile. The resulting imidazolium chloride salt was recrystallized in ethyl acetate and dried on a high vacuum line. The aluminum chloride was purified by sublimation in a sealed glass bomb tube containing aluminum wire and sodium chloride (3,19).

The chloroaluminate ionic liquids are highly moisture sensitive. To exclude the effect of water contamination all mixtures were prepared in a dry nitrogen atmosphere glove box. DSC samples were loaded into hermetically sealed aluminum pans in the same glove box and measured immediately afterward. The dielectric measurements were performed within

a cryostat which was constantly purged with dry nitrogen gas from an LN2 dewar. Dielectric sample capacitors were held in a plastic bag and purged with the same dry nitrogen gas for one hour prior to filling with a sealed syringe containing the ionic liquid sample. The sample capacitor was then lowered into the cryostat while continuously purging with dry nitrogen. In this way, reproducible dielectric measurements were accomplished which exclude any effect of water uptake.

Broadband dielectric spectroscopy (BDS) measurements were made over the frequency range 10^{-1} – 10^{9}Hz. Measurements from 10^{-1}-10^{6} Hz were made using a Novocontrol α-analyzer with a parallel plate sample capacitor geometry consisting of 20mm diameter gold-plated brass electrodes and a 1.0mm sample thickness maintained by 1.0mm thick Teflon spacers. Measurements from 10^{6}-10^{9} Hz were made on a HP E4991B impedance analyzer with a parallel plate sample capacitor geometry consisting of 10mm diameter gold-plated brass electrodes and a 0.1mm sample thickness maintained by 100μm fused silica rod spacers. Temperature control for all BDS measurements was provided by a Quatro temperature control system using nitrogen as a cooling and heating gas. The temperature accuracy was ±0.1°C.

Differential scanning calorimetry (DSC) measurements were made on a TA instruments Q2000 calorimeter. Samples were encased in aluminum hermetic pans and subjected to heating and cooling scans at a rate of 10°C/min. Calorimetric glass transition temperatures (T_g) were recorded on cooling and correspond to a maximum in the temperature derivative of heat flow.

Results

Insight into charge transport and dynamics of ion conducting liquids is obtained by analyzing the material response to a frequency-varying electric field by BDS (20). This response may be represented in terms of the complex conductivity, $\sigma^*(\omega) = \sigma'(\omega) + i\sigma''(\omega)$. The real part of complex conductivity, $\sigma'(\omega)$, is presented in Figure 2 for the 40mol% $AlCl_3$ + EMImCl ionic liquid. In this representation, the DC ionic conductivity, σ_0, corresponds to the frequency-independent plateau value. At frequencies below σ_0 the conductivity rapidly decreases due to electrode polarization processes associated with the development of ion layers at the electrode surfaces (21). These electrode polarization processes are not within the purview of this study and will not be discussed further. At higher frequencies, the real part of conductivity begins to increase above the DC ionic conductivity value. This high frequency dispersion is common to all ionic glasses and is associated with the transition from DC to AC ion conduction (22). The characteristic frequency at which this transition occurs is also known as the conductivity relaxation rate, ω_c. One approach to ascertaining this frequency is to convert the data into the complex electric modulus, $M^*(\omega) = 1/\varepsilon^*(\omega) = M'(\omega) + iM''(\omega)$, where $\varepsilon^*(\omega)$ is the complex dielectric permittivity and M' and M'' are the real and imaginary parts of the modulus, respectively (23,24). In this representation, the frequency of the peak in M'' coincides with the frequency of the up-turn in σ' (25,26). The frequency-dependent imaginary modulus of the 40 mol% $AlCl_3$ + EMImCl ionic liquid is presented in Figure 2.

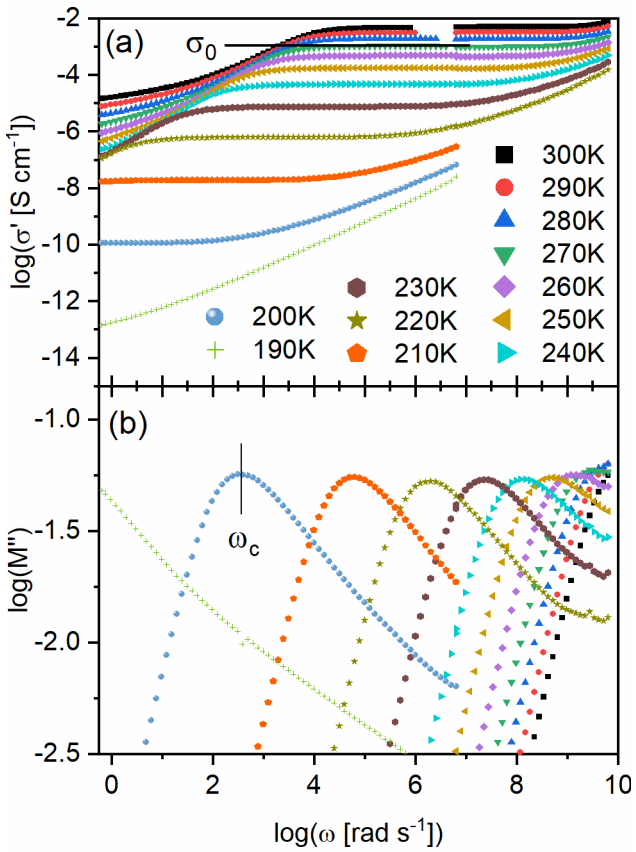

Figure 2. (a) Real part of complex conductivity, $\sigma^*(\omega) = \sigma'(\omega) + i\sigma''(\omega)$, and (b) imaginary part of complex electric modulus, $M^*(\omega) = M'(\omega) + iM''(\omega)$, for the 40mol% $AlCl_3$ + EMImCl ionic liquid. The frequency of the peak in the imaginary modulus corresponds to the ionic conductivity relaxation rate, ω_c.

The characteristic frequencies of the conductivity relaxation rate, ω_c, are presented in Figure 3 for all the studied ionic liquids. The gradual slowing of the conductivity relaxation rate with decreasing temperature is consistent with the gradual slowing of molecular motion common to all glass-forming materials. This temperature dependence is well-described by the VFT equation, Equation 1, where ω_∞ is the high temperature limiting relaxation rate, D is a constant, and T_0 is the Vogel temperature. The fit parameters extracted by fitting the data in Figure 3 with this equation are provided in Table I.

$$\omega_c = \omega_\infty e^{-DT_0/T-T_0} \quad [1]$$

The calorimetric glass transition temperatures, T_g, of the four ionic liquids are also presented in Figure 3 as star symbols. The conductivity relaxation rates coincide with this structural relaxation rate within the experimental accuracy of the T_g (± 2K). The inset of Figure 3 presents the conductivity relaxation *versus* temperature normalized by T_g. In this plot, ionic liquids with comparable fragilities are expected to scale by T_g and collapse onto a single curve (27). For the investigated chloroaluminates, the relaxation rates coincide only at lower temperatures and diverge considerably at intermediate temperatures. This divergence is reflected in the wide range of fragilities, m, calculated by Equation 2 and

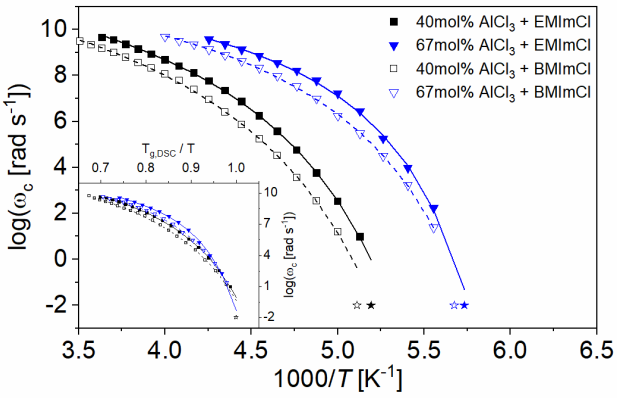

Figure 3. Temperature-dependence of the conductivity relaxation rates, ω_c, corresponding to the frequency of the peak in the imaginary part of the complex electric modulus. Lines correspond to fits by the VFT equation. Inset: Conductivity relaxation rates v*ersus* temperature normalized by the calorimetric glass transition temperatures, T_g.

presented in Table I (28). The strong influence of anion structure on fragility is unusual when compared to trends observed for air-and-water stable ionic liquids and will be discussed in more detail later.

$$m = \frac{DT_0}{2.303}\frac{T_g}{(T_g - T_0)^2} \qquad [2]$$

The temperature-dependent DC ionic conductivities, σ_0, of the four ionic liquids are presented in Figure 4. The data are well-described by the VFT equation. VFT fit parameters and calculated fragilities are provided in Table II. The fragilities are in good agreement with those obtained by VFT fits to the conductivity relaxation rates. As observed for the relaxation rates, the ionic conductivities do not scale by the T_g indicating the significant change in fragility (compare the values of m for the 40 mol% and 67 mol% $AlCl_3$ compositions in Table II). In addition to calculating the fragility, the influence of ion structure on the VFT temperature dependence may be observed by calculating the temperature-derivative of σ_0, see inset of Figure 4 (a and b). In the derivative representation, a VFT-type temperature dependence is observed as a line with a slope related to the fragility. The conductivity derivatives have clearly varying slopes with a strong influence from both the cation and anion chemical structure.

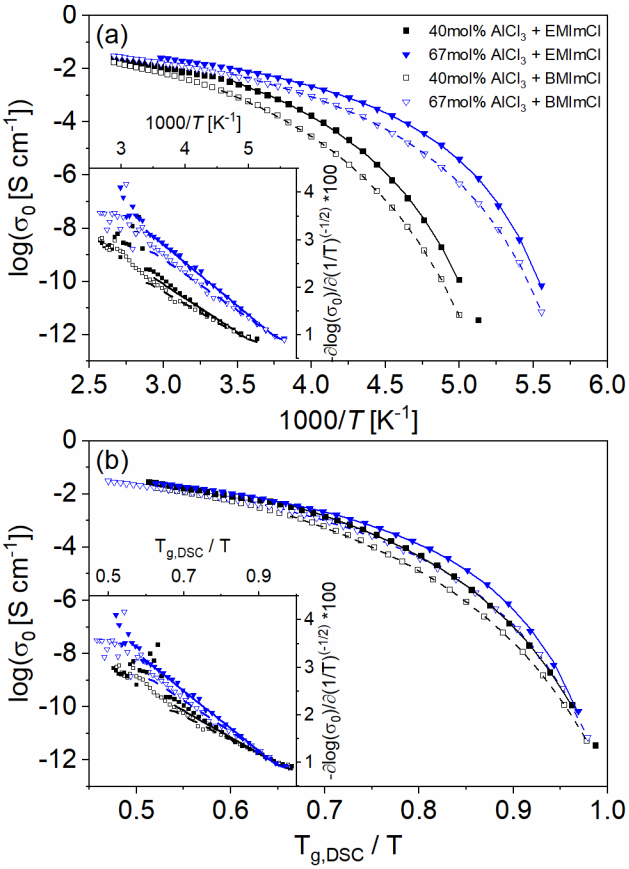

Figure 4. Temperature dependence of DC ionic conductivity *versus* (a) inverse temperature and (b) temperature normalized by the calorimetric glass transition temperature, T_g. Inset: Temperature derivative of DC ionic conductivity. Lines correspond to fits by the VFT equation.

Discussion

The DC ionic conductivity of ion-conducting materials is given by the expression, $\sigma_0 = \sum_i q_i n_i \mu_i$, where q is the charge, n the effective number density, and μ the mobility of all charge carriers *i* (20). Substituting the Einstein and Einstein-Smoluchowski relations for the ion mobility gives Equation 3 where k is Boltzmann's constant, T is temperature, and λ is the ion hopping length (29). From this relation it is evident that DC ionic conductivity of the chloroaluminate ionic liquids may be influenced by some combination of the ionic conductivity relaxation rate, ion hopping length, and effective number density of free ions. To investigate the relative importance of these factors in determining the temperature dependent ionic conductivity we utilize the Barton-Nakajima-Namikawa (BNN) plot of DC ionic conductivity *versus* the conductivity relaxation rate presented in Figure 5 (30–32). For the investigated ionic liquids, the conductivities collapse onto a single line over a very broad range of conductivities and relaxation rates. In addition, in the inset of Figure 5 we present the logarithm of the product $n\lambda^2/T$. The value of this product is approximately constant with chemical structure and is relatively independent of temperature. Together, these considerations indicate that it is the conductivity relaxation rate which predominantly determines the DC ionic conductivity of these chloroaluminate ionic liquids. This finding is in agreement with results from other classes of aprotic ionic liquids (29).

$$\sigma_0 = \sum_i \frac{q_i^2 n_i}{kT} \frac{\lambda^2 \omega_c}{2} \qquad [3]$$

Prior investigations of aprotic ionic liquids revealed a close coupling of ion dynamics with the structural relaxation which accompanies the dynamic glass transition (29,33). Charge transport in these systems is therefore attributed to a glass-transition-assisted ion-hopping mechanism where ions jump through a disordered matrix at the timescale of the structural relaxation. Charge transport of the chloroaluminate systems considered in this study is attributed to the same mechanism due to the overlap of the conductivity relaxation rates with the calorimetric glass transitions (see Figure 3). The dynamic glass transition is defined as the gradual slowing of molecular motion with decreasing temperature. All glass-

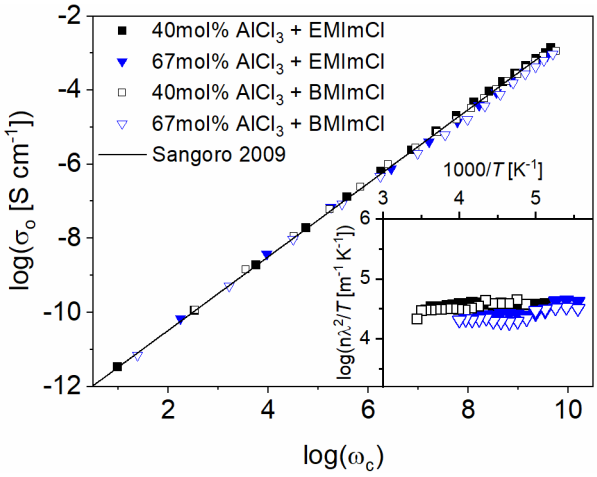

Figure 5. Barton-Nakajima-Namikawa plot of DC ionic conductivity versus ionic conductivity relaxation rate, ω_c, for the investigated ionic liquids. The line represents a linear fit to ionic liquid conductivity data from (33). Inset: Temperature dependence of the product of effective number density of ions, n, and square of ion hopping length, λ, divided by temperature, T.

formers have a characteristic calorimetric glass transition, T_g, conventionally defined as the temperature at which the structural relaxation reaches a timescale of 100s. In addition, each glass-former approaches the T_g at a different rate. This rate or steepness of approach is estimated by a factor termed the fragility, m (34,35). The coupling of ion transport and structural relaxation alongside the scaling of DC conductivity by the conductivity relaxation rate indicates that the strongest influence of chemical structure on charge transport is due to the effect on the dynamic glass transition. Therefore, an ionic liquid with a very low T_g and/or very high fragility is desired in order to increase DC ionic conductivity. It is therefore of interest to investigate how the cation and anion chemical structure alter the T_g and fragility.

TABLE I. Vogel-Fulcher-Tammann Fit Parameters – Conductivity Relaxation Rates, ω_c

Ionic Liquid	ω_∞ [rad s^{-1}]	D	T_o [K]	$T_{g,\,DSC}$ [K]	m	T_g/T_o
40mol% $AlCl_3$ + EMImCl	3.1E13	6.1	161	193	82	1.20
67mol% $AlCl_3$ + EMImCl	4.0E12	3.4	158	175	146	1.10
40mol% $AlCl_3$ + BMImCl	3.0E13	7.1	160	196	76	1.23
67mol% $AlCl_3$ + BMImCl	8.6E12	4.7	153	176	103	1.15

TABLE II. Vogel-Fulcher-Tammann Fit Parameters – DC Ionic Conductivity, σ_0

Ionic Liquid	σ_∞ [S cm^{-1}]	D	T_o [K]	$T_{g,\,DSC}$ [K]	m	T_g/T_o
40mol% $AlCl_3$ + EMImCl	3.2	5.1	165	193	95	1.16
67mol% $AlCl_3$ + EMImCl	0.43	3.0	159	175	148	1.10
40mol% $AlCl_3$ + BMImCl	3.9	6.5	162	196	76	1.21
67mol% $AlCl_3$ + BMImCl	0.78	4.2	154	176	104	1.14

The VFT fit parameters and the calculated fragilities for the four ionic liquids are presented in Table I and II alongside the calorimetric glass transition temperatures. The increase in $AlCl_3$ concentration from 40 to 67mol% $AlCl_3$ is accompanied by a significant increase in the fragility for both the EMImCl and BMImCl systems. This change is attributed to the shift in anion speciation from a mixture of chloride and tetrachloroaluminate ($AlCl_4^-$) in the 40mol% melt to predominantly heptachlorodialuminate ($Al_2Cl_7^-$) in the 67mol% melt. The fragility of the 67mol% $AlCl_3$ + EMImCl ionic liquid is among the highest reported for a glass forming liquid (34,36–38). The increase in fragility accompanying this shift in anion chemical structure is much more substantial than is seen in aprotic ionic liquids with air and water-stable anions (29,33,39–41). However, the increase in alky chain length of the BMImCl ionic liquid reduces this effect and leads to ionic liquids with overall lower fragility.

Summary

Charge transport in acidic and basic chloroaluminates based on 1-ethyl-3-methylimidazolium and 1-butyl-3-methylimidazolium follows the glass-transition-assisted mechanism of other aprotic ionic liquids. The glass transition temperature and fragility of these mixtures is highly dependent upon the anion speciation. The formation of complex $Al_2Cl_7^-$ anions produces ionic liquids with very low T_g's and high fragilities.

Acknowledgments

This work was funded by the Army Research Office [MIPR# 11370192]. We are grateful for facilities support from the U.S. Naval Academy. Any opinions, findings, conclusions, or recommendations expressed herein are those of the authors and do not reflect the views of the U.S. Navy or the U.S. Army.

References

1. J. S. Wilkes, *Green Chem.*, **4**, 73–80 (2002).
2. J. Braunstein, G. Mamantov, and G. P. Smith, Eds., *Advances in Molten Salt Chemistry*, p. 284, Plenum Press, New York, (1971).
3. R. J. Gale and R. A. Osteryoung, in *Molten Salt Techniques*, D. G. Lovering and R. J. Gale, Editors, p. 55–78, Plenum Press, New York (1983).
4. C. H. Hussey, in *Advances in Molten Salt Chemistry*, G. Mamantov and C. B. Mamantov, Editors, p. 185–229, Elsevier, New York (1983).
5. A. Kumar and D. Sarma, in *Ionic Liquids IIIB: Fundamentals, Progress, Challenges, and Opportunities*,, p. 350–370 (2005).
6. J. P. Hallett and T. Welton, *Chem. Rev.*, **111**, 3508–3576 (2011).
7. N. V. Plechkova and K. R. Seddon, *Chem. Soc. Rev.*, **37**, 123–150 (2008).
8. T. G. Tucker and C. A. Angell, *J. Electrochem. Soc.*, **161**, H796–H801 (2014).
9. J. S. Wilkes, *Room temperature molten salts for advanced energy storage and conversion*, p. 1–12, Colorado Springs, (1994).
10. T. Welton, *Chem. Rev.*, **99**, 2071–2084 (1999).
11. R. Kore, P. Berton, S. P. Kelley, P. Aduri, S. S. Katti, and R. D. Rogers, *ACS Catal.*, **7**, 7014–7028 (2017).
12. H. Wang, S. Gu, Y. Bai, S. Chen, N. Zhu, C. Wu, and F. Wu, *J. Mater. Chem. A*, **3**, 22677–22686 (2015).
13. A. A. Fannin, D. A. Floreani, L. A. King, J. S. Landers, B. J. Piersma, D. J. Stech, R. L. Vaughn, J. S. Wilkes, and J. L. Williams, *J. Phys. Chem.*, **88**, 2614–2621 (1984).
14. Y. Zheng, K. Dong, Q. Wang, J. Zhang, and X. Lu, *J. Chem. Eng. Data*, **58**, 32–42 (2013).
15. J. W. Vaughan, D. Dreisinger, and J. Haggins, *ECS Trans.*, **2**(3), 381–392 (2006).
16. C. L. Hussey, *J. Electrochem. Soc.*, **133**, 1389–1391 (1986).
17. M. Jasiurkowska, W. Kossack, R. Ene, C. Iacob, W. K. Kipnusu, P. Papadopoulos, J. R. Sangoro, M. Massalska-Arod, and F. Kremer, *Soft Matter*, **8**, 5194 (2012).
18. J. R. Sangoro, A. Serghei, S. Naumov, P. Galvosas, J. Karger, C. Wespe, F. Bordusa, and F. Kremer, *Phys. Rev. E*, **77**, 51202 (2008).
19 J. S. Wilkes, J. A. Levisky, R. A. Wilson, and C. L. Hussey, *Inorg. Chem.*, **21**, 1263–1264 (1982).
20. F. Kremer and A. Schönhals, *Broadband Dielectric Spectroscopy*, p. 729, Springer, Berlin, (2003).
21. A. Serghei, M. Tress, J. R. Sangoro, and F. Kremer, *Phys. Rev. B*, **80**, 5 (2009).
22. J. C. Dyre, *J. Appl. Phys.*, **64**, 2456–2468 (1988).
23. N. G. McCrum, B. E. Read, and G. Williams, *Anelastic and Dielectric Effects in Polymeric Solids*, p. 617, Dover Publications, (1967).
24. J. H. Ambrus, C. T. Moynihan, and P. B. Macedo, *J. Phys. Chem.*, **76**, 3287–3295 (1972).
25. F. S. Howell, C. T. Moynihan, and P. B. Macedo, *Bull. Chem. Soc. Jpn.*, **57**, 652–661 (1984).
26. K. Pathmanathan and J. R. Stevens, *J. Appl. Phys.*, **68**, 5128–5132 (1990).
27. L.-M. Martinez and C. A. Angell, *Nature*, **410**, 663–667 (2001).
28. R. Böhmer, K. L. Ngai, C. A. Angell, and D. J. Plazek, *J. Chem. Phys.*, **99**, 4201–4209 (1993).
29. J. R. Sangoro, M. Mierzwa, C. Iacob, M. Paluch, and F. Kremer, *RSC Adv.*, **2**,

5047–5050 (2012).
30. J. L. Barton, *Verres Refract.*, **20**, 328 (1966).
31. N. Nakajima, in *Annual Report - Conference on Electrical Insulation and Dielectric Phenomena*,, National Academy of Sciences, Washington, DC (1972).
32. H. Namikawa, *J. Non. Cryst. Solids*, **18**, 173–195 (1975).
33. J. R. Sangoro, C. Iacob, A. Serghei, C. Friedrich, and F. Kremer, *Phys. Chem. Chem. Phys.*, **11**, 913–916 (2009).
34. L.-M. Wang, C. A. Angell, and R. Richert, *J. Chem. Phys.*, **125**, 74505 (2006).
35. W. Xu, E. I. Cooper, and C. A. Angell, *J. Phys. Chem. B*, **107**, 6170–6178 (2003).
36. C. Austen Angell, Y. Ansari, and Z. Zhao, *Faraday Discuss.*, **154**, 9–27 (2012).
37. C. A. Angell, R. D. Bressel, J. L. Green, H. Kanno, M. Oguni, and E. J. Sare, *J. Food Eng.*, **22**, 115–142 (1994).
38. K. Niss and T. Hecksher, *J. Chem. Phys.*, **149**, 230901 (2018).
39. T. Cosby, Z. Vicars, E. U. Mapesa, K. Tsunashima, and J. Sangoro, *J. Chem. Phys.* (2017).
40. H. Shirota, H. Fukazawa, T. Fujisawa, and J. F. Wishart, *J. Phys. Chem. B*, **114**, 9400–9412 (2010).
41. J. Leys, M. Wübbenhorst, C. Preethy Menon, R. Rajesh, J. Thoen, C. Glorieux, P. Nockemann, B. Thijs, K. Binnemans, and S. Longuemart, *J. Chem. Phys.*, **128**, 064509 (2008).

ECS Transactions, 98 (10) 129-139 (2020)
10.1149/09810.0129ecst ©The Electrochemical Society

Conductivity of 1-Ethyl-3-methylimidazolium Chloride (EMIC) and Aluminum Chloride ($AlCl_3$) Ionic Liquids at different Temperatures and $AlCl_3$ Mole Fractions

Pravin S. Shinde[a], Aninda N. Ahmed[a], Md Khalid Nahian[a], Yuxiang Peng[a], and Ramana G. Reddy[a]

[a] Department of Metallurgical and Materials Engineering,
The University of Alabama, Tuscaloosa, AL 35487, USA
Corresponding author: rreddy@eng.ua.edu; Tel: 205-348-4246

The conductivity (κ) of ionic liquid (IL) comprising a melt of 1-ethyl-3-methylimidazolium chloride (EMIC) and aluminum chloride ($AlCl_3$) with different $AlCl_3$ mole fractions (X_{Al}) and temperatures (343-383 K) are reported. X_{Al} values of 0.6, 0.643, and 0.667 in EMIC-$AlCl_3$ IL are selected to maintain the desired Lewis acidity. Precise and fast conductivity measurements and the behavior of anion species in IL are studied using electrochemical impedance spectroscopy (EIS). The measured κ data followed the Arrhenius law from which the activation energies (E_a) of conduction are determined. The conductivity of EMIC-$AlCl_3$ IL decreased with the higher X_{Al}. EMIC-$AlCl_3$ with X_{Al}=0.6 exhibited higher κ (5.58 S m^{-1}) at 383 K and lowest E_a (4.25 KJ mol^{-1}) among studied compositions. Based on the thermodynamic calculations, the differences in conductivities are attributed to the interplay of anion concentration, the molecular structure, cation-anion interactions, and hydrogen bonds in the IL.

Introduction

Over the last few decades, ionic liquids (ILs) are widely investigated because of their several potential applications in catalysis, electrochemistry, synthesis, and separation processes (1-4). ILs are the solvents containing a mixture of asymmetric organic cations and organic/inorganic anions. ILs have several attractive properties such as high ionic conductivity, low vapor pressure, high thermal and electrochemical stability, and broad liquid temperature range (5-7). As a result, the ILs are continuously receiving a lot of scientific interest among the research community. However, despite a lot of progress in tuning the physical and chemical properties of ILs, the fundamental understanding of the intermolecular interaction between anions and cations is relatively unexplored (8, 9). The vital properties such as structure, diffusion, viscosity, conductivity, or melting points, depend largely on these interactions between cations and anions in ILs. We have reported several physicochemical properties such as the heat capacity (10), thermal stability (11-13), density (14, 15), viscosity (12, 14, 15), vapor pressure (15), thermal conductivity (15, 16), thermodynamic (17-19), and electroanalytical (20-23) properties of several ILs and molten salts, which are necessary to understand the electrochemistry of metals and alloys to tune their electrosynthesis parameters. In general, density, viscosity, electrochemical window, and conductivity are important physical properties that determine if an IL is suitable as an electrolyte for electrochemical devices. The conductivity (κ) is a critical

property of ILs in terms of their prospects as electrolytes for electrodeposition of metals. Electrodeposition of aluminum from imidazolium-based room-temperature chloroaluminate (RTC) ILs is one such example. Metals such as aluminum and their alloys can be electrodeposited from chloroaluminate-based electrolytes with the addition of the so1ute metal ion to the electrolyte. This can be accomplished by either anodic dissolution of the solute metal directly into the melt or addition of the appropriate chloride salt or combination of both. The RTC ILs can be obtained by combining aluminum chloride ($AlCl_3$) with certain dialkyl imidazolium chloride salts such as 1-ethyl-3-methylimidazolium chloride (EMIC). The chloro-acidity of such ILs is adjustable by controlling the mole fraction of $AlCl_3$ (X_{Al}). The ILs can be classified as acidic, neutral, and basic, depending on the $AlCl_3$ content. If $AlCl_3$ content is less (X_{Al} <0.5), the electrolyte contains $AlCl_4^-$ and Cl^- anions, exhibiting Lewis basic characteristics due to excess unbound chloride ions. On the other hand, at higher $AlCl_3$ (X_{Al} >0.5), the electrolyte possesses $AlCl_4^-$ and $Al_2Cl_7^-$ species exhibiting Lewis acidic properties mainly due to coordinately unsaturated $Al_2Cl_7^-$ species (24). Acidic RTCs are of interest as electrolytes for the electroplating of aluminum (Al) and its alloys because only the acidic compositions are active for Al plating and stripping at the anode, according to the reversible redox reaction given below (25, 26):

$$4(Al_2Cl_7)^- + 3e^- \leftrightarrow 7(AlCl_4)^- + Al \quad [1]$$

The electrochemical deposition of Al from such chloroaluminate ILs has been reported to be primarily due to contribution from the diffusion of $Al_2Cl_7^-$ species (27-29). The mobility and availability (concentration) of such anion species at the diffusion layer of respective electrodes dictate the conductivity of the electrolyte. Several researchers have studied different ILs to theoretically estimate information on ionic conductivities using rigorous methods with limited accuracy (30-38).

Fannin et al. were among the first to extensively evaluate the physical and chemical properties of dialkyl imidazolium-based ILs (39, 40). They investigated the ion-interactions as well as the phase transitions, densities, electrical conductivities, and viscosities for dialkyl imidazolium-based chloroaluminate ILs. Few other groups also investigated the electrical conductivities of such ILs. Despite several reports on the physicochemical properties, there are inconsistencies in the κ data available in the literature for imidazolium-based chloroaluminate ILs at higher temperatures (41-44). The discrepancies in conductivity values in the literature could be due to inconsistent sample purity, different measurement tools, and water contents. Thus, a systematic study on the conductivity data of imidazolium-based chloroaluminate ILs regarding electrolyte temperature and various mole fractions of $AlCl_3$ is needed. Most of the conductivity measurements in the literature have been obtained using conductivity meter probes (44-46), and the EIS technique has rarely been used for ionic liquids. The conductivity measurement by meter probes poses erroneous measurements because of several factors that include incomplete immersion of probe's surface, the boundary effects outside the electrode surfaces due to improper position of the sensor in the electrolyte, and the measurement limitation at higher temperatures. On the other hand, EIS measurement can be done in-situ in a precise manner with great accuracy even at high temperatures.

In this study, we have systematically investigated the conductivity behavior of EMIC-$AlCl_3$ ionic liquid as a function of the electrolyte composition ($AlCl_3$ mole fractions) and temperature. The conductivity of IL is studied using electrochemical impedance spectroscopy (EIS) technique to obtain accurate, non-empirical, and fast information about contributing anions on the IL conductivity. The κ values and activation energy of conduction for EMIC-$AlCl_3$ at different $AlCl_3$ mole fractions and temperatures IL determined and compared.

Experimental

Materials

The chemicals such as anhydrous $AlCl_3$ (95+%, Alfa-Aesar) and organic chloride salt 1-ethyl-3-methylimidazolium chloride (EMIC, 95%, Sigma-Aldrich) were purchased and used without further treatment. All the chemicals are heated to get rid of any moisture prior to their use for experiments. The nickel sheets (99.9%) were obtained from Sigma Aldrich company. The ultrahigh pure (UHP) Argon gas (99.999%) was obtained from Airgas.

Preparation of EMIC-$AlCl_3$ Ionic Liquid

The appropriate amount of EMIC organic chloride salt and the $AlCl_3$ were weighed for a given $AlCl_3$ mole fraction. Here, the $AlCl_3$ mole fraction of 0.667 was chosen to maximize the concentration of $Al_2Cl_7^-$ anion species in the EMIC-$AlCl_3$ IL. Both the ingredients were mixed in a Pyrex beaker on a preheated hot plate. The mixing is performed cautiously and slowly using a glass rod as the spontaneous reaction is vigorous. The mixture of two solid ingredients turns into a clear liquid as the eutectic condition is reached at room temperature. Upon stirring for 30 s, the mixture turns into a clear liquid, although few large chunks of EMIC might float in the solution, which eventually dissolves in about 30 min. The desired amount of clear IL solution is then transferred to the 50 mL electrochemical Pyrex cell placed on a hot plate, and IL was stirred for about 30 min using a magnetic stirrer at 60 RPM for homogeneous mixing at the set temperature. The IL was stored in a dry box until used for further measurements such as density and electrical conductivity. The mole fractions of $AlCl_3$, X_{Al}=0.60, 0.643, and 0.667 were chosen. Temperatures studied for EMIC-$AlCl_3$ IL at each X_{Al} were 343, 353, 363, 373, and 383 K. The UHP argon gas was purged over the surface of IL to keep it free from oxygen and moisture, and finally, the cell was sealed.

Electrical Conductivity Measurements

The electrical conductivities of EMIC-$AlCl_3$ IL at different mole fractions and temperatures were obtained using ac impedance spectroscopy through a potentiostat/galvanostat (VersaSTAT 3, M-100) in the argon environment. The conductivity experiments for ILs were performed in a two-electrode configuration with two nickel plates with identical dimensions as working and counter electrodes in a quartz cell. The working and counter electrodes are fixed in a quartz cell separated

by a distance of ~ 0.95 cm, such that one side of each electrode is tightly attached to the cell wall. Both the Ni electrodes were polished with 800 grit SiC abrasive paper, washed with ethanol and deionized water, and dried by air. The top of the cell is sealed with Teflon tape to exclude the possibility of atmospheric exposure of ionic liquid. Then, the whole-cell assembly is kept inside the oil bath on the hot-plate. The electrolyte temperature was monitored and controlled using a precision thermometer inserted into the bath. The conductivities were obtained in the temperature range of 343-383 K. The thermal equilibrium time set to measure conductivity for each given temperature was at least 30 min. The EIS curves (Nyquist plots) were obtained by applying an ac signal of amplitude 10 mV in the frequency range of 100 kHz-0.1 Hz at 0.2 V vs. Ni. The series resistance (R_s) is calculated by fitting Nyquist plots with an equivalent electrochemical circuit. Then, by using the area (A) of the electrode immersed in IL and the separation distance of electrodes (l), the conductivity (κ) is calculated using the following equation,

$$\kappa = l/R \cdot A \qquad [2]$$

Before actual conductivity measurements on ILs, the cell was calibrated by performing the EIS measurement at room temperature using three commercially available conductivity standards. The conductivity cell was carefully cleaned and dried before introducing each IL sample.

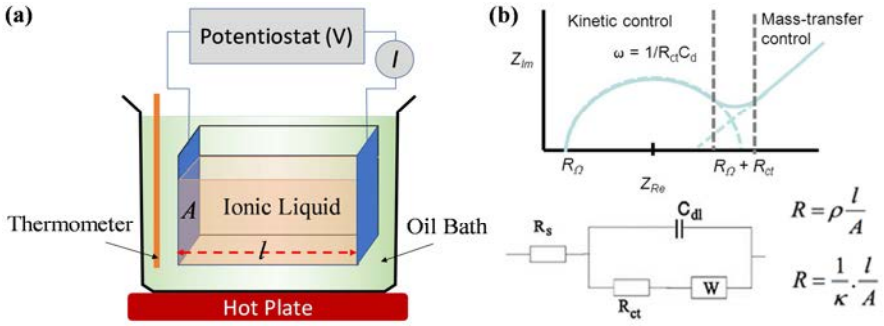

Figure 1. (a) Schematic of the experimental EIS set up. (b) Typical Nyquist plot from EIS measurement that shows a semicircle and a straight-line with an equivalent electrochemical circuit model to calculate the resistance or conductivity.

Results and Discussion

Figure 2 shows the Nyquist plots obtained for EMIC-$AlCl_3$ IL at different temperatures for the $AlCl_3$ mole fraction of 0.60. The semicircles of different diameters show up at different temperatures. The figure suggests that the diameter of arches (represented by charge transfer resistance, R_{ct}) decreases with temperature indicating faster diffusion of chloroaluminate ions in the electrolyte due to increased conductivity. Additionally, the series resistance (R_s) of the electrochemical circuit is decreasing with temperature. Before the EIS measurement of IL, the resistance of electrochemical circuits other than the electrolyte was first determined. The resistance of the cell determined using different conductivity standards as the electrolyte using the same set of Ni

electrodes and electrochemical cells was subtracted from R_s to get the actual resistance and hence to get the conductivity of the EMIC-$AlCl_3$ IL and are plotted in Figure 3.

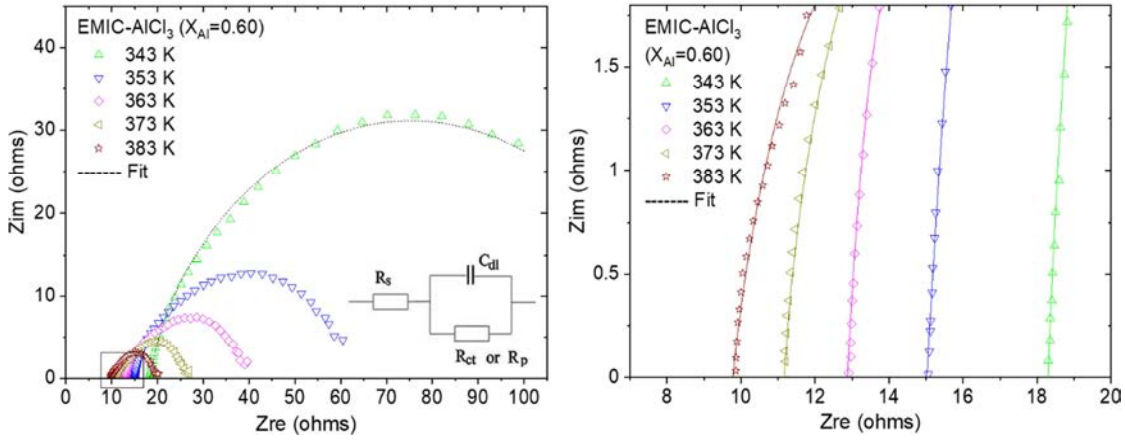

Figure 2. Nyquist plots of EMIC-$AlCl_3$ IL recorded on Ni plate vs. Ni for $AlCl_3$ mole fraction of 0.6 (left) at different temperatures and the corresponding magnified view of Nyquist plots in the high-frequency regime (right).

Figure 3 shows the temperature dependency of electrical conductivity for RTC ILs for different $AlCl_3$ mole fractions. As shown in the figure, the ionic conductivity shows an increasing trend with temperatures for all mole fractions of $AlCl_3$. Such enhancement is because of the weak attractive interaction between the ions at higher temperatures.

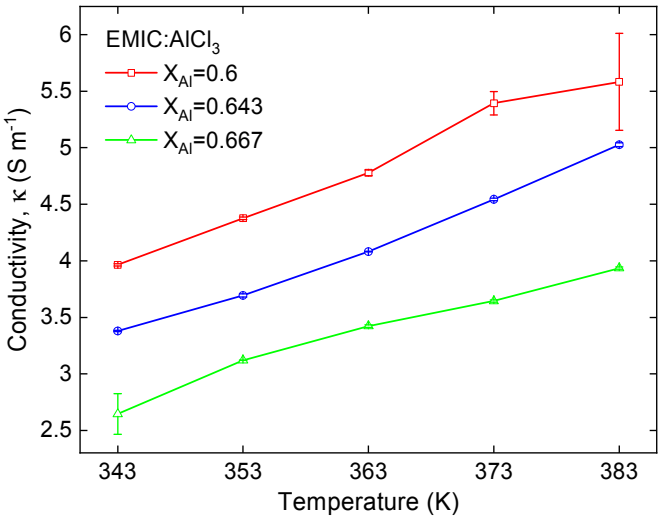

Figure 3. Conductivity plot as a function of temperature at different $AlCl_3$ mole fractions for EMIC-$AlCl_3$ IL.

All the measured conductivities are compared with literature data and are listed in TABLE I. The higher conductivity in the EMIC-$AlCl_3$ IL system has been attributed to the weaker cation-anion interaction and hydrogen bonding between $EMIC^+$-based ion pairs compared to higher alkyl-chained $HMIC^+$-based pairs (41).

TABLE I. Comparison of conductivity values obtained from EIS plots for EMIC-$AlCl_3$ IL with literature. Room temperature (RT) conductivity was obtained from the slope.

$AlCl_3$ mole fraction (X_{Al})	Conductivity, κ (S m^{-1}) at different temperatures						References
	RT	343 K	353 K	363 K	373 K	383 K	
0.6	2.43	3.96	4.38	4.78	5.39	5.58	This work
0.643	1.93	3.38	3.69	4.08	4.54	5.03	
0.667	1.61	2.65	3.12	3.42	3.64	3.94	
0.64	-	3.60	4.13	4.69	5.28	-	Fannin *et.al* (40)
0.66	-	3.40	3.91	4.44	5.00	-	
0.6	-	2.8	3.2	3.7	-	-	Ferrara *et.al* (43)
0.6	-	4.02	5.08	6.17	8.09	9.72	Vila *et.al* (44)
0.63	-	~2.5	~3.0	~3.3	-	-	

With higher mole fractions of $AlCl_3$ in EMIC-$AlCl_3$ IL, the electrical conductivities decrease in the order: $\kappa(X_{Al}=0.6) > \kappa(X_{Al}=0.643) > \kappa(X_{Al}=0.667)$. Similar behavior is found in other dialkyl imidazolium chloride chloroaluminate ILs such as MeMeImCl-$AlCl_3$, and MeBuImCl-$AlCl_3$ including EMIC-$AlCl_3$ (MeEtImCl-$AlCl_3$) (40, 41). To explain the decrease in conductivity with higher $AlCl_3$ mole fractions, it is essential to know the concentration and interplay of different anions present in the ionic liquids at a given temperature. Karpinsky et al. reported the formation of different chloroaluminate anions ($AlCl_4^-$, $Al_2Cl_7^-$, $Al_3Cl_{10}^-$, etc.) for different $AlCl_3$ mole fractions in EMIC-$AlCl_3$ (24). The equilibrium concentration (X_i) of various chloroaluminate anions in the EMIC-$AlCl_3$ IL system for different $AlCl_3$ mole fractions based on thermodynamic calculations (47) are shown in Figure 4.

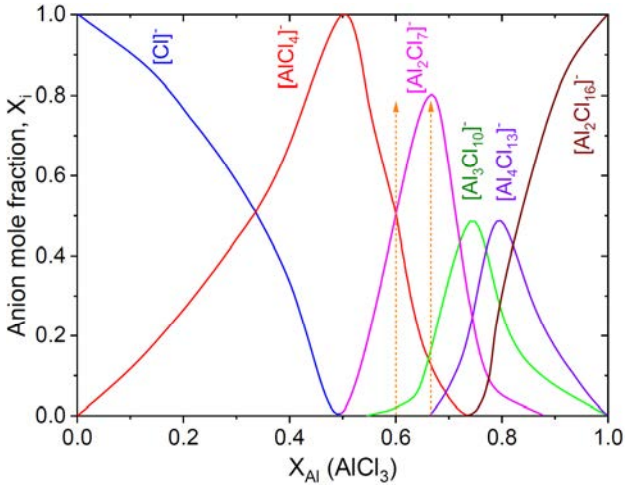

Figure 4. Equilibrium concentration (X_i) of various chloroaluminate anions (Cl^-, $AlCl_4^-$, $Al_2Cl_7^-$, $Al_3Cl_{10}^-$, $Al_4Cl_{17}^-$, and $Al_2Cl_{16}^-$) in EMIC-$AlCl_3$ IL (reproduced from (24, 47)).

As shown in Figure 4, for a studied $AlCl_3$ mole fraction range (X_{Al}=0.6-0.667), three anions, $Al_2Cl_7^-$, $AlCl_4^-$, and $Al_3Cl_{10}^-$, exist simultaneously in the IL. The relative concentrations of $Al_2Cl_7^-$ and $Al_3Cl_{10}^-$ anions increase, and that of $AlCl_4^-$ decreases with an increase in mole fraction of $AlCl_3$ from 0.6 to 0.667. At low $AlCl_3$ mole fraction (X_{Al}=0.6), an almost similar number of $Al_2Cl_7^-$ and $AlCl_4^-$ anions are present in the system. As $AlCl_3$ mole fraction increases, the concentration of $Al_2Cl_7^-$ anions increases until a maximum at X_{Al}=0.667 while the concentration of $AlCl_4^-$ anions decrease. At

higher $AlCl_3$ mole fractions, the cation-anion interaction and hydrogen bonding are reported to be stronger between $EMIC^+$ and $AlCl_4^-$ than that between $EMIC^+$ and $Al_2Cl_7^-$, due to a smaller volume and higher geometric symmetry of the $AlCl_4^-$ anion than the $Al_2Cl_7^-$ anion. Thus, the structural features make $AlCl_4^-$ more conductive in EMIC-$AlCl_3$ ionic liquid at the same conditions. This is the viable reason for the decrease in conductivity at higher mole fractions of $AlCl_3$ in EMIC-$AlCl_3$ IL. The actual concentration of these anions can be determined using mole fractions of these anions from Figure 4 and the formula weights of primary ingredients used to make the ionic liquid. The actual concentration of anions can be calculated in the following manner. The concentration of total anions ($Al_2Cl_7^-$, $AlCl_4^-$, and $Al_3Cl_{10}^-$, etc.) present in the IL are given by:

$$C_{total} = \frac{W_{total} \cdot W_{Al}}{W_{AlCl_3}}\ mol\ m^{-3} \quad [3]$$

where W_{total} is the measured weight of known volume (x mL) of EMIC-$AlCl_3$ for a given $AlCl_3$ mole fraction, W_{Al} is the weight% of $AlCl_3$ in the electrolyte, W_{AlCl_3} is the formula weight of $AlCl_3$ (133.34 g mol^{-1}). Then, the concentration of a specific anion, such as $Al_2Cl_7^-$, from the total concentration of anions (C_{total}) in EMIC-$AlCl_3$ (for a given $AlCl_3$ mole fraction, X_{Al}=0.6) electrolyte can be calculated as,

$$[Al_2Cl_7]^- = \frac{C_{total} \cdot X_{[Al_2Cl_7]^-}}{n_{[Al_2Cl_7]^-}}\ mol\ m^{-3} \quad [4]$$

where $X_{Al_2Cl_7^-}$ is the mole fraction of $Al_2Cl_7^-$ anion from equilibrium concentration data of anions (Figure 4) and $n_{Al_2Cl_7^-}$ represents the number of moles of $AlCl_3$ necessary to produce one mole of $Al_2Cl_7^-$ anion (n=2 in this case). The concentrations of $AlCl_4^-$, $Al_2Cl_7^-$ and $Al_3Cl_{10}^-$ anions determined using this method for EMIC-$AlCl_3$ for all the $AlCl_3$ mole fractions are tabulated in TABLE II.

TABLE II. Calculation of $AlCl_4^-$, $Al_2Cl_7^-$, and $Al_3Cl_{10}^-$ anion concentrations in EMIC-$AlCl_3$ IL electrolyte at different $AlCl_3$ mole fractions at 373 K. Here, n=1, 2, and 3 for $AlCl_4^-$, $Al_2Cl_7^-$, and $Al_3Cl_{10}^-$, respectively.

$AlCl_3$ mole fraction (X_{Al})	**Density of IL (g cm^{-3})**	**Total Conc. (mol m^{-3})**	**Anion mole fraction**			**Anion concentration (mol m^{-3})**		
			$AlCl_4^-$	**$Al_2Cl_7^-$**	**$Al_3Cl_{10}^-$**	**$AlCl_4^-$**	**$Al_2Cl_7^-$**	**$Al_3Cl_{10}^-$**
0.6	1.359	5.657	0.5037	0.4842	0.0121	2.850	1.370	0.023
0.643	1.387	6.176	0.2102	0.7321	0.0577	1.298	2.261	0.119
0.667	1.402	6.409	0.0918	0.7908	0.1174	0.588	2.534	0.251

The concentration of $Al_2Cl_7^-$ anions in EMIC-$AlCl_3$ IL increases while that of $AlCl_4^-$ decreases with increasing $AlCl_3$ mole fractions from 0.6 to 0.667. EMIC-$AlCl_3$ IL with 0.6 mole fraction (X_{Al}=0.6) possess maximum $AlCl_4^-$ concentration (2.839 mol m^{-3}).

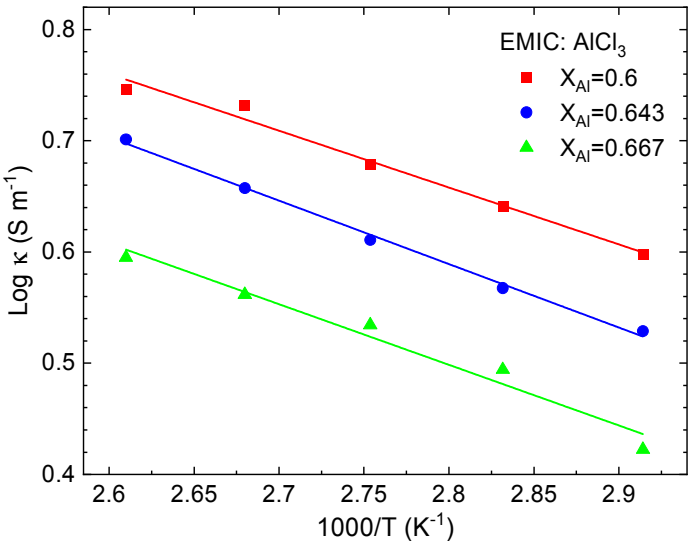

Figure 5. Arrhenius plots of EMIC-$AlCl_3$ IL with different $AlCl_3$ mole fractions.

In the literature, the effects of temperature on the electrical conductivity of ionic liquid electrolytes have been correlated by the Vogel−Tamman−Fulcher (VTF) equation (48). The experimental measurements show that the electrical conductivity follows the VTF model like literature for EMIC-$AlCl_3$ (43) as well as a typical Arrhenius law reported for several molten salts (49). Better least-square fits for the experimental data were observed with the Arrhenius plot than that of the VTF plot. The Arrhenius equation has been utilized to describe the temperature dependence of electrical conductivity as (50),

$$\kappa = A \exp\left[\frac{-E_a}{RT}\right] \qquad [5]$$

where A is the pre-exponential factor, E_a is the activation energy for ion transportation by migration, and R is the gas constant. The obtained conductivity data were fitted as a function of temperature using a linear fit of (ln κ) versus (1000/T). The experimental Arrhenius plots of the conductivities for all the ionic liquids with different $AlCl_3$ mole fractions are shown in Figure 5.

TABLE III. Activation energies obtained from Arrhenius plots for EMIC-$AlCl_3$ IL with different $AlCl_3$ mole fractions.

Ionic Liquid	$AlCl_3$ mole fraction (X_{Al})	Activation Energy (E_a), KJ mol^{-1}	References
EMIC-$AlCl_3$	0.6	4.250 ± 0.305	This work
	0.643	4.744 ± 0.172	
	0.667	4.533 ± 0.456	
	0.6	6.793	*Vila et. al.* (44)

TABLE III lists the activation energy (E_a) values determined from the slope of Arrhenius plots for EMIC-$AlCl_3$ IL with different $AlCl_3$ mole fractions. The table suggests that the activation energy of electrical conduction varies with temperature. Higher the activation energy, the slower will be the chemical reaction. EMIC-$AlCl_3$ IL gives the activation energy in the range of 4.25-10.9 kJ mol^{-1}. The E_a values increase

with $AlCl_3$ mole fraction. Thus, the findings suggest that EMIC-$AlCl_3$ ionic liquid with a 0.6-mole fraction of $AlCl_3$ can serve as an efficient electrolyte for Al-electrodeposition based on higher electrical conductivity and the lowest activation energy of conduction. The calculated activation energies are slightly less than the literature. The E_a value obtained by fitting the VTF model of conduction for EMIM-$AlCl_3$ ionic liquid with the $AlCl_3$ mole fraction of 0.60 is 6.793 kJ mol^{-1} (44).

Conclusions

In conclusion, the electrochemical impedance spectroscopy (EIS) tool was successfully used to obtain the electrical conductivities of imidazolium-based chloroaluminate ionic liquids at different temperatures (343-383 K) and different $AlCl_3$ mole fractions (0.6-0.667). The electrical conductivities of EMIC-$AlCl_3$ ionic liquid increased with temperature following an Arrhenius relationship. However, the conductivity of the EMIC-$AlCl_3$ ionic liquid is decreased at all the studied temperatures with increasing $AlCl_3$ concentration, possibly due to the depleted concentration of $AlCl_4^-$ anions, which have better structural features, such as smaller volume and higher geometric symmetry, in comparison to $Al_2Cl_7^-$ anions. The decrease in conductivity despite a larger concentration of highly conducting $Al_2Cl_7^-$ anions is attributed to the increase in internal resistance and strong cation-anion interactions in EMIC-$AlCl_3$, leading to suppressed movement of ions. A more detailed study involving the interaction of anions with high alkyl-group cations on the conductivity behavior is needed to gain further insights, which will be our future study. The experimentally obtained conductivities and activation energies of EMIC-$AlCl_3$ ionic liquid are compared with the literature data.

Acknowledgments

The authors acknowledge the financial support from the National Science Foundation (NSF) Award Number 1762522, Department of Energy (DOE) RAPID Manufacturing Institute and ACIPCO for this research project. Authors also thank the Department of Metallurgical and Materials Engineering, the University of Alabama, for providing the experimental and analytical facilities.

References

1. M. Galinski, A. Lewandowski and I. Stepniak, *Electrochim. Acta*, **51**(26), 5567 (2006).
2. J. Dupont, R. F. de Souza and P. A. Z. Suarez, *Chem. Rev.*, **102**(10), 3667 (2002).
3. X. Han and D. W. Armstrong, *Acc. Chem. Res.*, **40**(11), 1079 (2007).
4. W. S. Miao and T. H. Chan, *Org. Lett.*, **5**(26), 5003 (2003).
5. A. Marciniak and E. Karczemna, *J. Phys. Chem. B*, **114**(16), 5470 (2010).
6. C. M. Wang, H. M. Luo, H. R. Li and S. Dai, *Phys. Chem. Chem. Phys.*, **12**(26), 7246 (2010).
7. T. L. Greaves and C. J. Drummond, *Chem. Rev.*, **108**(1), 206 (2008).

8. D. R. MacFarlane, M. Forsyth, E. I. Izgorodina, A. P. Abbott, G. Annat and K. Fraser, *Phys. Chem. Chem. Phys.*, **11**(25), 4962 (2009).
9. H. Weingaertner, *Angew. Chem. Int. Ed.*, **47**(4), 654 (2008).
10. J. D. Holbrey, W. M. Reichert, R. G. Reddy and R. D. Rogers, in *Ionic Liquids as Green Solvents: Progress and Prospects,* , R. D. Rogers and K. R. Seddon Editors, p. 121, ACS Symposium Series 856, American Chemical Society, New York (2003).
11. V. Kamavaram and R. G. Reddy, *Int. J. Therm. Sci.*, **47**(6), 773 (2008).
12. V. Kamavaram and R. G. Reddy, in *Light metals 2005*, H. Kvande Editor, p. 501, Warrendale (2005).
13. Ramana G. Reddy, Zhijing Zhang, Mario F. Arenas and Daniel M. Blake, *High. Temp. Mater. Proc.*, **22**(2), 87 (2003).
14. V. Karmavaram and R. G. Reddy, in *Aluminum 2003*, S. K. Das Editor, p. 299 (2003).
15. Y. Peng and R. G. Reddy, in *Advances in Molten Slags, Fluxes, and Salts: Proceedings of the 10th International Conference on Molten Slags, Fluxes and Salts 2016*, p. 1169 (2016).
16. T. Wang, S. Viswanathan, D. Mantha and R. G. Reddy, *Sol. Energy Mater. Sol. Cells*, **102**, 201 (2012).
17. R. Reddy, A. Yahya and L. Brewer, *J. Alloys Compd.*, **321**(2), 223 (2001).
18. M. Zhang, V. Kamavaram and R. G. Reddy, *J. Phase Equilib. Diff.*, **26**(2), 124 (2005).
19. M. M. Zhang and R. G. Reddy, *Min. Proc. Ext. Met.*, **119**(2), 71 (2010).
20. A. Liu, Z. Shi and R. G. Reddy, *Ionics*, **26**(6), 3161 (2020).
21. A. Liu, Z. Shi and R. G. Reddy, *Electrochim. Acta*, **251**, 176 (2017).
22. A. Liu, Z. Shi and R. G. Reddy, *J. Electrochem. Soc.*, **164**(9), D666 (2017).
23. M. Li, Z. Wang and R. G. Reddy, *J. Electrochem. Soc.*, **161**(4), D150 (2014).
24. Z. J. Karpinski and R. A. Osteryoung, *Inorg. Chem.*, **23**(10), 1491 (1984).
25. T. Jiang, M. J. Chollier Brym, G. Dubé, A. Lasia and G. M. Brisard, *Surf. Coat. Technol.*, **201**(1), 1 (2006).
26. J. S. Wilkes, J. A. Levisky, R. A. Wilson and C. L. Hussey, *Inorg. Chem.*, **21**(3), 1263 (1982).
27. D. Pradhan and R. G. Reddy, *Mater. Chem. Phys.*, **143**(2), 564 (2014).
28. T. Jiang, M. C. Brym, G. Dubé, A. Lasia and G. Brisard, *Surf. Coat. Technol.*, **201**(1-2), 1 (2006).
29. J. Tang and K. Azumi, *Electrochim. Acta*, **56**(3), 1130 (2011).
30. A. P. Abbott, *ChemPhysChem*, **6**(12), 2502 (2005).
31. S. Tsuzuki, H. Tokuda, K. Hayamizu and M. Watanabe, *J. Phys. Chem. B*, **109**(34), 16474 (2005).
32. H. Matsuda, H. Yamamoto, K. Kurihara and K. Tochigi, *J. Comput. Aided Chem.*, **8**, 114 (2007).
33. J. M. Slattery, C. Daguenet, P. J. Dyson, T. J. S. Schubert and I. Krossing, *Angew. Chem. Int. Ed.*, **46**(28), 5384 (2007).
34. K. Tochigi and H. Yamamoto, *J. Phys. Chem. C*, **111**(43), 15989 (2007).
35. O. Borodin, *J. Phys. Chem. B*, **113**(36), 12353 (2009).
36. K. Ueno, H. Tokuda and M. Watanabe, *Phys. Chem. Chem. Phys.*, **12**(45), 15133 (2010).

37. P. Eiden, S. Bulut, T. Kochner, C. Friedrich, T. Schubert and I. Krossing, *J. Phys. Chem. B*, **115**(2), 300 (2011).
38. S. Tsuzuki, *ChemPhysChem*, **13**(7), 1664 (2012).
39. A. A. Fannin, L. A. King, J. A. Levisky and J. S. Wilkes, *J. Phys. Chem.*, **88**(12), 2609 (1984).
40. A. A. Fannin, D. A. Floreani, L. A. King, J. S. Landers, B. J. Piersma, D. J. Stech, R. L. Vaughn, J. S. Wilkes and J. L. Williams, *J. Phys. Chem.*, **88**(12), 2614 (1984).
41. Y. Zheng, K. Dong, Q. Wang, J. Zhang and X. Lu, *J. Chem. Eng. Data*, **58**(1), 32 (2013).
42. J. Lu and D. Dresinger, in *Ionic Liquids as Green Solvents Progress and Prospects*, R. D. Rogers and K. R. Seddom Editors, p. 495, American Chemical Society, Washington, DC (2003).
43. C. Ferrara, V. Dall'Asta, V. Berbenni, E. Quartarone and P. Mustarelli, *J. Phys. Chem. C*, **121**(48), 26607 (2017).
44. J. Vila, P. Gines, J. M. Pico, C. Franjo, E. Jimenez, L. M. Varela and O. Cabeza, *Fluid Phase Equilibria*, **242**(2), 141 (2006).
45. H. Xu, T. Bai, H. Chen, F. Guo, J. Xi, T. Huang, S. Cai, X. Chu, J. Ling, W. Gao, Z. Xu and C. Gao, *Energy Storage Mater.*, **17**, 38 (2019).
46. G. Zhu, M. Angell, C.-J. Pan, M.-C. Lin, H. Chen, C.-J. Huang, J. Lin, A. J. Achazi, P. Kaghazchi, B.-J. Hwang and H. Dai, *RSC Adv.*, **9**(20), 11322 (2019).
47. H. Øye, M. Jagtoyen, T. Oksefjell and J. Wilkes, in *Materials Science Forum*, p. 183 (1991).
48. B. S. Lalia, N. Yoshimoto, M. Egashira and M. Morita, *J. Power Sources*, **195**(21), 7426 (2010).
49. J. O. M. Bockris and A. K. N. Reddy, Modern Electrochemistry 2, in, Plenum Press, New York (1970).
50. H. Every, A. Bishop, M. Forsyth and D. R. Macfarlane, *Electrochim. Acta*, **45**(8-9), 1279 (2000).

ECS Transactions, 98 (10) 141-147 (2020)
10.1149/09810.0141ecst ©The Electrochemical Society

Preparation and Electrochemical Properties of Ambient Temperature Molten Chlorides Based on Quaternary Ammonium Chlorides and $MgCl_2$

H. Matsumoto*, R. Ooyabu, and N. Akai.

Department of Energy and Environment, Research Institute for Electrochemical Energy,
National Institute of Advanced Industrial Science and Technology (AIST),
1-8-31, Ikeda, Osaka 563-8577, JAPAN

Magnesium metal can be used as reversible anode in an inorganic molten chloride, such as an alkali metal chloride, however, it is necessary to significantly decrease the melting point of the chloride melts in order to use conventional battery components and materials in a magnesium battery. In this study, we report an organic binary molten chloride based on N,N-diethyl-N-methyl-N-(2-methoxyethyl)ammonium chloride (DEMECl) and $MgCl_2$ which melted near room temperature. The melting point of DEMECl (67 °C) decreased with the increasing amount of $MgCl_2$. The lowest melting point of 34 °C was obtained for $MgCl_2$ - DEMECl (1:5). Its physicochemical, thermal and electrochemical properties were preliminary investigated.

Introduction

The research and development of magnesium secondary batteries using a magnesium anode have attracted much attention as one of the prospective post-lithium ion batteries due to its high theoretical capacity (3830 Ah dm^{-3}) and no resource constraints. However, it has been quite difficult to construct magnesium batteries for a long time because practical electrolytes like a carbonate solvent containing $LiPF_6$ for a lithium ion battery have been currently under development (1). As a result of efforts in recent years regarding the research and development of organic electrolytes for the magnesium anode batteries, a few practical electrolyte systems have begun to be reported (2). The use of an organic electrolyte must be preferable to the future social implementation of magnesium battery systems that would be similar to the structure and the manufacture of lithium-ion batteries. Regarding the use of organic solvents, the safety issue based on the flammability and volatility must be more prominent in the magnesium batteries compared to a lithium-ion battery because the operating temperature of the magnesium batteries using a cathode based on a transition metal oxide should be much higher than that of the lithium batteries due to the large electrostatic field of Mg^{2+}. In such a case, ionic liquids would be promising candidates in terms of safety and use at high temperature. For example, the alkali metal binary molten amide ($Mg[Tf_2N]_2$-$Cs[Tf_2N]$) was used as a solvent for investigating the charge-discharge property of one of the promising cathodes of $MgCo_2O_4$ at 150 °C (3).

Ionic liquid electrolytes have been reported to be successfully applied to the lithium anode and also ~~the~~ lithium-ion batteries (4), however, a magnesium anode in such conventional ionic liquids containing perfluoroanions did not indicate a reversible

response at the magnesium standard potential (5, 6). We previously reported that Tf_2N-based ILs were not suitable for a Mg anode even in an alkali metal binary molten salt such as $Mg[Tf_2N]_2$-$K[Tf_2N]$, which indicated that the existence of the Tf_2N^-affected magnesium redox on the Mg electrodes (6). Furthermore, the existence of surface passivation films derived from the decomposition compounds from the perfluroanion was also reported (7). On the other hand, a relatively smooth magnesium redox could be observed in 1-butyl-3-methylimidazolium chloride melts containing $Mg[Tf_2N]_2$ (8). This indicate that the existence of halogen anions effectively improved magnesium redox. However, the electrochemical window of the imidazolium melt was limited by the reduction decomposition of the imidazolium.

In this study, we report that ambient temperature molten chlorides could be obtained by mixing a quaternary ammonium chloride and $MgCl_2$, which do not contain any perfluoroanions, such as the Tf_2N^-, and also imidazolium cations. The thermal properties and also the physicochemical properties were investigated. The electrochemical response of a magnesium metal in the binary melt were also shown to indicate the possibility as the electrolyte for a magnesium anode battery.

Experimental

N,N-Diethyl-N-methyl-N-(2-methoxyethyl)ammonium chloride (DEMECl) was prepared by an alkylation reaction of N,N-diethyl-N-methylamine with 2-chloroethylmethylether using an autoclave. After heating for 3 days at 120 °C, the unreacted raw materials in the crude products were removed by vacuum distillation. An activated carbon was used for removing the residual impurities in the DEMECl dissolved in methanol. The methanol solution was filtered, then the methanol was distilled off using a rotary-evaporator under vacuum. (89% yield). The purified DEMECl and anhydrous $MgCl_2$ (3N, Kojundo Chemical Laboratory Co., Ltd.) were mixed in an open dry chamber (DAIKIN, dew point < -50 °C). The resulting binary molten chlorides were dried under vacuum over 85°C for 12 h.

The physicochemical properties, such as viscosity (Brookfield DV-III+, cone spindle: CP-52) and ionic conductivity, were measured in the same dry chamber to avoid contact with moisture. The conductivity measurements were carried out using a computer-controlled Solartron SI-1260 impedance/gain-phase analyzer with a frequency range from 1 Hz to 500 kHz. The impedance data were analyzed by the complex impedance method. The measurement of the samples was carried out in a commercially-available conductivity cell using platinum black electrode cells (Radiometer Analytical, CDC749, cell constant: 1.9 cm^{-1}). The density was measured by a He gas pycnometer (Accupyc II 1340). The thermal behaviors of the DEMECl salts were investigated by DSC (Perkin-Elmer, Pyris 1) using a liquid N_2 cryostat system, which allows the DSC measurement from −150 °C.

The electrochemical measurements were carried out by a computer-controlled electrochemical analyzer (Bio-logic, VMP3) in a Ar-filled glove box (MIWA). The analyzer could obtain an electrode potential for not only the working electrode but also the counter electrode. An iodide redox reference electrode consisting of a platinum wire immersed in a small aliquot of $[C_2mim][Tf_2N]$ containing 60 mmol dm^{-3} *N,N,N,N*-

tetrapropylammonium iodide and 15 mM iodine was used. The iodide redox solution in the reference electrode was separated from the measurement solution by a porous Vycol glass top fitted onto the bottom of the reference electrode.

Results and Discussion

Thermal Properties

N,N-Diethyl-N-methyl-N-(2-methoxyethyl)ammonium ($DEME^+$) was chosen in this study because it contains a flexible alkoxy side-chain, which effectively decreases the melting point of the quaternary ammonium salts combined with various anions as already reported (9). As shown in Figure 1(a), the DEMECl did not melt at near room temperature, but the melting point (T_m = 67 °C) was much lower than that of quaternary tetraalkylammonium chloride, such as N,N,N,N-tetraethylammonium chloride (262 °C), N-methyl-N-propylpiperidinium chloride (225 °C), N-butylpyridinium chloride (132°C) and 1-ethyl-3-methylimidazolium (85°C) (10, 11). In the same figure, results for mixing $MgCl_2$ into the DEMECl are also shown. The T_m of the binary chloride (DEMECl + $MgCl_2$ (5:1)) was significantly decreased from that of the DEMECl single salt. During the successive second heating, no endothermic peak was observed and only a glass transition was observed. This indicates that the binary melt tends to remain as a

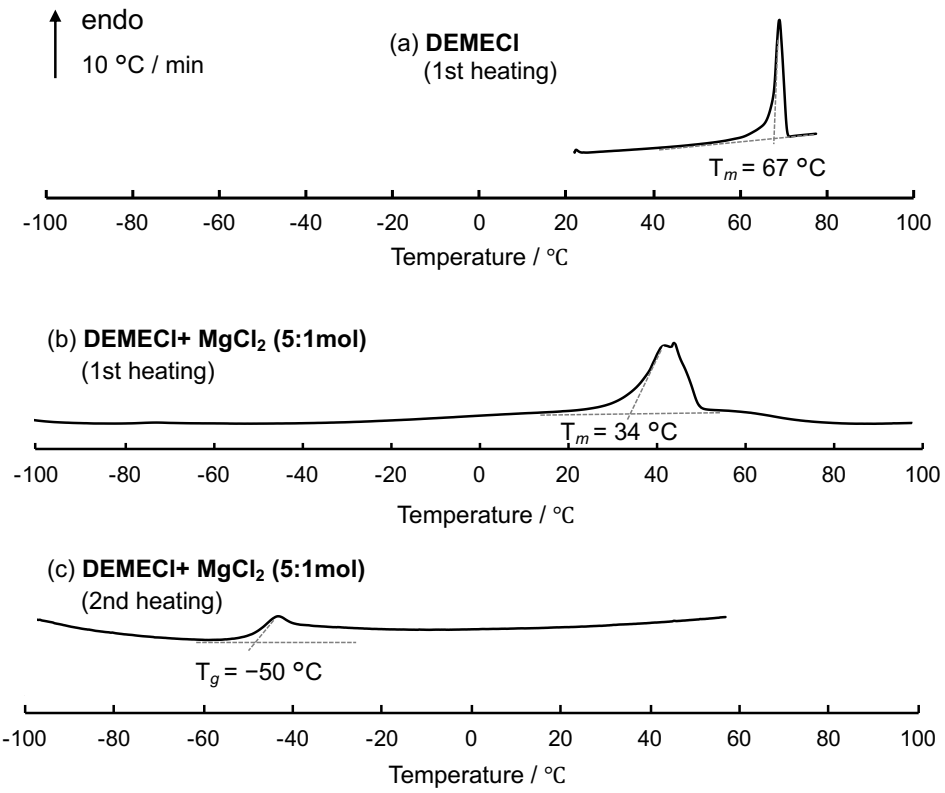

Figure 1. DSC results obtained by heating (10 °C min). (a) DEMECl; (b) DEMECl + $MgCl_2$ (5:1) during the first heating; (c) DEMECl + $MgCl_2$ (5:1) during the successive second heating.

supercooled liquid. The melting behavior as shown in Figure 1(b) was observed again after a few days later. The relatively high glass transition temperature (T_g = −50°C) suggests that the binary melt exhibits a very high viscosity compared to the conventional ionic liquids as described later. The amount of $MgCl_2$ was not able to be increased from this binary composition (DEMECl : $MgCl_2$ = 5:1) at room temperature. Therefore, the binary melt would be a basic melt, which means an excess amount of a free chloride existed in the melt.

Transport Properties

As already stated, the viscosity of the binary chloride (DEMECl + $MgCl_2$ (5:1)) might be expected to be much higher than that of conventional ionic liquids, such as DEME[Tf_2N] (Tf_2N^-, bis(trifluoromethylsulfonyl)amide), which exhibited a much lower T_g at −95 °C. As shown in Figure 2, the viscosity of DEMECl-$MgCl_2$(5:1) was about 2 orders of magnitude higher than that of the DEME[Tf_2N]. Such a high viscosity of the binary molten chloride inhibits the diffusivity of ions in the melt. Indeed, the molar conductivity of the binary molten chloride was also two orders of magnitude lower than that of DEME[Tf_2N] as shown in TABLE I. In case of chloroaluminate melts, an acidic composition, which means the molar ratio of $AlCl_3$ to the tetraalkylammonium chlorides, or alkali metal chlorides is greater than 1.0, could be easily prepared (12), however, $MgCl_2$ was quite difficult to dissolve into the DEMECl melt for such an acidic composition. This might be one of the reasons for the high viscosity of the DEMECl-

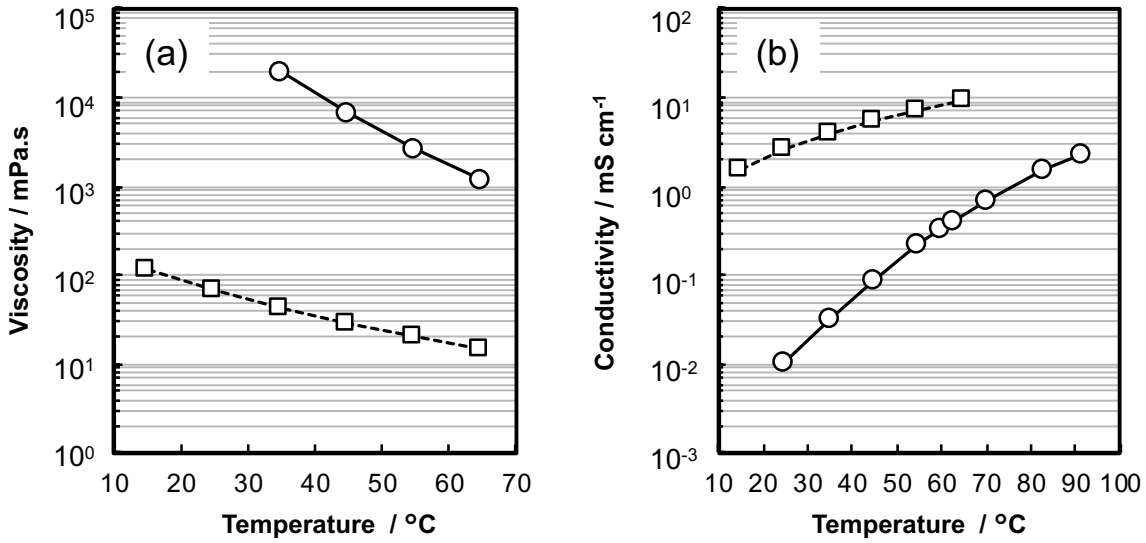

Figure 2. Transport properties of molten DEME salts; (a) viscosity; (b) conductivity. (○) DEMECl + $MgCl_2$ (5:1), (□) DEME[Tf_2N].

TABLE I. Transport properties of molten binary chloride and ionic liquids based on $DEME^+$ at 45 °C.

	d[a] / g mL^{-1}	**C**[b] / mol L^{-1}	**η**[c] / mPa.s	**κ**[d] / mS cm^{-1}	**Λ**[e] / S cm^2 mol^{-1}
DEMECl + $MgCl_2$ (5:1)	1.10	6.1	6800	0.087	0.014
DEME[Tf_2N]	1.42	3.3	29	5.2	1.6

a: Density; ***b***: Concentration; ***c***: Viscosity; ***d***: Specific conductivity; ***e***: Molar conductivity.

$MgCl_2$ binary melt. This situation also affected the electrochemical window especially for the anodic region due to the oxidation of Cl^- as stated below.

Electrochemical Properties

One of the motivations of this study was to prepare ambient temperature ionic liquids without using perfluoroanions, such as Tf_2N^-, for a magnesium anode because recent studies of ionic liquids for a magnesium anode have revealed that an irreversible passivation film was formed on the magnesium in these conventional ionic liquids based on perfluoroanions (7). One of the examples for such conventional ionic liquids such as [DEME][Tf_2N] containing 0.5 mol dm^{-3} $Mg[Tf_2N]_2$ is shown in Figure 3. In the conventional ionic liquids, Li deposition and stripping was reported by many researchers over the past two decade (4) but Mg could not be deposited on Pt, furthermore, more unfortunately, the potential of the magnesium counter electrode significantly changed during the cycling. All these results indicate that the conventional ionic liquids could not be used as an electrolyte for the magnesium battery system. The much stronger electrostatic force from the divalent Mg cation than that of the Li cation must more tightly attract Tf_2N^-, which might be maintained and does not dissociate during the electrodeposition process.

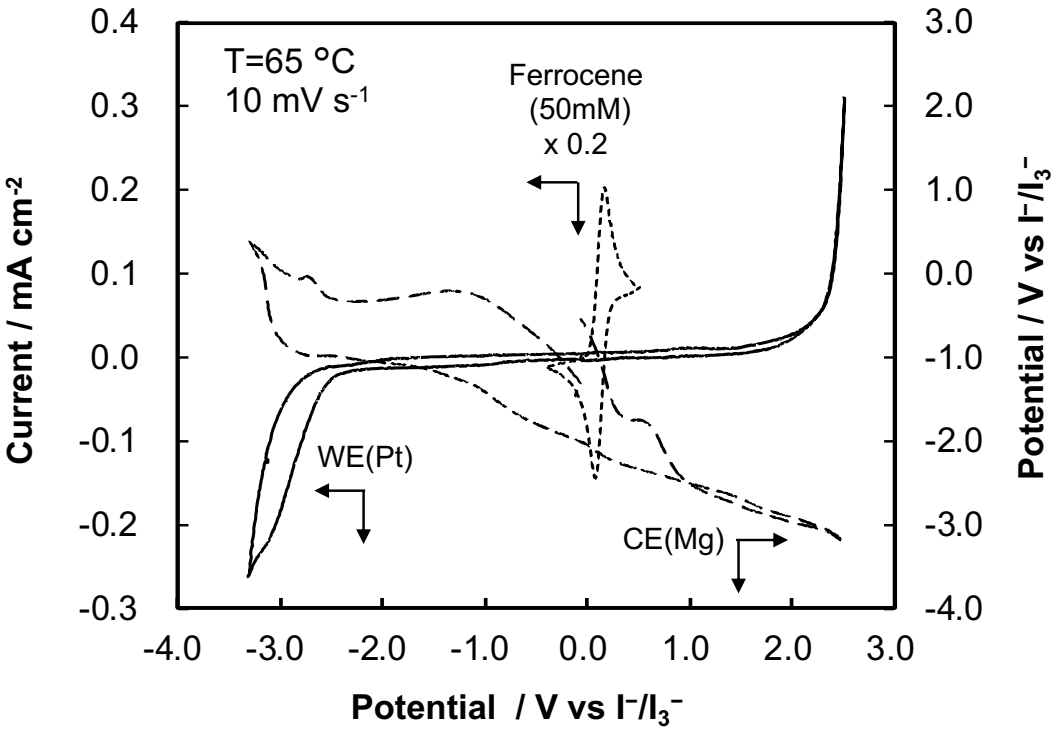

Figure 3. Cyclic voltammogram of Pt in a [DEME][Tf_2N] + $Mg[Tf_2N]_2$ (0.5 mol dm^{-3}) at 65 °C. The potential of the Mg counter electrode (CE(Mg)) simultaneously obtained is indicated (dashed line) and also the cyclic voltammogram of ferrocene added to the same ionic liquids is also shown (dotted line).

On the other hand, not only in organic electrolytes (2), but also in molten salts (13), the halogen ion seems to be essential for a good magnesium redox. In this study, we found the ambient temperature organic molten chloride as already stated, which does not

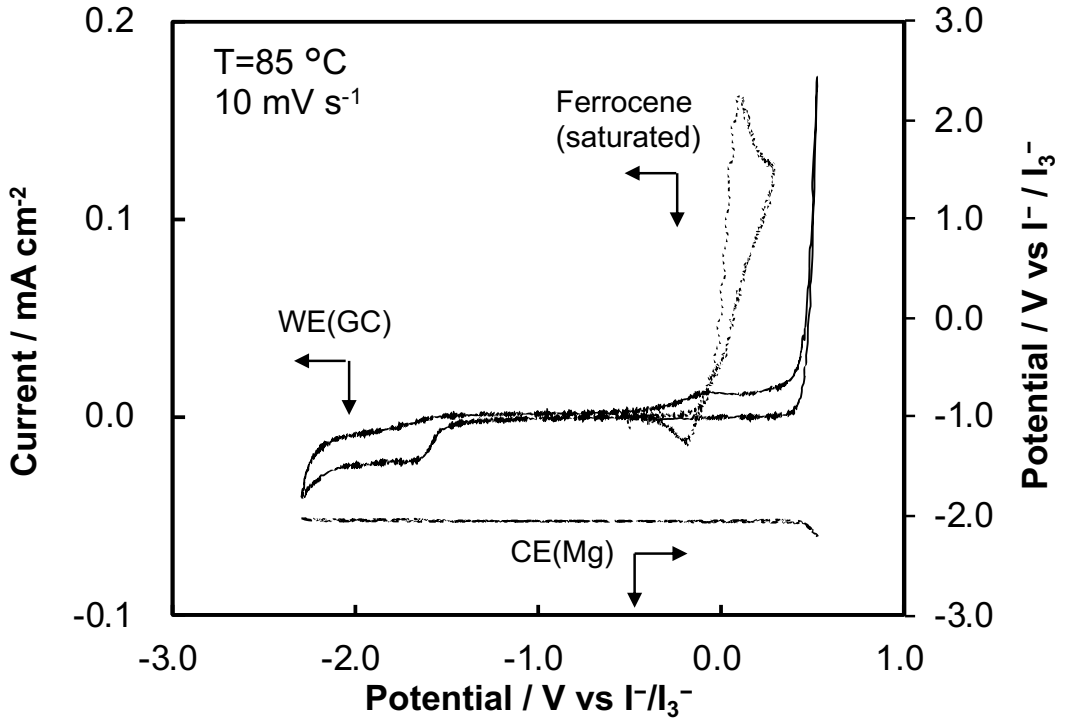

Figure 4. Cyclic voltammogram of a glassy carbon (GC) in a DEMECl + $MgCl_2$ (5:1) at 85 °C. The potential of the Mg counter electrode (CE(Mg)) simultaneously obtained is indicated (dashed line) and also the cyclic voltammogram of ferrocene added to the binary melt is shown (dotted line).

contain any perfluroanions. In this case, a cathodic peak and an anodic peak were observed, and very interestingly, the potential of the counter Mg during the cycling was fixed at -2.1 V, which suggested that a Mg anode could operate in the molten binary chloride as shown in Figure 4. The exact potential of the magnesium in the melt was not correctly calculated because the redox peak of the ferrocene as the internal potential standard was not clearly indicated in the binary melt, especially, the reduction peak current from the ferrocenium (Fc^+) was quite low compared to the oxidation peak current from the ferrocene (Fc). The reason for this is not yet understood, but the Fc^+ might be affected by the existence of a large amount of Cl^-.− However, the peak potential in the molten binary chloride was not very different from that in the conventional [DEME][Tf_2N] (+0.12 V vs I^-/I_3^- in [C_2mim][Tf_2N]) as shown in Figure 3; the potential of the Mg counter was about + 0.6 V (−2.1 V vs Fc/Fc^+) higher than the magnesium standard potential (14). ($E(Fc/Fc^+)$ = + 0.4 V vs SHE (15), $E^0(Mg/Mg^{2+})$ = -2.34 V vs SHE = -2.74 V vs Fc/Fc^+(14)). The limiting anodic potential, which might be the oxidation of Cl^- in the binary melt, was ca. +0.5 V vs I^-/I_3^-, which corresponds to 2.5 V higher than the magnesium anode. Therefore, the binary chloride melt could be used as a magnesium anode, but the cathode material was limited to below the operating potential under the oxidation limiting potential derived from Cl^-. To overcome this limitation, we need to develop a new strategy to prepare an acidic binary melt.

Conclusion

We developed a new ambient temperature molten chloride based on an organic cation and $MgCl_2$. The transport properties of the binary melt were poor compared to the corresponding conventional ionic liquids composed of Tf_2N^-. However, the potential of magnesium in the binary melt was quite stable and a relatively negative potential (+ 0.6 V vs Mg) was maintained during the voltammetry. The binary melt could be used as an anolyte for a magnesium anode. To choose the appropriate cathode material, which can be operated below the oxidation limiting potential of the binary melt, it is expected to construct an approximate 2.5 V battery using a magnesium metal anode. To increase the output voltage, it is necessary to find a new method to prepare an anodic composition using $MgCl_2$.

Acknowledgments

This work was supported by the ALCA-Specially Promoted Research for Innovative Next Generation Batteries (ALCA-SPRING) of Japan Science and Technology Agency (JST).

References

1. C. B. Bucur, *Challenges of a Rechargeable Magnesium Battery*, Springer International Publishing AG, Cham, Switzerland (2018).
2. R, Attias, M. Salama, B. Hirsch, Y. Goffer, and D. Aurbach, *Joule,* **3**(1), 27 (2019).
3. S. Okamoto, T. Ichitsubo, T. Kawaguchi, Y. Kumagai, F. Oba, S. Yagi, K. Shimokawa, N. Goto, T. Doi, and E. Matsubara, *Adv. Sci.,* **2**(8), 1500072 (2015).
4. H. Matsumoto, in *Electrolytes for Lithium-ion Batteries*, T. R. Jow, K. Xu, O. Borodin and M. Ue, Editors, chapter 4, Springer, New York (2014), and references therein.
5. G. Vardar, A. E. S. Sleightholme, J. Naruse, H. Hiramatsu, D. J. Siegel, and C. W. Monroe, *ACS Appl. Mater. & interfaces*, **6**, 18033 (2014).
6. K. Kubota, and H. Matsumoto, *J. Electrochem. Soc.*, **167**, 020541 (2020).
7. T. Shiga, Y. Kato, and M. Inoue, *ACS Appl. Mater. & interfaces*, **8**, 30933 (2016).
8. H. Matsumoto, and K. Kubota, *ECS Trans*., **86**(14), 21 (2018).
9. H. Matsumoto, H. Sakaebe, and K. Tatsumi, *ECS Trans.*, **16**(35), 59 (2009).
10. D. O. Abranches, L. P. Silva, M. A. R. Martins, L. Fernadez, S. P. Pinho, and J. A. P. Coutinho, *Fluid Phase Equilibria*, **493**,120 (2019).
11. A. A. Fannin, D. A. Floreani, L. A. King, J. S. Landers, B. J. Piersma, D. J. Stech, R. L. Vaughn, J. S. Wilkes, and J. L. Williams, *J. Phys. Chem.*, **88**(12), 2614 (1984).
12. S. D. Jones, and G. E. Blomgren, *J. Electrochem. Soc.*, **136**(2), 424 (1989).
13. X. Zhao, Q. Li, Z. Z-Karger, P. Gao, K. Fink, X. Shen, and M. Fichtner, *ACS Appl. Mater. & interfaces*, **6**, 10997 (2014).
14. S. Trasatti, *Pure & Appl. Chem*., **58**(7), 955 (1986).
15. R. R. Gagne, C. A. Koval, and G. C. Lisensky, *Inorg. Chem*., **19**, 2854 (1980).

ECS Transactions, 98 (10) 149-159 (2020)
10.1149/09810.0149ecst ©The Electrochemical Society

Limited Ionicity in Protic Ionic Liquids: Ionization Gibbs Energies in Organic Acid/Trialkylamine Mixtures

Devin O. Klapatiuk, Keith E. Johnson, and Allan L. L. East

Department of Chemistry and Biochemistry, University of Regina, Regina, SK S4S0A2, Canada

The nature of the ions present in mixtures of trialkylamines (B) with carboxylic acids (HA) is discussed. New ab initio molecular dynamics (AIMD) simulations of mixtures of triethylamine (TEA) with acids here reveal the same cation type, the large complex $[B(HA)_nHB]^+$, as seen earlier with pyridine (PYR). Since this indicates that the ionization equilibrium reaction 2 $B(HA)_n \rightleftarrows B(HA)_nHB^+ + A(HA)_{n-1}^-$ is perhaps more general than for pyridine systems, a new analysis derives ΔG for this equilibrium reaction from experimental conductivities, viscosities, and densities, as a function of x_B (mole fraction of B in the acid/base mixture). The results show that large Walden constant values, which might be indicative of Grotthuss H^+ conductivity mechanisms, are not needed except for formic-acid-rich mixtures.

Introduction

Protic ionic liquids (PILs) are a subset of ionic liquids formed by certain mixtures of a Bronsted acid with a Bronsted base, generating ionic species through proton transfer (1-4). The ionicity of PILs is not always as high as anticipated, often calling into question their inclusion into the category of ionic liquids, and the reasons for such limited conductivity is an active research topic.

In the classic cases of carboxylic acids with amines, not only are conductivities low, but they show maxima in conductivity at acid mole fractions near $x_B = 0.17$ (1:5 base:acid) (5-9), rather than the more commonly studied 1:1 mixtures. A second maximum of varying location is also occasionally seen (5,8,9). Additionally interesting is that this conductivity maximum location ($x_B \approx 0.2$) is often close to, or even coincident with, the viscosity maximum location ($x_B \approx 0.2$-0.3), which at first may seem counterintuitive. Table 1 provides motivating data.

We are in pursuit of a theory that can explain these phenomena, qualitatively and semiquantitatively, with an ultimate goal of predicting the conductivity of a given mixture at any mixing ratio. We had begun ("2018 theory") with a system (pyridine + acetic acid) in which the conductivity and viscosity maxima are coincident, at $x_B = 0.17$ (10). In this paper we begin the extension to *non-coincident* systems. We present here an examination of the thermodynamics and plausible Walden constants of five triethylamine systems (TEA + carboxylic acids) and one tributylamine system (TBA + propionic acid).

TABLE I. Mole fractions of property extrema in amine/acid mixtures: VE = volume excess, η = viscosity, [ions] = total ion concentration, σ = specific (ionic) conductivity.

Mixture [a]	$x_B(VE_{min})$	$x_B(\eta_{max})$	$x_B([ions]_{max})$ [b]	$x_B(\sigma_{max})$
TEA/a1	≥ 0.40	≥ 0.40	0.19 ± 0.01	0.10 ± 0.01
TEA/a2	0.35 ± 0.02	0.28	0.19 ± 0.01	0.13 ± 0.02
TEA/a3	0.35 ± 0.02	0.28	0.20 ± 0.01	0.16 ± 0.01
TEA/a4	0.34 ± 0.02	0.25	0.23 ± 0.01	0.18 ± 0.02
TEA/a5	0.33 ± 0.02	0.25	0.24 ± 0.01	0.20 ± 0.02
PYR/a2	0.19 ± 0.03	0.17	0.17 ± 0.01	0.17

[a] a1-a5 refer to acids formic-pentanoic; TEA = triethylamine, data from Huyskens (7); PYR = pyridine, data from Venkatesan (11).
[b] The location of the maximum of the product ησ; see Eq. [17].

Huyskens and co-workers had developed a very similar theory for the TEA systems already in 1980 (7). They, like us, use Walden's (Viscosity) Rule as the central relation:

$$\sigma = W\, C / \eta \qquad [1]$$

where σ and η are the specific conductivity (S cm^{-1}) and viscosity (cP) of the electrolyte, C the ion or electrolyte concentration (mol L^{-1}), and W a proportionality constant known as the Walden constant (units S cP cm^2 mol^{-1}) (12). Eq. [1], though originally empirical, can be derived from Stokes' Law (see Theory section). Huyskens et al. began their paper by agreeing with the hypothesis of Kohler et al. that an apparent preference of the mixtures for $B(HA)_3$ complexes (B = base amine, HA = carboxylic acid) explains the viscosity maximum at $x_B = 0.25$ (13). Huyskens et al. then proposed (based on some assumptions about W magnitudes in Eq. [1]) that the apparent ion concentration maximum at $x_B = 0.20$ is due to the ionization equilibrium

$$B(HA)_3 + HA \rightleftarrows BH^+ + A(HA)_3^- \qquad [2]$$

and, further, that the different conductivity magnitudes among the heavier acids could be ascribed to their dielectric constants. This proposed equilibrium was indeed a clever way to explain how a conductivity maximum could be displaced from a viscosity maximum. Their notion of a complexed anion $A(HA)_n^-$ with A = carboxylate is quite analogous with the halide cases (A = Cl- or Br-) that were detected by Angell (14) and Johnson (15) and assumed in very old studies of amines with strong mineral acids (16).

A flaw was quickly spotted. In the following year (1981), Kohler and co-workers presented ^{1}H-NMR data which placed the acidic proton at 8-12 ppm, too far downfield to indicate a free BH^+ entity, and instead indicative of a partially bridged proton, strongly hydrogen bonded (8). Kohler et al. gave a counterproposal: that the conductivity is occurring not by translating ionic aggregates but by "a flipping over of hydrogen bonds," possibly a reference to a Grotthuss H^+ mechanism. This counterproposal, however, has two problems of its own. First, Kohler et al. erringly stated that the conductivity maximum was at $x_B = 0.25$ like viscosity (which might support a Grotthuss claim), when in fact their own data shows the conductivity maxima at $x_B = 0.17$ or lower. Second, Angell (1) used Walden plots to show that these systems do not show any enhanced ion mobility afforded by a supposed Grotthuss mechanism: the conductivities are poorer than those of the most highly ionic 1:1 PILs from the strongest acid/base combinations, which,

like aprotic ILs, conduct via molecular ions or ion aggregates (the so-called "vehicular" mechanism).

There is, fortunately, a resolution at hand. The ^{1}H-NMR data can be explained by our discovery, via ab initio molecular dynamics (AIMD) simulations of pyridine + acetic acid mixtures, that the cationic species at equilibrium in that system are not free BH^+ but larger $[B(HA)_nHB]^+$ cationic aggregates (n = 0, 1, 2, …) (10). Those simulations, of the mixtures at equilibrium, showed no evidence of H^+ hopping. There was rare hopping of "monomeric" acetic acid or pyridinium ions from complex to complex, which as we pointed out might contribute to conductivity, but the relative rarity of their hops at room temperature caused us to pursue a theory based on ordinary vehicular transport of charge, as Huyskens et al. had done (7), but with an updated ionization equilibrium:

$$B(HA)_m + B(HA)_n + \rightleftarrows [B(HA)_mHB]^+ + A(HA)_{n-1}^- \qquad [3]$$

and further mathematical development (10). We note in passing that this reaction requires two base molecules to generate two ions, unlike the Huyskens equilibrium which requires just one.

In that same 2018 paper we went on to produce an equation for conductivity as a function of viscosity, molar volume, dielectric constant, and ion size (10). Using fitted experimental data for the first two properties, linearly interpolated dielectric constants, the Fuoss equation (17) for degree of dissociation of ion pairs (from ion size and dielectric constant of the medium), and only two fitting parameters to represent the poorly known ion sizes needed for the Fuoss (ions that are pairing) and Walden (big ions that are translating) equations, the conductivity equation successfully reproduced the experimental conductivity curve in the pyridine/ethanoic acid system. The resulting fit gave reasonable effective conduction ion sizes of 6 Å (cations) and 11 Å (anions) for the pyridine/acetic acid system. It was noted, however, that an exploratory fit to the triethylamine/acetic acid system predicted overly large ions (10).

In this preliminary Communication, we first present results from AIMD simulations of the TEA/acid systems to examine ion speciation, supporting the continued use of Eq. [3] as the ionization reaction. Second, we derive ionization Gibbs energies for this reaction from experimental conductivities and viscosities and a selection of assumed Walden constant values W. The resulting relationship of ΔG_{ioniz} with mole fraction is discussed, and the limitations on plausible W values are used to test the assumption of vehicular (vs. Grotthuss) conductivity.

In a later full paper we intend to present an updated conductivity theory that merges the 2018 and 1980 ideas and can hopefully fit (and thus explain) the conductivities of several of these amine + organic acid systems.

Theory (Derivation of Walden's Rule)

This is improved upon our earlier presentation (10) by (i) generalizing to handle mixtures having more than two kinds of ions, and (ii) avoiding the superfluous step of converting ion velocities to ion diffusion constants. Conductivity σ is the proportionality constant relating the external electric field X to the induced electrolyte current *i*:

$$i = \sigma X \qquad [4]$$

The current, in terms of ion velocities v_j, is:

$$i = \Sigma\, q_j\, \rho_j\, v_j \qquad [5]$$

where the sum runs over all ion types *j*, and q_j and ρ_j are the ion charge and ion density (concentration). The ion velocities achieve steady ("terminal") values because the constant force F_j on the ion *j* due to the field X,

$$F_j = q_j X\,, \qquad [6]$$

accelerates the ions faster and faster until the rising viscous drag force F_j' finally matches the field force F_j, at which point acceleration stops and velocities are steady. The viscous drag force on spherical particles in a structureless medium is given by Stokes' Law:

$$F_j' = -6\pi\eta r_j v_j \qquad [7]$$

where r_j is the ion radius (Stokes radius). Thus, when the velocities are steady, $F_j' = F_j$ and equating the last two equations gives

$$v_j = q_j X /(6\pi\eta r_j) \qquad [8]$$

which inserts into Eq. [5] to give

$$i = \Sigma\, q_j\, \rho_j\, [q_j X /(6\pi\eta r_j)]$$
$$i = [\, \Sigma\, q_j^2 \rho_j/(6\pi\eta r_j)\,]\, X \qquad [9]$$

This matches Eq. [4], revealing σ to be

$$\sigma = [1/(6\pi\eta)]\, \Sigma\, (q_j^2 \rho_j / r_j) \qquad [10]$$

A second way of writing this uses $q_j = z_j e_0$ (integer times electron charge) $\rho_j = N_{AVO}\, c_j$ (Avogadro's number times ion molarity), and $F = N_{AVO}\, e_0$:

$$\sigma = [e_0 F/(6\pi\eta)]\, \Sigma\, (z_j^2 c_j / r_j) \qquad [11]$$

A third way of writing this is

$$\sigma = (1/\eta)\, \Sigma\, W_j c_j\,, \qquad [12]$$
$$W_j = [e_0 F/(6\pi)]\, (z_j^2 / r_j) \qquad [13]$$

where W_j is the *ion-specific Walden constant.* The constant factor $e_0F/(6\pi)$ is 81.9 S cP cm^2 Å mol^{-1}.

To accommodate ion pairing, we relate each ion concentration c_j to a formal electrolyte concentration $c = V_m^{-1}$ with a degree of ionization α_j:

$$c_j = \alpha_j\, c \qquad [14]$$

With this, a fourth way of writing the conductivity expression is

$$\sigma = (c/\eta)\, \Sigma\, \alpha_j W_j \qquad [15]$$

Furthermore, if the electrolyte is a simple 1:1 salt, $\alpha_+ = \alpha_- = \alpha$, which produces the expressions

$$\sigma = 2\alpha c W/\eta \qquad [16]$$
$$\sigma = WC/\eta \qquad [17]$$

where W is the *average* W_j and C is the *total* ion concentration:

$$W = ½\, (W_+ + W_-) \qquad [18]$$
$$C = c_+ + c_- = 2\alpha c \qquad [19]$$

It is Eq. [17] that is Walden's Rule, often written as $\Lambda\eta = W$ where Λ is the molar or equivalent conductivity σ/C. The expression for W in Eq. [18] was erroneously missing the factor of ½ previously (10), due to confusion with an alternative formalism that takes C to be c instead of 2αc, i.e. that takes C in Walden's Rule (Eq. [17]) to be formal electrolyte concentration instead of total ion concentration. We shall keep W and C as defined in Eqs. [18] and [19].

There is an additional convention decision to make, regarding the definition of the formal electrolyte concentration c itself in these acid+base mixtures, due to the various ions formed as mole fraction x_B is varied. As before (10) we take c to be total initial concentration of acid + base (roughly 5-15 M),

$$c = V_m^{-1} = [B]_{init} + [HA]_{init} \qquad [20]$$

This is unlike Huyskens et al. (7) who chose c to be initial concentration of base only, $[B]_{init}$. The choice of convention affects the values of c and hence $\alpha_j = c_j/c$, but not the ion concentrations c_j.

Methodology

Simulations were performed as before (10) using the Vienna Ab-initio Simulation Package (VASP) software (19). VASP simulations assign each atom nucleus a randomized velocity and direction of motion, and moves them in steps (timestep 1 fs, as before) dictated by Newton's laws of motion, with the forces applied on each individual nucleus coming from the approximate solution of the Schrodinger equation for electronic energy. VASP performs periodic replication of a unit cell to model condensed phases. Initial Cartesian coordinates were generated using Gaussview 5.0. Unit cell side lengths were chosen to match the experimentally known density of the mixture at the given mixing ratio.

Results and Discussion

Simulations

Initially, several short 10 ps simulations (1 fs timesteps) were performed on three systems, TEA with formic (a1), acetic (a2), or propanoic (a3) acids, at selected acid-rich mixing ratios (2:18, 3:15, 4:6, 5:5), starting from neutral monomer molecules. These established that triethylamine, like pyridine, readily forms ion-pair "kites" $B(HA)_n$ of various lengths *n*, up to n=8 for TEA/a1 and n=5 for TEA/a2 or TEA/a3. Such short simulations would not be expected to achieve equilibration; indeed, none of these short simulations generated any free ions or ion complexes. The long lengths of kites, however, are noteworthy, as such lengths were not anticipated by either Huyskens et al. (7) or Kohler et al. (8).

One simulation was run for 630 ps, in hopes of observing ions to learn their nature. For this we chose the 3:15 TEA/a1 mixture, the system and mixture thought to have the highest concentration of ions. This simulation began with 10 neutral HA (HCOOH), 2 neutral B (Et_3N), and one ion-pair kite $B(HA)_5$. One of the free base molecules was protonated rather quickly. Between 100 and 200 ps the species observed were one each of $[B(HA)_7HB]^+$, $A(HA)_5^-$, B, and $(HA)_2$. The other free base was not protonated until ~ 540 ps (540000 timesteps), with a noticeable step drop in the plot of energy vs. time. At the end of the run, the species observed (Fig. 1) were one each of $[BHAHB]^+$, $A(HA)_6^-$, $B(HA)_5$, and $(HA)_2$. Hence the cations produced by the simulation were the "two-headed kites" $[B(HA)_7HB]^+$ and not the BH^+ ions assumed by Huyskens (7). This observation of the cations as two-headed kites matches what we found previously in pyridine/acetic acid simulations (10).

The insight gleaned from simulations allow us to update the past explanations of excess volume and viscosity data vs mixing ratio. Table 2 shows our summary of the expected sizes of the neutral molecules and complexes, at various mixing mole fractions, with comparison to the hypotheses put forward in 1980-81.

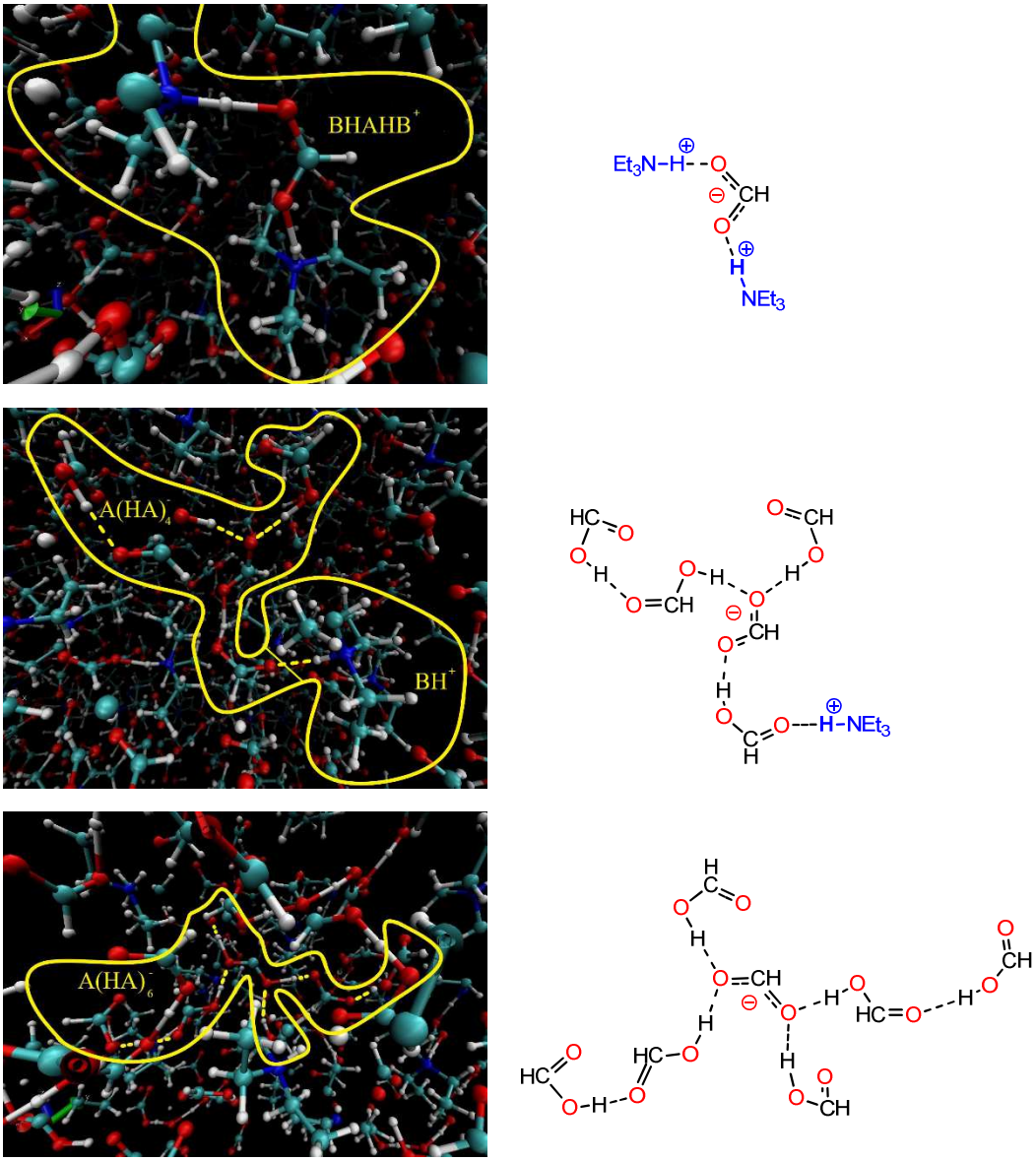

Figure 1. Snapshots of portions of the simulation cell at the final timestep of the long $(Et_3N)_3(HCOOH)_{15}$ simulation, showing (top) the $BHAHB^+$ cation, (middle) the $B(HA)_5$ ion pair "kite," and (bottom) the $A(HA)_6^-$ "free tail" anion.

TABLE II. Improvements in "minimalist" descriptions of the neutral complexes in TEA/acid mixtures (x_B = mole fraction of base, A = acid molecule HA).

x_B	ba_3 idea [a]	ba_3 + ba idea [b]	current work
0.05	$BA_3 + 8\ A_2$	$BA_3 + 8\ A_2$	$BA_{9+2y} + (5\text{-}y)\ A_2$ [c]
0.10	$BA_3 + 3\ A_2$	$BA_3 + 3\ A_2$	BA_9
0.25	$y\{BA_3\}$ + $z\{B + 1.5\ A_2\}$	$y\{BA_3\}$ + $z\{BA + A_2\}$	BA_3
0.33	$y\{BA_3 + 0.5\ B\}$ + $z\{B + A_2\}$	$y\{BA_3 + BA\}$ + $z\{BA + 0.5\ A_2\}$	BA_2
0.50	$BA_3 + 2\ B$	BA	BA
0.90	$BA_3 + 26\ B$	BA + 8 B	BA + 8 B

[a] In the spirit of Kohler et al. (8) [b] In the spirit of Huyskens et al. (7)
[c] At very small x_B such as 0.05, the maximum kite length varies with the acid involved, e.g. y=0 for pentanoic and butanoic acid, but larger for propanoic and acetic acids.

Ionization Gibbs Energies

To simplify the mathematics, we do as before (10) and reduce the number of Eq. [3] equilibria to one at each value of x_B:

$$2\ B(HA)_n + \rightleftarrows [B(HA)_nHB]^+ + A(HA)_{n-1}^- \quad [21]$$

$$K_{ioniz} = [B(HA)_nHB^+][A(HA)_{n-1}^-]/[B(HA)_n]^2 = (\alpha c)(\alpha c) / (x_i c - 2\alpha c)^2 \quad [22]$$

The generation of $\Delta G_{ioniz}(x_B)$ values from experimental conductivities can be achieved if one assumes (a) that all the conductivity arises from translation of these product ions, and (b) the error made by adopting a "minimalist" model (of one Eq. [21] ionization reaction at each x_B value) is negligible. With these assumptions, the generation of $\Delta G_{ioniz}(x_B)$ values occurs via Eqs. [17-19]:

$$\alpha = \sigma_{expt}\eta_{expt} / 2c_{expt}W \quad [23]$$

$$K_{ioniz} = \alpha^2 / (x_i - 2\alpha)^2 \quad [24]$$

$$\Delta G_{ioniz} = -RT \ln K_{ioniz} \quad [25]$$

where $c_{expt} = \rho_{expt}/(x_AM_A+x_BM_B)$ is the formal concentration of monomers before complexation and ionization (Eq. [20]), 2α is the degree of ionization (of the monomers, Eq. [19]), and x_i is the mole fraction of the *minority* ingredient (x_B if $x_B < 0.5$, x_A if $x_A < 0.5$). The reasoning for needing the minority x_i for kite concentration $[B(HA)_n] = x_ic - 2\alpha c$ is the following. If $x_B < 0.5$, the system consists initially of only kites $[B(HA)_n]$, whose concentration is limited by and equal to the initial base concentration, x_Bc. However, if $x_A < 0.5$, the system consists initially of minimal-length kites [BHA] and excess free base [B], and hence the kite concentration is limited by and equal to the initial acid concentration, x_Ac. Eq. [24] is Eq. [22] simplified, and Eq. [23] is Eq. [16] rearranged.

Results appear in Fig. 2. The shape of these ΔG_{ioniz} curves is driven principally by the dielectric constant $\varepsilon(x_B)$, which affects the stability of ions. While the pure acids and bases generally have low ion-destabilizing dielectric constants (except formic acid), the "kite" complexes $B(HA)_n$, especially for $n > 1$, have large dipoles, creating significantly larger dielectric constants in the range $x_B = 0.1$-0.5. Huyskens et al. (7) predicted 10-fold increases in dielectric constant at ideal mixing ratios; Orzechowski and co-workers (19) confirmed this for one system (TEA/propionic acid), their results only disagreeing with the earlier predictions on the exact dependence of ε upon x_B. The large dipoles (and their concentration) at $x_B = 0.1$-0.5 stabilizes ions, lowering ΔG_{ioniz} to be near or below zero at these mole fractions. In the limits of $x_B \rightarrow 0$ or 1, the dielectric constant falls considerably, causing ΔG_{ioniz} to rise and greatly disfavouring the existence of ions. The case involving pyridine has a different (lower) $x_B \rightarrow 1$ limit for ΔG_{ioniz} than the TEA cases because ε_{PYR} (= 13.3) is not as low as that of ε_{TEA} (= 2.4).

The case involving formic acid has a very low apparent $x_B \rightarrow 0$ limit for ΔG_{ioniz} due to the high dielectric constant of formic acid ($\varepsilon = 51$).

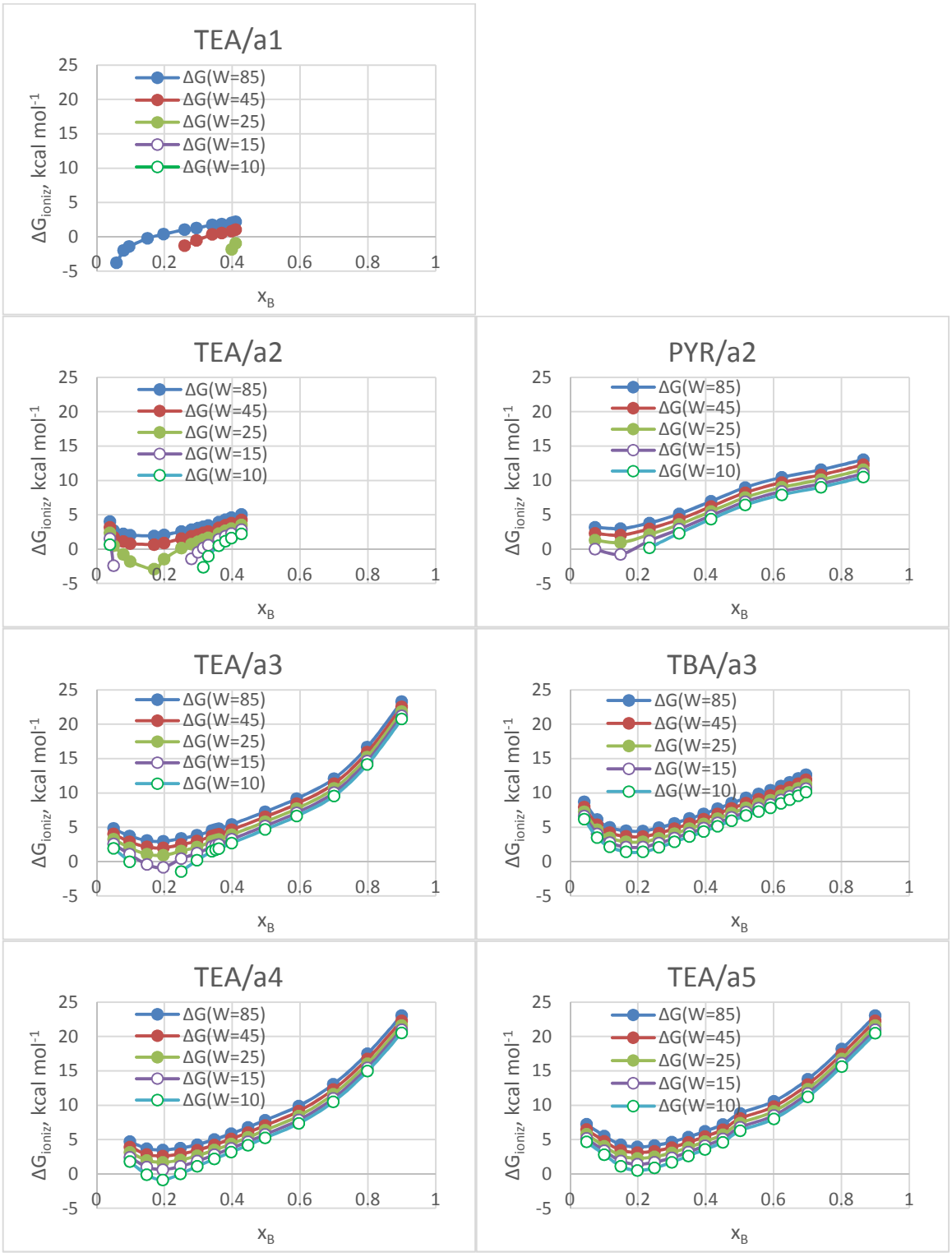

Figure 2. ΔG_{ioniz} curves from Eqs. [23-25] and the following experimental data: for TEA systems, Huyskens et al. (7); for PYR/a2, Venkatesan et al. (11); for TBA/a3, Orzechowski et al. (20) (using accurate interpolated values of their viscosities and densities).

The Walden constant (W) values tested were {10, 15, 25, 45, 85} S cP cm^2 mol^{-1}, which via Eq. [13] correspond to effective Stokes radii of {8.2, 5.5, 3.3, 1.8, 1.0} Å for the translating ions. We have chosen an extreme range of W values to demonstrate that the nature of the curves, qualitative and quantitative, depend rather little on this choice. Huyskens et al. had considered W = 31 for free BH^+ and values of 20-31 for $AHAHA^-$ anions (7). Given that our simulations do not show free BH^+, values below 30 and closer to 20 should be more realistic for the translating complexes. As x_B falls from 0.5 to 0.1, the ion complex sizes should get larger (arising from larger and larger kites), and hence the W "constant" probably decreases mildly (say from ~25 to ~15).

The more interesting question, perhaps, is if this data itself shows any particular evidence or need for unexpectedly large W values (i.e. small conducting ions) that might contradict the assumed "vehicular" conductivity mechanism involving the large translating ions of Eq. [3] and [21]. Electric fields could hypothetically induce hopping ion fragments or even relays (such as BH^+ or A^- or the classic Grotthuss H^+ mechanism). For the heavier acids, we do not think so: reasonable looking ΔG_{ioniz} curves are generated by W≈15 (TEA/a4 and TEA/a5) and W≈25 (TEA/a3 and PYR/a2). For TEA/a2, the requirement that % ionization be 100% or less requires that W be 24 or greater; W≈30 gives a reasonable curve without requiring a terribly small ion.

It is only the formic acid case (TEA/a1) where the assumptions must be questioned. In this system, W must be greater than 80 at x_B = 0.04 and 0.06 (1:20 mixing ratios); otherwise, impossibly high ion concentration (i.e. > 100% ionization) would be required to explain the high conductivities there. Huyskens et al. (7), whose incorrect equilibrium Eq. [2] would generate twice as many ions at these 1:20 mixing ratios as equilibrium Eq. [3], also had this problem for TEA/a1, needing W to be greater than about 40 in their case. At the time, they commented that the impossibly high ion concentration prediction for 1:20 TEA/a1 "is due to the inaccuracy of the Walden relation in such high polar medium." The conductivity from autoionization of formic acid is insufficient to account for the excess conductivity at 1:20 ratios. The "inaccuracy of the Walden relation" there is, possibly, the need for a particularly large W there, i.e. a Grotthuss H^+ mechanism. At such ratios, there is certainly an abundance of formic acid molecules, which are perhaps arranged into long H-bonded chains by the small amount of base present. A kite of length 13 was the result seen in our 1:15 PYR/a2 simulation (10).

Note, however, that at the most commonly used mixing ratio (x_B = 0.5), W only needs to be greater than about 23 for TEA/a1 to avoid impossible ion concentrations, and furthermore a Grotthuss-friendly H-bond network is not expected at this mixing ratio. Therefore, even with formic acid, a Grotthuss mechanism at x_B = 0.5 is unlikely.

Conclusions

AIMD simulations of mixtures of triethylamine with various carboxylic acids at several mixing ratios produce neutral "kite" structures $B(HA)_n$, with the only cations being "two-headed kites" $B(HA)_nHB^+$ and not BH^+. This is in accord with what was seen with pyridine mixtures in our previous work (10). Hence, a similar conductivity theory should apply, with a conductivity mechanism of large translating ion complexes.

A means of deriving ionization Gibbs energies from measured conductivities was presented, and curves of such values versus mole fraction of base were derived and plotted (Fig. 2). They exhibit a minimum near $x_B = 0.15$-0.20, due to an expected maximum in dielectric constant there, in turn due to the high dipole moments of the large kite structures $B(HA)_n$, $n \approx 4$. A variety of possible Walden constant values were employed to show their minor effect upon ΔG_{ioniz}. However, the limitation of no more than 100% ionization places restrictions on W values, and a problem first spotted by Huyskens et al. (7) exists in explaining the high conductivity of the TEA/formic acid mixtures at extreme 1:20 mixtures. There, very large W values would be needed in the theory, hinting that only there would there be a need to consider very small conducting ions, i.e. a Grotthuss mechanism.

Acknowledgements

The work was supported by NSERC Canada (RGPIN-2017-06247), with supercomputer funding from CFI Canada (LEF 2009-21625), and ISF Saskatchewan.

References

1. M. Yoshizawa, W. Xu, and C. A. Angell, *J. Am. Chem. Soc.* **125**, 15411 (2003).
2. C. A. Angell, N. Byrne, and J. Belieres, *Acc. Chem. Res.* **40**, 1228 (2007).
3. T. L. Greaves and C. J. Drummond, *Chem. Rev.* **108**, 206 (2008).
4. T. L. Greaves and C. J. Drummond, *Chem. Rev.* **115**, 11379 (2015).
5. H. E. Patten, *J. Phys. Chem.* **6**, 554 (1902).
6. L. E. Swearingen and R. F. Ross, *J. Phys. Chem.* **38**, 1141 (1934).
7. P. Huyskens, N. Felix, A. Janssens, F. Van den Broeck, and F. Kapuku, *J. Phys. Chem.* **84**, 1387 (1980).
8. F. Kohler, R. Gopal, G. Goetze, H. Atrops, M. A. Demiriz, E. Liebermann, E. Wilhelm, F. Ratkovics, and B. Palagyi, *J. Phys. Chem.* **85**, 2524 (1981).
9. R. G. Treble, K. E. Johnson, and E. Tosh, *Can. J. Chem*. **84**, 915 (2006).
10. N. P. Aravindakshan, K. E. Gemmell, K. E. Johnson, and A. L. L. East, *J. Chem. Phys*. **149**, 094505 (2018).
11. V. K. Venkatesan and C. V. Suryanarayana, *J. Phys. Chem*. **60**, 777 (1956).
12. J. O'M. Bockris and A. K. N. Reddy*, Modern Electrochemistry*. Vol. 1, p. 385, Plenum Press, New York (1973).
13. F. Kohler, E. Liebermann, G. Miksch, and C. Kainz*, J. Phys. Chem*. **76**, 2764 (1972).
14. J. W. Shuppert and C. A. Angell, *J. Chem. Phys*. **67**, 3050 (1977).
15. J. L. E. Campbell and K. E. Johnson*, Inorg. Chem*. **32**, 3809 (1993).
16. F. Kaufler and E. Kunz, *Ber. Dtsch. Chem. Ges*. **42**, 2482 (1909).
17. R. M. Fuoss*, J. Am. Chem. Soc*. **80**, 5059 (1958).
18. G. Kresse, J. Furthmuller, *Vienna Ab-initio Simulation Package: the Guide* (2003).
19. K. Orzechowski, M. Pajdowska, K. Fuchs, U. Kaatze, *J. Chem. Phys*. **119**, 8558 (2003).
20. K. Orzechowski, M. Pajdowska, J. Przybylski, J. Gliński, and H.A. Kolodziej, *Phys. Chem. Chem. Phys*. **2**, 4676 (2000).

ECS Transactions, 98 (10) 161-169 (2020)
10.1149/09810.0161ecst ©The Electrochemical Society

Electrochemical Methods for Analysis of Hydroxide and Oxide Impurities in Li, Mg/Na, and Ca Based Molten Chloride Salts

M.Gonzalez[a], E. Faulkner[a], C. Zhang[b], S.Choi[a], and M.F. Simpson[a]

[a] University of Utah, Salt Lake City, Utah, USA
[b]Lawrence Livermore National Laboratory, Livermore, California, USA

Due to their highly hygroscopic nature, molten chloride salts are known to resist complete thermal dehydration, resulting in incomplete water removal prior to use in high temperature applications. At temperatures required to melt these salts, this can result in hydrolysis, leading to formation of oxides or hydroxides. Depending on application, these hydrolytic impurities can cause further adverse effects through the formation of insoluble oxides and oxychlorides. In this paper, previously published work is reviewed to discuss electrochemical methods used for identification and measurement of hydrolytic impurities in LiCl and $CaCl_2$ as well as their effect on electrolytic processes. Cyclic voltammetry shows that thermal dehydration of LiCl and $CaCl_2$ promotes LiOH and CaO formation, respectively. The presence of CaO in a $CaCl_2$-$CeCl_3$ salt meant to emulate a typical actinide-chloride electrorefining salt causes insoluble Ce_2O_3 and CeClO to form, reducing electrochemical signals as the active species is precipitated as an insoluble phase.

Introduction

With applications that include thermal energy storage in Gen3 concentrated solar power (CSP), molten salt batteries in grid scale energy storage, fuel and coolant in molten salt reactors (MSR), and oxide reduction/electrorefining of spent nuclear fuel; molten salts are potentially the most important all-around medium for advanced energy systems. In particular, molten halide salts are known to be extremely hygroscopic, typically resisting complete thermal dehydration. Incomplete removal of water leads to hydrolysis; promoting formation of volatile HCl and insoluble oxide/hydroxide impurities in the molten salt. Depending on the application, this can accelerate corrosion, lower product yield through formation of insoluble oxides and oxychlorides, and/or reduce cell efficiency in electrolytic processes. Consequently, the generation, speciation, and electrochemical response of oxide and hydroxide impurities in various molten chloride salts have been widely studied. In this paper, previously published work by our group in LiCl-Li_2O, $MgCl_2$-KCl-NaCl, $CaCl_2$, and $CaCl_2$-CaO-$CeCl_3$ molten chloride salts is reviewed and discussed to reveal underlying commonality and lessons learned. The electrochemical methods used for identification of impurities in each system will be reviewed alongside the methodology used to develop electrochemical methods for in situ measurement techniques. Electrochemical methods in all cases were further substantiated through sample analyses including titration, thermogravimetric analysis (TGA), quadrupole mass spectrometry (QMS), X-ray diffraction (XRD), and inductively coupled plasma mass spectrometry (ICP-MS).

Studies with Molten LiCl

While hydrolysis was not explicitly shown to be the cause of impurity formation in work done by Gonzalez et al., the study was motivated to determine the cause of unexpected cathodic reactions preceding UO_2 and Li_2O reduction during direct electrolytic reduction (DER) in LiCl-Li_2O, as shown in work published by Herrmann et al. (1,2). In the work published by Herrmann et al., a broad cathodic current began to develop at -1.0 V vs Ni/NiO as Li_2O was added to the salt (2). The magnitude of the cathodic current increased as larger quantities of Li_2O were added. Due to the hygroscopic nature of LiCl, Gonzalez et al. suspected that moisture-induced contamination could be the cause of this pre-reduction current; resulting in the formation of LiOH as residual moisture is expected was interact with LiCl or Li_2O as shown in Equations [1] and [2] (1).

$$H_2O + LiCl \rightarrow LiOH + HCl \quad [1]$$

$$H_2O + Li_2O \rightarrow 2LiOH \quad [2]$$

A reaction mechanism was proposed (Equations [3-5]) where electrolysis of LiOH results in the formation of H_2, Li_2O, and Cl_2.

$$LiOH + e^- \rightarrow LiO^- + \tfrac{1}{2} H_2 \quad [3]$$

$$LiCl + LiO^- \rightarrow Li_2O + Cl^- \quad [4]$$

$$Cl^- \rightarrow \tfrac{1}{2} Cl_2 + e^- \quad [5]$$

Analysis of voltammetric data from cyclic voltammetry (CV) tests performed on a matrix of LiCl-based salt compositions containing LiOH, Li_2O, and Li_2O_2 indicated that LiOH is the most stable moisture-based impurity in this system. It was noted that electrochemical responses were complicated when both LiOH and Li_2O were present in the melt as it appears that the addition of LiOH results in an increase of both O^{2-} and OH^- in the salt. It was hypothesized that speciation occurs according to an ionic equilibrium model (Equation [6]), where OH^- and H^+ each generate a unique electrochemical response as shown in their respective half-cell reactions (Equations [7] and [8]).

$$OH^- \rightarrow O^{2-} + H^+ \quad [6]$$

$$OH^- + e^- \rightarrow O^{2-} + \tfrac{1}{2} H_2 \quad [7]$$

$$H^+ + e^- \rightarrow \tfrac{1}{2} H_2 \quad [8]$$

While interactions were reported between Li_2O and LiOH, LiOH contamination of LiCl manifested as a broad baseline reduction current (B_c), as shown in Figure 1.

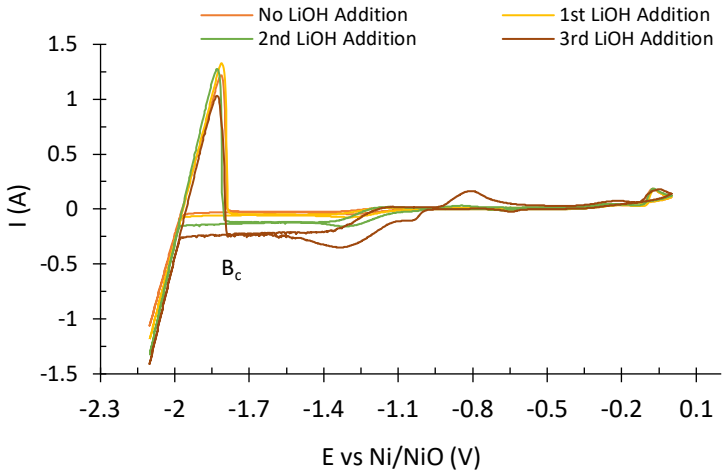

Figure 1. CV of LiCl, LiCl-0.07wt%LiOH, LiCl-0.20wt%LiOH, and LiCl-0.40wt%LiOH at 650°C and scan rate of 100mVs^{-1} with tungsten WE/CE

A method for the creation of calibration curves at set scan rates was developed for use in *in situ* measurement of LiOH. First a LiCl-Li_2O melt was prepared after which incremental additions of LiOH were made, followed by CV scans. A calibration curve (Figure 2) was established by correlating LiOH reduction baseline current densities to corresponding nominal LiOH concentrations (Table I) and fixing the y-intercept of the resulting linear regression at 0. This was done with the understanding that in the absence of LiOH no baseline current would be present. Interestingly, results indicated that LiOH was present in pre-dried and treated melts prior to any intentional additions. Estimated LiOH concentrations using the calibration curve and corrected nominal LiOH concentrations are presented in Table I.

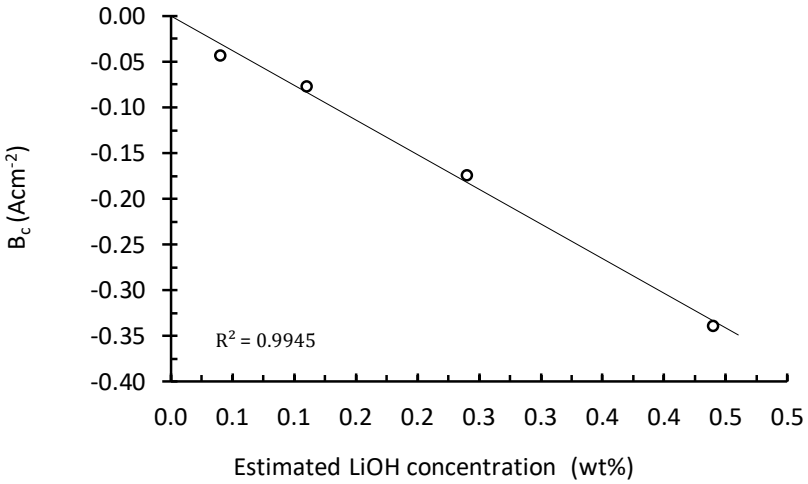

Figure 2. Calibration curve using baseline current density (Figure 1) at 100 mVs^{-1} and 650°C versus estimated LiOH concentration.

TABLE I. Summary of results for LiOH measurements using baseline calibration curve

Condition	Nominal LiOH wt%	Estimated LiOH wt%	LiOH Baseline (Acm^{-2})
No LiOH Addition	0.00	0.04	-0.034
1st LiOH Addition	0.07	0.11	-0.060
2nd LiOH Addition	0.20	0.24	-0.137
3rd LiOH Addition	0.40	0.44	-0.266

Studies with Molten $MgCl_2$-KCl-NaCl

Under the direction of the U.S. Department of Energy (DOE), $MgCl_2$-KCl has been identified as a mixture of interest for Gen3 concentrating solar power (CSP) (3), while the addition of NaCl is expected to lower the melting temperature of the mixture (4). As it was expected that OH^- would be present in the salt, Choi et al. performed a series of electrochemical tests to identify and measure OH^- levels in the salt as well as open-circuit potential (OCP) measurements to characterize redox potentials for the CSP melt ($MgCl_2$-KCl-NaCl) (5). Here, OCP data were reported for the CSP salt, CSP salt with Mg^0 added, and CSP salt with Mg^0 and NaOH additions.

Results indicated that the $MgCl_2$-KCl-NaCl redox potential can be affected through the addition of Mg^0 and NaOH; where addition of Mg^0 causes the OCP to become more negative, while addition of NaOH causes the OCP to increase (see Figure 3). While it was not possible to distinguish between OH^- associated with Mg, Na, or K with methods employed, it was hypothesized that the contrasting effects of Mg^0 and NaOH on the salt's OCP could be explained by a class of reactions that deserve further studying, of the following type:

$$Mg + 2NaOH = MgO + Na_2O + H_2 \quad [9]$$

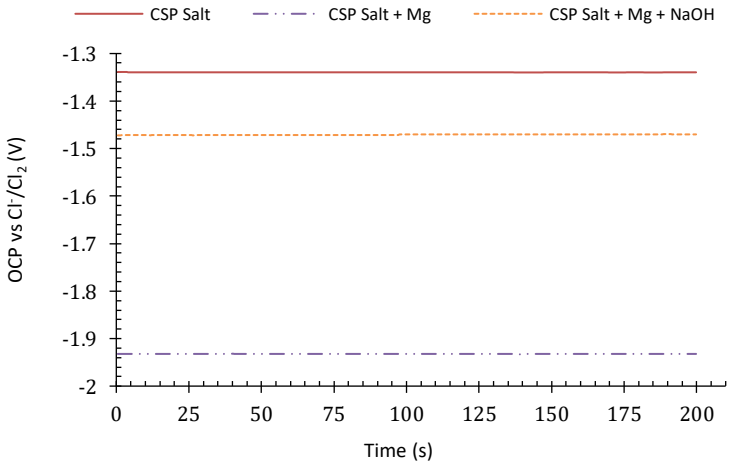

Figure 3. OCP measurements of CSP salt ($MgCl_2$–KCl–NaCl), CSP salt containing 0.3 wt% Mg, and CSP salt containing 0.46 wt% NaOH and 0.31 wt% Mg at 500ºC with tungsten WE/CE

Choi et al. also applied similar methods to those reported for OH^- measurements in LiCl above to study OH^- formation and electrochemical response in $MgCl_2$-KCl-NaCl, correlating cathodic currents preceding Mg^{2+} reduction, with NaOH additions to the salt (Figure 4a) (5). The cathodic peaks beginning at -2.1 V grew with every addition of NaOH. Incremental additions of NaOH, followed by CV scans were used to correlate these cathodic peak current densities with nominal concentrations of NaOH ranging from 0.0 to 1.0 wt% to create a the curve shown in Figure 4b, where a y-intercept of 0 was once again forced on the linear regression. The non-zero current for the salt composition containing 0.0 wt% added NaOH suggests that the salt contained OH^- impurities prior to any intentional additions. Nevertheless, while it was not possible to ascribe OH^- to any particular metal present in the melt with these methods, these results show the advantage of using a curve such at that in Figure 4b to estimate OH^- impurities in the melt.

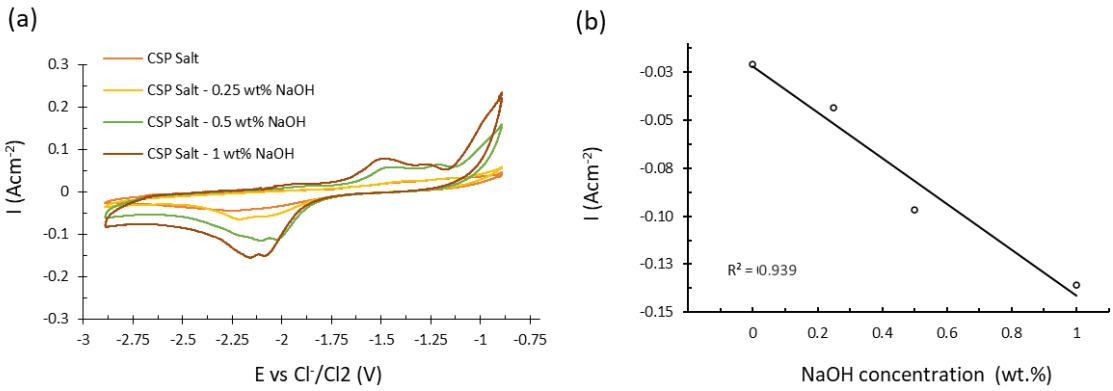

Figure 4. (a) CV of $MgCl_2$–KCl–NaCl with varying NaOH concentration at 200 mVs^{-1} at 500°C with tungsten WE/CE (b) Calibration curve using cathodic peak current density (Figure 4a) at 200 mVs^{-1} versus nominal NaOH concentration.

Studies with Molten $CaCl_2$

Faulkner et al. studied the effect of hydrolysis in $CaCl_2$ and the subsequent impact on electrolytic oxide reduction and electrorefining processes (6). Due to the hygroscopic nature of $CaCl_2$, it was suspected that hydrolysis would result in the formation of CaO and/or $Ca(OH)_2$ as shown in Equations [10] and [11]. Yan and Zhao showed that $Ca(OH)_2$ begins decomposing at temperatures above 400°C following the reaction shown in Equation [12] (7).

$$H_2O + CaCl_2 \rightarrow CaO + 2HCl \quad [10]$$

$$H_2O + CaCl_2 \rightarrow Ca(OH)_2 + HCl \quad [11]$$

$$Ca(OH)_2 \rightarrow CaO + H_2O \quad [12]$$

Figure 5 shows CV scans of molten $CaCl_2$ reported by Faulkner et al. with incremental additions of CaO and $Ca(OH)_2$ to show that $Ca(OH)_2$ is unstable at operating temperatures (>772°C) (6). Here, subsequent additions of CaO to molten $CaCl_2$ resulted in the formation

and growth of reduction and oxidation peaks around 0.0 V. No new peaks developed following the addition of $Ca(OH)_2$, revealing CaO as the most stable consequence of hydrolysis in $CaCl_2$.

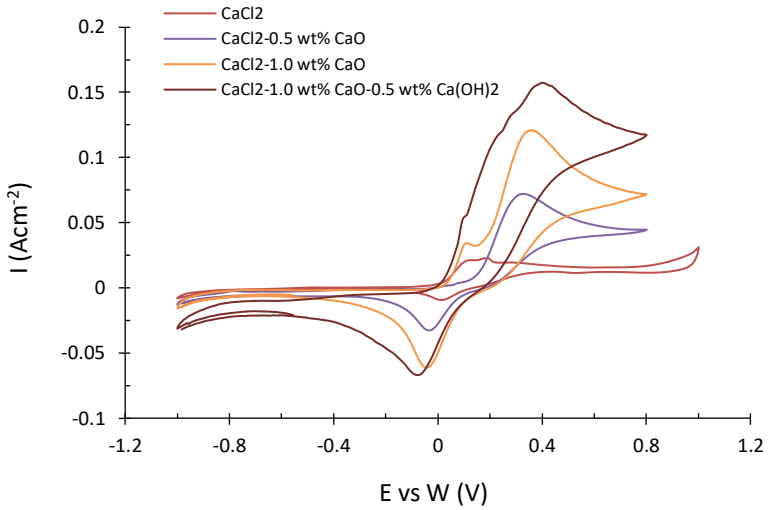

Figure 5. CV of molten $CaCl_2$ with varying CaO and $Ca(OH)_2$ at 300 mVs^{-1} at 850°C with tungsten WE/CE

Following the identification of CaO as the main consequence of hydrolysis in $CaCl_2$, Faulkner et al. ran CV scans of $CaCl_2$ salt with incremental additions of CaO (Figure 6a) and in a manner after methods previously described, correlated oxidation peak current densities of at 0.0 V to subsequent nominal concentrations of CaO (6). Again, non-zero current prior to intentional additions of CaO suggested that the $CaCl_2$ contained CaO prior to any intentional additions. After correction of the nominal concentrations using the estimated initial contamination, a calibration curve was created for use in estimating CaO contamination in molten $CaCl_2$ (Figure 6b).

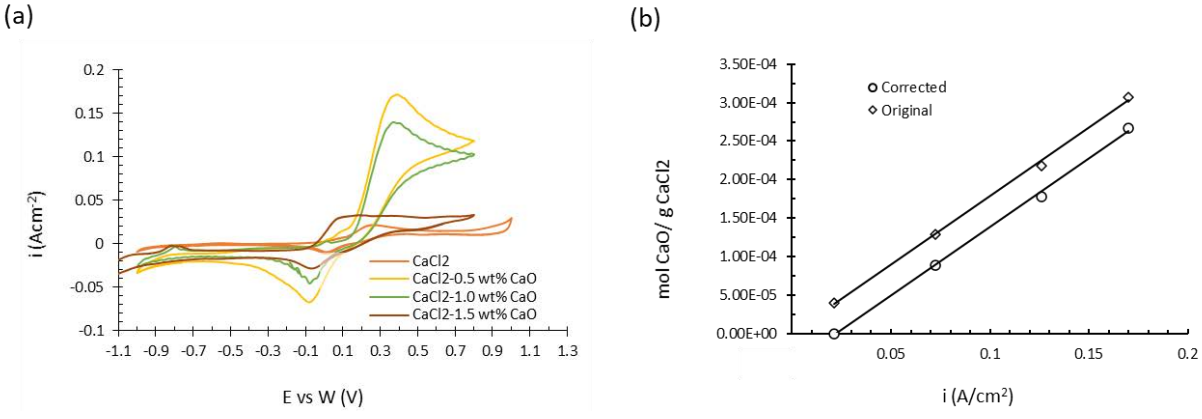

Figure 6. (a) CV of $CaCl_2$ with varying CaO concentration at 850°C using tungsten WE/CE at 300 mVs^{-1} (b) Calibration curve using corrected estimated CaO concentration vs oxidation peak current density (Figure 6a) at 300 mVs^{-1}.

$CaCl_2$ can also be used for electrorefining of metals such as plutonium or uranium. Here, CaO contamination in the salt can lead to a series of undesirable reactions, as oxides are incompatible with electrorefiner chemistry. The potential for formation and precipitation of oxide or oxychloride phases, is of particular concern, as they have the ability to lower product yield and purity. The precipitation of insoluble actinide species would make them largely unrecoverable. In the case of extreme contamination, the induced drawdown of actinide-chloride concentrations necessary so support the electrochemical processes could drive considerable contamination of the metal deposit. Faulkner et al. further studied $CaCl_2$-CaO to emulate contaminated electrorefining salt (6). Here, CaO was to act as the hydrolysis-generated impurity and $CeCl_3$ as a surrogate for a typical actinide chloride such as UCl_3 or $PuCl_3$. CV scans of $CaCl_2$-CaO-$CeCl_3$ (Figure 7) indicated that the peaks ascribed to CaO reduction and oxidation peaks (around 0.0 V) became smaller in response to subsequent $CeCl_3$ additions to the melt.

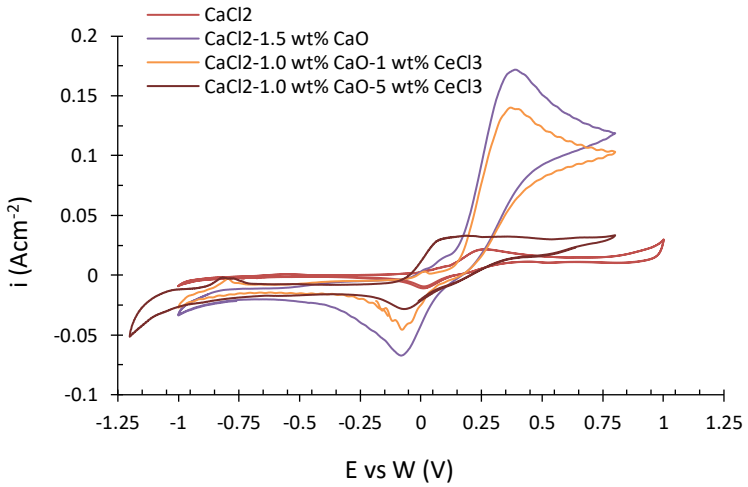

Figure 7. CV of $CaCl_2$ and $CaCl_2$-CaO with varying $CeCl_3$ concentration at 300 mV/s at 850°C using tungsten WE/CE

The presence of CaO in the electrorefining salt was shown to result in the formation of insoluble Ce_2O_3 and CeOCl, verified through XRD analysis of a mixture of $CaCl_2$-CaO-$CeCl_3$ after melting and resolidification. Both the oxide and oxychloride phases were insoluble, settling at the bottom of the crucible. Faulkner et al. proposed the following mechanisms for the formation of Ce_2O_3 and CeOCl (6).

$$2CeCl_3 + 3CaO \rightarrow Ce_2O_3 + 3CaCl_2 \quad [13]$$

$$CeCl_3 + CaO \rightarrow CeOCl + CaCl_2 \quad [14]$$

Conclusions

Cyclic voltammetry performed on molten chloride salts with controlled additions of OH^- and O^{2-} provides evidence of their stability at operating temperatures and allows for classification of unique electrochemical responses associated with their presence in the salts. Electrochemical reactions consistent with the presence of OH^- observed during CV

of LiCl and $MgCl_2$-KCl-NaCl indicated that OH^- contamination was present prior to any intentional additions. This indicates the need to develop processes for complete water removal prior to use of the molten sat. Although the speciation of OH^- and O^{2-} was not determined, additions of LiOH to LiCl and NaOH to $MgCl_2$-KCl-NaCl resulted in a net increase of electrochemical signals ascribed to either OH^- and O^{2-} or interactions between them. The presence of CV peaks associated with both OH^- and O^{2-} in LiCl and $MgCl_2$-KCl-NaCl suggests that an equilibrium exists between ionic species in cases where both OH^- and O^{2-} are stable. In $CaCl_2$, however, OH^- is unstable and addition of $Ca(OH)_2$ results in an increase of O^{2-} signals ascribed to CaO. The presence of hydrolytic impurities in each of these salt systems has different implications. During oxide reduction of spent nuclear fuel, the presence of OH^- and its interaction with O^{2-} present in the system, as studied in LiCl, lowers cell efficiency as current is spent on non-productive reduction processes. The presence of OH^- in $MgCl_2$-KCl-NaCl CSP salt implies hydrolysis has occurred and is indicative of the likelihood of favorable corrosion reactions with structural materials containing the salt. Hydrolytic contamination of electrorefining salt, as studied in $CaCl_2$-CaO, results in the precipitation of active species as O^{2-} leads to the formation of insoluble oxides and oxychlorides. Consequently, measurement of impurity levels prior to processing is of critical importance. The correlation of characteristic cathodic (in LiCl and $MgCl_2$-KCl-NaCl) and anodic (in $CaCl_2$) current densities in CV with varying concentrations of OH^- and O^{2-} yields a powerful and versatile analytical tool for determination of OH^- and O^{2-} contamination levels. The extension of cyclic voltammetry to develop in situ methods for creating calibration curves for OH^- and O^{2-} enables development of real-time, in-line sensors to support the efficiency and efficacy of many molten salt processes continues to be explored extensively.

Acknowledgments

The authors gratefully acknowledge funding from Oak Ridge National Laboratory and the U.S. Department of Energy's Solar Energy Technology Office which provided financial support for S. Choi, and Los Alamos National Laboratory, which provided financial support for E. Faulkner. Collaboration with Prof. Jinsuo Zhang's research group (Virginia Tech) and their valuable contributions to this work was paramount in the success of these projects.

References

1. M. Gonzalez, A. Burak, S. Guo, M.F. Simpson. *J. Nucl. Mater.* **510,** 513 (2018).
2. Herrmann SD, Li SX., *Nucl Technol*. 171 (3), 247-265 (2010).
3. M. Mehos, C. Turchi, J. Vidal, M. Wagner, Z. Ma, C. Ho, W. Kolb, C. Andraka, A. Kruizenga, Concentrating Solar Power Gen3 Demonstration Roadmap, (January 2017) National Renewable Energy Laboratory Technical Report NREL/ TP-5500-67464.
4. D. Williams, Assessment of Candidate Molten Salt Coolants for the NGNP/NHI Heat Transfer Loop, (2006) ORNL/TM-2006/69, Oak Ridge, TN.

5. Choi, S.; Orabona, N.E.; Dale, O.R.; Okabe, P.; Inman, C.; Simpson, M.F., *Sol. Energy Mater. Sol. Cells*, **202**, 110087 (2019).
6. E. Faulkner, M. Monreal, M. Jackson, an M.F. Simpson, *J. Rad. Nuc. Chem*, in submission.
7. J. Yan and C. Y. Zhao, *Chem. Eng. Sci.*, **138**, 86–92, (2015).

ECS Transactions, 98 (10) 171-178 (2020)
10.1149/09810.0171ecst ©The Electrochemical Society

Real-time Monitoring for Electrochemical Analysis in Molten LiCl-KCl Eutectic Salt

H. L. Cha, J. W. Park, and J. -I. Yun

Department of Nuclear and Quantum Engineering, KAIST, Yuseong-gu, Daejeon 34141, Republic of Korea

In the present work, a real-time monitoring system for molten LiCl-KCl eutectic salt medium is set up with optically accessible quartz windows mounted on the furnace and the CMOS camera. Based on the designed system, the real-time monitoring was carried out to investigate the electrode behavior in various electrochemical systems, such as (1) differences in Co morphology deposited in molten $CoCl_2$-LiCl-KCl system by various electrochemical deposition methods, (2) a reoxidation behavior of electrochemically reduced lithium, and (3) a reduction of Zr(IV) ions to Zr(III) ions in the molten $ZrCl_4$-LiCl-KCl system. By delivering the video signal from the CMOS camera to the PC which controls the potentiostat, the visual changes can also be synced with the measured current or potential during the experiment. This enables us to compare the visualized morphological properties on the surface of the working electrode under different applied potential conditions during the application of electroanalytical methods.

Introduction

Molten salts are one of the promising alternative classes of new materials for electrochemical processing. They have high chemical stability and offer a much wider electrochemical window than conventional aqueous media. This enables various electrochemical reactions to be conducted without decomposing electrolyte. In addition, the high operating temperature of the molten salt not only promotes the mass transfer of the reactants, but also provides relatively more energy to overcome the energy barrier of the electrochemical reaction, so that the processing time is shortened. Owing to these advantages, the molten salt electrolytes have intensively dealt with the electrowinning of metal and electrochemical separation processes (1-4).

Knowing the chemical behavior of electrodes during such processes is crucial to understand the mechanism of electrochemical reactions that occur during the process. One of the most powerful methods of examining the system is to monitor the visual status of electrodes in real time while the electrochemical process is running. However, due to some practical limitations, it has rarely been applied to the molten salt electrochemical system.

In this work, the real-time monitoring system for molten LiCl-KCl eutectic salt medium is designed and built for our electrical furnace installed in the glove box system. Based on the self-built real-time monitoring system, several electrochemical experiments with molten LiCl-KCl eutectic salt medium are carried out to observe the morphological and visual changes at the electrode/electrolyte interface.

Experimental

Electrochemical system

All experiments were performed in a glove box (Koreakiyon Co.) under high-purity argon gas (99.999% Ar) at concentrations of H_2O and O_2 below 1 ppm to prevent hydration and oxidation of hygroscopic chloride salts. A cylindrical tungsten rod (99.95%, Nilaco) was used as a working electrode and a counter electrode (ϕ = 1~2 mm) for all electrochemical experiments. The reference electrode consisted of a silver wire (ϕ = 1 mm, 99.99%, Nilaco) and molten AgCl-LiCl-KCl ([AgCl] = 1 wt%), which was filled in a cylindrical pyrex tube (inner diameter = 2.4 mm). Anhydrous LiCl-KCl eutectic salt (99.99%, [LiCl] = 44 wt%, Sigma-Aldrich) was used to prepare the electrolyte for the electrochemical cell. The temperature of the molten salt was regulated at 773K for all experiments. $CoCl_2$ beads (99.999%, Sigma-Aldrich), or $ZrCl_4$ powder (99.99% Sigma-Aldrich) were utilized to control the concentration of metal ions in LiCl for each experiment. Due to the sublimation effect of $ZrCl_4$, a solidified $ZrCl_4$-LiCl-KCl stock was prepared prior to electrochemical experiments to control the concentration of zirconium ion in the molten LiCl-KCl. Electrochemical measurements were carried out in a cylindrical quartz electrochemical cell with an inner diameter of 27 mm using a potentiostat (SP-240, Bio-Logic Science Instruments). A customized Teflon cap was utilized to precisely position the three-electrode system.

Real-time monitoring system

A temperature-controlled electric furnace was directly connected to the glove box system. Four optically accessible quartz windows were mounted on the electrical furnace so that the interior of the furnace is visible from the outside. A commercially-available CMOS camera (Sony ILCE-7M2) with the macro lens (Tamron 90mm) was utilized to get a photo or video of the electrochemical system during the experiment. In order to improve the image quality, the brightness of the quartz cell should be maintained adequately. Since the fluorescent light from the glove box does not reach the quartz cell due to the Teflon cap, an auxiliary flashlight was installed at the right angle of the CMOS camera to illuminate the quartz cell. By installing the optical rail at the bottom of the electric furnace, the CMOS camera and flashlight can be fixed (Figure 1).

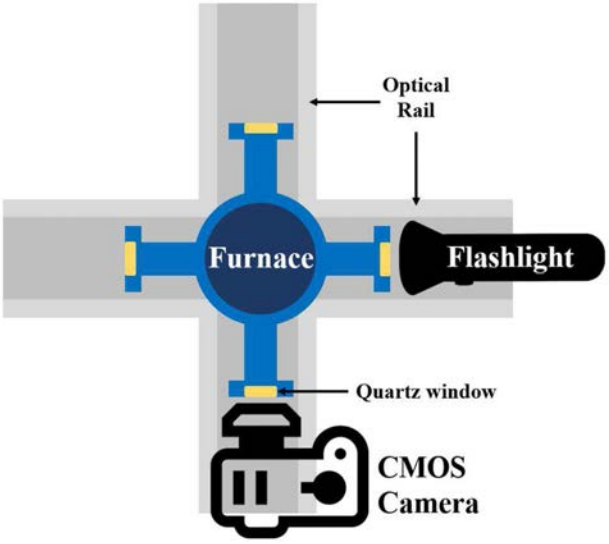

Figure 1. A top view of the electric furnace with the real-time monitoring system. Note that furnace is directly connected to the glove box.

The thickness of the tungsten rod can be measured by a Vernier caliper in prior of the experiment. With the high resolution of 24.0 megapixel of the CMOS camera that has received photography, the immersed electrode area can be determined from the photograph by analyzing the aspect ratio between the immersed depth (vertical) and the thickness of the rod (horizontal). Since the thickness of the rod in photographs is at least 100 pixels, the uncertainty can be less than 1% (Figure 2).

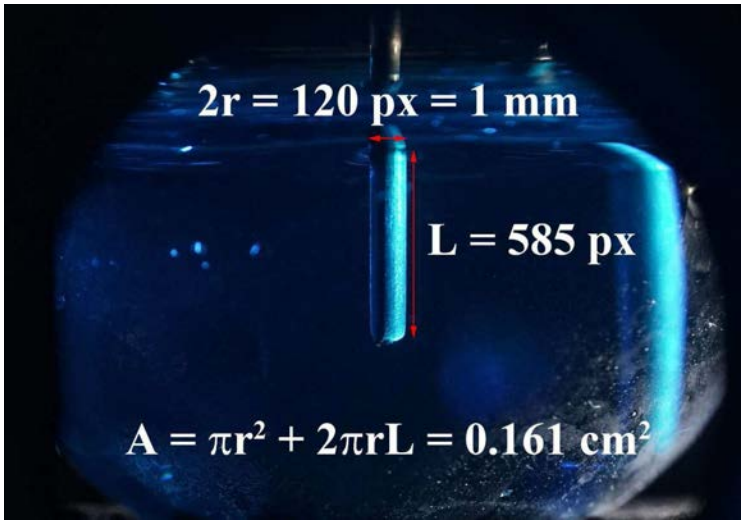

Figure 2. A representative photograph of the working electrode (W rod, ϕ = 1 mm) (center) and the counter electrode (W rod, ϕ = 1.5 mm) (right) immersed in the molten $CoCl_2$-LiCl-KCl (0.5 wt% $CoCl_2$). The pixel values marked adjacent to the electrode are obtained from the original unprocessed photograph. Note that the visualized counter electrode is out of focus and distorted due to the curvature of the quartz cell. The reference electrode is not observed in this photograph (located far left).

Result and Discussions

Based on the constructed real-time monitoring system, several electrochemical experiments have been carried out to investigate the morphological characteristics of metal/ion species during the redox reaction. Especially in electrochemical systems with molten salts that do not produce solid phase products, it is difficult to elaborately understand the behavior of chemical species during the experiment with indirect methods. However, real-time monitoring makes it possible to obtain direct morphological information at the interface between the working electrode and the electrolyte.

Deposition of cobalt with galvanostatic and potentiostatic method

The deposition behavior of cobalt in the molten $CoCl_2$-LiCl-KCl system (1 wt% $CoCl_2$) was investigated on a tungsten working electrode. Two different electrodeposition methods are applied: the galvanostatic method, in which a constant reduction current was applied to maintain the working electrode potential at the reduction potential of Co(II)/Co(0), and the potentiostatic method, in which a constant reduction potential is applied to the reduction potential of Co(II)/Co(0). As shown in Figure 3, there is a clear morphological differences in cobalt deposits between the galvanostatic and the potentiostatic electrodeposition. While the metallic cobalt was deposited uniformly on the surface of the working electrode by galvanostatic electrodeposition, a rapid growth of the dendritic structure was observed using the potentiostatic electrodeposition.

Figure 3. Images of metallic cobalt deposits on a tungsten working electrode in the molten $CoCl_2$-LiCl-KCl system (1 wt% $CoCl_2$) at 773K. The deposition conditions are -18 mA/cm^2 for 1 hour galvanostatic electrodeposition and -1.6 V vs. Cl_2/Cl^- for 30 minutes potentiostatic electrodeposition.

These morphological difference can also be observed in the scanning electron microscope (SEM) image of each deposit. In order to separate the solidified LiCl-KCl adhering to the working electrode, a deposit removed from molten LiCl-KCl salt is immersed in methanol (anhydrous, 99.9%, Sigma-Aldrich) and dried in the glove box. As depicted in Figure 4, the galvanostatic electrodeposition product consisted of uniformly grown hexagonal metallic cobalt particles, while the growth of metallic cobalt is relatively slow and irregular for the potentiostatic electrodeposit product.

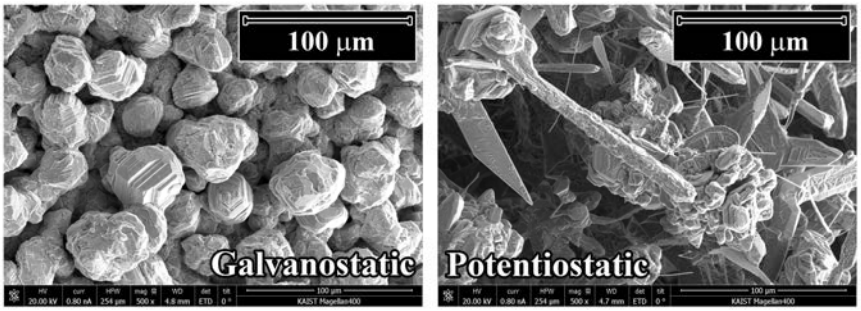

Figure 4. SEM images of metallic cobalt deposits on the tungsten working electrode in the molten $CoCl_2$-LiCl-KCl system (1 wt% $CoCl_2$) at 773K.

The mechanism of this phenomenon could be related to the rate of reduction on the surface of the electrode. In the case of potentiostatic electrodeposition, the reduction rate is set to the maximum that the working electrode maintains such an electrode potential. Thus, the concentration of Co(II) on the surface of the working electrode reaches zero during the deposition and creates a stiff concentration gradient near the surface of the working electrode (5). On the other hand, the galvanostatic electrodeposition can control the reduction rate below the maximum, so that the concentration gradient is lower than in the potentiostatic case. A higher concentration gradient in the vicinity of the working electrode during electrodeposition can lead to an unruly diffusion behavior of metal ions, for instance due to local turbulence. Accordingly, this may affect the nucleation behavior of reduced metal on the working electrode in the early stage of electrodeposition, which is closely related to the morphological properties of the end product. Consequently, this phenomenon suggests that the structural properties of deposits can vary significantly due to the nature of the electrodeposition methods.

Reduction and re-oxidization of liquid lithium

During the galvanostatic lithium reduction in the molten LiCl-KCl system, the liquefied metallic lithium formed the oval bulge on the surface of tungsten working electrode with a measured electrode potential of -3.6 V vs. Cl_2/Cl^-. At the same time, the unknown indigo-colored flow was observed on the surface of the deposited metallic lithium (Figure 5). This unknown flow was consistently confirmed even after the reduction process has ended. It eventually disappeared when the oval bulge of metallic lithium gradually re-oxidized to Li(I) ions due to the open circuit potential of tungsten working electrode (-1.1 V vs Cl_2/Cl^-). Based on the observations, the clear mechanism, although still to be explored, appeared to be related to the re-oxidization of metallic lithium to Li(I) ions.

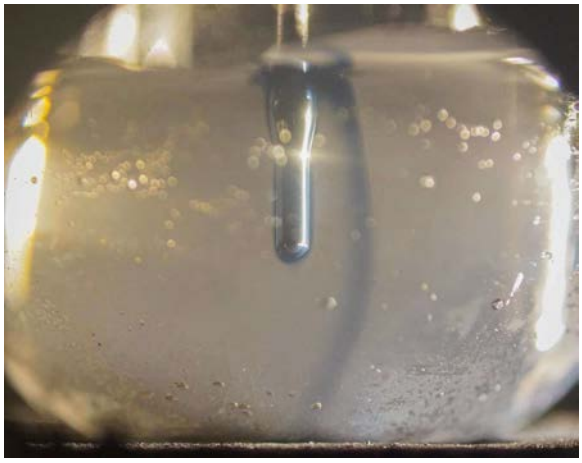

Figure 5. Image of metallic lithium deposition at -3.6 V vs. Cl_2/Cl^- on the tungsten working electrode in the molten LiCl-KCl system at 773K.

Reduction of Zr(IV) ions to Zr(III) ions

The redox behavior of zirconium in molten LiCl-KCl salt is reported to be complicated, at least three reduction peaks and four oxidation peaks are confirmed by cyclc voltammetry (CV) (Figure 6a) (6). According to the literature, the color of Zr(III) ion is reported to be brown-colored by UV-Vis spectroscopy (6). In the molten $ZrCl_4$-LiCl-KCl system (1 wt% $ZrCl_4$) with tungsten working electrode, the reduction of Zr(IV) ions to Zr(III) ions during the potentiostatic electroreduction at -2.0 V vs. Cl_2/Cl^- was identified by the formation of a brown-colored flow near the surface of the working electrode (Figure 6b). This confirms the result of our previous work which suggests that the Zr(IV) ion is reduced to a brown-colored Zr(III) ion in the first step of cyclic voltammetry (CV) at an applied potential of -2.0 V vs. Cl_2/Cl^- in molten $ZrCl_4$-LiCl-KCl system (6).

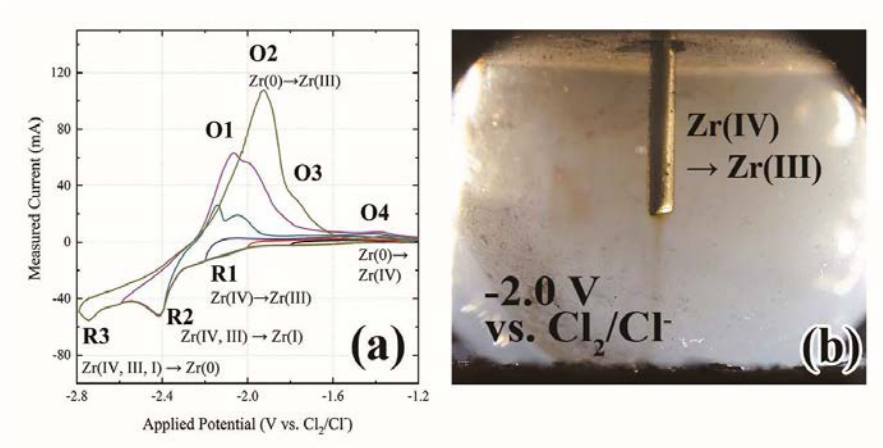

Figure 6. (a) Typical cyclic voltammograms of $ZrCl_4$-LiCl-KCl system on tungsten working electrode. (b) Image of Zr(IV) reduction at -2.0 V vs. Cl_2/Cl^- on tungsten working electrode in the molten $ZrCl_4$-LiCl-KCl system (1 wt% $ZrCl_4$) at 773K.

Synchronization of the electroanalytical data with visual monitoring

When the CMOS camera was connected to the PC that controls the potentiostat, the video signal can be sent to the PC so that the visual changes can be monitored simultaneously during the electroanalytical measurement. This makes it possible to compare the morphological properties on the surface of the working electrode under different applied potential conditions during the CV experiment.

The visual change during the multi-step reduction of Zr(IV) in molten LiCl-KCl is recorded during the CV measurement in the molten $ZrCl_4$-LiCl-KCl system (1 wt% $ZrCl_4$) with tungsten working electrode. The silvery lusting surface (Figure 7a) changed to black with the applied potential of -2.4 V vs. Cl_2/Cl^- (Figure 7b). This can be explained by the electrodeposition of insoluble ZrCl from the reduction of Zr(IV) and Zr(III) ions in the bulk (7). When the applied potential reaches -2.7 V vs. Cl_2/Cl^-, the surface of the working electrode changes again from black to gray due to the reduction of insoluble ZrCl to metallic Zr (Figure 7c) (7).

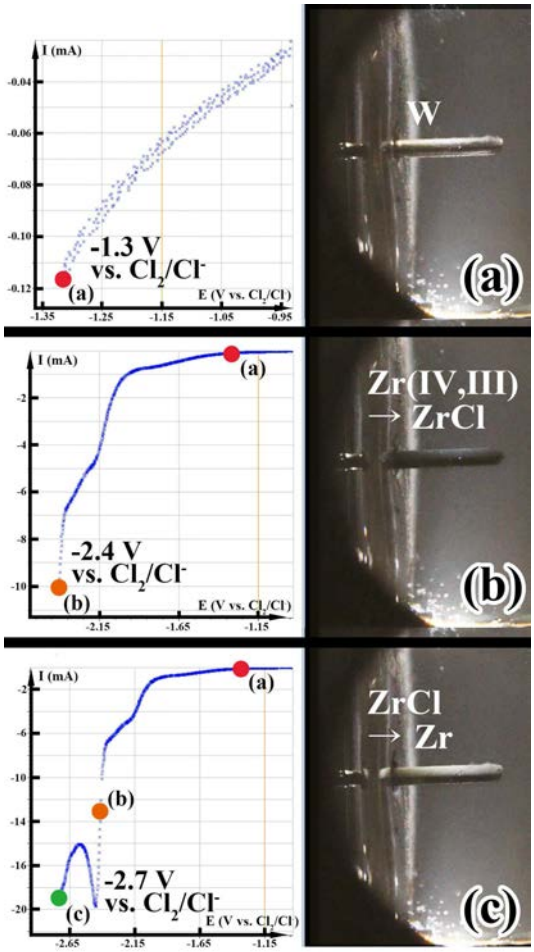

Figure 7. Potential-current (E-I) graphs and images of the reduced zirconium on the tungsten working electrode in the molten $ZrCl_4$-LiCl-KCl system (1 wt% $ZrCl_4$) at 773K when applying the potentials during cyclic voltammetry, (a) -1.3 V vs. Cl_2/Cl^-, (b) -2.4 V vs. Cl_2/Cl^-, (c) -2.7 V vs. Cl_2/Cl^- (scan rate of 200 mV/s, starting potential of -0.9 V vs. Cl_2/Cl^-).

Conclusion

In this work, a real-time monitoring system for the high-temperature molten LiCl-KCl salt system has been proposed, which can be used to monitor the visual status of the electrochemical system during the experiments. With the use of a commercially available CMOS camera and flashlight, the real-time monitoring system can be easily constructed for any electric furnace system that enables spectroscopic analysis with optically accessible quartz windows. Thanks to the high-resolution image quality and video performance, real-time monitoring can be used to a large extent to investigate the morphological properties of metal/ion species during the redox reaction and to clearly determine the immersed working electrode surface area in the molten salts. Through practical application to several electrochemical systems, new observations could be obtained that are difficult to achieve with conventional analytical methods, such as the formation of an indigo-color flow during the re-oxidation of the reduced lithium in the molten LiCl-KCl salt. Real-time monitoring system for molten LiCl-KCl system allows to examine the electrochemical reactions with a new perspective and to find out the curious reaction mechanism of various electrochemical reactions.

Acknowledgments

This work was supported by the National Research Foundation of Korea (NRF) grant funded by the Korea government (NRF-2016M2B2A9911780 and NRF-2017M2A8A5014801).

References

1. A. Girginov, T. Z. Tzvetkoff and M. Bojinov, *J. Appl. Electrochem.*, **25**, 993 (1995).
2. Y. Xiao, D. W. van der Plas, J. Bohte, S. C. Lans, A. van Sandwijk and M. A. Reuter, *J. Electrochem. Soc.*, **154** (6), D334 (2007).
3. H. Lee, G. -I. Park, J. -W. Lee, K. -H. Kang, J. -M. Hur, J. -G. Kim, S. Paek, I. -T. Kim and I. -J. Cho, *Sci. Technol. Nucl. Ins.*, **2013**, 1 (2013).
4. W. Han, W. Wang, M. Li, J. Wang, Y. Sun, X. Yang and M. Zhang, *Sep. Purif. Technol.,* **232**, 115965 (2020).
5. A. J. Bard and L. R. Faulkner, *Electrochemical methods: Fundamentals and applications*, p. 29, 2nd ed., John Wiley & Sons, New York (2001).
6. H. L. Cha and J. -I. Yun, *Electrochem. Commun.*, **84**, 86 (2017).
7. J. Park, S. Choi, S. Sohn, K. -R. Kim and I. S. Hwang, *J. Electrochem. Soc.*, **161** (3), H97 (2014).

Chapter 7

L02 – Electrodeposition

ECS Transactions, 98 (10) 181-187 (2020)
10.1149/09810.0181ecst ©The Electrochemical Society

Electrodeposition of Aluminium Containing Alloys from Molten Fluoride Electrolytes Containing Metal Oxides

Geir Martin Haarberg[a]

[a] Department of Materials Science and Engineering, Norwegian University of Science and Technology (NTNU), Trondheim, Norway

Aluminium is produced by the Hall-Heroult process by electrowinning in a molten fluoride electrolyte with dissolved alumina at ~955 ^{o}C. Several metallic impurities typically end up in the produced metal due to the fact that most metals are more noble than aluminium. Such co-deposition of metals may be utilized to form aluminium alloys. Another advantage is that many metal oxides are readily soluble in molten cryolite based electrolytes. The more noble metals will deposit at the limiting current density. The alloy composition is essentially determined by the bath concentration of the dissolved cations of the alloying element. Therefore it is possible to produce alloys of certain compositions by controlled addition of metal oxides. Interesting candidate alloying elements are silicon, titanium and manganese but also more valuable elements such as scandium are possible. Electrochemical studies were carried out in laboratory experiments and the behaviour of dissolved metal oxides was studied in industrial cells. High current efficiencies for the codeposition of the alloying elements Si, Ti and Mn were confirmed. Significant savings for producing alloys by this method are expected.

Introduction

Aluminium is produced by electrolysis in molten NaF-AlF_3-Al_2O_3 at ~955 ^{o}C, where dissolved alumina is reduced to liquid aluminium at the cathode and CO_2 is evolved at consumable carbon anodes. The current efficiency with respect to aluminium can be as high as 96 % in modern Hall-Heroult cells. The total cell reaction is:

$$Al_2O_3 \text{ (diss)} + 3/2 \text{ C (s)} = 2 \text{ Al (l)} + 3/2 \text{ } CO_2 \text{ (g)} \quad [1]$$

More than 60 million tons aluminium were produced by this process globally in 2019 (1). China is the dominating country but also India, Canada, Russia and countries in the Middle East have significant production of primary aluminium.

Drawbacks of the process are related to high specific electric energy consumption (~13 kWh/kg Al), low energy efficiency (~50 %) and emissions of CO_2 due to consumption of carbon anodes and generation of electricity. Another challenge is to eliminate the emissions of PFC gases (CF_4 and C_2F_6) that are formed during so-called anode effect due to depletion of dissolved alumina.

Today various aluminium based alloys are made by adding pure alloying elements to the produced liquid aluminium before casting. The most common alloying elements of commercial alloys are silicon, copper, zinc, magnesium, iron, and manganese. More valuable elements are titanium and scandium which may give alloys with improved properties in terms of strength and corrosion resistance. Many of these elements can be co-deposited during electrolysis since aluminium is a reactive metal with a high deposition potential. Another interesting feature is that most metal oxides are readily soluble in the molten fluoride electrolyte used in the Hall-Heroult process.

Metallic impurities that are more noble than aluminium tend to deposit at the liquid aluminium cathode in the industrial process (2). It has been shown (3, 4) that cations of such impurities are reduced at the cathode at the limiting current density (i_{lim}) which is given by the following equation:

$$i_{lim} = nFkc^o \qquad [2]$$

where k is the mass transfer coefficient and c^o is the concentration of the dissolved impurity element species in the bulk of the electrolyte. Studies of impurities in industrial cells have been carried out by analyses of samples of electrolyte and metal as a function of time after additions of known amounts of compounds containing impurities. The concentration of the impurity species under investigation versus time after addition can be expressed as follows (4)

$$c = c_o \exp\left(-\frac{A}{V}kt\right) \qquad [3]$$

where A is the area of the active cathode and V is the volume of the electrolyte. By knowing the latter quantities, the mass transfer coefficient can be determined. Typical values have been reported to be in the range from 10^{-5} - 10^{-6} m/s (3, 4), iron giving slightly higher values than silicon and titanium. However, such mass transfer coefficients will depend more on design, technology and operation of industrial cells. High convection of electrolyte and metal pad or unstable cells will cause higher values.

Experimental

Laboratory experiments were carried out in a standard furnace under argon atmosphere. A tungsten wire (2.0 mmØ) was used as working electrode, while the counter electrode was made of platinum or carbon. A wire of platinum served as a quasi reference electrode. In experiments with dissolved alumina an aluminium reference electrode was used, where liquid aluminium was placed inside an alumina tube with a slot for electrolyte contact and a tungsten wire. High purity and dried chemicals of NaF, AlF_3, Al_2O_3, SiO_2, TiO_2 and Mn_2O_3 were used. The electrolyte was contained in a platinum or a sintered alumina crucible. Electrochemical studies and electrolysis experiments were performed. Recent experiments were carried out by adding minority elements throughout the course of electrolysis to maintain constant conditions.

Other experiments were carried out in industrial aluminium producing cells. Known amounts of metal oxides were added and samples were taken for analysis from electrolyte (bath) and metal before and at certain intervals for up to 24 h.

Results and discussion

Laboratory experiments

Fig. 1 shows cyclic voltammograms in pure molten cryolite saturated with alumina at 1020 ^{o}C recorded using a tungsten electrode. J and K represent deposition and oxidation of Al, while L is the anodic potential limit due to oxidation of tungsten. The considerable background current before Al deposition is due to the formation of dissolved Al as well as dissolved Na. The formation of an alloy of Al-W may also contribute to some cathodic current. Co-deposition of iron, silicon, manganese and titanium take place within the potential window where alumina is thermodynamically stable.

The electrochemical behaviour of dissoved titanium species was studied by cyclic voltammetry in molten cryolite with dissolved TiO_2 (5). The results suggested that titanium is reduced in two steps according to the following scheme:

$$Ti\ (III)\ (diss) + 3\ e^- \rightarrow Ti\ (s) \qquad [4]$$

$$Ti\ (IV)\ (diss) + e^- \rightarrow Ti\ (III)\ (diss) \qquad [5]$$

These results are in agreement with reports from other studies in fluoride melts where titanium is deposited from Ti (III) because Ti (II) species are not formed (6).

Industrial experiments

It was found that all the studied minority elements of silicon, manganese and titanium were efficiently reduced at the cathode. Of special interest is manganese, where essentially all the added manganese was found to end up in the metal regardless of the compound that was added to the electrolyte; Mn_2O_3, MnO_2 or MnO. Figure 2 shows the concentration of manganese in the electrolyte and metal as a function of time before and after addition of Mn_2O_3. For the other elements about 90 % of the metal containing additions were found to be co-depositing on the cathode. One reason for the loss may be poor dissolution or inefficiency due to the presence of species of different oxidation states.

Figure 3 shows a plot of the data for manganese after addition of Mn_2O_3 according to equation [3]. The good linear fit suggests that manganese is reduced at the cathode at diffusion controlled conditions. Similar results were obtained for the other elements. Figure 4 shows concentration of silicon and titanium in the bath as a function of time before and after adding SiO_2 and TiO_2.

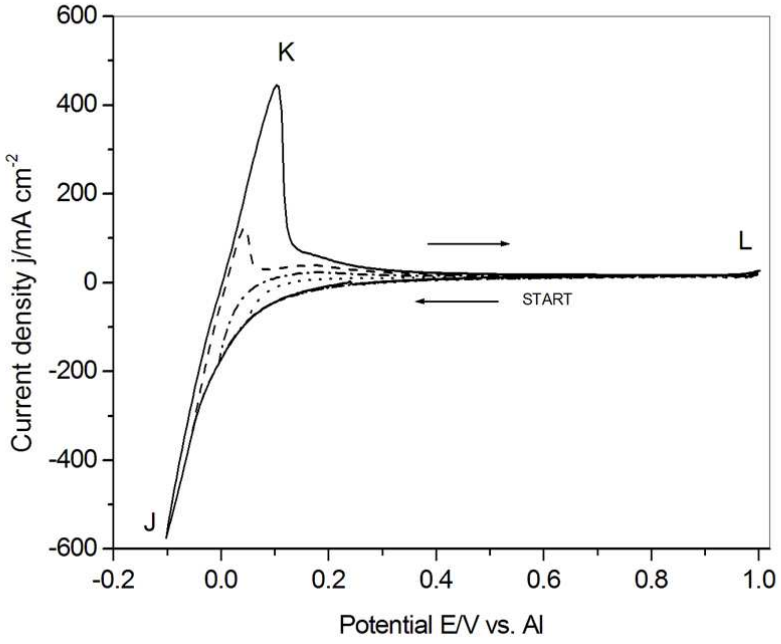

Figure 1. Voltammograms recorded on a tungsten working electrode in molten cryolite (Na_3AlF_6) saturated with Al_2O_3 at 1020 ^oC. Sweep rate 0.1 V s^{-1}.

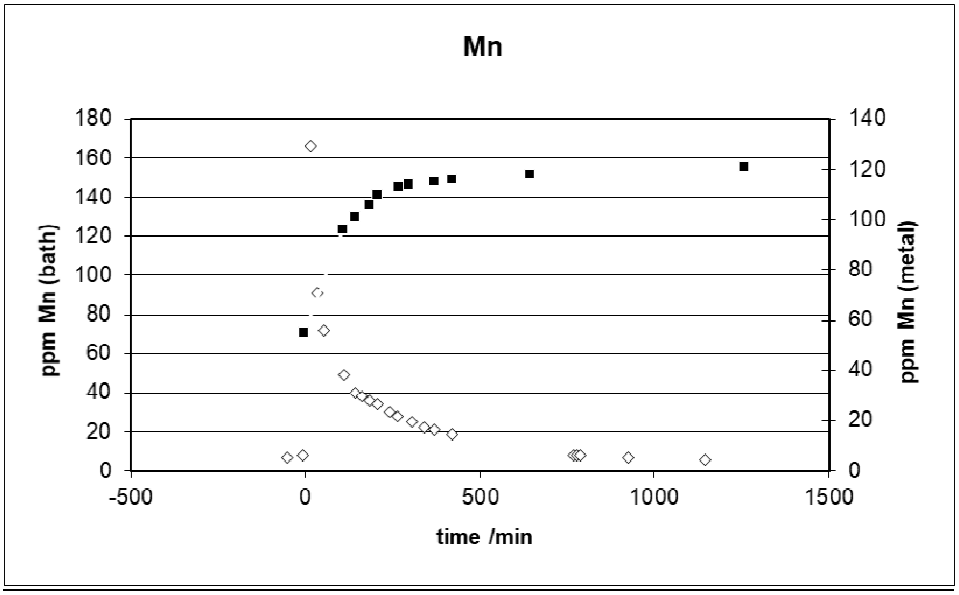

Figure 2. Concentration of manganese in bath and metal as a function of time before and after addition of Mn_2O_3. The addition was made at t = 0. Open symbols: Mn in bath. Filled symbols: Mn in metal.

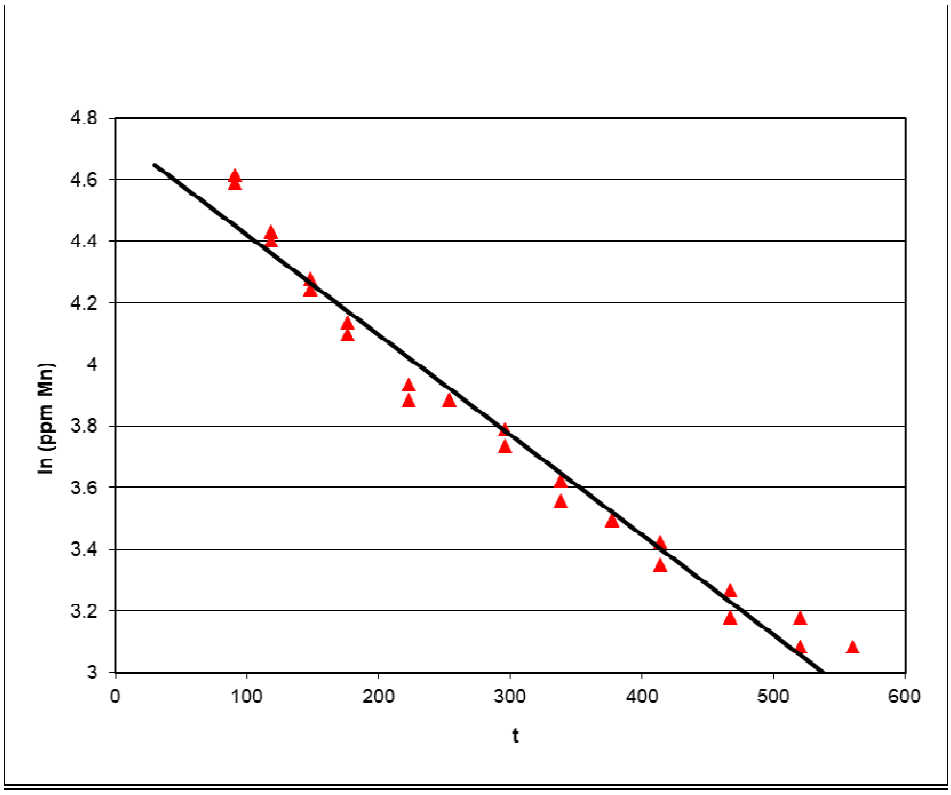

Figure 3. Plot of log concentration of manganese in the bath as a function of time after addition of Mn_2O_3. The solid line is a linear fit of the data.

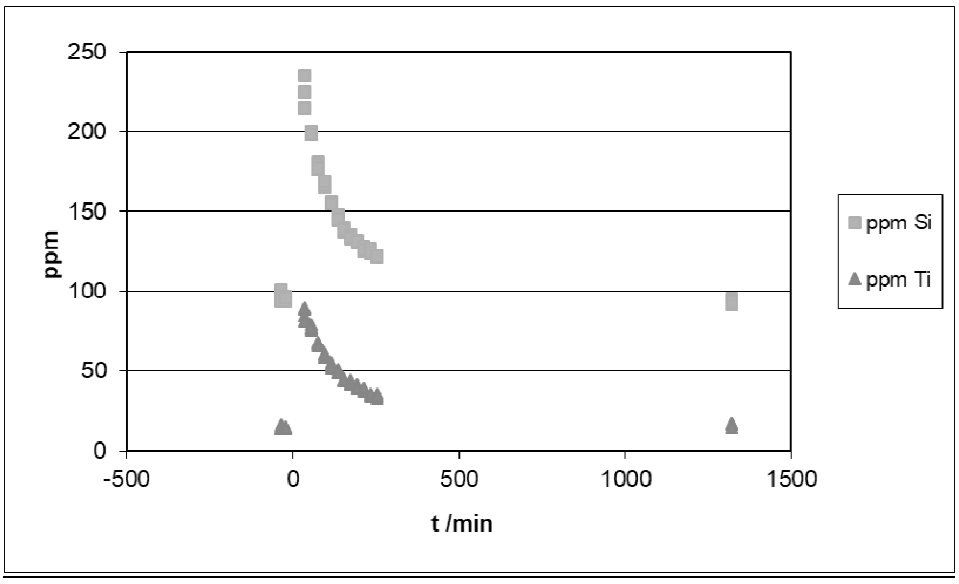

Figure 4. Concentration of silicon and titanium in the bath as a function of time before and after adding SiO_2 and TiO_2. The addition was made at t = 0.

From plots like that shown in Figure 3 and using equation [2], the mass transfer coefficient was found to be of the order of $1 \cdot 10^{-5}$ m/s for all the investigated metals. This is in agreement with literature (3, 4).

Ongoing laboratory experiments are focussing on investigating the conditions where the concentration of dissolved metal oxides is kept constant by addtion throughout the electrolysis. Quantitative results are not avaiable because electrolyte and metal samples have not yet been analysed. Preliminary results indicate that electrolysis time, concentration of dissolved metal oxides and electrolysis temperature or superheat may influence the dissolution of the metal oxides and affect the content of the alloying element.

It is expected that successful co-deposition of alloying elements may give big savings compared to the current practice. New valuable such as $TiAl_3$ may be produced by controlled co-deposition. Another benefit by using co-deposition is the possibility to use inexpensive raw materials containing impurities which can be utilized for producing alloys.

Conclusions

Laboratory studies of the electrochemical behaviour of candidate alloying elements with aluminium were carried out for silicon, manganese and titanium. These elements can be reduced from their dissolved metal oxides in molten cryolite-alumina based electrolytes.

Experiments were also carried out in industrial aluminium cells. Large quantities (kg) of metal oxides were added to the electrolyte during electrolysis, and samples of electrolyte and produced metal were taken and analysed as a function of time after addition. The results suggested all these metals were co-depositing with liquid aluminium at their limiting current density. The apparent current efficiency for metal co-deposition was estimated to be of the order of 90 % for silicon and titanium and close to 100 % for manganese.

Significant savings for implementing this method for producing aluminium based alloys are expected.

Acknowledgments

Hydro Aluminium is thanked for financial support.

References

1. https://pubs.usgs.gov/periodicals/mcs2020/mcs2020-aluminum.pdf.
2. K. Grjotheim, K. Matiasovsky, *Aluminium*, **59**, 687 (1983).
3. H. Grini Johansen, J. Thonstad and Å. Sterten, *Light Metals*, 253 (1977).
4. T.E. Jentoftsen, G.M. Haarberg, B.P. Moxnes, A. Buen and J. Thonstad: ”Mass Transfer of Iron, Silicon and Titanium in Hall-Heroult Cells”, Proceedings, 11th Int. Aluminium Symposium, ed. A. Solheim and G.M. Haarberg, Trondheim-Bergen-Trondheim, Norway, 217 (2001).

5. G.M. Haarberg: "Electrochemical Behaviour of Dissolved Titanium Oxides during Aluminium Deposition from Molten Fluoride Electrolytes", *Mater. Trans.* **58** (3), 406 (2017).
6. E. Chassaing, F. Basile and G. Lorthiair, *J. Appl. Electrochem.*, **11**, 187 (1981).

ECS Transactions, 98 (10) 189-198 (2020)
10.1149/09810.0189ecst ©The Electrochemical Society

Electrodeposition of Tungsten from Molten KF–KCl–WO_3 and CsF–CsCl–WO_3

T. Nohira[a], X. Meng[a], T. Ide[a], Y. Norikawa[a], and K. Yasuda[b,c],[*]

[a] Institute of Advanced Energy, Kyoto University, Uji 611-0011, Japan
[b] Graduate School of Energy Science, Kyoto University, Kyoto 606-8501, Japan
[c] Agency for Health, Safety and Environment, Kyoto University, Kyoto 606-8501, Japan
[*]Present address: Graduate School of Engineering, Kyoto University, Kyoto 606-8501, Japan

The electrodeposition of W films was investigated in KF–KCl eutectic melts after adding 0.5–2.0 mol% of WO_3 at 923 K. Cyclic voltammetry at a Ag electrode suggested that the electrodeposition of W from W(VI) ions proceeds from 1.65 V vs. K^+/K. Electrodeposition of α-W was confirmed by XRD analysis. The effect of current density and added amount of WO_3 on the morphology of W films was investigated by surface and cross-sectional SEM, which indicated that the best W film having thickness of ca. 15 μm was obtained at 12.5 mA cm^{-2} and 2.0 mol% of WO_3. Although the film thickness was increased to ca. 30 μm by increasing the charge density, the surface roughness was significantly increased. To suppress the growth of crystal grains, electrodeposition of W was also investigated in CsF–CsCl eutectic melts at lower temperature of 873 K. The XRD confirmed the existences of both α-W and β-W in the W films. The SEM observations revealed that dense and smooth W films having thickness of ca. 30 μm were successfully obtained.

Introduction

Tungsten metal is known for its robustness, especially for high melting and boiling points, and high hardness. However, its hardness and brittleness make it difficult to work. Thus, electrodeposition of flat and dense tungsten films is worth investigating. There are a number of reports on the electrodeposition of tungsten from high temperature molten salts such as fluorides (1), chlorides (2), oxides (3), etc. It is known that dense and coherent tungsten deposits are more easily obtained from molten fluorides compared to molten chlorides. One drawback of typical fluoride melts like LiF–NaF–KF is difficulty in removing the adhered molten salts by water washing because LiF and NaF have limited solubility to water (4). Although good tungsten deposits can be electrodeposited from molten oxides (3), the operation temperature tends to be very high, typically over 1123 K.

Incidentally, we proposed new electrolyte baths, molten KF–KCl (T_{eu} = 878 K at 45:55 mol%), for the electrodeposition of crystalline Si films (5) and Ti films (6-8). Since all the component salts of KF and KCl have large solubility to water (4), solidified salts on deposited films can be easily removed by water washing. So far, we have successfully obtained crystalline Si films from molten KF–KCl–K_2SiF_6 at 923 K (5) and smooth Ti films from KF–KCl–K_3TiF_6 at 923 K (6–8).

From this background, we applied the KF–KCl molten salt to the electrodeposition of W films in the present study. We selected WO_3 as a tungsten source because it is easy to handle compared to gaseous WF_6. We investigated the effect of W(VI) ion concentration and current density on the morphology of W films at 923 K. Furthermore, to suppress the growth of crystal grains, we selected molten CsF–CsCl (T_{eu} = 713 K at 50:50 mol%) as a lower temperature molten salt. Here, the component salts of CsF and CsCl have even larger solubility to water than KF and KCl (4). The electrodeposition of W films was also investigated in the at CsF–CsCl–WO_3 at 873 K.

Experimental

For molten KF–KCl, reagent-grade KF (FUJIFILM Wako Pure Chemical Corp., >99.0%) and KCl (FUJIFILM Wako Pure Chemical Corp., >99.5%) were mixed in the eutectic composition (molar ratio of KF:KCl = 45:55, melting point = 878 K, 400 g) and loaded in a graphite crucible (Toyo Tanso Co., Ltd., O.D. 100 mm, I.D. 90 mm, and height 120 mm). They were first dried under vacuum at 453 K for over 72 h and further dried under vacuum at 773 K for 24 h. For molten CsF–CsCl, reagent-grade CsF (Furuuchi Chemical Corp., >99.0%) and CsCl (FUJIFILM Wako Pure Chemical Corp., >99.0%) were mixed in the eutectic composition (molar ratio of CsF:CsCl = 50:50, melting point = 713 K, 500 g) and loaded in a graphite crucible. They were first dried under vacuum at 453 K for over 72 h and further dried under vacuum at 673 K for 24 h. The mixture in the crucible was placed at the bottom of a stainless steel vessel in an airtight Kanthal container. The electrochemical measurements were conducted in dry Ar atmosphere.

Electrochemical measurements and galvanostatic electrolysis were performed using a three-electrode method with an electrochemical measurement system (Hokuto Denko Corp., HZ-7000). The working electrodes were Cu foil (Nilaco Corp., 20 mm × 5 mm, thickness: 0.030 mm, 99.9%), Ag flag (Nilaco Corp., diameter: 2.0 mm, thickness: 0.1 mm, 99.98%), and Au flag (Nilaco Corp., diameter: 2.0 mm, thickness: 0.10 mm, 99.95%) electrodes. The structure of the flag electrodes was reported in our previous paper (5). A glass-like carbon rod (Tokai Carbon Co., Ltd., diameter: 3.0 mm) was used as the counter electrode. A Pt wire (Nilaco Corp., diameter: 1.0 mm, 99.98%) was used as the quasi-reference electrode. The potential of the quasi-reference electrode was calibrated with respect to dynamic K^+/K or Cs^+/Cs potential determined by cyclic voltammetry at a Ag electrode. The melt temperature was measured with a type-K thermocouple. The electrolyzed samples on the Cu foils were soaked in distilled water for 60 min at 333 K to remove the salt adhered on the deposits.

The phase identification of the samples was conducted by X-ray diffractometry (XRD; Rigaku Ultima IV, Cu Kα, 40 kV, 40 mA). The surface and cross-section of the samples were observed by using scanning electron microscopy (SEM; Keyence E8800). Before the observation of the cross section, the samples were cut at the center and embedded in acrylic resin. The samples were polished with emery papers and buffing compounds. The samples were then coated with Au using an ion-sputtering apparatus (Hitachi, Ltd., E-1010) to impart conductivity. The surface roughness (R_a and S_a) of the samples was measured by Laser microscope (Keyence VK-X 1000).

Result and Discussion

KF–KCl–WO_3 melts

Cyclic Voltammetry and XRD Analysis. Figure 1 (a) shows the cyclic voltammogram at a Ag flag electrode after the addition of WO_3 (2.0 mol%) in molten KF–KCl at 923 K. For comparison, the voltammogram measured before the addition of WO_3 is also plotted. After the addition of WO_3, new cathodic currents are observed from 1.65 V, which suggests the electrodeposition of W metal from W(VI) ions. The W(VI) ions are believed to exist in the form of $WO_3F_3^{3-}$ because the Raman spectrum of this melt was approximately identical to the reported one for $K_3WO_3F_3$ crystal (9). After the reversal of the scan direction to positive, new anodic currents arise from 1.65 V, which is explained by the anodic dissolution of the electrodeposited W metal.

A sample was prepared at a Cu foil electrode by galvanostatic electrolysis at 12.5 mA cm^{-2} for 120 min (Charge density: 90 C cm^{-2}). The electrode potential maintained a stable value of ca. 1.56 V during the electrolysis. Figure 2 (a) shows optical images of the sample before and after the electrolysis. The appearance changed from copper color to bright grey. Figure 2 (b) shows an XRD pattern of the sample, which clearly confirms the electrodeposition of W metal (α-W). The current efficiency based on the weight increase was calculated to be as high as 97%.

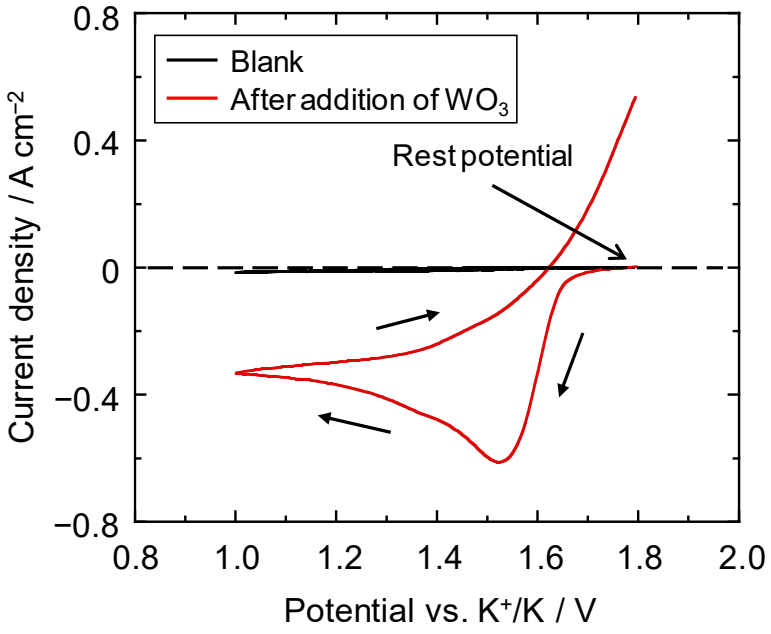

Figure 1. Cyclic voltammogram at a Ag flag electrode in molten KF–KCl before and after addition of WO_3 (2.0 mol%) at 923 K. Scan rate: 0.5 V s^{-1}.

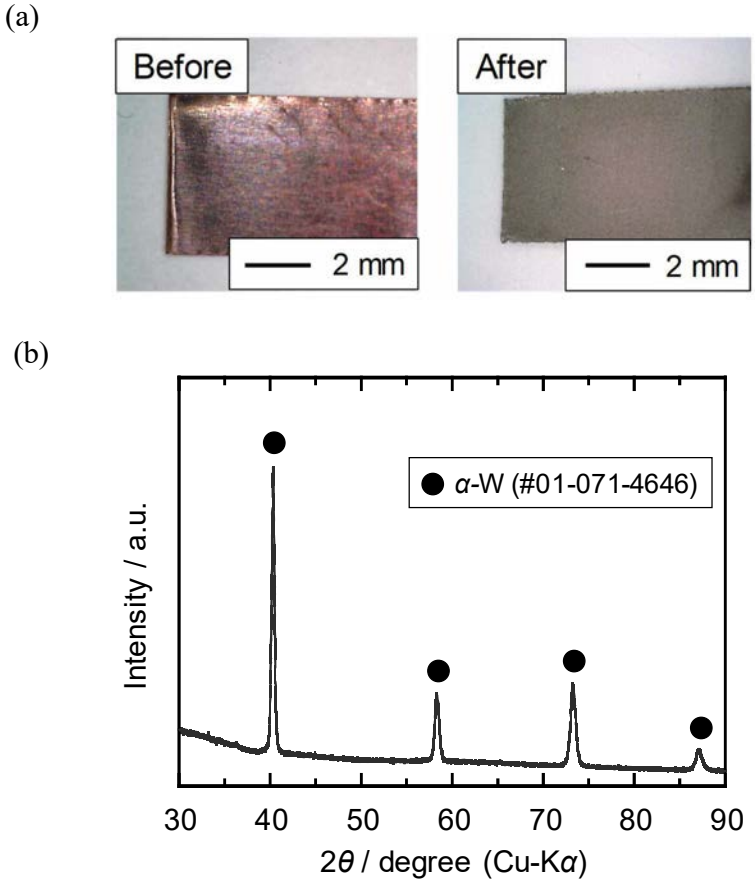

Figure 2 (a) Optical images of the sample before and after galvanostatic electrolysis of a Cu foil electrode at 12.5 mA cm^{-2} for 120 min in molten KF–KCl–WO_3 (2.0 mol% added) at 923 K. (b) An XRD pattern of the sample.

Effect of Current Density and W(VI) Ion Concentration. To study the optimum electrodeposition condition for obtaining dense and smooth W films, we conducted galvanostatic electrolysis at various current densities (12.5, 25, 50, 100 mA cm^{-2}) and various added amounts of WO_3 (0.50, 1.0, 1.5, 2.0 mol%). Here, the charge density was unified to 90 C cm^{-2} for accurate comparison. Figure 3 shows optical images of the samples after washing with distilled water. In the cases of higher current densities and lower W(VI) ion concentrations, no deposits were obtained or most of the deposits were detached from the substrate during the water washing. Such conditions are indicated with yellow background in the figure. In other conditions than above, black or grey deposits were obtained.

Figure 4 compares the SEM images of the samples. Relatively smooth W films were deposited at lower current densities (12.5 and 25 mA cm^{-2}) and higher W(VI) ion concentrations (1.5 and 2.0 mol% added); these conditions are indicated with pale red background in the figure. The size of crystal grains ranges from 3 μm to 8 μm. In the cases of slightly larger current densities and slightly higher W(VI) ion concentrations, which are indicated with pale green background in the figure, the W films exhibit rough surfaces.

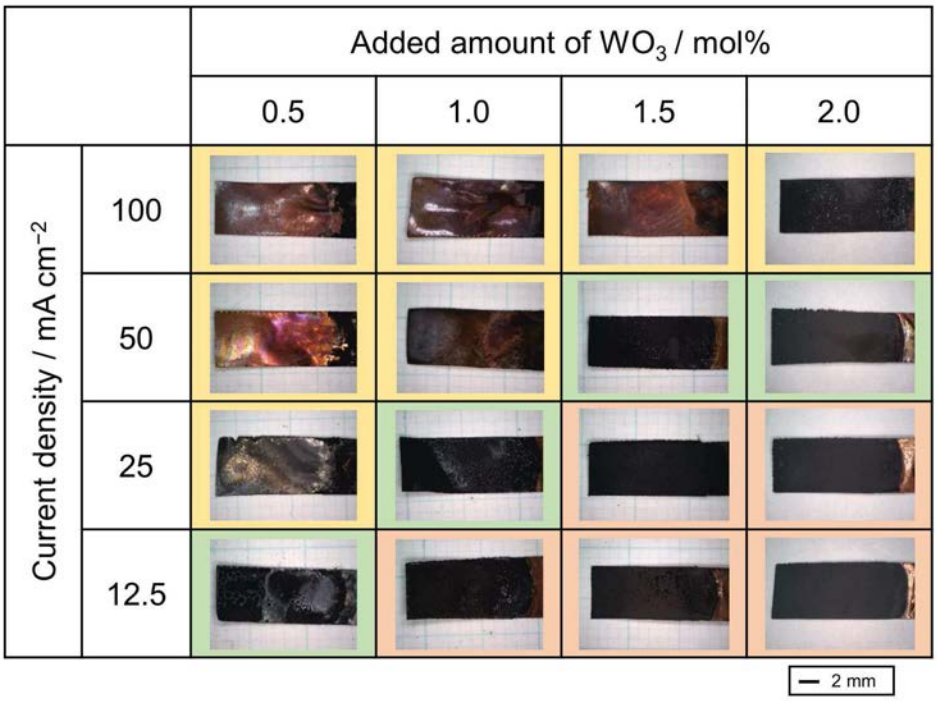

Figure 3. Optical images of the samples obtained by galvanostatic electrolysis of Cu foil electrodes at various current densities and added amounts of WO_3 in molten KF–KCl at 923 K. Charge density: 90 C cm^{-2}. The scale bar is common for all images.

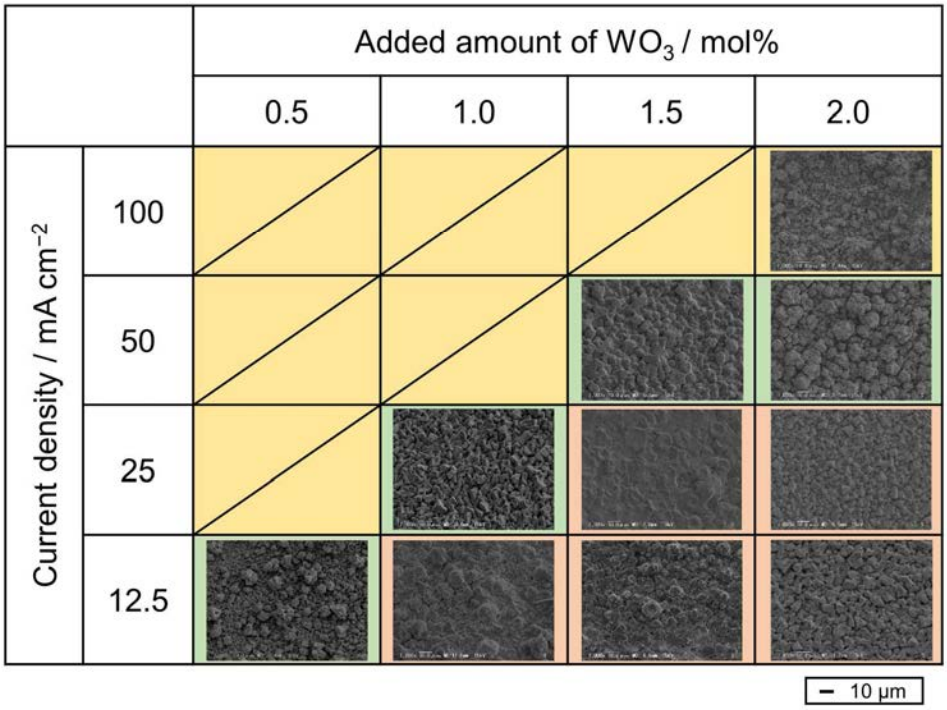

Figure 4. Surface SEM images of the samples obtained by galvanostatic electrolysis of Cu foil electrodes at various current densities and added amounts of WO_3 in molten KF–KCl at 923 K. Charge density: 90 C cm^{-2}. The scale bar is common for all images.

Figure 5 shows cross-sectional SEM images of the samples. Dense W films are observed for the samples at lower current densities and higher W(VI) ion concentrations. The thicknesses of the W films are approximately 10–15 μm. The smoothest surface is confirmed for the sample prepared at 12.5 mA cm^{-2} and 2.0 mol%. For this W film, the average R_a was calculated to be 1.02±0.11 μm. On the other hand, rougher deposits were obtained in the conditions indicated with pale green background.

We tried to obtain thicker W films by prolonging the electrolysis time at 12.5 mA cm^{-2} and 2.0 mol%. Figure 6 shows surface and cross-sectional SEM images of samples electrolyzed for 40, 120, 200, and 360 min; the time periods correspond to 30, 90, 150, and 210 cm^{-2}, respectively. As is evident from the surface SEM, the size of crystal grains increases with the electrolysis time. Although the film thickness successfully increased to ca. 30 μm at 210 cm^{-2}, the surface roughness also increased significantly.

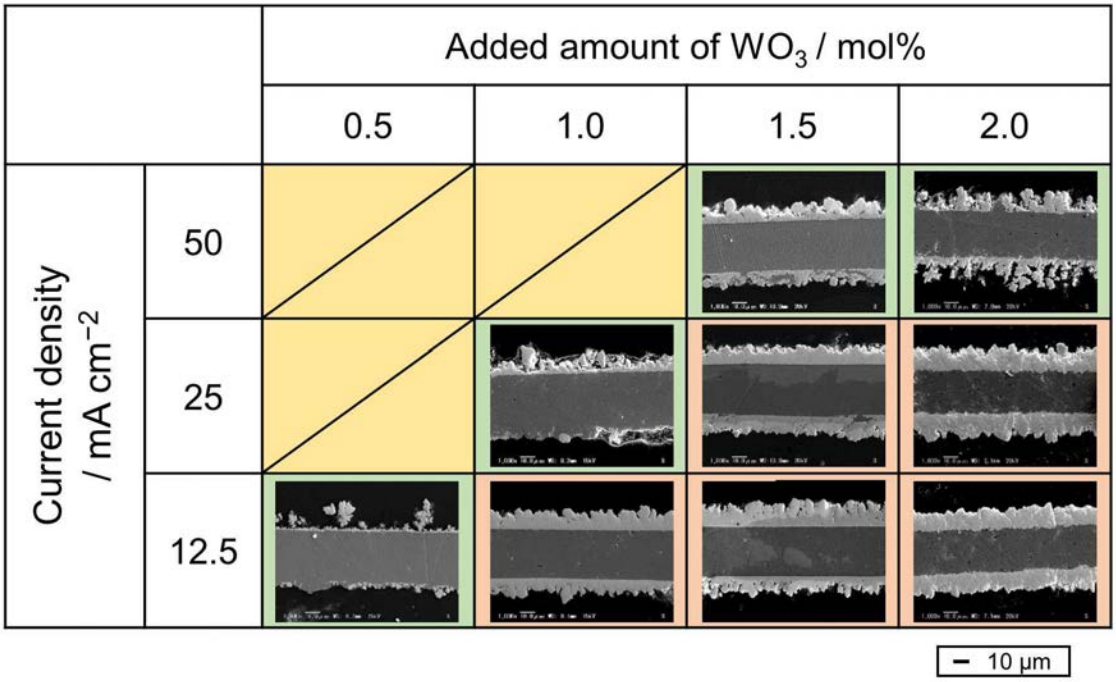

Figure 5. Cross-sectional SEM images of the samples obtained by galvanostatic electrolysis of Cu foil electrodes at various current densities and added amounts of WO_3 in molten KF–KCl at 923 K. Charge density: 90 C cm^{-2}. The scale bar is common for all images.

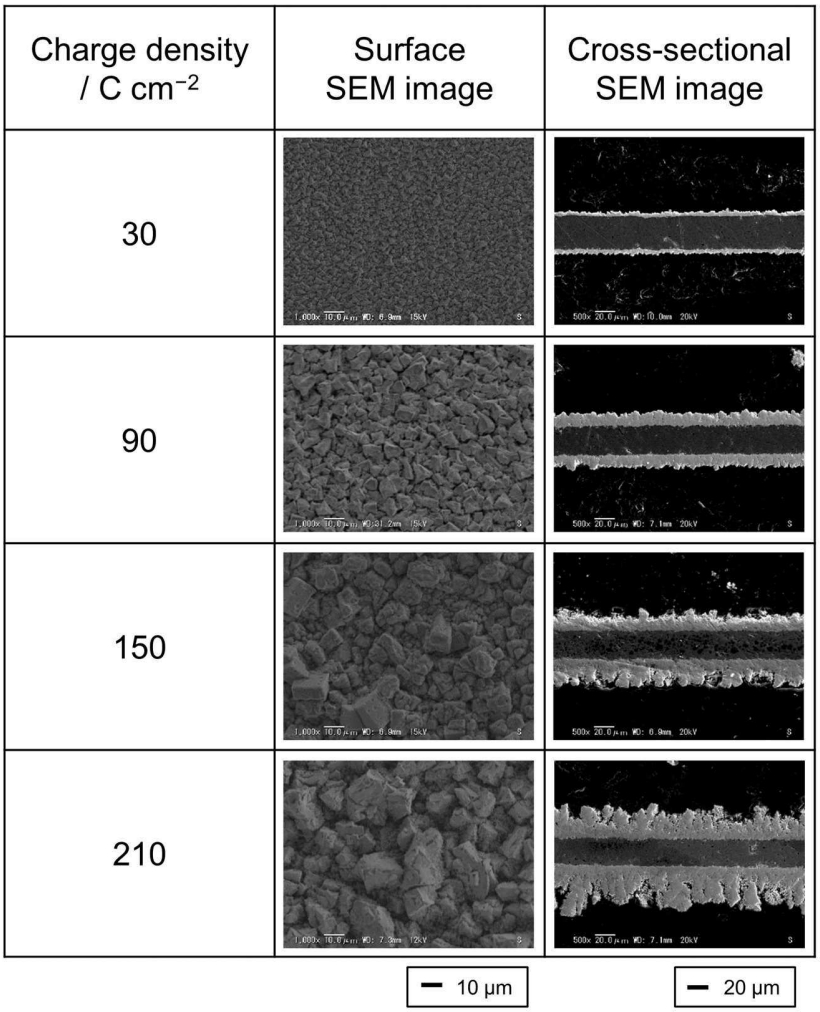

Figure 6. Surface and cross-sectional SEM images of the samples obtained by electrolysis of Cu foil electrodes at 12.5 mA cm^{-2} at various charge densities in molten KF–KCl–WO_3 (2.0 mol% added) at 923 K. The scale bar is common for all surface/cross-sectional images.

CsF–CsCl–WO_3 melts

In our previous study on the electrodeposition of Ti films in molten LiF–LiCl–Li_3TiF_6, the growth of crystal grains could be effectively suppressed and smoother deposits were obtained by lowering the temperature from 923 K to 823 K (10, 11). Thus, in the present study, we attempted to lower the temperature by utilizing CsF–CsCl eutectic melts. Figure 7 show cyclic voltammograms at a Au flag electrode in molten CsF–CsCl–WO_3 (2.0 mol% added) at 823–923 K. As with the KF–KCl–WO_3 (2.0 mol% added) at 923 K, cathodic currents are observed from approximately 1.5 V vs. Cs^+/Cs at all temperatures, indicating the electrodeposition of W. However, the peak current densities were smaller at lower temperatures and especially small at 823 K, which suggests that the solubility of WO_3 at the lower temperatures are less than 2.0 mol%.

A sample was prepared at a Cu foil electrode by galvanostatic electrolysis at 12.5 mA cm^{-2} for 120 min (Charge density: 90 C cm^{-2}). Figure 8 shows an XRD pattern of the

sample after washing with water. Interestingly, the existence of β-W is confirmed in addition to α-W. It is known that β-W is a meta-stable phase of W and has A15 type crystal structure (12). Recently, β-W is attracting much attention because it exhibits giant spin Hall effect (12). The current efficiency based on the weight increase was calculated to be 94%.

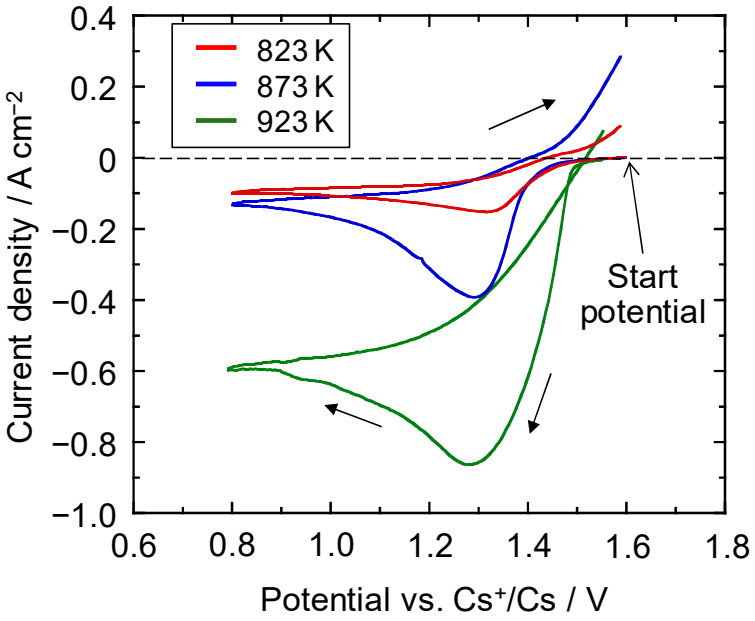

Figure 7. Cyclic voltammograms at a Au flag electrode in molten CsF–CsCl–WO_3 (2.0 mol% added) at 823–923 K. Scan rate: 0.5 V s^{-1}.

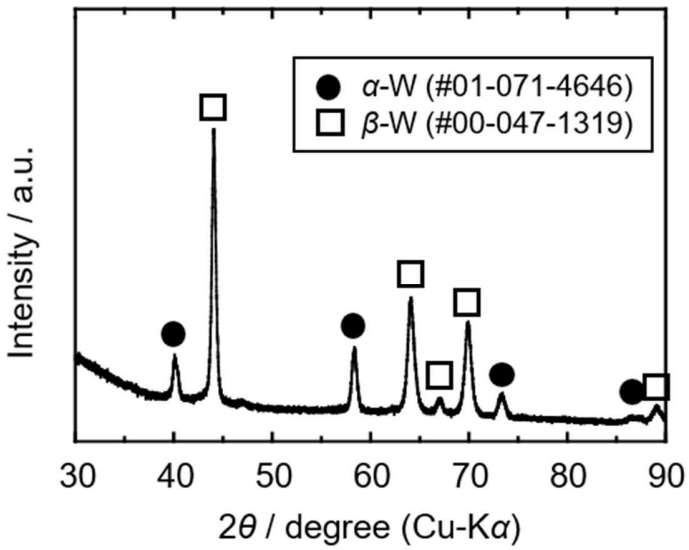

Figure 8. An XRD pattern of the sample obtained by galvanostatic electrolysis of a Cu foil electrode at 12.5 mA cm^{-2} for 120 min in molten CsF–CsCl–WO_3 (2.0 mol% added) at 873 K. Charge density: 90 C cm^{-2}.

We also attempted to obtain thicker W films by prolonging the electrolysis time for 360 min (Charge density: 210 cm^{-2}). Figure 9 shows surface and cross-sectional SEM images of the samples obtained at 90 and 210 C cm^{-2}. As seen from the surface SEM, the sizes of crystal grains are considerably smaller compared with the deposits in the KF–KCl–WO_3 (2.0 mol% added) at 923 K. The value of S_a was 0.61 μm for the W films at 90 C cm^{-2}. The cross-sectional SEM revealed that the film thickness successfully increased to ca. 30 μm at 210 C cm^{-2} without a significant increase of the surface roughness.

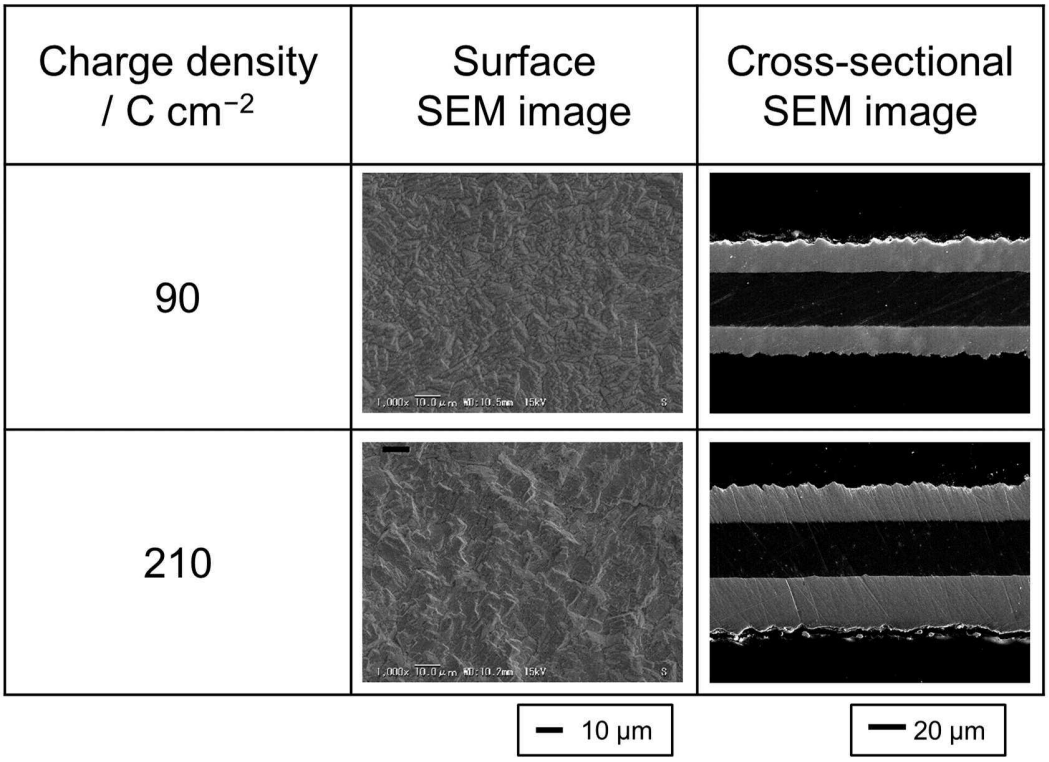

Figure 9. Surface and cross-sectional SEM images of the samples obtained by galvanostatic electrolysis of Cu foil electrodes at 12.5 mA cm^{-2} in molten CsF–CsCl–WO_3 (2.0 mol% added) at 873 K. Charge density: 90 and 210 C cm^{-2}.

Conclusion

The electrodeposition of W films was investigated at 923 K in KF–KCl eutectic melts to which 0.5–2.0 mol% of WO_3 were added. Cathodic currents at a Ag electrode from 1.65 V vs. K^+/K were interpreted as the electrodeposition of W metal from W(VI) ions. Electrodeposition α-W was confirmed by XRD analysis for the sample prepared at Cu foil. Among various current densities (12.5–100 mA cm^{-2}) and added amounts of WO_3 (0.5–2.0 mol%), the optimum condition was found to be 12.5 mA cm^{-2} and 2.0 mol%. The surface and cross-sectional SEM indicated that the dense and smooth W films with thickness of ca. 15 μm were obtained at the optimum condition. Although the film thickness was increased to ca. 30 μm by increasing the charge density to 210 C cm^{-2}, the surface

roughness was significantly increased. On the other hand, galvanostatic electrolysis at 12.5 mA cm^{-2} and 90 C cm^{-2} in molten CsF–CsCl–WO_3 (2.0 mol% added) at 873 K gave better W films with smoother surface. The XRD analysis indicated that the obtained W films consisted of both α-W and β-W. The surface and cross-sectional SEM revealed that dense and smooth W films having thickness of ca. 30 μm was successfully obtained at 12.5 mA cm^{-2} and 210 C cm^{-2}.

Acknowledgments

A part of this study was conducted as collaborative research with Sumitomo Electric Industries, Ltd.

References

1. S. Senderoff and G. Mellors, *Science*, **153**, 1475 (1966).
2. M. Masuda, H. Takenishi, and A. Katagiri, *J. Electrochem. Soc.*, **148**, C59 (2001).
3. K. Koyama, M. Morishita, and T. Umezu, *Electrochemistry*, **67**, 667 (1999).
4. D. R. Lide (Ed.), *CRC Handbook of Chemistry and Physics*, 88th Edition, Chap.4, p.43-101, CRC Press, Boca Raton (2007).
5. K. Maeda, K. Yasuda, T. Nohira, R. Hagiwara, and T. Homma, *J. Electrochem. Soc.*, **162**, D444 (2015).
6. Y. Norikawa, K. Yasuda, and T. Nohira, *Mater. Trans*., **58**, 390 (2017).
7. Y. Norikawa, K. Yasuda, and T. Nohira, *Electrochemistry*, **86**, 99 (2018).
8. Y. Norikawa, K. Yasuda, and T. Nohira, *J. Electrochem. Soc*., **166**, D755 (2019).
9. A.S. Krylov, S.N. Sofronova, E.M. Kolensnikova, Y.N. Ivanov, A.A. Sukhovsky, S.V. Goryainov, A.A. Ivanenko, N.P. Shestakov, A.G. Kocharova, and A.N. Vtyurin, *J. Solid State Chem.*, **218**, 32 (2014).
10. Y. Norikawa, K. Yasuda, and T. Nohira, *J. Electrochem. Soc*., **167**, 082502 (2020).
11. M. Unoki, Y. Norikawa, K. Yasuda, and T. Nohira, *ECS Trans.*, this volume (2020).
12. Q. Hao, W. Chen, and G. Xiao, *Appl. Phys. Lett.*, **106**, 182403 (2015).

ECS Transactions, 98 (10) 199-208 (2020)
10.1149/09810.0199ecst ©The Electrochemical Society

Nucleation Study on Deposition of Aluminum from 1-butyl-3-methylimidazolium chloride (BMIC) and Aluminum chloride ($AlCl_3$) Ionic Liquid Electrolyte

Yuxiang Peng, Pravin. S. Shinde, and Ramana G. Reddy
Department of Metallurgical and Materials Engineering
The University of Alabama, Tuscaloosa, AL 35487, USA
Corresponding author: rreddy@eng.ua.edu; Tel: 205-348-4246

The aluminum is electrodeposited from an ionic liquid comprising a eutectic mixture of 1-butyl-3-methylimidazolium chloride (BMIC) and aluminum chloride ($AlCl_3$) at the $AlCl_3$ mole fraction of 0.667 (molar ratio of 1:2). The electrochemical behavior of chloroaluminate species in the ionic liquid (IL) is investigated by the chronoamperometry (CA) technique at different temperatures. The diffusion coefficients (D) of $Al_2Cl_7^-$ anion species in BMIC-$AlCl_3$ IL are calculated at various temperatures based on the chronoamperometric method. The calculated number densities of nucleation of Al deposits are 0.7×10^{10}, 1.0×10^{10}, and 1.4×10^{10} m^{-2} at 363 K with the applied potentials of −1.7, −1.75, and −1.8 V versus Pt, respectively. The scanning electron microscopy (SEM) result indicated that the calculated data is comparable to the experimental electrodeposition data. In addition, the rate of nucleation was also investigated during the electrodeposition experiment.

1. Introduction

In recent years, the room-temperature ionic liquid (IL) has been investigated as the electrolyte in the field of electrodeposition of metals or alloys (1). The IL is eco-friendly and efficient electrolyte due to its non-corrosive property, the wide temperature range for the liquid phase, the excellent thermal stability, low vapor pressure, wide electrochemical window, and low pollutant emission (2-4). In addition, they have recently been used as the electrolyte to reduce the Al element (2,5-8). However, the conventional processes of reducing Al require high temperatures that not only consume lots of energy but also release the unwanted greenhouse gases (9). Several ILs have been used to electrodeposit Al, which are synthesized by the combination of $AlCl_3$ with alkyl imidazolium chlorides (10-14). In fact, to understand the electrosythesis conditions and electrochemistry of this kind of ionic liquid, several properties have been reported in our group, such as the heat capacity (15), thermal stability (16,17), density (18), viscosity (18,19), thermodynamic (20-22), and electroanalytical (23-26) properties. One of the interesting ILs is BMIC-$AlCl_3$, which is liquid at room temperature. The mixture of the melt leads to the formation of several chloroaluminate anions, which exist in equilibrium, according to the following reactions (1-3) (10,11).

$$AlCl_3 + Cl^- \overset{room\ temperature}{\Longleftrightarrow} AlCl_4^- \quad [1]$$

$$AlCl_3 + AlCl_4^- \overset{room\ temperature}{\Longleftrightarrow} Al_2Cl_7^- \quad [2]$$

$$AlCl_3 + Al_2Cl_7^- \overset{room\ temperature}{\Longleftrightarrow} Al_3Cl_{10}^- \quad [3]$$

The amount of $AlCl_3$ determines the Lewis acidity of the BMIC-$AlCl_3$ melt. When the molar ratio of $AlCl_3$ and BMIC is less than 1, the melt consists of organic cation and tetra-chloroaluminate ions ($AlCl_4^-$). In the melts containing excess amount of $AlCl_3$ (molar ratio > 1), the excess $AlCl_3$ reacts with $AlCl_4^-$ anions to form Lewis acidic hepta-chloroaluminate ions ($Al_2Cl_7^-$) (27).

The electrochemical process of reduction of Al-species in the ILs is necessary to discuss before the utilization of ILs as the electrolyte. In fact, it has been illustrated previously that the electrodeposition process is due to the diffusion of $Al_2Cl_7^-$ species (2,14,28). And the nucleation of aluminum from BMIC-$AlCl_3$ IL follows the instantaneous process (2,29). However, the nucleation number densities at different conditions are still unclear in such IL. Even a few research studies illustrate the calculated and experimental nucleation number density in other ILs (1,30), the nucleation rate in the BMIC-$AlCl_3$ IL still unclear and needs to be investigated.

In this study, the melt of $AlCl_3$ with BMIC is employed for the nucleation study of the Al electrodeposition process. The CA experiments are performed to analyze the mechanism of diffusion and nucleation of aluminum-species from BMIC-$AlCl_3$ IL. Besides, Samples after electrodeposition were analyzed by Scanning Electron Microscope (SEM) and Energy Dispersive X-Ray Spectroscopy (EDS).

2. Experimental

The chemicals such as $AlCl_3$ (95%, Alfa-Aesar) and BMIC (98%, Sigma-Aldrich, HPLC grade) single salts were purchased and used as received. In the present work, the BMIC to $AlCl_3$ molar ratio of 1:2 was used to maximize the concentration of $Al_2Cl_7^-$ anion species in the ILs. Before the mixing process, the BMIC was placed in a vacuum oven to dry for at least 6 hours. Then, the chemicals were weighed in an appropriate ratio in a glove box under dry ultra-high purity (UHP, 99.995%) argon (Ar) gas. The BMIC was taken in a 250 mL beaker, and then $AlCl_3$ was slowly added into it at room temperature. A glass rod was used to stir while adding the $AlCl_3$. When the IL becomes a clear solution, it is transferred to another 50 mL beaker outside the glove box. The 50 mL beaker is covered by parafilm and placed on a hot plate and stirred for about 30 min for homogeneous mixing using a magnetic stirrer at 60 RPM. The temperature of the preheated hot plate was set to the experimental temperature (353 K).

The electrochemical experiments were performed with an EG&G PARC model 273 A potentiostat/galvanostat instrument controlled by Power Suite software. The CA curves were obtained by varying the overpotentials. The experiments were performed from BMIC-$AlCl_3$ IL using a three-electrode cell configuration. And each experiment was repeated at least two times to ensure repeatability. Figure 1 shows the schematic of the CA experimental setup.

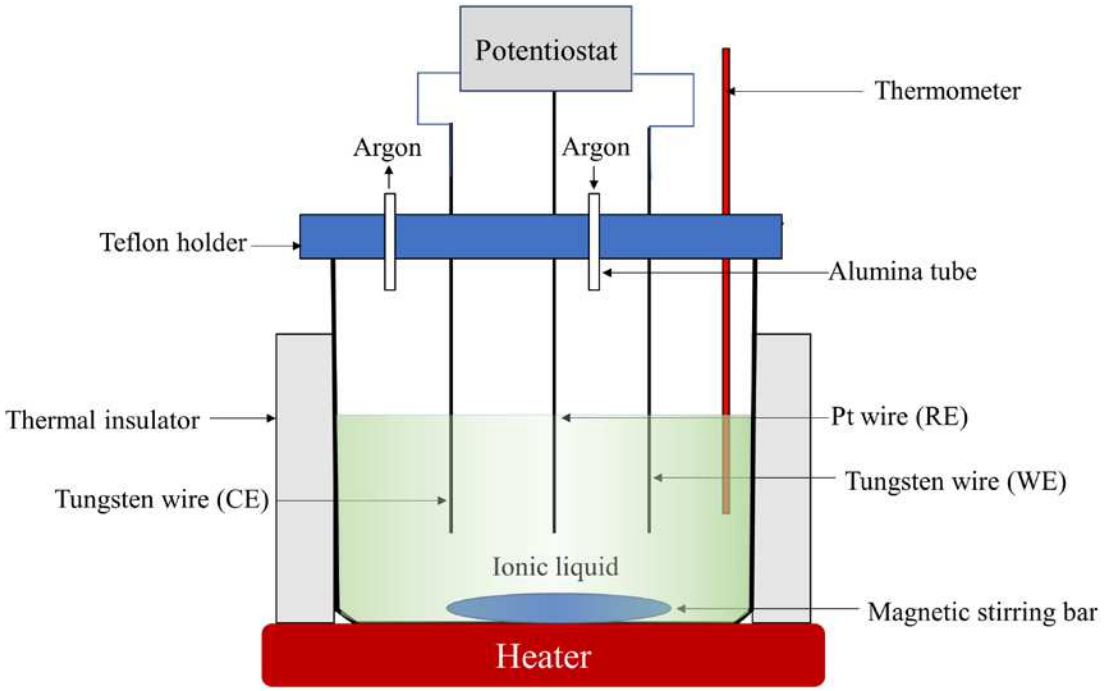

Figure 1. Schematic of an electrochemical cell for CA experiments in IL.

As shown in Figure 1, the temperature was controlled by a hot plate and was precisely monitored by the inserted thermometer. Tungsten wires (99.9%) with a diameter of 0.45 mm were used as working and counter electrodes, and the quasi-reference electrode was Pt wire (99.9%) with a 0.5 mm diameter. The Ar gas flow was continuously maintained through the alumina tube during the experiment. Thus, the whole system was under the Ar gas atmosphere. For the electrodeposition experiment, the experimental setup was similar to the CA experiment. But the working electrode was a Ni plate, and the counter electrode was an aluminum sheet. All the electrodes were ground with 800-grit SiC abrasive paper, washed with acetone and deionized water, and then dried by air right before the experiment. The height of the electrode immersed into the IL was measured after the experiment for area normalization.

3. Results and Discussion

3.1. Chronoamperometry (CA)

The chronoamperometric current-time transients for the BMIC-$AlCl_3$ IL at different applied potentials and different temperatures are shown in Figure 2. The area of a tungsten working electrode immersed in the IL is 2.8×10^{-5} m^2, and the quasi-reference electrode is Pt.

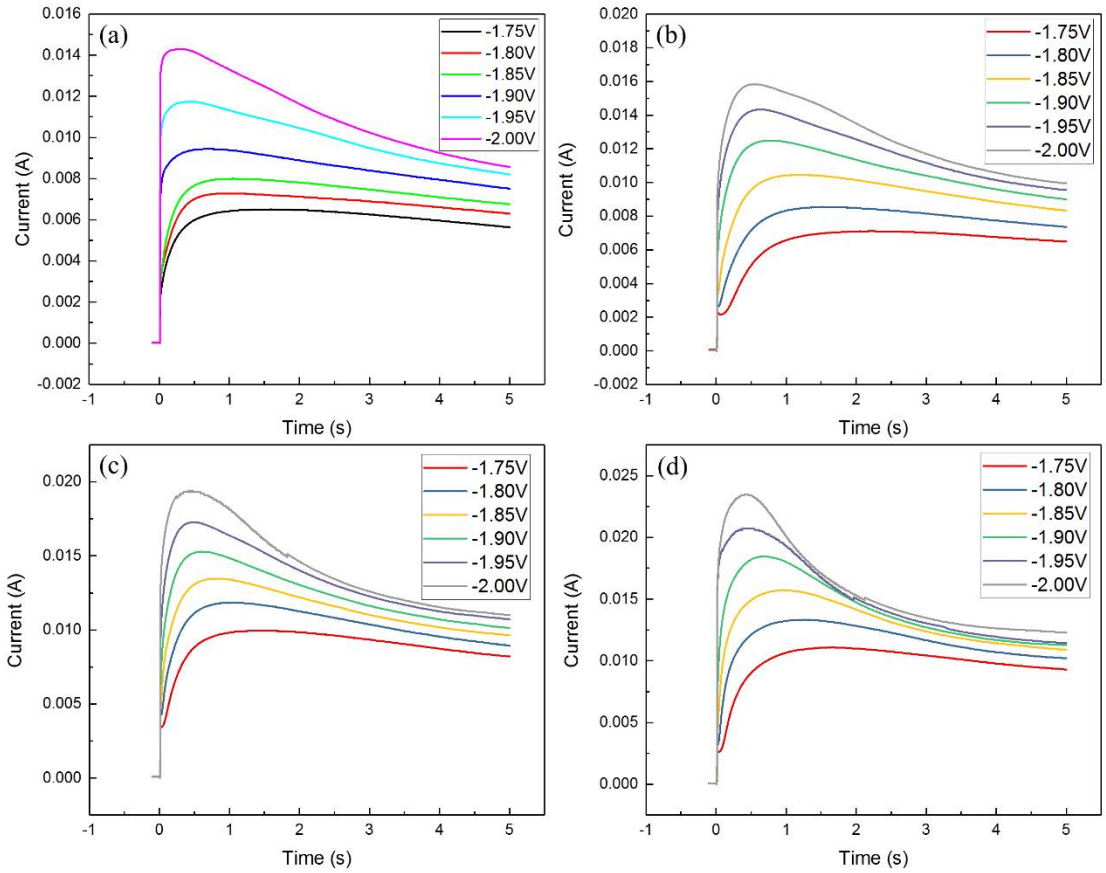

Figure 2. The chronoamperometric current-time transients for Al deposition from BMIC-$AlCl_3$ IL with different overpotentials at (a) 353 K, (b) 363 K, (c) 373 K, and (d) 383 K.

As shown in Figure 2, the applied overpotentials are sufficient to initiate the nucleation and growth of aluminum as the maximum current (I_m) and corresponding time (t_m) were observed. The current increased initially at a specific maximum value and then dropped. Moreover, when the applied overpotential is more negative, the value of the maximum current is increased while the corresponding time is decreased. As the cathodic potential increased, the nucleation rate and density of aluminum are increased (31).

3.2. Number density of nucleation and average radius

The dimensionless experimental current-time transients are compared with the dimensionless theoretically instantaneous and progressive nucleation model, which is described by Scharifker and Hills (32). The detailed expression is listed in equations [4-5], which present the relationship between dimensionless current density (j/j_m) to the dimensionless time (t/t_m).

$$Instantaneous: (j_{inst}/j_m)^2 = 1.9542(t_{inst}/t_m)^{-1}\{1 - exp[-1.2564(t_{inst}/t_m)]\}^2 \quad [4]$$

$$Progressive: (j_{prog}/j_m)^2 = 1.2254(t_{prog}/t_m)^{-1}\left\{1 - exp\left[-2.3367(t_{prog}/t_m)^2\right]\right\}^2 \quad [5]$$

where j is the current density (A m^{-2}) at any experimental time t, j_m is the maximum current density, and t_m time (s) is its corresponding time. The dimensionless current-time

transients for different potentials in BMIC-$AlCl_3$ IL along with theoretical nucleation processes are compared, as shown in Figure 3.

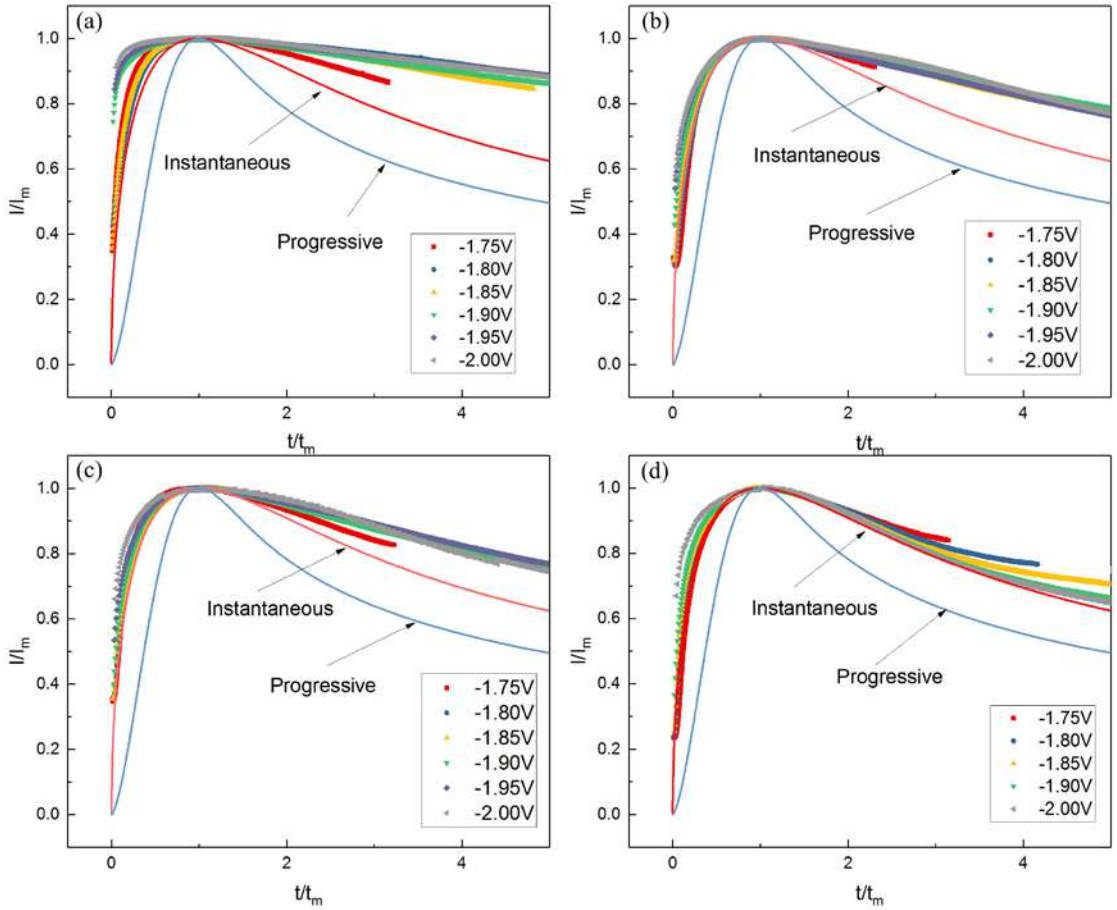

Figure 3. Comparison between experimental current-time transients at different potentials, in BMIC-$AlCl_3$ IL and theoretical instantaneous and progressive nucleation at (a) 353 K, (b) 363 K, (c) 373 K, and (d) 383 K.

As shown in Figure 3, the experimental results are closely relatable to the instantaneous nucleation process. At longer times, the experimental currents are larger than the theoretical values from the instantaneous nucleation model, reportedly due to partial kinetic control of the growth process (24,31).

As the electrodeposition of Al in BMIC-$AlCl_3$ IL follows three-dimension instantaneous nucleation and diffusion-control process, the number density of nucleation at different overpotentials can be calculated based on the model developed by Gunawardena *et al*. (33). The relation is given by equations [6-8].

$$j_m = 0.6382nFCD(kN)^{0.5} \quad [6]$$

$$j_m^2 t_m = 0.1629(nFC)^2 D \quad [7]$$

$$\mathrm{k} = (8\pi CM/\rho)^{0.5} \quad [8]$$

where the values of j_m and t_m are obtained from Figure 2, n is transferred electrons (0.75 mole for 1 mole $Al_2Cl_7^-$ diffusion), F is Faraday constant (96485C mol^{-1}), C is the concentration of $Al_2Cl_7^-$ (mol L^{-1}), D is diffusion coefficient (m^2 s^{-1}), k is a numerical constant, M is the atomic weight of aluminum (26.98 g mol^{-1}), ρ is the density of metallic aluminum (2700 g m^{-3}), and N is nucleation number density.

Based on the distribution of Al species in IL using the thermodynamic calculations (27) and the literature density data (34), the concentration of $Al_2Cl_7^-$ is calculated, which is listed in TABLE I.

TABLE I. Densities of BMIC-$AlCl_3$ IL and concentration of $Al_2Cl_7^-$ in the IL

Temperature (K)	Density × 10^6 (g m^{-3})	Concentration of $Al_2Cl_7^-$ (mol L^{-1})
353	1.29	2.34
363	1.28	2.32
373	1.27	2.30
383	1.26	2.28

Thus the average radius can be calculated based on the number density of nucleation (35) using equation [9].

$$r = (1/\pi N)^{0.5} \quad [9]$$

where r is the average radius (m), and N is the number density of nucleation (m^{-2}). And the calculated number density of nucleation at 363 K at different overpotentials is listed in TABLE II.

TABLE II. The calculated number density of nucleation (N) and the average radius (r) of the deposition of Al in BMIC-$AlCl_3$ at 363 K.

Potential (V) vs. Pt	N (m^{-2})	r (m)
-1.70	0.7×10^{10}	6.74×10^{-6}
-1.75	1.0×10^{10}	5.64×10^{-6}
-1.80	1.4×10^{10}	4.77×10^{-6}

As shown in TABLE II, the number density of nucleation is increased, while the average radius of deposition is decreased as the potential becomes more negative. To determine the influence of potential on the morphology of Al deposits, the electrodeposition experiments were performed on Ni plate at 363 K and different potentials (-1.7, -1.75, and -1.8 V vs. Pt). The working electrode and counter electrode used were Ni and Al plate in this experiment. The result is shown in Figure 4.

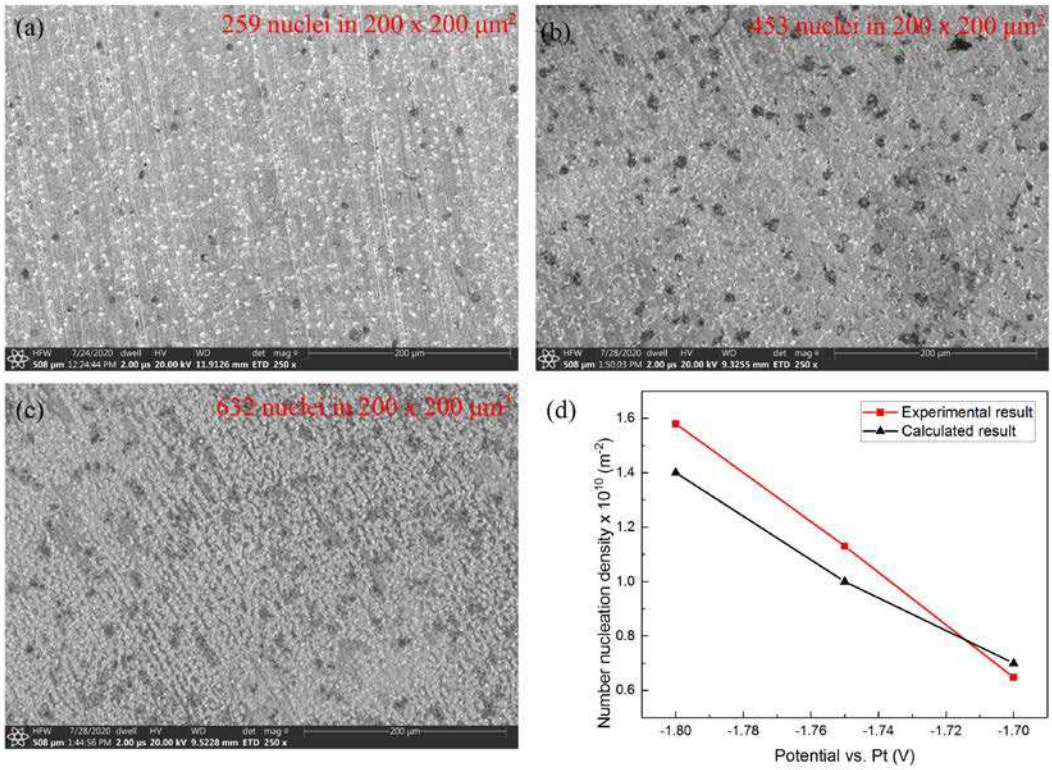

Figure 4. SEM micrographs of Al deposition on Ni substrates obtained in BMIC-$AlCl_3$ (1:2) IL for 1 min at 363 K and different potentials ((a) -1.7 V, (b) -1.75 V, and (c) -1.8 V) as well as (d) comparison of number nucleation density between experimental and calculated result.

As shown in Figure 4, the sphere depositions of Al are found on the Ni substrates at different constant potentials. In addition, the deposition is denser at a more negative potential. The number density of nucleation is counted in the 200 × 200 μm^2 area in the SEM micrographs and then calculated in 1 m^2 area. As shown in Figure 4(d), the calculated data (TABLE II) is comparable to the experimental result. The small difference may due to the formation of an exclusion zone in the model calculation (2).

The electrodeposition experiments were performed for different durations at -1.7 V vs. Pt at 363 K to investigate the growth rate of nucleation. And the result is shown in Figure 5.

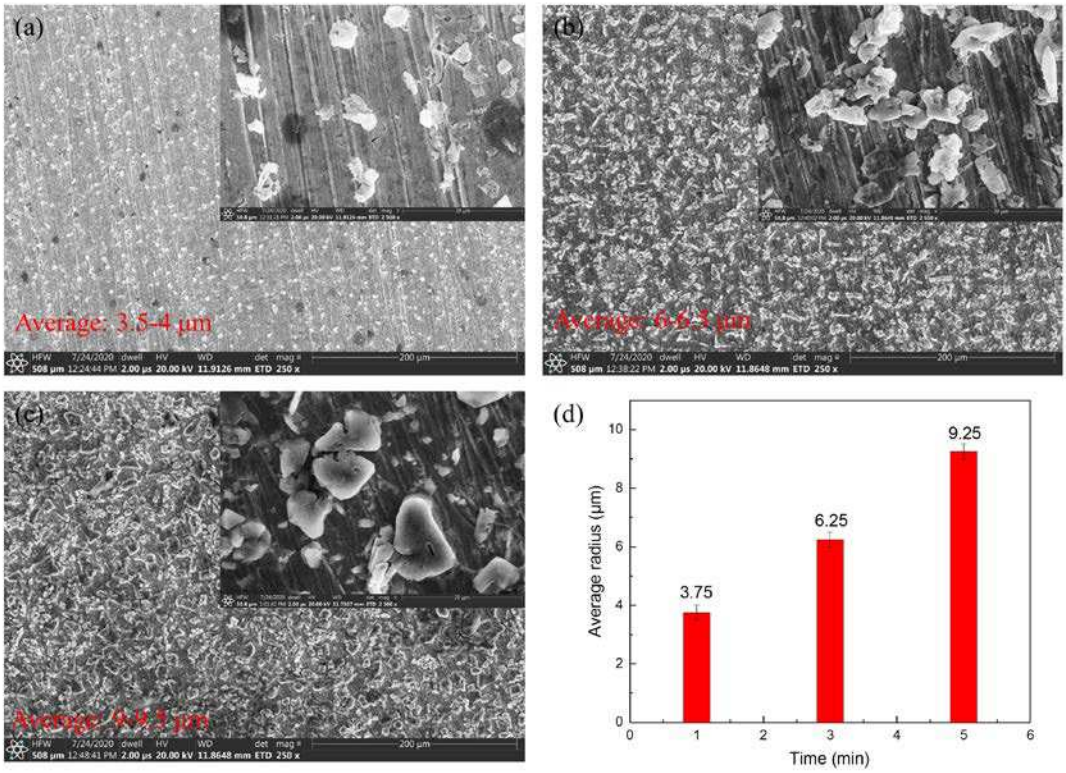

Figure 5. SEM micrographs of Al deposition on Ni substrates obtained in BMIC-$AlCl_3$ (1:2) IL at -1.7 V vs. Pt and 363 K for different time ((a) 1 min, (b) 3 min, and (c) 5 min); (d) a plot of the average radius of nucleation against time.

As shown in Figure 5, the average radius of the nucleation increases at a longer time and reaches to 9.25 μm for 5 min deposition. In addition, the growth rate is decreased for a long duration as the deposition becomes denser. The calculated average radius is 6.74 μm, as listed in TABLE II, which is slightly different from the experimental data. The little difference is due to the spherical grain assumed in the model calculation. In the real experiment, the deposition of nuclei growth is not spherical.

4. Conclusions

The nucleation process of Al electrodeposition in BMIC-$AlCl_3$ (1:2) is successfully evaluated by chronoamperometry in present work at different temperatures and different overpotentials. The result showed that deposition of Al involved in a three-dimension instantaneous nucleation process. In addition, the number density of nucleation is calculated at different applied potentials at 363 K based on the known concentration and diffusion coefficient of $Al_2Cl_7^-$ species. The morphological studies indicated that the deposition becomes denser at a more negative potential. And the number densities of nucleation are comparable between calculated and experimental results. Moreover, the growth rate of Al deposition is also studied in present work. It is found that the growth rate decreased for longer-time depositions. The calculated average nucleation radius is in a good agreement with experimental data.

Acknowledgments

The authors acknowledge the financial support received from the National Science Foundation (NSF) award number 1762522, Department of Energy (DOE) RAPID Manufacturing Institute and ACIPCO for this research project. Authors also thank the Department of Metallurgical and Materials Engineering, the University of Alabama for providing experimental and analytical facilities.

References

1. T. Jiang, M.C. Brym, G. Dubé, A. Lasia, G. Brisard, S*urf. Coat. Technol*. **201**(1-2) (2006) 10-18.
2. D. Pradhan, R.G. Reddy, *Mater. Chem. Phys*. **143**(2) (2014) 564-569.
3. R.G. Reddy, *J. Phase Equilib. Diff.* **27**(3) (2006) 210.
4. H. Yang, R.G. Reddy, *Electrochim. Acta* **178** (2015) 617-623.
5. R.T. Carlin, P.C. Trulove, H.C. De Long, *J. Electrochem. Soc.* **143**(9) (1996) 2747-2758.
6. J. Robinson, R. Osteryoung, *J. Electrochem. Soc.* **127**(1) (1980) 122-128.
7. P. Lai, M. Skyllas-Kazacos, *J. Electroanal. Chem. Interf. Electrochem.* **248**(2) (1988) 431-440.
8. D. Pradhan, R. Reddy, *Electrochim. Acta* **54**(6) (2009) 1874-1880.
9. D. Pradhan, R.G. Reddy, *Metall. Mater. Tran. B* **43**(3) (2012) 519-531.
10. P. Koronaios, D. King, R.A., *Inorg. Chem.* **37**(8) (1998) 2028-2032.
11. V. Kamavaram, D. Mantha, R. Reddy, *Electrochim. Acta* **50**(16-17) (2005) 3286-3295.
12. Q. Liao, W.R. Pitner, G. Stewart, C.L. Hussey, G.R. Stafford, *J. Electrochem. Soc.* **144**(3) (1997) 936.
13. Y. Zhao, T. VanderNoot, *Electrochim. Acta* **42**(11) (1997) 1639-1643.
14. T. Jiang, M.C. Brym, G. Dubé, A. Lasia, G. Brisard, *Surf. Coat. Technol.* **201**(1-2) (2006) 1-9.
15. J.D. Holbrey, W.M. Reichert, R.G. Reddy, R.D. Rogers, ACS Publications **856**(11) (2003) 121-133.
16. V. Kamavaram, R.G. Reddy, *Int. J. Therm. Sci.* **47**(6) (2008) 773-777.
17. R.G. Reddy, Z. Zhang, M.F. Arenas, D.M. Blake, *High Temp. Mater. Proc.* (London) **22**(2) (2003) 87-94.
18. V. Karmavaram, R.G. Reddy, Aluminum 2003, S.K. Das Ed., TMS, (2003) 299-308.
19. V. Kamavaram, R. Reddy, Light Metals 2005, TMS, Warrendale, PA (2005) 501-05.
20. R. Reddy, A. Yahya, L. Brewer, *J. Alloy. Compd.* **321**(2) (2001) 223-227.
21. M. Zhang, V. Kamavaram, R.G. Reddy, *J. Phase Equilib. Diff.* **26**(2) (2005) 124-130.
22. M.M. Zhang, R.G. Reddy, *Min. Proc. Ext. Met.* **119**(2) (2010) 71-76.
23. A. Liu, Z. Shi, R.G. Reddy, *Ionics* **26**(6) (2020) 3161-3172.
24. A. Liu, Z. Shi, R.G. Reddy, *Electrochim. Acta* **251** (2017) 176-186.
25. A. Liu, Z. Shi, R.G. Reddy, *J. Electrochem. Soc.* **164**(9) (2017) D666-D673.
26. M. Li, Z. Wang, R.G. Reddy, *J. Electrochem. Soc*. **161**(4) (2014) D150-D153.
27. V. Kamavaram, D. Mantha, R. Reddy, *J. Min. Metall. B* **39**(1-2) (2003) 43-58.

28. J. Tang, K. Azumi, *Electrochim. Acta* **56**(3) (2011) 1130-1137.
29. Y. Zheng, C. Peng, Y. Zheng, D. Tian, Y. Zuo, Y. Zheng, *Int. J. Electrochem. Sci.* **11** (2016) 6095-6109.
30. J.J. Lee, B. Miller, X. Shi, R. Kalish, K.A. Wheeler, *J. Electrochem. Soc.* **147**(9) (2000) 3370-3376.
31. H. Yang, R.G. Reddy, *J. Electrochem. Soc.* **161**(10) (2014) D586-D592.
32. B. Scharifker, G. Hills, *Electrochim. Acta* **28**(7) (1983) 879-889.
33. G. Gunawardena, G. Hills, I. Montenegro, *Electrochim. Acta* **23**(8) (1978) 693-697.
34. V. Kamavaram, Novel electrochemical refining of aluminum based materials in low temperature ionic liquid electrolytes, Dissertation, The University of Alabama, 2004.
35. R.T. Carlin, W. Crawford, M. Bersch, J. *Electrochem. Soc.* **139**(10) (1992) 2720-2727.

ECS Transactions, 98 (10) 209-214 (2020)
10.1149/09810.0209ecst ©The Electrochemical Society

Electrochemical Behavior of Silver Halogenocomplexes in an Amide-Type Ionic Liquid

Nobuyuki Serizawa, Suguru Kuwahara, and Yasushi Katayama

Department of Applied Chemistry, Faculty of Science and Technology, Keio University, 3-14-1 Hiyoshi, Kohoku-ku, Yokohama, Kanagawa 223-8522, Japan

The electrochemical behavior of halogenocomplexes of Ag was investigated in an amide-type ionic liquid, 1-butyl-1-methylpyrrolidinium bis(trifluoromethylsulfonyl)amide (BMPTFSA) in the presence of the corresponding halogen anion. Silver halides, AgX (X^- = Cl^-, Br^-, and I^-) were found to be soluble in BMPTFSA containing 0.5 M BMPX by forming $[AgX_3]^{2-}$. The cathodic reduction of $[AgX_3]^{2-}$ to metallic Ag was possible within the electrochemical window of BMPTFSA. The reduction potentials were in the order of $[AgCl_3]^{2-}$ > $[AgBr_3]^{2-}$ > $[AgI_3]^{2-}$. The morphology of Ag deposits depended on the reduction potential. The diffusion coefficients of $[AgCl_3]^{2-}$, $[AgBr_3]^{2-}$, and $[AgI_3]^{2-}$ were 2.5, 2.0, and 1.6 × 10^{-7} cm^2 s^{-1}, respectively. Formation of Ag nanoparticles dispersed in the ionic liquids was confirmed after potentiostatic cathodic reduction at –2.5 V using transmission electron microscopy.

Introduction

Amide-type ionic liquids composed of bis(trifluoromethylsulfonyl)amide anion ($TFSA^-$) have been investigated as an alternative electrolyte for electroplating because of wide electrochemical window, hydrophobicity, non-flammability, and low-volatility. Besides delivering deposits onto a substrate, metal nanoparticles can also be dispersed in an ionic liquid by the cathodic reduction at the negative potential (1). However, metal ions are introduced into the ionic liquids, in many cases, by dissolution of their $TFSA^-$ salts, which are expensive or commercially unavailable. It is desired to use such inexpensive and common metal salts as metal halides for practical application. We have already reported that some metal chlorides are soluble in an amide-type ionic liquid, BMPTFSA (BMP^+: 1-butyl-1-methylpyrrolidinium) in the presence of Cl^- and that electrodeposition of the metals is possible (2-6).

Silver halides, AgX (X^- = Cl^-, Br^-, and I^-), are not very soluble salts in aqueous solution. The solubility of AgCl is reported very low in an amide-type ionic liquid (7). However, AgX has been known to dissolve in such organic electrolytes as acetonitrile and dimethyl sulfoxide in the presence of X^- by forming halogenocomplexes, $[AgX_n]^{(n-1)-}$ (8, 9). Dissolution of AgCl has also been reported in basic chloroaluminate ionic liquids (10) and a deep eutectic solvent containing Cl^- (11).

Electrodeposition of Ag has been investigated some amide-type ionic liquids (12-17). However, electrochemical behavior of $[AgX_n]^{(n-1)-}$ has not been studied in the ionic liquids in the presence of X^-. In the present study, dissolution of AgX has been investigated in

BMPTFSA with addition of BMPX. Furthermore, electrodeposition of Ag and electrochemical preparation of Ag nanoparticles have been examined in the Lewis basic ionic liquids.

Experimental

BMPX were synthesized by the reaction of 1-methylpyrrolidine (Tokyo Chemical Industry) and butyl chloride (Fujifilm Wako Pure Chemical Corp.), butyl bromide (Tokyo Chemical Industry), or butyl iodide (Tokyo Chemical Industry) in acetonitrile (Junsei Chemical), respectively. 1-Methylpyrrolidine was purified by distillation under reduced pressure before use. BMPX was recrystallized from its acetonitrile solution using ethyl acetate (Junsei Chemical) and dried under vacuum. BMPTFSA was prepared by the metathesis reaction between LiTFSA (Solvay) and BMPBr. AgCl (Kojundo Chemical Laboratory), AgBr (Sigma Aldrich), and AgI (Fujifilm Wako Pure Chemical Corp.) were used as received.

Electrochemical measurements were conducted using a three-electrode cell at 323 K in an Ar-filled glove box (Miwa MFG, DBO-1KP-K03) with a continuous gas purification apparatus. Glassy Carbon (GC, Tokai Carbon) was used as a working electrode. Ag wire was used as a counter electrode. Ag wire immersed in BMPTFSA containing 0.1 M $AgCF_3SO_3$ (Sigma Aldrich) was used as a reference electrode. The inner electrolyte of the reference electrode was isolated from the sample electrolyte with a porous glass (Vycor). The equilibrium potential of the reference electrode, denoted as Ag|Ag(I) in this paper, was +0.43 V vs. ferrocene|ferrocenium in BMPTFSA at 298 K (18). The potentiostatic anodic dissolution of Ag wire was conducted at –0.8 V vs. Ag|Ag(I) using a two-compartment cell separated by a porous glass filter with a Pt counter electrode.

Ag deposits obtained by galvanostatic or potentiostatic electrodeposition were characterized by a scanning electron microscope (SEM, Keyence, VE-9800, detector: secondary electron) and an X-ray diffractometer (XRD, Rigaku, MiniFlex 600) after washing the sample with acetonitrile. Ag nanoparticles dispersed in the ionic liquids were characterized by a transmission electron microscope (TEM, FEI, TECNAI F20) equipped with an energy dispersive X-ray analyzer (EDX, Oxford Instruments, X-Mat 80T). The ionic liquids after potentiostatic electrolysis were dropped on a TEM grid. The excess ionic liquid was removed by washing with acetonitrile.

Results and Discussion

AgX was found to dissolve in 0.5 M BMPX/BMPTFSA at 323 K, suggesting the formation of some halogenocomplexes, $[AgX_n]^{(n-1)-}$. Figure 1 shows the cyclic voltammograms of a GC electrode in 0.5 M BMPX/BMPTFSA containing 50 mM AgX. A pair of cathodic and anodic current peaks was observed in each ionic liquid. The deposits on a GC substrate after potentiostatic cathodic reduction at –2.0 V were identified as metallic silver by XRD, indicating the cathodic and anodic reactions were attributed to the electrodeposition of Ag from $[AgX_n]^{(n-1)-}$ and the dissolution of Ag deposited during the preceding cathodic scan, respectively.

$$[AgX_n]^{(n-1)-} + e^- \rightleftharpoons Ag(s) + n[X^-] \quad [1]$$

The current crossover corresponding to the 3-dimensional nucleation of deposits was observed in each CV, suggesting the overpotential for the nucleation of Ag on a GC electrode was large regardless of the kind of halide.

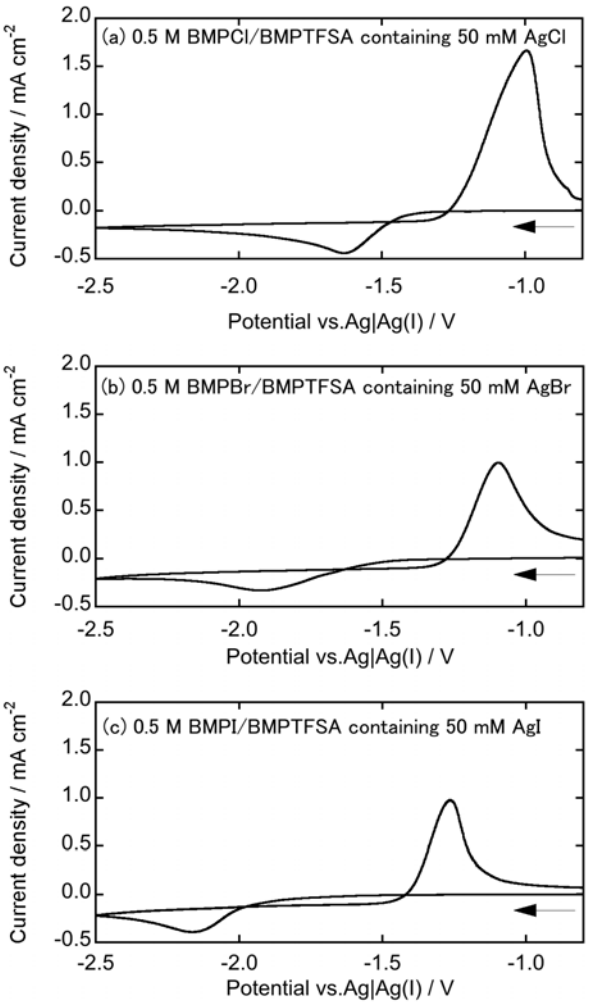

Figure 1. Cyclic voltammograms of a GC electrode in 0.5 M BMPX/BMPTFSA containing 50 mM AgX at 323 K (X^- = Cl^-, Br^-, and I^-). Scan rate: 10 mV s^{-1}.

In order to determine the dissolved species of Ag(I) in the ionic liquids, the open circuit potentials of a Ag electrode were measured in 0.5 M BMPX/BMPTFSA containing different concentrations of Ag(I). Ag(I) was introduced into the ionic liquids by the potentiostatic anodic dissolution of Ag assuming the current efficiency of 100%. The formation of some halogenocomplexes can be described as the following equilibrium.

$$Ag^+ + n[X^-] \rightleftharpoons [AgX_n]^{(n-1)-} \quad [2]$$

The open circuit potentials are expected to reflect the concentration of $[AgX_n]^{(n-1)-}$ and X^- according to the Nernst equation for reaction [1]. Figure 2 shows the Nernst plot of a Ag

electrode in 0.5 M BMPBr/BMPTFSA. The slope of the Nernst plot (64 mV decade^{-1}) was closest to the theoretical value of an one-electron transfer reaction at 323 K (64 mV decade^{-1}) assuming the formation of $[AgBr_3]^{2-}$ (n = 3). The similar results were obtained for BMPTFSA containing BMPCl and BMPI, suggesting the dissolved species of Ag(I) in 0.5 M BMPX/BMPTFSA was $[AgX_3]^{2-}$. On the other hand, $[AgCl_2]^-$ (n = 2) was reported as the predominant chlorocomplex in acetonitrile containing Cl^- (8). Both $[AgCl_2]^-$ and $[AgCl_3]^{2-}$ were detected in a deep eutectic solvent composed of choline chloride and ethylene glycol by extended X-ray absorption fine structure (EXAFS) analysis (11). The dissolved species of Ag(I) were determined as $[AgCl_2]^-$, $[AgCl_3]^{2-}$, and $[AgCl_4]^{3-}$ in basic chloroaluminate ionic liquids composed of butylpyridinium or 1-methyl-3-ethylimidazolium by the potentiostatic titration of Cl^-, although the concentrations of these chlorocomplexes depended on the basicity of the chloroaluminate ionic liquids (10). As the same manner, the coordination number of Ag^+ in BMPX/BMPTFSA possibly depends on the concentration of free X^- in the electrolyte.

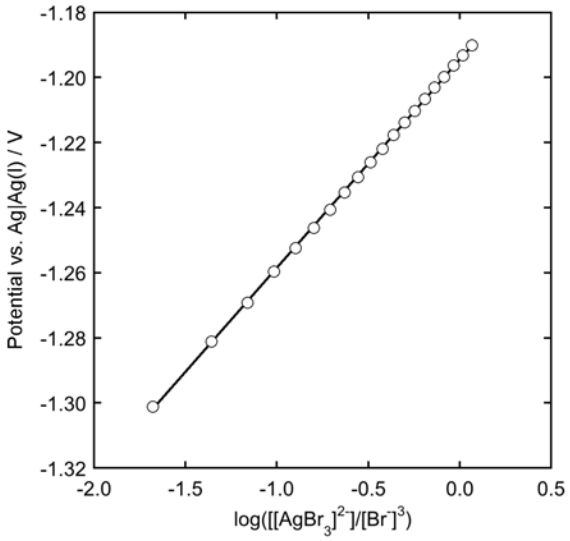

Figure 2. Open circuit potentials of a Ag electrode in 0.5 M BMPBr/BMPTFSA with different concentrations of Ag(I) at 323 K.

The reduction potentials of these halogenocomplexes were more negative than that of $[Ag(TFSA)_3]^{2-}$, reflecting the difference in the donor properties of X^- and $TFSA^-$ (16, 19). The reduction potentials were in the order of $[AgCl_3]^{2-} > [AgBr_3]^{2-} > [AgI_3]^{2-}$, suggesting the formation of $[AgI_3]^{2-}$ was most stable among these halogenocomplexes in 0.5 M BMPX/BMPTFSA. The same order of the reduction potentials was reported in dimethyl sulfoxide, while the coordination number of Ag^+ was not determined (9).

The diffusion coefficients of $[AgX_3]^{2-}$ were determined by chronoamperometry. The diffusion coefficients of $[AgCl_3]^{2-}$, $[AgBr_3]^{2-}$, and $[AgI_3]^{2-}$ were 2.5, 2.0, and 1.6 × 10^{-7} cm^2 s^{-1}, respectively, at 323 K. The difference in the diffusion coefficients probably reflected the viscosity of the electrolytes and the sizes of $[AgX_3]^{2-}$.

Figure 3 shows the SEM images of the Ag deposits obtained by galvanostatic electrodeposition at –30 μA cm^{-2}. Granular deposits were observed regardless of the kind

of halide. On the other hand, the morphology of the Ag deposits obtained by potentiostatic electrodeposition strongly depended on the reduction potential as is the case for the deposits from $[Ag(TFSA)_3]^{2-}$ in BMPTFSA (16). The dendritic deposits were obtained at negative potentials, suggesting the accumulation of BMP^+ on the negatively charged GC electrode hindered the nucleation of Ag.

Nanoparticles were found to be dispersed in the ionic liquids after potentiostatic cathodic reduction of $[AgX_3]^{2-}$ at –2.5 V. The TEM image of the nanoparticles obtained in 0.5 M BMPBr/BMPTFSA containing 10 mM AgBr is shown in Fig. 4. The EDX spectrum of the nanoparticles indicated these nanoparticles contained Ag.

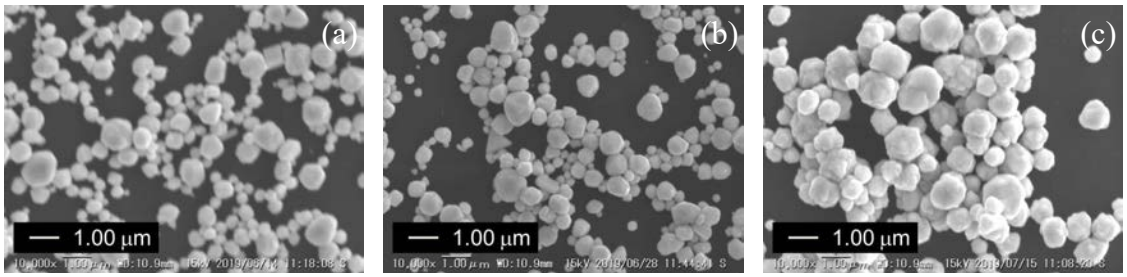

Figure 3. SEM images of Ag deposits on a GC substrate obtained by galvanostatic cathodic reduction of (a) $[AgCl_3]^{2-}$, (b) $[AgBr_3]^{2-}$, and (c) $[AgI_3]^{2-}$ in 0.5 M BMPX/BMPTFSA containing 50 mM AgX at 323 K. Current density: –30 μA cm^{-2}. Electric charge: 1.0 C cm^{-2}.

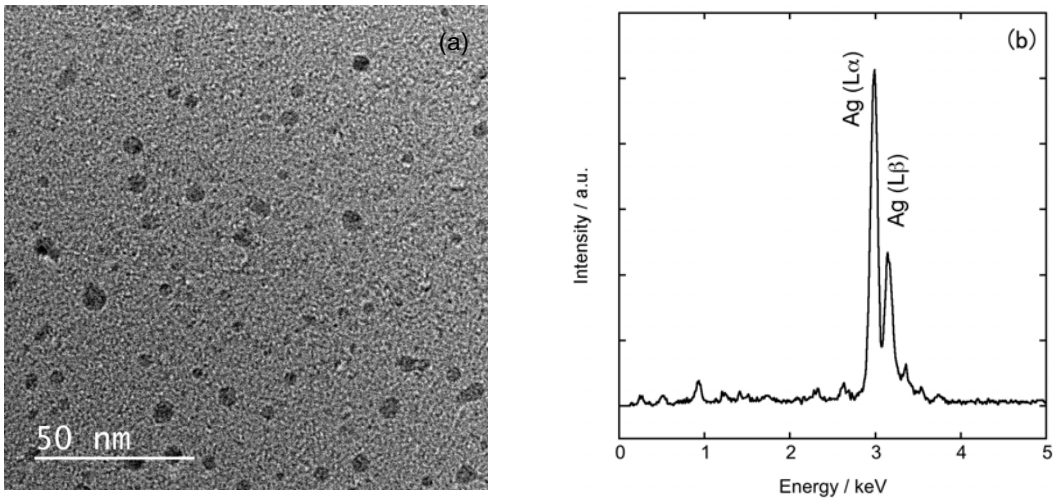

Figure 4. TEM image (a) and EDX spectrum (b) of the silver nanoparticles obtained after potentiostatic cathodic reduction at –2.5 V vs. Ag|Ag(I) in 0.5 M BMPBr/BMPTFSA containing 10 mM AgBr at 323 K.

Acknowledgments

Part of this study was supported by the Impulsing Paradigm Change through Disruptive Technologies Program (ImPACT) from Cabinet Office, Government of Japan.

References

1. M. H. G. Prechtl (Ed.) *Nanocatalysis in Ionic Liquids*, 1st edition, Wiley-VCH Verlag GmbH & Co. kGaA, Weinheim, p. 207 (2017).
2. Y. Bando, Y. Katayama, and T. Miura, *Electrochim. Acta*, **53**, 87 (2007).
3. S. Saha, N. Tachikawa, K. Yoshii, and Y. Katayama, *J. Electrochem. Soc*., **163**, D259 (2016).
4. S. Saha, N. Tachikawa, K. Yoshii, N. Serizawa, and Y. Katayama, *Electrochemistry*, **86**, 229 (2018).
5. M. Sano, N. Tachikawa, K. Yoshii, N. Serizawa, and Y. Katayama, *Electrochemistry*, **86**, 260 (2018).
6. K. Ando, N. Tachikawa, N. Serizawa, and Y. Katayama, *J. Electrochem. Soc*., **167**, 062505 (2020).
7. T. Kakiuchi, T. Yoshimatsu, and N. Nishi, *Anal. Chem*., **79**, 7187 (2007).
8. M. Skompska, M. A. Vorotyntsev, A. Rajchowska, and O. V. Levin, *Phys. Chem. Chem. Phys*., **12**, 10525 (2010).
9. R. Kimura, A. Tsuboi, K. Nakamura, and K. Kobayashi, *Sol. Energy Mater. Sol. Cells*, **177**, 128 (2018).
10. T. M. Laher and C. L. Hussey, *Inorg. Chem*., **22**, 1279 (1983).
11. A. P. Abbott, K. E. Ttaib, G. Frisch, K. S. Ryder, and D. Weston, *Phys. Chem. Chem. Phys*., **14**, 2443 (2012).
12. E. I. Rogers, D. S. Silvester, S. E.W. Jones, L. Aldous, C. Hardacre, A. J. Russell, S. G. Davies, and R. G. Compton, *J. Phys. Chem. C*, **111**, 13957 (2007).
13. N. Serizawa, Y. Katayama, and T. Miura, *J. Electrochem. Soc*., **156**, D503 (2009).
14. N. Serizawa, Y. Katayama, and T. Miura, *Electrochim. Acta*, **56**, 346 (2010).
15. A. Ispas, M. Pölleth, K. H. T. Ba, A. Bund, and J. Janek, *Electrochim. Acta*, **56**, 10332 (2011).
16. R. Fukui, Y. Katayama, and T. Miura, *J. Electrochem. Soc*., **158**, D567 (2011).
17. T. Uematsu, J-T. Han, T. Tsuda, and S. Kuwabata, *J. Phys. Chem. C*., **116**, 20902 (2012).
18. Y. Yamato, Y. Katayama, and T. Miura, *J. Electrochem. Soc*., **160**, H309 (2013).
19. T. Liu, Y. Danten, J. Grondin, and R. Vilar, *J. Raman Spectrosc*., **47**, 449 (2016).

ECS Transactions, 98 (10) 215-222 (2020)
10.1149/09810.0215ecst ©The Electrochemical Society

Dissolution Behavior of SiO_2 and Electrochemical Reduction of Dissolved SiO_2 in Molten Chlorides

Y. Ma[a], T. Yamamoto[a], K. Yasuda[b, c, *], and T. Nohira[a]

[a] Institute of Advanced Energy, Kyoto University, Uji 611-0011, Japan
[b] Agency for Health, Safety and Environment, Kyoto 606-8501, Japan
[c] Graduate School of Energy Science, Kyoto University, Kyoto 606-8501, Japan
[*] Present address: Graduate School of Engineering, Kyoto University, Kyoto 606-8501, Japan

To develop a new production process for SOG-Si with high productivity and low energy consumption, the structure of silicate ions in molten eutectic NaCl–$CaCl_2$ containing dissolved SiO_2 was investigated by Raman spectroscopy. The existence of SiO_3^{2-} was indicated in melts containing 1.0 mol% of $CaSiO_3$ ($O^{2-}/SiO_2 = 1.0$). When 1.0 mol% of CaO was further added to the melt ($O^{2-}/SiO_2 = 2.0$), the existence of SiO_4^{4-} was indicated. Cyclic voltammetry and potentiostatic electrolysis were conducted in molten NaCl–$CaCl_2$ with different silicate ions. From cyclic voltammograms, XRD analysis and SEM observation, silicate ions with different structure indicated different electrochemical reduction behavior; and the SiO_3^{2-} ion is likely to be more suitable than SiO_4^{4-} ion for the electrodeposition of Si.

Introduction

Photovoltaic (PV) power generation is considered as a source of clean and inexhaustible energy, which could substitute the conventional fossil-fuel power generation. The global production of PV cells achieved 102.4 GW in 2018, approximately 350 times the value in 2000 (1). Since crystalline silicon solar cells accounted for 96.9 % of the worldwide production in 2018 (2), they are expected to remain mainstream in the PV industry for the time being. Thus, the global demand for high-purity crystalline Si, which is known as solar-grade Si (SOG-Si), will also continue to increase in the future.

To develop a new production process for SOG-Si, experimental studies such as purification of metallurgical-grade silicon (3) and metallothermic reduction of silicon halides by metal reductants (4) have been conducted. Over the past two decades, we have been studying the electrochemical reduction of solid SiO_2 to Si in molten $CaCl_2$ to as a new production process for SOG-Si (5–7). In molten $CaCl_2$, electrochemical reduction of insulating SiO_2 proceeds by using a SiO_2 contacting electrode, which provides a three-phase interface of conductor/SiO_2/$CaCl_2$.

$$SiO_2(s) + 4\ e^- \rightarrow Si(s) + 2\ O^{2-} \qquad [1]$$

With the aim of efficient recovery of reduced Si, we also proposed an electrochemical reduction process of SiO_2 using a liquid Zn cathode in molten $CaCl_2$ (8–10). The overall process consists of three major steps: electrolysis, precipitation, and refining. In the

electrolysis step, solid SiO_2 is reduced to form Si–Zn liquid alloy. Then, solid Si is precipitated by decreasing the temperature of the liquid Si–Zn alloy in the precipitation step. The recovered Si is subjected to a refining step that comprises vacuum refining to remove residual Zn and directional solidification to manufacture SOG-Si ingots.

In our previous study, we found that direct electrochemical reduction of SiO_2 mainly occurred at the three-phase interface of $Zn/SiO_2/CaCl_2$. Although, the liquid Ca–Zn alloy, which formed at negative potentials, also contributed to the indirect reduction of SiO_2 below the $Zn/CaCl_2$ interface, i.e. in the liquid Zn cathode, the current efficiency was low since only part of Ca–Zn alloy contributed to the reduction of SiO_2 (10). In order to improve the productivity of the process, we focused on the electrochemical reduction of dissolved SiO_2, i.e., silicate ions (SiO_4^{4-}, SiO_3^{2-}, $Si_2O_5^{2-}$ etc.). When O^{2-} ion is added into molten salt, the dissolution of SiO_2 could be expressed as

$$x\ SiO_2(s) + y\ O^{2-} \rightarrow Si_xO_{(2x+y)}^{2y-} \qquad [2]$$

Electrodeposition of crystalline Si film from silicate ions has been reported by Bard and co-workers (11, 12). However, the structure of silicate ions has not been investigated.

In the present study, we focused on eutectic $NaCl–CaCl_2$, which has a lower melting point (777 K) than that of pure $CaCl_2$ (1045 K). The structure of silicate ions in molten eutectic $NaCl–CaCl_2$ with various concentrations of CaO was investigated by Raman spectroscopy. In our previous study, we have found that the structure of dissolved SiO_2 is identical to that of dissolved $CaSiO_3$ when the ratio of O^{2-}/SiO_2 is less than 1.0. Thus, $CaSiO_3$ was used as the source of SiO_3^{2-} ion, and CaO as the source of O^{2-} ion in this study. Also, electrochemical reduction of silicate ions was investigated at a solid graphite substrate, as the preliminary study for liquid Zn cathode.

Experimental

All experiments were conducted in a dry Ar atmosphere at 1023 K.

Structural Analysis of Silicate Ions by Raman Spectroscopy

NaCl and $CaCl_2$ powders (FUJIFILM Wako Pure Chemical Corp., reagent grade) were mixed in an eutectic composition ($NaCl:CaCl_2$ = 47.9:52.1 mol%), and then certain amounts of CaO (FUJIFILM Wako Pure Chemical Corp., reagent grade, 0 or 1.0 mol%) and $CaSiO_3$ (ALDRICH Chemistry, 200 mesh, 99%, 1.0 mol%) powders were added to the eutectic mixture. The mixture was loaded into a graphite crucible (Toyo Tanso Co., Ltd., IG-110 grade, o.d. 55 mm × i.d. 49 mm × height 150 mm) and dried under vacuum at 453 K for 2 days, then 723 K for 1 day. After the temperature was raised to 1023 K and maintained at that temperature for 1 day to sufficiently dissolve CaO and $CaSiO_3$, the salt was sampled by a Pyrex tube.

The sampled salt was then loaded into a Pt pan (Rigaku Corp., o.d. 5 mm × height 2.5 mm) and was placed in an air-tight high-temperature stage (Japan High Tech Co., Ltd., 10042). After the mixture was heated to 1023 K, the structure of silicate ions was investigated by Raman spectroscopy (Tokyo Instruments, Nanofinder 30). Figure 1 shows a schematic drawing of experimental apparatus for Raman spectroscopy.

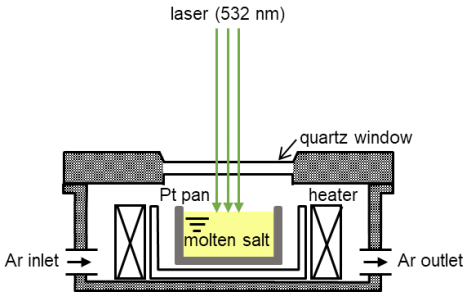

Figure 1. Schematic illustration of experimental apparatus for Raman spectroscopy of molten salt.

Electrochemical Reduction of Silicate Ions

NaCl and $CaCl_2$ powders were mixed in an eutectic composition and loaded into a graphite crucible (Toyo Tanso Co., Ltd., IG-110 grade, o.d. 80 mm × i.d. 70 mm × height 200 mm). The eutectic mixture was dried under vacuum at 453 K for 2 days and 723 K for 1 day. After the temperature was raised to 1023 K, certain amounts of CaO (0 or 1.0 mol%) and $CaSiO_3$ (1.0 mol%) powders were added to the eutectic mixture.

Figure 2 shows a schematic drawing of experimental apparatus for electrochemical reduction of silicate ions. As the working electrodes, a flag-like graphite plate (Toyo Tanso Co., Ltd., 3 mm × 3 mm × thickness 0.5 mm) was used for cyclic voltammetry and that with a size of 10 mm × 10 mm was used for electrolysis. The counter electrodes were glass-like carbon (Tokai Carbon Co., Ltd., diam.: 3.0 mm) for cyclic voltammetry and graphite square bar (Toyo Tanso Co., Ltd., 5 mm × 5 mm × height 50 mm) for electrolysis. A Si square bar (Furuuchi Chemical Corp., 5 mm × 5 mm × height 50 mm, 10 N) was used as the reference electrode.

The obtained samples were washed in a HCl solution (pH = 1) at 333 K and analyzed by X-ray diffraction (XRD, Rigaku, Ultima 4, Cu-*K*α, λ = 1.5418 Å, 40 kV, 40 mA) and SEM (Phenom, Pro-SED).

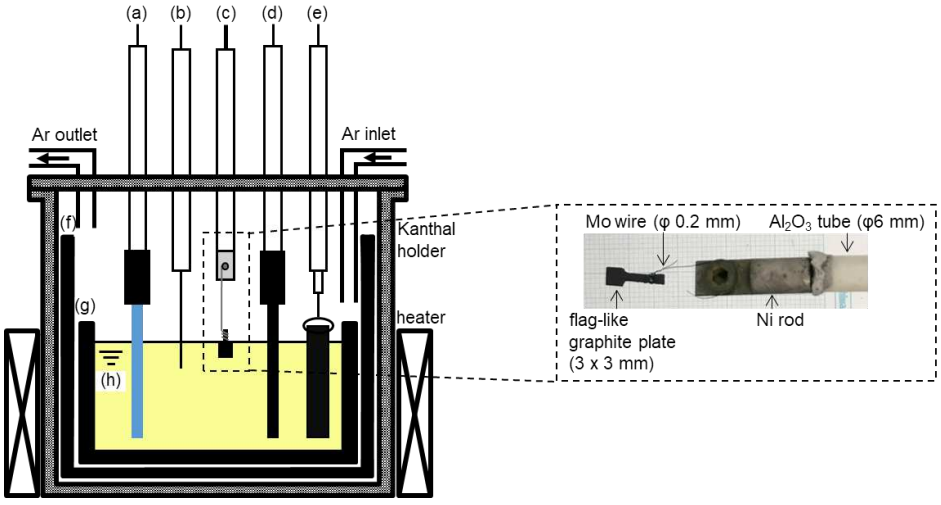

Figure 2. Schematic illustration of the electrolysis cell. (a) Si reference electrode, (b) Na^+/Na dynamic reference electrode on a Mo wire, (c) flag-like graphite working electrode, (d) glass-like carbon counter electrode, (e) graphite counter electrode, (f) graphite holder, (g) graphite crucible, and (h) molten NaCl–$CaCl_2$ containing CaO and $CaSiO_3$.

Results and Discussion

Structure of Silicate Ions

Figure 3 shows Raman spectra of molten (a) NaCl–$CaCl_2$–1.0 mol% $CaSiO_3$ and (b) NaCl–$CaCl_2$–1.0 mol% CaO–1.0 mol% $CaSiO_3$ at 1023 K. Within the wave number range of 700–1200 cm^{-1}, a strong band at 972 cm^{-1} and weak bands at 915, 1051 cm^{-1} were observed for molten salt (a). On the other hand, a strong band was detected at 830 cm^{-1} for molten salt (b). The main Raman bands for the stretch vibration of Si–O structures have been reported as 850–870 cm^{-1} for SiO_4^{4-}, 905–920 cm^{-1} for $Si_2O_7^{6-}$, 950–970 cm^{-1} for SiO_3^{2-}, and 1050–1100 cm^{-1} for $Si_2O_5^{2-}$, respectively (13–17). Therefore, the main structure is SiO_3^{2-} in molten salt (a) and SiO_4^{4-} in molten salt (b), which is consistent well with the O^{2-}/SiO_2 ratio in the melts. The weak bands of $Si_2O_7^{6-}$ and $Si_2O_5^{2-}$ ions are observed due to the disproportionation reaction of SiO_3^{2-} ion (reaction [3]).

$$4\ SiO_3^{2-} \rightarrow Si_2O_7^{6-} + Si_2O_5^{2-} \qquad [3]$$

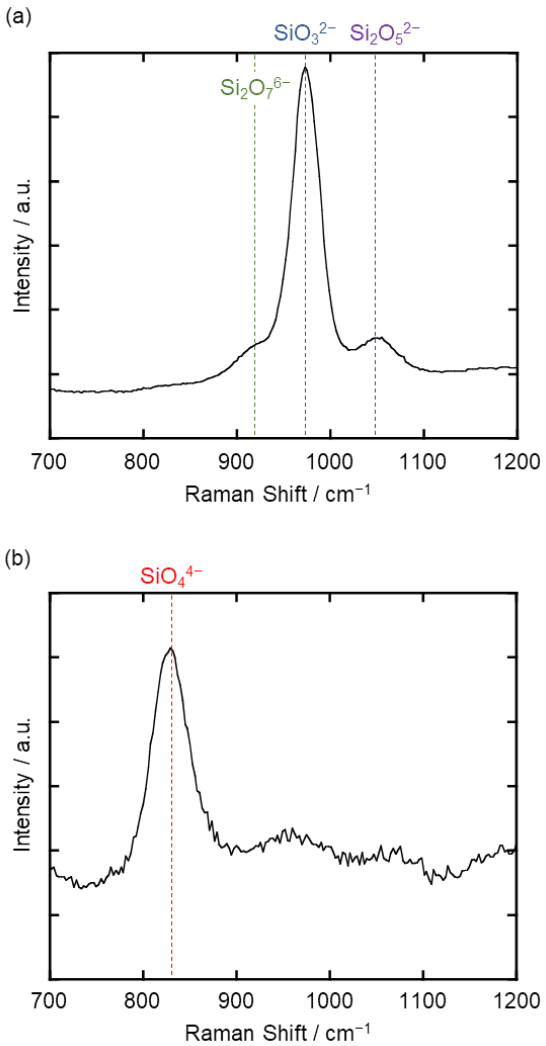

Figure 3. Raman spectra of molten NaCl–$CaCl_2$ containing (a) 1.0 mol% $CaSiO_3$, and (b) 1.0 mol% CaO–1.0 mol% $CaSiO_3$ at 1023 K.

Electrochemical Reduction of Silicate Ions

Figure 4 (a) shows cyclic voltammograms at a graphite electrode in molten NaCl–$CaCl_2$ before and after the addition of 1.0 mol% of $CaSiO_3$. The cathodic current observed in blank melt is likely due to the intercalation of Na or Ca metal into graphite. After the addition of $CaSiO_3$, cathodic currents increase from 1.2 V (vs. Na^+/Na), suggesting the electrochemical reduction of SiO_3^{2-} ion. The sharp increase in cathodic current around 0.6 V is considered as the formation of Na–Si or Ca–Si alloy. Figure 4 (b) shows the voltammogram measured after the addition of 1.0 mol% of CaO and 1.0 mol% $CaSiO_3$. Cathodic currents were observed from the rest potential (1.8 V), which suggests the electrochemical reduction of SiO_4^{4-} ion. The sharp increase from 0.6 V is supposed to be the same as that for SiO_3^{2-} ion in Figure 4 (a).

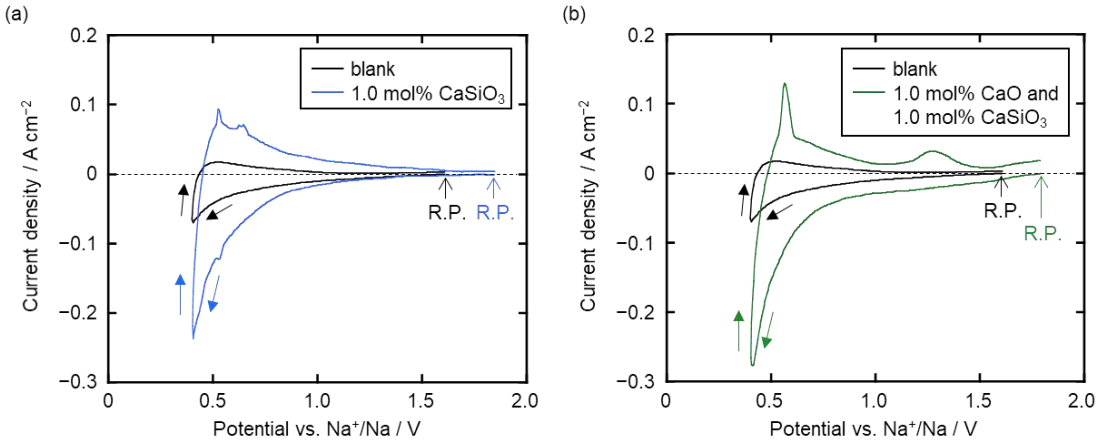

Figure 4. Cyclic voltammograms at a graphite electrode in molten NaCl–$CaCl_2$ before and after the addition of (a) 1.0 mol% of $CaSiO_3$, and (b) 1.0 mol% of CaO and 1.0 mol% of $CaSiO_3$ at 1023 K. Scan rate: 50 mV s^{-1}.

On the basis of the voltammetric results, potentiostatic electrolysis was conducted at 0.90, 0.70, and 0.50 V for −14 C cm^{-2} in molten NaCl–$CaCl_2$ containing 1.0 mol% of $CaSiO_3$ (molten salt (a)), and 1.0 mol% of CaO and 1.0 mol% of $CaSiO_3$ (molten salt (b)). The optical images of the graphite substrate and electrolyzed samples are shown in Figure 5. For samples obtained in molten salt (a), small amount of deposits were observed at 0.90 V and 0.50 V, and quite amount of deposit in brown color at 0.70 V. For samples obtained in (b), no significant deposit was observed at 0.90 V, deposits in brown and gray colors were obtained at 0.70 V, and deposit in gray color at 0.50 V.

Figure 6 shows XRD patterns of a graphite substrate and the electrolyzed samples. For samples obtained at 0.90 and 0.70 V in molten salt (a), the formation of Si was confirmed, indicating that the increase in cathodic current from 1.2 V in Figure 4 (a) is the electrochemical reduction of SiO_3^{2-} ion to solid Si.

$$SiO_3^{2-} + 4\ e^- \rightarrow Si(s) + 3\ O^{2-} \qquad [4]$$

Since $CaSi_2$ was identified for the sample at 0.50 V, the sharp increase from 0.6 V corresponds the formation of $CaSi_2$.

$$2\ Si(s) + Ca^{2+} + 2\ e^- \rightarrow CaSi_2(s) \qquad [5]$$

For samples obtained in molten salt (b), only graphite was detected at 0.90 V. The existence of Si was confirmed at 0.70 V, and both Si and $CaSi_2$ were detected at 0.50 V. Since Si deposition was only observed at potentials more negative than 0.70 V, the electrochemical reduction of SiO_4^{4-} ion to Si is considered to be more difficult than that of SiO_3^{2-} ion. Similarly, the formation of $CaSi_2$ seems to be less favorable for SiO_4^{4-} ion compared with SiO_3^{2-} ion.

Figure 7 shows surface SEM images of deposits. In molten salt (a), wire-like Si was obtained at 0.90 V and particle Si at 0.70 V. Dense $CaSi_2$ was observed at 0.50 V. For samples obtained in molten salt (b), wire-like Si was observed at 0.70 V and particle Si at 0.50 V.

From the results of XRD and SEM, the electrodeposition of Si from SiO_3^{2-} ion started from a more positive potential than that of SiO_4^{4-} ion. Thus, SiO_3^{2-} ion will be more suitable for the electrodeposition of Si at liquid Zn cathode as well as at solid graphite electrode.

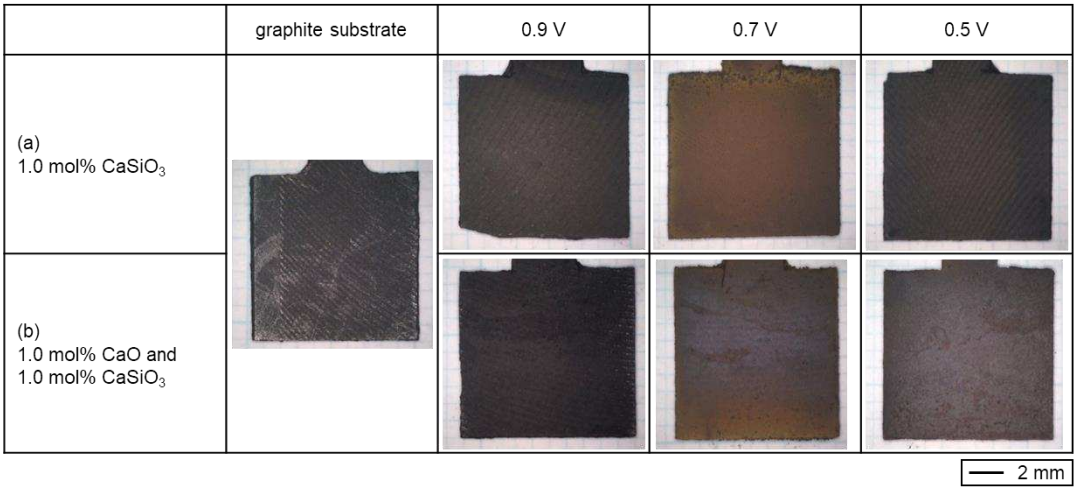

Figure 5. Optical images of the graphite substrate and samples obtained by electrolysis at graphite plates in molten NaCl–$CaCl_2$ containing (a) 1.0 mol% of $CaSiO_3$, and (b) 1.0 mol% of CaO and 1.0 mol% of $CaSiO_3$. Charge density: −14 C cm^{-2}.

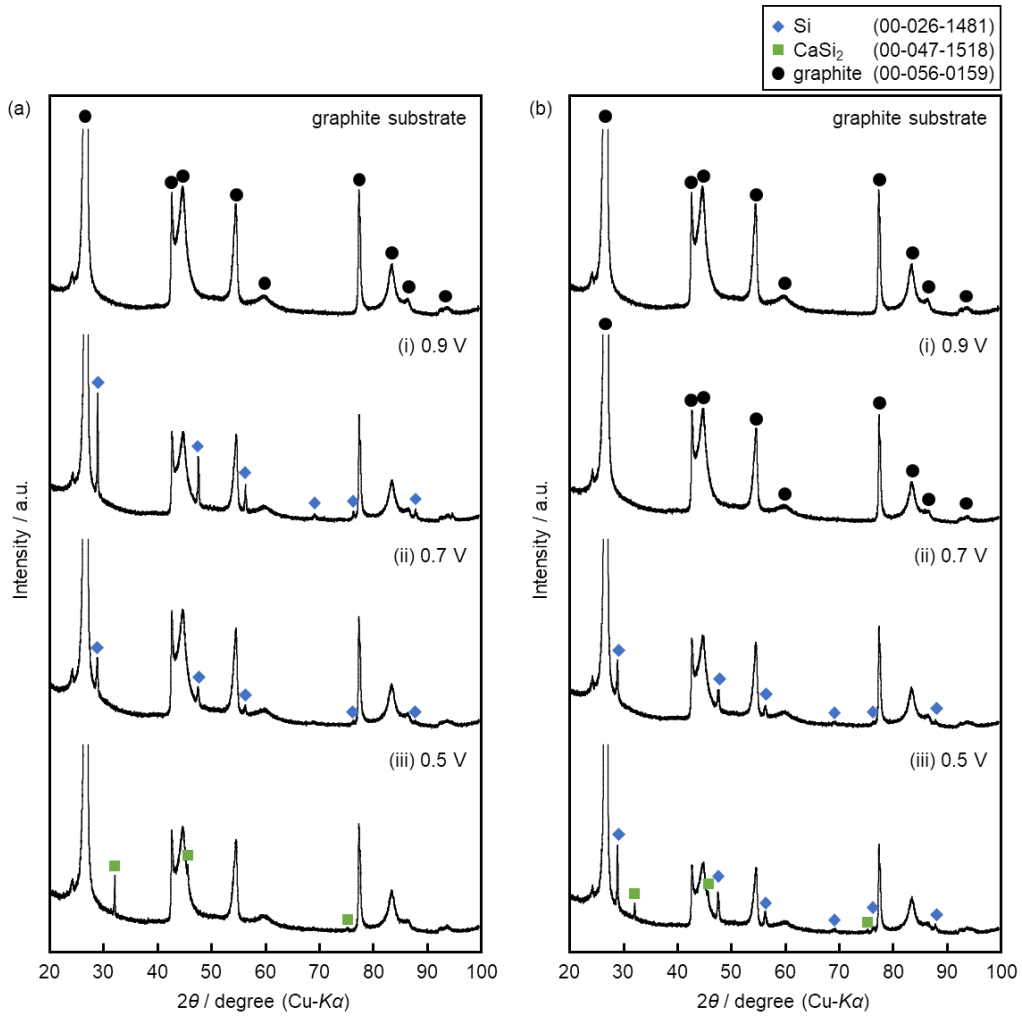

Figure 6. XRD patterns of the graphite substrate and samples obtained by electrolysis at graphite plates in molten NaCl–$CaCl_2$ containing (a) 1.0 mol% of $CaSiO_3$, and (b) 1.0 mol% of CaO and 1.0 mol% of $CaSiO_3$. Charge density: −14 C cm^{-2}.

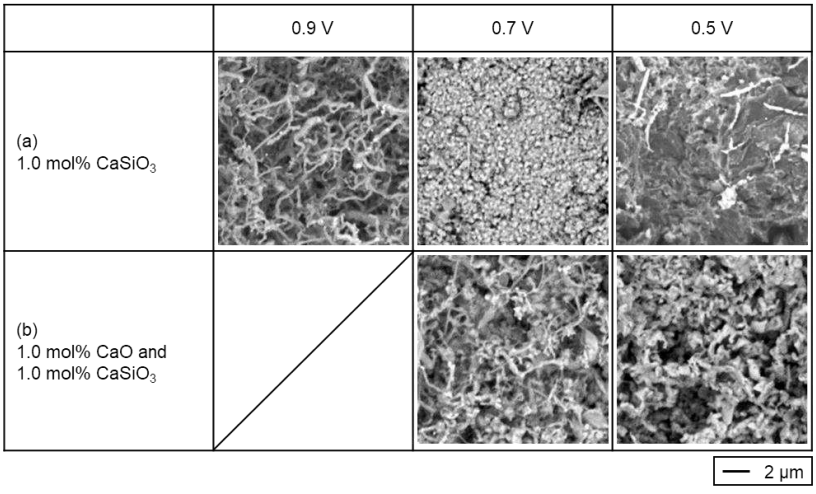

Figure 7. SEM images of the samples obtained by electrolysis at graphite plates in molten NaCl–$CaCl_2$ containing (a) 1.0 mol% of $CaSiO_3$, and (b) 1.0 mol% of CaO and 1.0 mol% of $CaSiO_3$. Charge density: −14 C cm^{-2}.

Conclusion

The structural analysis and electrochemical reduction of silicate ions at the solid graphite substrate were conducted as the preliminary study for liquid Zn cathode. The structure of silicate ions in molten NaCl–$CaCl_2$ containing (a) 1.0 mol% of $CaSiO_3$ and (b) 1.0 mol% of CaO and 1.0 mol% of $CaSiO_3$ was investigated by Raman spectroscopy. The main structure is SiO_3^{2-} ion in molten salt (a) and SiO_4^{4-} ion in molten salt (b), which is consistent well with the O^{2-}/SiO_2 ratio in the melts. In molten salt (a), electrodeposition of Si was confirmed at 0.70–0.90 V and formation of $CaSi_2$ at 0.50 V. In molten salt (b), pure Si deposition was only confirmed at 0.70 V and the mixture of Si and $CaSi_2$ was observed at 0.50 V. Thus, SiO_3^{2-} ion is likely to be more suitable for the electrodeposition of Si at liquid Zn cathode as well as at solid graphite electrode.

Acknowledgement

This study was partially supported by Grant-in-Aid for Scientific Research A, Grant Number 16H02410, from the Japan Society for the Promotion of Science (JSPS) and the Joint Usage/Research Program on Zero-Emission Energy Research, Institute of Advanced Energy, Kyoto University (ZE30A-04, ZE31A-05).

Reference

1. *Industrial Rare Metal 2019*, Arumu Publ. Co. (2019).
2. *Photovoltaic Market 2019*, RTS Corp. (2019).
3. X. Ma, T. Yoshikawa and K. Morita, *Sep. Purif. Technol.*, **125**, 264 (2014).
4. S. Honda, M. Yasueda, S. Hayashida and M. Yamaguchi: Japanese Patent, Toku Kai H19-145663 (2007).
5. T. Nohira, K. Yasuda and Y. Ito, *Nat. Mater.*, **2**, 397 (2003).
6. K. Yasuda, T. Nohira, R. Hagiwara and Y. H. Ogata, *J. Electrochem. Soc.*, **154**, E95 (2007).
7. T. Toba, K. Yasuda, T. Nohira, X. Yang, R. Hagiwara, K. Ichitsubo, K. Masuda and T. Homma, *Electrochemistry*, **81**, 559 (2013).
8. T. Nohira, A. Ido, T. Shimao, X. Yang, K. Yasuda, R. Hagiwara and T. Homma, *ECS Trans.*, **75**(15), 17 (2016).
9. K. Yasuda, T. Shimao, R. Hagiwara, T. Homma and T. Nohira, *J. Electrochem. Soc.*, **164**, H5049 (2017).
10. Y. Ma, A. Ido, K. Yasuda, R. Hagiwara and T. Nohira, *J. Electrochem. Soc.*, **166**, D162 (2019).
11. X. Yang, L. Ji, X. Zou, T. Lim, J. Zhao, E. T. Yu and A. J. Bard, *Angew. Chem. Int. Ed.*, **56**, 15078 (2017).
12. X. Zou, L. Ji, J. Ge, D. R. Sadoway, E. T. Yu and A. J. Bard, *Nat. Commun.*, **10**, 5772 (2019).
13. C. R. Masson, *Jour. Iron Steel Inst.*, **210**, 89 (1972).
14. S. A. Brawer and W. B. White, *Chem. Phys.*, **63**, 2421 (1975).
15. P. Sen and M. Thorpe, *Phys. Rev. B*, **15**, 4030 (1977).
16. F. L. Galeener, *Phys. Rev. B*, **19**, 4292 (1979).
17. H. Verweij, *Jour. Non-Cryst. Solids*, **33**, 41 (1979).

ECS Transactions, 98 (10) 223-230 (2020)
10.1149/09810.0223ecst ©The Electrochemical Society

Investigation on Operating Conditions Influencing the Aluminum Electrolysis using Chloroaluminate Ionic Liquids

Koichi Ui[a], Satoshi Kobayashi[a], Tatsuya Takeguchi[a], Tetsuya Tsuda[b], Mikito Ueda[c], Jyunji Nunomura[d], Yukio Honkawa[d], and Yoichi Kojima[d]

[a] Graduate School of Science and Engineering, Iwate University, Iwate, Japan
[b] Graduate School of Engineering, Osaka University, Osaka, Japan
[c] Faculty of Engineering, Hokkaido University, Hokkaido, Japan
[d] Research and Development Division, UACJ Corporation, Nagoya, Japan

$AlCl_3$-EMIC (1-ethyl-3-methylimidazolium chloride) melt has attracted attention as an efficient electrolyte for Al electrolysis. However, several problems such as the low deposition rate and rough surface limit its practical use. In this study, we have investigated the influence of the electrolytic condition on the surface roughness of electrolytic Al foil by using the $AlCl_3$-EMIC (molar ratio 2 : 1) melt with/without 20 mmol dm^{-3} of an OP (1,10-phenanthroline anhydrate) additive as an electrolyte. The AFM image revealed that the surface roughness (Sa) value of the electrolytic Al foil obtained on the Ti plate substrate from the melt with the OP additive at 50 ℃ was 45.8 nm at the current density of 52.6mA cm^{-2}. A smooth electrolytic Al foil was found to be obtained even at high current density by increasing the operating temperature and adding OP to the melt.

Introduction

Our group has focused on the Al electrolysis using room-temperature ionic liquids (RTILs). Al can be deposited from the chloroaluminate ILs, but a practical technology for depositing Al from the ILs has not been established. There are several problems such as the low limiting current density and the deposition in a dendritic form. In particular, the surface smoothness of electrolytic Al foil is required for practical application.

Many articles on the Al electrodeposition using the ILs have ever been reported. Bakkar and co-worker reported that the grain size decreased clearly as electrolysis potential shifted to negative (1). The grain size and crystallite size were controlled on the electrolysis potential. On the other hand, the method of using additives has been reported. Wang and co-workers reported that a bright Al coating was obtained by adding nicotinic acid or methyl nicotinate to a Lewis acidic $AlCl_3$-BMIC (1-butyl-3-methylimidazolium chloride) (2). Ueda and co-workers reported that the surface roughness was improved by adding 1,10-phenanthroline anhydrate (OP) (Figure 1) to a Lewis acidic $AlCl_3$-EMIC (1-ethyl-3-methylimidazolium chloride) melt (3). However, few articles systematically investigate the correlation between the Al deposits and the operating conditions (parameters). In order to effectively scale up from the laboratory level to the practical level, it is desirable to make the above correlation sufficiently clear.

In this study, we investigated on the parameters influencing to obtain a smooth electrolytic Al foil at higher current density.

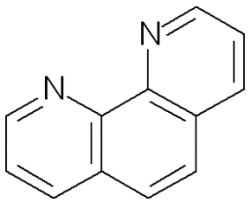

Figure 1. Structural formula of 1,10-phenanthroline anhydrate (OP).

Experimental

Preparation of electrolyte

In order to remove residual moisture, anhydrous $AlCl_3$ (Sigma Aldrich, ≥ 99.99%) and EMIC (Kanto Chemical Co., Inc., ≥ 98%) were dried at 60 °C for 10 h in vacuo, respectively. A chloroaluminate ionic liquid consisting of anhydrous $AlCl_3$ and EMIC for 2:1 molar ratio was mixed in an Ar-filled glove box (Vacuum Atmospheres Co., VAC101965-OMNI-LAB). This ionic liquid was purified by a substitution method (4). Al wires were immersed in the above liquid for *ca* 1 month, and a colorless and transparent electrolyte was obtained. 20 mmol dm^{-3} OP (Sigma Aldrich) was added to the electrolyte as an additive.

Electrochemical experiments

A constant-current electrolysis method was carried out in a conventional three-electrode cell with stirring at room temperature (RT) and 50 ℃. A Ti plate (Nilaco, thickness: 0.2 mm, purity: 99.5%) was employed as a cathode. A reference electrode (Al(III)/Al) was constructed by placing an Al wire (0.99-mm-diameter) into a Pyrex tube terminated with a porous G4 glass frit. The electrolyte for the reference electrode was a 66.7mol%$AlCl_3$–33.3mol%EMIC melt. An Al plate (Nilaco, thickness: 1.2 mm, purity: 99.99%) was employed as an anode.

The conditions of constant-current electrolysis were as follows: the operating temperature of RT and 50 ℃, the stirring speed of 1500 rpm, the current density of 21.1～63.2 mA cm^{-2}, and the total charge of 30 C cm^{-2}. A magnetic stirrer hot plate with a stir bar of 1.5 cm long was used to control the operating temperature and the stirring speed of the electrolyte. Electrochemical experiments were performed using a computer-controlled electrochemical measuring system (Hokuto Denko, HZ-7000).

Analysis of the samples

Surface morphology was observed using a field-emission scanning electron microscope (FE-SEM, JSM-7001F, JEOL). Arithmetic mean roughness (Sa) was observed using an atomic force microscope (AFM, Park Systems, NX-10). The crystal structure was analyzed by X-ray diffraction (XRD) using an X-ray diffraction meter (Rigaku Denki, MiniFlex600)

with Cu Kα radiation (λ = 0.15418 nm). The obtained deposits were washed with ethanol and acetone to remove the electrolyte prior to analysis.

Results and Discussion

Figure 2 shows the chronopotentiograms for depositing of Al on the Ti plate substrate under various operating conditions. These cathodic polarization curves mean the reaction of Al deposition ($4Al_2Cl_7^- + 3e^- \rightarrow Al + 7AlCl_4^-$). The electrolytic potential at RT shifted to negative with increasing the current density. Although the initial electrolytic potential approached to −2.0 V *vs*. Al/Al(Ⅲ), it did not reach to the reductive decomposition of EMI^+ cation (−2.2 V *vs*. Al / Al (Ⅲ)) even at the high current density (52.6 mA cm^{-2}) (5). By increasing the operating temperature to 50 ℃, both electrolytic potentials shifted to positive. This would be because as the operating temperature increases, the electrolyte viscosity decreases and the diffusion of reactive ion species ($Al_2Cl_7^-$ ions) becomes faster. Moreover, it should be noted that the OP addition had almost no effect on the electrolytic potential.

Here we defined the current efficiency as the ratio between the actual amount of deposits to that calculated theoretically from Faraday's laws in percent (6). The current efficiency of the resulting Al foil at the operating temperature of RT and 50 ℃ was 99.6% in the latter as compared to 84.8% in the former at a current density of 52.6 mA cm^{-2}. The current efficiencies at the operating temperature of 50 ℃ were higher than those of RT also at other current densities. Regardless of the OP addition, the current efficiencies were more than 90% even at the current density of 52.6 mA cm^{-2}.

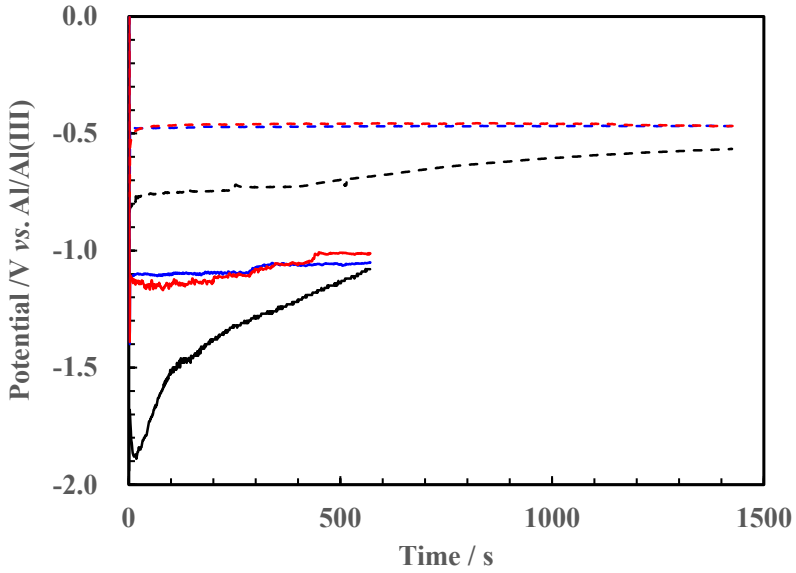

Figure 2. Chronopotentiograms for depositing of Al on the Ti plate electrode in the $AlCl_3$-EMIC melt at (black) room temperature, (blue) 50 ℃, and (red) 50 ℃ with 20 mmol dm^{-3} of OP additive; current density: (dashed line) 21.1, (solid line) 52.6 mA cm^{-2}, total charge for all deposits: 30 C cm^{-2}.

Figure 3 shows the photographs of the electrolytic Al foil obtained on the Ti plate substrate under various operating conditions. As shown in Figure 3 (a), the edge of the electrolytic Al foil obtained from the OP-free bath at RT was remarkably rough. As shown in Figure 3 (b), by increasing the operating temperature, the roughness of the edge was clearly improved. As shown in Figure 3 (c), by adding OP to the bath, a matt finish electrolytic Al foil was obtained, suggesting that the smoothness is improved by chemical action rather than thermodynamic action.

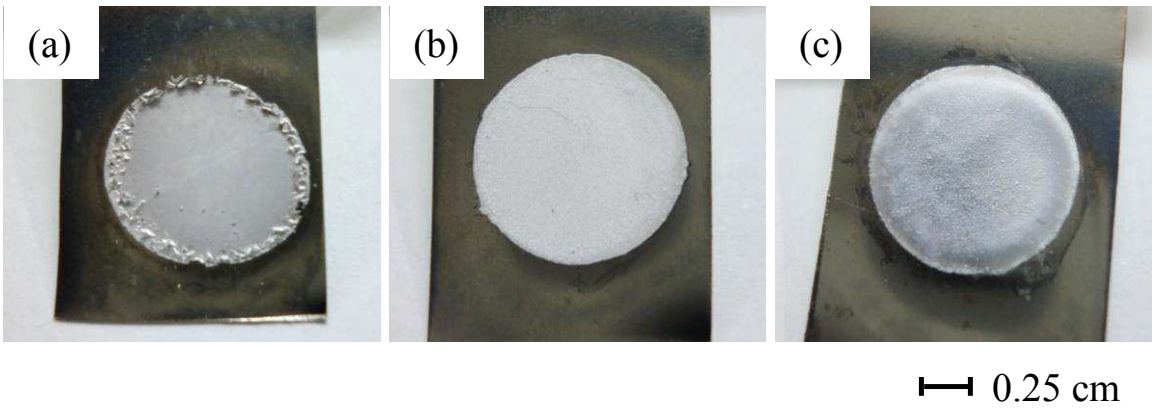

Figure 3. Photographs of electrolytic Al foils obtained on the Ti plate substrate from the $AlCl_3$-EMIC melt at (a) room temperature, (b) 50 ℃, and (c) 50 ℃ with 20 mmol dm^{-3} of OP additive; current density: 42.1 mA cm^{-2}, total charge for all deposits: 30 C cm^{-2}.

Figure 4 shows the FE-SEM images of the electrolytic Al foil obtained on the Ti plate substrate under various operating conditions. The crystal grain shape was the same, like a texture, regardless of the operating conditions. As shown in Figure 4 (a-I, b-I), in the OP-free bath, the crystal grain size became smaller with increasing the current density. At high current densities, many Al nuclei are generated and then each nucleus grows as the current disperses, resulting in smaller crystal grains (7, 8).

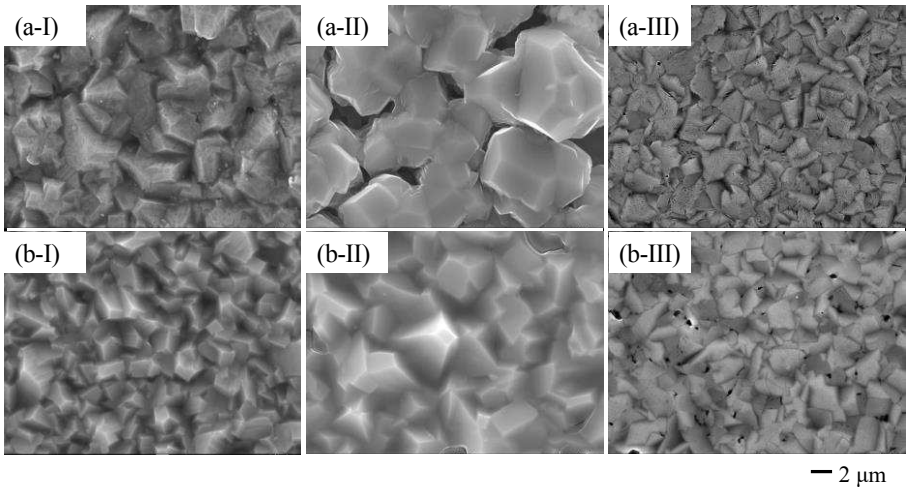

Figure 4. FE-SEM images of electrolytic Al foils obtained on the Ti plate substrate from the $AlCl_3$-EMIC melt at (I) room temperature, (II) 50 ℃, and (III) 50 ℃ with 20 mmol dm^{-3} of OP additive; current density: (a) 21.1, (b) 52.6 mA cm^{-2}, total charge for all deposits: 30 C cm^{-2}.

As shown in Figure 4 (a-II, b-II), both crystal grain sizes grew with increasing the operating temperature. When the operating temperature increases, the surface diffusion distance of the deposited Al atoms increases, forming large nuclei, and the current concentrates on them, resulting in the growth of large crystals (7, 8). As shown in Figure 4 (a-III, b-III), at both current densities, the crystal grain size became smaller by the OP addition. The addition of OP to the $AlCl_3$-EMIC melt at 50 ℃ also affected the crystal grain size to be small while the addition of OP did not affect the overpotential for the electrolysis. This suggests that the crystal growth of Al is suppressed by the adsorption of OP itself or the complex of OP and Al(Ⅲ) ions on the Al nucleus (9).

Figure 5 shows the AEM images and the surface roughness (Sa) values of the electrolytic Al foil obtained on the Ti plate substrate under various operating conditions. As shown in Figure 5 (a-I, b-I), in the OP-free bath, the Sa value became smaller with increasing the current density (Sa = 0.2429 μm → 0.1273 μm). As shown in Figure 5 (a-II, b-II), both Sa values became larger with increasing the operating temperature. Moreover, as shown in Figure 5 (a-III, b-III), the OP addition drastically reduced both Sa values and showed the values of about 1/10. In particular, in the case of Figure 5 (b-III), 45.8 nm of Sa was obtained, which was smoother than the Sa value (105.8 nm) of the commercial Al foil for a battery current collector. By adding OP to the melt, the Sa value became extremely smaller, indicating that the OP addition strongly suppresses the roughness. The above results are consistent with the trend in the crystal grain sizes shown in Figure 4.

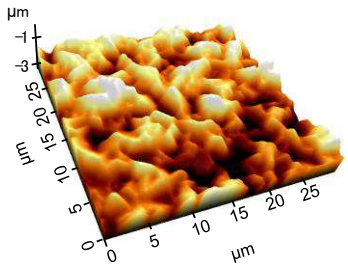

(a-I) Sa = 0.2429 μm

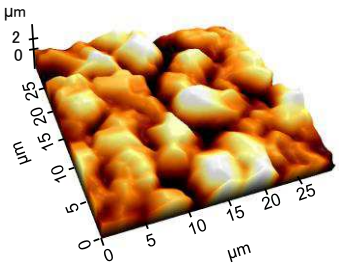

(a-II) Sa = 0.7735 μm

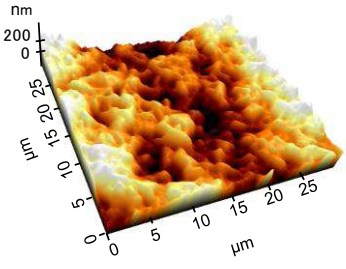

(a-III) Sa = 87.4 nm

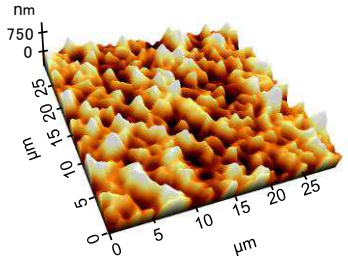

(b-I) Sa = 0.1273 μm

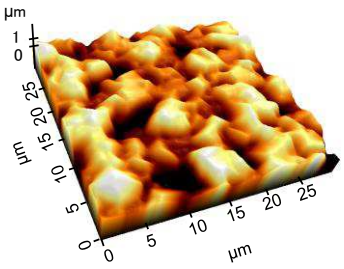

(b-II) Sa = 0.4245 μm

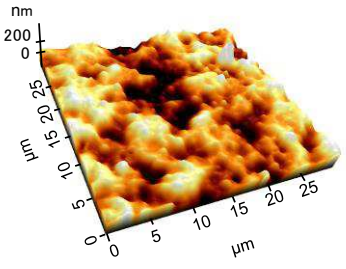

(b-III) Sa = 45.8 nm

Figure 5. AEM images of electrolytic Al foils obtained on the Ti plate substrate from the $AlCl_3$-EMIC melt at (I) room temperature, (II) 50 ℃, and (III) 50 ℃ with 20 mmol dm^{-3} of OP additive; current density: (a) 21.1, (b) 52.6 mA cm^{-2}, total charge for all deposits: 30 C cm^{-2}.

Figure 6 shows the XRD patterns of the electrolytic Al foil obtained on the Ti plate substrate under various operating conditions. The XRD peaks were identified and indexed by the comparison to the standard obtained from the JCPDS card. All the peaks were attributed to Al (fcc), so that the single phases were obtained. In the OP-free bath, the (200) reflection became strong as the operating temperature was high. Moreover, the orientations of the (200) and (220) reflections were strong by the OP addition.

From the (200) reflection of the XRD patterns, the crystallite sizes were calculated using the Scherrer's equation:

$$D = K\lambda / \beta \cos\theta \qquad [1]$$

where D is the crystallite size (nm); K is the Scherrer constant (0.9); λ is the is the X-ray wavelength (0.15418 nm); β is Full width of half maximum (FWHM, rad); θ is the Bragg angle. The relation between operating conditions and crystallite size of electrolytic Al foil is listed in Table 1. The crystallite size became small with increasing the current density. Increasing the operating temperature, both crystallite sizes grew. Moreover, both crystallite sizes were dramatically decreased by the OP addition.

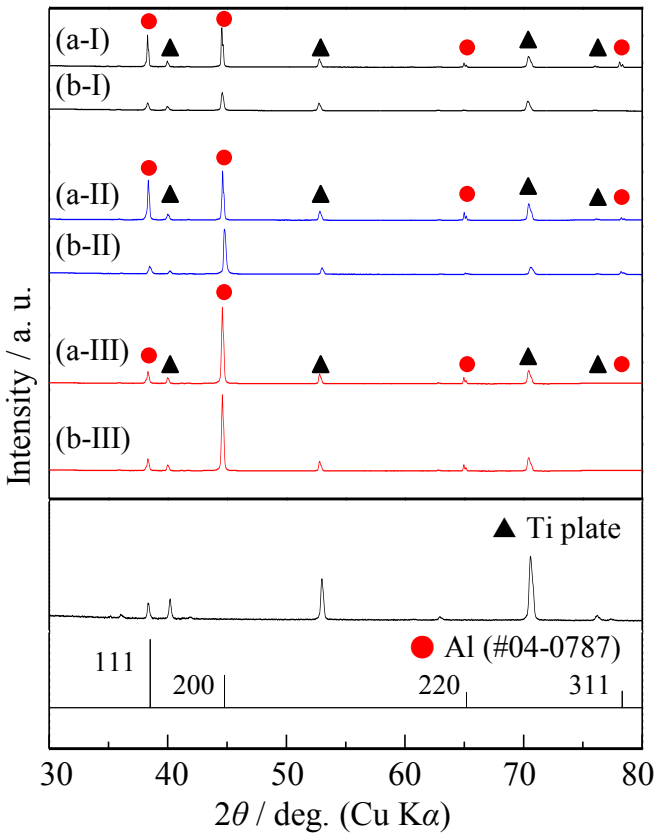

Figure 6. XRD patterns of electrolytic Al foils obtained on the Ti plate substrate from the $AlCl_3$-EMIC melt at (I) room temperature, (II) 50 ℃, and (III) 50 ℃ with 20 mmol dm^{-3} of OP additive; current density: (a) 21.1, (b) 52.6 mA cm^{-2}, total charge for all deposits: 30 C cm^{-2}.

TABLE I. Relation between operating conditions and crystallite size of electrolytic Al foil (XRD).

Additives	**Operating temperature** ℃	**Current density** mA cm^{-2}	**Crystallite size** nm
None	Room temp.	21.1	80.1
		52.6	75.4
None	50	21.1	90.0
		52.6	78.3
OP	50	21.1	70.3
		52.6	49.3

The current density and the operating temperature are closely related to the electrolytic potential (10), so it is considered that the factor that determines the crystallite sizes is the electrolytic potential. Figure 7 shows the relation between the electrolytic potential and crystallite size of electrolytic Al foils obtained on the Ti plate substrate under various operating conditions. In fact, when the relation between the electrolytic potential and the crystallite size was plotted, a proportional relation was clearly demonstrated. In the OP-free bath, it is suggested that the crystallite size depends on the overvoltage rather than the operating temperature.

By increasing the operating temperature, the surface roughness became larger and the crystallite size grew. Therefore, when OP was added to the electrolyte at the operating temperature of 50 ℃, OP exhibited an effect of improving surface roughness without affecting the electrolytic potential. While no luster was observed in the electrolytic Al foil obtained from the OP-free bath, matt finish surface was observed in the electrolytic Al foil obtained from the OP-added bath, independent of the current density (21.1～63.2 mA cm^{-2}).

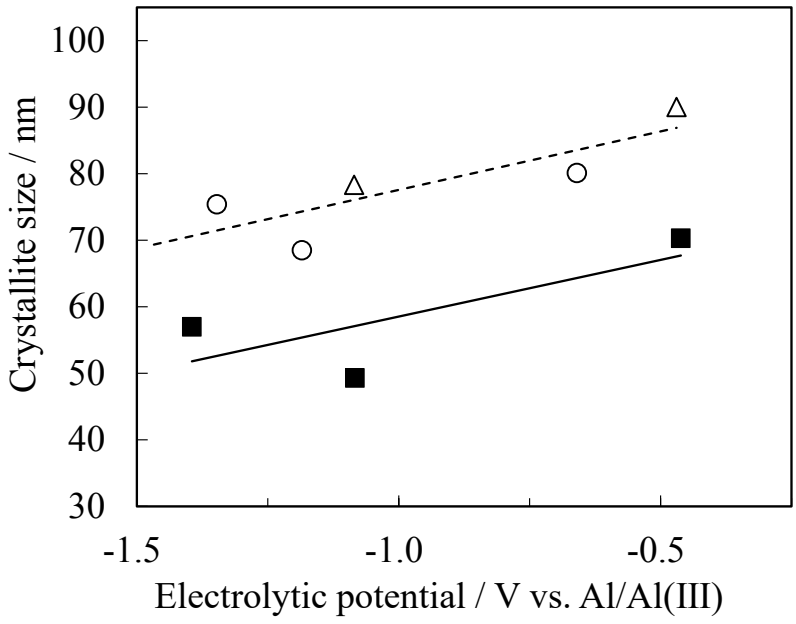

Figure 7. Relation between the electrolytic potential and crystallite size of electrolytic Al foils obtained on the Ti plate substrate from the $AlCl_3$-EMIC melt at (○) room temperature, (△) 50 ℃, and (■) 50 ℃ with 20 mmol dm^{-3} of OP additive; total charge for all deposits: 30 C cm^{-2}.

Based on these results, it was clarified that the crystal grain size and the crystallite size of the electrolytic Al foil were reduced by the addition of OP, which improved the surface roughness regardless of overvoltage.

Conclusions

We investigated on the parameters influencing to obtain a smooth electrolytic Al foil at higher current density. The AFM image revealed that the surface roughness (Sa) value of the electrolytic Al foil obtained from the melt with the OP additive at 50 ℃ was 45.8 nm at the current density of 52.6mA cm^{-2}. The smooth electrolytic Al foil was successfully obtained even with high operating temperature and high current density by adding OP to the $AlCl_3$-EMIC melt.

Acknowledgments

This work is based on results obtained from a project commissioned by the New Energy and Industrial Technology Development Organization (NEDO).

References

1. A. Bakkar and V. Neubert, *Electrochim. Acta.*, **103**, 211 (2013).
2. Q. Wang, Q. Zhang, B. Chen, X. Lu, and S. Zhang, *J. Electrochem. Soc.*, **162**, D320 (2015).
3. H. Takahashi, C. Namekata, T. Kikuchi, H. Matsushima, and M. Ueda, *J. Surf. Finish. Soc. Jpn.*, **68**, 208 (2017).
4. S. Takahashi and N. Koura, *J. Electroanal. Chem.*, **188**, 245 (1985).
5. M. Lipsztain and R. A. Osteryoung, *J. Electrochem. Soc.*, **130**, 1968 (1983).
6. M. Paunovic and M. Schlesinger, *Fundamentals of Electrochemical Deposition, John Wiley & Sons*, p. 198, New York, NY (1998).
7. T. Watanabe, *Metals*, **66**, 339(2002).
8. T. Watanabe, *Metals*, **66**, 350 (2002).
9. X. Fang, K. Uehara, S. Kaneko, S. Sato, T. Tanabe, T. Gunji, and F. Mathumoto, *Electrochemistry*, **84**, 17 (2016).
10. M. Paunovic and M. Schlesinger, *Fundamentals of Electrochemical Deposition, John Wiley & Sons*, p. 250, New York, NY (1998).

ECS Transactions, 98 (10) 231-243 (2020)
10.1149/09810.0231ecst ©The Electrochemical Society

Electroanalytical study of Active Species to Deposit Ti Alloy from 1-Butyl-3-methylimidazolium Chloride-Aluminum Chloride Ionic Liquid

Pravin S. Shinde[a], Yuxiang Peng[a], and Ramana G. Reddy[a]

[a] Department of Metallurgical and Materials Engineering,
The University of Alabama, Tuscaloosa, AL 35487, USA
Corresponding author: rreddy@eng.ua.edu; Tel: 205-348-4246

The electrochemical behavior of titanium-chloroaluminate anion species in Lewis acidic 1-butyl-3-methyl imidazolium chloride (BMIC)-aluminum chloride ($AlCl_3$) ionic liquid (IL) electrolyte with 0.667 $AlCl_3$ mole fraction is investigated at 383K by cyclic voltammetry (CV), chronoamperometry (CA), and chronopotentiometry (CP). The effect of scan rate on peak potential and peak current, constant current density, constant applied potential, and the electrolyte temperature are discussed. The redox reaction of the Ti^{2+}/Ti^0 deposition from titanium hepta-chloroaluminate ($[Ti(Al_2Cl_7)_4]^{2-}$) anions is a reversible process with a 2-electron transfer while that of Al^{3+}/Al^0 deposition from hepta-chloroaluminate ($[Al_2Cl_7]^-$) anions is quasi-reversible with the 3-electron transfer. The cyclic voltammograms indicated that the reduction of $[Al_2Cl_7]^-$ and $[Ti(Al_2Cl_7)_4]^{2-}$ species to corresponding Al and Ti forms is a diffusion-controlled phenomenon. The diffusion coefficients (D) of the anion-species in BMIC-$AlCl_3$ IL determined at 383 K using CV and CP methods are 9.74×10^{-10} m^2 s^{-1} and 6.36×10^{-10} m^2 s^{-1}, respectively.

Introduction

Titanium (Ti) is the ninth most abundant element and fourth among common metals in the earth's crust. The Ti and its alloys have been widely employed in aerospace, military, automotive, medical, and several other fields due to their excellent thermomechanical properties such as low density, exceptional strength, high melting point, and good oxidation resistance and structural stability. The Kroll process invented in the 1940s has been the primary method of Ti production (1). Several research efforts have been focused on developing a cost-effective approach to produce low-cost and high-purity titanium (2-12). Electrochemical synthesis from low-temperature ionic liquid (IL) electrolytes is one of the fascinating methods of producing Ti metal or its alloys (13). Unfortunately, the electrochemical mechanism for titanium deposition is more complicated than other metals such as aluminum because of its different oxidation states (II, III, and IV). Therefore, it is often electrodeposited in the form of alloys, such as titanium aluminide (Ti-Al). The ILs are still continuously receiving a lot of scientific interest due to their lack of understanding at the fundamental molecular level, e.g., the ion-ion interactions, leading to different observed properties (14, 15). In general, density, viscosity, electrochemical potential window, and conductivity are important physical properties that determine if an IL is suitable for a given application. Our research group has been

instrumental in studying several physicochemical properties such as the heat capacity (16), thermal stability (17-19), density (20, 21), viscosity (18, 20, 21), vapor pressure (21), thermal conductivity (21, 22), thermodynamic (23-25), and electroanalytical (26-29) properties of several ILs and molten salts, which are necessary to understand the electrochemistry of metals and alloys to tune their electrosynthesis parameters. Electrodeposition of Ti and its alloys from low-temperature ILs, especially in chloroaluminate-based alkyl imidazolium chloride, is very challenging as the electrochemistry of Ti in such IL is very complicated. Such ILs are used to electrodeposit Al using a eutectic mixture of $AlCl_3$ with alkyl imidazolium chlorides (30-34). For instance, in an IL consisting of BMIC and $AlCl_3$, several anion species such as $[AlCl_4]^-$, $[Al_2Cl_7]^-$, and $[Al_2Cl_{10}]^-$ with different concentrations are in equilibrium for a given mole fraction (X_{Al}) of $AlCl_3$. The amount of X_{Al} dictates the acidity or basicity of electrolyte and impacts the electrodeposition conditions. At higher $AlCl_3$ (X_{Al} >0.5), the electrolyte mainly possesses $AlCl_4^-$ and $Al_2Cl_7^-$ species exhibiting Lewis acidic properties primarily due to coordinately unsaturated $Al_2Cl_7^-$ species (35). The electrochemical deposition of Al from such chloroaluminate ILs has been reported to be primarily due to contribution from the diffusion of $Al_2Cl_7^-$ species (34, 36, 37). Acidic IL compositions are active for Al plating and stripping at the anode, according to the reversible redox reaction given below (38, 39).

$$4[Al_2Cl_7]^- + 3e^- \leftrightarrow Al\ (Cathode) + 7[AlCl_4]^- \quad [1]$$

Our group previously performed the electrodeposition of Ti-Al alloys from BMIC-$AlCl_3$-$TiCl_4$ (1:2:0.019 molar ratio) at different applied potentials voltages (1.5-3.0 V) and temperatures (343-398 K) (11). Ti foils were used as cathode and anode, and Ti wire was used as a reference electrode. The possible reactions are given by Eq. (2-5)

$$\text{Cathode reactions: } [Ti(Al_2Cl_7)_4]^{2-} + 2e^- \leftrightarrow Ti\ (Cathode) + 7[AlCl_4]^- \quad [2]$$
$$4[AlCl_4]^- + 3e^- \leftrightarrow Al\ (Cathode) + 7[AlCl_4]^- \quad [3]$$

$$\text{Anode reactions: } Ti\ (Anode) + 4[Al_2Cl_7]^- - 2e^- \leftrightarrow [Ti(Al_2Cl_7)_4]^{2-} \quad [4]$$
$$AlCl_3 + 4[AlCl_4]^- - 3e^- \leftrightarrow 4[Al_2Cl_7]^- + 1.5\ Cl_2 \quad [5]$$

The electrochemical process of reduction of Al-species in the ILs is relatively well studied. However, there are no reports on electrochemical studies of ILs to deposit Ti-Al alloy without the addition of $TiCl_4$ with regard to studying the nucleation and growth mechanisms. In our previous work, the potentiostatic electrodeposition of smooth, compact, and dendrite-free growth of Ti-Al alloy on the copper substrate was demonstrated at −1.3 V vs. Ti for 1 h using BMIC-$AlCl_3$ IL with $AlCl_3$ mole fraction of 0.667 at low temperature (40). However, nucleation and growth mechanisms at constant potential and current densities were not performed.

In this work, the electrodeposition behavior, especially the initial crystallization nucleation and growth mechanism of the Ti-Al alloy electrodeposition on Pt wire electrodes from IL electrolyte consisting of a eutectic mixture melt of BMIC and $AlCl_3$ are investigated using a CV, CA, and CP techniques. Furthermore, the diffusion coefficient (D) values are estimated from using CV and CP methods. The CA experiments are performed to analyze the mechanism of diffusion and nucleation of Ti-Al-species

from BMIC-$AlCl_3$ IL. The diffusion coefficient of $[Ti(Al_2Cl_7)_4]^{2-}$ or $Al_2Cl_7^-$ ions in BMIC-$AlCl_3$ IL with $AlCl_3$ mole fraction of 0.667 are calculated and compared using CP and CV methods at 383 K.

Experimental

Materials

The chemicals such as anhydrous $AlCl_3$ (95%, Alfa-Aesar) and organic chloride salt 1-butyl-3-methylimidazolium chloride (BMIC, 98%, Sigma-Aldrich, HPLC grade) were purchased and used as received. The Pt wire (0.5 mm diameter, 99.99%) was obtained from Sigma Aldrich company. Pure titanium wire (0.25 mm diameter, 99.99%) was obtained from Alfa Aesar®. The ultrahigh pure (UHP) Argon gas (99.999%) was obtained from Airgas.

Preparation of BMIC-$AlCl_3$ Ionic Liquid

The appropriate amount of BMIC organic chloride salt and the $AlCl_3$ were weighed for a given $AlCl_3$ mole fraction. Here, the $AlCl_3$ mole fraction of 0.667 was chosen to maximize the concentration of $Al_2Cl_7^-$ anion species in the BMIC-$AlCl_3$ IL. Both the ingredients were mixed in a Pyrex beaker on a preheated hot-plate. The mixing is performed cautiously and slowly using a glass rod as the spontaneous reaction is vigorous. The mixture of two solid ingredients turns into a clear liquid as the eutectic condition is reached at room temperature. Upon stirring for 30 s, the mixture turns into a clear liquid, although few large chunks of BMIC might float in the solution, which eventually dissolves in about 30 min. The desired amount of clear IL solution is then transferred to the 50 mL electrochemical Pyrex cell placed on a hot plate, and IL was stirred for about 30 min using a magnetic stirrer at 60 RPM for homogeneous mixing at the set temperature. The IL was stored in a dry box until used for further measurements such as density and electrical conductivity. The $AlCl_3$ mole fraction (X_{Al}) of 0.667 in BMIC-$AlCl_3$ IL and at a fixed electrolyte temperature of 383 K was chosen for the electrochemical measurements. The UHP argon gas was purged over the surface of IL to keep it free from oxygen and moisture, and the cell is sealed.

Electrochemical Measurements

The electrochemical measurements were performed from BMIC-$AlCl_3$ IL at 383K using CV, CA, and CP methods using an EG&G PARC model 273A potentiostat/galvanostat instrument controlled by Power Suite software. The electrochemical cell for the measurements consisted of a 40 mL Pyrex® glass beaker fitted with Teflon/Perspex cover, which has provisions for introducing electrodes, thermometer, and inert gas inlet and outlets, as shown schematically in Figure 1.

The experiments were performed from BMIC-$AlCl_3$ IL using a three-electrode cell configuration, where Pt wire served as working electrode (WE), Ti wire as the counter electrode (CE), and Ti or Pt wire as a quasi-reference electrode (RE). The Ti-species

were incorporated from the electrolysis experiment for one hour before starting the electrochemical measurements. The working distance between WE and CE was 0.025 m. The temperature was controlled by a hot plate and was precisely monitored by the inserted thermometer. The Ar gas flow was continuously maintained through the alumina tube during the experiment. All the electrodes were polished with 800-grit SiC abrasive paper, washed with acetone and deionized water, and then dried by air right before the experiment. The height of the electrode immersed in the IL was measured after the experiment.

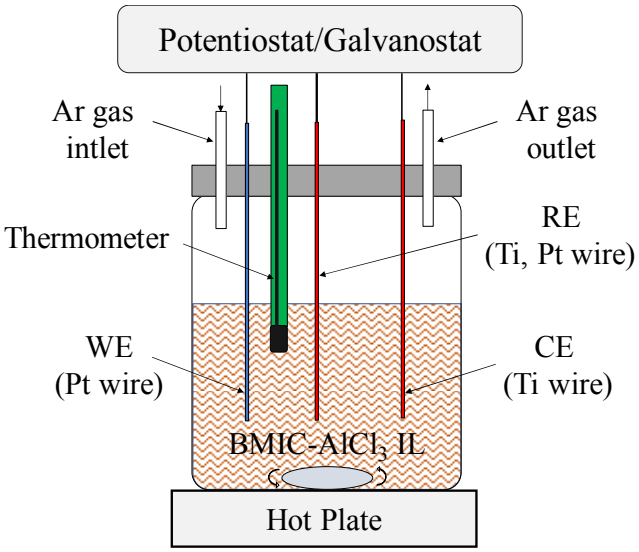

Figure 1. Schematic of the electrochemical cell set-up for CV, CP, and CA experiments in BMIC-$AlCl_3$ IL.

Results and Discussion

Cyclic Voltammetry (CV)

The nucleation and growth studies of metals or alloys are commonly investigated by electroanalytical methods such as CV and CA, which can be served both as the deposition method as well as the diagnostic tools for determining the reaction mechanisms. One can predict the growth models using the experimental measurements, based on certain assumptions involving the nucleation mode (instantaneous, progressive), the dimensional type of growth (2D, 3D), the geometry of growth centers, and the rate-determining step of the entire process. The electrochemical synthesis parameters such as electrolyte temperature, viscosity, and concentration of ionic species play a critical role by controlling the nucleation and growth of electrodeposits in electrodeposition. The diffusion or mass transfer coefficient of ionic species in the IL is one such essential parameters. As mentioned earlier, $Al_2Cl_7^-$ are predominant ionic species in BMIC-$AlCl_3$ IL at an $AlCl_3$ molar fraction of 0.667. Therefore, it is necessary to understand the mass transfer or diffusion of such ions and their complexes to/from the bulk electrolyte to the electrode surface during electrodeposition.

The cyclic voltammograms are obtained from BMIC-$AlCl_3$ IL at Pt electrode with Ti as reference and Ti as a sacrificial anode at 383K. The scan rates are varied from 100 to 300 mV s^{-1}. Figure 2 shows the cyclic voltammograms recorded on polished Pt wire at different scan rates from BMIC-$AlCl_3$ IL. The area of WE immersed inside the electrolyte was 0.118×10^{-4} m^2. The reduction and oxidation peaks are seen in the CV curves. When the CV is swept from 1 V or open circuit potential towards a negative direction, a tiny reduction peak at 0.187 V vs. Ti appears. This peak is due to the two-electron reduction of Ti-hepta-chloroaluminate complex ions from ionic liquid according to reaction [2] to deposit metallic Ti on a copper substrate. As the potential sweeps further toward more negative potentials, the cathodic current becomes steady until −1.0 V vs. Ti and increases rapidly, giving rise to a reduction peak at −1.4 V vs. Ti, which signifies the deposition of Al according to the reaction [3].

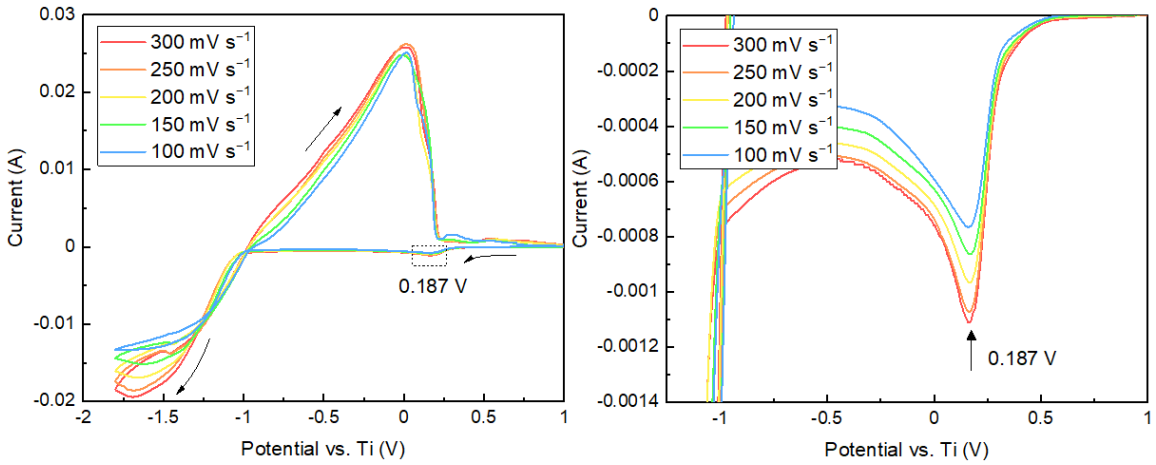

Figure 2. Cyclic voltammograms recorded at different scan rates from BMIC-$AlCl_3$ IL (0.667 $AlCl_3$ mole fraction) with 1.11987×10^{-2} mol L^{-1} $Ti[(Al_2Cl_7)_4]^{2-}$ ions at 383 K.

During the reverse sweep, a broad oxidation peak at −0.06V vs. Ti, followed by a tiny peak at 0.475 V vs. Ti, appears, which dictates the anodic stripping of Al and Ti complex species, respectively. The ratio of cathodic peak current (E_{pc}) and anodic peak current (E_{pc}) measured for reduction/oxidation reactions for Ti during the forward and reverse sweeps is close to unity (E_{pc}/E_{pa}~1). Moreover, the interpeak distance (ΔE_p) is 0.288 V. That is, $(\Delta E_p)=|E_{pc}-E_{pa}|=28.8$ mV. For an entirely reversible reaction, the $\Delta E_p=2.303RT/nF=59.2$ mV/n, where n represents the number of electrons exchanged during the reduction or oxidation reaction. The number of electrons involved in reduction or oxidation reaction according to the reaction [3] is 2. For the two-electron reduction or oxidation reaction, the value of ΔE_p should be 29.6 mV, which is close to the observed value of 28.8 mV. This suggests that the charge transfer processes involving deposition/stripping of Ti reversible.

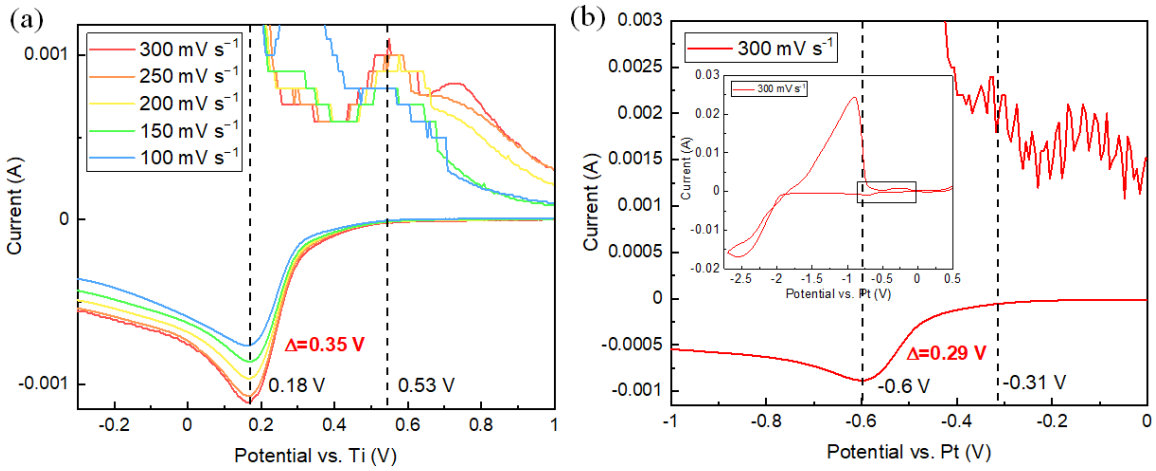

Figure 3. Cyclic voltammograms recorded from BMIC-$AlCl_3$ IL (0.667 $AlCl_3$ mole fraction) at 383 K versus (a) Ti at different scan rates (magnified view) and (b) Pt at the scan rate of 300 mV s^{-1} for comparison.

The reduction peak at −1.4 V vs. Ti and anodic stripping peak at −0.06 V vs. Ti in Figure 2 are separated by ΔE_p = ~1.34 V. Higher value of ΔE_p (> 59.2 mV/*n*, considering a three-electron reduction reaction, *n*=3) for Al deposition indicates that the electrochemical process is quasi-reversible. To further confirm the electrochemical deposition of Ti, cyclic voltammogram of BMIC-$AlCl_3$ ($AlCl_3$ mole fraction of 0.667) electrolyte was re-recorded on titanium wire using platinum reference electrode as shown in Figure 3(b). The reduction peak at −0.6 V vs. Pt (Figure 2b) confirms the deposition of Ti, which is in line with the reduction peak for Ti from [EMIm]Tf_2N containing 0.25 M $TiCl_4$ electrolyte (41). Alternatively, we performed the CV for BMIC-$AlCl_3$ IL with a 0.667-mole fraction of $AlCl_3$ without any Ti content. The CVs at different scan rates do not exhibit any reduction peaks in the regime of potentials where Ti redox peaks are observed from Ti-containing BMIC-$AlCl_3$ electrolyte.

As seen in Figure 2, the overall shapes of CVs for different scan rates are similar. However, there are noticeable shifts in the peak potentials for deposition of Al during cathodic sweeps. With an increase in scan rate, the reduction peak current increases. The reduction peak at 0.187 V vs. Ti signifying the reduction of $[Ti(Al_2Cl_7)_4]^{2-}$ to metallic Ti does not change with respect to the scan rate, as shown in the magnified view of the reduction peaks in Figure 3a. This suggests that this two-electron reduction reaction is a reversible process. No discernible shifts in anodic stripping peaks related to Al during anodic sweep are seen, although anodic stripping peaks for Ti shows irregular peak potentials due to complex electrochemistry involving quasi-reversible reaction. We rule out the possibility of the occurrence of redox peaks of Ti due to underpotential deposition (UPD). The deposition of metal on a substrate of the same material is deposited by the UPD process (42). The thickness of such materials deposited by UPD is of few monolayers. If it is due to the UPD process, then a considerable amount of Ti may not be deposited. The formation of the Ti-Al deposit (with ~3 at.% Ti at lower potential) from the same composition was confirmed from SEM-EDS previously (43). The cathodic reduction potentials are used for estimating the diffusion coefficients of $[Ti(Al_2Cl_7)_4]^{2-}$ anions. The diffusion coefficient for $Al_2Cl_7^-$ anions can also be estimated. However, our primary purpose in the present study is to investigate the electrochemical parameters for

the electrodeposition of Ti. Hence, we have focused on determining the diffusion coefficient calculation for $[Ti(Al_2Cl_7)_4]^{2-}$ anion species.

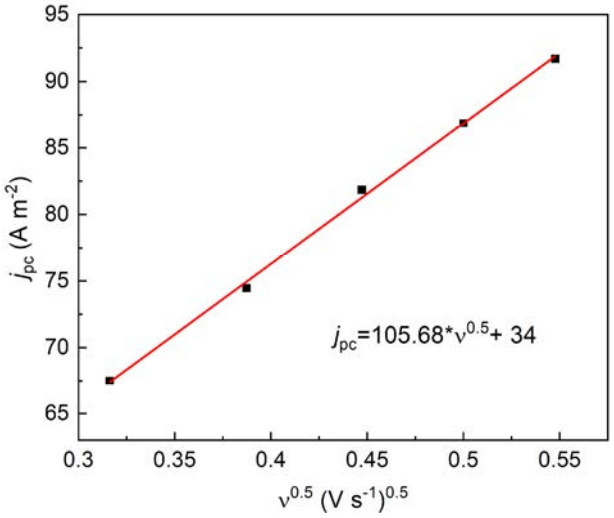

Figure 4. A plot of j_{pc} versus $\nu^{0.5}$ at 383 K (from redox peaks of Ti-species in BMIC-$AlCl_3$ IL).

To get insights into the rate of electron transfer or diffusion current (only the cathodic reaction considered), the diffusion coefficient of $[Ti(Al_2Cl_7)_4]^{2-}$ ions is calculated from the Randell–Sevcik relation (44),

$$j_{pc} = 0.4958nFC_i(\frac{\alpha nF}{RT})^{0.5}D^{0.5}v^{0.5} \quad [6]$$

where j_{pc} is the cathodic peak current density (obtained by dividing the current by area A of the working electrode), C_i is the bulk concentration of $[Ti(Al_2Cl_7)_4]^{2-}$ ions (*ca.* 1.11987 × 10^{-5} mol L^{-1}), R is the gas constant (8.314 J K^{-1} eq^{-1}), T is the experimental temperature (K), α is the charge transfer coefficient, n is the number of electrons transferred/molecule or ion (n=2), and F is the Faraday constant (96485 C mol^{-1}), D is the diffusion coefficient (m^2 s^{-1}), and ν is the scan rate (V s^{-1}). For quasi-reversible reaction, α can be determined by Nicholson and Shain relation (45) as,

$$\left|E_{pc} - E_{pc/2}\right| = 1.857RT/\alpha nF \quad [7]$$

where E_{pc} is the cathodic peak potential (V), and $E_{pc/2}$ is the cathodic half-peak potential (V). From Figure 4, the D can be calculated from the slope of a linear plot between cathodic peak current density (j_{pc}) versus $\nu^{0.5}$ once the C_i and α are known from the slope $0.4958nFC_i(\frac{\alpha nF}{RT})^{0.5}D^{0.5}$. The D value is calculated using the slope from Figure 4 and is listed in TABLE I, along with all the parameters obtained from CV curves.

TABLE I. Electrochemical parameters obtained from Figure 3(a) and Figure 4 at 383k. The area of a working electrode immersed in the liquid is 0.1178×10^{-2} m^2.

Scan rate ($mV\ s^{-1}$)	E_{pc} (mV)	$E_{pc/2}$ (mV)	E_{pa} (mV)	$\lvert E_{pc}-E_{pa}\rvert$ (mV)	$\lvert E_{pc}-E_{pc/2}\rvert$ (mV)	$\lvert j_{pc}\rvert$ ($A\ m^{-2}$)	α	D, $\times 10^{-10}$ ($m^2\ s^{-1}$)
100	86.85	205.23	246.15	159.30	118.38	65.2287	0.26	This work
150	97.90	209.61	342.60	244.69	111.71	72.1613	0.27	
200	103.45	211.70	433.30	329.84	108.24	78.5135	0.28	
250	109.00	220.05	430.50	321.50	111.05	82.2519	0.28	
300	114.56	223.64	452.44	337.88	109.08	85.4532	0.28	
						Average	0.27	9.74

Chronopotentiometry (CP)

Chronopotentiometry (CP) can be used to study the mechanism and kinetics of chemical reactions involving one or more redox species. CP method involves galvanostatic mode to control current and measure voltage. For systems involving only one redox species, an S-shaped current-voltage response is observed. The potential of the electrode changes from open-circuit potential to an approximately constant value, until the concentration of the redox species at the electrode is depleted. When this species is depleted at the electrode surface, the potential rapidly shifts to a potential that is able to sustain the applied current. This sudden shift is called the transition time (τ). If only one redox species is present, the potential shifts to a value that causes either the supporting electrolyte or solvent to be reduced/oxidized. If the redox process is reversible, the potential response during the plateau of the sigmoidal curve is controlled by the concentration of the oxidized and reduced forms of the redox couple at the electrode surface. Therefore, one can use the Nernst equation to evaluate the formal potential for the reduction process, as long as the diffusion coefficients of the oxidized and reduced form of the redox couple are known (46).

The quantitative relationship between transition time and current density using CP technique using the Sand equation (47) given by equation [8],

$$j\,\tau^{0.5} = 0.5nFCD^{0.5}\pi^{0.5} = constant \qquad [8]$$

The advantage of CP is that the Sand equation is appropriate for both planar and spherical electrodes to determine the diffusion coefficient, unlike the Cottrell equation (for CA method) representing the diffusion-controlled reaction. A better precision can be achieved using CP and Sand equation because the measured parameters τ and j vary linearly with D and non-linearly with $D^{0.5}$ for the Sand and Cottrell equations, respectively. The average value of the diffusion coefficient can be calculated by measuring the transition times at several current densities using equation [9] or from the slope of $\tau^{0.5}$ versus j,

$$D = \frac{4j^2\tau}{\pi\,(nFC)^2} \qquad [9]$$

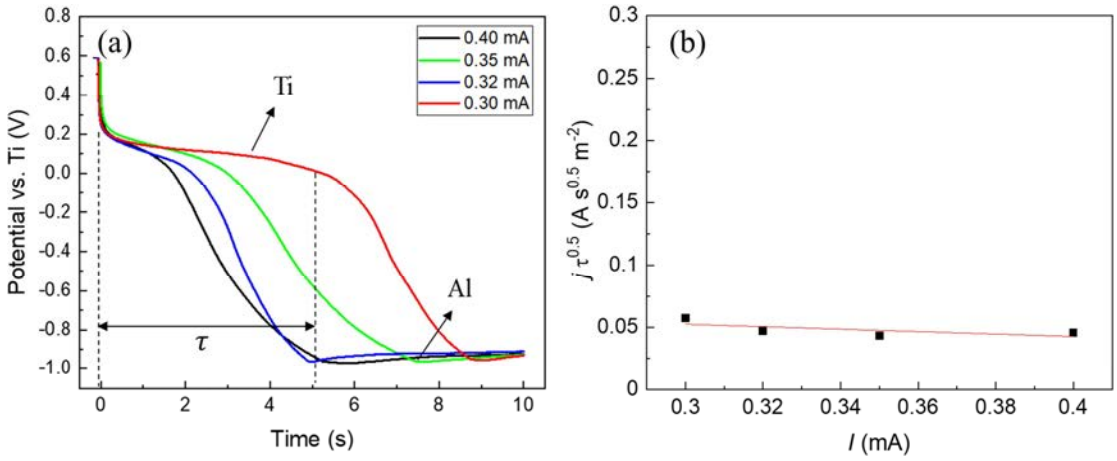

Figure 5. (a) Chronopotentiometric transients at different currents for 10 s duration at 383 K from BMIC-$AlCl_3$ IL and (b) Plot of $j\tau^{0.5}$ versus different applied currents.

Figure 5a shows the CP curves recorded for different currents, clearly revealing the distinct plateau regions for Ti and Al in the various potential regimes. Then, by plotting the transition time versus current density, as shown in Figure 5, the D values are estimated at 383 K. The average value of $j\tau^{0.5}$ at 383 K is 48.3 A $s^{0.5}$ m^{-2}, and the calculated D value is 6.36×10^{-10} m^2 s^{-1}. The D value calculated from the CV method is higher than that calculated by the CP method. The discrepancy could be because the CV method uses a modified Randles-Sevcik equation, which is a kinetically driven process. In contrast, the CP method uses the Scharifker-Hills and Cottrell equations, which is a static measurement.

Chronoamperometry (CA) and Nucleation and growth mechanism

The chronoamperometry (CA) study was performed to study the nucleation and growth mechanism of Ti or Ti-Al alloy deposits from BMIC-$AlCl_3$ (0.667 $AlCl_3$ mole fraction) containing 1.11987×10^{-2} mol L^{-1} of $[Ti(Al_2Cl_7)_4]^{2-}$ anions at 383 K. Since no nucleation peaks were observed near the reduction potential of Ti, the CA method was not used to estimate the D values. Figure 6 shows the CA plots at different overpotentials. The potentials were varied from −1.00 to −1.35 V *vs*. Ti, which was sufficient to initiate the nucleation and growth of Ti along with Al. The potentials higher than the deposition potentials of Ti were chosen because no nucleation peaks were noticed due to lower concertation of Ti species relative to that of Al-species in the ionic liquid. The current rises first due to the onset of nucleation and growth of the Ti and Al nuclei and then follows a current decay slowly after t_m (reaching a maximum peak) due to mass-transfer limitation (27).

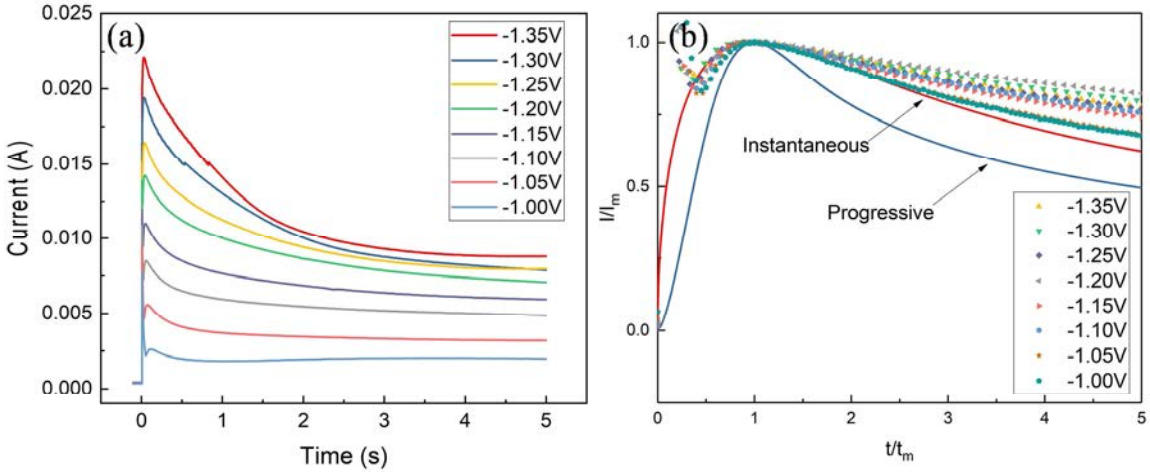

Figure 6. (a) Chronoamperometric current-time transients for TiAl deposition from BMIC-$AlCl_3$ IL with different overpotentials at 383 K. (b) Comparison of experimental current-time transients with simulated data using theoretical instantaneous and progressive nucleation model for BMIC-$AlCl_3$ IL with different overpotentials at 383 K.

In Figure 6a, as the potential increases, the value of I_m seems to increase while the value of t_m tends to decrease. This is due to the increase in nucleation rate and nucleation density (48). The maximum current and corresponding time values obtained from Figure 6a were further used to investigate the nucleation mechanism and diffusion coefficient of $[Al_2Cl_7]^-$ and $[Ti(Al_2Cl_7)_4]^{2-}$ anion species in the BMIC-$AlCl_3$ IL. It is known that the electrodeposition of metal follows a three-dimensional nucleation process at the initial stages. There are mainly two nucleation growth models, viz. instantaneous and progressive, as described by Scharifker and Hills (49). The dimensionless experimental current–time transients is compared with the dimensionless theoretically instantaneous and progressive nucleation model, which can be expressed by equations [10-11], which represent the relationship between dimensionless current density (j/j_m) to the dimensionless time (t/t_m).

Instantaneous: $(j_{inst}/j_m)^2 = 1.9542(t_{inst}/t_m)^{-1}\{1 - exp[-1.2564(t_{inst}/t_m)]\}^2$ [10]

Progressive: $(j_{prog}/j_m)^2 = 1.2254(t_{prog}/t_m)^{-1}\{1 - exp[-2.3367(t_{prog}/t_m)^2]\}^2$ [11]

where j is the current density (A m^{-2}) at any time t, j_m is the maximum current density at t_m time (s) where it occurs. To determine the nucleation mechanism of Ti-Al alloy in BMIC-$AlCl_3$ IL, the data from Figure 6a are compared with the theoretical instantaneous and progressive nucleation model. Such dimensionless current-time transients for different potentials at 383K along with theoretical nucleation processes are plotted and compared in Figure 6b. Hence, it is clear that the electrodeposition of Ti-Al alloy follows instantaneous nucleation at a lower temperature, suggesting a 3D instantaneous nucleation process.

Conclusions

The electrochemical behavior of titanium-chloroaluminate anion species in Lewis acidic BMIC-$AlCl_3$ ionic liquid with 0.667 $AlCl_3$ mole fraction is investigated by cyclic voltammetry (CV) and chronopotentiometry (CP) at 383K to calculate the diffusion coefficient (*D*). The *D* values obtained from CV and CP methods are 9.74×10^{-10} m^2 s^{-1} and 6.36×10^{-10} m^2 s^{-1}, respectively. Further, the nucleation and growth mechanism of Ti-Al alloy deposition from BMIC-$AlCl_3$ ionic liquid is studied from chronoamperometry (CA). The three-electron reduction process of $Al_2Cl_7^-$ to metallic Al is quasi-reversible, while the two-electron reduction of $[Ti(Al_2Cl_7)_4]^{2-}$ to metallic Ti is a reversible process. The CA study indicated that the nucleation of Ti-Al alloy is an instantaneous nucleation process.

Acknowledgments

The authors acknowledge the financial support from the National Science Foundation (NSF) award number 1762522 and ACIPCO for this research project. Authors also thank the Department of Metallurgical and Materials Engineering, the University of Alabama, for providing the experimental and analytical facilities.

References

1. W. Kroll, *Trans. Electrochem. Soc.*, **78**(1), 35 (1940).
2. K. H. Stern, in *Metallurgical and Ceramic Protective Coatings*, p. 9, Springer (1996).
3. D. Wei, M. Okido and T. Oki, *J. Appl. Electrochem.*, **24**(9), 923 (1994).
4. T. Oishi, H. Kawamura and Y. Ito, *J. Appl. Electrochem.*, **32**(7), 819 (2002).
5. J. H. Von Barner, P. Noye, A. Barhoun and F. Lantelme, *J. Electrochem. Soc.*, **152**(1), C20 (2004).
6. Y. Song, S. Jiao, L. Hu and Z. Guo, *Metall. Mater. Trans. B*, **47**(1), 804 (2016).
7. D. R. Sadoway, *JoM*, **43**(7), 15 (1991).
8. S. Hai-bin, Z. Xiu-rong, Z. Zhi-guo and H. Xue-hui, *J. Electrochem.*, **14**(1), 104 (2008).
9. C. Guang-Sen, M. Okido and T. Oki, *Electrochim. Acta*, **32**(11), 1637 (1987).
10. D. Pradhan and R. Reddy, Production of Al-Ti Alloys Using Ionic Liquid Electrolytes at Low Temperatures, in *Innovation in Titanium Technology: Novel Materials and Processes I*, p. 79, TMS, The Minerals, Metals and Materials Society (2007).
11. D. Pradhan and R. G. Reddy, *Electrochim. Acta*, **54**(6), 1874 (2009).
12. D. Pradhan, R. Reddy and A. Lahiri, *Metall. Mater. Trans. B*, **40**(1), 114 (2009).
13. M. Zhang, V. Kamavaram and R. G. Reddy, *Mining Metall. Explor.*, **23**(4), 177 (2006).
14. D. R. MacFarlane, M. Forsyth, E. I. Izgorodina, A. P. Abbott, G. Annat and K. Fraser, *Phys. Chem. Chem. Phys.*, **11**(25), 4962 (2009).
15. H. Weingaertner, *Angew. Chem. Int. Ed.*, **47**(4), 654 (2008).

16. J. D. Holbrey, W. M. Reichert, R. G. Reddy and R. D. Rogers, in *Ionic Liquids as Green Solvents: Progress and Prospects,* , R. D. Rogers and K. R. Seddon Editors, p. 121, ACS Symposium Series 856, American Chemical Society, New York (2003).
17. V. Kamavaram and R. G. Reddy, *Int. J. Therm. Sci.*, **47**(6), 773 (2008).
18. V. Kamavaram and R. G. Reddy, in *Light metals 2005*, H. Kvande Editor, p. 501, Warrendale (2005).
19. Ramana G. Reddy, Zhijing Zhang, Mario F. Arenas and Daniel M. Blake, *High. Temp. Mater. Proc.*, **22**(2), 87 (2003).
20. V. Karmavaram and R. G. Reddy, in *Aluminum 2003*, S. K. Das Editor, p. 299 (2003).
21. Y. Peng and R. G. Reddy, in *Advances in Molten Slags, Fluxes, and Salts: Proceedings of the 10th International Conference on Molten Slags, Fluxes and Salts 2016*, p. 1169 (2016).
22. T. Wang, S. Viswanathan, D. Mantha and R. G. Reddy, *Sol. Energy Mater. Sol. Cells*, **102**, 201 (2012).
23. R. Reddy, A. Yahya and L. Brewer, *J. Alloys Compd.*, **321**(2), 223 (2001).
24. M. Zhang, V. Kamavaram and R. G. Reddy, *J. Phase Equilib. Diff.*, **26**(2), 124 (2005).
25. M. M. Zhang and R. G. Reddy, *Min. Proc. Ext. Met.*, **119**(2), 71 (2010).
26. A. Liu, Z. Shi and R. G. Reddy, *Ionics*, **26**(6), 3161 (2020).
27. A. Liu, Z. Shi and R. G. Reddy, *Electrochim. Acta*, **251**, 176 (2017).
28. A. Liu, Z. Shi and R. G. Reddy, *J. Electrochem. Soc.*, **164**(9), D666 (2017).
29. M. Li, Z. Wang and R. G. Reddy, *J. Electrochem. Soc.*, **161**(4), D150 (2014).
30. P. Koronaios, D. King and R. A. Osteryoung, *Inorg. Chem.*, **37**(8), 2028 (1998).
31. V. Kamavaram, D. Mantha and R. G. Reddy, *Electrochim. Acta*, **50**(16), 3286 (2005).
32. Q. Liao, W. R. Pitner, G. Stewart, C. L. Hussey and G. R. Stafford, *J. Electrochem. Soc.*, **144**(3), 936 (1997).
33. Y. Zhao and T. VanderNoot, *Electrochim. Acta*, **42**(11), 1639 (1997).
34. T. Jiang, M. C. Brym, G. Dubé, A. Lasia and G. Brisard, *Surf. Coat. Technol.*, **201**(1-2), 1 (2006).
35. Z. J. Karpinski and R. A. Osteryoung, *Inorg. Chem.*, **23**(10), 1491 (1984).
36. D. Pradhan and R. G. Reddy, *Mater. Chem. Phys.*, **143**(2), 564 (2014).
37. J. Tang and K. Azumi, *Electrochim. Acta*, **56**(3), 1130 (2011).
38. T. Jiang, M. J. Chollier Brym, G. Dubé, A. Lasia and G. M. Brisard, *Surf. Coat. Technol.*, **201**(1), 1 (2006).
39. J. S. Wilkes, J. A. Levisky, R. A. Wilson and C. L. Hussey, *Inorg. Chem.*, **21**(3), 1263 (1982).
40. J. Tang and K. Azumi, *Electrochim. Acta*, **56**(3), 1130 (2011).
41. F. Endres, S. Zein El Abedin, A. Y. Saad, E. M. Moustafa, N. Borissenko, W. E. Price, G. G. Wallace, D. R. MacFarlane, P. J. Newman and A. Bund, *Phys. Chem. Chem. Phys.*, **10**(16), 2189 (2008).
42. A. Bakkar and V. Neubert, *Electrochem. Commun.*, **51**, 113 (2015).
43. P. S. Shinde, Y. Peng and R. G. Reddy, in, p. 1659, TMS 2020 149th Annual Meeting & Exhibition Supplemental Proceedings, Cham (2020).
44. A. J. Bard, L. R. Faulkner, J. Leddy and C. G. Zoski, *Electrochemical Methods: Fundamentals and Applications*, Wiley New York (1980).

45. R. S. Nicholson and I. Shain, *Anal. Chem.*, **36**(4), 706 (1964).
46. A. J. Bard and L. R. Faulkner, Fundamentals and Applications, New York: Wiley, 2001, in, Wiley & Sons (2001).
47. J. E. Baur, in *Handbook of Electrochemistry*, C. G. Zoski Editor, p. 829, Elsevier, Amsterdam (2007).
48. H. Yang and R. G. Reddy, *J. Electrochem. Soc.*, **161**(10), D586 (2014).
49. B. Scharifker and G. Hills, *Electrochim. Acta*, **28**(7), 879 (1983).

ECS Transactions, 98 (10) 245-251 (2020)
10.1149/09810.0245ecst ©The Electrochemical Society

Electroplating of Bright Aluminum on The ABS Resin Substrate Covered with Cu Film in EmImCl-$AlCl_3$ Ionic Liquid

Mikito Ueda

Faculty of Engineering, Hokkaido University, Sapporo, Hokkaido,060-8628 Japan

To form bright and uniform Al electroplated film on Cu substrate, stirring effect in 1-ethyl-3-methylimidazolium chloride (EmImCl) and $AlCl_3$ mixture ionic liquid was investigated, then supporting electrodes were arranged for the Cu electrode. Al electroplating film with bright surface from the ionic liquid containing the additive formed depend on rotation rate of ionic liquid electrolyte. By arranging the supporting electrodes, current concentration on the substrate was dispersed from the edge to the whole of substrate. The Al electroplated film having a uniform thickness was also formed on the ABS resin substrate covered with Cu plating. The electroplated film formed on the ABS substrate was anodized and showed pink, blue and orange.

Introduction

Aluminum (Al) has excellent corrosion resistance, and its surface hardness can be increased by alloying with other elements. From these characteristics, Al is widely used as daily necessities, building materials and plating materials. Further, since Al formed into a mirror surface has a reflectance of 90% or more in the visible light region, it has been used as an optical device such as a microscope and a reflector of an LED light in the optical field. To form Al thin film, there are a vacuum vapor deposition method (1-2), a hot dipping method (3), and an electroplating method (4-8). The vacuum vapor deposition method can form a glossy surface, but it is difficult to form a thin film in a complicated shape or thicken the film. In the hot dip plating method, a large amount of plating can be possible on a large area substrate with low cost, but it is difficult to control the thin film. In the electroplating method, if it has conductive surface, it is possible to plate even a surface having a complicated shape, and it is easy to control the film thickness by the amount of electricity. Our group aims to form a bright aluminum electroplating on a resin that is even lighter than aluminum. This study may contribute to further weight reduction of mobile devices.

− When Al plating is formed by the electroplating method, an aqueous solution electrolyte can't use, therefore non-aqueous liquids must be used. Molten salts, organic solvent, and ionic liquids are candidates for Al electroplating. Since the heat resistant temperature of ABS resin is about 100 ^oC, Al electroplating on ABS resin cannot be achieved in molten salt electrolysis (150 ^oC). These results were achieved by using an EmImCl-$AlCl_3$ ionic liquid.

In this study, we investigated bright Al plating using an ionic liquid that enables Al plating at ionic liquid. The ionic liquid as an electrolyte with a higher electrical conductivity is desirable because a larger current can flow in electroplating process. In this

study, an ionic liquid of 1-ethyl-3-methylimidazolium chloride (EmImCl) and $AlCl_3$ mixture was used as an electrolyte for Al electroplating from the viewpoint of electrical conductivity. Conditions for bright plating using an electrolyte containing additives and arrangement of supporting electrodes for uniform thickness electroplated film were studied.

Experimental

The electrolyte is EmImCl -$AlCl_3$ ionic liquid (Kanto Chemical Co., Ltd.) with molar ratio of 1 : 2. Then 1,10-Phenanthroline (Wako Pure Chemical, 99.9%) is added to the ionic liquid as an additive. Concentration of additive is 20 mM. The electrolysis cell was made by a Pyrex glass, and this was filled with 180 ml of electrolyte. All Al plating experiments were performed in the temperature of 60°C in a glove box under Ar atmosphere. A magnetic stirrer was used for stirring the electrolyte. A Cu plate and ABS resin covered with Cu film were used as substrate for electroplating and the substrates were sealed by PTFE (polytetrafluoroethylene) tape.

The counter electrode is Al plate (Nippon Light Metal Co., 99.99%) or Al mesh were used. The Al surface was polished with #800 water-resistant SiC paper and then ultrasonically cleaned with acetone. The Cu electrode and the Al electrode were placed with distance of 5 mm. Electrodeposition experiments were carried out by current pulse electrolysis with 20 $mAcm^{-2}$ and duty ratio of 0.83 (t_{on} = 1.0 s, t_{off} = 0.2 s). Charge density was 59.7 Ccm^{-2} (Theoretical film thickness of 20μm). A potentiostat (HZ-5000, Hokuto Denko) was used to control the electroplating current.

In order to quantitatively evaluate the electroplated surface, the reflectance was measured using a fiber optical reflection probe (Halogen white light source: HL-2000+, spectroscope: USB2000+, Ocean Optics, USA). Reflectance of the aluminum mirror (reflectance: 90%) was used as a reference. The average roughness of the Al plating was measured using an atomic force microscope (AFM; Nanocute, SII Nano Technology) in the Dynamic Force mode at a scanning frequency of 0.91 Hz. Al electroplated samples with and without support electrodes were filled with cured resin, cut, and polished, and then observed by SEM.

The Al plating sample on Cu-coated ABS substrate was anodized at 20°C in sulfuric acid solution. The electroplated sample after the anodizing was washed with water and then colored in three colors of pink, blue and orange.

Results and discussion

Pulse electrolysis was carried out using an Al plate counter electrode, and when the stirring rate was 100 to 600 rpm, the glossiness of the plating surface was improved with increasing stirring rate from 0 to 400 rpm. However, at 500 rpm, a non-glossy plating was formed in the center, and at 600 rpm, most of surface was not formed a glossy surface. It was found that there is appropriate rate in the stirring of the electrolyte.

The reflectance of the center of the electroplating samples formed at 0 to 400 rpm were measured. Figure 1 shows the reflectance of electroplated samples in the visible light

range (500 to 800 nm). These reflectance values are the ratio of the reflectance of samples when the reflectance of the reference aluminum mirror is 100%. From this figure, the reflectance of each sample changes slightly depending on the wavelength, but increases in sequence from 0 to 400 rpm. At a wavelength of 500 nm, reflectance was 8.76% at 0 rpm, 27.8% at 100 rpm, 52.6% at 200 rpm, 67.7% at 300 rpm, and 74.7% at 400 rpm.

In order to investigate the electrodeposition morphology on the electroplating surface, SEM observation of the Al electroplating surface was performed under the condition that the glossiness was increased (0 to 400 rpm). SEM images of the center of the plating surface at each stirring speed are shown in Fig. 2 (a)-(e).

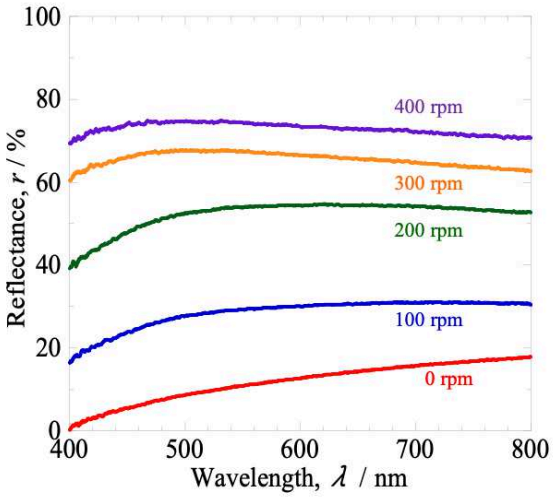

Figure 1. Reflectance of the center parts of Al electroplated samples formed stirring condition from 0 to 400 rpm (9).

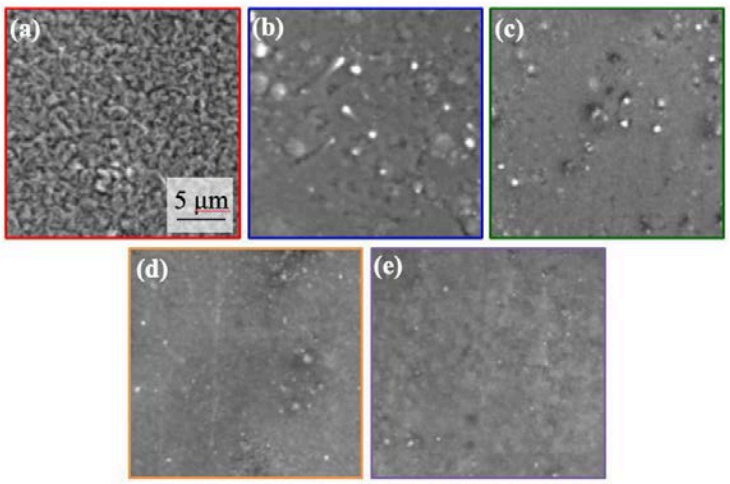

Figure 2. SEM images of the center parts of Al electroplated surface formed stirring condition of (a)0 rpm, (b)100 rpm, (c)200 rpm, (d)300 rpm, and (e)400 rpm (9).

From the figures, comparing the samples obtained without stirring in (a) and with stirring in (b)-(e), grain boundaries were clearly confirmed in the sample without stirring, but it was difficult to distinguish the grain boundaries in other samples. The particle size without stirring is about 1 μm, but the particle under the condition of 100 to 400 rpm were not clearly observed. From this result, it is considered that the particles become finer by stirring the electrolyte. Further, the results of surface roughness measurement by AFM for a plated sample of 0 to 400 rpm are shown in Fig. 3(a) to (e). From the figures, relatively large roughness was observed on the plated surface without stirring (a), and the average arithmetic roughness (Ra) value was about 26 nm. It was found that the roughness gradually became smaller as the stirring rate increased, and a smoother surface was formed. The Ra value of the surface at 400 rpm in Fig. 3(e) was 2.3 nm, which corresponds to about 1/10 of that without stirring.

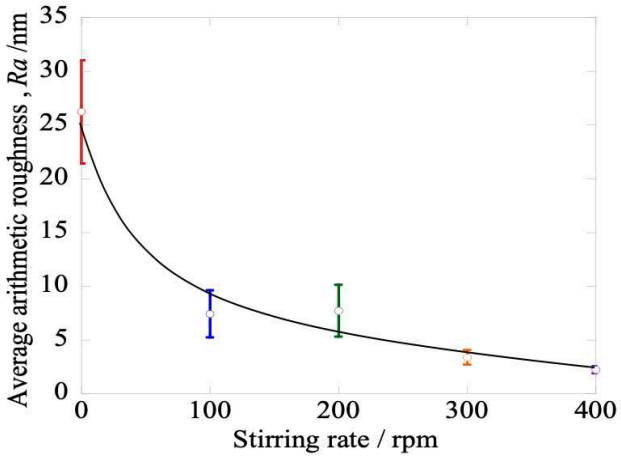

Figure 3. Average arithmetic roughness (Ra) of the Al electroplated surface at stirring rate from 0 to 400 rpm (9).

The Al electroplating experiment using a meshed Al counter electrode was performed under the same electrolysis conditions without stirring. Fig. 4 shows a photograph of the outside view of the electroplated sample after electrolysis. From the photograph, it was found that bright Al plating was formed on almost the entire surface. When the reflectance of this sample was measured, it showed a reflectance of about 80% compared to the Al mirror. Therefore, it was confirmed that a glossy surface formed in a wide area even without stirring with the use of a meshed Al counter electrode.

Figure 4. Photograph of the Al electroplating on Cu plate using Al mesh counter electrode in EmimCl-$AlCl_3$ ionic liquid at 60 °C without stirring (9).

The results of film thickness measurement without a supporting electrode and with a supporting cathode are shown in Fig. 5 and Fig. 6 respectively. When the supporting electrode was not used, the film thickness was 16.1 μm at the center, 36.7 μm at the left end, and 57.1 μm at the corner at the right end, and it was observed that the film thickness increased from the center to both ends. When the supporting cathode was used, the film thickness was 23.0 μm at the center, 22.7 μm at the left end, and 19.8 μm at the right end. In the case of without supporting electrode, the current may flow from both edge sides of the working electrode. As a result, the growth rate of film becomes faster than the center part. In case of with supporting cathode, the current flowing at the edge sides flows into also the supporting cathode, therefore concentration of the current at the edge sides of the working electrode hardly occurs.

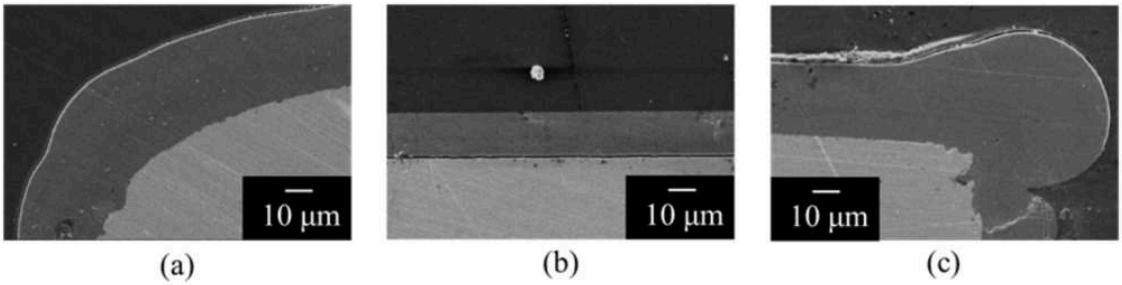

Figure 5. SEM images of cross section of the Al electroplated film on Cu plate formed without supporting electrode; (a) left edge, (b) center and (c) right edge (10).

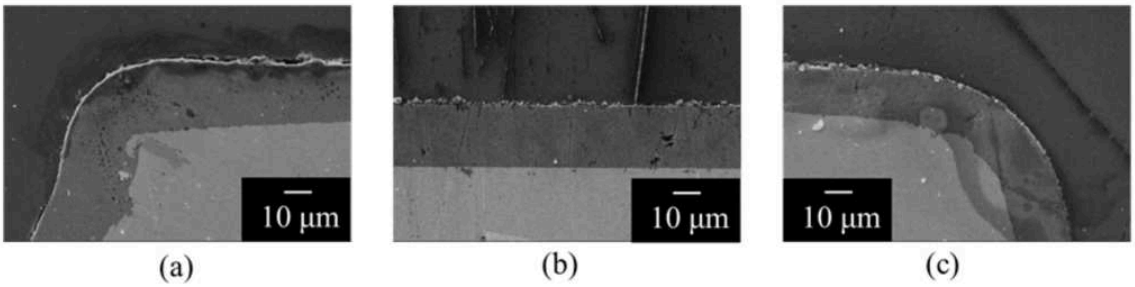

Figure 6. SEM images of cross section of the Al electroplated film on Cu plate formed with parallel supporting cathode; (a) left edge, (b) center and (c) right edge (10).

Photographs of an ABS resin substrate coated with a copper plating and electroplating sample on the substrate are shown in Fig. 7. From the photograph, it can be seen that the Al electroplated surface also exhibits the same gloss as before the electroplating. Photographs of the electroplated sample which was treated by color almite in sulfuric acid solution are shown in Fig. 8 (a)-(c). From this photograph, the color-anodized surface shows vivid pink, blue and orange. The cracks are obserbed at the part where weak plating adhesion for the Cu substrate. The findings in this study result are that the Al film formed by electroplating can be anodized as with bulk Al.

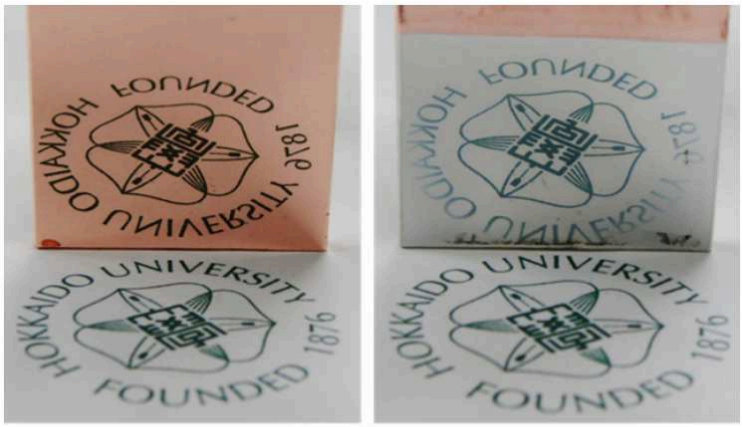

Figure 7. Photographs of ABS resin substrate covered with Cu plating (a) and (b) after Al electroplating treatment (10).

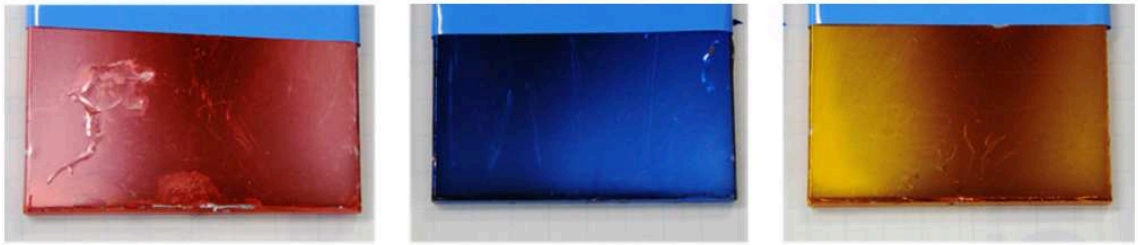

Figure 8. Photographs of Al electroplated film after color alumite treatment; (a) pink, (b) blue, and (c) orange (10).

Conclusions

To form bright and uniform Al electroplated film, Al electroplating experiment was carried out in EmImCl and $AlCl_3$ mixture ionic liquid containing 1,10-Phenanthroline at 60°C.

(1)The roughness of the electroplated surface becomes smaller as the stirring rate of the electrolyte increases (0-400 rpm) in counter electrode of Al plate.

(2)When the Al mesh was used as the counter electrode, the smoothness of the electroplated surface was improved without stirring.

(3)The arrangement of the supporting electrodes dispersed the current concentration on the electrode and forms a uniform film thickness. The Al film formed by electroplating can be anodized and colored as bulk Al.

Acknowledgments

I would like to thank Prof. Dr. Kikuchi (Hokkaido University), Prof. Dr. Matsushima (Hokkaido University), C. Namekata (DENSO Corporation), H. Takahashi (DENSO Corporation), and T. Hirai (Nippon Light Metal Co., Ltd) for supporting this experiments.

References

1. H. Yamamoto, *Kinzoku Hyomen Gijutsu,* **30**(5), 225 (1979).
2. M. Sugiyama, *Kinzoku Hyomen Gijutsu,* **4** (3), 116 (1953).
3. *6th edition Denkikagaku Binran*(Ed. Electrochemical Society Japan), Maruzen, P. 493 (2013).
4. *6th edition Denkikagaku Binran*(Ed. Electrochemical Society Japan), Maruzen, P. 507 (2013).
5. T. Jiang, MJC. Brym, G. Dube, A. Lasia, and GM. Brisard, *Surface & Coatings Technology*, **201**, 1 (2006).
6. JK. Chang, SY. Chen, WT. Tsai, MJ. Deng, and IW. Sun, *Electrochemistry Communications*, **9**, 1602 (2007).
7. B. Li, CH. Fan, Y. Chen, JW. Lou, and LG. Yan, *Electrochimica Acta*, **56**(16), 5478 (2011).
8. AP. Abbott, CA. Eardley, NRS. Farley, GA. Griffith, and A. Pratt, *Journal of Applied Electrochemistry*, **31**(12), 1345 (2001).
9. H. Takahashi, C. Namekata, T. Kikuchi, H. Matsushima, and M. Ueda, *J. Surf. Finish. Soc. Jpn*, **68**, 208 (2017).
10. T. Hirai, H. Matsushima, and M. Ueda, *J. Surf. Finish. Soc. Jpn,* **71**, 32 (2020).

ECS Transactions, 98 (10) 253-260 (2020)
10.1149/09810.0253ecst ©The Electrochemical Society

Anodic Behavior of $MoSi_2$ in Molten $MgCl_2$-NaCl-$CaCl_2$ Containing Oxide Ions

Takamasa Miyoshi[a], Taiki Morishige[b] and Toshihide Takenaka[b]

[a] Graduate School of Science and Engineering, Kansai University,
Suita, Osaka 564-8680, Japan
[b] Department of Chemistry and Material Engineering, Kansai University,
Suita, Osaka 564-8680, Japan

Abstract

The anodic behavior of $MoSi_2$ in molten $MgCl_2$-NaCl-$CaCl_2$ containing oxide ions has been investigated in this study to aim at developing an inert anode in this melt. A sharp anodic current peak appeared around 1.8V (vs. Mg / Mg^{2+}) in a cyclic voltammogram, which suggested that $MoSi_2$ was passivated in the melt with oxide ions. An oxide film consisting of SiO_2 and $MgSiO_3$ was formed on $MoSi_2$ by potentio-static electrolysis more positively than 1.6V (vs. Mg / Mg^{2+}), and gas bubbles kept generating during the electrolysis. The current contributions assuming that the dissolution of Mo and the formation of $MgSiO_3$ were estimated from the weight change and the film thickness after potentio-static electrolysis. The current contribution other than the Mo dissolution and the oxide film formation enlarged with the increase in the electrolysis duration and the raise in the electrolysis potential, and became above 90%. These results imply that $MoSi_2$ is potential as an inert anode in molten $MgCl_2$-NaCl-$CaCl_2$ containing oxide ions.

Introduction

Mg and Li are smelted by electrolysis in molten chloride, and carbon-based material is used for the anode. carbon-based material has advantages in chemical stability in the bath. However, since chloride salt has a high hygroscopic property, carbon-based material is consumed by electrochemical reaction with dissolved O^{2-}, for example, the reaction [1].

$$C + xO^{2-} \rightarrow CO_x + 2xe^- \quad [1]$$

The so-called inert anode is desired, and it has been reported that glassy carbon (1) and boron-doped diamond (2) behaved as an inert anode in molten LiCl-KCl at 700K. However, an inert anode which can be used at higher current density and at higher temperature has not been studied well.

The authors proposed an inert anode by forming a stable passivation film on the electrode. The anodic behavior of SiC and $MoSi_2$ in molten LiCl-KCl containing oxide ions had been studied (3-8). SiO_2 was formed on a surface of SiC with CO_2 gas generation by potentio-static electrolysis. However, the protection by the SiO_2 film seemed insufficient and SiC was consumed severely. SiO_2 was also formed on $MoSi_2$ surface in the bath. The likely reaction to form SiO_2 is shown as [2]. The consumption of $MoSi_2$ was inhibited by the film formation, but the protection was insufficient so far.

$$MoSi_2 + 4O^{2-} \rightarrow Mo^{3+} + 2SiO_2 + 11e^- \quad [2]$$

In this paper, the anodic behavior of $MoSi_2$ in molten $MgCl_2$-NaCl-$CaCl_2$ at higher temperatures was investigated, and the inhibition of $MoSi_2$ consumption by the formed oxide layer is discussed.

Experimental

The experimental apparatus is illustrated in Fig. 1. In a glove box filled with Ar, about 50 g of $MgCl_2$-NaCl-$CaCl_2$ (about 20: 50: 30 in weight) was put in a transparent quartz glass crucible, and about 1.0 mass% of MgO (99.9%, anhydrous) was added. The mixture was placed in an electric furnace with observation ports. The furnace was heated about 973K, and electrolysis was carried out under Ar atmosphere.

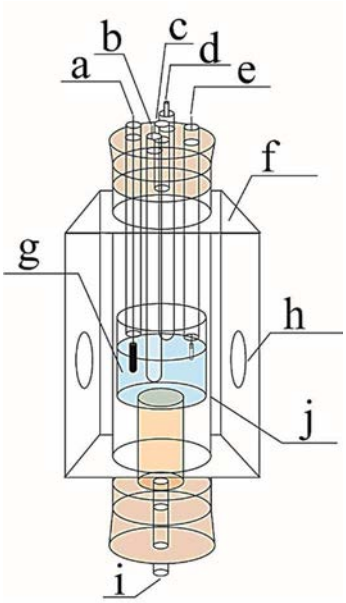

a. reference electrode
b. counter electrode
c. Ar inlet
d. thermocouple
e. working electrode
f. electrolysis device
g. observation window
h. Ar outlet
i. Core tube

Figure 1 Apparatus for electrochemical measurement and electrolysis.

Polished $MoSi_2$ rod (ϕ3.0mm) was used as the working electrode. The counter electrode was a Cu plate with a large surface area. A couple of Ag/AgCl in the same melt in a ceramic membrane was used as the reference electrode. Since the electrode potential of the Ag/AgCl reference electrode changes easily with the concentration of AgCl, its potential was calibrated via the Mg deposition potential. All the potential in this paper was represented with this potential as Mg/Mg^{2+}.

The anodic behavior of $MoSi_2$ was investigated by cyclic voltammetry and potentio-static electrolysis. The appearance around the $MoSi_2$ electrode during electrolysis was simultaneously observed with a CCD camera, and recorded by a video system. The electrochemical response was synchronized and superimposed to the recorded view. The change in the $MoSi_2$ surface by electrolysis was analyzed by XRD (RINT 2500V) and SEM(JCM-6000)-EDX(Ex-5441). The protective property was evaluated by the weight change, the thickness of the formed film after the potentio-static electrolysis and the quantity of electricity during electrolysis.

Results and Discussion

Anodic Behavior of $MoSi_2$

Fig. 2 shows a cyclic voltammogram at the $MoSi_2$ in the bath with MgO. The anodic

current increased above 1.6 V with bubbles generation. An anodic current peak appeared at about 1.8V, and the current density decreased sharply thereafter. This phenomenon was not observed in the bath without MgO. Since oxide film was found after potentio-static electrolysis, it was thought that the passivation phenomenon occurred in the bath containing MgO.

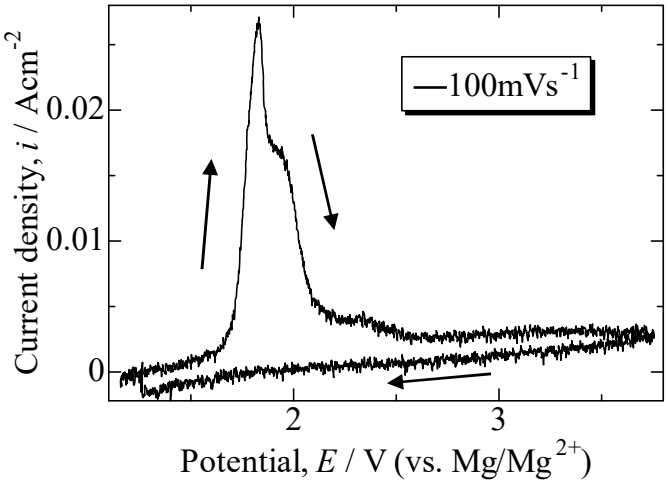

Figure 2 Cyclic voltammogram in the bath with MgO.

$MoSi_2$ after Potentio-Static Electrolysis

Potentio-static electrolysis was performed at 1.9 V, 3.1 V, and 6.3V. The $MoSi_2$ surface was covered with a dense film after the electrolysis at 3.1V and 6.3V, while the film formation seemed irregular by the electrolysis at 1.9V.

Fig. 3 shows the SEM image and element distributions of the cross-section of the $MoSi_2$ electrode after potentio-static electrolysis at 3.1V. A thin film was seen on the surface, and Mg and O were concentrated in it. A similar oxide film was formed by the electrolysis at 3.1V and 6.3V. However, it was seen by visual observation that the surface film peeled off during the electrolysis at 6.3V with sudden change in electrolysis current.

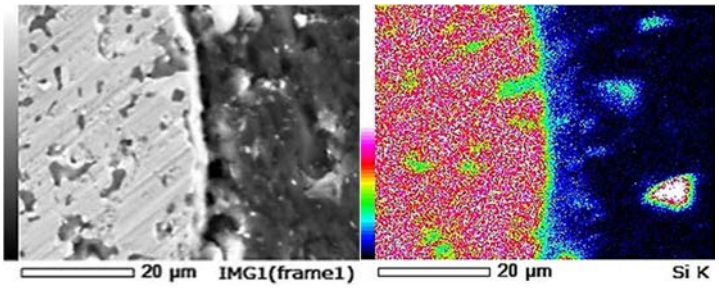

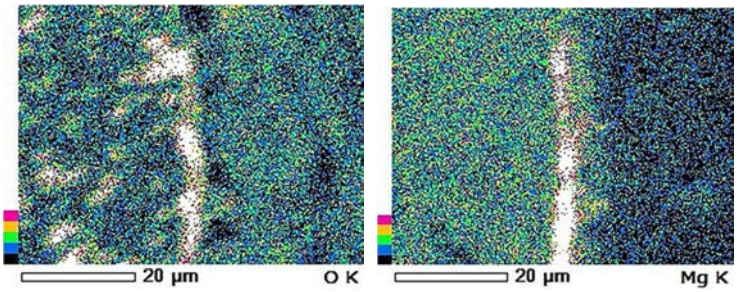

Figure 3 SEM image and element distribution cross-section of the $MoSi_2$ electrode after potentio-static electrolysis at 3.1V.

$MgSiO_3$ and SiO_2 were detected by XRD analysis as shown in Fig. 4, so the reaction [2] and the following reactions were thought to take place on the surface of the anode electrode.

$$SiO_2 + MgO \rightarrow MgSiO_3 \quad [3]$$

$$Mg^{2+} + 3O^{2-} + Si \rightarrow MgSiO_3 + 4e^- \quad [4]$$

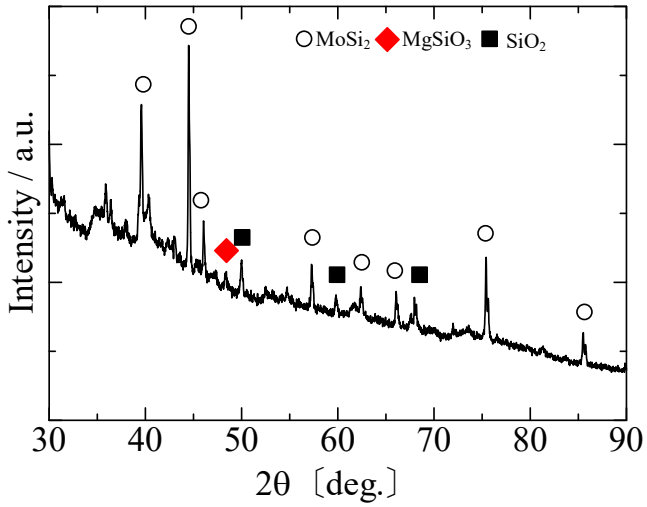

Figure 4 X-ray diffraction pattern of electrode after potentio-static electrolysis at

Weight Change of $MoSi_2$

Fig. 5 shows the weight change of the $MoSi_2$ with electrolysis duration. The anodic current was very small during the potentio-static electrolysis at 1.9V, so the weight of the $MoSi_2$ rarely changed. In the electrolysis at 3.1V, the weight increased at the early stage and became small with electrolysis. The weight change was very small by the short electrolysis at 6.3V even though the anodic current was observed. However, the weight

apparently decreased with the electrolysis time. It is thought that the film on the electrode surface peeled off under the condition.

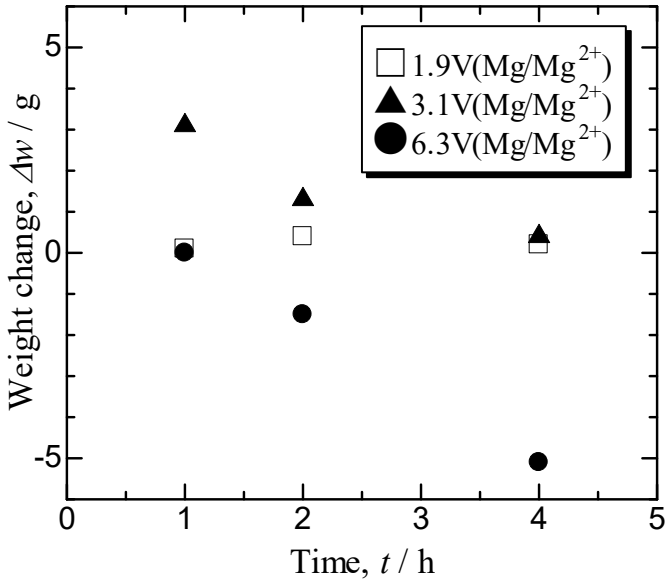

Figure 5 Weight change of $MoSi_2$ under various conditions.

Current Contribution to Anodic Reactions

The current contribution was calculated from the weight change of the $MoSi_2$ and thickness of the oxide layer under the assumption that the reactions during potentio-static electrolysis were only $MgSiO_3$ formation and Mo dissolution by reaction [2] and [3]. The amounts of the formed $MgSiO_3$ layer: n_{MgSiO3}(mol) and dissolved Mo: n_{Mo}(mol) are given as follows;

$$n_{MgSiO_3} = \frac{V_{layer}\rho_{MgSiO_3}}{M_{MgSiO_3}} \quad [5]$$

$$n_{Mo} = \frac{\Delta w - n_{MgSiO_3}M_{MgSiO_3}}{M_{Mo}} \quad [6]$$

where M_i, V_{MgSiO3}, ρ_{MgSiO3} and Δw are the atomic weight of substance i (kg/mol), film volume(cm^3), $MgSiO_3$ density(kg/cm^3) and weight change by electrolysis, respectively. The current contribution by the $MgSiO_3$ formation P_{MgSiO3} and Mo dissolution P_{Mo} are caluculated as follows;

$$P_{MgSiO_3} = \frac{4n_{MgSiO_3}F}{Q} \times 100 \quad [7]$$

$$P_{Mo} = \frac{3n_{Mo}F}{Q} \times 100 \quad [8]$$

where Q is the quantity of electricity during potentio-static electrolysis (C) and F is Faraday constant (C/mol). The electrolysis current seemed to be spent partly other than the $MgSiO_3$ formation and Mo dissolution, and its contribution P_{other} is given as follow;

$$P_{other} = 100 - P_{MgSiO3} - P_{Mo} \quad [9]$$

Table 1 shows the contribution rate in the anodic reaction at each potential. P_{MgSiO3} and P_{Mo} were very large in the electrolysis at 1.9V. Under this condition, the $MoSi_2$ was not passivated sufficiently, which seemed to cause the strange result. In the electrolysis at 3.1V, both P_{MgSiO3} and P_{Mo} decreased with the electrolysis duration. P_{MgSiO3} and P_{Mo} were very small in the electrolysis at 6.3V for 1h, though the contributions in the longer electrolysis could not be estimated because of peeling-off of the film. P_{MgSiO3} and P_{Mo} tended to decrease with long-term electrolysis and higher electrolysis potential, which indicated that the formation of an oxide layer and Mo dissolution were inhibited by the progress of passivation.

The current contribution other than the $MgSiO_3$ formation and Mo dissolution P_{other} tended to increase with the electrolysis time and potential, and reached more than 90% under a suitable condition. Since gas bubbles kept generating during the electrolysis, P_{other} is thought due to this gas generation mainly. Since the theoretical decomposition voltages of pure $MgCl_2$ and MgO at 973K were estimated as 2.35V and 2.40V (9), respectively, the generated gas under the condition cannot be identified. Further research on the analysis of the gas is necessary.

From the estimation on the current distribution, it is suggested that $MoSi_2$ has a potential as an inert anode under this condition.

Table 1. Current contribution for reactions at 1.9V, 3.1V and 6.3V.

		P_{Mo} /%	P_{MgSiO3} /%	P_{other} /%
1.9V	1h	17.9	122	—
	2h	23.0	272	—
	4h	1.02	36.0	63.0

3.1V	1h	57.0	24.2	18.8
	2h	20.8	21.5	57.7
	4h	3.70	1.40	94.9
6.3V	1h	1.77	9.90	88.3
	2h	—	—	—
	4h	—	—	—

Conclusion

The $MoSi_2$ anode shows the passivation phenomenon in the melt $MgCl_2$-NaCl-$CaCl_2$, and an oxide film containing $MgSiO_3$ and SiO_2 was formed. The current contributions by the oxide film formation and Mo dissolution were calculated from the thickness of the film and the weight change, and it is shown that the current contribution other than the oxide film formation and Mo dissolution reached more than 90% under the suitable condition. The current contribution other than the oxide film formation and Mo dissolution is thought due to gas generation, which suggest that $MoSi_2$ is a potential as an inert anode in molten $MgCl_2$-NaCl-$CaCl_2$ containing O^{2-}.

Acknowledgements

This research was supported by the Salt Science Research Foundation 2019 Research Grant (#1906).

References

1. S. Paek, Si-Hyung Kim, D. Yoon, Tack-Jim Kim, Doo-Hee Ahn and Hansoo Lee, *J. Rad. Nuc. Chem.*, **295**, 439-444(2013).
2. W. Park, Jong-Kook Kim, Jin-Mok Hur, Eun-Young Choi, Hun Suk lm, Sun-Seok Hong, *J. Nuc. Mater.*, **432**, 175-181 (2013).
3. T. Takenaka and M. Kawakami: *ECS Trans*., **3(35)** (2007), 385.
4. T. Takenaka, K. Iwasa, Y. Hashigaya and M. Izaki: *Electrochemistry*, **77** (2009), 633.
5. M. Umehara, Taiki Morishige, Toshihide Takenaka: Proc. 4th Asian Conf. on Molten Salt Chem.and Tech., (2012), 388-389.
6. T. Takenaka, M. Umehara, D. Araki and T. Morishige: *ECS Trans.*, **50(11)** (2012), 127.
7. D. Araki, T. Morishige and T. Takenaka: Proc. 4th Asian Conf. on Molten Salt Chem. and Tech., (2012), 312-313.
8. Y. Takahashi, T. Morishige and T. Takenaka: *ECS Trans.*, **75(15)** (2016), 207.
9. *HSC chemistry for Windows, ver 5.1*, Outokumpu Research Oy, Finland (2002).

Chapter 8

L02 – Monday Poster Session

ECS Transactions, 98 (10) 263-270 (2020)
10.1149/09810.0263ecst ©The Electrochemical Society

Synthesis of Refractory Metal Carbides on Carbon Fibers in Molten Salts and Their Electrochemical and Electrocatalytic Properties

D. G. Miklashov, S. O. Luneva, V. S. Dolmatov, and S. A. Kuznetsov

Tananaev Institute of Chemistry of the Federal Research Centre "Kola Science Centre of the Russian Academy of Sciences", Apatity, Russia

TaC and NbC coatings and Mo_2C crystals on carbon fibers were obtained by currentless transfer in molten salts. Investigation of electrocatalytic properties of these compositions in the reaction of the hydrogen peroxide decomposition was carried out. The kinetic parameters of this reaction were determined. It has been established that NbC on carbon fibers has a higher electrocatalytical properties in comparison with other carbides.

Introduction

Carbides of refractory metals with a high melting point, heat resistance, high microhardness, etc., are widely used as protective coatings on parts and assembly units in order to improve performance and reduce the production cost of parts made from inexpensive materials (1-4). Carbides of refractory metals also have catalytic and electrocatalytic properties.

The most popular methods for producing different coatings are chemical and physical vapor deposition. However, electrochemical synthesis methods in molten salts have a number of advantages over other synthesis methods (4-6). Electrochemical synthesis is relatively simple in the technical organization of the process and allow to produce non-porous coatings of refractory metal carbides. Carbides of refractory metals obtained by electrochemical methods have a good adhesion to the substrate, a wear resistance and tribotechnical characteristics.

Coatings of refractory metal carbides on substrates with high specific surface area can be used as electrocatalytic systems in reduction and oxidation reactions (7). The advantage of using electrocatalysis is the ability to carry out various reactions in a wide range of conditions from an extremely reducing environment to an extremely oxidizing one. The next is the ability to control the course of the reaction by accurately adjusting the potential, and to carry out some processes that are impossible in practice. Unlike conventional catalysis, electrocatalytic reactions do not contain reagents in products in the form of oxides, hydroxides or salts. In electrochemical processes, an electron acts as a reducing or oxidizing agent, resulting in the formation of high-purity products (8).

Oxidative reactions are the most numerous and most used in the industry, at the same time, they are listed as polluting and hazardous to nature. Therefore, the overriding importance of green chemistry is the development of alternative oxidation methods that produce less harmful wastes. Hydrogen peroxide is an ideal oxidation reagent, which in turn becomes highly effective and selective when activated with transition metals or their carbides. Therefore, we have considered the reaction of

hydrogen peroxide decomposition as an example of the electrocatalytic reaction on the surface of refractory metal carbides synthesized on carbon fiber.

Experiments

Synthesis of the Refractory Metal Carbide Coatings on Carbon Fibers

The following salt components were used in the work. Background melt was an equimolar mixture of NaCl and KCl. Salts of K_2NbF_7 and K_2TaF_7 of high purity were recrystallized in a solution of hydrofluoric acid. The production of these salts was carried out in the experimental workshop of the Institute of Chemistry, Kola Science Centre RAS. The Na_2MoO_4 of analytical grade was used in the experiments without additional treatment.

Storage and handling of salts was carried out in an argon atmosphere in a glove box MBraun LabMaster 130 (M.Braun Inertgas-Systeme GmbH, Germany) to exclude the appearance of moisture in the electrochemical cell.

A glassy carbon crucible (brand SU-2000) was used as a container for molten salts. Glassy carbon crucible was filled with a mixture of salts with a given ratio and then placed into retort. A retort was a thick-walled stainless steel tube, the upper part of which was equipped with a water-cooled refrigerator. The retort was closed with a lid with special technological holes for electrodes and salt additions.

The electrochemical cell was evacuated to a pressure 0.6 Pa with stepwise heating, first at room temperature and then at higher temperatures (200, 400 and 600 ^{0}C). After this the retort was filled with high purity argon and the electrolyte was melted.

The synthesis was carried out at temperatures of 800-900 ^{0}C.

Carbon fibers of the Carbopon-B-22 brand (Svetlogorsk, Belarus) were used as substrate for deposition. The dimensions of the carbon fiber samples were 8x20x5 mm^3, which were fixed on a molybdenum rod using a tungsten wire of a hook-shape.

The identification and study of the compounds was carried out by X-ray phase analysis (DRON-2 diffractometer, Russia), crystal optics – Leica DM 2500P (Leica Microsystems Wetzlar GmbH, Germany), IR spectroscopy – Nicolet 6700 (Thermo Scientific, USA), scanning electron microscopy – SEM LEO-420 (CARL ZEISS, Germany), X-ray microprobe analysis – INCA ENERGY-400 (OXFORD Instruments, Great Britain).

Evaluating the Electrocatalytic Activity of Refractory Metal Carbide Coatings

To study the kinetics of electrocatalytic decomposition of hydrogen peroxide on the surface of refractory metal carbides, it is possible to use the method based on measuring the volume of evolved gas in time, collected in a volumetric cylinder.

The substrate from carbon fibers with refractory metal carbides was fixed with a copper wire. The contact point of these two materials was hermetically sealed. The copper did not contact with hydrogen peroxide during experiments. Polarization of the electrodes made of fibers with coatings of refractory metal carbides was carried out

using a B5-71/1-m (Profi Group, Russia) power supply at a voltage of 30 V and the current in the circuit was monitored with a universal digital voltmeter GDM-8145-2 (GW Instek, Taiwan). Uncoated carbon fibers served as the cathode.

Oxygen was released at the anode and hydrogen at the cathode. With the accumulation of gaseous reaction product in a certain volume, the electrolysis process was completed.

The electrocatalytic activity of niobium and tantalum carbide coatings and molybdenum carbide crystals on carbon fibers in the reaction of hydrogen peroxide decomposition, was compared with each other and electrodes from copper and platinum. The surface area of metallic electrodes was 5 mm^2.

It should be noted that the value of the surface area of refractory metal carbides cannot be accurately determined. We can only say about the specific surface area, which is 5-15 m^2/g. In our experiments the linear dimensions of samples were the same and the immersion depth of samples with carbide coatings into hydrogen peroxide was the same too.

In this work, we used two integral methods for determining the order of reaction for the decomposition of hydrogen peroxide: the substitution method (calculating the reaction rate constants using equations for different reaction orders) and graphical (plotting the graphs of concentration functions versus the time and determining the linear dependence of one of them). The reaction rate constant was determined by the slope of the straight line in the corresponding coordinates.

The activation energies of the process were calculated based on the experimental data obtained at different temperatures of the experiment: 25, 30, 40, 50, 60, 70, 80 ^0C.

Results and Discussion

Synthesis of Refractory Metal Carbide Coatings on the Carbon Fibers

Interaction between metal and its own salt leads to the formation of refractory metal complexes with a lower oxidation state (5):

$$(m\text{-}n)Me + nMe^{m+} \rightarrow mMe^{n+}, \quad [1]$$

where m>n.

Complexes with an intermediate oxidation state diffuse through the melt, and disproportionate on the surface of carbon fibers:

$$mMe^{n+} + (m\text{-}n)C \rightarrow (m\text{-}n)MeC + nMe^{m+} \quad [2]$$

The driving force of reaction [2] is the energy of carbide formation $\Delta G_{MeC.}$ The disproportionation is accompanied by the formation of metal carbide and metal complexes with the higher oxidation state of m^+, where $m^+ = 5$ for tantalum and niobium, and $m^+ = 6$ for molybdenum. The complexes of the higher oxidation state emerging in the melt due to reaction [2] diffuse to the metal and interact with it [1] with the formation of reduced form complexes. Thus, the process of refractory metal

transfer onto the carbon fibers surface closes into a cycle, and the resulting reaction, with account for reactions [1] and [2] can be written as:

$$Me + C \rightarrow MeC \qquad [3]$$

Fig. 1 presents the micrographs of carbon fiber with TaC coatings and the cross-section of separate fiber with TaC coating. It was not observed the splicing of fibers with each other; coatings were uniform in a cross section as well as along the fiber. According to XRD analysis data tantalum carbide TaC had a cubic modification with the border-centered crystal lattice.

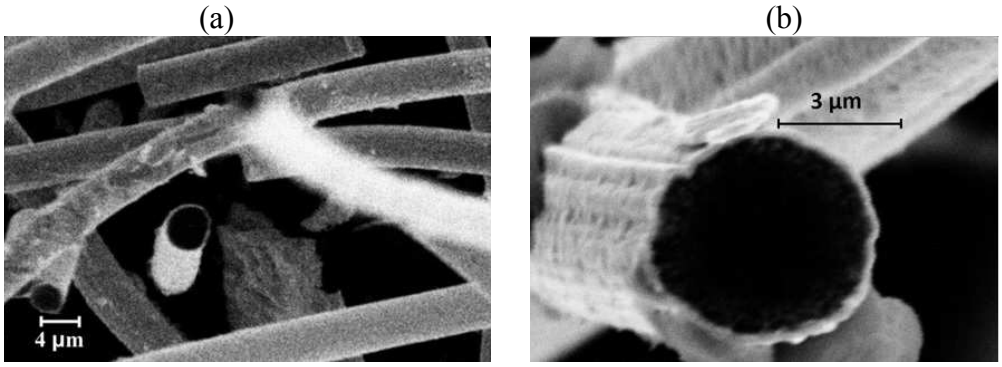

Figure 1. Micrographs of the carbon fiber with TaC coating obtained in the NaCl – KCl – K_2TaF_7 – Ta melt by currentless transfer. Temperature 850 ^{0}C, time = 24 h.

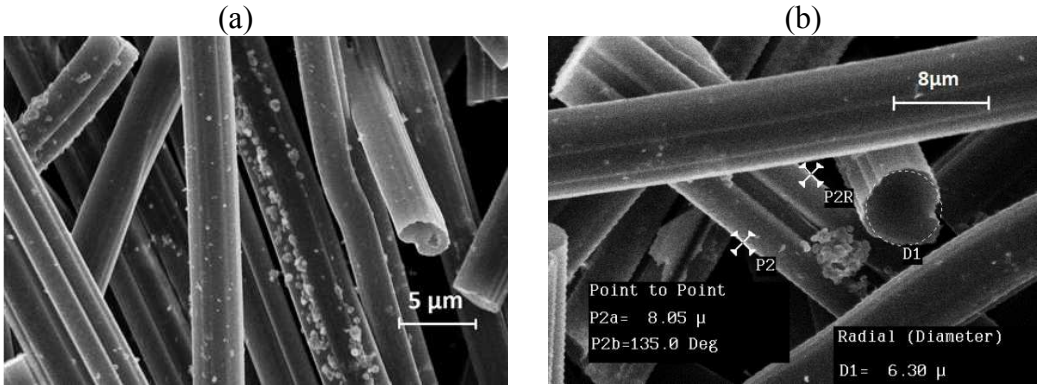

Figure 2. Micrographs of carbon fibers with NbC coating obtained in the NaCl – KCl – K_2NbF_7 – Nb melt by currentless transfer. Temperature 850 ^{0}C, time = 24 h.

Carbon fibers with NbC coatings are presented on Fig. 2. XRD analysis determined that niobium carbide NbC had a cubic crystal lattice. The marks in Fig. 2b give an information about geometric dimensions of individual carbon fibers. Fiber diameters range was 6-8 µm. Thickness of tantalum and niobium carbides coatings on carbon fiber varied of 50 – 250 nm. Clear boundary without a transition zone between the carbon fiber and coating was observed.

The phase of Mo_2C was detected on carbon fibers after the currentless transfer in the Na_2MoO_4-containing melt. XRD analysis of this phase indicated on the formation of crystals with the hexagonal structure as shown in SEM image of Fig. 3. It was

determined that the quantity of Mo_2C crystals increased with the rise of process time. Crystals of Mo_2C had a well-defined structure with the size approximately 8-20 μm.

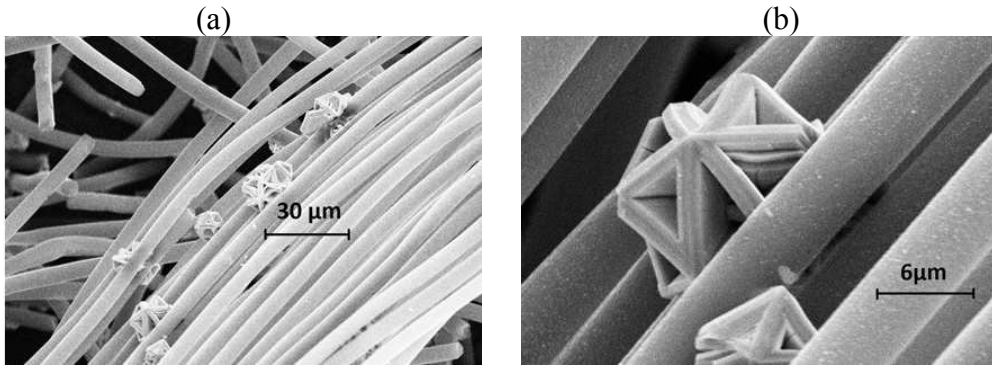

Figure 3. Micrographs of carbon fibers with Mo_2C crystals obtained in the NaCl – KCl – Na_2MoO_4 – Mo melt by currentless transfer. Temperature 850 ^{0}C, time = 1 h.

Electrocatalytic Activity of Refractory Metal Carbide Coatings in the Decomposition of Hydrogen Peroxide

The decomposition of hydrogen peroxide proceeds with the evolution of oxygen. The rate of this reaction can be measured by the volume of oxygen collected in a graduated cylinder, which displaces the hydrogen peroxide solution.

Kinetics data were plotted to determine the reaction order of the electrocatalytic decomposition of hydrogen peroxide obtained on the NbC/C electrode at a temperature of 30 ^{0}C, as shown in Figure 4. Data for the same reaction and temperature obtained on different electrodes are presented in Figure 5.

In this work we used integral methods for determining the order of the reaction for the hydrogen peroxide decomposition including the substitution method and the graphic one. Since the graph of the function of changing the reaction product volume (oxygen) versus time $\Delta V(t)$ on TaC/C, NbC/C, Mo_2C/C, platinum and copper electrodes is linear, the reaction of the hydrogen peroxide decomposition has a zero order and is characterized by the kinetic equation: $\upsilon = k$ (where υ is a rate of reaction, and k is a reaction rate constant). This situation is the same for all electrodes; therefore, graphs are shown only for NbC/C electrode (Fig. 4).

The reaction rate constants were determined by the tangent of the straight line in the corresponding coordinates. The activation energies of the process were calculated based on the experimental data obtained at different temperatures. Fig. 5 shows the kinetic data the hydrogen peroxide decomposition at a temperature of 30 ^{0}C on different electrodes. Similar graphs were observed at a higher temperature, but with a faster reaction rate. Therefore, only one example is given in Fig. 5. From the data in Fig. 5 it follows that the reaction rate increases in the next row: Mo_2C < TaC < Pt < Cu < NbC.

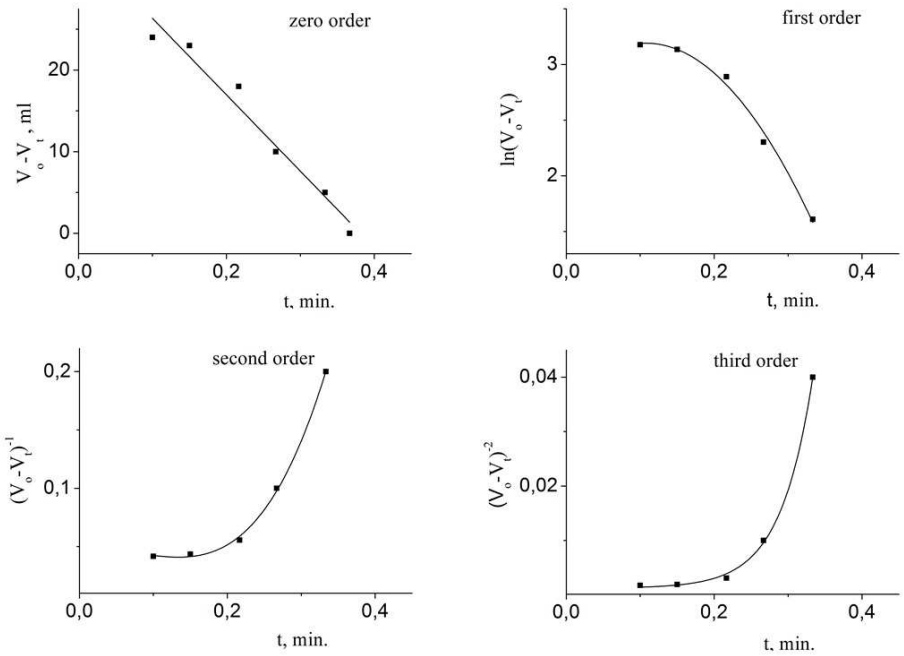

Figure 4. Kinetic dependences for the different reaction's order of the electrocatalytic decomposition of hydrogen peroxide obtained on the NbC/C electrode at a temperature of 30 ^{0}C.

Using the values of the rate constants for the reaction of the hydrogen peroxide decomposition at different temperatures, the values of the activation energy on Mo_2C/C, platinum, TaC/C, copper and NbC/C electrodes were calculated using the Arrhenius equation, which amounted to 107.2; 82.2; 74.8; 48.2 and 37.1 kJ/mol, respectively.

It was established that the reaction rate is constant in time, does not depend on the concentration of reactants, and the rate of diffusion reactants to the surface is less than the rate of their chemical transformation. The electrocatalytic reaction of the hydrogen peroxide decomposition is irreversible.

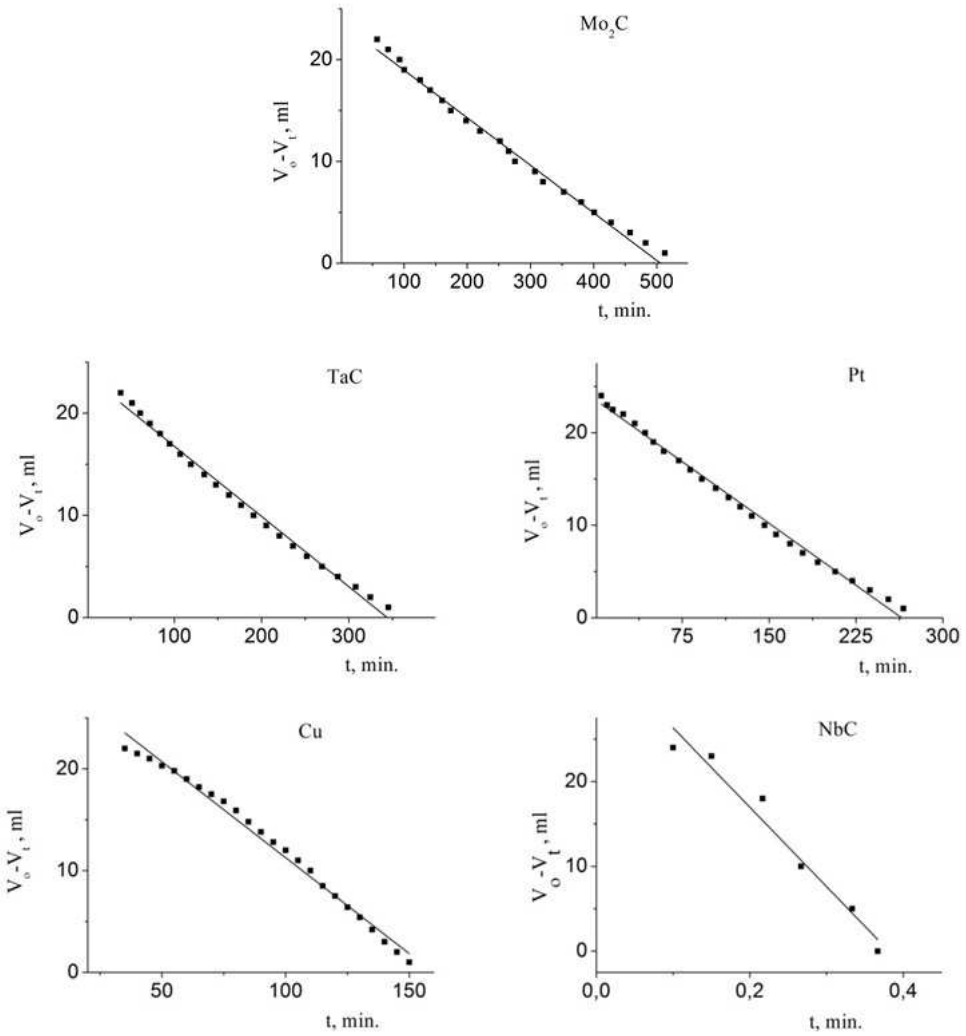

Figure 5. Kinetic dependences of the electrocatalytic decomposition of the hydrogen peroxide obtained on different electrodes at a temperature of 30 ^{0}C.

Conclusions

Tantalum and niobium carbide coatings on carbon fibers were obtained by the currentless transfer in molten salts. At the same time only crystals of molybdenum carbides were obtained by the same method. It was found that there is no splicing of fibers with each other; coatings were uniform in a cross section as well as along the fiber, and clear boundary without a transition zone between the carbon fiber and coating was observed.

The electrocatalytic properties of TaC/C, NbC/C, Mo_2C/C compositions and platinum and copper in the reaction of the hydrogen peroxide decomposition were studied and the kinetic parameters of the reaction were determined. It was found that the reaction rate increases in the next row: Mo_2C<TaC <Pt <Cu <NbC.

References

1. V.S. Dolmatov, S.A. Kuznetsov, *Russ. J. Promising Materials,* **1** (2011).
2. V.S. Dolmatov and S.A. Kuznetsov, *ECS Trans.,* **50** (11), 711 (2012).

3. Y.V. Stulov, V.S. Dolmatov, and S.A. Kuznetsov, *ECS Trans.,* **75** (15), 409 (2016).
4. S.A. Kuznetsov, A.L. Glagolevskaya, and S.V. Kuznetsova, *Russ. J. of Appl. Chem*., **63** (9), 2078 (1990).
5. S.A. Kuznetsov, *Russ. J. of Appl. Chem*., 72, (7), 1127 (1999).
6. L. Massot, P. Chamelot, P. Winterton, and P. Taxil, *J. Alloys Compd.*, **471**, 561 (2009).
7. A. Goti, F. Cardona, *Hydrogen Peroxide in Green Oxidation Reactions: Recent Catalytic Processes*, P. Tundo and V. Esposito, Editors, p. 191, Green Chemical Reactions. NATO Science for Peace and Security Series, Series C: Environmental Security, (2008).
8. Electrochemistry: The past thirty and the next thirty years, H. Bloom and F. Gutmann, Editors, p. 368, Plenum Press, New York and London (1982).

ECS Transactions, 98 (10) 271-281 (2020)
10.1149/09810.0271ecst ©The Electrochemical Society

A Method of Producing Al–REE Master Alloys Using Exchange Reduction Reaction

K. V. Maksimtsev, A. S. Mukhamadeev, G. L. Fofanov, O. I. Rebrin,
V. A. Volkovich, and I. B. Polovov

Department of Rare Metals and Nanomaterials,
Ural Federal University, Ekaterinburg, 620002, Russia

A novel method of aluminium-based master alloy manufacturing using high-temperature exchange processes between aluminium and halides of various rare-earth metals (Ce, Nd, Gd) was proposed. Samples with REE content from 1 to 10 wt. % were synthesised. The yields in excess of 90, 86 and 80 % were achieved for Al–Ce, Al–Nd and Al–Gd alloys, respectively. Microstructure of the alloys consisted of a metal matrix of aluminium in which intermetallic compounds were distributed. Mechanical properties of synthesised master alloys were determined.

Introduction

Modern aerospace engineering relies on Al-based alloys with enhanced high-temperature strength properties and oxidation resistance. These requirements can be fulfilled by modifying alloys' structure employing rare earth metal doping. These alloys are particularly strong, heat-resistant and have a wide range of applications in both the automotive and aerospace industries. The main problem of high-strength light metal alloys production is the high cost of pure rare earth metals that results in considerable expenses for manufacturing aluminum alloys with rare earth elements (REE) in an industrial scale.

Most of previous studies of Al–REE alloys production were mainly performed using melting of pure aluminum (99.99 %) and high-purity metallic REE and differed only in the conditions of the process or in apparatus design (1-10). In the most cases the melting was carried out in arc furnace under argon atmosphere (1-8). Vacuum melting furnace was used to manufacture the required alloys (9). An original method of Al–REE alloy manufacturing employed a high-temperature extruder (10). However direct addition of metallic rare earths to aluminum is complicated due to high chemical activity of molten rare-earth metals and significant vapor pressure of aluminum at elevated temperatures. Another route for obtaining the master Al–Nd alloy involved electrolysis of KCl–NaCl–$NdCl_3$ (6.95 wt. %) melt on liquid aluminum cathode (11). However, in this case the additional problem of anode gas recycling arises.

The current study was focused on the results of experiments and characteristics of master alloys obtained using the method of exchange reactions. The proposed method is based on the exchange reaction between REE fluoride and metallic aluminum. This technology allows reducing the cost of production of master alloys compare to direct melting and electrolysis. The main advantage of this method is that there is no need to produce individual REE and heat them to the melting point. Also the process of pure REE fluoride synthesis is much easier and cheaper than the manufacturing an individual metal of the same purity.

Thermodynamic Calculations

At the first stage preliminary thermodynamic calculations were performed. The exchange reaction between REE fluorides and aluminium [1] can be represented in two following steps [2, 3]:

$$(REE)F_3 + Al_{liquid} = (REE) - Al_{alloy} + AlF_3, \quad [1]$$
$$(REE)F_3 + Al_{liquid} = (REE) + AlF_3, \quad [2]$$
$$(REE) + Al_{liquid} = (REE) - Al_{alloy}. \quad [3]$$

The free Gibbs energy change for the reaction [1] can be defined as:

$$\Delta G^T_{(1)} = \Delta G^T_{(2)} + \Delta G^T_{(3)}, \quad [4]$$

where $\Delta G^T_{(2)}$ can be determined using standard thermodynamic procedures in the HSC Chemistry software package; $\Delta G^T_{(3)}$ can be determined using activity measurement according to the following equations:

$$\Delta G^T_{(3)} = -nFE_{(REE)\text{-}Al(alloy)}, \quad [5]$$
$$E_{(REE)\text{-}Al(alloy)} = E_{REE^{3+}/REE(alloy)} - E_{REE^{3+}/REE}, \quad [6]$$
$$E_{(REE)\text{-}Al(alloy)} = (RT \ln\alpha_{REE(Al)})/(3F), \quad [7]$$
$$\Delta G^T_{(3)} = -RT \ln\alpha_{REE(Al)}. \quad [8]$$

Using the literature data on the temperature dependences of REE activity in liquid Al-REE alloys, we calculated the Gibbs energy change of the formation of the alloy $\Delta G^T_{(3)}$, and then obtained the thermodynamic parameters $\Delta G^T_{(1)}$ for the reaction [1] (8). It was found that decreasing temperature leads to decreasing Gibbs free energy change and increasing equilibrium constant. However, the exchange process would be successful only if the process temperature exceeds the melting point of aluminium.

Experimental

For the high-temperature reactions, the following parameters were selected. Since the temperature of at least 933 K is needed to produce molten aluminium and it is necessary to prevent contact of molten metal with the surrounding air we proposed to use an equimolar mixture of potassium and sodium chlorides with the melting point of 940 K as a cover flux. This salt composition is less aggressive in contrast to complex fluoride systems with higher melting temperatures. Therefore, we propose that the required temperature for the exchange reaction should be equal to 1023 K.

The following procedure was used to produce the master alloys. At the first step we grinded and thoroughly mixed the salt composition consisting of equimolar quenched melt NaCl–KCl with the necessary addition of REE fluoride. REE fluoride was added with an excess of about 15–20 % compare to stoichiometry for reaction [1]. Aluminium metal was melted in a high-density alumina crucible under a layer of pure NaCl–KCl

equimolar mixture. Then the salt composition containing REE fluoride was added to the crucible. Duration of the exchange process was about 30 minutes from the moment of introduction of the NaCl–KCl with of REE fluoride salt mixture. Solid aluminium fluoride produced during the process acted as a slag deposited on the walls of the crucible serving as a protector against aggressive salt melt. The obtained master alloy was poured into a copper mould along with the salt melt. High crystallization rate prevented noticeable liquation of the sample and significantly improved the microstructure of the master alloys. Solidified salt was easily separated from the metallic sample.

X-ray fluorescence (XRF) and X-ray diffraction (XRD) analysis were performed to characterise the produced master alloys. The microstructure of the obtained samples was examined by scanning electronic microscopy (JEOL JSM 6490) and energy dispersive X-ray microanalysis (Oxford INCA).

Results and Discussion

Al–Ce Master Alloys

Binary Al–Ce phase diagram is presented in Fig. 1. There is the eutectic between metallic aluminium and Ce_3Al_{11}/$CeAl_4$. Increase of cerium content in Al–Ce system leads to the formation of intermetallic compounds, i.e. $CeAl_2$, CeAl, etc. In addition, Ce_3Al_{11} and $CeAl_4$ compounds undergo polymorphic transformations at temperatures of 1010 and 1250 °C, respectively.

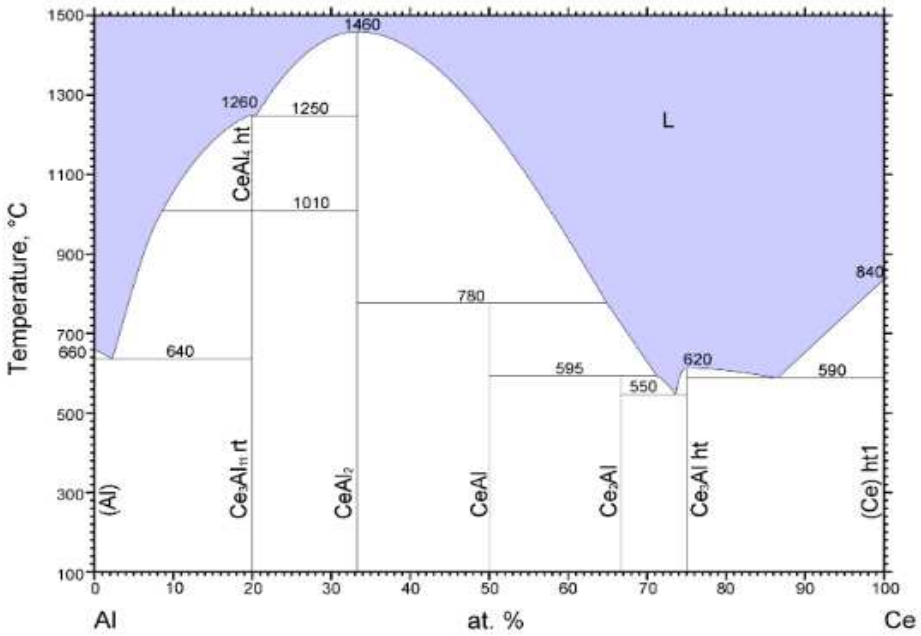

Figure 1. Al–Ce binary system phase diagram.

A series of experiments was performed to investigate the exchange reaction between aluminium metal and CeF_3-containing salt composition. Al-Ce alloys were formed and the obtained results are presented in Table I. From the technological point the process characteristics were acceptable; the yield of Ce into the alloy ($Ce^{found}/Ce^{expected}$ value) was above 90 %.

TABLE I. Synthesis of Al–Ce master-alloys using the exchange reaction between aluminum and cerium fluoride at 1023 K

Al Mass, g	CeF_3 Mass, g	Mass of Alloy Obtained, g	Ce concentration, wt. %	$Ce^{found}/Ce^{expected}$, %
45.06	0.66	45.43	1.0	96.3
45.36	2.17	46.53	3.1	94.0
45.66	3.52	47.53	4.9	92.2
44.94	5.49	47.80	7.4	90.8
45.22	7.42	48.11	10.0	90.1

According to X-ray microanalysis and X-ray diffraction, all the prepared samples consisted of the following phases: metallic aluminum and intermetallic compounds of the compositions $Al_{11}Ce_3$ and Al_4Ce (Figures. 2 and 3). The results of SEM microstructure examination performed are shown in Figure 4.

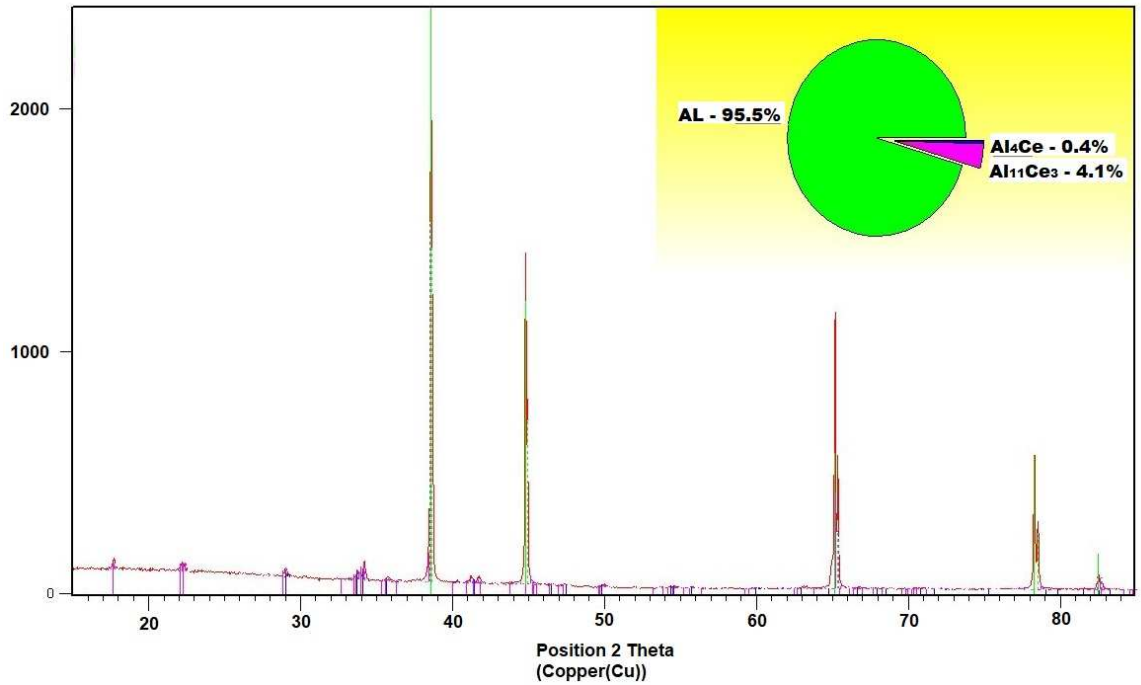

Figure 2. XRD pattern of Al–Ce (1 % wt.) master alloy.

The composition of Al_4Ce is a high-temperature phase. Its appearance can be caused by the high rate of crystallization of the metallic melt.

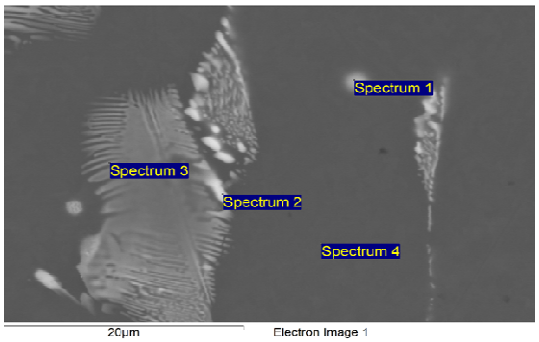

Spectrum	Al	Ce	Total
Spectrum 1	79.5	20.5	100.00
Spectrum 2	75.1	24.9	100.00
Spectrum 3	90.7	9.3	100.00
Spectrum 4	99.7	0.3	100.00

Figure 3. EDS analysis of Al–Ce (1 %) alloy sample.

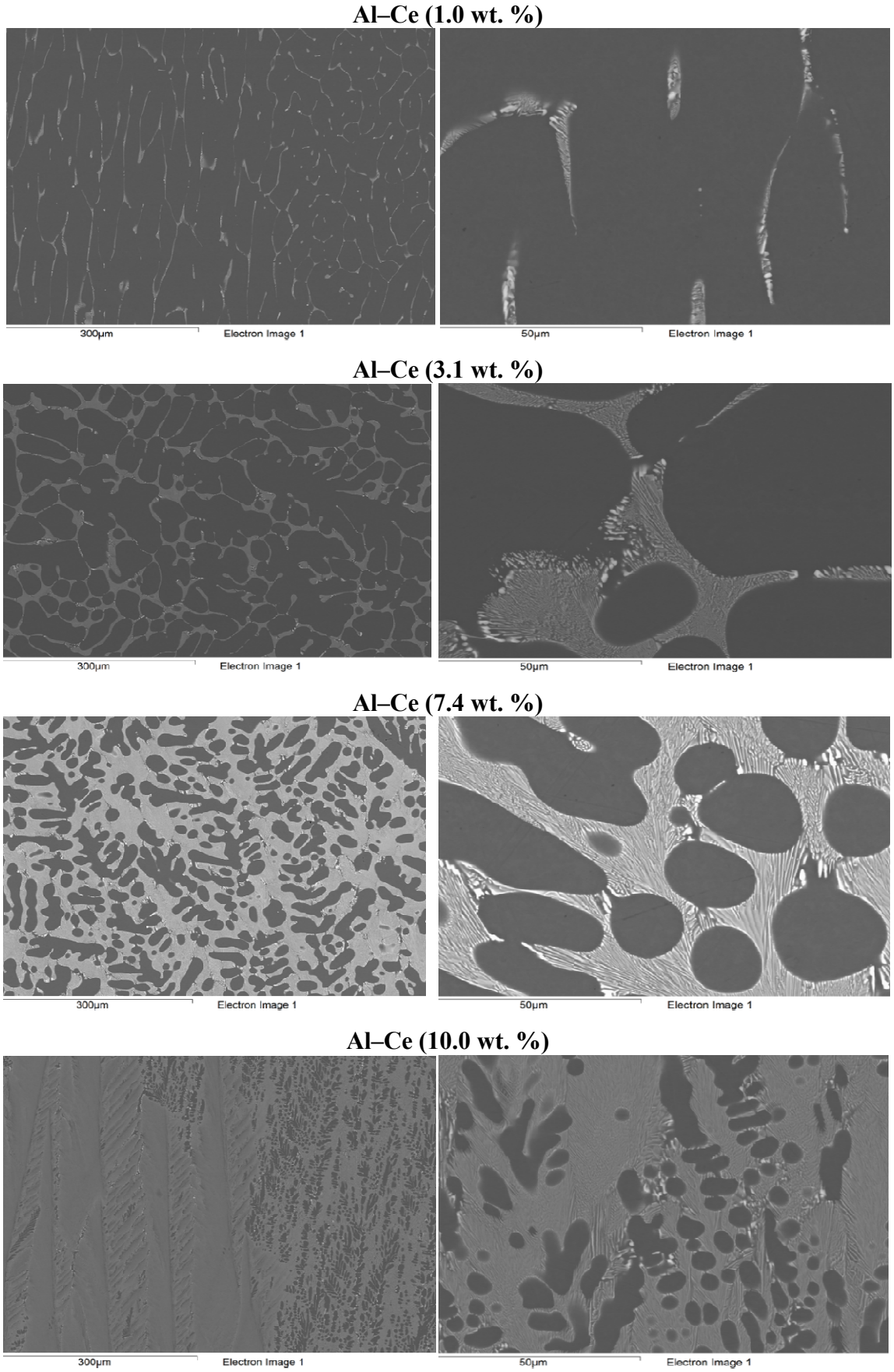

Figure 4. SEM images of the synthesized Al–Ce master alloys.

Al–Nd Master Alloys

Samples of Al–Nd master alloys were produced using the same methodology, Experimental results areshown in Table II. The yield of neodymium into the alloy was above 86 %.

TABLE II. Synthesis of Al–Nd master-alloy using the exchange reaction between aluminum and neodymium fluoride at 1023 K.

Al Mass, g	NdF_3 Mass, g	Mass of Alloy Obtained, g	Nd Concentration, wt. %	$Nd^{found}/Nd^{expected}$, %
45.24	0.67	45.62	1.0	97.4
44.62	2.13	45.80	3.2	96.1
45.38	3.70	47.40	5.2	93.7
44.69	4.82	47.26	6.7	91.6
44.68	8.40	48.41	10.7	86.1

According to X-ray microanalysis and X-ray diffraction, all the prepared samples consisted of the following phases: aluminum-based solid solution and intermetallic compound $Al_{11}Nd_3$ (Figures 5 and 6). This result correlates well with literature data (13). The results of SEM microstructure examination performed are shown in Figure 7.

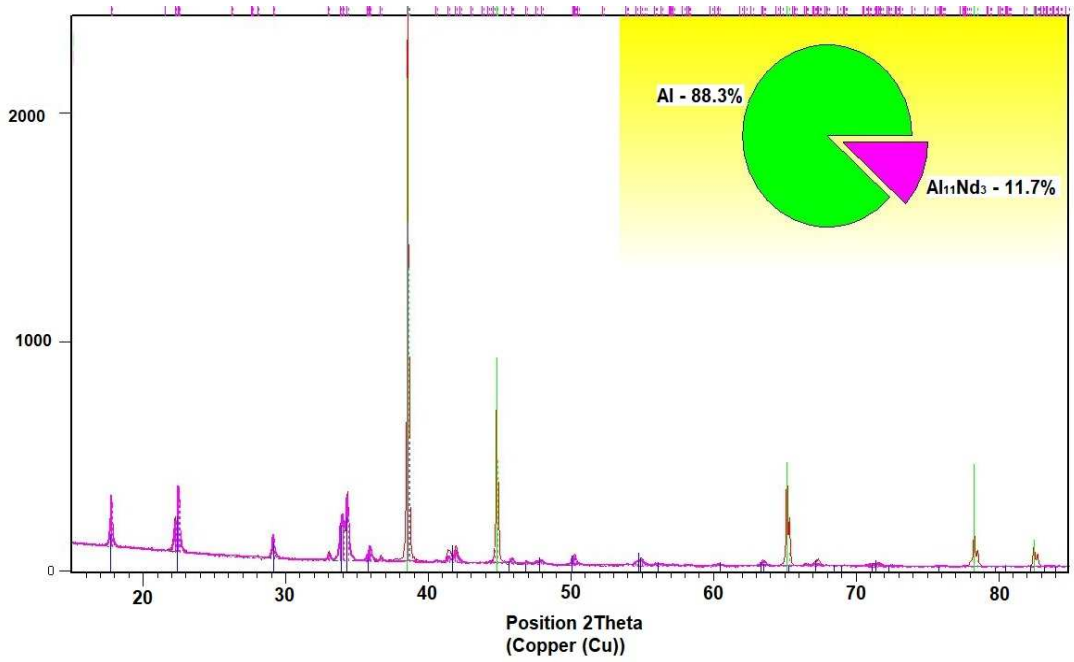

Figure 5. XRD pattern of Al–Nd (5.2 wt. %) master alloy.

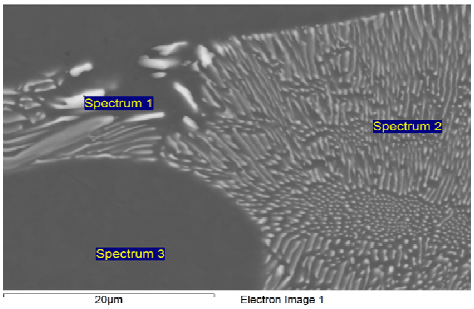

Spectrum	Al	Nd	Total
Spectrum 1	62.4	37.6	100.0
Spectrum 2	85.1	14.9	100.0
Spectrum 3	100.0	0.0	100.0

Figure 6. EDS analysis of the Al–Nd (5.2 wt. %) alloy sample.

Al–Nd (1.0 wt. %)

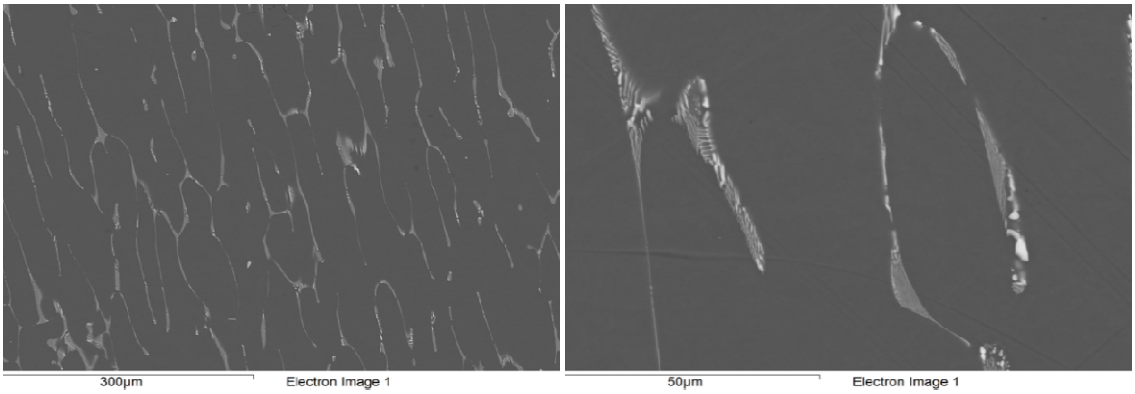

Al–Nd (3.2 wt. %)

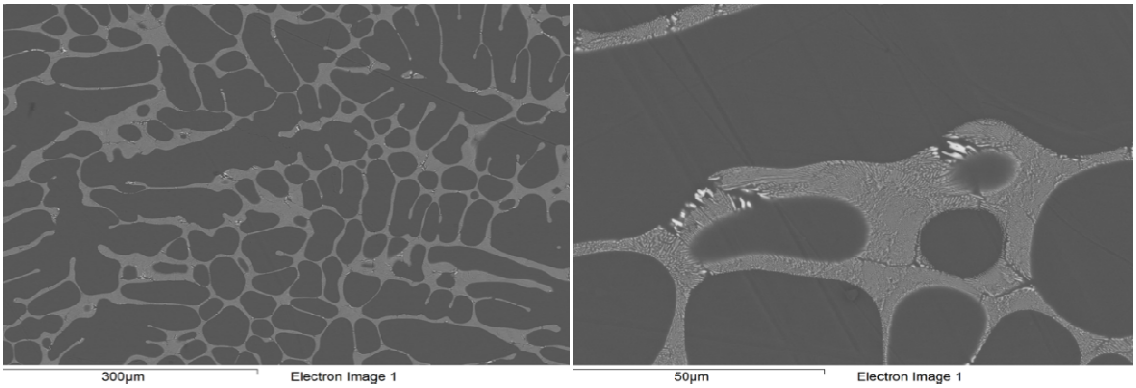

Al–Nd (6.7 wt. %)

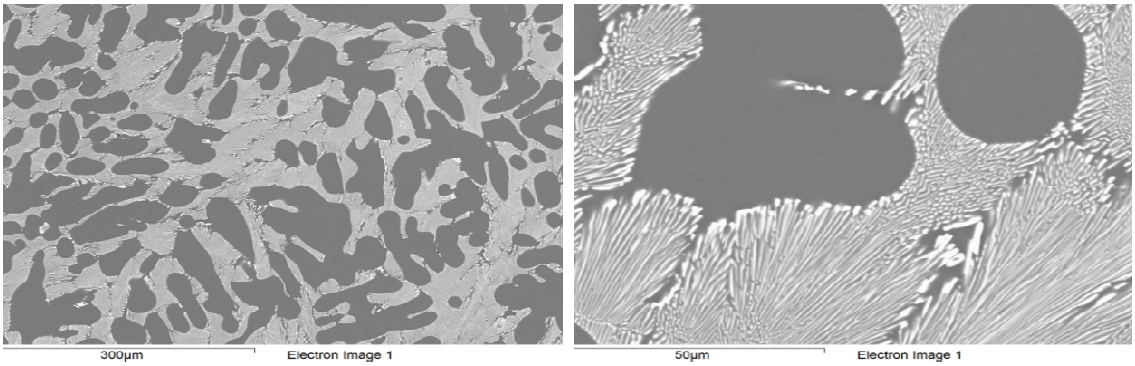

Al–Nd (10.7 wt. %)

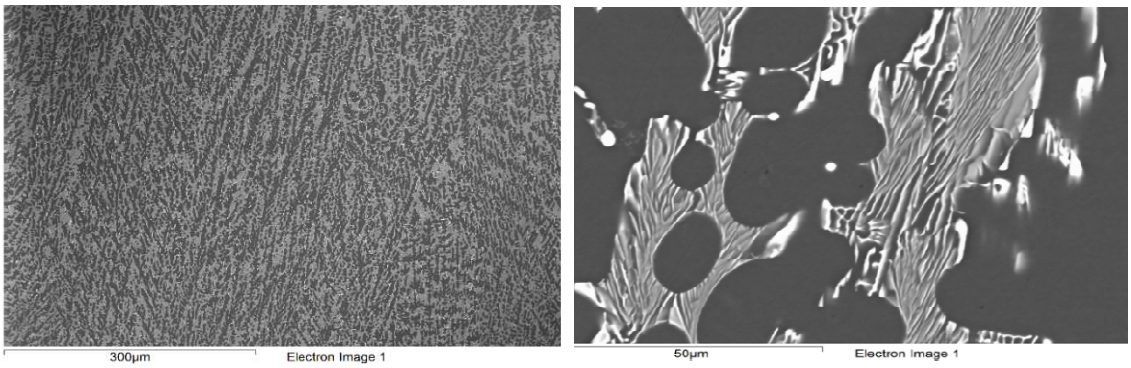

Figure 7. SEM images of synthesized Al–Nd master alloys.

Al–Gd Master Alloys

Synthesis of Al–Gd master alloys was performed according to exchange reactions procedure between gadolynium fluoride and aluminum in chloride melt based systems. Experimental results shown in Table III. The yield of gadolinium into the alloy exceeded 80 %.

TABLE III. Synthesis of Al–Gd master-alloy using the exchange reaction between aluminum and gadolinium fluoride at 1023 K

Al Mass, g	GdF_3 Mass, g	Mass of Alloy Obtained, g	Gd Concentration, wt. %	$Gd^{found}/Gd^{expected}$, %
10.45	1.51	11.03	8.80	80.1
11.90	0.83	12.16	4.72	85.0
11.37	0.31	11.41	1.91	81.2

According to XRD analysis results (Figure 8) the following phases were detected: metallic aluminum and intermetallic compounds of the composition of Al_3Gd and additional phase that is isostructural to the orthorhombic UAl_4. Based on the performed analysis we propose the formation Al_4Gd phase that is absent from Al–Gd phase diagram. However, such intermetallic phase was previously identified by XRD analysis in the aluminum-rich zone of the Al–Gd binary system (14). We suppose that the indicated phase was formed due to rapid quenching of the metallic alloy.

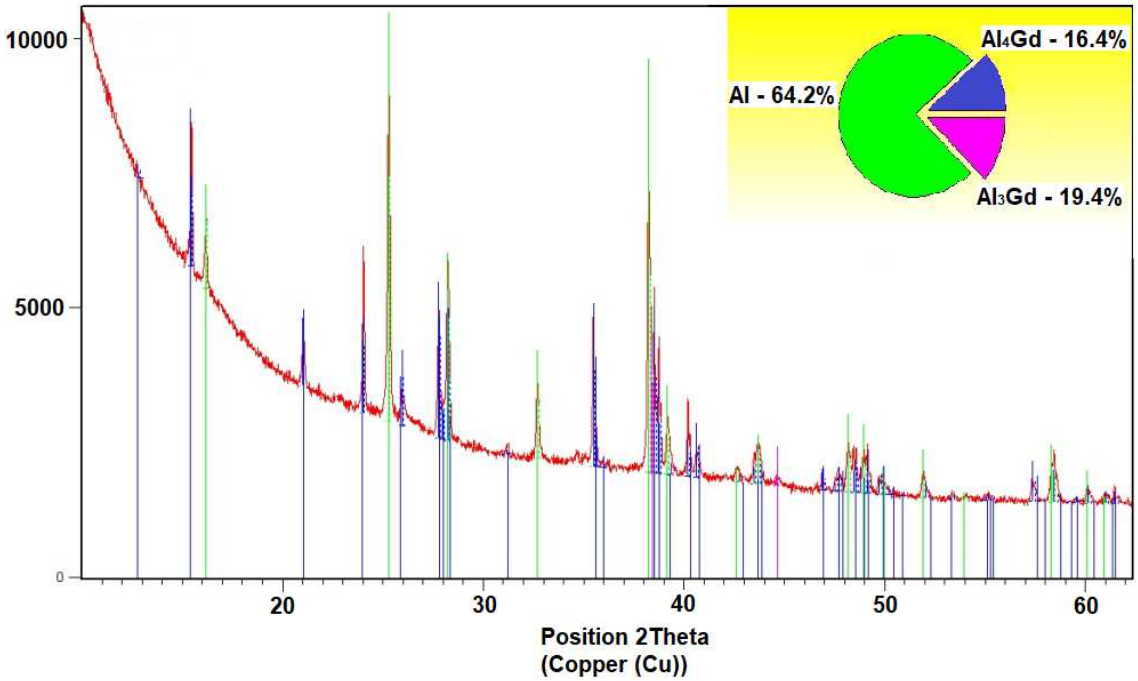

Figure 8. XRD. Phase composition of Al–Gd (8.8% wt.) alloy.

SEM images of the synthesized Al–Gd master alloys are shown in Figure 9. The obtained microstructure was uniform and correlated well with other Al–REE systems.

Al–Gd (1.9 wt. %)

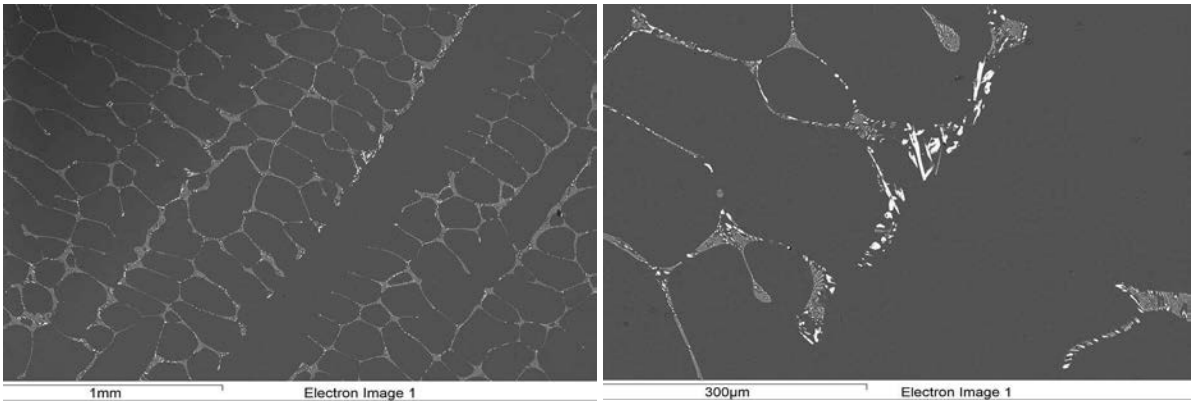

Al–Gd (4.7 wt. %)

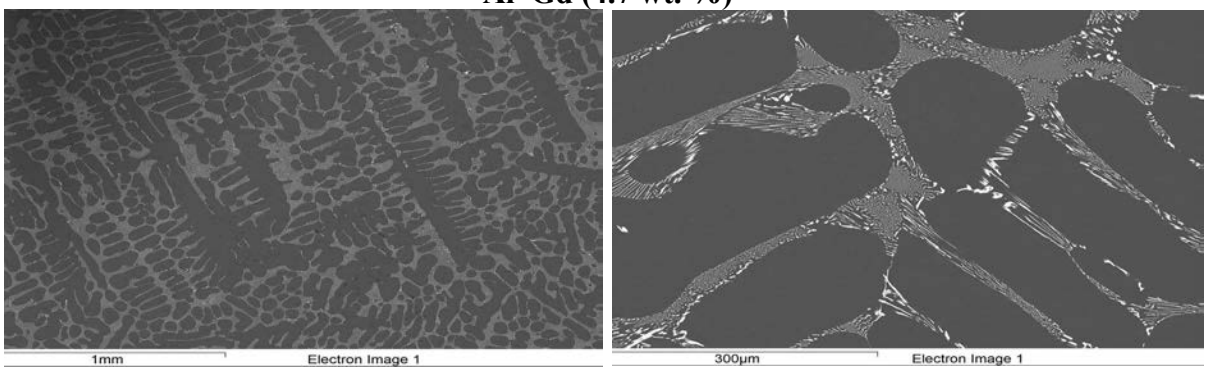

Al–Gd (8.8 wt.%)

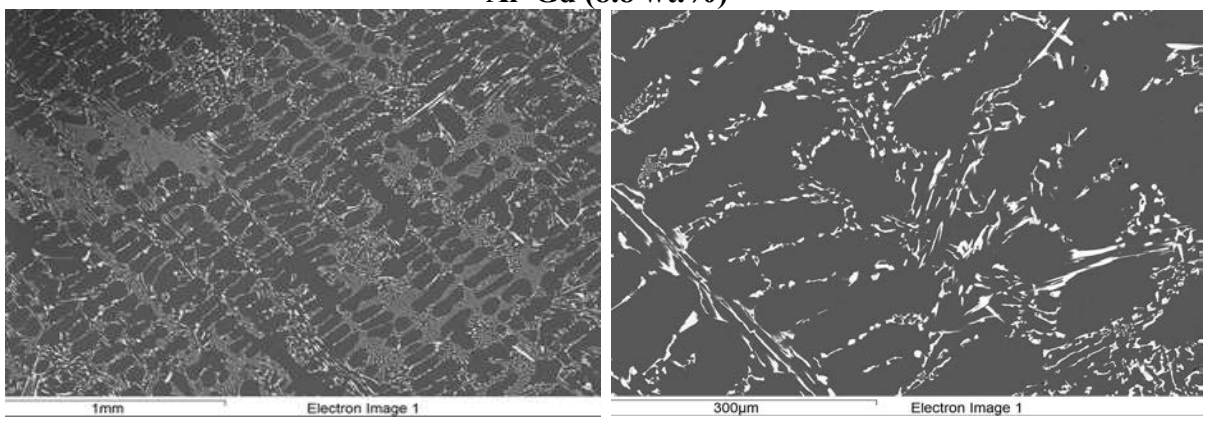

Figure 9. SEM images of the synthesized Al–Gd master alloys.

Mechanical Tests

In a special series of experiments mechanical properties of the synthesized master alloys were studied. The samples of Al–REE master alloys with length of 20 mm and diameter of about 3.7 mm were prepared. The mechanical properties were studied using an Instron 3382 test machine at the ambient temperature. Results of the tests are summarized in Table IV. Addition of REE to aluminum increased the ultimate tensile strength of the alloy. However, the industry uses more dilute alloys with a REE content of 0.001–1 wt. % and usually these systems consist of three or four components, which causes an additional number of advantages compare to aluminum metal.

TABLE IV. Mechanical properties of Al–REE master-alloys

Sample	REE Concentration, wt. %	Yield Strength, MPa	Uniform Elongation δ,%	Ultimate Tensile Strength σ, N/mm^2
Al	-	108	30	88.3
Al-Ce	7.42	62	5.3	131.2
Al-Nd	6.68	48	5.2	123.4
Al-Gd	8.8	35	0	124,5

Conclusions

The proposed method of synthesis of aluminium based master alloys using a high-temperature exchange reaction has been successfully tested for manufacturing Al–Ce, Al–Nd, and Al–Gd master alloys. Samples with REE content from 1 to 10 wt. % were synthesised. The yields higher than 90, 86 and 80 % were achieved for Al–Ce, Al–Nd and Al–Gd correspondingly. The use of a copper mould for crystallization of the aluminium master alloy melt at a high speed allows producing the materials with uniform microstructure. Possible orthorhombic Al_4Ce and Al_4Gd phases were detected after rapid quenching of metallic melt. Mechanical properties of Al–REE master alloys were investigated showing enhanced strength properties compared to pure aluminum.

References

1. Z. Mao, D. N. Seidman and C. Wolverton, *Acta Mater.*, **59**(9), 3659 (2011).
2. Z. C. Sims, O. R. Rios, D. Weiss, P. E. A. Turchi, A. Perron, J. R. I. Lee, T. T. Li, J. A. Hammons, M Bagge-Hansen, T. M. Willey, K. An, Y. Chen, A. H. King and S. K. McCall, *Mater. Horiz.,* **4**(6), 1070 (2017).
3. D. Weiss, O. Rios, Z. Sims, S. McCall and R. Ott, in *Light Metals 2017*, A. Ratvik, Editor, p. 1492, Springer, Cham (2017).
4. B. Sun, X. Bian, J. Hu, T. Mao and Y. Zhang, *Mater. Charact.*, **59**(6), 820 (2008).
5. M. Yu. Murashkin, I. Sabirov, A. E. Medvedev, N. A. Enikeev, W. Lefebvre, R. Z. Valiev and X. Sauvage, *Mater. Des.*, **433**, 90 (2016).
6. C. Zujun, K. Gang and C. Chunshan. *J. Rare Earths,* **35**(10), 1022, (2017).
7. M. Razazi, R. N. Amini, B. B. Eshov and A. B. Badalov, *Mater. Sci. Res. India,* **9**(1), 1 (2012).
8. M. C. Gao, N. Ünlü, G. J. Shiflet, M. Mihalkovic and M. Widom, *Metall. Mater. Trans. A,* **36**(12), 3269 (2005).
9. J. Sarkar, S. Saimoto, B. Mathew and P.S. Gilman, *J. Alloys Compd.*, **479**(1-2), 719 (2009).
10. I. Matveeva, N. Dovzhenko, S. Sidelnikov, L. Trifonenkov, V. Baranov and E.Lopatina, in *Light Metals 2013,* B. Sadler, Editor, p.1377, Springer, Cham (2013).
11. M. C. Akhmedov and V. A. Lebedev, in *Innovations in materials science and metallurgy: Proceedings of the IV International interactive research and practical conference*, N. N. Ozerets, Editor, p. 468, UrFU, Yekaterinburg (2015) *(in Russian)*.
12. V. I. Kober, V. A. Lebedev and L. F. Yamshchikov, *Thermochemistry of Alloys of Rare Earth and Actinide,* p. 335, Metallurgy, Chelyabinsk (1989) *(in Russian)*.

13. H. Okamoto, *J. Phase. Equilib. Diff.*, **37**(3), 350 (2016).
14. O. J. C. Runnalls, R. R. Boucher, *J. Less Common Met.,* **13**(4), 431 (1967).

ECS Transactions, 98 (10) 283-294 (2020)
10.1149/09810.0283ecst ©The Electrochemical Society

Application of Phosphate Precipitation for Removing Strontium and Barium from Alkali Chloride Based Melts

A. B. Ivanov[a], E. D. Byzova[a], V. A. Volkovich[a], A. V. Chukin[b], and T. R. Griffiths[c]

[a] Department of Rare Metals and Nanomaterials, Institute of Physics and Technology, Ural Federal University, Ekaterinburg 620002, Russian Federation
[b] Department of Theoretical Physics and applied Mathematics, Institute of Physics and Technology, Ural Federal University, Ekaterinburg 620002, Russian Federation
[c] Energy Process Developments Ltd., London SE1 4AG, United Kingdom

The reaction of solutions of barium and strontium chlorides in LiCl–KCl, NaCl–KCl and NaCl–KCl–CsCl based melts with sodium orthophosphate was studied at 450 and 750 ^{o}C. The initial phosphate-to-alkaline earth molar ratio varied from 0.5 to 14 and the excess of phosphate required for the complete conversion of $AECl_2$ (AE = Sr, Ba) to phosphates as well as phase composition of the phosphates produced were determined. Normal orthophosphates alongside with lithium phosphate were formed in lithium chloride containing melts, whilst double alkali–alkaline earth phosphates and chloro-phosphates were obtained in NaCl–KCl and NaCl–KCl–CsCl based melts. Size of the particles comprising solid precipitates was determined; the values varied from 0.1 to tens microns. Increasing the initial PO_4^{3-} : AE^{2+} molar ratio did not have a pronounced effect on the particle size.

Introduction

Alkali metal chloride based melts have a number of prospective applications in technology including nuclear fuel cycle where various ways of reprocessing spent nuclear fuels (SNFs) are currently being developed. Separation of remaining or newly formed fissile materials from fission products (FPs) is the primary goal of reprocessing. Pyrochemical reprocessing of SNF from solid (oxide or nitride) fuel nuclear reactors in molten salts normally involves separation of actinides of interest (uranium and plutonium) from FPs using electrochemical processes or separation in a "molten salt – liquid metal" system (reductive extraction, etc.). In terms of the electrochemical or redox properties all fission products can be separated in two groups in relation to uranium and plutonium, i.e. those with more positive electrode potentials (electropositive) and with more negative electrode potentials (electronegative). After electropositive FPs, uranium and plutonium are extracted from the molten salt electrolyte the melt contains electronegative FPs including rare earth (yttrium, lanthanum and lanthanides), alkaline earth (strontium and barium) and alkali (rubidium and cesium) metals. Returning the melt into the head-end of the technological process requires removing (at least partial) these electronegative FPs.

There are several approaches for purifying molten salts from the electronegative fission product elements including reductive extraction by liquid metal alloys, treating the

melt with oxygen, adding boric acid or alkali phosphates (1–11). All these methods were, however, mostly developed for dealing with the rare earth fission product elements. Considerably less attention was paid to the alkaline earths (strontium and barium).

SNF of a thermal neutron reactor contains several isotopes of strontium (from Sr-87 to Sr-92) and barium (from Ba-136 to Ba-140) (12). Depending on the reactor neutron spectrum, nuclear fuel type, burnup and cooling time SNF arriving for reprocessing can contain ca. 1–2.2 kg strontium and 2.5–5.6 kg barium per ton. Typical SNF of thermal neutron reactors arriving for reprocessing contains 1.8 kg Sr and 4.3 kg Ba per ton with the total activity of 5100 and 7600 TBq, respectively.

Strontium and barium form sparingly soluble phosphates and phosphate precipitation can therefore be employed for removing these elements from molten salts similar to rare earths. Preliminary experiments on precipitating strontium and barium phosphates from chloride melts showed that $NaSr(Ba)PO_4$ phases were formed in NaCl–KCl based melts and unidentified phases in LiCl–KCl eutectic beads melt (7). Effect of temperature, melt composition, excess of phosphate added on the precipitation process parameters were not considered.

The aim of the present work was therefore performing a more detailed study of precipitation of strontium and barium phosphates from alkali chloride based melts of various compositions, considering the effect of the initial phosphate-to-metal molar ratio on completeness of precipitation, determining phase composition and size of particles of the precipitates produced.

Experimental

The experiments were performed in LiCl–KCl and NaCl–KCl–CsCl eutectic, and NaCl–KCl equimolar mixture based melts. Commercially available lithium, sodium, potassium and cesium chlorides were dried under vacuum, melted and treated with gaseous hydrogen chloride (13). Then the salts prepared were fused in the required proportions. Anhydrous strontium and barium chlorides were obtained from the corresponding crystal hydrates ($SrCl_2 \cdot 6H_2O$ and $BaCl_2 \cdot 2H_2O$) by drying at 180 ^oC tio the constant weight. Salt mixtures containing strontium and barium chlorides were prepared by fusing together the metal chloride and the solvent salt mixture under vacuum followed by sparging the melt with gaseous hydrogen chloride to remove trace moisture. The resulting melt was fully transparent. Salts thus prepared were stored and manipulated in an argon filled glove box.

Phosphate precipitation experiments were conducted under static conditions using the procedure described previously (14). The initial phosphate-to-AE (AE – alkaline earth metal) molar ratios were varied from 0.3–0.5 to 10. The quenched salt was treated with a weak solution of hydrochloric acid to remove soluble salts, the precipitate filtered, washed with distilled water and dried. The filtrate and washing water were combined and used for chemical analysis to determine the amount of AE element that did not precipitate.

Phase composition of the phosphates was determined by X-ray powder diffraction (X'Pert PRO instrument, $Cu_{K\alpha}$ radiation with a Ni β-filter). The diffraction patterns were

analyzed using the PDF-2 file and Rietveld full profile refinement. Particle size of the precipitated phosphates was determined by a laser diffraction method using an ANALYSETTE 22 NanoTec (Fritsch) instrument with a measuring range of 0.02–2100 μm using the procedure described previously (14). Particle size measurements were performed with ultrasonic treatment to destroy particle agglomerates that could be formed.

Results and Discussion

Precipitation of Barium and Strontium Phosphates from LiCl–KCl Eutectic Based Melts

The eutectic mixture of lithium and potassium chlorides is currently considered as a prime candidate for the practical realization of SNF pyrochemical reprocessing. The experiments were performed at 450 ^{o}C. Increasing the initial PO_4^{3-} : AE^{2+} molar ratio resulted in an expected increasing degree of the alkaline earth element precipitation. An example of the dependence of the degree of precipitation on the initial phosphate-to-alkaline earth metal molar ratio is shown in Fig. 1.

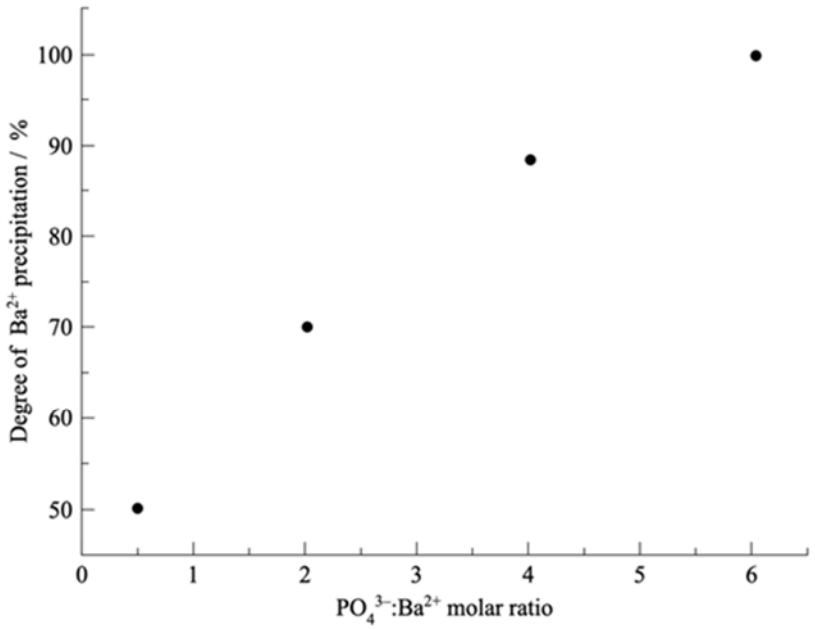

Figure 1. Effect of the initial PO_4^{3-} : Ba^{2+} molar ratio on the degree of barium precipitation by sodium phosphate from LiCl–KCl–$BaCl_2$ melts at 450 ^{o}C.

X-ray powder diffraction analysis was used to identify the reaction products. Examples of the X-ray diffraction patterns of the precipitates obtained at various initial PO_4^{3-} : Ba^{2+} molar ratios are presented in Fig. 2. The majority of peaks belong to lithium orthophosphate, Li_3PO_4. The formation of lithium phosphate is similar to the results obtained previously for the rare earths, where excess phosphate ions added to LiCl–KCl melts reacted with lithium ions forming sparingly soluble lithium phosphate (5). The principle barium containing phase was normal barium orthophosphate $Ba_3(PO_4)_2$, Fig. 2.

Only one sample, formed at the initial phosphate-to-barium molar ratio of four, additionally contained small amount of double sodium-barium phosphate, $NaBaPO_4$. None of the other samples contained this phase in a detectable amount, Fig. 2. The results of the experiments on precipitating strontium and barium phosphates are summarized in Table I. The results obtained for LiCl–KCl eutectic based melts showed much similarity in precipitation of phosphates of alkaline earth and rare earth elements. For both groups of the elements the reaction in LiCl–containing melts resulted in the formation of normal orthophosphates and excess added phosphate was mostly converted to lithium phosphate.

TABLE I. Precipitation of strontium and barium phosphates from alkali chloride based melts.

AE	PO_4^{3-} : AE^{2+} Molar Ratio	Degree of AE Precipitation / %	Solid Phase Composition
		LiCl–KCl based melts, 450 °C	
Ba	0.50	50.2	Li_3PO_4, $Ba_3(PO_4)_2$
	2.02	70.0	Li_3PO_4, $Ba_3(PO_4)_2$
	4.02	88.4	Li_3PO_4, $Ba_3(PO_4)_2$, $NaBaPO_4$
	6.04	99.9	Li_3PO_4, $Ba_3(PO_4)_2$
		NaCl–KCl based melts, 750 °C	
Ba	1.88	99.7	$NaBaPO_4$, $Ba_3(PO_4)_2$, $Ba_5(PO_4)_3Cl$
	3.29	99.1	$NaBaPO_4$, $Ba_3(PO_4)_2$
	4.38	98.8	$NaBaPO_4$, $Ba_3(PO_4)_2$
	5.25	99.1	$NaBaPO_4$, $Ba_3(PO_4)_2$
Sr	1.12	97.3	$Sr_5(PO_4)_3Cl$
	4.46	98.6	$Sr_{10}O(PO_4)_6$, $NaSrPO_4$
	6.66	99.2	$Sr_{10}O(PO_4)_6$, $NaSrPO_4$
	8.81	99.9	$Sr_{10}O(PO_4)_6$, $NaSrPO_4$
		NaCl–KCl–CsCl based melts, 750 °C	
Ba	0.58	91.0	$Ba_5(PO_4)_3Cl$
	1.07	95.7	$Ba_5(PO_4)_3Cl$, $NaBaPO_4$
	2.16	98.4	$NaBaPO_4$, $Ba_3(PO_4)_2$
	4.35	99.5	$NaBaPO_4$, $Ba_3(PO_4)_2$, $Ba_5(PO_4)_3Cl$
	6.52	99.2	$NaBaPO_4$, $Ba_3(PO_4)_2$, $Ba_5(PO_4)_3Cl$
	8.71	99.8	$Ba_5(PO_4)_3Cl$
Sr	0.87	77.6	$Sr_5(PO_4)_3Cl$
	1.75	94.1	$Sr_5(PO_4)_3Cl$, $NaSrPO_4$
	3.48	98.6	$NaSrPO_4$
	6.99	97.8	$NaSrPO_4$
	10.40	97.8	$Sr_3(PO_4)_2$, $NaSrPO_4$
	13.93	97.8	$Sr_3(PO_4)_2$, $NaSrPO_4$

Similar to rare earths, phosphate precipitation of strontium and barium resulted in the formation of solids consisting of micron sized particles. Examples of particle size distribution (PSD) curves for strontium phosphates are given in Fig. 3. The results obtained for barium phosphates were similar. The majority of particles had the size within 1–30 microns. PSD curves generally had profiles with two maxima around 1.5–3.0 and 14–20 μm. There was no obvious dependence of the particle size on the PO_4^{3-} : AE^{2+} molar ratio. For strontium phosphates first maxima on PSD curves were around 1.5 μm for the samples obtained at phosphate-to-strontium molar ratios of 0.48–2.88. For the molar ratio of 3.86 the position of the first maximum shifted to 4 μm. The position of second maximum for all the samples was around 8–20 μm.

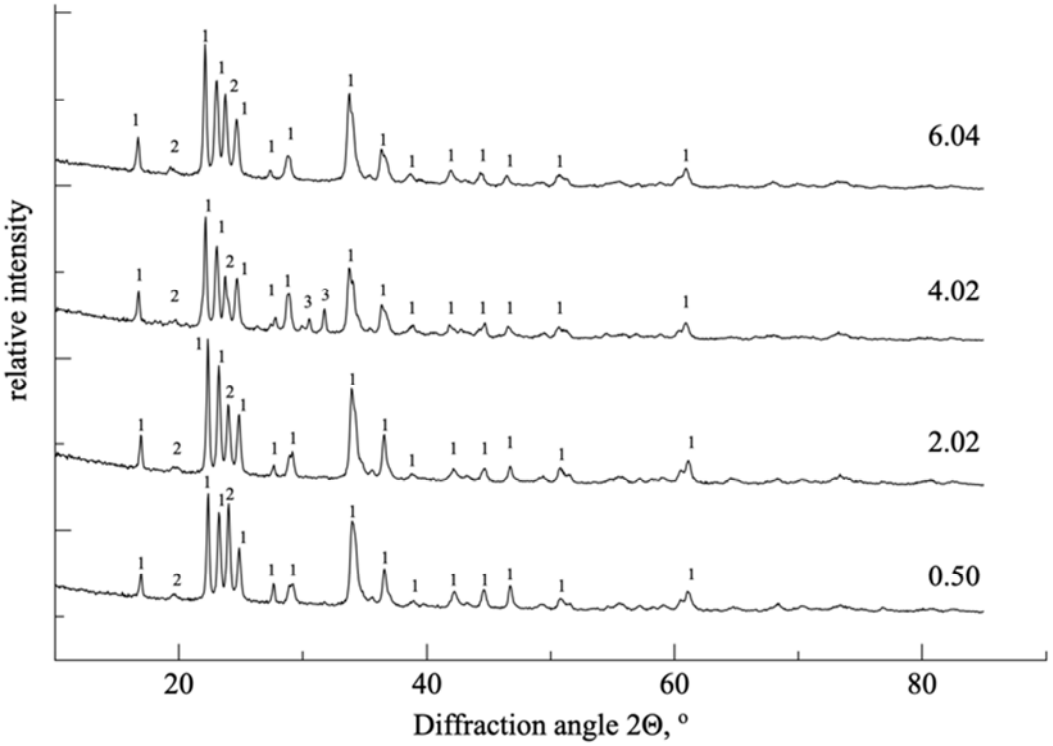

Figure 2. X-ray diffraction patterns of barium phosphates formed in LiCl–KCl–$BaCl_2$ melts at various initial PO_4^{3-} : Ba^{2+} mole ratios (shown on the plot for each set of data). The phases present were Li_3PO_4 (1); $Ba_3(PO_4)_2$ (2) and $NaBaPO_4$ (3).

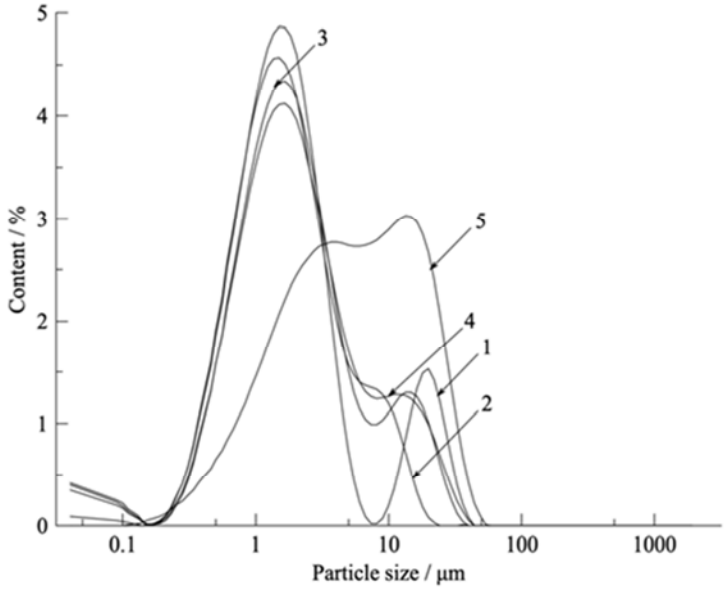

Figure 3. Differential PSD curves of strontium phosphates formed in LiCl–KCl–$SrCl_2$ melts at the initial PO_4^{3-} : Sr^{2+} mole ratios of 0.48 (1); 0.91 (2); 1.69 (3); 2.88 (4) and 3.86 (5).

Precipitation of Barium and Strontium Phosphates from NaCl–KCl Equimolar Mixture Based Melts

The experiments were performed at 750 °C. Addition of sodium phosphate in the equimolar to the alkaline earth metal amount was sufficient for over 97 % precipitation of barium and strontium, Table I and Fig. 4. X-ray powder diffraction analysis performed on strontium phosphate precipitates, Fig. 5, showed that the solid phase consisted of double sodium-strontium orthophosphate $NaSrPO_4$ and strontium oxo-orthophosphate $Sr_{10}O(PO_4)_6$. Comparison of the relative intensity of peaks belonging to these phases showed that there was no a uniform dependence of the phase composition on the phosphate-to-strontium molar ratio in the melt. The peaks of $NaSrPO_4$ double phosphate were the strongest in the samples obtained at the molar ratios of 4.46 and 8.81, whilst in the sample formed at the intermediate molar ratio of 6.66 the reflections from $NaSrPO_4$ phase were quite weak compare to the reflections from the oxo-orthophosphate $Sr_{10}O(PO_4)_6$. Normal strontium orthophosphate $Sr_3(PO_4)_2$ was not detected in any of the samples analyzed. There was a difference between strontium and barium precipitates' phase composition, Table I. Barium containing phosphate precipitates formed at the phosphate-to-barium molar ratios above 3 consisted of a mixture of double sodium-barium orthophosphate $NaBaPO_4$ and barium orthophosphate $Ba_3(PO_4)_2$. No evidence of barium oxo-orthophosphate presence was found. At the low $PO_4^{3-} : AE^{2+}$ molar ratios (1.12 for Sr and 1.88 for Ba) chlorophosphates $AE_5(PO_4)_3Cl$ were formed, Table I, and this phase was the only one identified in the strontium containing sample. In the barium containing sample there was a mixture of $Ba_5(PO_4)_3Cl$, $NaBaPO_4$ and $Ba_3(PO_4)_2$.

Particles of the precipitate were of micron size, Figs. 6 and 7. Particles were larger than in the samples obtained in LiCl–KCl based melts. For strontium phosphates the

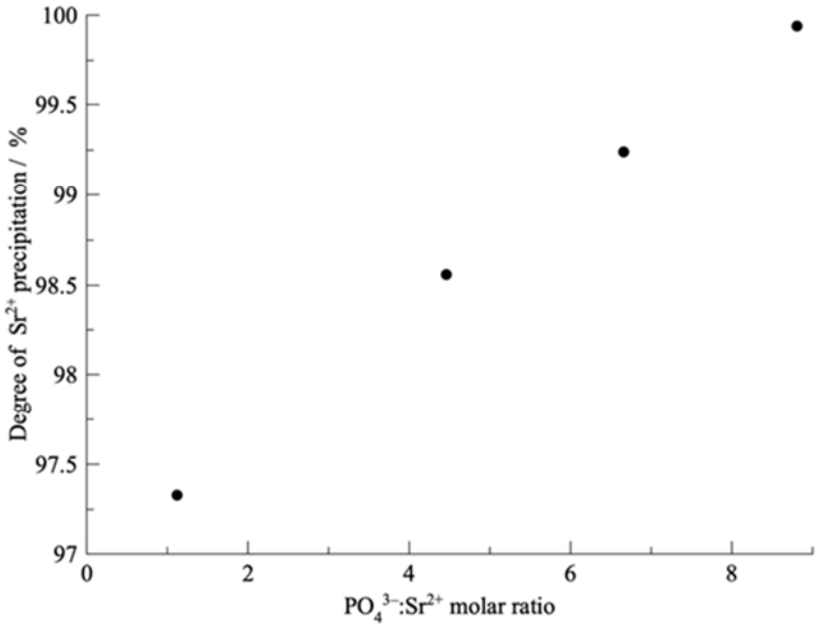

Figure 4. Effect of the initial $PO_4^{3-} : Sr^{2+}$ molar ratio on the degree of strontium precipitation by sodium phosphate from NaCl–KCl–$SrCl_2$ melts at 750 °C.

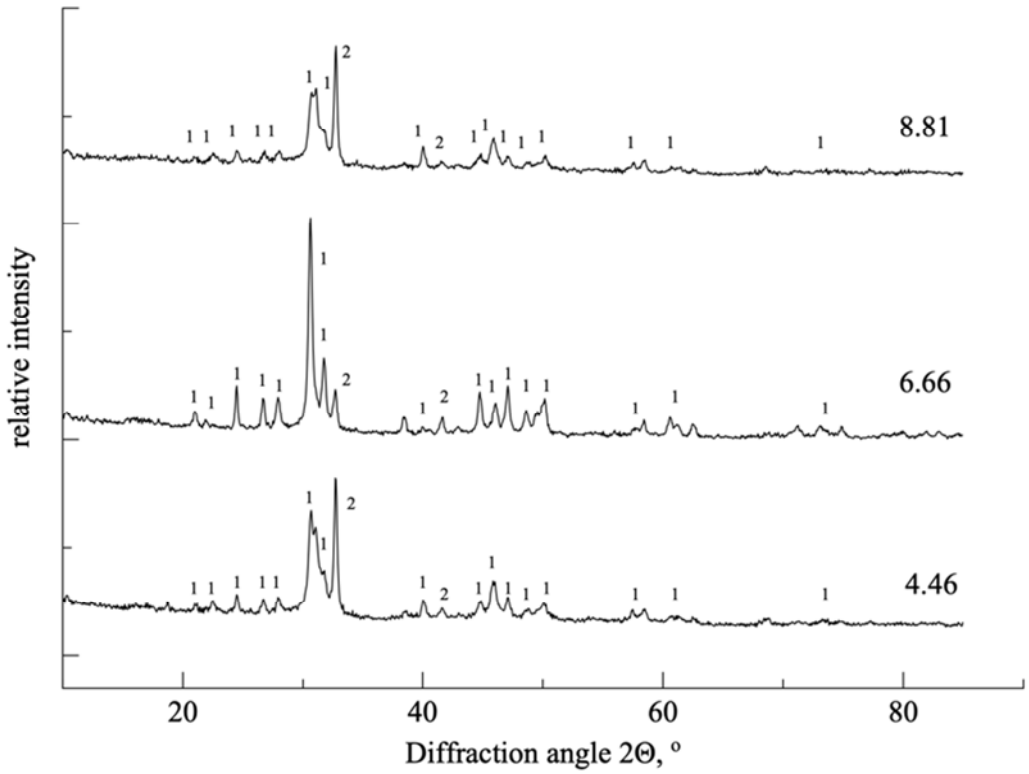

Figure 5. X-ray diffraction patterns of strontium phosphates formed in NaCl–KCl–$SrCl_2$ melts at various initial PO_4^{3-} : Sr^{2+} mole ratios (shown on the plot for each set of data). The phases present were $Sr_{10}O(PO_4)_6$ (1) and $NaSrPO_4$ (2).

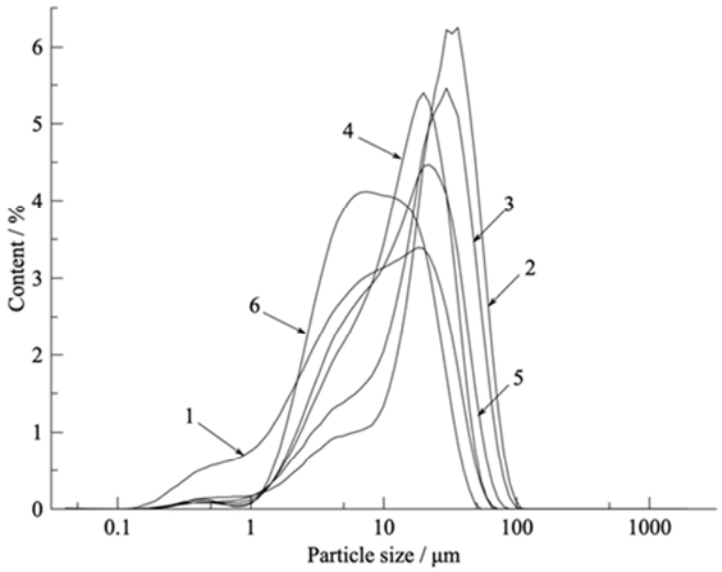

Figure 6. Differential PSD curves of strontium phosphates formed in NaCl–KCl–$SrCl_2$ melts at the initial PO_4^{3-} : Sr^{2+} mole ratios of 0.68 (1); 1.12 (2); 2.23 (3); 4.46 (4); 6.66 (5) and 8.81 (6).

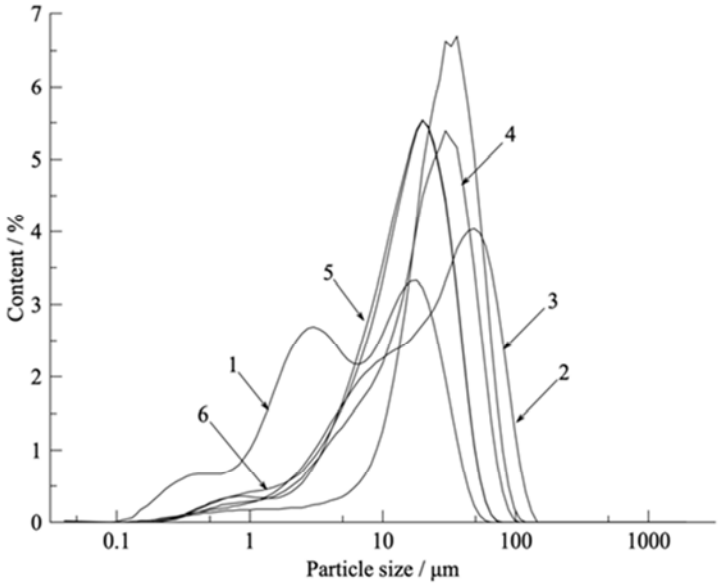

Figure 7. Differential PSD curves of barium phosphates formed in NaCl–KCl–$BaCl_2$ melts at the initial PO_4^{3-} : Ba^{2+} mole ratios of 0.53 (1); 1.02 (2); 1.88 (3); 3.29 (4); 4.38 (5) and 5.25 (6).

majority of particles were less than 50 microns. Maximum in PSD curve of the sample formed at PO_4^{3-} : Sr^{2+} molar ratio of 8.81 was around 6 μm. For the molar ratios of 0.68, 4.46 and 6.66 maxima on PSD curves were close around 25 μm. For the molar ratios of 1.12 and 2.23 the maxima were around 30 μm. The smallest particles were observed for the sample formed at the molar ratio of 0.68 and the largest for the molar ratio of 1.12.

For barium containing samples smallest particles were observed for the sample produced at the phosphate-to-barium molar ratio of 0.53; first maximum on the PSD curve was around 3 μm. Second maximum was around 20 μm, as for the samples obtained at the phosphate-to-barium molar ratios of 4.38 and 5.25. For the samples formed at PO_4^{3-} : Ba^{2+} molar ratios of 1.02 and 3.29 second maximum was around 30 μm. Largest particles were (up to 150 μm) were found in the sample produced at PO_4^{3-} : Ba^{2+} molar ratio of 1.88. Fig. 7 shows that increasing the initial phosphate-to-barium molar ratio did not result in a monotonous increase of the particle size.

Precipitation of Barium and Strontium Phosphates from NaCl–KCl–CsCl Eutectic Based Melts

The experiments were conducted at 750 ^{o}C and the results are summarized in Table I. Over 98 % strontium and barium could be precipitated at the phosphate-to-alkaline earth molar ratios over three, Fig. 8. Increasing the initial phosphate-to-strontium molar ratio resulted in a gradual change of the precipitate composition. Examples of X-ray diffraction patterns are shown in Fig. 9. At lower molar ratios the precipitate consisted of mostly strontium chloride-phosphate ($Sr_5(PO_4)_3Cl$) (patterns for the samples formed at the molar ratios of 0.87 and 1.75 in Fig. 9). Increasing the initial PO_4^{3-} : Sr^{2+} molar ratio to 1.75 also resulted in appearance of double sodium-strontium orthophosphate and the precipitate consisted of a mixture of mostly $Sr_5(PO_4)_3Cl$ and some $NaSrPO_4$, Fig. 9. At

the molar ratios from around 3.5 and higher the predominant phase was double sodium-strontium orthophosphate and only at the molar ratio of over 13 some normal strontium orthophosphate $Sr_3(PO_4)_2$ was produced in addition to $NaSrPO_4$. The results obtained for the barium system were mostly similar but there were some differences. Barium chloro-phosphate $Ba_5(PO_4)_3Cl$ was found practically in all the samples of the precipitates obtained at the phosphate-to-barium molar ratios from 0.58 to 8.71. Double sodium-barium orthophosphate $NaBaPO_4$ appeared in the samples formed at the molar ratios over one and normal barium orthophosphate $Ba_3(PO_4)_2$ – in the samples formed at the molar ratios over two.

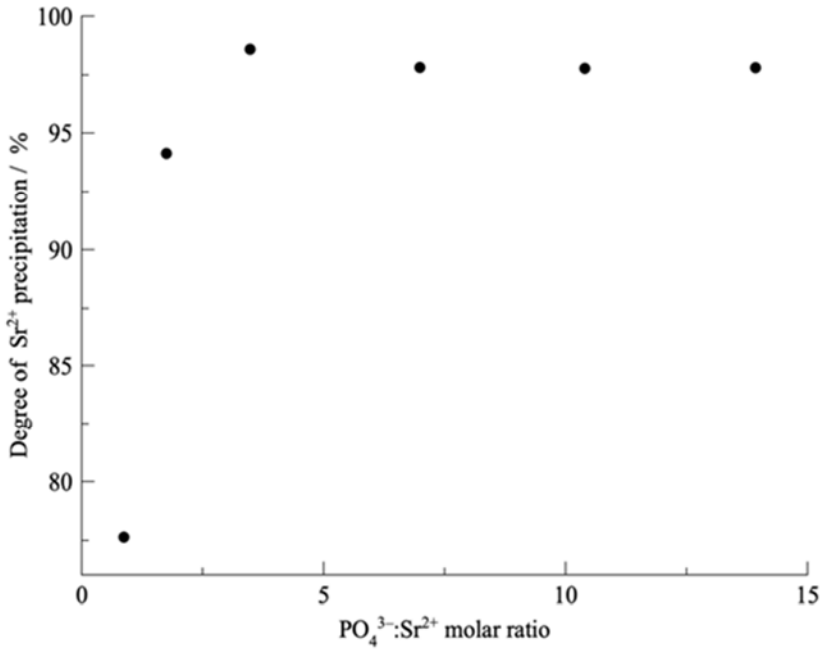

Figure 8. Effect of the initial PO_4^{3-} : Sr^{2+} molar ratio on the degree of strontium precipitation by sodium phosphate from NaCl–KCl–CsCl–$SrCl_2$ melts at 750 °C.

The results of determining particle size of strontium and barium phosphates precipitated from NaCl–KCl–CsCl eutectic based melts are shown in Figs. 10 and 11. Strontium phosphate precipitates were formed of micron size particles. For the samples obtained at low initial molar ratios of phosphate-to-strontium in the reaction mixture first maximum on PSD curves was around 2 μm and second around 25 μm. At higher molar ratios first maximum on PSD curves was weak and position of the second (main) maximum was around 20, 15 and 8 microns for the molar ratios of 6.99, 3.48 and 10.40, respectively.

Barium phosphate particle were 1–100 microns in size. Maximum on the PSD curves of the precipitates formed at the initial PO_4^{3-} : Ba^{2+} mole ratios of 0.58 and 1.07 was around 25 μm. Position of the maximum shifted to ca. 15 μm for the sample obtained at the molar ratio of 2.16. Further increase of the molar ratio to 4.35–8.71 resulted in more complicated profiles of PSD curves with two maxima. Thus, again, similar to LiCl–KCl and NaCl–KCl melts there was no obvious and monotonous dependence of the particle size on the initial phosphate-to-alkaline earth metal molar ratio in the reaction mixture.

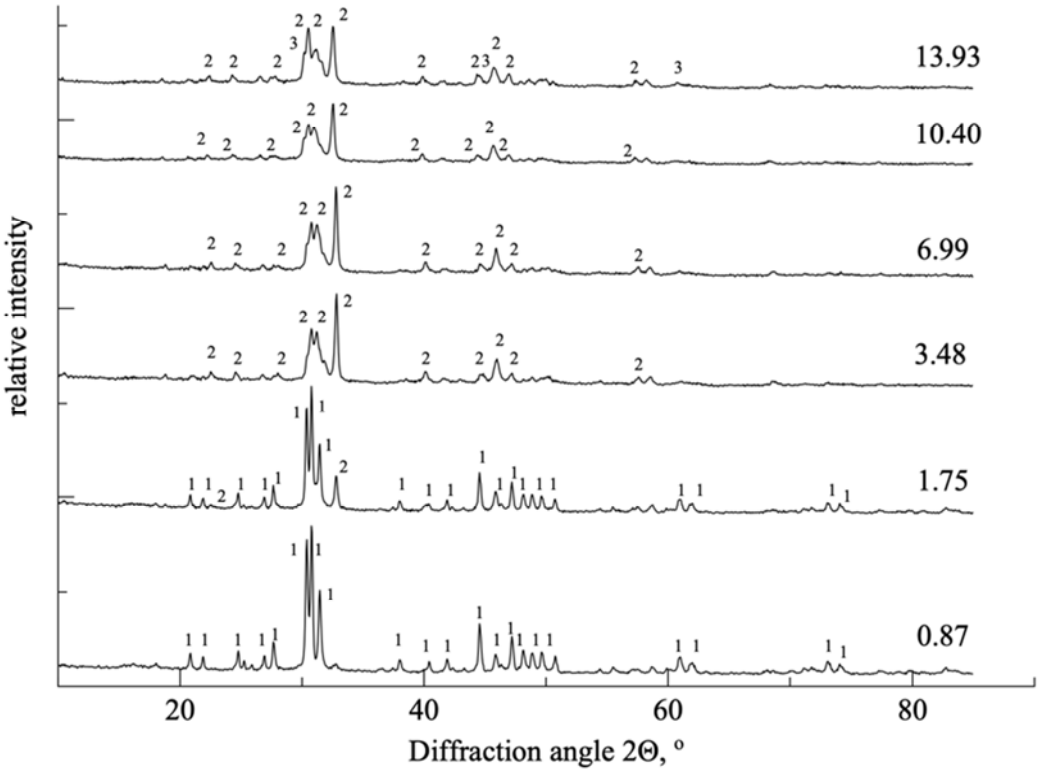

Figure 9. X-ray diffraction patterns of strontium phosphates formed in NaCl–KCl–CsCl–$SrCl_2$ melts at various initial PO_4^{3-} : Sr^{2+} mole ratios (shown on the plot for each set of data). The phases present were $Sr_5(PO_4)_3Cl$ (1); $NaSrPO_4$ (2) and $Sr_3(PO_4)_2$ (3).

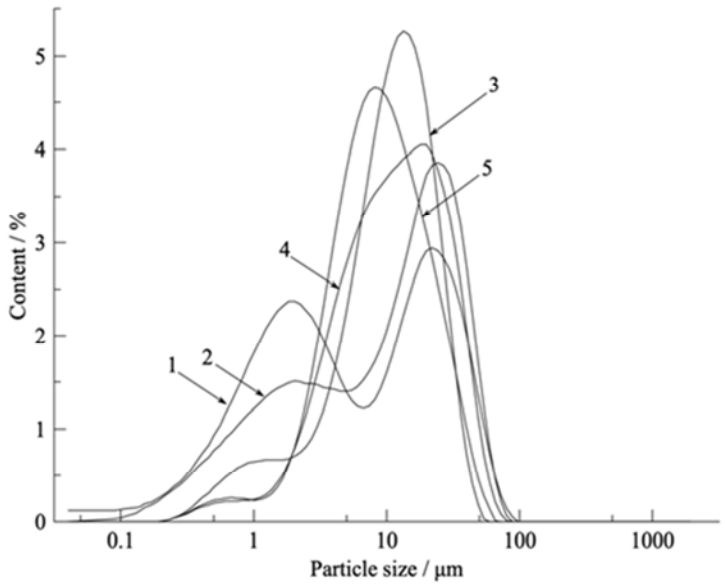

Figure 10. Differential PSD curves of strontium phosphates formed in NaCl–KCl–CsCl–$SrCl_2$ melts at the initial PO_4^{3-} : Sr^{2+} mole ratios of 0.87 (1); 1.75 (2); 3.48 (3); 6.99 (4) and 10.40 (5).

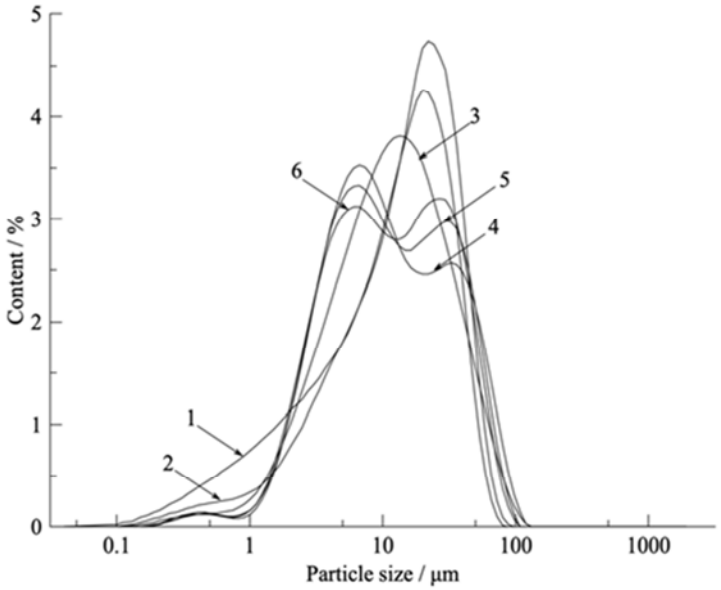

Figure 11. Differential PSD curves of barium phosphates formed in NaCl–KCl–CsCl–$BaCl_2$ melts at the initial PO_4^{3-} : Ba^{2+} mole ratios of 0.58 (1); 1.07 (2); 2.16 (3); 4.35 (4); 6.52 (5) and 8.71 (6).

Comparing the results obtained here for strontium and barium with previous findings for the rare earth phosphates showed that the size of particles forming phosphate precipitates is very weakly affected by the nature of the metal (11, 13). For both rare earth and alkaline earth metals phosphate precipitates are mostly made of particles smaller than 30–50 microns. Therefore the same process for separating solid precipitate from the melt can be applied in case of rare earth and alkaline earth phosphates.

Conclusions

Reaction of Na_3PO_4 with LiCl–KCl–$AECl_2$, NaCl–KCl–$AECl_2$ and NaCl–KCl–CsCl–$AECl_2$ (AE = Ba, Sr) melts resulted in the formation of alkaline earth phosphates that were essentially insoluble in the chloride melts. Phosphate precipitation process can be effectively used for purifying chloride electrolytes from alkaline earth fission products in pyrochemical technologies of spent nuclear fuel reprocessing.

Depending on the melt composition and the initial phosphate-to-alkaline metal chloride molar ratio barium and strontium can form normal, $AE_3(PO_4)_2$, double, $NaAEPO_4$, or more complex, $AE_{10}O(PO_4)_6$, $AE_5(PO_4)_3Cl$, phosphates. In lithium containing melts mostly normal $AE_3(PO_4)_2$ phosphates were produced; excess phosphate ions reacted with lithium chloride forming sparingly soluble lithium phosphate.

References

1. J. P. Ackerman and T.R. Johnson, *Process to Remove Rare Earth From IFR Electrolyte,* US Patent 5336450, 09.08.1994.

2. Y. Ikeda, Y. Yasuike, M. Yamaguchi, H. Kobayashi and H. Igarashi, *Process for Treating Salt Waste Generated in Dry Reprocessing of Spent Metallic Nuclear Fuel*, US Patent 5264159, 23.11.1993.
3. Y.-J. Cho, H.-C. Yang, H.-C. Eun, E.-H. Kim and I.-T. Kim, *J. Nucl. Sci. Techn*., **43**, 1280 (2006).
4. Y.-J. Cho, H.-C. Yang, H.-C. Eun, E.-H. Kim and J.-H. Kim, *J. Ind. Eng. Chem*., **11**, 707 (2005).
5. H. C. Eun, Y. Z. Cho, H. S. Park, T. K. Lee, I. T. Kim, K. I. Park and H. S. Lee, *J. Nucl. Mater.*, **408**, 110 (2011).
6. V. A. Volkovich, T. R. Griffiths and R. C. Thied, *Phys. Chem. Chem. Phys.*, **5**, 3053 (2003).
7. V. A. Volkovich, T. R. Griffiths and R. C. Thied, *J. Nucl. Mater.*, **323**, 49 (2003).
8. V. A. Volkovich, B. D. Vasin, T. R. Griffiths, I. B. Polovov, E. O. Medvedev and S. M. Yakimov, *ECS Trans.*, **3**(35), 493 (2007).
9. V. A. Volkovich, A. B. Ivanov, S. M. Yakimov, I. B. Polovov, B. D. Vasin, T. R. Griffiths, A. V. Chukin and A. K. Shtolts, *ECS Trans*., **50**(11), 517 (2012).
10. T.-K. Lee, Y.-Z. Cho, H.-C. Eun, S.-M. Son, G.-I. Park and T.-S. Hwang, *J. Nucl. Sci. Techn.*, **50**, 742 (2013).
11. A. B. Ivanov, V. A. Volkovich, D. S. Malltsev, V. V. Sukhikh and T. R. Griffiths, *ECS Trans.*, **75**(15), 313 (2016).
12. P. D. Wilson, *The Nuclear Fuel Cycle: From Ore to Wastes*, p. 314, Oxford University Press, Oxford (1996).
13. V. A. Volkovich, A. B. Ivanov, A. V. Chukin, V. V. Sukhikh and T. R. Griffiths, *ECS Trans.*, **86**(14), 329 (2018).
14. V. A. Volkovich, A. B. Ivanov, S. M. Yakimov, B. D. Vasin, A. V. Chukin and A. K. Shtolts, *Rasplavy*, (6), 36 (2014).

ECS Transactions, 98 (10) 295-305 (2020)
10.1149/09810.0295ecst ©The Electrochemical Society

Electrochemical Behavior of Titanium Complexes in the KCl-KF Melt with Additions of Alkaline Earth Metal Cations

D.A. Vetrova, S.A. Kuznetsov

Tananaev Institute of Chemistry of the Federal Research Centre "Kola Science Centre of the Russian Academy of Sciences", Apatity, Russia

The charge transfer kinetics for the redox couple Ti(IV)/Ti(III) in the KCl-KF(10 wt.%)-K_2TiF_6 melt was studied. The standard rate constants of charge transfer (k_s) for the redox couple Ti(IV)/Ti(III) in the KCl-KF(10 wt.%)-K_2TiF_6 melt and the activation energy of charge transfer were calculated. Influence of strongly polarizing cations (Mg^{2+}, Ca^{2+}, Sr^{2+} and Ba^{2+}) on the charge transfer kinetics was studied. It was determined the linear dependence of k_s on the ionic potential of alkaline earth metal cations. The activation energies of charge transfer in case of strongly polarizing cations addition were found.

Introduction

The electrochemical behavior of titanium in chloride and chloride-fluoride melts has studied in works (1–9). Electrochemical studies (1, 2) showed that in these melts the electroreduction of Ti(IV) complex to the metal occurs in two stages:

$$Ti(IV)+e^-\rightarrow Ti(III) \quad [1]$$
$$Ti(III)+3e^-\rightarrow Ti. \quad [2]$$

The diffusion coefficients of Ti(IV) complexes were determined in the NaCl-KCl melt for different temperature in investigations (1, 2). In our studies (8, 9), the standard rate constants of charge transfer (k_s) for the redox couple Ti(IV)/Ti(III) in the NaCl-$KCl_{(equimol.)}$-NaF(10 wt.%)-K_2TiF_6 melt and the activation energies of charge transfer were defined.

Electrochemical studies of titanium in the KCl-KF melt are extremely few. Only in works (3, 6, 7) the titanium electrochemical behavior was studied in the KCl-KF eutectic mixture. However, there are no data on the diffusion coefficients and the standard rate constants of charge transfer for the Ti(IV)/Ti(III) redox couple in the KCl-KF melt.

The goal of the present work was to study the charge transfer kinetics of the redox couple Ti(IV)/Ti(III) in the KCl-KF(10 wt.%)-K_2TiF_6 melt and to determine the influence of strongly polarizing cations of Mg^{2+}, Ca^{2+}, Sr^{2+} and Ba^{2+} on the electrochemical behavior of titanium complexes.

Experimental

Electrochemical Cell and Salt Preparation

Electrochemical studies were performed by cyclic voltammetry method using a VoltaLab 40 dynamic electrochemical laboratory, equipped with "VoltaMaster 4"

(version 6) software. The potential scan rate (*v)* varied from 0.1 to 2.0 V s^{-1} range. Experiments were carried out in the temperature range 1073-1173 K.

A glassy carbon crucible used as container for the melt was placed in a sealed retort of the Kh18N10T stainless steel. Glassy carbon rods (SU-2000) were used as working and quasi-reference electrode. The diameter of the glassy carbon rods was 2 mm. The glassy carbon crucible served as the auxiliary electrode.

The salts were prepared as follows: potassium chloride (analytical grade) were recrystallized, sintered in a muffle oven and then put into quartz retort. The retort was evacuated to the residual pressure of 0.66 Pa, firstly at room temperature, then upon gradual stepwise heating to 873 K. After that, it was filled by inert gas (argon) and the electrolyte was melted.

Potassium fluoride was dried at 673–773 K in a vacuum, heated to the temperature by 50 K higher than the melting point, kept at this temperature for several hours, and then cooled at a rate of 3–4 deg h^{-1} to the temperature lower than the melting point by 50 K. After solidification, the salt was transported at 393 K to a glove box with a controlled atmosphere (O_2 and H_2O content $\leq$ 2 ppm), and contaminations were mechanically removed in the box.

Potassium hexafluorotitanate of pure grade was dissolved in hot water (363-373 K). The solution was passed through a hot filter and cooled. The resulting K_2TiF_6 crystals were dried in a vacuum, first at 363 K for 24 h and then at 423 K for 6 h. (10).

Barium chloride (chemical pure) is dried in a vacuum oven in 433 K for 24 hours. Barium fluoride (analytically pure grade), magnesium fluoride (high pure) and calcium chloride (pure grade) was used without additional processing.

Strontium chloride (reagent grade) was dried in a vacuum oven in 523 K for 12 hours. Then salt was placed into quartz tubes and immersed into a retort. The retort was evacuated to the residual pressure 0.66 Pa with simultaneous heating to 823 K at a rate of 100 deg h^{-1}.

The KCl-KF (10 wt%) electrolyte was placed into a glassy carbon crucible, loaded into a retort of the electrochemical cell, the above described vacuum-melting operations were repeated and K_2TiF_6 was introduced into the melt.

The Procedure for the Determination of the Standard Rate Constants of Charge Transfer

The theory of the standard rate constants of charge transfer (k_s) determining for quasi-reversible redox processes without formation of an insoluble product based on the method of cyclic voltammetry has been developed by Nicholson (11). He established a correlation between the function Ψ, related to the potential difference between the cathodic and anodic peaks, and the standard rate constant:

$$\psi_T = (k_s(D_{ox}/D_{red})^{\alpha/2})/((\pi D_{ox} n F v)/RT)^{1/2}, \quad [3]$$

where α is the transfer coefficient, n is the number of electrons involved in the reaction, D is the diffusion coefficients of Ti(IV) and Ti(III) complexes (D_{ox} and D_{red} respectively), v is the polarization rate.

In the calculating of the standard rate constants of charge transfer we used a = 0.5 because this value is for which the interrelation between ΔE_p and Ψ has been found in (11).

Since usually $D_{ox}/D_{red} \approx 1$ equation [3] can be simplified and takes the form:

$$\psi_T = (k_s)/((\pi D_{ox} nF\nu)/RT)^{1/2} \quad [4]$$

For determining of the standard rate constants of charge transfer, the data ΔE_p and Ψ, reported in work (11) for the temperature 298 K, should be recalculated for the operation temperature by equations (12):

$$(\Delta E_p)_{298} = (\Delta E_p)_T 298/T, \quad [5]$$

$$\psi_T = \psi_{298}(T/298)^{1/2}. \quad [6]$$

By using the values of the function Ψ_T obtained from equation [6] and combined with the diffusion coefficients, the standard rate constants of charge transfer may be calculated by equation [4].

Results and Discussion

The Ti(IV) + e^- ↔ Ti(III) Redox Process Diagnostics in the KCl-KF(10 wt.%)-K_2TiF_6 melt

Typical cyclic voltammograms for the Ti(IV)/Ti(III) redox couple obtained at different polarization rates in the KCl-KF(10 wt.%)-K_2TiF_6 melt are shown in Fig. 1.

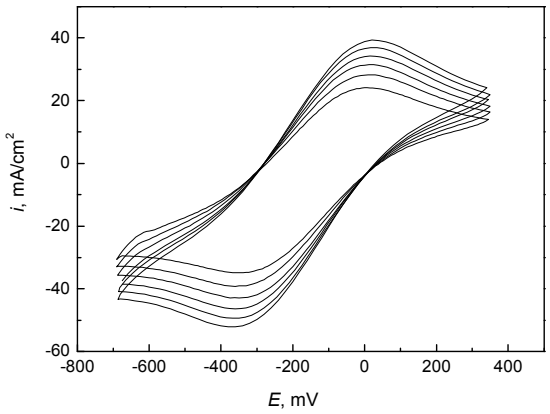

Figure 1. Cyclic voltammograms for the Ti(IV) + e^- ↔ Ti(III) process in the KCl-KF(10 wt.%)-K_2TiF_6 melt obtained on a glassy carbon electrode. T=1023 K. Scan rate (V s^{-1}): 0.75 (inner curve), 1.0, 1.25, 1.5, 1.75, 2.00 (outer curve).

It was found that the peak current of the electroreduction process is directly proportional to the square root of the polarization rate (Fig. 2a), while the peak potential does not depend on the polarization rate up to ν=0.75 V s^{-1} (Fig. 2b). The peak current is

linear function on the K_2TiF_6 concentration, while the peak potential does not depend on the concentration of K_2TiF_6 in the melt. According to the theory of cyclic voltammetry (13), up to polarization rate of 0.75 V s^{-1}, the electrode process is controlled by the rate of mass transfer and yields a reduced form soluble in the melt.

Since the Nicholson's theory was developed for quasi-reversible processes, it is necessary to establish a region of polarization rates at which process [1] is quasi-reversible. According to cyclic voltammetry diagnostic criteria (13) the deviation of the experimental points from a straight line in Fig. 2a at a scan rate higher than 0.75 V s^{-1} indicates that the electroreduction of Ti (IV) to Ti(III) at $v > 0.75$ V s^{-1} is quasi-reversible. This is also confirmed by the curvilinear dependence of $E_p(C)$ on log v (Fig. 2b).

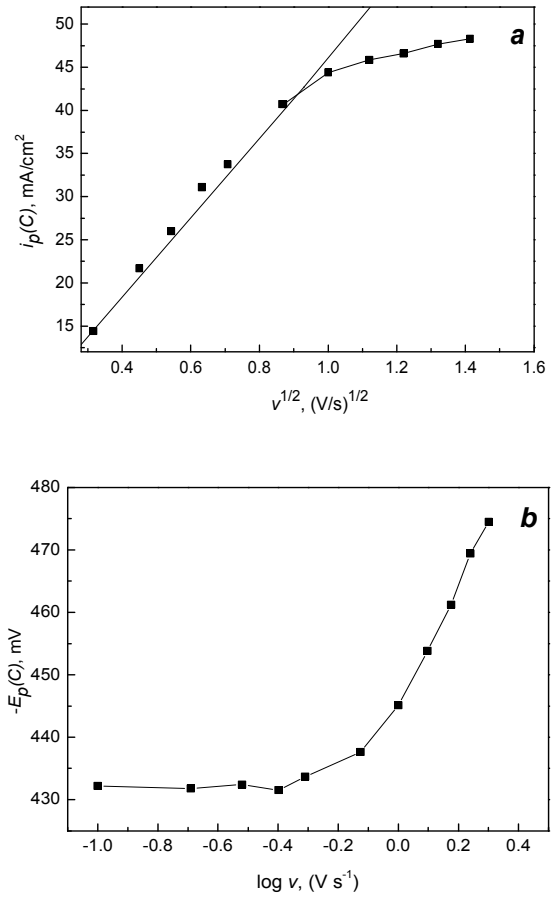

Figure 2. The dependences of peak currents (a) and peak potentials (b) for the redox process [1] on the polarization rate in the KCl-KF(10 wt.%)-K_2TiF_6 melt; T=1023 K.

Determination of the Ti(IV) Diffusion Coefficients in the KCl-KF(10 wt.%)-K_2TiF_6 Melt

The Ti(IV) diffusion coefficients in the KCl-KF(10 wt.%)-K_2TiF_6 melt were determined at v = 0.1 V s^{-1} using Randles-Sevchik equation (14), which is valid for reversible process with formation of soluble product:

$$I_p = 0.4463F^{3/2}R^{-1/2}T^{-1/2}n^{3/2}ACD^{1/2}v^{1/2}, \quad [7]$$

where I_p is the cathodic current peak (A), A is the electrode area (cm^2), C is the bulk concentration active species (mol cm^{-3}), D is the diffusion coefficient (cm^2 s^{-1}), n is the number of electrons involved in the reaction, v – the sweep rate (V s^{-1}).

The Ti(IV) diffusion coefficients were found to be (1.34±0.5) 10^{-5} cm^2 s^{-1} at 1073 K, (1.72±0.5) 10^{-5} cm^2 s^{-1} at 1123 K and (2.5±0.5) 10^{-5} cm^2 s^{-1} at 1173 K.

The temperature dependence of the diffusion coefficients (Fig. 3) is described by the equation:

$$\log D = -1.62 - 3496/T \pm 0.03 \quad [8]$$

Relation [8] was used to calculate the diffusion activation energy according to the equation:

$$-\Delta U/2.303R = \partial \log D/\partial(1/T). \quad [9]$$

The activation energy of diffusion in the KCl-KF(10 wt.%)-K_2TiF_6 melt turned out to be (70±11) kJ mol^{-1}.

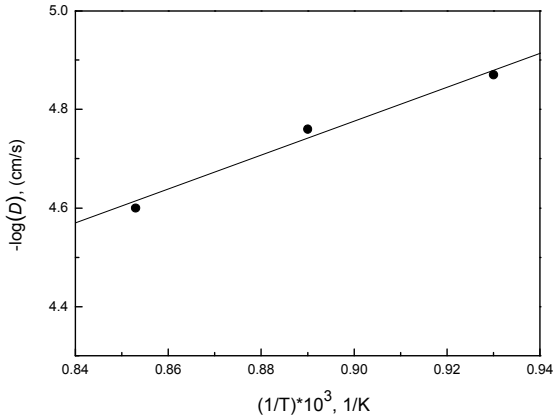

Figure 3. The dependence of diffusion coefficients on the temperature. The sweep rate is 0.1 V·s^{-1}.

Determination of the Standard Rate Constants of Charge Transfer for the Ti(IV)/Ti(III) Redox Couple in the KCl-KF(10 wt.%)-K_2TiF_6 Melt

The values of k_s were calculated by using the Nicholson's method. It was shown that k_s are independent on the polarization rate and increase with temperature increasing (Fig. 4). It is due to increase in the number of particles with the energy that necessary for overcoming the potential barrier for the electron transfer process.

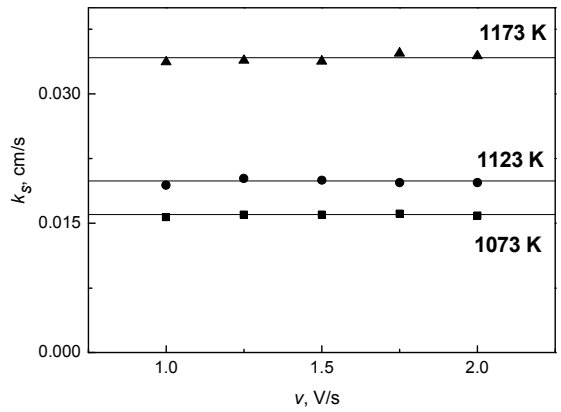

Figure 4. Standard charge transfer rate constants (k_s) on the polarization rate (v) for different temperature in the KCl-KF(10 wt.%)-K_2TiF_6 melt.

The temperature dependence of the standard rate constants of charge transfer (Fig. 5) is described by the empirical equation:

$$\log k_s = (2.01\pm0.40)–(4178\pm810)/T \qquad [10]$$

A correlation coefficient $R^2 = 0.95$.

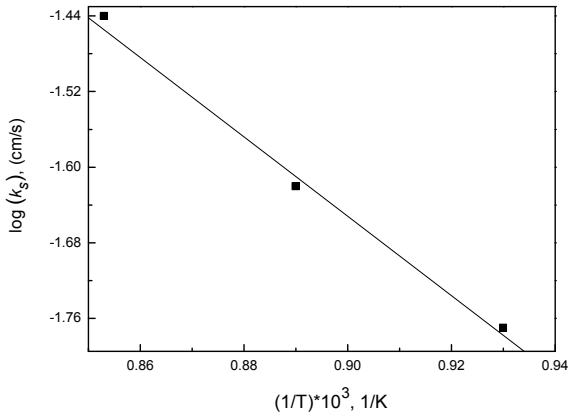

Figure 5. The dependence of log k_s on 1/T. The polarization rate is 1.5 $V \cdot s^{-1}$.

Relation [10] was used to calculate the activation energy of charge transfer to be (80±15) kJ mol^{-1}. This value is significantly higher than the activation energy for the melt NaCl-$KCl_{(equimol.)}$-NaF(10 wt.%)-K_2TiF_6. (8)

The temperature dependences of the standard rate constants of charge transfer for the Ti(IV)/Ti(III) redox couple in the NaCl-$KCl_{(equimol.)}$-NaF(10 wt.%)-K_2TiF_6 melt (8) and KCl-KF(10 wt.%)-K_2TiF_6 melt are shown in Fig.6. The k_s values are decreasing from NaCl-$KCl_{(equimol.)}$-NaF(10 wt.%)-K_2TiF_6 melt to KCl-KF (10 wt.%) melt because the titanium complexes strength increase due to the decrease of the counter-polarizing effect in transition from sodium to potassium cations in the second coordination sphere.

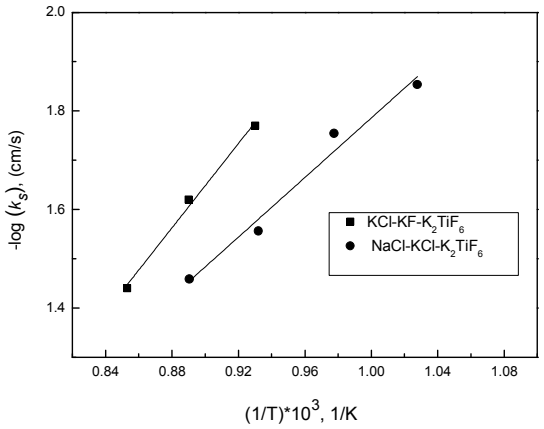

Figure 6. The dependences of log k_s on 1/T for KCl-KF(10 wt.%)-K_2TiF_6 and NaCl-$KCl_{(equimol.)}$-NaF(10 wt.%)-K_2TiF_6 melts. The polarization rate is 1.5 V·s^{-1}.

Determination of the Standard Rate Constants of Charge-Transfer for the Ti(IV)/Ti(III) Redox Couple in the KCl-KF(10 wt.%)-K_2TiF_6 melt with Addition of Alkaline Earth Metal Cations

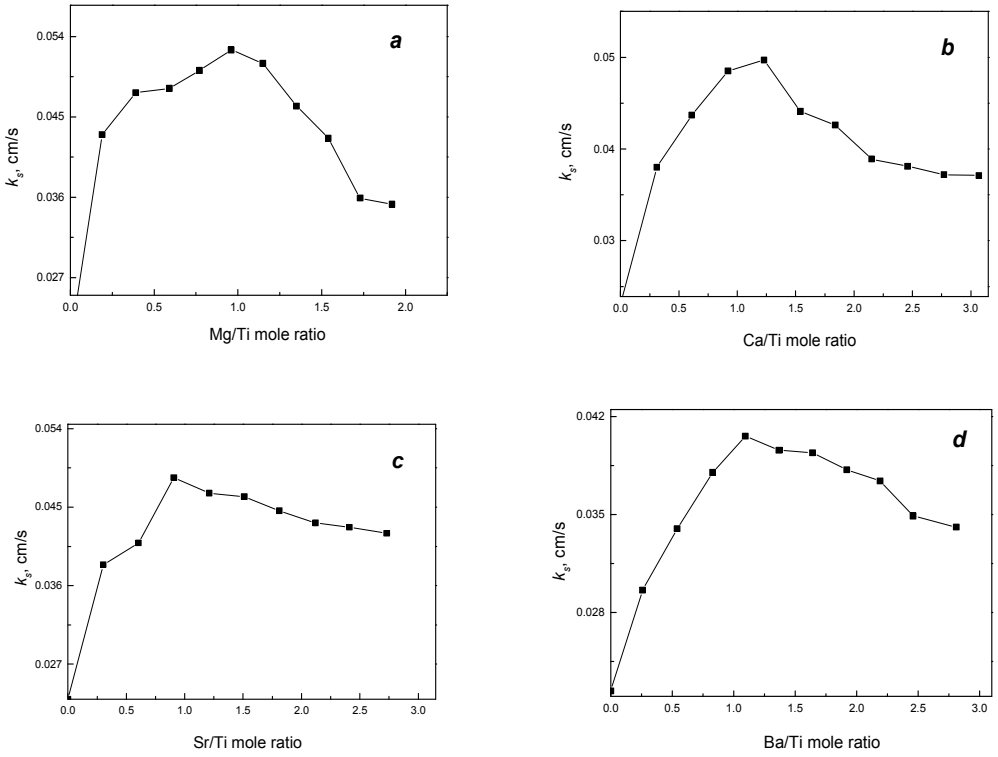

Figure 7 The dependence of the standard rate constant of charge transfer on the Me^{2+}/Ti(IV) mole ratio (Mg^{2+} (*a*), Ca^{2+} (*b*), Sr^{2+} (*c*) and Ba^{2+} (*d*)). The polarization rate is 1.5 V·s^{-1}, *T*=1073 K.

Addition of alkaline earth metal cations (Mg^{2+}, Ca^{2+}, Sr^{2+} and Ba^{2+}) into the initial melt resulted in increasing of k_s to the certain ratio of Me^{2+}/Ti(IV) for the all alkaline earth metal cations (Fig .7). It is related to the replacement of potassium cations with Me^{2+} in the second coordination sphere of complexes since the ionic potential of strongly polarizing cations is significantly higher than that of alkali metal cations. The Me^{2+}/Ti(IV) ratio (for k_s maximum) is lower for alkaline earth metal cations with the higher the ionic potential because the lower Me^{2+}/Ti(IV) ratio needs to the replacement of cations of alkali metals with Me^{2+} in the second coordination sphere of titanium complexes.

Decrease of k_s at the definite ratio of components can be explained by a change in the structure of the double layer or increasing of the melts viscosity (viscosity of alkaline earth metal halides are higher than alkali metal halides), which brings to decreasing of the diffusion coefficients.

The same results (within the experimental error) were obtained using chlorides or alkaline earth metal fluorides as additives (Fig. 8).

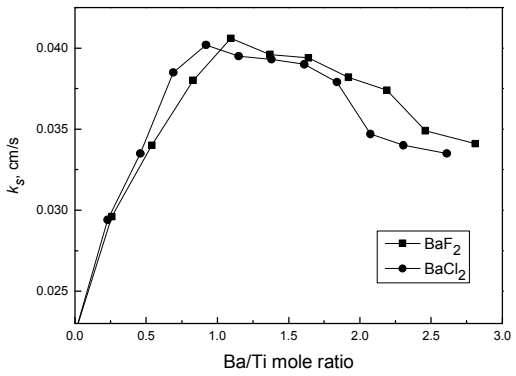

Figure 8. The dependences of the standard rate constant of charge transfer on the Ba^{2+}/Ti(IV) mole ratio; T=1073 K.

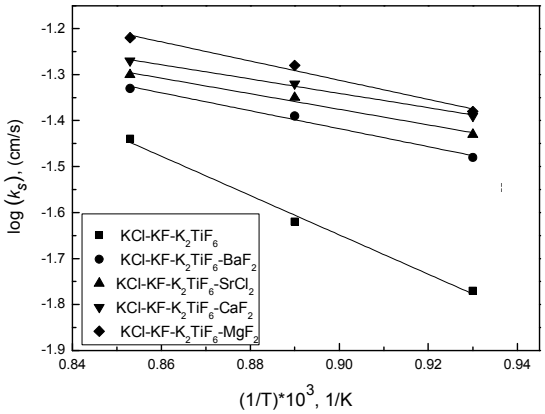

Figure 9. The dependences of log k_s on 1/T. The polarization rate is 1.5 $V \cdot s^{-1}$.

The temperature dependences for maximum values of k_s for strongly polarizing cations are shown in Fig. 9 and described by the empirical equations:

$$\log k_{s(Mg^{2+})} = -(0.31\pm0.06) - (927\pm180)/T \quad [11]$$

$$\log k_{s(Ca^{2+})} = -(0.35\pm0.06) - (972\pm196)/T \quad [12]$$

$$\log k_{s(Sr^{2+})} = -(0.23\pm0.04) - (1128\pm215)/T \quad [13]$$

$$\log k_{s(Ba^{2+})} = -(0.13\pm0.02) - (1223\pm235)/T \quad [14]$$

The calculated activation energies of charge transfer are shown in the Table I. Values of activation energy are less than activation energy for the initial system. According to theory of elementary act (15) the activation energy of charge transfer is smaller if the standard rate constants of charge transfer are higher. That is in an agreement with obtained data.

TABLE I. The Activation Energies of Charge Transfer in the KCl-KF(10 wt.%)-K_2TiF_6 Melt for Systems with Addition of Strongly Polarizing Cations.

Cation	E_a, kJ mol^{-1}
Mg^{2+}	22±4
Ca^{2+}	26±5
Sr^{2+}	28±5
Ba^{2+}	33±7

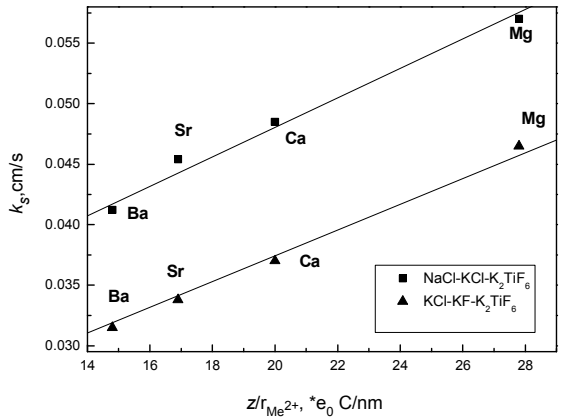

Figure 10. The dependences of k_s maximum values on the ionic potential of alkaline earth metal cations in KCl-KF(10 wt.%)-K_2TiF_6 and NaCl-$KCl_{(equimol.)}$-NaF(10 wt.%)-K_2TiF_6 melts; T=1073 K.

The dependences of maximum values of k_s on the ionic potential of alkaline earth metal cations for the NaCl-$KCl_{(equimol.)}$-NaF(10 wt.%)-K_2TiF_6 melt (8) and for the KCl-KF(10 wt.%)-K_2TiF_6 melt are shown in Fig.10. As can be seen from Fig. 10, k_s for the redox couple Ti(IV)/Ti(III) in systems with the addition of alkaline earth cations are higher for the NaCl-KCl based melt.

The standard rate constants increase with an increasing of the ionic potential and reach maximum values for the complexes with outer sphere magnesium ions. The dependences of k_s on the ionic potential point out that the electron transfer to the complex occurs through the bridging mechanism, i.e. through electrolyte cations.

Conclusions

1) In this work the kinetics of charge transfer for the Ti(IV)/Ti(III) redox couple in the KCl-KF(10 wt.%)-K_2TiF_6 melt was studied by cyclic voltammetry method. The electrochemical redox process $Ti(IV) + e^- \leftrightarrow Ti(III)$ was classified as quasi-reversible at a sweep rate 0.75 V $s^{-1} \leq v \leq$ 2.0 V s^{-1}. The standard rate constants of charge transfer (k_s) were calculated by Nicholson method.

2) The values of k_s increase with the increasing of temperature due to increase in the number of particles capable of overcoming the potential barrier for the electron transfer process.

3) The influence of the strongly polarizing cations Mg^{2+}, Ca^{2+}, Sr^{2+} and Ba^{2+} on the charge transfer kinetics for the Ti(IV)/Ti(III) redox couple in the KCl-KF(10 wt.%)-K_2TiF_6 melt was investigated. It was determined that the k_s increasing with the ionic potential and reach a maximum for complexes with magnesium outer sphere cations.

4) The activation energies of charge transfer in the KCl-KF(10 wt.%)-K_2TiF_6 melt and in the melts with additions of strongly polarizing cations Mg^{2+}, Ca^{2+}, Sr^{2+} и Ba^{2+} were calculated. Values of activation energy for systems with strongly polarizing cations are considerably less than activation energies of the initial system and decrease in case of ionic potential increasing.

References

1. L.P. Polyakova, P.T. Stangrit and E.G. Polyakov, *Electrochim. Acta*, **31**, 159 (1986).
2. C.A. Sequeira, *J. Electroanal. Chem.*, **239** (1-2), 203(1988).
3. L.P. Polyakova, T.V. Stogova, *Zh. Prikl. Khim.*, **7**, 1470 (1985).
4. L.P. Polyakova, P. Taxil, E.G. Polyakov, *Alloys and Compd.*, **359**, 244 (2003).
5. V. Malyshev, A. Gab, D.-M. Bruskova et al., *Revue Roumaine de Chimie*, **54 (**1), 5 (2009).
6. Y. Norikawa, K. Yasuda, T. Nohira, *The Electrochem. Soc. of Japan*, **86** (2), 99 (2018).
7. Y. Norikawa, K. Yasuda, T. Nohira, *Materials Transactions*, **58**(3), 390 (2017).
8. D. A. Vetrova, O.S. Kazakova, S.A. Kuznetsov, *Zh. Prikl. Khim.*, **87**(4), 446 (2014).
9. D. A. Vetrova, S.A. Kuznetsov, *Russ. Metallurgy (Metally),* **2**, 100 (2017).
10. M.A. Strinberg, *J. Electrochim.Soc.*, **102**, 332 (1955).
11. R.S. Nicholson, *Anal. Chem.*, **37**(11), 1351(1965).
12. S.A. Kuznetsov, S.V. Kuznetsova, P.T. Stangrit, *Russ. J. Electrochem*, **26**, 63, (1990).
13. R. S. Nicholson, Shain *J. Anal.Chem.,* **36** (4), 706 (1964).
14. P. Delahay, *New devices and methods in electrochemistry,* IL, Moscow, (1957).

15. B.B. Damaskin and O.A. Petriy, *Introduction of electrochemical kinetics*, Vysshaya Shkola Publ., Moscow, (1975).

ECS Transactions, 98 (10) 307-315 (2020)
10.1149/09810.0307ecst ©The Electrochemical Society

Corrosion of Metallic Materials in 3LiCl–2KCl and (3LiCl–2KCl)–UCl_3

R. R. Alimgulov[a], A.V. Abramov[b], A. N. Trubcheninova[a], I. B. Polovov[a], A. Y. Zhilyakov[c], S.V. Belikov[c], and O. I. Rebrin[b]

[a] Department of Rare Metals and Nanomaterials, Ural Federal University, Ekaterinburg, 620002, Russia
[b] Department of Physical and Chemical Methods of Analysis, Ural Federal University, Ekaterinburg, 620002, Russia
[c] Department of Heat Treatment and Physics of Metals, Ural Federal University, Ekaterinburg, 620002, Russia

The corrosion of various metallic materials was investigated in 3LiCl–2KCl and 3LiCl–2KCl–UCl_3 (5 wt. % U) melts under inert atmosphere. Metallic tantalum and molybdenum, nickel-chromium-molybdenum alloys (VDM® Alloy C-4, Hastelloy® G-35® and specially designed KhN62M alloy) were investigated. The corrosion tests run for 100 h, and the temperature was varied from 450 to 750 °C. The corrosion rates were determined by gravimetric technique and chemical analysis of quenched melts.

Introduction

High-temperature molten salts are widely used in production and refining of non-ferrous and rare metals, in nuclear technology and solar storage systems. For example, in the nuclear industry a large amount of spent nuclear fuel (SNF) was accumulated and it continues to grow rapidly. The estimated amount of heavy metals, HM (Pu, U, Th and minor actinides) in SNF from nuclear reactors worldwide amounted to 370 000 tons by the end of 2013 (1). Approximately one third (120 000 t HM) has been reprocessed resulting in the separation of fissile materials and residual waste, but the remaining two thirds are currently being stored, awaiting either future direct disposal or reprocessing. Unfortunately, currently used solvent extraction methods are often not suitable for processing of high-level wastes due to the limitations imposed by the water environment. Today, the most optimal way to solve this problem is pyrochemical method of reprocessing of SNF in molten salts. Such technologies were developed in the 1980s at the Idaho National Laboratory and other countries (2, 3). However, application of such technologies is limited by the problem of finding suitable corrosion resistant materials for prolonged contact with molten salts. The current study is focused on the corrosion of metallic materials in 3LiCl–2KCl based melts.

The reduction potentials of salt cations Li(I), K(I) are far below corresponding potentials of refractory metals (molybdenum, tantalum) and main components of Ni-based alloys (4). This fact indicates that alkali metal cations are not expected to cause considerable corrosion of these materials. Uranium (III) also has relatively low electrode potential. Different research group confirmed high corrosion resistance of nickel–based alloys in molten chloride salts. For example, Vignarooban et al. studied corrosion behavior of Hastelloy® C-276, C-22® and SS 304 in molten NaCl–KCl–$ZnCl_2$ from 200 to 800 °C in the inert and air conditions (5). Under inert atmosphere, Hastelloy® alloys showed remarkably low corrosion rates in molten chloride salts even at 800 °C.

Recently our group investigated corrosion resistant (Hastelloy® N, B-3®, G-35®, C-2000®) and high temperature (Haynes® 230®, Hastelloy® S and X) alloys in KCl–$AlCl_3$ melts (6). It was found that the mechanisms of corrosion of high-temperature alloys and corrosion-resistant alloys in KCl–$AlCl_3$ based melts were different. At a critical temperature phase structure of the high-temperature alloys changed after contact with chloroaluminate melts resulting in formation of intermetallic or carbon-containing phases along the grain boundaries that resulted in increasing strength of the alloys but initiated intense intergranular corrosion. Higher temperatures also can cause structural changes in majority of the corrosion-resistant alloys. It was shown that both types of alloys undergo intergranular corrosion below the critical conditions. Later we also found that VDM® Alloy C-4 and Hastelloy® G-35® had the highest phase stability and can be used in molten chloroaluminates under 650 °C (7). VDM® Alloy C-4 in as-received state demonstrated high resistance against intergranular corrosion in 3LiCl-2KCl below 650 °C (8).

Therefore, the aim of the current investigation was conducting preliminary corrosion tests on refractory metals and corrosion-resistant of nickel-based alloys in 3LiCl–2KCl and 3LiCl–2KCl–UCl_3 (5 wt. % U) melts under inert atmosphere and static conditions with detailed analysis of temperature influence on corrosion properties and phase stability of these metallic materials.

Materials and Methods

Preparation of Molten Salt Systems

Anhydrous lithium chloride (A.C.S., 99 %+, Aldrich) and potassium chloride (99.99 %) were used in the present study. Individual alkali chlorides were dried under vacuum at 300 °C for 3–5 h. After that the salts were melted and sparged with a mixture of chlorine and hydrogen chloride for 5 h. Molten salts were then poured into alumina crucibles and cooled in a desiccator. Salts thus prepared were kept in an argon filled dry box (Glovebox Systemtechnik Gmbh). The eutectic mixture of lithium and potassium chlorides (44 wt. % LiCl) was prepared by fusing together LiCl and KCl in the required proportion at 600 °C for 2 h with hydrogen chloride bubbled through the melt. After that the melt was held under vacuum to remove dissolved HCl, then poured into alumina crucibles and allowed to solidify.

Uranium containing melts based on 3LiCl–2KCl eutectic were prepared by dissolving the required amount of UCl_3. Uranium trichloride was prepared according to the scheme described previously (9). To ensure that uranium remained in the melt as ions in the oxidation state +3, a piece of metallic uranium was also added into the melt during this stage. Uranium containing melts were prepared in the argon filled drybox (Glovebox Systemtechnik Gmbh) and the melt was held in the molten state for 6 h. Concentration of uranium in the electrolytes was 5.0 wt. %.

Sample Preparation for Corrosion Srudies

Samples of selected metallic materials were cut by a cold mechanical method, alloys were in the form of parallelepipeds with dimensions of 10x5x4 mm^3 and individual metals were prepared as cylinders of 8 mm height and 9 mm diameter; the surface area of the samples was about 4–6 cm^2. Each sample of the alloy was sandpapered in five stages (SiC papers were used in the following order: 80→220→320→1200→2400). Prior to the experiments the samples were washed in distilled water, rinsed in ethanol, dried and weighted. Corrosion experiments were conducted according to the scheme described previously (10). Composition of the alloys in the as received state are listed in Table I

TABLE I. Chemical composition of studied alloys.

Type of Alloy	Ni	Fe	Cr	Mo	Al	Ti	Si	Mn	Cu	W
Hastelloy G-35	base	≤2	33	8	≤0.4	0.01	0.6	≤0.5	0.03	0.11
VDM Alloy C-4	base	≤1	16.12	15.62	—	0.1	0.1	0.02	0.003	—
KhN62M	base	0.47	23.2	13	0.11	0.08	0.03	0.03	0.01	0.05

Quenched melt samples taken after each experiment were analyzed to determine the content of the elements of interest using X-ray fluorescence spectroscopy (ADVANT'X 4200, ARL) and inductively coupled plasma mass spectrometry (Elan 9000, Perkin Elmer). The surface of the corroded samples was examined by metallographic analysis (Olympus GX-71F), scanning electronic microscopy (JEOL JSM 6490) and energy dispersive X-ray microanalysis (Oxford INCA®).

Results and Discussion

Corrosion Processes in 3LiCl – 2KCl Eutectic Melts

To study the corrosion activity of molten 3LiCl–2KCl eutectic mixture, the materials were tested for 100 h in the temperature range of 450–750 °C. Based on obtained results, the corrosion rates were calculated and the obtained values are given in Table II. The corrosion rates were determined by the gravimetric method, which is considered as one of the most accurate methods for assessing the corrosion rate in molten salts. The main advantages of this method are the simplicity of setting up the experiment and the maximum closeness of the tests to real operating conditions.

TABLE II. Corrosion rates in mm/year in molten 3LiCl-2KCl after exposure for 100 hours in 3LiCl–2KCl melt.

Temperature, ºC	VDM® Alloy C-4	Hastelloy® G-35®	KhN62M	Ta	Mo
450	<0.001	<0.001	<0.001	<0.001	<0.001
550	0.003	0.004	0.003	<0.001	<0.001
650	0.030	0.021	0.036	0.006	0.005
750	0.065	0.037	0.099	0.006	0.009

According to the results thus obtained, individual metals demonstrated high corrosion resistance over the entire temperature range. The damage of the surface of both metals was uniform and no localization of corrosion processes was observed (Fig. 1). Therefore, it can be concluded that molybdenum and tantalum exhibit high corrosion resistance in this media up to 750 ºC and can be recommended as a promising construction material.

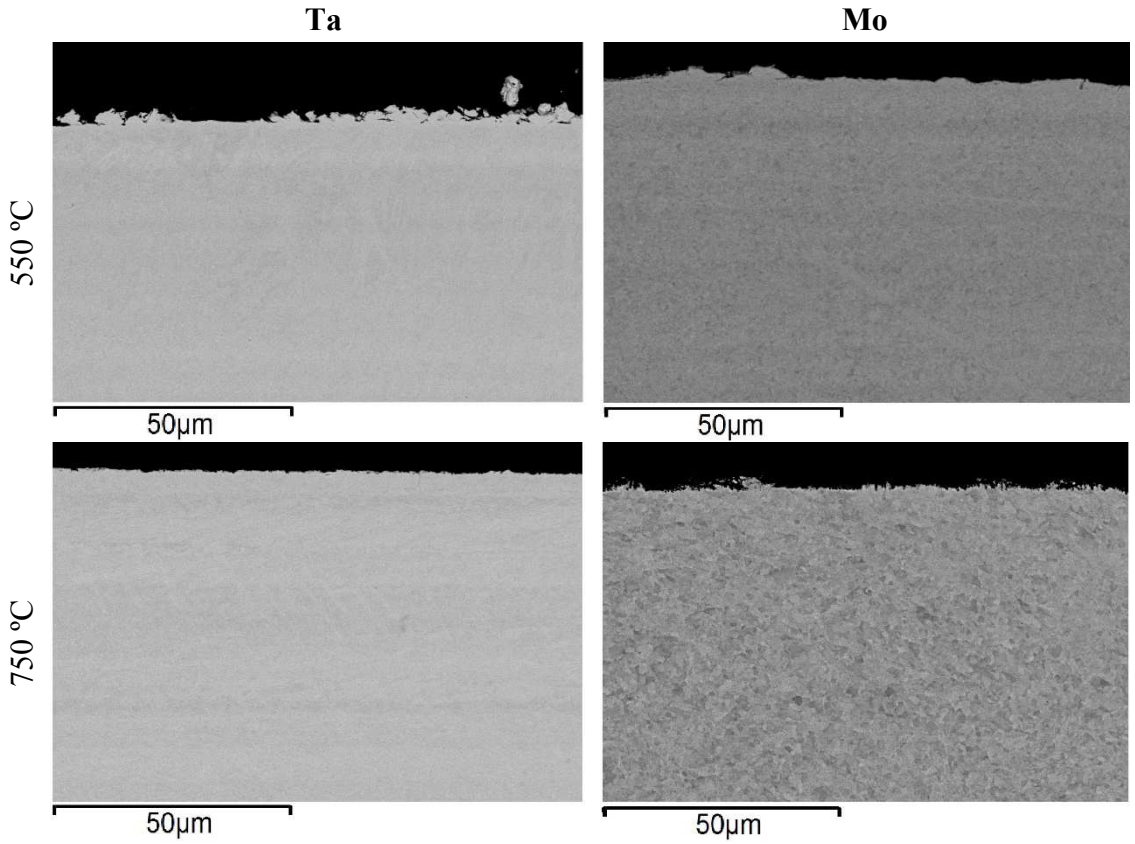

Figure 1. SEM images of Mo and Ta surface after 100 h contact with molten 3LiCl-2KCl at 550 ºC and 750 ºC.

Nickel-based alloys remained unchanged under low temperature conditions, at 450 °C and 550 °C respectively. The uniform corrosion of the materials surface was observed (Fig. 2), associated with the etching of chromium from the bulk of the material. These results allow us to conclude that these alloys can be used in 3LiCl–2KCl molten salt media as structural materials at temperatures that not exceed 550 °C. However, several technologies of SNF pyrochemical reprocessing scheme must be implemented at higher temperatures.

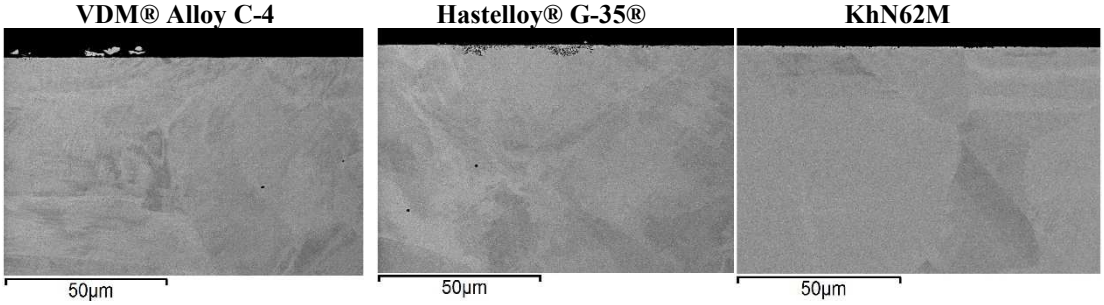

Figure 2. SEM images of alloys surface after 100 h contact with molten 3LiCl–2KCl at 550 ºC.

When temperature increased to 650 ºC and 750 ºC, the corrosion rates of all alloys increased rapidly (Table II). Our experience shows that the temperature of 650 ºC constitutes the limit for the studied nickel-based alloys (7). Above this temperature, the corrosion rate increases significantly, and intergranular corrosion is also activated due to

the rapid growth of secondary phases of intermetallides along the grain boundaries of the alloys. The penetration depths at 750 ºC (Fig. 3) were 20-30 microns for alloys VDM® Alloy C-4 and KhN62M, in case of Hastelloy® G-35® corrosion penetrated up to 70–90 microns. In case of Hastelloy® G-35®, the depth of damage was so high due to the high content of chromium in this alloy, which was selectively etched out of the alloy during the corrosion.

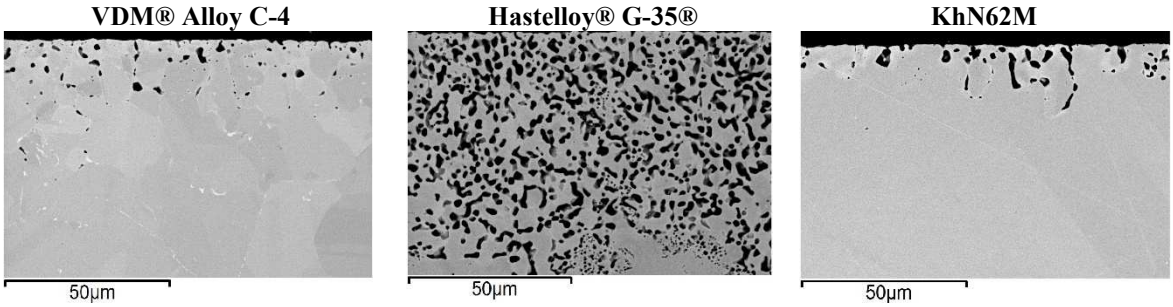

Figure 3. SEM images of alloys surface after 100 h contact with molten 3LiCl–2KCl at 750 ºC.

The processes of formation of excess phases were observed both in the surface layer and in the bulk of the samples, as shown by the example of Hastelloy® G-35® alloy (Fig. 4). Appearance of the secondary phases along the grain boundaries in the bulk of the nickel alloy samples was due to the thermal effect, which caused the decomposition of the metastable structure of the γ-solid solution based on nickel (7). Formation of these phases in the surface layer of the samples was also due to a change in the chemical composition of the surface layer of the alloy as a result of continuous corrosion. A change in the chemical composition and increase in the number of defects in the zone resulted in continuous corrosion. These processes created favorable conditions for the rapid formation of secondary phases.

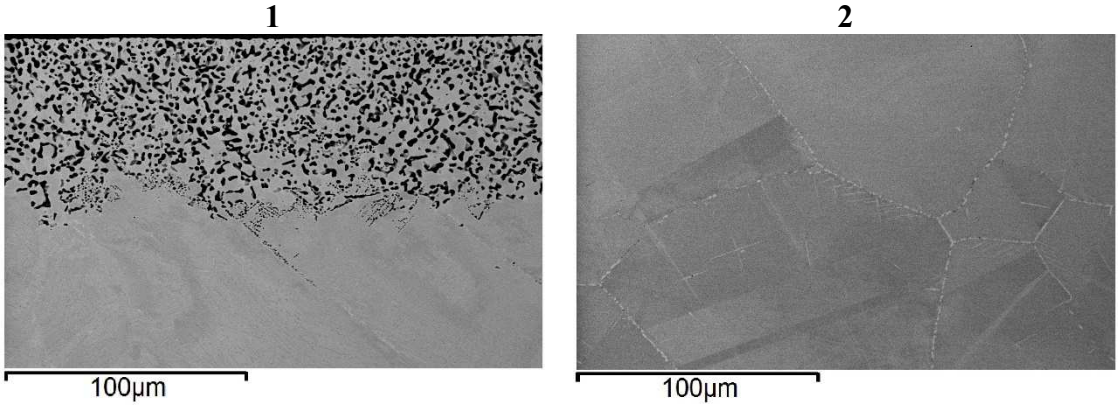

Figure 4. SEM images of surface (1) and in the bulk (2) of Hastelloy® G-35® after 100 hours of exposure in molten 3LiCl–2KCl at 750 ºC.

Secondary phases accelerate the corrosion process even more due to the fact that chromium easily passes there and then diffuses through them into the melt (Fig. 5).

Element	Composition %	
	wt.	at.
Al	0.14	0.30
Si	0.30	0.62
Cr	**42.34**	**48.04**
Fe	0.42	0.44
Ni	40.15	40.35
Mo	16.66	10.25

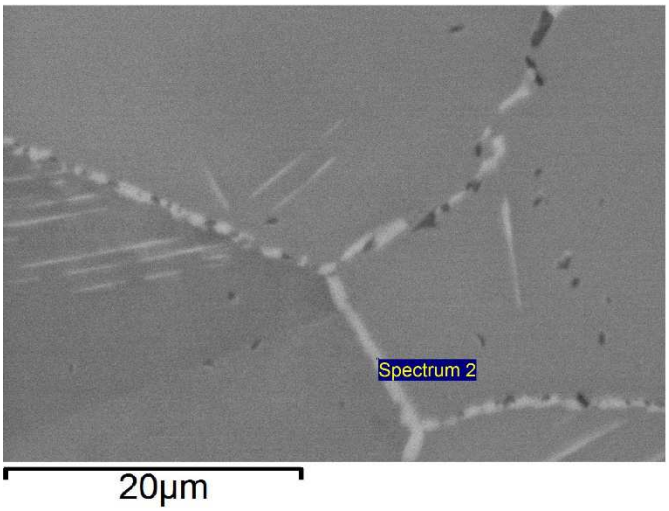

Figure 5. SEM image and chemical composition of grain boundary of Hastelloy® G-35® in molten 3LiCl-2KCl at 750 ºC after 100 hours of exposure.

Corrosion Processes in 3LiCl–2KCl–UCl_3 Melts

Corrosion tests of materials in uranium-containing melt were carried out at 550 °C and 750 °C. It was found that weight of nickel-based alloys at 550 °C increased. Therefore, analytical techniques were more convenient for estimation of the corrosion rates in 3LiCl–2KCl–UCl_3. The salt phase was analyzed using XRF analysis of quenched melts after the corrosion tests and the obtained concentrations of the corrosion products were used to calculate the corrosion rates. Table III contains the corrosion rates determined by both gravimetric and analytical methods.

TABLE III. Corrosion rates in mm/year in molten 3LiCl–2KCl–UCl_3 after exposure for 100 hours.

Temp. / °C	Calculation Method	VDM® Alloy C-4	Hastelloy® G-35®	KhN62M	Ta	Mo
550	gravimetric	growth*	growth*	growth*	<0.001	<0.001
	analytical	0.07	0.06	0.01	<0.001	<0.001
750	gravimetric	0.16	0.08	0.15	<0.001	<0.001
	analytical	0.12	0.06	0.16	<0.001	<0.001

* – specimens after exposure and washing showed weight gain

Refractory metals after exposure at 550 and 750 °C demonstrated a continuous uniform character of surface destruction (Fig. 6). The metal concentration in the quenched salt melts was below the detection limit. Taking into account the extremely low corrosion rate, it can be concluded that molybdenum and tantalum after 100 h of exposure in uranium-containing melts at temperatures up to 750 °C exhibit high corrosion resistance and can be suitable for further research as promising structural materials.

To determine the reasons for the mass increase of samples of nickel-based alloys at 550 °C and the increased corrosion rates at 750 °C, their surface was examined using SEM. The microstructures of their surface after exposure in 3LiCl–2KCl–UCl_3 at 550 and 750 °C are presented in Fig. 7.

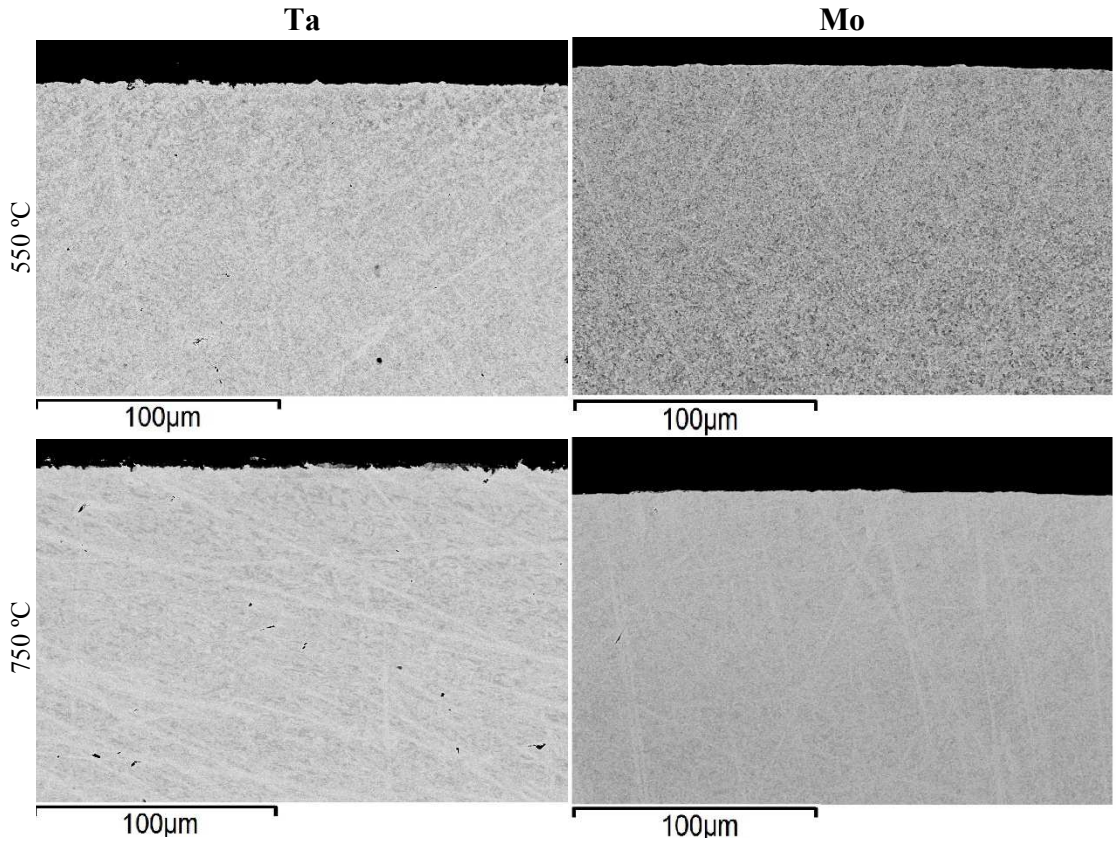

Figure 6. SEM images of Mo and Ta surface after 100 h contact with molten 3LiCl-2KCl-UCl_3 at 550 ºC and 750 ºC.

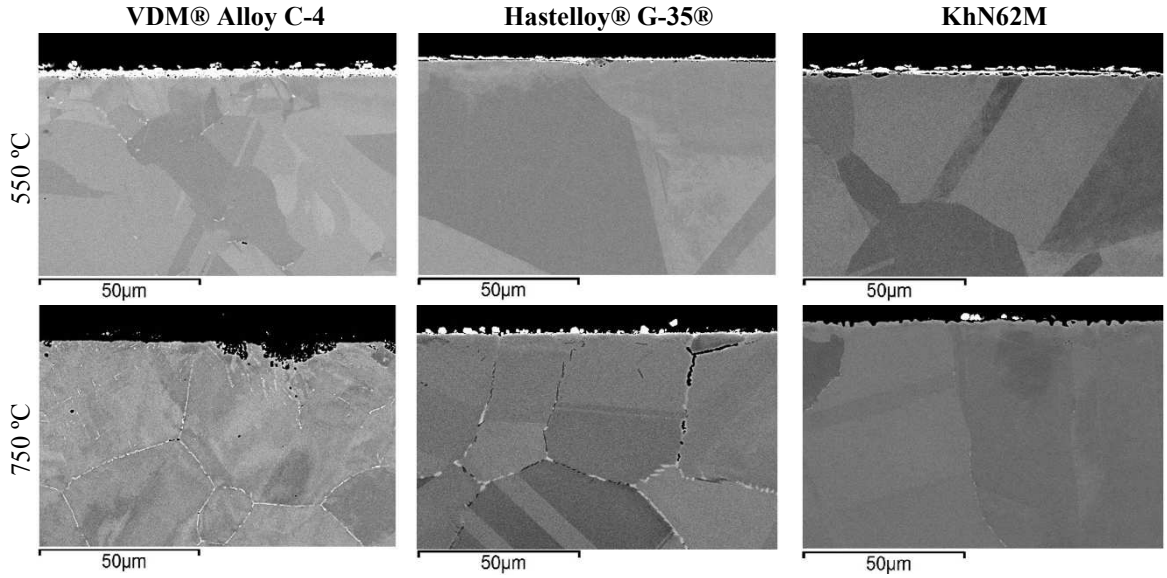

Figure 7. SEM images of alloys surface after 100 h contact with molten 3LiCl-2KCl-UCl_3 at 550 ºC and 750 ºC.

We observed thin layers of the new phase formed on the surface of the samples at temperatures higher both 550 and 750ºC. In the last case these coatings were poorly adhered. The X-ray spectral microanalysis of the coatings showed that they consist of mostly uranium and nickel (Fig. 8). According to the U–Ni binary phase diagram, these metals form intermetallic compounds. Therefore, we concluded that the oxidation process of the nickel alloy was accompanied by a process of fusion of nickel with uranium.

Formation of intermetallic compounds of uranium with nickel can shift the potential of U^{3+}/U^0 couple to more positive values and result in more intensive dissolution of the alloy components.

One can see that corrosion degradation at 750 °C was more pronounced for all the alloys. In this case localization of the corrosion processes along the grain boundaries was observed, that was caused by the intensive formation of chains of excess phases along the grain boundaries. The observed increased corrosion rates at 750 °C can also be explained by enhanced diffusion processes at higher temperatures that resulted in the lack of time for the dense coating formation.

VDM® Alloy C-4

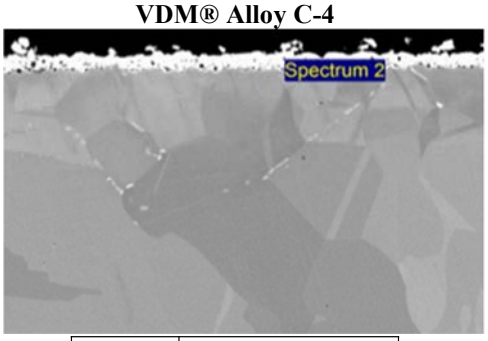

Element	Content, wt.%
Cr	8.4
Fe	0.5
Ni	45.0
Mo	6.9
U	39.2

KhN62M

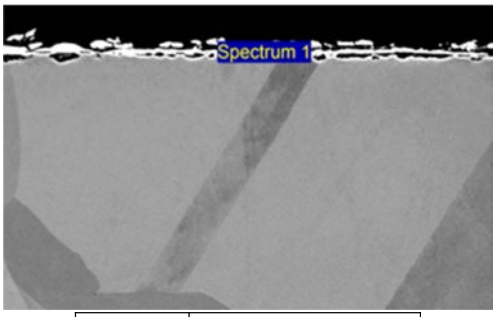

Element	Content, wt.%
Cr	1.8
Fe	0.5
Ni	52.9
Mo	1.3
U	43.5

Figure 8. The composition of VDM® Alloy C-4 (Spectrum 2) and KhN62M (Spectrum 1) surface layers after exposure for 100 hours in molten 3LiCl-2KCl-UCl_3 in 550 ºC.

Conclusions

The corrosion behavior of metallic tantalum, molybdenum and Ni-based alloys Hastelloy® G-35®, VDM® Alloy C-4, KhN62M was studied in 3LiCl-2KCl and 3LiCl-2KCl-UCl_3 (5 wt. % U) molten salts in various temperatures. The undesirable intergranular corrosion was noticed for the nickel-based alloys at 750 °C and this was induced by the formation of secondary phases at the grain boundaries. Metallic tantalum and molybdenum were subjected to only gradual etching even at 750 °C. Their corrosion rates did not exceed 0.01 mm/year and these materials can be recommended for the application in contact with molten chlorides at 750 °C.

Addition of uranium(III) chloride to the melt led to increasing corrosion rate for all the materials. The corrosion mechanism, however, remained almost the same with changing temperature. The presence of oxidant (U^{3+}) resulted in acceleration of corrosion etching. The rate of the exchange reaction between uranium chlorides and components of materials can be accelerated by the formation of U–Ni alloys.

Molybdenum therefore is the most prospective material for the high-temperature SNF reprocessing. However, it should be remembered that their mechanical properties, weldability, and high temperature resistance in air are noticeably worse compared to the

nickel-based alloys. Nickel-based alloys demonstrated satisfactory corrosion resistance at temperature below 650 °C both in 3LiCl–2KCl and 3LiCl–2KCl–UCl_3. Formation of metallic uranium-containing layers on the surface of nickel-based samples deserves a separate attention as an element of possible currentless protection coatings.

Acknowledgements

This research was financially supported by the JSC "Proryv" of the State Corporation "Rosatom".

References

1. *Status and Trends in Spent Fuel and Radioactive Waste Management*, IAEA Nuclear energy series No. NW-T-1.14, (2018).
2. M. F. Simpson, *Developments of Spent Nuclear Fuel Pyroprocessing Technology at Idaho National Laboratory*, Idaho National Lab., (2012).
3. M.V. Kormilitsyn, A.V. Bychkov, V.S. Ishunin, in *Proceedings of Global 2003*, New Orleans, November 16–20, p. 782, (2003).
4. S. Guo, J. Zhang, W. Wu and W. Zhou, *Prog. in M. S.* **97**, 448 (2018).
5. K. Vignarooban, X. Xu, K. Wang, E.E. Molina, P. Li, D. Gervasio and A. M. Kannan, *App. Energ*, **159**, 206 (2015).
6. A. V. Abramov, V. V. Karpov, A. Y. Zhilyakov, A. F. Gibadullina, I. B. Polovov, V. A. Volkovich, S. V. Belikov, A. V. Shak and O. I. Rebrin, *ECS Trans*. **64** (4), 217 (2014).
7. I. B. Polovov, A. V. Abramov, V. V. Karpov, A. F. Gibadullina, A. Yu. Zhilyakov, K. V. Dedov, S. V. Belikov, A. V. Shak, V. A. Volkovich, O. I. Rebrin, *ECS Trans.,* **77** (11), 753 (2017).
8. I. B. Polovov, A. V. Abramov, A. F. Gibadullina, R. R. Alimgulov, V. V. Karpov, A. Yu. Zhilyakov, V.A. Khotinov and S. V. Belikov, *J. Alloys Compd*., **810**, 151758 (2019).
9. I.B. Polovov, A.V. Abramov, K.V. Dedov, V.V. Karpov, A.Yu. Zhilyakov, A.F. Gibadullina, S.V. Belikov, V.A. Volkovich and O.I. Rebrin, *ECS Trans*, **77** (11), 847 (2017).
10. A. V. Abramov, V. V. Karpov, A. Yu. Zhilyakov, S. V. Belikov, V. A. Volkovich, I. B. Polovov and O. I. Rebrin, *AIP Conf. Proc.* **1886**, 020029 (2017).

ECS Transactions, 98 (10) 317-331 (2020)
10.1149/09810.0317ecst ©The Electrochemical Society

Cationic Catalysis during the Discharge of Carbonate Anions in Molten Salts

Inessa Novoselova[a], Serhii Kuleshov[a], Anatoliy Omelchuk[a], Veniamin Soloviev[b], Natalia Solovyova[c]

[a]V.I. Vernadskii Institute of General and Inorganic Chemistry, Kyiv, Ukraine
[b]Poltava National Technical Yuri Kondratyuk University, Poltava, Ukraine
[c]Ukrainian medical stomatological academy, Poltava, Ukraine

The paper presents a quantum-chemical model and experimental confirmation of cation catalysis mechanism during the cathodic discharge of carbonate anion in chloride melt. The model of cationized carbonate complex which describes the effect of the acid-base properties of the melt on the electronic, energetic, structural and electrochemical properties of the carbonate anion was proposed. Cation-anion interaction between CO_3^{2-} anion and the strongly polarized Li^+, Ca^{2+}, Mg^{2+} cations result either in the formation of cationized anions (metal complexes) or in anion dissociation. Dissociation of CO_3^{2-} anions can occur directly or through an intermediate stage of formation of "short-lived" metal complexes. The changes in the electrochemical behavior of CO_3^{2-} anion were studied by voltammetry by the sequential addition of cations with different ionic strength to the Na,K,Rb|Cl eutectic. The potentiostatic electrolyses carried out in three electrolytes Na,K,Rb|Cl–Na_2CO_3–LiCl($CaCl_2$,$MgCl_2$) at a same potential of -1.1 V against Ag/AgCl reference electrode gave a carbon powder.

Introduction

In the recent years, much attention has been focused on the synthesis of various carbon nanomaterials (CNMs). CNMs (fullerenes, carbon nanotubes and nanofibers, graphene, onions, carbon films of different structure etc) have great potential for application in various fields of modern science and technology, including anode materials for Li and Na ion batteries, supercapacitors, ceramic-based composites, adsorbents for removal of organic pollutants, coverings for implants in medicine and many others (1-4). Some applications of CNMs are shown at **Figure 1.**

In spite of a great variety of methods used to prepare CNMs (laser and arc evaporation of graphite, catalytic pyrolysis of hydrocarbons, disproportionation of CO on metal-catalysts etc.), none of the currently known methods allows one to obtain a monophasic and monodisperse product with given physicochemical properties in one stage.

One promising method for production of CNMs with various structure and morphology is high-temperature electrochemical synthesis (HTES) in molten salts. In this method, the electrochemical splitting of the carbon-containing precursor (carbonate anion or carbon dioxide) can take place as a result of their reduction on the cathode.

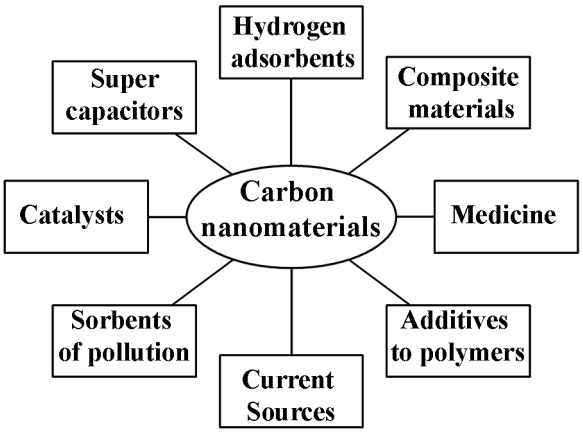

Figure 1. Fields of application of carbon nanomaterials.

The method allows one to control the structure and morphology of the carbon products being produced by using the different modes and conditions of electrolysis. The advantages of the method also are: simplicity of equipment, low energy consumption for electrolysis, cheap expendables, and the possibility to dope the carbon frame structure in one synthesis stage. If carbon dioxide is used as a carbon precursor, a vista opens for creating an environmentally friendly technology for electrochemical CO_2 utilization.

Carbon dioxide utilization (capture, storage and splitting), especially in the gas emissions of industrial enterprises, are becoming basic processes for the sustainable development of the humanity. Electrochemical reduction is one of possible ways of CO_2 conversion and can take place in gases, aqueous, non-aqueous (organic and ionic liquid based), solid-phase and salts melt conducting media in a wide temperature range (from room temperatures to 1000 °C). A peculiarity of the electroreduction of CO_2 dissolved in molten salts is the deposition of a solid carbon phase on the cathode in contrast to aqueous, organic (ionic liquids) and solid-phase electrolytes, in which hydrocarbons (methane (CH_4), ethylene (C_2H_4)); organic acids and alcohols (formic acid (HCOOH), oxalic acid ($H_2C_2O_4$), methanol (CH_3OH), ethanol (C_2H_5OH)); carbon monooxide (CO) can be obtained. In molten media, the direct and indirect electroreduction of CO_2 can be effected. In the former case, carbon dioxide dissolved in a molten salt is reduced, and which is introduced into the electrolyzer either by flow or under pressure. The production of excessive pressure is necessary to increase the solubility of the gas in the electrolyte. Indirect CO_2 reduction takes place in salt melts (carbonate, chloride-carbonate, chloride-oxide), when a carbon dioxide atmosphere is created over the melt. Depending on the electrolysis conditions and modes, the discharge of the carbonate anion at the cathode can result in the formation of a carbon monoxide or a solid carbon phase and in the release of oxide anions. The oxide anion in the melt can bind carbon dioxide from the gas phase to form a carbonate anion. In this way the carbonate anion consumed in the electrolyte is regenerated. The investigation of these processes is dealt with in a large number of original papers, reviews and books (5-8).

Although much research has been devoted to this subject, there is disagreement about the mechanism and fundamental reactions that occur during this process. In this work, the cathodic discharge of the carbonate anion in molten salts will be considered from the point of view of the concept of acid-base interactions (cation-anion interaction between the strongly polarizing Li^+, Ca^{2+}, Mg^{2+} cations and CO_3^{2-} anion).

Experimental

Cation-anion interaction was studied by the voltammetry method in a low-temperature Na,K,Rb|Cl eutectic and in an equimolar mixture NaCl–KCl. The process was studied mainly at temperatures of 550–580 °C, which are much lower than the thermal decomposition temperature of alkali metal carbonates. Several experiments were carried out at 700–800 °C. In this research, we gave up the use of platinum as working electrode because preliminary research showed that platinum to be not indifferent electrode to both cathodic and anodic processes. Glassy carbon (GC) was mainly used as the cathodic material.

The background electrolyte was prepared from ultrapure potassium, sodium, and rubidium chlorides. The ultrapure anhydrous lithium, calcium and magnesium chlorides were prepared by the procedure presented in (9). The purity of the background electrolyte and anhydrous chlorides was monitored by the residual currents on voltammograms. The experiments were carried out with carefully dehydrated reagents in a visualized electrochemical cell in an atmosphere of purified argon. To service the cell (loading the studied reagents, electrodes, etc.), we used a dry box filled with argon.

A quartz electrochemical cell was used (**Figure 2**), which allows making additions of anhydrous chlorides without its depressurization. A glassy carbon rod (d = 2 mm) and a platinum wire (d = 0.5 mm) were used as the cathode. The anode and melt container were glassy carbon and platinum crucibles. The reference electrode was a silver-chloride electrode. The reference electrode consisted of a silver wire placed in an alumina tube filled with Na,K,Rb|Cl melt containing 0.5 mol% AgCl.

The voltammetric studies were carried out using a Pi–50–1 pulsed potentiostat and LKD–4 X–Y recorders or a PO 5122 oscillograph. The electrolysis products were investigated with an electron probe microanalyzer (CAMEBAX SX–50 device), by X-ray fluorescence spectroscopy (XFS) (Expert 3L elemental composition analyzer), X-ray diffraction analysis (XRD) (DRON–3M diffractometer with CuKa radiation), scanning electron microscopy (SEM) (JSM–35).

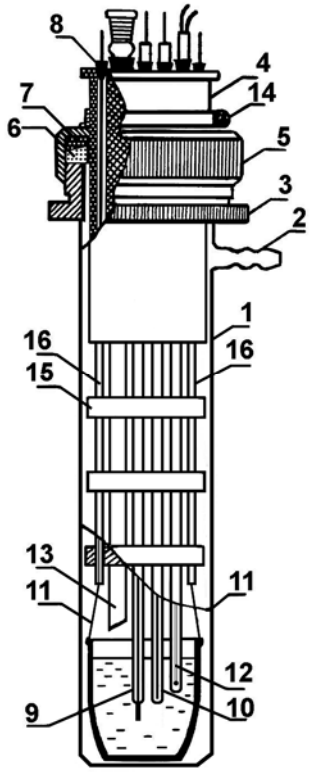

Figure 2. Schematic of an electrochemical cell for operation in an inert atmosphere: (1) quartz beaker, (2) evacuation tube, (3) threaded ring, (4) teflon bushing, (5) steel nut, (6) vacuum rubber ring, (7) teflon ring, (8) vacuum rubber stoppers, (9) indicator electrode, (10) Ag|AgCl reference electrode, (11) current leads to the anode, (12) thermocouple, (13) salt filling tube, (14) locking ring, (15) serpentine washers, (16) alundum tubes.

Results and Discussion

Acid-Base Equilibria in Molten Salts

In comparison with aqueous electrolytes, ionic melts give the researchers greater possibilities of controlling electrode processes. For these purposes, the following approaches can be used: (a) acid-base equilibria; (b) complex formation; (c) action of surfactants (10, 11). In molten electrolytes, some discharging elements (tungsten, silicon, carbon) are in the form of stable anionic complexes, which can be reduced at the cathode without electrolytic pre-dissociation. An important approach of controlling electrode processes is the change of the "basicity" or "acidity" of the ionic melt. The measures of the "basicity" or "acidity" of ionic melts are the concentrations of such ions as O^{2-} or Hal^{-} (Hal – Cl, F, Br, I).

The problem of the effect of acid-base equilibria on the kinetics of electrode processes in ionic melts was considered in (12, 13). By shifting acid-base equilibria by adding oxygen ion acceptors or donors to the electrolyte, one can conduct the electrolysis in the desired direction within definite limits. Ions and molecules, such as PO_3^{-}, CO_2, MoO_3, WO_3, can serve as oxygen ion acceptors. Oxygen ion donors are Na_2O_2 and other peroxides, as well as alkalis.

Shapoval and coworkers (9) have extended the concept of acid-base equilibria to melts containing WO_4^{2-}, MoO_4^{2-}, CrO_4^{2-}, CO_3^{2-}, SO_4^{2-}, PO_3^{-}, NO_3^{-} oxyanions and described the effect of the following acid-base equilibrium [1] on the electroreduction kinetics of the above anions:

$$[MO_{n/2+1}]^{2-} \rightleftarrows MO_{n/2} + O^{2-} \quad [1]$$

where M – W, Mo, Cr, C, S, P, N: n – valence of element M

The authors established a law, according to which in the presence of such equilibrium in the melt, the species with the most acidic properties, namely $MO_{n/2}$ species, are reduced in the first place. If reaction [1] and the process of discharge of the electrophilic species $MO_{n/2}$ according to [2] are reversible:

$$MO_{n/2} + n\bar{e} \rightleftarrows M + n/2\ O^{2-} \quad [2],$$

and acid-base equilibrium [1] is characterized by the constant:

$$K = [MO_{n/2}] * [O^{2-}] / [MO_{n/2+1}]^{2-} \quad [3],$$

then the Nernst equation for the potential of electrode process [2] will take the form:

$$E = E^o + RT / nF * \ln \{K [MO_{n/2+1}]^{2-} / [O^{2-}]^{n/2+1} * [M]\} \quad [4]$$

It is generally accepted that the activities of the solid phase [M] and the reducible particle $[MO_{n/2+1}]^{2-}$ in concentrated salt media are high and do not change over time. On this basis and in accordance with the stoichiometry of the reaction [1], the ratio of activities $[M]/[MO_{n/2+1}]^{2-}$ equation [4] can be conditionally equated to unity. In this case the electrode process potential will depend only on the activity of the oxide ion $[O^{2-}]$.

$$E = const - \{2,3(n/2 +1) * RT / nF\} * \lg[O]^{2-} \quad [5]$$

The acid-base equilibria of the types [1] is often called in literature Lux-Flood equilibria (14), and basicity of the melt is expressed by the pO value, which is equal to the negative logarithm of oxide ion activity. The pO value is the same ionic characteristic for oxygen-containing molten systems as pH for aqueous solutions.

The prelogarithmic factor of the equation of dependence of equilibrium potential for CO_3^{2-} on the basicity of the melt is:

$$E = E^o + 1,725RT / F * pO \quad [6]$$

Thus, the change in melt basicity must affect the values of carbonate ion discharge potential.

The carbon deposition potential is greatly affected by the form of the electrochemically active species (EAS). The kinetic peculiarities of the electroreduction of carbonate ion from molten chlorides showed that the process occurs by the CE

mechanism (15), i.e., with a preceding chemical reaction of acid-base type, which is conjugated with the electrode process:

$$CO_3^{2-} \rightleftarrows CO_2 + O^{2-} \quad [7]$$

and the subsequent discharge of a more electrophilic species, carbon dioxide:

$$CO_2 + 4\bar{e} \rightarrow C + 2O^{2-} \quad [8]$$

In this particular case, the action of acidic dopants consist firstly in a shift of equilibrium [8] to the right and an increase in CO_2 depolarizer concentration and secondly in an increase in the rate of the electrode process itself owing to the acidification of the near-electrode layer. This must first of all affect the discharge wave current, the discharge potential changing only slightly. The ten-fold increase of the concentration in the melt must shift the discharge potential at 1023 K by 0.051 V. The form of the EAS in this case will not change, which is associated with the higher stability of CO_2 molecules in halide melts.

Cationic Catalysis in the Formation of Electrochemically Active Species during the Discharge of CO_3^{2-} in Molten Salts

In salt melts, acid-base interactions manifest themselves explicitly; however, the mechanism of these interactions has a complex nature. References (16-19) proposed a model which describes the effect of the acid-base properties of the ionic medium on the electronic, energetic, structural and electrochemical properties of the anions of polyvalent elements in melts. According to this approach, the properties of the medium can be modeled by gradually increasing the number of cations in the first solvation shell of the complex anion, modeling the formation of a “cationized” anionic complex. The possible changes in the energy, electronic and structural state of the anion under investigation were considered using quantum-chemical calculations. The changes in the electrochemical behavior of the anion were studied by voltammetry by the sequential addition of cations of different ionic strength to the electrolyte.

The physicochemical properties of anionic melts containing the coordination anion $[CO_3]^{2-}$ are determined by the electronic structure of the anion and the mode of interaction with the cations of the molten medium. The consideration of the existence of only short ones-range order in the carbonate anion creates difficulties both in the interpretation of experimental data and in the theoretical description of the structure of melts.

The isolated anion $[CO_3]^{2-}$ and its metal complexes (up to five-coordinate ones) with lithium cations $\{nLi^{+}...CO_3^{2-}\}$ were chosen as model compounds for quantum-chemical estimations. An energetic evaluation of cation-anion interaction paths for a carbonate-containing melt from the results of a semi-empirical calculation (16, 17) showed the possibility of formation of a wide range of metal complexes of the CO_3^{2-} anion with lithium cations and the effect of the nature of the cation on increase in the ability to be reduced of cation-anion interaction products.

When analyzing the energy profiles of the potential surfaces of the interaction of the anion $[CO_3]^{2-}$ with Li^+ or Be^{2+}, the preferential interaction of cations along the bisectrix of any of the valence angles of the anion in the presence of local energy minima in the monodentate position of the cation relative to anions has been established (19). A calculation showed that under the conditions of bi-dentate anion-cation interaction, a migration of the electron density from the 2s, $2p_x$ and $2p_y$ orbitals of the O(1) and O(2) atoms under the influence of the cation takes place to form σ bonds. As a result, an effective positive σ^+ charge is transferred to the oxygen atoms (**Figure 3**, schemes 1 and 2). This, in turn, contributes to the manifestation of the electron-donor effect of the O(3) atom p_z orbitals to form π bonds.

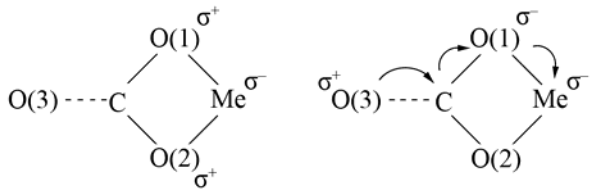

Scheme 1 Scheme 2

Figure 3. Schemes of the electron density redistribution in the carbonate anion.

Thus, the role of metal cations consists in anion polarization on the whole by the σ, π interaction mechanism with the predominance of one of the modes of interaction. In the carbonate anion and the corresponding metal complexes, the σ mechanism of electron density redistribution has a priority, which leads to a significant weakening of the C–O bond. When the number of the cations of the first solvate shell in the $[CO_3]^{2-}$ anion sequentially increases, the C–O bond sequentially weakens. On the whole, when the $[CO_3]^{2-}$ anion is cationized, the energy gap between the highest filled and the lowest vacant molecular orbitals decreases, indicating an increase in its reducing ability because of a decrease in activation barriers to reduction for the entire series of complexes (15).

Another important factor affecting the reduction process in melts is electric field. The effect of field on acid-base interaction and the elementary act of charge transfer has been assessed from the results of quantum-chemical calculations. A uniform electric field was modeled by a system of unlike charges, located symmetrically at a large distance from the molecule. Reference (18) shows that by enhancing the specificity of cation-anion interaction (mainly σ-type interaction in the carbonate anion), the field affects greatly the reducing ability of the products of this interaction, viz reduces the activation barrier.

As applied to the carbonate anion, the cation-anion interaction process can be represented by the following scheme 3 at **Figure 4**, where m – is the cation charge, n – is the order of reaction with respect to cation or coordination number (CN).

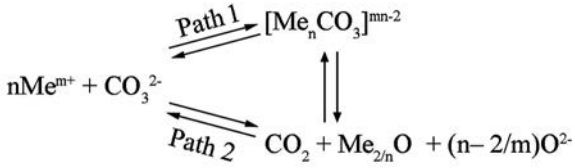

Scheme 3

Figure 4. Possible reaction paths of the cation-anionic interaction of the carbonate anion.

Thus, cation-anion interaction can result either in the formation of cationized anions (metal complexes) or in anion dissociation both under the direct influence of cations and through the intermediate stage of formation of "short-lived" metal complexes.

When estimating the contributions to the change in C–O bond energies in the carbonate anion under the influence of the electrode surface and electricity field, it has been found that last influence predominates, i.e., within the framework of the proposed model; the electrode surface does not affect in principle the mechanism of EAS formation. The mechanism is mainly determined by the cationic composition of the melt.

When comparing the energy characteristics and charges on atoms and the populations of atomic orbitals in an anion that is near the electrode surface under the action of cations and an external electric field ($E = 2 \times 10^{10}$ Vm^{-1}), it has been found that a rupture of C–O bonds takes place to form CO_2. In the opinion of the authors of (18), under the influence of the electrode surface, the activation barriers to the two- and four-electron reduction of the carbonate anion decrease relative to the analogous values for an isolated anion. The additional influence of the electric field enhances the effect (by a factor of about 2) and facilitates the direct discharge of the CO_2 molecule.

The conclusions drawn from the calculations made have been confirmed by the results of a voltammetric study of the cathodic discharge of a carbonate anion in chloride melts on adding cations of different ionic strength.

Peculiarities of the Discharge of CO_3^{2-} Anion in Chloride Electrolytes

The electroreduction of the CO_3^{2-} anion in a NaCl–KCl melt as the base electrolyte, which was considered in (15), was performed at a temperature of 700 °C, at which the thermal decomposition of carbonates in the presence of strongly polarizing Li^+, Ca^{2+} cations is possible. The authors assumed that the electrochemically active species is carbon dioxide, which is formed as a result of acid-base interactions in the melt. The further development of the concepts of the cation-anion interaction mechanism in melts, which is based on quantum-chemical calculations, showed that the interaction reaction between CO_3^{2-} and strongly polarizing cations can proceed in two ways: formation of $[Me_nCO_3]^{mn-2}$ metal complex and destruction of the CO_3^{2-} anion (17-19).

Therefore, an important task was to confirm experimentally the mechanism of cation-anion interaction between the CO_3^{2-} anion and the strongly polarizing Li^+, Ca^{2+}, Mg^{2+} cations by the voltammetry method and to elucidate the mechanism of formation of electroactive species and process kinetics.

Figure 5 shows voltammograms of a Na,K,Rb|Cl chloride melt, containing sodium carbonate, under sequential addition of lithium chloride. In this melt, the carbonate ion exhibits no electrochemical activity. Increasing the temperature up to 700 °C does not lead to the appearance of a CO_3^{2-} electroreduction wave without additions of lithium chloride. The addition of a 470-fold excess of LiCl relative to the concentration of CO_3^{2-} also does not manifest itself in voltammograms (**Figure 5**, curve 2). Only when the lithium ion concentration is further increased, a small CO_3^{2-} electroreduction wave, extended along the potential axis, observed in the potential range of -0.7 to -0.9 V (**Figure 5**, curves 3, 4). The replacement of the glassy carbon cathode by a platinum one results in a more pronounced manifestation of the CO_3^{2-} reduction wave (**Figure 6**).

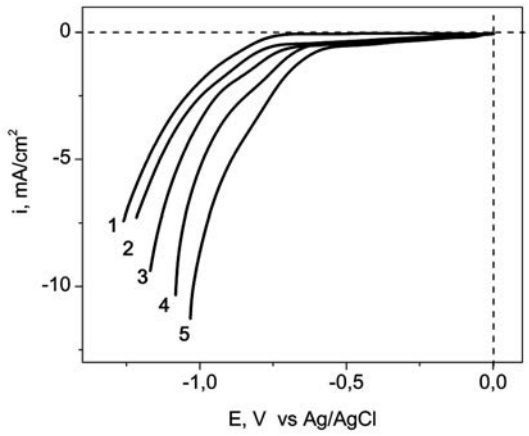

Figure 5. Voltammograms of the system K,Na,Rb|Cl–Na_2CO_3–LiCl: base electrolyte K,Na,Rb|Cl (1); (2÷5) the concentration of Na_2CO_3 is 2.5 $\times 10^{-5}$ mol·cm^{-3}; concentration of LiCl ($\times 10^{-3}$ mol·cm^{-3}): (2) 11.8; (3) 15.6; (4,5) 19.1. Polarization rate (Vs^{-1}): (1 ÷ 4) 1; (5) 2; cathode and anode – GC; t = 580 °C.

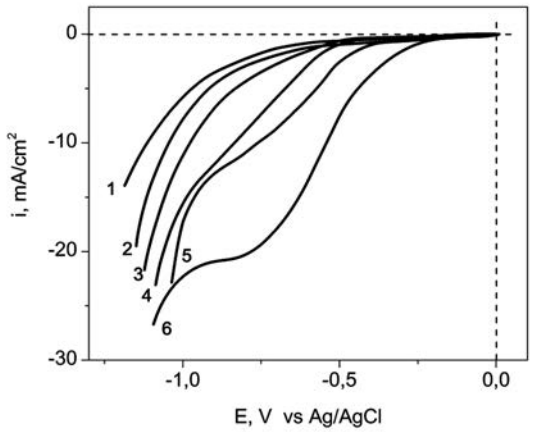

Figure 6. Voltammograms of the system K,Na,Rb|Cl–Na_2CO_3–LiCl: base electrolyte K,Na,Rb|Cl (1); (2÷6) the concentration of Na_2CO_3 is 2.5 $\times 10^{-5}$ mol·cm^{-3}; concentration of LiCl ($\times 10^{-3}$ mol·cm^{-3}): (2) 0; (3) 12.0; (4) 25.6; (5) 31.2; (6) 92.3. Polarization rate 1 V·s^{-1}; cathode – Pt, anode – GC; t = 580 °C.

When using platinum electrodes, the electroreduction wave appears at a lower LiCl concentration and is in the more positive potential range. Hence it can be concluded that the platinum electrode is not indifferent to carbonate-containing melts. When CO_3^{2-} is reduced at platinum electrodes, different catalytic and depolarization effects are possible.

It was discovered in a number of works (20-24) that the cathodic reduction waves of the carbonate anion and carbon dioxide in chloride-carbonate and pure carbonate melts are better observed not on inert materials (glassy carbon), but on active (non-indifferent) cathode materials (oxidized titanium, platinum, tungsten, nickel, etc.). In our view, this is associated with the electrocatalytic properties of the latter. It can be assumed that the catalytic mechanism of the above metals is due to their interaction with carbon deposited as a result of discharge and the formation of a carbide phase:

$$CO_3^{2-} + 4\bar{e} + xMe \rightarrow Me_xC + 3O^{2-} \quad [9]$$

$$CO_2 + 4\bar{e} + xMe \rightarrow Me_xC + 2O^{2-} \quad [9a]$$

The passivation of the platinum surface does not occur, apparently due to the high values of the electronic conductivity of the formed carbide phase. Subsequently, depending on the stability of the carbide phase, it can persist and be found in the cathodic product or decompose partly or completely according to the equation:

$$Me_xC \rightarrow xMe + C \quad [10]$$

Then process [9] can be represented, in view of reaction [10], as:

$$CO_3^{2-} + 4\bar{e} + xMe \rightarrow xMe + C + 3O^{2-} \quad [11]$$

Thus, these metals can act as catalysts for the discharge of carbonate anions. Such a mechanism explains the detection of metallic platinum (cathode material) in the cathodic carbon product, which was recorded in Refs (23, 25, 26).

The calcium cation exerts a stronger effect on the CO_3^{2-} electroreduction process compared with the lithium cation. A noticeable CO_3^{2-} discharge wave (**Figure 7**) is observed at as small as 200-fold excess of Ca^{2+} ions. The CO_3^{2-} reduction waves in the presence of calcium ions are also extended along the potential axis. There is no explicit dependence of the wave height on the cation concentration.

The effect of the Mg^{2+} cation on the reduction of the carbonate anion is most clearly observed (**Figure 8**). A well-defined wave manifests itself at as small as four-fold excess of Mg^{2+} ions relative to CO_3^{2-} (**Figure 8a**, curve 4). Further increasing the Mg^{2+} concentration leads to an increase in wave height, and at the 100-fold excess of Mg^{2+}, it reaches the maximum value (**Figure 8a**, curves 6-7). Independent of the concentration of Mg^{2+} cations in the melt, the wave is in the same potential range. The evacuation of the system when reaching the wave height maximum leads to a decrease in wave height (**Figure 8b**, curves 1, 2). The further addition of Mg^{2+} (after evacuation) leads again to an increase in wave height (**Figure 8b**, curves 2, 3).

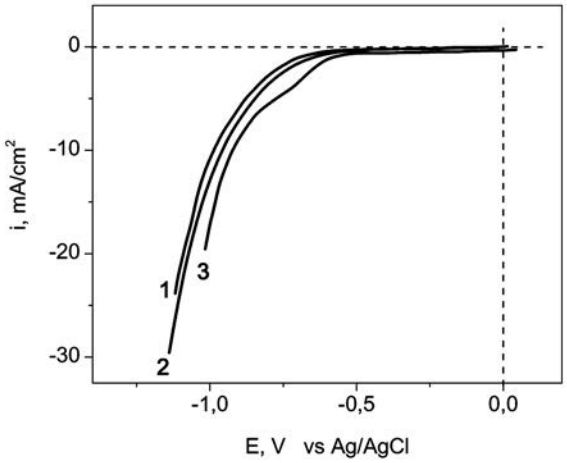

Figure 7. Voltammograms of the melts: (1) K,Na,Rb|Cl; (2) K,Na,Rb|Cl – 2.5 $\times 10^{-5}$ mol·cm^{-3} Na_2CO_3 – 5.54 $\times 10^{-3}$ mol·cm^{-3} $CaCl_2$; (3) K,Na,Rb|Cl – 2.5 $\times 10^{-5}$ mol·cm^{-3} Na_2CO_3 – 13.7 $\times 10^{-3}$ mol·cm^{-3} $CaCl_2$. Polarization rate 1 V·s^{-1}; cathode and anode – GC; t = 580 °C.

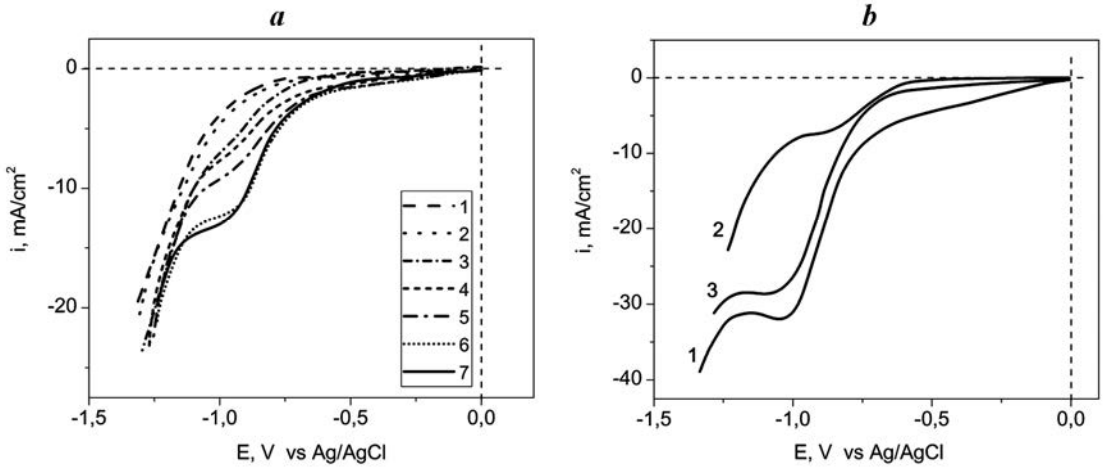

Figure 8. Voltammograms of the melt K,Na,Rb|Cl – 2.5 $\times 10^{-5}$ mol·cm^{-3} Na_2CO_3, cathode and anode – GC; V = 1 V·s^{-1}; t = 580 °C: (a) under sequent addition of $MgCl_2$ ($\times 10^{-5}$ mol·cm^{-3}): (1) 0.78; (2) 1.70; (3) 5.50; (4) 11.20; (5) 98.00; (6) 138.00; (7) 183.00; (b) under sequential addition of $MgCl_2$ ($\times 10^{-5}$ mol·cm^{-3}): (1) 308.00; (2) 308.00, after evacuation; (3) 531.00.

Thus, cation-anion interaction between CO_3^{2-} and strongly polarizing cations can be represented by the scheme 3 (**Figure 4**).

The reaction path in which equilibrium (**Figure 4**) will shift is determined by the concentration and polarizing power of Me^{m+} cations. In any case, cation-anion interaction occurs via the formation of cationized species, $[Me_nCO_3]^{mn-2}$ metal complexes, i.e., in the presence of Li^+ and Ca^{2+} cations, the main form of existence of CO_3^{2-} in the melt is metal

complexes. However, we failed to electrochemically detect the existence of metal complexes. This may be due to the fact that the reduction potential of metal complexes is close to the cathodic decomposition potential of the base electrolyte.

The action of the more strongly polarizing Mg^{2+} cation leads to a significant polarization of the carbonate ion and to its destruction to form CO_2. The presence of well reproducible waves of the electroreduction of CO_3^{2-} in the presence of Mg^{2+} makes it possible to estimate some parameters of the electrode process. The nature of the charge transfer step was determined according to generally accepted criteria, viz:

- from the peak half-width value ($\Delta E = E_{pk}-E_{pk/2}$) (Matsuda-Ayabe criterion (27): $\Delta E = 1.857\ RT/\alpha n_\alpha F$;

- from the dependence of the peak potential on the polarization rate (Delahay criterion (28):

$$E_{p/2} = - C\ RT/\alpha n_\alpha F - \ln(D^{1/2})RT/\alpha n_\alpha F + \ln(k^0_{fh})RT/\alpha n_\alpha F - \ln(\alpha n_\alpha v^{1/2})RT/\alpha n_\alpha F);$$

The trend of the $i_p/v^{1/2}$ -$v^{1/2}$ plot (**Figure 9**) shows that the electrode process has a diffusion nature, i.e., is controlled by the rate of carbon dioxide delivery to the electrode surface. The values of n = (0.8 – 1.0), obtained by analyzing the half-widths of peaks and the $\varphi_{p/2}$- *lg v* plot, indicate the cathodic discharge to be irreversible.

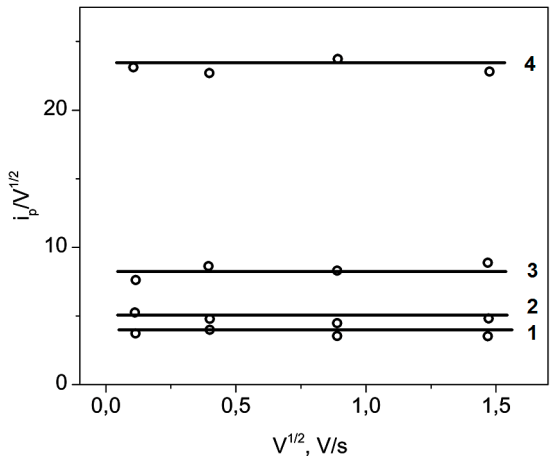

Figure 9. Dependence of $i_p \cdot v^{-1/2}$ on $v^{1/2}$ for the system K,Na,Rb|Cl–Na_2CO_3–$MgCl_2$; concentration of Na_2CO_3 is 2.5 ×10^{-5} mol·cm^{-3}; concentration of $MgCl_2$, ×10^{-5} mol·cm^{-3}: (1) 11.2; (2) 98.0; (3) 183.0; (4) 531.0. t = 580 °C.

The electrolyses carried out in all of the three electrolytes under the potentiostatic modes at a same potential of -1.1 V against Ag/AgCl reference electrode at the concentrations of lithium, calcium and magnesium chlorides, corresponding to the clear observation of cathodic waves, gave a black powder as the cathodic product. According to the data of a chemical and an X-ray diffraction analysis, it was amorphous carbon (**Figure 10a**). Morphology of electrolytical carbon is presented in **Figure 10b**. Carbon particles are crystallites composed of degraded graphite sheets. The general appearance resembles to "crumpled paper".

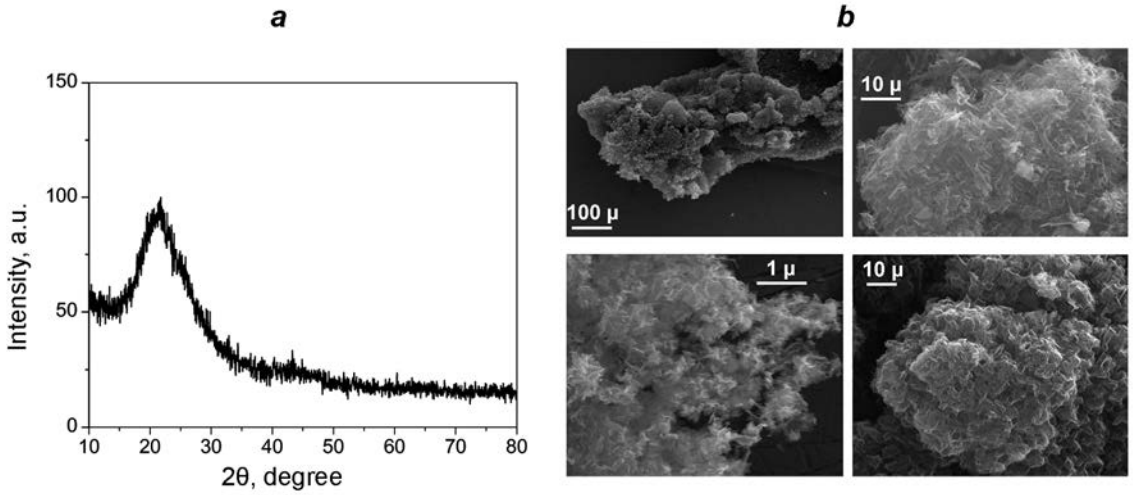

Figure 10. XRD pattern (a) and SEM images (b) of carbon powder, produced in the Na,K,Rb|Cl–Na_2CO_3–LiCl melt at 600 °C.

Conclusions

Based on the theoretical and experimental results, the following conclusions can be down:

- Based on quantum-chemical calculations, a model of cation catalysis mechanism during the cathodic discharge of carbonate anion in chloride melt is proposed. This model of cationized carbonate complex describes the effect of the acid-base properties of the melt on the electronic, energetic, structural and electrochemical properties of the carbonate anion.

- In the Na,K,Rb|Cl melt containing weakly polarizable Na^+, K^+, Rb^+ cations, the CO_3^{2-} anion shows no electrochemical activity within the "potential window" of the background electrolyte and in the temperature range of 570–700 °C. The addition of strongly polarizable cations (cations with high specific charge) results in the activation of the carbonate ion, which is caused by a large excess of Li^+ cations (500-fold excess) and Ca^{2+} cations (300-fold excess). In the case of Mg^{2+} cations, the carbonate ion shows electroactivity at much lower concentrations (4-fold excess). The more strong effect of magnesium ions on the discharge of the carbonate anion can be explained by comparing the polarizing (electrostatic) force of the cations, which present in the studied melts. In Ref. (29), the calculated values of the electrostatic force of cations (Z/r^2_k , where Z is the charge number of the cation and r_k is the cationic radius) for 126 metals are given. These values for all cations of the investigated electrolytes (taken from [29]) are presented in Table 1.

The table shows that the cations of the background electrolyte (Na+, K+, Rb+) have low values of the polarizing force (less than unity), the polarizing force of magnesium cation has the highest value (2.704) among the introduced additives.

TABLE I. Electrostatic Forces of Cations in the Studied Melts.

Cations	Na^+	K^+	Rb^+	Li^+	Ca^{2+}	Mg^{2+}
Z/r^2_k	0.743	0.433	0.363	1.235	1.539	2.704

- Independent of the polarizing power of the cation (melt acidity), the CO_3^{2-} reduction process in molten chlorides occurs in the same potential range of -0.7 to -0.9 V versus a silver reference electrode. It can be concluded that the same species, viz CO_2, is involved in the electrode process in melts of different cationic composition. The experimental fact (22) of the direct reduction of CO_2 in KCl–NaCl at the same potentials can serve as a confirmation of this conclusion.

- The CO_3^{2-} electroreduction process under the action of strongly polarizable cations occurs at temperatures much lower than the thermal decomposition temperature of the corresponding carbonate. This suggests that the formation of CO_2 is not the result of thermal decomposition, but is a consequence of the cations action.

References

1. Yu. Gogotsi, V. Presser, *Carbon Nanomaterials*. *2nd ed.* 529 p, CRC Press Taylor & Francis Group, (2017).
2. G. Hong, S. Diao, A. Antaris and H. Dai, *Chem. Rev.,* **115**(19), 10816 (2015).
3. X. Lin, K. Adair and X. Sun, in *Carbon Nanomaterials for Electrochemical Energy Technologies: Fundamentals and Applications*, p 111–130, S. Sun, X. Sun, Z. Chen, Y. Liu, D.P. Wilkinson and J. Zhang, Editors, CRC Press Taylor & Francis Group; (2018).
4. R. Alshehri, A.M. Ilyas, A. Hasan, A. Arnaout, F. Ahmed and A. Memic, *J. Med. Chem.,* **59(**18), 8149 (2016).
5. I.A. Novoselova, N.F. Oliinyk, S.V. Volkov, A.A. Konchits, I.B. Yanchuk, V.S. Yefanov, S.P. Kolesnik and M.V. Karpets. *Physica E,* **40**(7), 2231 (2008).
6. J. Qiao, Y. Liu, J. Zhang, Editors, *Electrochemical Reduction of Carbon Dioxide: Fundamentals and Technologies*, 394 p, CRC press. Taylor and Francis Group, (2016).
7. R. Jiang, M. Gao, X. Mao and D. Wang, *Curr. Opin. Electrochem.***, 17**, 38 (2019).
8. R. Küngas, *J. Electrochem. Soc.* **167**(4), 044508 (2020).
9. G. Brauer, *Handbook of preparative inorganic chemistry. 3rd edn.* F. Enke, Stuttgart. Russian translation: Moscow: Mir (1985) (in Russian).
10. Yu.K Delimarskii, *Electrochim. Acta* **30**, 1007 (1985).
11. Yu.K. Delimarskii and V.I. Shapoval, *Theor. Exp. Chem.,* **8**, 378 (1972).
12. Yu.K. Delimarskii and V.I. Shapoval, *Theor. Exp. Chem*., **9**, 748 (1973).
13. V.I. Shapoval, Yu.K. Delimarskii and V.F. Grishchenko, in *Ionic Melts*, *Issue 1*, p 222–240, Naukova Dumka, Kiev (1974) (in Russian).
14. H. Flood and T. Forland, *Discuss. Faraday Soc.,* **1**, 302 (1947).
15. Yu.K. Delimarskii, V.I.Shapoval and V.A. Vasilenko, *Russ. J. Electrochem.,* **7**, 1301 (1971) (in Russian).

16. V.I. Shapoval, E.D. Lavrinenko-Ometsinskaya, and V.V. Soloviev, *Ukr. Khim. Zh.*, **49**, 704 (1983) (in Russian).
17. V.I. Shapoval, V.V. Soloviev, E.D. Lavrinenko-Ometsinskaya and Kh.B. Kushkhov, *Ukr. Khim. Zh.*, **50,** 917 (1984) (in Russian).
18. V.I. Shapoval, V.V. Soloviev, E.D. Lavrinenko-Ometsinskaya and Kh.B. Kushkhov, *Ukr. Khim. Zh.*, **51,** 951 (1985) (in Russian).
19. V.V. Soloviev, *Interaction of Anions NO_3^- and CO_3^{2-} with cations Li^+ and Be^{2+} on the background of ionic melts*. PhD diss., V. I. Vernadskii Institute of General and Inorganic Chemistry, Kiev (1985) (in Russian).
20. Kh.B. Kushkhov, I.A. Novoselova, V.I. Shapoval and A.A. Tishenko, *Russ. J. Electrochem.*, **28**(5), 779 (1992) (in Russian).
21. I. Novoselova, N. Oliynyk and S. Volkov, p 459–465, in Hydrogen Materials Science and Chemistry of Carbon Nanomaterials. NATO Security through Science Series A: Chemistry and Biology, T.N. Veziroglu et al. Editors, Springer, Dordrecht (2007).
22. I.A. Novoselova, N.F. Oliinyk, A.B.Voronina and S.V. Volkov, *Z. Naturforsch., A: Phys. Sci.,* **63a**, 467 (2008).
23. A.B. Voronina, I.A. Novoselova, V.F. Kozin and A.A. Omelchuk. *Ukr. Khim. Zh.,* **74**, 37 (2008) (in Russian).
24. Q. Song, Q. Xu and Y. Wang, *Thin Solid Films*, **520** 6856 (2012).
25. H.P. Boehm, *Carbon,* **16,** 77 (1978).
26. I.A. Novoselova, S.V. Kuleshov, S.V. Volkov and V.N. Bykov, *Electrochim. Acta,* **211**, 343 (2016).
27. H. Matsuda and Y. Ayabe, *Z. Elektrochem.,* **59**, 494 (1955).
28. P. Delahay, *J. Americ. Chem. Soc.*, **75**, 1190 (1953).
29. Y. Zhang, *J. Inorg. Chem*., **21,** 3889 (1982).

ECS Transactions, 98 (10) 333-340 (2020)
10.1149/09810.0333ecst ©The Electrochemical Society

Al electrodeposition in molten $CaCl_2$ with various calcium aluminates

Yuta Iwai[a], Taiki Morishige[b], Toshihide Takenaka[b]

[a] Graduate School of Science and Engineering, Kansai University,
Suita, Osaka 564-8680, Japan
[b] Department of Chemistry and Material Engineering, Kansai University,
Suita, Osaka 564-8680, Japan

In this study, direct production of liquid Al metal was attempted in molten $CaCl_2$ with various calcium aluminates, based on our previous studies on Ti and Si electrolysis. Al and Al-Mo alloys were detected on the electrode surface after electrolysis at -1.8V (Mo vs. dissolution) at 1573K, and the molar ratio of CaO to Al_2O_3 did not affect Al deposited strongly. By using the electrode with a BN receiver, the electrodeposited Al was kept around the cathode and Al was obtained from the cathode surface. It was shown that calcium aluminate was dissolved in molten $CaCl_2$ above 1573 K and liquid Al metal could be obtained electrochemically with little dependence on the molar ratio of CaO to Al_2O_3.

Introduction

An innovative production process of Al metal is desired to reduce CO_2 and perfluorocarbon gases generation. Attention has been paid to the use of molten chloride bath to realize Al production with a lower environmental load and lower cost than in molten fluoride.[1] In our laboratory, direct electrowinning of liquid Ti and Si in molten $CaCl_2$ has been studied.[2-6] These studies indicated that calcium titanate and calcium silicate could be dissolved in molten $CaCl_2$, and that Ti and Si could be obtained electrochemically. It was also shown that the molar ratio of CaO to TiO_2 had a strong effect on Ti electrodeposition while the molar ratio of CaO to SiO_2 did not influence Si electrodeposition apparently.

In this study, direct production of liquid Al metal was attempted in molten $CaCl_2$ with various calcium aluminates above the melting point of Al. The solubility of calcium alminate in molten $CaCl_2$ and the influence of the molar ratio of CaO to Al_2O_3 on Al depositied were also discussed.

Experimental

Preparation of calcium aluminate

A mixture of CaO and Al_2O_3 was prepared as follows; CaO (Kishida Chem., >98%) and Al_2O_3 (Kishida Chem., >99.5%) was mixed as a molar ratio of CaO to Al_2O_3: 1.0, 12/7 or 3.0. The mixture was compacted and sintered at 1573K, and then ground to powder. In this paper, the molar ratio of CaO to Al_2O_3 is represented as $R_{CaO/Al2O3}$, and the bath containing calcium alminate is shown as $R_{CaO/Al2O3}$, for example, the bath of $R_{CaO/Al2O3} = 1.0$.

Electrochemical measurement

The apparatus for electrochemical measurement and electrolysis is shown in Fig.1. Calcium chloride (Kishida Chem., >95%) containing the CaO-Al_2O_3 powder was put in a Mo crucible, and vacuum dried at 373K for a day. The mixture with the crucible was set in an air-tight furnace and melted under a pure Ar atmosphere. In this study, electrochemical measurement was conducted at 1573K, and the concentration of calcium aluminate in molten $CaCl_2$ was represented by the added amount of Al_2O_3.

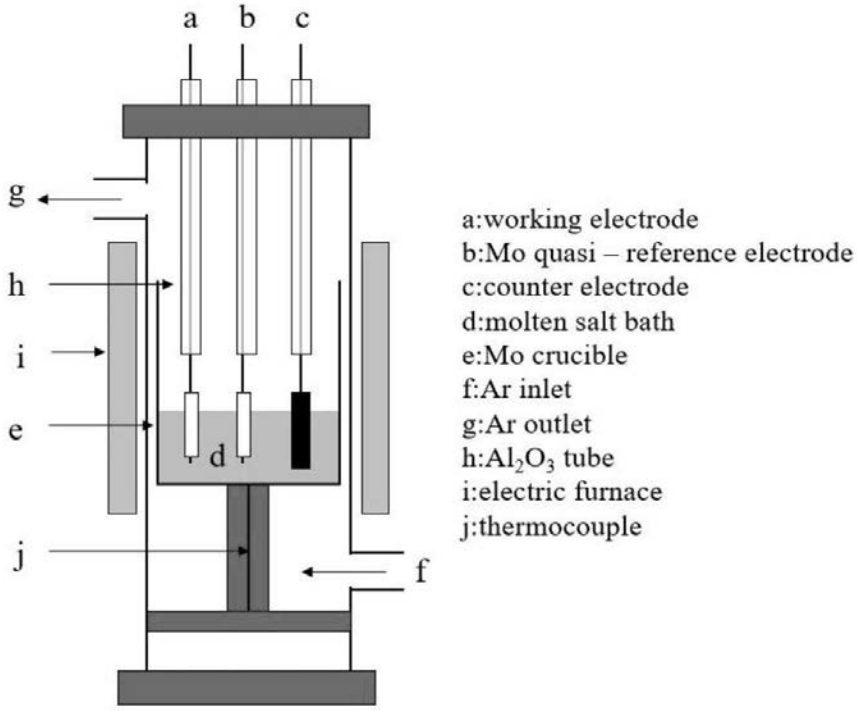

Fig.1 Apparatus for electrochemical measurement and electrolysis.

A Mo wire (Nilaco, ϕ1.0mm) covered with pure Al_2O_3 sheath was used as a working electrode. A graphite rod (Nippon Techno-Carbon, MF-307, ϕ5.0mm) was used as a counter electrode. Another Mo wire was used as a quasi-electrode, and its potential was calibrated with the Mo dissolution potential. The electrochemical behavior of Al was investigated by cyclic voltammetry. Based on the results by cyclic voltammetry, potentio-static electrolysis (Hokuto Denko Co., Ltd., HZ-5000) was carried out. The electrodeposit was washed with distilled water, and then analyzed by XRD (Rigaku, RINT-2550V) and SEM (JEOL, JCM-6000) -EDX (JEOL, EX-5441).

Results and Discussion

Analysis of sintered calcium aluminate

The XRD pattern of the powder of $R_{CaO/Al2O3}$ = 1.0 is shown in Fig.2. The powder of $R_{CaO/Al2O3}$ = 1.0 was mainly composed of $CaAl_2O_4$. The powders of $R_{CaO/Al2O3}$ = 12/7 and of $R_{CaO/Al2O3}$ = 3.0 were also mainly consisted of $Ca_{12}Al_{14}O_{33}$ and $Ca_3Al_2O_6$, respectively.

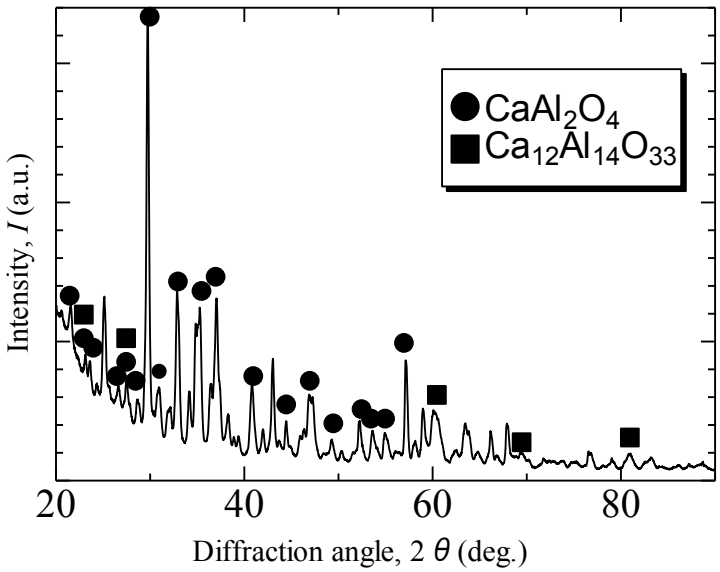

Fig.2 XRD pattern of prepared calcium aluminate of $R_{CaO/Al2O3}$ = 1.0.

Change in cyclic voltammogram with various calcium aluminates

Typical cyclic voltammograms in the bath of various calcium aluminate are shown in Fig. 3. The current in the bath containing calcium aluminate except for $R_{CaO/Al2O3}$ = 1.0 was larger overall than in the melt without calcium aluminate, but no sharp current peak was seen. The overall current also became lager with the increase in potential scan rate, but a clear relationship between the current and scan rate was hardly seen. These results suggest that electrochemical reduction of Al occurred under the influence of strong convection in the bath, the shape of cyclic voltammograms slightly changed with $R_{CaO/Al2O3}$, but the influence of $R_{CaO/Al2O3}$ was not significant in comparison with that of calcium titanate.

Figure 4 shows the relationship between the added amount of Al_2O_3 and the reduction current density at -1.6V. Except for $R_{CaO/Al2O3}$ = 1.0, the reduction current increased with the increase in the added amount of Al_2O_3 up to the addition of 7 mol% Al_2O_3. However, the reduction current in the bath containing 9 mol% Al_2O_3 rather decreased in comparison with that in 7mol%-Al_2O_3 bath. In previous studies on Ti and Si, [5-7] it was shown that the excess addition of calcium titanate and silicate caused the decrease in the reduction current. The solubility of $Ca_{12}Al_{14}O_{33}$ and $Ca_3Al_2O_6$ was about 7mol% as Al_2O_3 concentration, while that of $CaAl_2O_4$ was low. However, it is still unknown why excessive addition inhibited Al reduction. Further study on this dependence should be necessary.

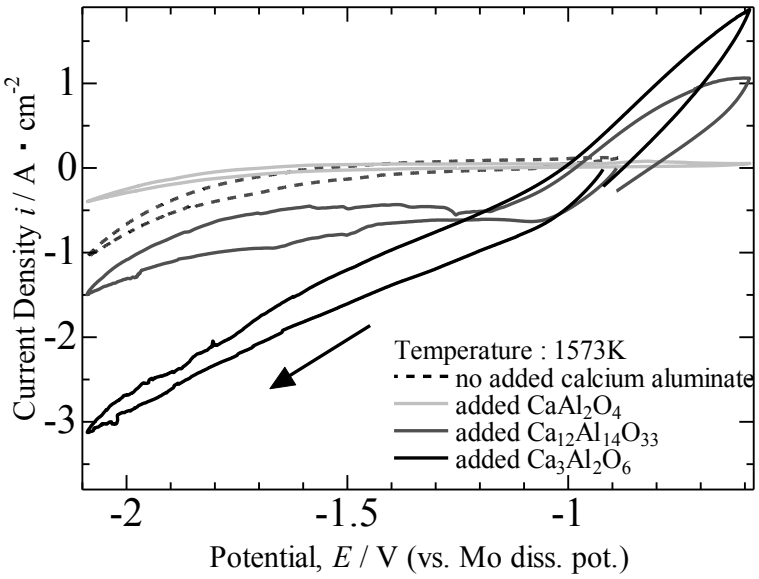

Fig.3 Typical cyclic voltammograms in bath of various $R_{CaO/Al2O3}$.
(x_{Al2O3} = 7 mol%, scan rate: 50 mV s^{-2})

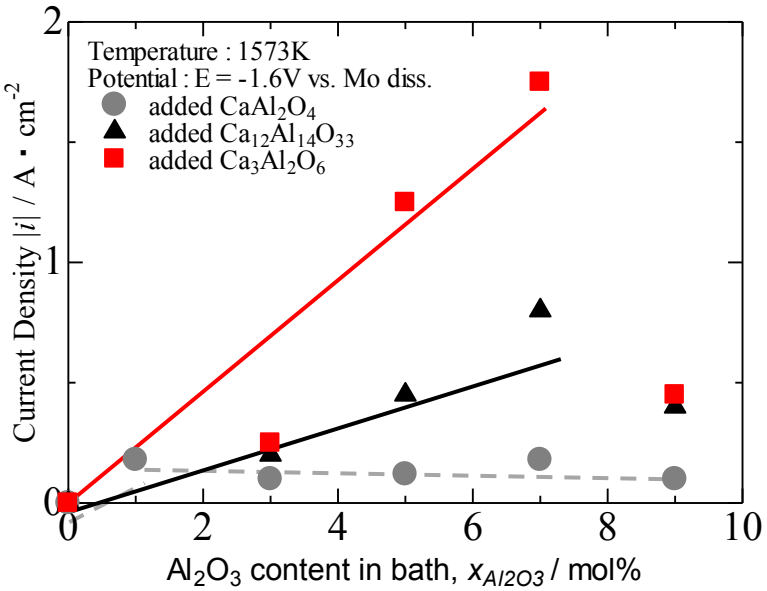

Fig.4 Relationship between cathodic current at -1.6V in cyclic voltammograms and Al_2O_3 content in bath.

Al electrodeposition

Potentio-static electrolysis was performed in the baths of various $R_{CaO/Al2O3}$ at -1.8V at 1573K. The appearance of electrode after electrolysis and its XRD pattern are shown in Fig. 5. Al metal, Al-Mo alloy and Al_2O_3 were detected on the electrode surface. In the cross section of electrode, Al was concentrated on the outer edge, but the thickness was extremely thin (50 μm or less). A small amount of Al metal particles was also found in the bottom of the crucible, which suggested the electrodeposited Al metal flew down from the electrode. The current efficiency which was calculated from the weight of Al metal particles, was about 2.7%.

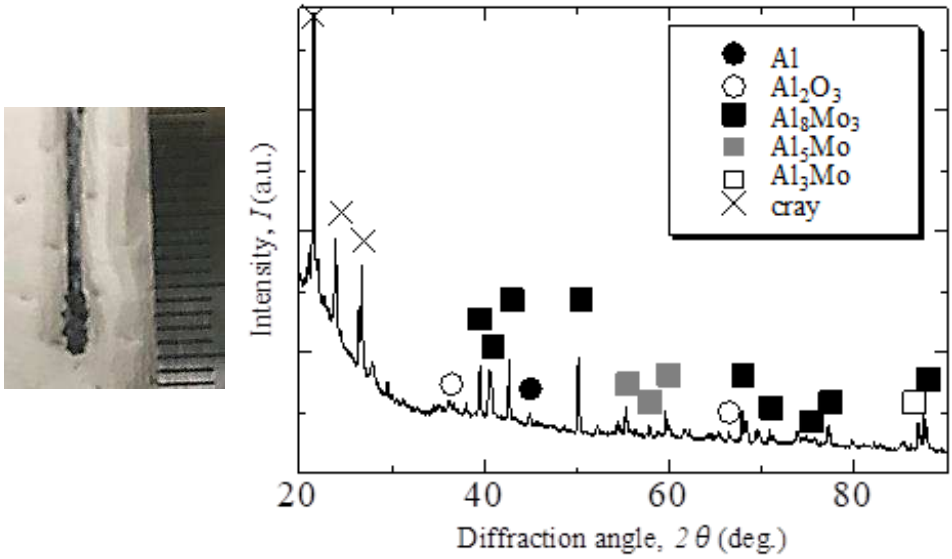

Fig.5 Appearance and XRD pattern of electrode after electrolysis in bath of $R_{CaO/Al2O3}$ = 12/7. (x_{Al2O3} = 7 mol%, E = -1.8V, t = 7200 s)

Potentio-static electrolysis using an electrode with a BN receiver as shown in Fig. 6 was carried out to keep the electrodeposit around the electrode. The appearance of the electrode after removing the receiver after electrolysis at -1.8V, and its XRD pattern are shown in Fig. 7. A black deposit was observed at the tip of the electrode, and the deposit mainly consisted of Al metal. Figure 8 shows the elemental mapping of the cross section. The layer consisted of Al and Mo, and its thickness was about 300 μm. The current efficiency, which was calculated from the thickness assuming the layer was Al_8Mo_3, was about 3.4%, which was larger than that without BN mentioned before.

It was suggested that Al was obtained in molten $CaCl_2$ containing calcium aluminate, and the influence of the molar ratio of CaO and Al_2O_3 on Al electrodeposition was not so significant. However, only a small amount of Al was obtained, and the current efficiency was insufficient. The condition for better electrolysis should be studied.

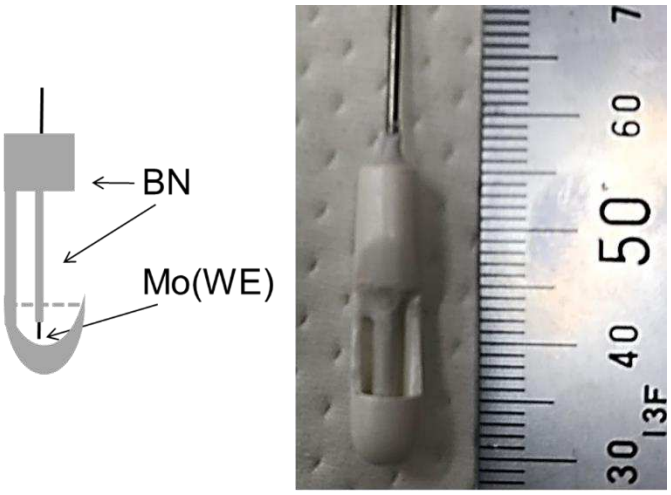

Fig.6 A Mo cathode with BN receiver.

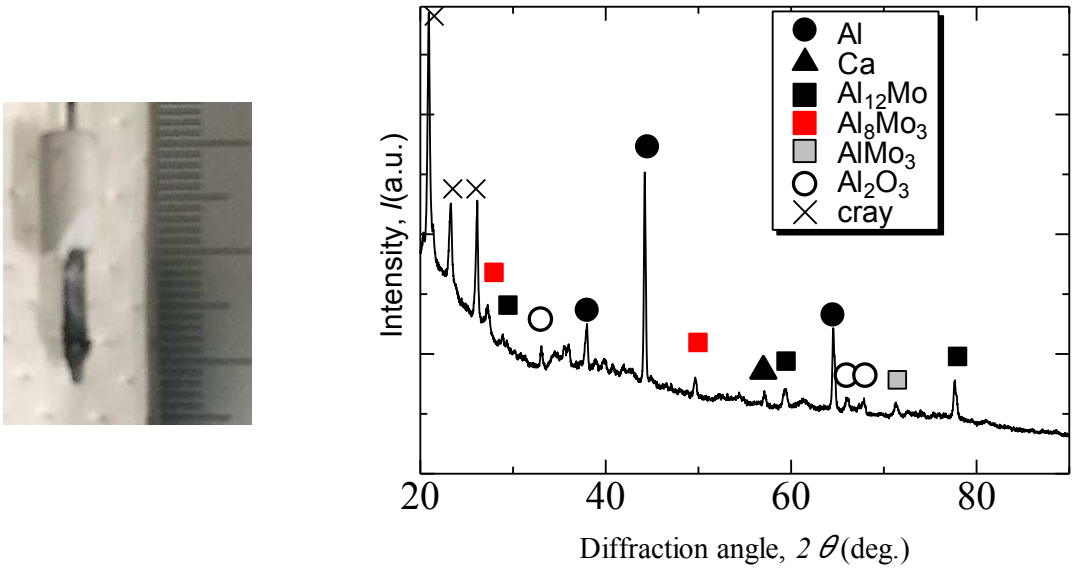

Fig.7 Appearance and XRD pattern of the electrode removing BN receiver after electrolysis in bath of $R_{CaO/Al2O3}$ = 1.0.
(x_{Al2O3} = 7 mol%, E = -1.8V, t = 7200 s)

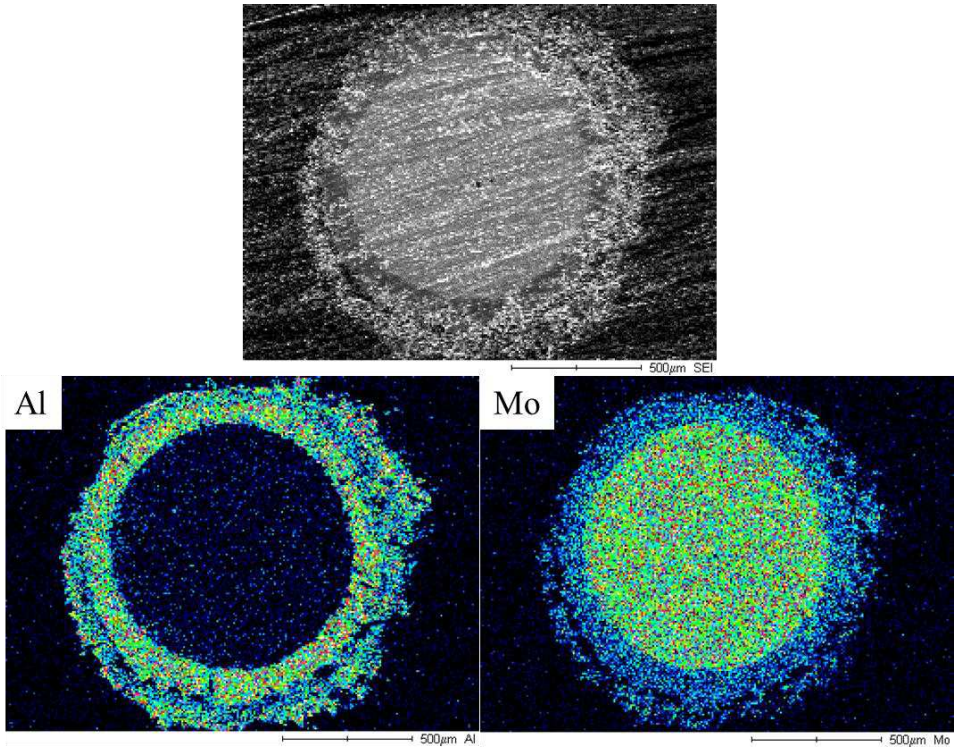

Fig.8 SEM image and EDS mapping image of the electrode removing BN receiver after electrolysis in bath of $R_{CaO/Al2O3}$ = 1.0.
(x_{Al2O3} = 7 mol%, E = -1.8V, t = 7200 s)

Conclusion

Calcium aluminate dissolved in molten $CaCl_2$ at 1573K. Al and Al-Mo was obtained electrochemically, and the influence of the molar ratio of CaO to Al_2O_3 on Al electrodeposition was not significant in comparison with Ti electrolysis. However, the current efficiency was still very small, so further study for better electrolysis should be necessary.

Acknowledgements

The study was supported by the Ministry of Education, Culture, Sports, Science and Technology, Japan (Grant-in-Aid for Scientific Research (B), #18H01763) and by Kansai University Grant-in-Aid for progress of research in graduate course, 2011.

References

1. H. Kadowaki, Y. Katasho, K. Yasuda and T. Nohira, *ECS Trans.*, **165**, 83-89, (2018).

2. T. Takenaka, M. Sugawara, H. Matsuo, A. Matsuyama and M. Kawakami, *ECS Trans.*, **16**, 139-143, (2009).
3. Y. Yamanaka, T. Morishige and T. Takenaka, *ECS Trans.*, **64**, 275-283, (2014).
4. T. Takenaka, K. Shimokawa, K. Nishikawa, H. Okada and T. Morishige, *Material Trans.*, **58**, 350-354, (2017).
5. H. Okada, K. Shimokawa, T. Morishige and T. Takenaka, *Material Trans.*, **59**, 690-693, (2018).
6. H. Okada, M. Murata, T. Morishige, T. Takenaka, *ECS Trans*., **86** 117, (2018)
7. T. Takenaka , R. Shimokawa , H. Okada , T. Morishige, *ECS Trans*., **86** 29, (2018)

ECS Transactions, 98 (10) 341-354 (2020)
10.1149/09810.0341ecst ©The Electrochemical Society

Kinetic and Thermodynamic Properties of Samarium Chlorides Dissolved in Alkali Chloride Melts Obtained by Electrochemical Transient Techniques

S.A. Kuznetsov[a], Yu.V. Stulov[a], and M. Gaune-Escard[b]

[a] Tananaev Institute of Chemistry of the Federal Research Centre "Kola Science Centre of the Russian Academy of Sciences", Apatity, Russia
[b] Ecole Polytechnique, CNRS UMR 6595, Technopole de Château Gombert, 13453 Marseille Cedex 13, France

The electrochemical behavior of samarium in NaCl-KCl, KCl and CsCl melts was studied in the temperature range 973-1173 K by different electrochemical methods. The diffusion coefficients (D) of Sm(III) and Sm(II) were determined by linear sweep voltammetry, chronopotentiometry and chronoamperometry methods. The standard rate constants of charge transfer (k_s) for the Sm(III)/Sm(II) redox couple were calculated on the basis of cyclic voltammetry data using Nicholson's equation. The nature of working electrode on the standard rate constants of charge transfer for the Sm(III)/Sm(II) redox couple was studied. The formal redox potentials $E^*_{Sm(III)/Sm(II)}$ were obtained in alkali chlorides melts from the cyclic voltammetry data.

Introduction

Up to now, the various elements present in nuclear wastes are separated by hydrometallurgical processes. The Purex process is widely used technique, but permits to recover only U and Pu, and is not capable to separate the trivalent transuranium elements like americium and curium from trivalent fission products represented by lanthanides. Several pyrochemical processes are being investigated at the international level in order to propose compact and economically competitive fuel cycle (1). The study of lanthanide halides is of particular interest for recycling spent nuclear fuel since the lanthanide elements present in spent fuel from fast nuclear reactors and samarium belongs to the group of the most abundant fission elements in nuclear reactors (2). A pyrochemical process may be coupled with a dedicated system such as an accelerator driven sub-critical reactor. The whole aim is to remove the minor actinides from the spent fuel while the lanthanides can be extracted by the molten salt electrorefining.

Thus a knowledge of the electrochemistry and thermodynamics of samarium chlorides in molten salts is crucial for the understanding of spent fuel recycling. In pyrochemical processes chlorides of lanthanides are usually diluted in molten salt medium and, as we already showed (3-7) in this case the electrochemical transient techniques is not only a powerful method for studying electrode kinetics, but also an effective method for the determination of thermodynamic properties.

Electrochemistry of samarium was studied in the LiCl–KCl melt of eutectic composition by Cordoba et al (8). The authors found a two-step reduction process, but

only the first one was observed in on a molybdenum electrode because the discharge potential of Sm(II) to Sm more negative than discharge potential of Li^+ cations. The redox potentials of Sm(III)/Sm(II) in a eutectic LiCl-KCl were determined in (9). In study (10) by potentiometric method the redox potentials of samarium were defined in alkali chlorides melts. The preliminary results on the diffusion coefficients (D) for oxidation states of Sm(III) and Sm(II) were determined by cyclic voltammetry, chronoamperometry and chronopotentiometry in an equimolar mixture NaCl-KCl and in KCl, CsCl melts (11). The standard rate constants of charge transfer (k_s) were calculated on the basis of cyclic voltammetry data for the Sm(III)/Sm(II) redox couple and formal redox potentials were found by electrochemical transient techniques (11). Nikolaeva et al. by linear and cyclic voltammetry determined the diffusion coefficients of Sm(III) and Sm(II) and the formal redox potential in a eutectic NaCl-CsCl (12-13). The electrochemical properties of samarium have been studied at a tungsten electrode in two molten chlorides with different acidity properties in a eutectic LiCl–KCl and in an equimolar $CaCl_2$-NaCl mixture by Castrillejo et al (14).

This paper describes a study of Sm(III) and Sm(II) electrochemical behavior in an equimolar mixture NaCl-KCl and in KCl, CsCl melts. The main goal of this study is the determination of Sm(III) and Sm(II) kinetic parameters such as: diffusion coefficients and the standard rate constants of charge transfer for the Sm(III)/Sm(II) redox couple. Another aim is to define the formal standard redox potentials $E^*_{Sm(III)/Sm(II)}$ and calculation the Gibbs energies and equilibrium constants for the reaction of $SmCl_3$ formation.

Experimental Details

Chemicals; Preparation of Salts

Samarium trichloride was prepared by chlorinating the oxide (Merck, 99.9%) with a current of high purity argon (water and oxygen content less than 2 and 0.5 ppm, respectively) saturated with $SOCl_2$ vapor in a quartz reactor, at 793-813 K for 24 hours (15).

Due to the highly hygroscopic property, $SmCl_3$ was stored in sealed glass ampoules under vacuum. All further handling of samarium trichloride were performed in a controlled purified argon atmosphere glove-box (water content less than 2 ppm.).

Alkali chlorides (NaCl, KCl, and CsCl) were purchased from Prolabo (99.5 % min.). They were dehydrated by continuous and progressive heating just above the melting point under gaseous HCl atmosphere in quartz ampoules. Excess HCl was removed from the melt by argon. The salts were handled in the glove box and stored in sealed glass ampoules. The total concentration of samarium was determined by inductively coupled plasma atomic emission spectroscopy (ICP-AES) using the device (Optima 8300 Cross Flow, Perkin Elmer, USA).

Procedures and Electrochemical Cell

Chlorides of alkali metals were placed in an ampoule made of glassy carbon (SU-2000 type) and transferred to a hermetically sealed retort of stainless steel. The latter was

evacuated to a residual pressure of $5 \cdot 10^{-3}$ Torr, first at room temperature and then at higher temperatures (473, 673 and 873 K). After this the retort was filled with high purity argon and the electrolyte was melted.

Linear sweep voltammetry (LSV), cyclic voltammetry (CV), chronopotentiometry (CP) and chronoamperometry (CA) were employed, using a VoltaLab-40 potentiostat (Radiometer Analytical, Lyon, France) with complementarily packaged software "VoltaMaster 4", version 6. The potential scan rate was varied between $5 \cdot 10^{-3}$ and 5.0 V s^{-1}. Experiments were carried out in the temperature range 973-1173 K. The cyclic voltammetric curves, chronopotentiograms and chronoamperograms were recorded at a glassy carbon and molybdenum electrodes of 1.0-2.0 mm diameter with respect to a glassy carbon plate quasi-reference electrode. The glassy carbon ampoule served as the counter electrode. While the potential of this quasi-reference electrode does not constitute a thermodynamic reference, the use of this electrode was preferred in order to avoid any contact between the melt and oxygen-containing material as used in classical reference electrodes. An Ag/NaCl-KCl-AgCl (2 wt.%) reference electrode was used in order to obtain more reliable potential values. At the final stage of each experimental set, this reference electrode was immersed in the melt for a short time for the determination of the potential peaks, the melt being no longer used after these measurements (3-7) The potentials from silver reference electrode were converted to a Cl^-/Cl_2 reference electrode (3).

Results and Discussion

Electrochemistry of the Redox Process Sm(III) + e^- ↔ Sm(II)

Cyclic Voltammetry. The cyclic voltammograms for the redox process:

$$Sm(III) + e^- \leftrightarrow Sm(II) \qquad [1]$$

obtained at a glassy carbon electrode in the NaCl-KCl-$SmCl_3$ melt at a temperature 1073 K are given in Fig. 1.

A similar voltammograms were obtained for KCl and CsCl melts.

It was found that in alkali chloride melts the peak current of the electroreduction process is directly proportional to the square root of the polarization rate, while the peak potential does not depend on the polarization rate up to ν=0.1 V s^{-1}. The peak current is linearly dependent on the $SmCl_3$ concentration, while the peak potential does not depend on the concentration of samarium trichloride in the melt. The potentiostatic electrolysis at potentials of the cathodic peak did not lead to the formation of any solid phase at the electrode and no visible transformation of the electrode itself was observed. According to the theory of cyclic voltammetry (16), up to the polarization rate 0.1 V s^{-1}, the electrode process is controlled by the rate of mass transfer and yields a reduced form soluble in the melt.

The diffusion coefficients (D) for the chloride complexes of Sm(III) and Sm(II) in NaCl-KCl, KCl and CsCl melts were determined at ν=0.1 V s^{-1} using of the Randles-Shevchik equation (17):

$$I_p^C = 0.4463 F^{3/2} R^{-1/2} T^{-1/2} n^{3/2} A C D^{1/2} \nu^{1/2} \quad [2]$$

where I_p^C is the peak cathodic current (A), A is the electrode area (cm^2), C is the bulk concentration of active species (mol cm^{-3}), D is the diffusion coefficient (cm^2 s^{-1}), ν is the potential sweep rate (V s^{-1}), and n is the number of electrons involved in the reaction.

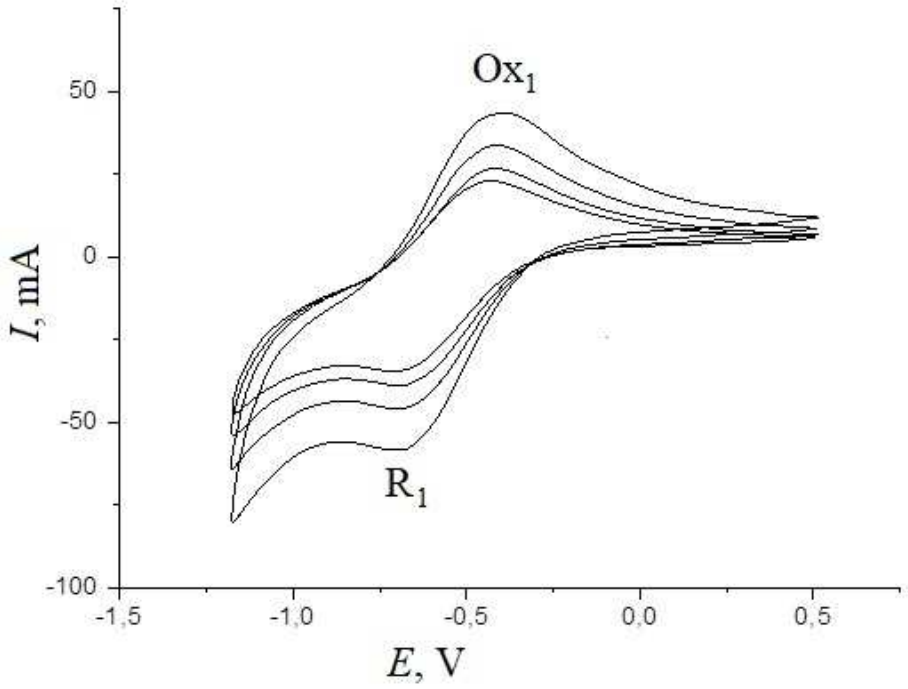

Figure. 1. Cyclic voltammograms at a glassy carbon electrode for various scan rates in the NaCl-KCl-$SmCl_3$ melt. Area: 0.494 cm^2. Temperature: 1073 K. Concentration of $SmCl_3$: $8.21 \cdot 10^{-5}$ mol cm^{-3}. Quasi-reference electrode: glassy carbon. Sweep rate:(1) 0.075 (inner curve); (2) 0.010; (3) 0.150; (4) 0.200 V s^{-1}.

For the determination of Sm(II) diffusion coefficients were used melts containing only Sm(II) complexes. Such melts were obtained by contact of Sm metal with the molten salt systems. The Sm metal can react not only with Sm(III) species, but also with the solvent to produce alkali metals. Alkali metals dissolve in the solvent and ionic-electronic melt is formed. For the melts with the electronic conductivity the usual electrochemical equations are not applicable. At the same time from thermodynamic and kinetics points of view follow that Sm metal initially interact with Sm(III) complexes. An approach, which includes the monitoring by voltammetry (curves registered each 5 minutes) of the melts after addition of Sm was used. The voltammetric curves clear indicated the transformation of cathodic wave to cathodic-anodic (due to appearance of

Sm(II) species) and finally to anodic wave. The anodic peak currents at the time point when the anodic-cathodic wave completely transformed to electrooxidation of Sm(II) to Sm(III) wave were used for calculation of Sm(II) diffusion coefficients by Eq. [2].

Chronopotentiometry. The electrochemical behavior of the redox couple Sm(III)/Sm(II) was further investigated by means of chronopotentiometry. A chronopotentiogram for the Sm(III) to Sm(II) electroreduction in the KCl-$SmCl_3$ melt at a glassy carbon electrode is shown in Fig. 2. The transition time (τ) is determined by the duration of the potential plateau (Fig. 2). Straight lines were obtained for the plots of I *vs.* $\tau^{-1/2}$ for various concentration of Sm(III). It was found that the square root of the transition time also increased linearly with increasing of added $SmCl_3$ amounts at various applied current densities. The chronopotentiometric curve did not shift towards negative potentials when current density was increased. Thus, on the basis of chronopotentiometric data, it is possible to conclude that the electrochemical reduction of Sm(III) to Sm(II) is a diffusion controlled process (18). The chronopotentiometric curve for the reversible electroreduction with a soluble substance formation is described by the following equation (18):

$$E=E^0_{Sm(III)/Sm(II)}+(RT/nF)\ln(D_{red}/D_{ox})^{1/2}+(RT/nF)\ln(\gamma_{ox}/\gamma_{red})+(RT/nF)\ln[(\tau^{1/2}-t^{1/2})/t^{1/2}] \quad [3]$$

where: D_{ox}, D_{red} and γ_{ox}, γ_{red} are, respectively, the diffusion coefficients and the activity coefficients of the oxidized and reduced forms.

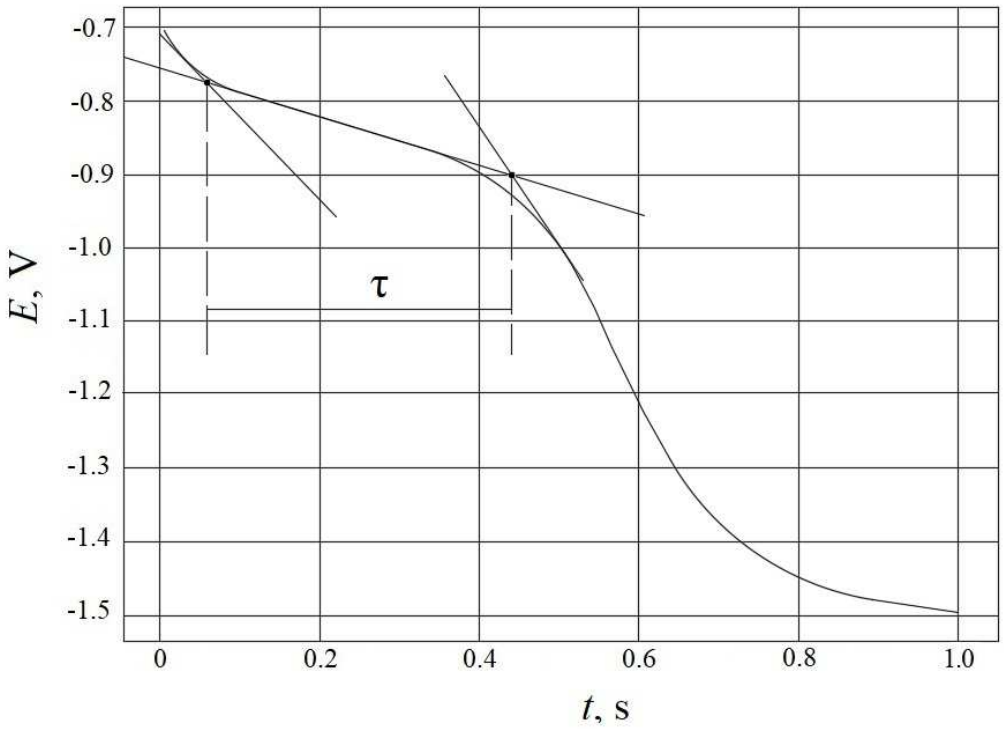

Figure. 2. Chronopotentiogram of the electroreduction process Sm(III) + $e^- \rightarrow$Sm(II) in the KCl melt at a glassy carbon electrode. Current: 25 mA. Area: 0.320 cm^2. Temperature: 1100 K. Concentration of $SmCl_3$: $7.12 \cdot 10^{-5}$ mol cm^{-3}. Quasi-reference electrode: glassy carbon.

It was determined that the plot E vs. $log\ [(\tau^{1/2} - t^{1/2})/t^{1/2}]$ is a straight line with a slope which is very close to the value 2.3 RT/F corresponding to a one electron transfer. For reversible process, the Sand's equation is valid (18):

$$I\tau^{1/2} = (nFCD^{1/2}\pi^{1/2}A)/2 \qquad [4]$$

where I is the current (A), A is the area (cm^2) of the working electrode, τ is the transition time (s), C is the bulk concentration of the reactant (mol cm^{-3}), and D is the diffusion coefficient of the reactant ($cm^2\ s^{-1}$).

Utilizing the Sand's equation and the slope of the plot I - $\tau^{-1/2}$ (Fig. 3), the diffusion coefficient of Sm(III) is estimated to be $4.13 \cdot 10^{-5}$ $cm^2\ s^{-1}$ at 1100 K.

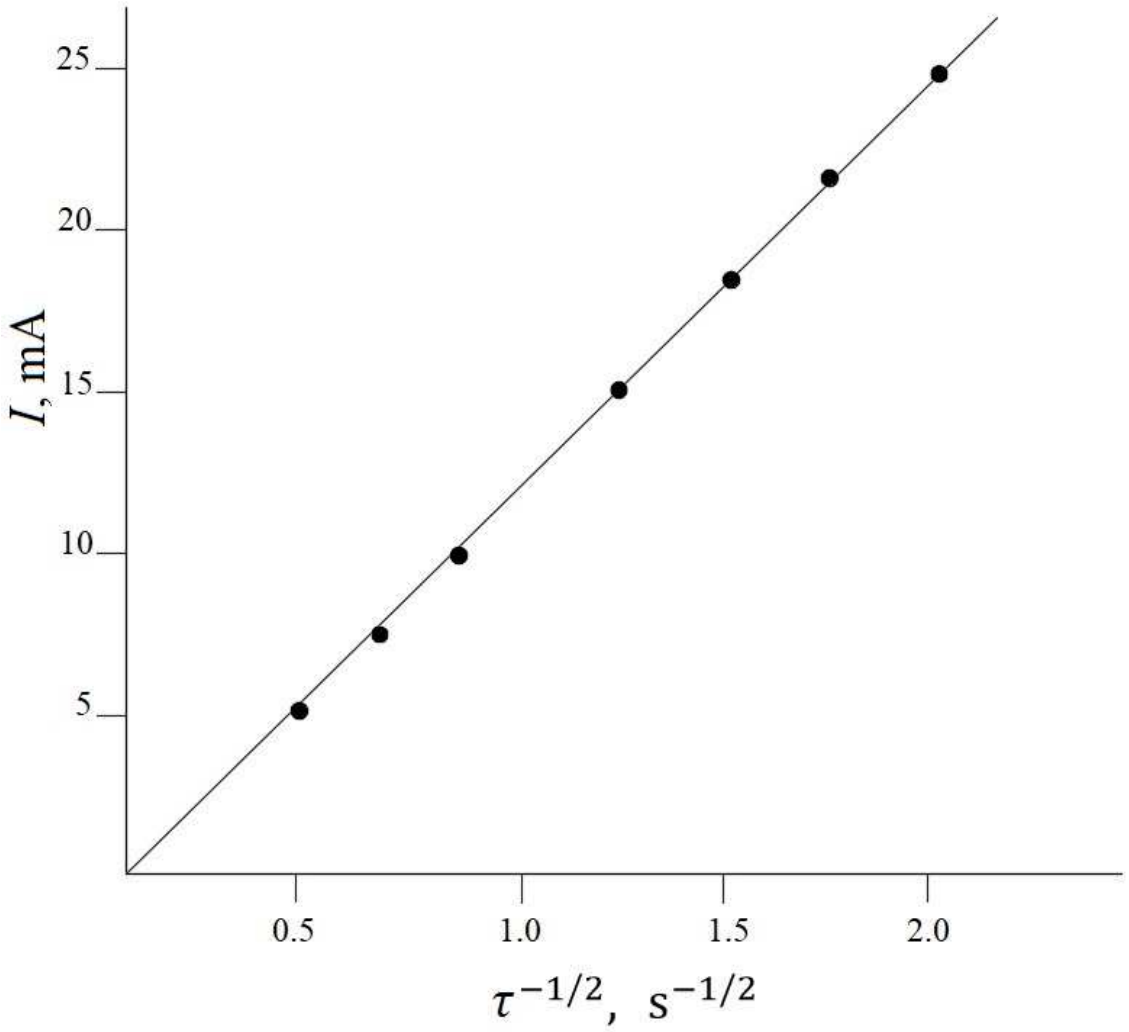

Figure. 3. The relation between I and $\tau^{-1/2}$ for the process Sm(III) + $e^- \rightarrow$Sm(II) in the KCl melt. Area: 0.320 cm^2. Temperature: 1100 K. Concentration of $SmCl_3$: $7.12 \cdot 10^{-5}$ mol cm^{-3}.

Chronoamperometry. Fig. 4 shows a typical chronoamperogram for electroreduction of Sm(III) to Sm(II) at a glassy carbon electrode in the CsCl-$SmCl_3$ melt. A linear relationship between the current and reciprocal square root of time was obtained (Fig. 5). Accordingly, the cathodic current can be expressed by the Cottrell's equation (18):

$$I=nFD^{1/2}_{Sm(III)}AC/\pi^{1/2}t^{1/2} \quad [5]$$

From the slope of the corresponding plot (Fig. 5), the diffusion coefficient of Sm(III) at 973 K was obtained as $1.17 \cdot 10^{-5}$ cm^2 s^{-1}.

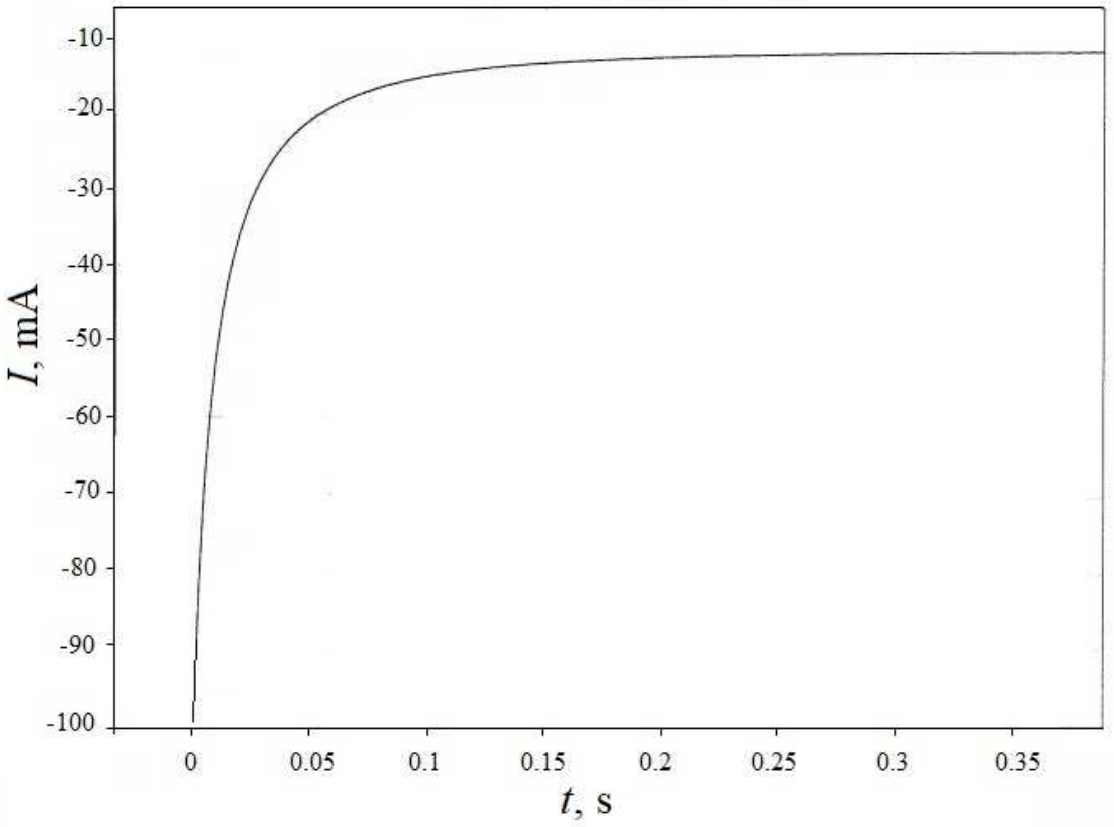

Figure. 4. Typical chronoamperogram for electroreduction of Sm(III) to Sm(II) in the CsCl melt at a glassy carbon electrode. Potential step: -0.82 V. Area: 0.320 cm^2. Temperature: 973 K. Concentration of $SmCl_3$: $7.96 \cdot 10^{-5}$ mol cm^{-3}. Quasi-reference electrode: glassy carbon.

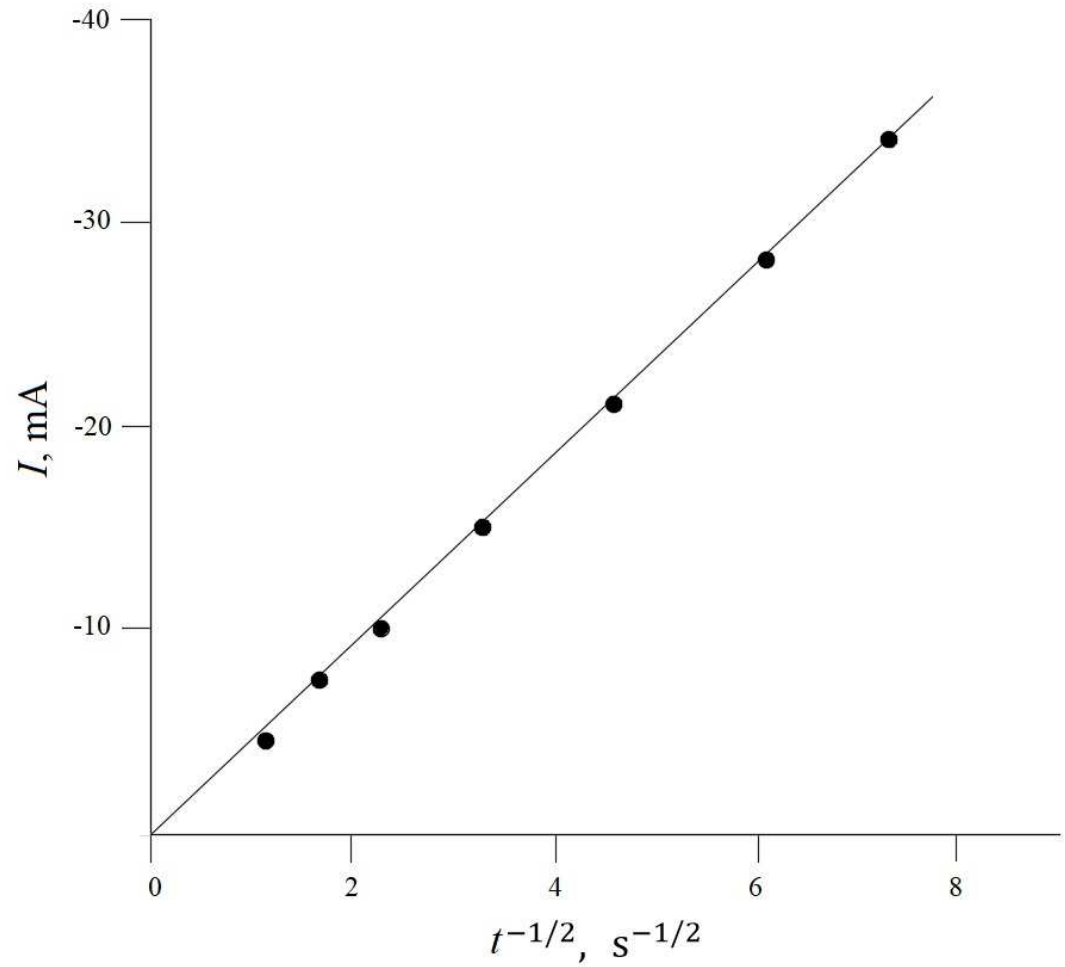

Figure. 5. Plot of current against the inverse square root of time for chronoamperogram (Fig. 4).

Diffusion Coefficients. As shown above, diffusion coefficients of Sm(III) were obtained by different methods. These results are summarized in Table I.

As can be seen from Table I, the diffusion coefficients of Sm(III) obtained by different methods are in a good agreement altogether. Temperature dependences of diffusion coefficients for Sm(III) and Sm(II) were determined in the temperature range 973-1173 K using linear sweep voltammetry at $\nu = 0.1$ V s^{-1}, because reproducibility of D values obtained by voltammetry method was better than that in CP and CA methods.

The coefficients of the equation:

$$\log D = -A - B/T \pm \Delta \qquad [6]$$

and diffusion coefficients at 1100 K, for Sm(III) and Sm(II) in NaCl-KCl, KCl and CsCl melts are given in Tables II and III. The activation energies for diffusion (ΔU) of Sm(III) and Sm(II) are also included in these tables. They were calculated from the equation:

$$-\Delta U/2.303R = \partial \log D/\partial(1/T) \quad [7]$$

Table I. Diffusion coefficients of Sm(III) in NaCl-KCl, KCl and CsCl melts at 1100 K obtained by various methods.

Methods	NaCl-KCl melt $D_{Sm(III)}\cdot10^5$, cm^2s^{-1}	KCl melt $D_{Sm(III)}\cdot10^5$, cm^2s^{-1}	CsCl melt $D_{Sm(III)}\cdot10^5$, cm^2s^{-1}
LSV	4.33	4.13	2.39
CP	4.19	3.98	2.21
CA	4.51	4.27	2.54

As evidenced in Tables II and III, smaller values of *D* were obtained when the cation in the second coordination sphere changes from Na^+ to Cs^+. Similar changes in *D* values are well-known (19). They are due to the decrease of the counter-polarizing effect of cations from Na^+ to Cs^+, resulting in a decrease of metal-ligand bond length. Diffusion coefficients decrease when samarium oxidation state increases while the activation energies for diffusion increase. Thus *D* decreases and ΔU increases with increasing ionic moment of the diffusing species. These results are in agreement with numerous data showing that diffusion coefficients and activation energies for diffusion of complexes strongly depend on the oxidation state of central atoms (20).

Table II. Coefficients *A* and *B* in equation [6], diffusion coefficients *D* at 1100 K for Sm(III) complexes and activation energy for diffusion (ΔU) in alkali chloride melts

Melt	*A*	*B*	Δ	$D\cdot10^5$ $sm^2\cdot s^{-1}$	ΔU $kJ\cdot mol^{-1}$
NaCl-KCl	2.52	2028	0.03	4.33	38.8
KCl	2.40	2182	0.03	4.13	41.8
CsCl	2.30	2554	0.03	2.39	48.9

Table III. Coefficients *A* and *B* in equation [6], diffusion coefficients *D* at 1100 K for Sm(II) complexes and activation energy for diffusion (ΔU) in alkali chloride melts

Melt	*A*	*B*	Δ	$D\cdot10^5$ $sm^2\cdot s^{-1}$	ΔU $kJ\cdot моль^{-1}$
NaCl-KCl	2.35	1929	0.03	7.88	36.9
KCl	2.33	2002	0.03	7.08	38.3
CsCl	2.29	2301	0.03	4.15	44.1

The Influence of the Second Coordination Sphere on the Standard Rate Constants of the Electrode Reaction Sm(III) + e^- ↔ Sm(II) in Alkali Chloride Melts

A mixed diffusion and electron-transfer control for the process (1) was observed in the potential sweep rate range $0.1<\nu\leq 0.3$ V s^{-1}. This mechanism is clearly evidenced by the deviation of experimental points from linearity in the I^C_p vs. $\nu^{1/2}$ plot, and by the magnitude of the difference between E^A_p and E^C_p, which is larger than is required for a reversible process (Fig. 1).

The problem of determining kinetic parameters on the basis of cyclic voltammetry was addressed by Nicholson (21). The standard rate constant of the electrode process is related to the function ψ as follow:

$$\psi = \frac{k_S \left(\frac{D_{ox}}{D_{red}} \right)^{\alpha/2}}{\pi^{1/2} D_{ox}^{1/2} \left(\frac{nF}{RT} \right)^{1/2} v^{1/2}} \qquad [8]$$

Here ψ is a function related to the difference between the peak potentials E^A_p-E^C_p (mV), k_s is the standard rate constant of electrode process (cm s^{-1}), α=0.5 is the transfer coefficient.

The dependences E^A_p-E^C_p on the function ψ reported in (21) at the temperature of 298 K, must be recalculated for the present working temperature, and the following equations (22) were used:

$$(\Delta E_p)_{298} = (\Delta E_p)_T 298/T \qquad [9]$$

$$\psi_T = \psi_{298}(T/298)^{1/2} \qquad [10]$$

The values of the ψ_T function, obtained from equation [9] and [10], and used in conjunction with expression [8] made it possible to calculate the standard rate constants of charge transfer. The influence of the second coordination sphere and temperature on the standard rate constants of the electrode reaction [1] is presented in Table IV.

Table IV. Standard rate constants k_s (cm s^{-1}) of the electrode reaction Sm(III)+e^- ↔ Sm(II) in alkali chloride melts at different temperatures

Melt	k_s 973 K	k_s 1023 K	k_s 1073 K	k_s 1123 K	k_s 1173 K
NaCl-KCl	$0.87 \cdot 10^{-2}$	$1.47 \cdot 10^{-2}$	$2.59 \cdot 10^{-2}$	$4.22 \cdot 10^{-2}$	-
KCl			$1.11 \cdot 10^{-2}$	$1.61 \cdot 10^{-2}$	$2.58 \cdot 10^{-2}$
CsCl	$0.71 \cdot 10^{-2}$	$1.28 \cdot 10^{-2}$	$2.05 \cdot 10^{-2}$	$3.12 \cdot 10^{-2}$	-

As seen from Table IV, the following nonmonotonic dependence of k_s on the nature of the outer sphere cation was found: k_s (KCl) < k_s (CsCl) < k_s (NaCl-KCl). The quantum-chemical calculation should be performed for explanation of experimental results.

The Influence of the Electrode Material on the Standard Rate Constants of Charge Transfer for the Redox Reaction Sm(III) + e^- ↔ Sm(II).

Cyclic voltammograms for the Sm(III)/Sm(II) redox couple obtained at a glassy carbon and molybdenum electrodes in the NaCl-KCl-$SmCl_3$ melt are shown in Fig. 6. The values of the standard rate constants determined at a glassy carbon and molybdenum electrodes in the NaCl-KCl-$SmCl_3$ melt are presented in Table V.

Table V. Standard rate constants k_s (cm s^{-1}) of the electrode reaction Sm(III)+e^- ↔ Sm(II) in the NaCl-KCl melt obtained at a glassy carbon and molybdenum electrodes

Electrode	973 K	1023 K	1073 K
Glassy carbon	$0.87 \cdot 10^{-2}$	$1.47 \cdot 10^{-2}$	$2.59 \cdot 10^{-2}$
Molybdenum	$1.81 \cdot 10^{-2}$	$2.90 \cdot 10^{-2}$	$5.63 \cdot 10^{-2}$

As can be seen from the Table V, the standard rate constants of charge transfer increase when a glassy carbon electrode is replaced by a molybdenum electrode. It is known from the theory of the elementary act that in general, the effect of the electrode nature on the rate of the discharge-ionization stage is due to both the change in the structure of the double layer and the difference in the energies of adsorption of reactants and reaction products on different materials (23). In our case, based on the diagnostic criteria of the cyclic voltammetry, it is established that neither the reactant nor the reaction product exhibit specific adsorption. Thus, higher values of k_s on a molybdenum electrode compared to the glassy carbon electrode are associated with a change in the structure of the electric double layer upon passing from one material to another.

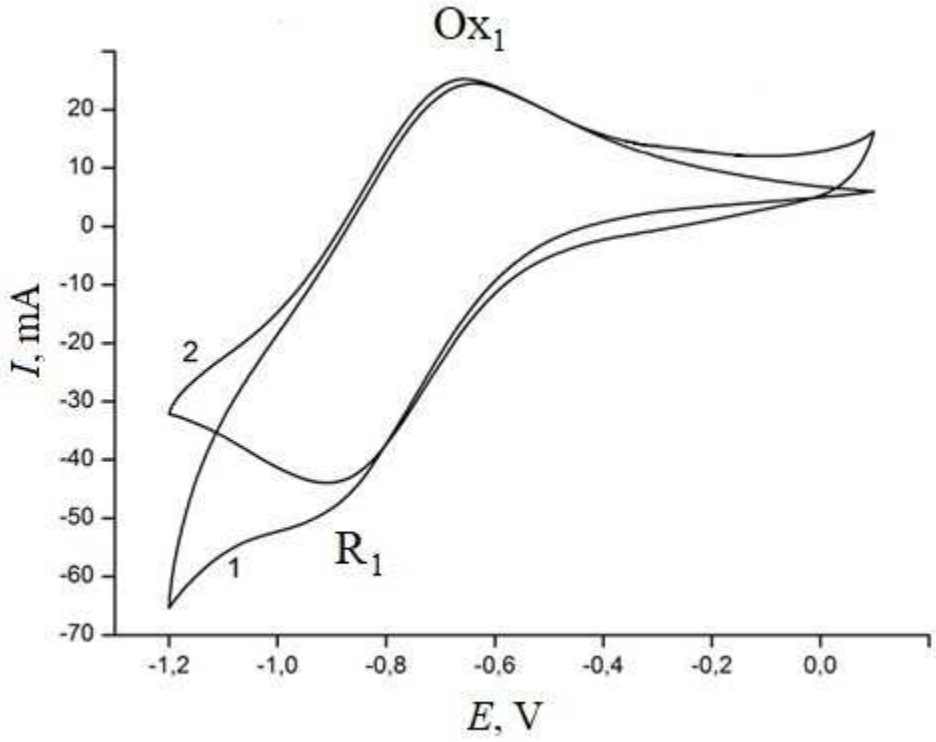

Figure. 6. Cyclic voltammograms for the Sm(III)/Sm(II) redox couple obtained at a glassy carbon (1) and molybdenum (2) electrodes in the NaCl-KCl-$SmCl_3$ melt. Sweep rate: 1.0 V s^{-1}. Temperature:1023 K. Area (GC): 0.324 cm^2. Area (Mo): 0.191 cm^2. Concentration of $SmCl_3$=5.70·10^{-5} моль$^{-3}$. Quasi-reference electrode: glassy carbon.

Formal Standard Potentials $E^*_{Sm(III)/Sm(II)}$ in Alkali Chloride Melts

According to the theory of cyclic and steady state voltammetry the following relations are valid for the reversible electrochemical reduction [1] between the cathodic and anodic peak potentials and half-wave potential (24):

$$E_P^C = E_{1/2} - 1.11(RT/F) \quad [11]$$

$$E_p^A = E_{1/2} + 1.11(RT/F) \quad [12]$$

$$(E_p^C + E_p^A)/2 = E_{1/2} \quad [13]$$

where

$$E_{1/2} = E^0_{Sm(III)/Sm(II)} + (RT/F)\ \ln(D_{red}/D_{ox})^{1/2} + (RT/F)\ \ln(\gamma_{ox}/\gamma_{red}) \quad [14]$$

In the concentration range of ions with mole fraction (N) less than $(3\text{-}5)\cdot10^{-2}$ the activity coefficients in molten salts remain constant which leads up to the following formal standard potentials (25):

$$E^*_{Sm(III)/Sm(II)} = E^0_{Sm(III)/Sm(II)} + (RT/F)\ \ln(\gamma_{ox}/\gamma_{red}) \quad [15]$$

The formal standard redox potentials of $E^*_{Sm(III)/Sm(II)}$ were calculated from the following equations:

$$E^*_{Sm(III)/Sm(II)} = E_p^C + 1.11(RT/F) + (RT/F)\ \ln(D_{ox}/D_{red})^{1/2} \quad [16]$$

$$E^*_{Sm(III)/Sm(II)} = E_p^A - 1.11(RT/F) + (RT/F)\ \ln(D_{ox}/D_{red})^{1/2} \quad [17]$$

$$E^*_{Sm(III)/Sm(II)} = (E_p^C + E_p^A)/2 + (RT/F)\ \ln(D_{ox}/D_{red})^{1/2} \quad [18]$$

Thus using the potential peaks values of the redox process and the diffusion coefficients of Sm(III) and Sm(II) it was found that the formal standard redox potentials are described relatively to a Cl^-/Cl_2 reference electrode by the following empirical dependences:

$$E^*_{Sm(III)/Sm(II)}/V = -(2.671\pm0.006) + (6.7\pm0.2)\cdot10^{-4}T/K \text{ (NaCl-KCl)} \quad [19]$$

$$E^*_{Sm(III)/Sm(II)}/V = -(2.789\pm0.006) + (7.3\pm0.2)\cdot10^{-4}T/K \text{ (KCl)} \quad [20]$$

$$E^*_{Sm(III)/Sm(II)}/V = -(2.990\pm0.005) + (8.4\pm0.2)\cdot10^{-4}T/K \text{ (CsCl)} \quad [21]$$

It can be seen that redox potential shifts toward more negative values with increasing of alkali metal radius. This is due to a greater stabilization of Sm(III) complexes as compared with the Sm(II) complexes, occurring with the increase of the radius of sodium, potassium and cesium cations in the melt.

From the redox potentials [19-21] it is possible to calculate the Gibbs free energy for the reaction:

$$SmCl_{2(sol.)} + 1/2\ Cl_{2(g.)} \leftrightarrow SmCl_{3(sol.)} \quad [22]$$

using the equation:

$$\Delta G^* = nF\ E^*_{Sm(III)/Sm(II)} \quad [23]$$

The temperature dependences of the formal Gibbs energy are described by the well-known equation:

$$\Delta G^* = \Delta H^* - T\Delta S^* \quad [24]$$

The change in the formal Gibbs energy during the formation of samarium trichloride in molten chlorides was calculated based on the dependences [19-21]:

$$\Delta G^*/\text{kJ}\cdot\text{mol}^{-1} = -(258\pm0.6) + (65\pm1.9)\cdot10^{-3}\ T/\text{K (NaCl-KCl)} \quad [25]$$

$$\Delta G^*/\text{kJ}\cdot\text{mol}^{-1} = -(269\pm0.6) + (70\pm1.9)\cdot10^{-3}\ T/\text{K (KCl)} \quad [26]$$

$$\Delta G^*/\text{kJ}\cdot\text{mol}^{-1} = -(288\pm0.6) + (81\pm1.9)\cdot10^{-3}\ T/\text{K (CsCl)} \quad [27]$$

The first terms in these equations [25-27] represent the formal enthalpy of the reaction, the exothermicity of which increased with increasing stability of the samarium chloride complexes. The temperature coefficient, taken with their signs reversed, give the formal standard values of partial entropy of the reaction. The increase of the formal standard partial entropy of the reaction from NaCl-KCl to CsCl is due both to a higher degree of order of the reactions products as the result of complex formation and to changes in their natural frequency with increasing stability (25).

Since $\Delta G^* = -2.303\ RT \log K^*$, the formal equilibrium constants can be calculated for the reaction [22]. The calculated values of the logarithm equilibrium constant linearly depend on the inverse temperature in melts of alkali metal chlorides:

$$\log K^* = -3.395 + 13475/T \pm 0.2 \text{ (NaCl-KCl)} \quad [28]$$

$$\log K^* = -3.656 + 14045/T \pm 0.2 \text{ (KCl)} \quad [29]$$

$$\log K^* = -4.230 + 15041/T \pm 0.2 \text{ (CsCl)} \quad [30]$$

The values of the formal equilibrium constants in alkali chloride melts indicate that the equilibrium of reaction [22] is completely shifted to the right side.

Conclusions

The electrochemical behavior of the Sm(III)/Sm(II) redox couple in alkali chloride melts (NaCl-KCl, KCl, CsCl) was studied in the temperature range 973-1173 K by different electrochemical methods. The diffusion coefficients (D) for Sm(III) and Sm(II) were determined by linear sweep voltammetry, chronopotentiometry and chronoamperometry methods showing that D decreases with increase of samarium oxidation state, while the activation energy for diffusion increases.

The standard rate constants of charge transfer (k_s) for the Sm(III)/Sm(II) redox couple were calculated on the basis of cyclic voltammetry data using Nicholson's equation. The following row of the standard rate constants of charge transfer has been experimentally determined: k_s (KCl) < k_s (CsCl) < k_s (NaCl-KCl). The nature of working electrode on the rate of charge transfer for the Sm(III)/Sm(II) redox couple was studied. It was found that

the values of k_s determined on a molybdenum electrode were higher than those at a glassy carbon electrode.

The formal redox potentials $E^*_{Sm(III)/Sm(II)}$ were obtained in alkali chloride melts from the cyclic voltammetry data. From the values of the formal redox potentials were calculated the Gibbs energies and equilibrium constants for the $SmCl_3$ formation.

References

1. J. P. Glatz, R. Malmbeck, P. Soucek, B. Claux, R. Meir, M. Ougier and T. Murakami, in *Molten Salts Chemistry from Lab to Applications,* F. Lantelme and H. Groult Editors, p. 541, Elsevier, Burlington MA (2013).
2. J. P. Ackerman*, Ind. Eng. Chem.Res.,* **30,** 141 (1991).
3. S. A. Kuznetsov and P.T. Stangrit, *Rasplavy*, **4,** 44 (1990).
4. S. A. Kuznetsov and M. Gaune-Escard, *Electrochim. Acta,* **46,** 1101 (2001).
5. S. A. Kuznetsov, H. Hayashi, K. Minato and M. Gaune-Escard, *J. Electrochem. Soc.,* **152,** C203 (2005).
6. S. A. Kuznetsov and M. Gaune-Escard, *J. Electroanal. Chem.,* **595,** 11 (2006).
7. S. A. Kuznetsov and M. Gaune-Escard, *J. Nucl. Mater.,* **389,** 108 (2009).
8. G. Cordoba, and C. Caravaca, *J. Electroanal. Chem.,* **572,** 145 (2004).
9. K. E. Johnson and J. R. Mackenzie, *J. Electrochem. Soc.,* **116,** 1697 (1969).
10. A. Novoselova, V. Shishkin and V. Khokhlov, *Z. Naturforsch.,* **56a,** 754 (2001).
11. S. A. Kuznetsov and M. Gaune-Escard, in *Proceedings of the Seventh International Symposium on Molten Salts Chemistry and Technology,* Toulouse, France, **2,** 855 (2005).
12. E. V. Nikolaeva, A. L. Bove and N. I. Moskalenko, *Rasplavy,* **18,** 64 (2008).
13. E. V. Nikolaeva, A. L. Bove and N. I. Moskalenko*, Russian Metallurgy (Metally),* **2011,** 142 (2010).
14. Y. Castrillejo, C. de la Fuente, M. Vega, F. de la Rosa, R. Pardo and E. Barrado, *Electrochim. Acta,* **51,** 120 (2013).
15. L. Rycerz and M. Gaune-Escard, *Z. Naturforsch.,* **57a,** 79 (2002).
16. R. S. Nicholson and I. Shain, *Anal. Chem.,* **36,** 706 (1964).
17. P. Delahay, *New Instrumental Methods in Electrochemistry: Theory, Instrumentation and Application to Analytical and Physical Chemistry,* Interscience, New York, 1954.
18. Z. Galus, *Fundamentals of Electrochemical Analysis,* Ellis Horwood, London (1994).
19. G. J. Janz, and N. P. Bansal, *J. Phys. Chem. Data,* **11,** 505 (1982).
20. A. V. Popova, V. G. Kremenetsky and S. A. Kuznetsov, *J. Electrochem. Soc.,* **161,** H447 (2014).
21. R. S. Nicholson, *Anal. Chem.,* **37,** 1351 (1965).
22. S. A. Kuznetsov, S. V. Kuznetsova and P. T. Stangrit, *Russ. J. Electrochem.,* **26,** 55 (1990).
23. B. B. Damaskin and O. A. Petriy, *Introduction to the Electrochemical Kinetics,* Vysshaya Shkola Publ., Moscow, (1975).
24. H. Matsuda, and Y. Ayabe, *Z. fur Elektrochem.,* **59,** 494 (1955).
25. M. V. Smirnov, *Electrode Potentials in Molten Chlorides,* Nauka, Moscow, (1973).

ECS Transactions, 98 (10) 355-364 (2020)
10.1149/09810.0355ecst ©The Electrochemical Society

Separation of Uranium and Zirconium in Alkali Chloride Melts Using Liquid Metal Cathodes

V. A. Volkovich[a], D. S. Maltsev[a, b], M. N. Soldatova[a], A. A. Ryzhov[a], and A. B. Ivanov[a]

[a] Department of Rare Metals and Nanomaterials, Institute of Physics and Technology, Ural Federal University, Ekaterinburg 620002, Russian Federation
[b] Department of Chemistry, University of Tennessee, Knoxville, TN 37996, USA

Cyclic voltammetry and cathodic polarization measurements were employed to study zirconium and uranium electrochemical behavior in LiCl–KCl eutectic based melts on solid (tungsten) and liquid (zinc, gallium, indium, Gz–Zn eutectic alloy) working electrodes. Deposition potentials of zirconium and uranium were determined. Ga–Zn alloy showed a difference of ca. 0.9 V in U and Zr deposition potentials. Thermodynamically achievable Zr/U separation factor in a "LiCl–KCl salt melt – liquid Ga–Zn alloy" system was experimentally determined.

Introduction

Alkali chloride melts are considered as prospective working media for non-aqueous pyrochemical reprocessing of spent nuclear fuels (SNFs). Separation of fissile materials from fission products in pyrochemical reprocessing can be achieved electrochemically. Amongst all the fission products zirconium has the closest electrochemical properties to uranium making separation of uranium and zirconium a challenging task. Uranium and plutonium fission produces several zirconium isotopes (1). For example, thermal neutron fission of U-235 produces Zr-91 (stable, 5.84 % yield); Zr-92 (stable, 6.03 % yield); Zr-93 ($1.53 \cdot 10^6$ years half-life, 6.45 % yield); Zr-94 (stable, 6.4 % yield); Zr-95 (64.02 days half-life, 6.2 % yield); Zr-96 (stable, 6.33 % yield) and Zr-97 (16.8 hours half-life, 5.9 % yield). In addition, decay of Y-91 (58.5 days half-life) produces Zr-91, and that of Y-93 (10.2 hours half-life) gives Zr-92. Depending on the reactor neutron spectrum, nuclear fuel type, burnup and cooling time SNF arriving for reprocessing can contain ca. 5–13 kg of zirconium (as the fission product excluding cladding) per ton. Typical SNF of thermal neutron reactors arriving for reprocessing contains 8.3 kg Zt/t with the total activity of 28.3 TBq. Fast neutron reactors also produce zirconium isotopes (from Zr-90 to Zr-96).

Electrochemical properties of zirconium in fused alkali chlorides are being studied for nearly seven decades but there is still no complete agreement concerning the mechanism of Zr(IV) ions reduction and oxidation states of zirconium ions present in the melt in the equilibrium with zirconium metal. Equilibrium electrode potentials of zirconium were measured in individual LiCl, NaCl, KCl, CsCl, as well as LiCl–KCl eutectic, NaCl–KCl equimolar and LiCl–CsCl mixtures of different compositions. Zirconium ions were introduced into the melt either by anodic dissolution of the metal or by dissolving zirconium tetrachloride, and the results obtained in the earlier works were reviewed by Smirnov (2). In addition to potentiometry, polarization studies were also performed

including polarization of zirconium anode in NaCl–KCl melts and molybdenum cathode in NaCl–KCl–$ZrCl_4$ melts (3, 4).

At present, eutectic mixture of lithium and potassium chlorides is considered as a prime candidate working media for pyrochemical SNF reprocessing. Therefore behavior of zirconium in LiCl–KCl eutectic based melts received close attention. Application of molten salts for separating zirconium from contaminated zirconium alloys was considered (5–8). Cyclic voltammetry is one of the most often employed techniques for studying zirconium electrochemistry in LiCl–KCl melts but there are some contradictions in the reported data (6, 8–12). According to the literature, zirconium in LiCl–KCl based melts at 500 ^{o}C can present in two soluble (Zr^{4+}, Zr^{2+}) and two insoluble (ZrCl, Zr) forms. Number of the oxidation waves in the voltammograms varied from two to four and number of the reduction waves was reported as two or three (6, 8–10). Each wave was assigned a particular redox reaction. In addition to the solid cathodes liquid metal electrodes can be utilized. Alloying processes and formation of intermetallic compounds in this case would affect the electrode potential values. Selecting suitable metal can result in increasing selectivity of the electrode reaction and improving separation factor for the metals of interest. Low melting metals (zinc, cadmium, aluminum, lead, etc.) are normally used as the liquid metal cathodes.

Uranium electrochemistry in fused alkali chlorides was studied in depth. Results of potentiometry measurements on solid electrodes (both for U/(U(III) electrode and U(III)/U(IV) redox potentials) in various melts were compared and showed satisfactory agreement (13). In addition, electrochemistry of uranium in chloride melts was studied on various liquid metal electrodes (14, 15).

The present work was devoted to studying cathodic processes in zirconium and uranium containing melts based on 3LiCl–2KCl eutectic mixture on solid and liquid metal electrodes aiming to determining conditions for possible electrochemical separation of these two metals.

Experimental

The experiments were performed in 3LiCl–2KCl eutectic mixture based melts. Commercially available anhydrous lithium and potassium chlorides were additionally dried under vacuum, melted and treated with gaseous hydrogen chloride. Then the salts prepared were fused in the required proportion. Zirconium containing melts were obtained by dissolving zirconium tetrachloride (either commercially available or prepared by reacting metallic zirconium with chlorine) in the solvent salt using the approach described previously (16). Melts containing uranium chlorides were prepared by dissolving the required amount of anhydrous uranium tetrachloride or uranium trichloride in molten LiCl–KCl eutectic. Prepared salts were kept and handled in an inert atmosphere glove box (Glovebox Systemtechnik), oxygen and moisture content in the atmosphere was kept below 2 and 0.1 ppm, respectively. The experiments were also performed in this glove box. The electrochemical measurements were conducted using an Autolab PGSTAT 302N potentiostat/galvanostat.

Cyclic voltammetry measurements were performed in standard three-electrode cells. A tungsten rod sheathed by alumina or beryllium oxide tube to control working surface area served as the solid working electrode. Low melting metals were placed in small (5–6 mm i.d.) beryllium oxide crucibles. Thin tungsten wire sheathed by a ceramic (Al_2O_3 or BeO) capillary tube served as the current conductor to the liquid metal. Silver chloride reference electrode consisting of a silver wire submerged into 1 mol. % solution of silver chloride in an alkali chloride melt was used for the measurements. A glassy carbon rod served as the counter electrode.

Similar three-electrode cells were used for the cathodic polarization measurements. Depending on the metal and system studied counter electrodes were zirconium, uranium or glassy carbon rods. Temperature was measured by a K-type thermocouple dipped into the melt in a beryllium oxide sheath. To obtain a polarization curve first waited until the working electrode potential reached a stationary value. Then a constant cathodic current was passed through the system for 30 seconds followed by a 60 seconds currentless pause. The duration of the polarization and the rest periods was determined in a preliminary series of experiments. Potential value was recorded after switching off the polarization current. Polarization current values varied from 0.001 to 1 A. Examples of the potential–time dependencies thus obtained and used to construct the polarization curves are shown in Fig. 1.

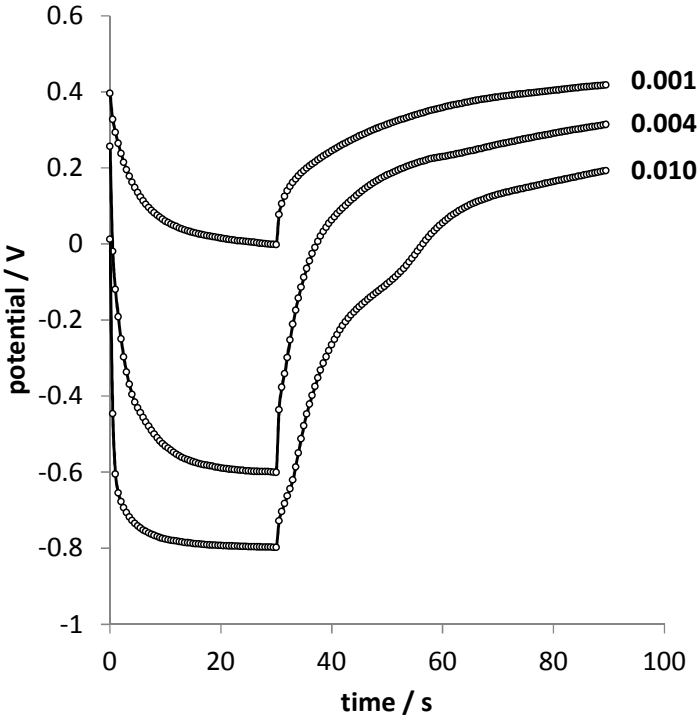

Figure 1. Examples of the potential–time dependencies obtained during cathodic polarization measurements in LiCl–KCl–$ZrCl_4$ melts (0.3 wt. % Zr, 544 ^oC) on a tungsten working electrode (0.661 cm^2). Silver chloride reference electrode. Polarization current (A) is shown on the graph for each set of data.

Results and Discussion

Cyclic Voltammetry Measurements in LiCl–KCl–$ZrCl_4$ Melts

An example of cyclic voltammogram recorded in LiCl–KCl–$ZrCl_4$ melt is shown in Fig. 2. There are peaks associated with reduction and subsequent oxidation of lithium from the solvent salt and a number of peaks associated with zirconium. In order to clarify the relationship between various peaks a series of voltammograms was recorded at varied cathodic potential limit. An example of the results is presented in Fig. 3. At the cathodic limit of –0.4 V (relative to silver chloride reference electrode) there were no cathodic and anodic peaks. Shifting the potential limit to –0.9 V resulted in one cathodic (Red3) and two anodic (Ox2 and Ox3) waves at –0.59, –0.33 and +0.07 V, respectively. Cathodic peak Red2 corresponds to the reduction of Zr(IV) to Zr(II) ions, and anodic Ox2 to oxidation of Zr(II) to Zr(IV). Anodic peak Ox3 is probably associated with oxidation of zirconium dichloride monolayer on the working electrode surface (8). Shifting the cathodic limit to –1.4 V produced two cathodic peaks (Red 2 and Red 1 at –1.04 and –1.4 V, respectively) and one anodic peak (Ox1) at –0.69 V. It is likely that the peak Ox1 is a superposition of two closely situated oxidation peaks, corresponding to the reduction peaks Red2 1nd Red 1. Sakamura et al. reported the results of X-ray diffraction analysis of the cathodic deposits obtained after electrolysis of a LiCl–KCl–$ZrCl_4$ melt at potentials around –1.1 and –1.4 V (10). Deposit obtained at the former potential consisted entirely of ZrCl and at that at the latter also contained metallic zirconium. Thus it is possible that the peak Red2 corresponds to the reduction of Zr(IV) and Zr(II) ions to ZrCl, and the peak Red1 to the reduction of ZrCl, Zr(II) and Zr(IV) to Zr metal.

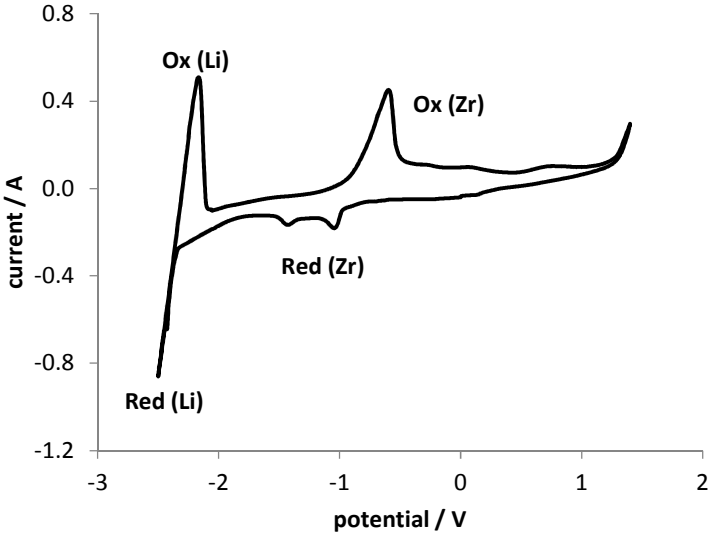

Figure 2. Cyclic voltammogram recorded in LiCl–KCl–$ZrCl_4$ melt (0.314 wt. % Zr, 550 ^oC) on tungsten working electrode (0.557 cm^2) at 0.2 V/s scan rate. Ag/AgCl (1 mol. % in NaCl–2CsCl) reference electrode.

Similarly cyclic voltammograms were also recorded on liquid gallium, indium and zinc working electrodes. Differential pulse voltammetry was used to complement cyclic voltammetry for more precise determination of zirconium deposition potentials. The

results obtained are summarized in Table I. Maximum positive shift of the potential was observed on gallium and indium electrodes.

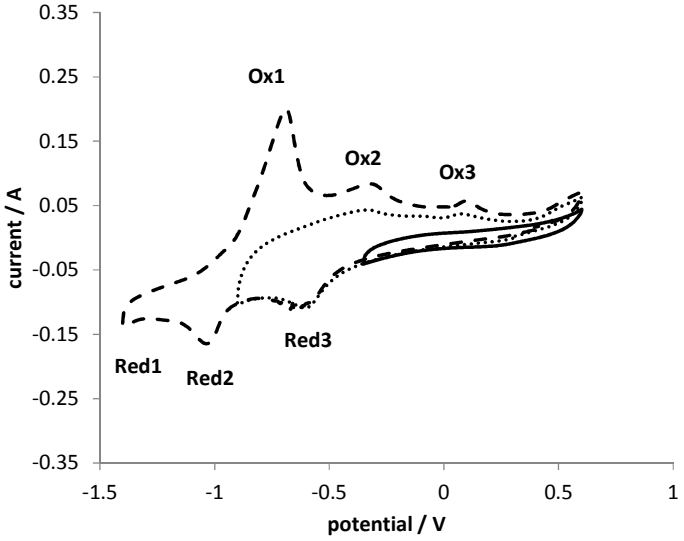

Figure 3. Effect of cathodic potential limit on cyclic voltammograms recorded in LiCl–KCl–$ZrCl_4$ melt (0.314 wt. % Zr, 550 ^oC) on tungsten working electrode (0.557 cm^2) at 0.2 V/s scan rate. Ag/AgCl (1 mol. % in NaCl–2CsCl) reference electrode.

TABLE I. Effect of cathode material on zirconium deposition potentials from LiCl–KCl–$ZrCl_4$ melts.

T / ^oC	Cathode	[Zr] / wt. %	Zr Deposition Potential / V	
			vs. Ag/AgCl	vs. $2Cl^-/Cl_2$
550	W	0.314	–1.08	–2.38
650	W	0.991	–0.93	–2.23
750	W	0.621	–0.88	–2.18
600	Ga	0.814	–0.85	–2.15
600	In	0.814	–0.83	–2.13
600	Zn	0.814	–1.03	–2.33

Cathodic Polarization Measurements in Zirconium and Uranium Containing Melts

First, polarization of the solid tungsten cathode was studied in LiCl–KCl–$ZrCl_4$ melts. Examples of the polarization curves are shown in Fig. 4. Increasing polarization current density resulted in a gradual change of the potential to negative values. Rising part of the polarization curves around –2.1 V (vs. $2Cl^-/Cl_2$ couple) reflects reduction of zirconium ions to the metal. Increasing temperature resulted in an expected shift of the potentials to slightly more positive values. Limiting current density for zirconium deposition was around 0.08–0.15 A/cm^2. At higher current densities co-reduction of zirconium and alkali metal (lithium) ions took place and the potential shifted to the negative values until there was deposition of lithium at –(3.1–3.3) V (second rising part of the polarization curves in Fig. 4).

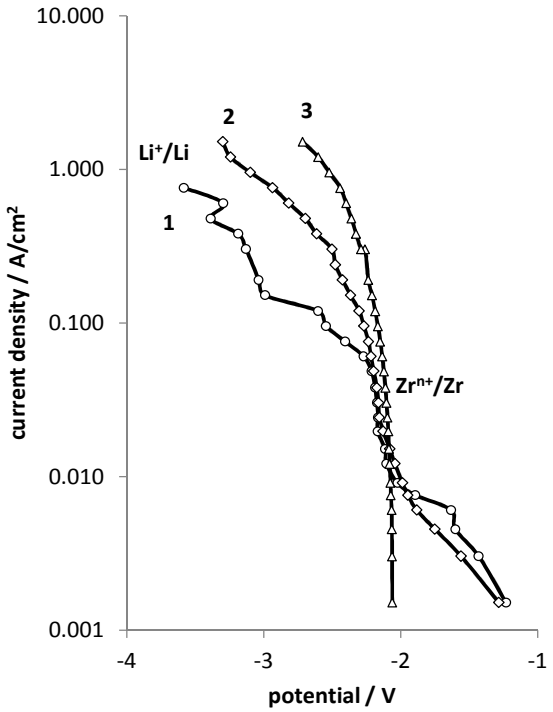

Figure 4. Polarization of tungsten cathode in LiCl–KCl–$ZrCl_4$ melts at 532 ^oC (1); 544 ^oC (2) and 637 ^oC (3). $2Cl^-/Cl_2$ reference electrode.

Cathode material can have a pronounced effect on the deposition potential, Table 1. Gallium and indium showed the biggest positive shift. However, these metals are not particularly attractive from the technological point of view; they are relatively expensive and have high boiling points that make difficult further separation of them from the alloys for recycling. Therefore at the present stage zinc and gallium–zinc eutectic alloy (3.64 wt. % Zn, m.p. 25.5 ^oC) were tested. Comparison of cathodic polarization of solid W and liquid Zn and Ga–Zn electrodes in in LiCl–KCl–$ZrCl_4$ melts at around 550 ^oC is shown in Fig. 5. The results showed that changing from tungsten to zinc resulted in ca. 0.13 V positive shift of zirconium deposition potential. Gallium–zinc alloy exhibited the most positive zirconium deposition potential value of –1.75 V, i.e. 0.4 V more positive than on tungsten, making this alloy an interesting candidate material for a further study.

To assess deposition potentials of uranium on Ga–Zn cathode polarization measurements were performed in LiCl–KCl–UCl_4 and LiCl–KCl–UCl_3 melts, Fig. 6. First rising part of the polarization curves around –1.8 V corresponded to the reduction of U(IV) to U(III) ions. The results obtained showed that the LiCl–KCl–UCl_3 melt contained some U(IV) ions as there also was a short rising part at ca. –1.85 V at low current densities (to 0.006 A/cm^2). Increasing current density shifted the potential to the negative direction and the part of the polarization curves between –(2.6–2.9) V corresponds to the deposition of uranium metal. At the current densities exceeding 1 A/cm^2 reduction of lithium takes place.

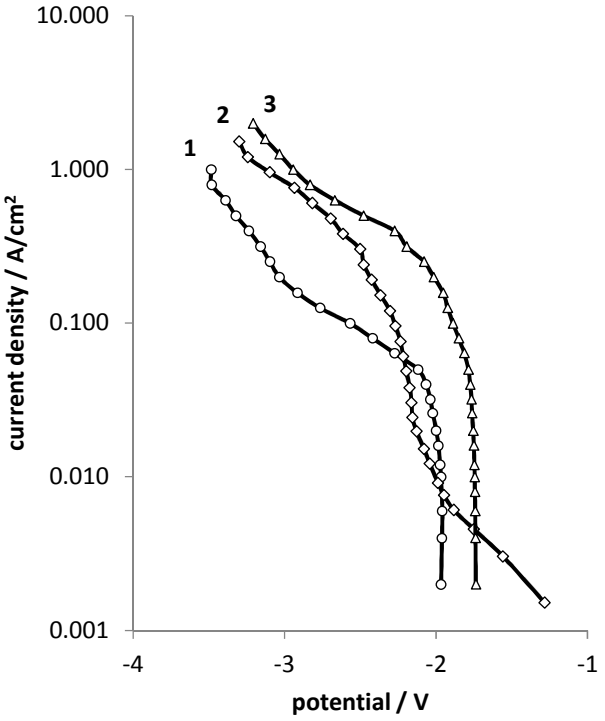

Figure 5. Polarization of zinc (1), tungsten (2) and Ga–Zn (3) cathodes in LiCl–KCl–$ZrCl_4$ melt at 567, 544 and 550 °C, respectively. $2Cl^-/Cl_2$ reference electrode.

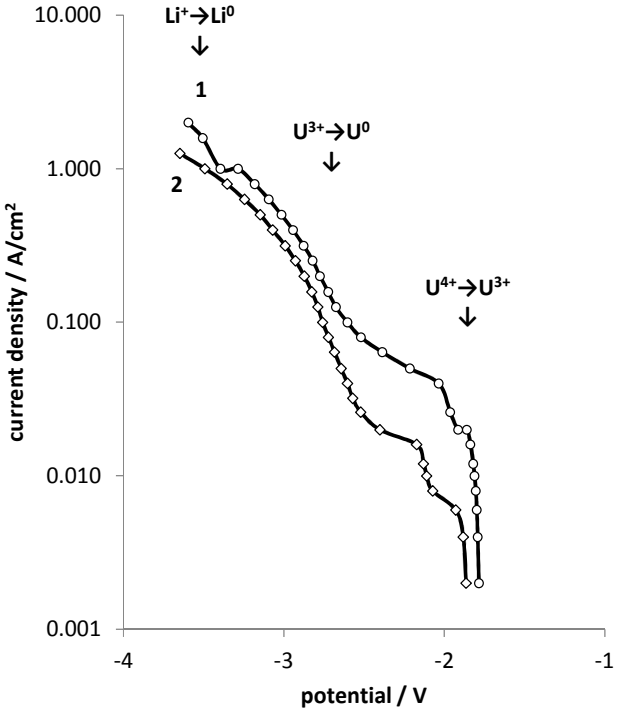

Figure 6. Polarization of gallium–zinc eutectic alloy cathode in LiCl–KCl–UCl_4 melt at 524 °C (1) and LiCl–KCl–UCl_3 melt at 541 °C (2). $2Cl^-/Cl_2$ reference electrode.

A comparison of the polarization curves measured on the Ga–Zn cathode in LiCl–KCl–UCl_4, LiCl–KCl–$ZrCl_4$ and LiCl–KCl–$ZrCl_4$–UCl_4 melts is shown in Fig. 7. As expected, reduction of U^{4+} to U^{3+} and Zr^{n+} to Zr^0 took place at very close potentials (first rising part of the polarization curve 3 in Fig. 7). Reduction of U^{3+} to U^0 in LiCl–KCl–$ZrCl_4$–UCl_4 melt took place around –2.7 V and current densities over 0.4 A/cm^2. Thus there is a noticeable difference in the deposition potentials of zirconium and uranium on Ga–Zn eutectic alloy cathode making this cathode promising for achieving deep separation of these two metals.

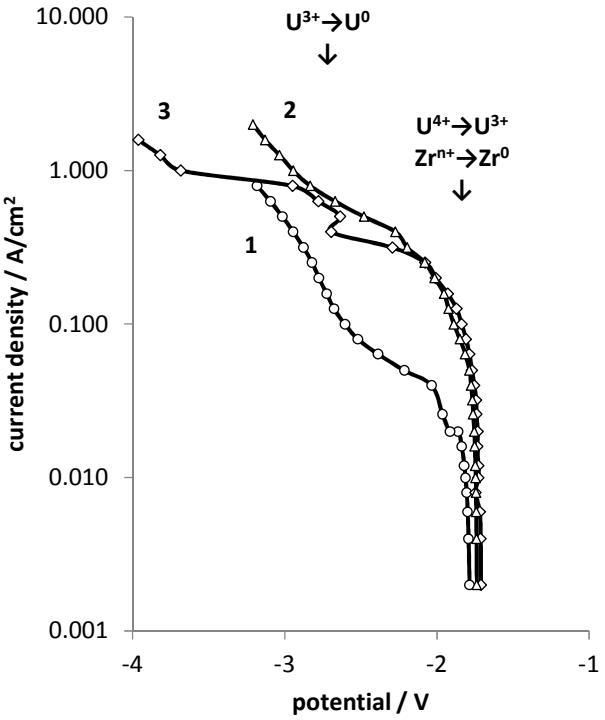

Figure 7. Polarization of gallium–zinc eutectic alloy cathode in LiCl–KCl–UCl_4 melt at 524 ^oC (1), LiCl–KCl–$ZrCl_4$ melt at 550 ^oC (2) and LiCl–KCl–$ZrCl_4$–UCl_4 melt at 534 ^oC (3). $2Cl^-/Cl_2$ reference electrode.

Determination of Zirconium and Uranium Separation Factor

To determine thermodynamically achievable Zr/U separation factor in a "LiCl–KCl melt – liquid Ga–Zn alloy" system the experiment was conducted in the following manner. A sample of (Ga–Zn)–U–Zr alloy was held in contact with LiCl–KCl–UCl_3–$ZrCl_4$ salt melt under static conditions (without stirring) at 540 ^oC. The course of the reaction was followed by recording the potential of the liquid alloy. The experiment lasted for 29 hours. Composition of the salt and metallic phases before and after the experiment are listed in Table II.

TABLE II. Composition of salt melt and metallic alloy in the experiment on assessing U/Zr separation factor in a "LiCl–KCl melt – liquid Ga–Zn alloy" system.

Element	Initial Concentration / wt. %		Final Concentration / wt. %	
	LiCl–KCl Melt	Ga–Zn Alloy	LiCl–KCl Melt	Ga–Zn Alloy
U	0.568	12.060	1.23	0.10
Zr	0.275	2.663	0.029	6.08

Calculations showed that the mass balance of the process agreed very well with the stoichiometry of the following exchange reaction:

$$4\ U(0) + 3\ Zr(IV) = 4\ U(III) + 3\ Zr(0) \quad [1]$$

Uranium distribution coefficient between metallic and salt phases was 0.081 and that of zirconium was 209.655. Therefore thermodynamically achievable separation factor of zirconium and uranium in the "LiCl–KCl salt melt – liquid Ga–Zn alloy" system equals to 2580. This value confirms that the liquid cathode based on Ga–Zn eutectic alloy can be effectively used for separating uranium and zirconium.

Conclusions

Effective separation of uranium and zirconium in a pyrochemical process of SNF reprocessing depends on the difference in potentials of deposition of these metals. Changing from solid tungsten to liquid low melting metal cathode shifted the potential of zirconium deposition to the positive values. This shift was reaching 0.2 V for gallium and indium based cathodes. Gallium–zinc eutectic alloy also showed a large positive shift of zirconium deposition potential and this alloy was tested as a possible cathode material for separating uranium and zirconium in a "molten salt – liquid metal" system. Thermodynamically achievable Zr/U separation factor in the "LiCl–KCl based salt melt – liquid Ga–Zn eutectic alloy" system was determined experimentally. The value of the separation factor obtained under static conditions at 540 ^{o}C was 2580 confirming the prospective of using Ga–Zn cathode in the separation process.

Acknowledgments

The study was supported by the Russian Science Foundation, project no. 17-73-20156.

References

1. P. D. Wilson, *The Nuclear Fuel Cycle: From Ore to Wastes*, p. 314, Oxford University Press, Oxford (1996).
2. M. V. Smirnov, *Electrode Potentials in Fused Chlorides*, p. 109, Nauka, Moscow (1973) (in Russian).
3. A. N. Baraboshkin, M. V. Smirnov and N. A. Saltykova, in *Proceedings if the Institute of Electrochemistry UBAS USSR*, Iss. 3, p. 25, Sverdlovsk (1962) (in Russian).
4. V. E. Komarov, M. V. Smirnov and A. N. Baraboshkin, in *Proceedings if the Institute of Electrochemistry UBAS USSR*, Iss. 2, p. 41, Sverdlovsk (1961) (in Russian).
5. G. J. Kipouros, *J. Electrochem. Soc*., **132**, 1087 (1985).
6. C. H. Lee, K. H. Kang, M. K. Leon, C. M. Heo and Y. L. Lee, *ECS Trans.*, **50**(11), 491 (2012).

7. H. Li, H. H. Nersisyan, K. T. Park, S. B. Park, J. G. Kim, J. M. Lee and J. H. Lee, *J. Nucl. Mater*., 413, 107 (2011).
8. J. Park, S. Choi, S. Sohn, K. R. Kim and I. S. Hwang, *J. Electrochem. Soc*., **161**, H97 (2013).
9. S. Ghosh, S. Vandarkuzhali, P. Venkatesh, G. Seenivasan, T. Subramanian, B. Prabhakara Reddy and K. Nagarajan, *J. Electroanal. Chem*., **627**, 15 (2009).
10. Y. Sakamura, *J. Electrochem. Soc.*, **151**, C187 (2004).
11. Z. Chen, M. Zhang, W. Han, X. Wang and D. Tang, *J. Alloys Compd*., **459**, 209 (2008).
12. C. P. Fabian, V. Luca, T. H. Le, A. M. Bond, P. Chamelot, L. Massot, C. Caravaca, T. L. Hanley and G. R. Lumpkin, *J. Electrochem. Soc*., **160**, H81 (2013).
13. D. S. Maltsev, V. A. Volkovich, B. D. Vasin and E. N. Vladykin, *J. Nucl. Mater*., **467**, 956 (2015).
14. K. Liu, H.-B. Tang, J.- W. Pang, Y.-L. Liu, Y.-X. Feng, Z.-F. Chai and W.-Q. Shi, *J. Electrochem. Soc.*, **163**, D554 (2016).
15. V. Smolenski, A. Novoselova, P. Mushnikov and A. Osipenko, J. Radioanal. Nucl. Chem., **311**, 127 (2017).
16. V. A. Volkovich, I. B. Polovov, R. V. Kamalov, B. D. Vasin and T. R. Griffiths, in *Molten Salts Chemistry and Technology*, M. Gaune-Escard and G.M. Haarberg, Editors, p. 489, John Wiley & Sons Inc., Hoboken (2014).

ECS Transactions, 98 (10) 365-372 (2020)
10.1149/09810.0365ecst ©The Electrochemical Society

Kinetics of Reaction of Oxygen with Uranium(IV) Chloride in Alkali Chloride Melts

V. A. Volkovich[a], A. B. Ivanov[a], A. A. Ryzhov[a], D. S. Maltsev[a, b], and T. R. Griffiths[c]

[a] Department of Rare Metals and Nanomaterials, Institute of Physics and Technology, Ural Federal University, Ekaterinburg 620002, Russian Federation
[b] Department of Chemistry, University of Tennessee, Knoxville, TN 37996, USA
[c] Energy Process Developments Ltd., London SE1 4AG, United Kingdom

The reaction of oxygen with solutions of uranium tetrachloride in molten alkali chlorides was studied. The experiments were performed in LiCl–KCl, NaCl–KCl–CsCl, and NaCl–CsCl eutectic based melts at 450–750 ^{o}C. Pure oxygen and argon–oxygen mixtures (containing *ca*. 1 and 10 % O_2) were used. Amount of oxygen passed through the melt varied from less than one to over 100 moles per mole of uranium present. In addition the reaction of oxygen with the melts containing a mixture of uranium(IV) and neodymium chlorides was investigated. The course of the reactions was followed by in situ electronic absorption spectroscopy measurements with the spectra recorded at the certain time intervals. Depending on temperature, cationic melt composition and oxygen-to-uranium molar ratio, the reaction resulted in oxidation of uranium(IV) to soluble uranyl chloride and/or precipitation of uranium oxide. Analysis of the spectra provided the information on kinetics of U(IV) concentration change and the reaction rates were determined. Increasing temperature, O_2 : U(IV) molar ratio or decreasing mean radius of alkali cations of the solvent melt resulted in faster decrease of U(IV) concentration in the melt.

Introduction

Alkali chloride melts have numerous potential applications in the nuclear fuel cycle including pyrochemical reprocessing of spent nuclear fuels, uranium electrowinning and electrorefining. Oxygen is a common technological impurity that can affect uranium speciation and behavior in fused salts. From the other side bubbling oxygen through molten salt electrolytes can be of practical use, for example for precipitating actinides (as oxides) or rare earth fission products (in the form of oxychlorides and oxides) from the melt. Gho et al. suggested a method for removing rare earth fission products from chloride melts by bubbling oxygen containing gaseous mixtures through the fused salt (1). Converting rare earth chlorides to oxides required temperatures in excess of 750 ^{o}C. Below this temperature rare earth chlorides are converted mostly to oxychlorides (1–4). Water can also act as a source of oxygen species and reaction of wet argon was studied with the melts containing neodymium, uranium or plutonium chlorides (5, 6).

Reaction of uranium chloride containing melts with oxygen was very little but studied. Thermodynamics of the reaction of uranium tri- and tetrachlorides with oxygen in NaCl–

KCl equimolar mixture based melts was considered by Smirnov and Skiba (7). The most probable process was the formation of uranyl chloride species. Subsequently Vavilov et al. studied the reaction of uranium tetrachloride solution in NaCl–2CsCl eutectic melt with oxygen and also detected the formation of uranyl species (8). Very little is however known on the kinetics of the reaction of solutions of uranium chlorides in molten salts with oxygen. Uranium chloride containing melts have distinct electronic absorption spectra (EAS) in the visible region and therefore electronic absorption spectroscopy can be employed to follow the course of the reaction involving U(III) or U(IV) ions, including the reaction with oxygen (9). The aim of the present work was applying high temperature electronic spectroscopy measurements for studying the reaction of solutions of uranium tetrachloride in alkali chloride based melts with gaseous oxygen and oxygen containing mixtures and determining kinetic characteristics of the reactions taking place.

Experimental

The experiments were performed in LiCl–KCl, NaCl–CsCl, and NaCl–KCl–CsCl eutectic mixtures. Commercially available anhydrous alkali metal chlorides were dried under vacuum, melted and treated with gaseous hydrogen chloride. Then the salts prepared were fused in the required proportions. Uranium(IV) containing melts were prepared by dissolving the desired amount of anhydrous uranium tetrachloride in the solvent salt melt. The procedure was performed in glassy carbon crucibles inside an argon filled glove box. Some experiments were also performed in the melts containing a mixture of uranium and neodymium chlorides. In this case melts containing neodymium chloride were prepared first (by reacting required amount of neodymium oxide with hydrogen chloride in the solvent salt melt) and then uranium tetrachloride was added.

Reaction of oxygen or oxygen containing gas mixtures with molten salts was investigated in silica cells. First, a salt mixture containing uranium chloride was melted under vacuum, then the cell was filled with argon and a desired amount of oxygen passed through the melt using a capillary tube that could be lowered into the melt or lifted up as desired. After completing the reaction a sample of the salt was taken for the chemical analysis. Similar experimental procedure was used for performing electronic absorption spectroscopy measurements. The difference was that the melt was held in 1 cm path length optical silica cells. The experimental setup employed for recording electronic absorption spectra at high temperatures was described in detail elsewhere (10). To record the spectrum passage of the gas through the melt was interrupted, any solid particles formed in the melt were allowed to settle and the spectrum was recorded. Then the gas flow was resumed.

Uranium(IV) and, when added, neodymium(III) ions exhibit characteristic EAS. Following the changes in the spectra allowed to determine changes in the concentration of the species of interest as well as to monitor possible appearance of new solutes. An example of the series of EAS recorded during bubbling oxygen through a chloride melt containing a mixture of uranium and neodymium chlorides is shown in Fig. 1.

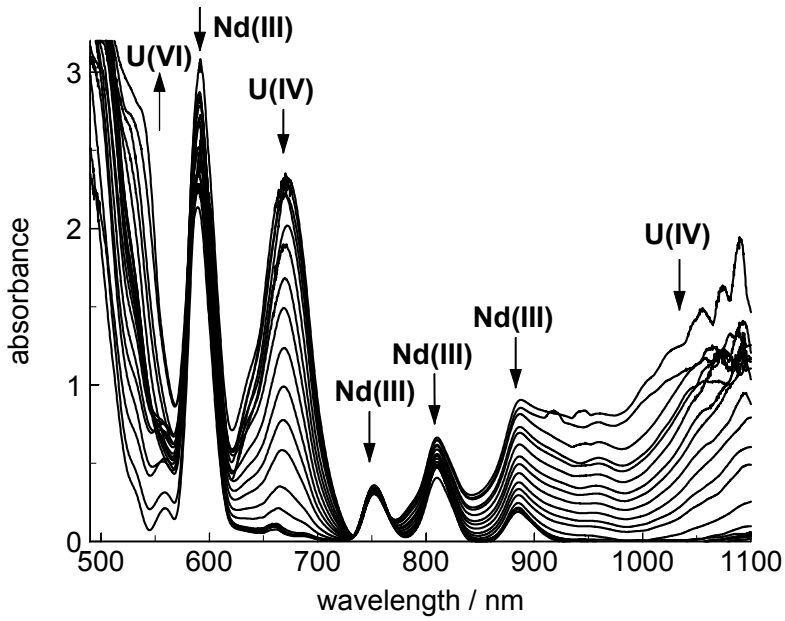

Figure 1. Spectra recorded in the course of reaction of O_2 with LiCl–KCl–UCl_4–$NdCl_3$ melt at 550 ^oC. Arrows show the direction spectra changed.

Results and Discussion

Reaction of U(IV) Containing Melts with Oxygen

In the first series of experiments the reaction of LiCl–KCl–UCl_4 melts with various amounts of oxygen was investigated. Solutions of uranium(IV) chlorides in molten LiCl–KCl eutectic have a characteristic green color. Bubbling oxygen through the melts resulted in a gradual change of the color from green to yellow, typical for uranyl chloro species. Red-ox titration was employed to assess the mean oxidation state of uranium in the melt samples and the results obtained showed that increasing amount of oxygen passed through the melt resulted in a steady increase of the mean oxidation state of uranium from four (in the initial melt) to nearly six when a large excess oxygen was used. The main reaction taking place can therefore be described by the following equation:

$$UCl_6^{2-} + O_2 = UO_2Cl_4^{2-} + Cl_2 \qquad [1]$$

In addition, a small amount of black precipitate was formed. X-ray powder diffraction analysis showed that this solid was mostly triuranium octaoxide U_3O_8. The results of this series of experiments are summarized in Table I.

In the second series of experiments the effect of cationic melt composition as well as temperature and concentration of oxygen in the gas bubbled through the melt were considered. The course of the reaction was followed by recording electronic absorption spectra. Changes in the EAS were similar in all the experiments. The intensity of the absorption bands associated with U(IV) ions gradually decreased and the low energy edge of the spectra around 550 nm gradually shifted to longer wavelengths due to increasing absorption of uranyl ions produced, Fig. 1. No evidence of formation of any

other uranium ions, e.g. in the oxidation state of +5, were obtained. The results allowed to conclude that the oxidation of U(IV) to U(VI) proceeded in one stage without any soluble intermediates formed.

TABLE I. Reaction of oxygen with LiCl–KCl–UCl_4 (3.72 wt. % U) melts.

t / °C	Total O_2 : U(IV) Molar Ratio	Fraction of U Remained in the Melt / %	Mean Oxidation State of Uranium in the Final Melt
550	5	95.7	4.40
	15	82.0	4.84
	30	85.2	5.45
	50	97.6	5.97
750	5	98.4	n/d*
	15	100	n/d
	30	83.1	n/d
	50	87.6	n/d

* n/d – not determined.

The results of the experiments are summarized in Table II. To see the effect of diluting oxygen by an inert gas two argon–oxygen mixtures were used, containing 9.62 and 0.966 % oxygen. Varying amount of oxygen in the gas did not result in any qualitative differences in the EAS recorded in the course of the reaction. Chemical analysis showed that the mean oxidation state of uranium in the melts sparged with oxygen of Ar–O_2 mixtures was between four and six reflecting various ratios of UCl_6^{2-} ions remaining and $UO_2Cl_4^{2-}$ ions formed in the melt. No formation of solid precipitates was observed in the melts not containing lithium chloride, i.e. NaCl–CsCl and NaCl–KCl–CsCl eutectics. In addition, when LiCl–KCl eutectic based melts were sparged with oxygen diluted by argon there also was no change in uranium concentration in the melt, only the oxidation state of uranium increased.

TABLE II. Reaction of oxygen and oxygen containing gas mixtures with alkali chloride melts containing uranium(IV) chloride.

Melt	*t* / °C	Gas Composition	Initial U(IV) Conc. / wt. %	Total O_2 : U(IV) Molar Ratio	Fraction of U Remained in the Melt / %	Mean Oxidation State of Uranium in the Final Melt
LiCl–KCl	450	O_2	1.843	28.6	91	5.45
	450	O_2	1.837	80.5	84	4.82
	550	O_2	1.835	63.6	100	5.26
	650	O_2	1.810	92.3	88	4.94
	750	O_2	1.834	69.0	90	5.48
	550	Ar–O_2 (9.62 %)	1.814	6.7	100	5.71
	550	Ar–O_2 (0.966 %)	1.843	0.7	100	5.61
NaCl–CsCl	550	O_2	1.616	87.7	100	n/d
	550	O_2	1.646	123.5	100	n/d
	550	O_2	2.449	43.0	100	n/d
NaCl–KCl–CsCl	550	O_2	2.427	58.6	100	n/d

* n/d – not determined.

Analysis of the experimental data showed that temperature had a relatively small effect on the process. Increasing temperature from 450 to 550 ^{o}C in LiCl–KCl based melts resulted in noticeable increase of the rate of oxidation but further increase of temperature to 650 and 750 ^{o}C did not have such pronounced effect. Diluting oxygen with argon slowed down the rate of oxidation but this slow down was apparent. If only volume of oxygen but not the entire gas mixture was taken into account, then oxidation of uranium in the melt was the fastest when the gas mixture with the lowest oxygen content was used. Increasing average cationic size of the solvent melt (from LiCl–KCl to NaCl–KCl–CsCl and then to NaCl–CsCl) resulted in some decrease of the rate of U(IV) oxidation. This can be connected with increased stability of UCl_6^{2-} ions in the melts with larger alkali cations.

Reaction of Oxygen with the Melts Containing U(IV) and Nd(III) Ions and Kinetics of U(IV) Oxidation

The results presented in Tables I and II show that under certain conditions U(IV) can be oxidized to $UO_2Cl_4^{2-}$ without precipitation of uranium oxide. From the other side, reaction of oxygen with the melts containing dissolved rare earth chlorides results in precipitation of rare earths in the form of oxychlorides and/or oxides insoluble in alkali chloride melts (1–4). Therefore sparging the melt with oxygen can be used as a possible mean of separating uranium from certain fission products, for example rare earth elements. In the last series of experiments interaction of oxygen with melts containing a mixture of uranium and neodymium chlorides was investigated. The course of the reaction was followed by recording EAS at certain points of time.

Uranium(IV) concentration in the melt could be followed using the absorption peak around 670 nm. Monitoring neodymium concentration was more difficult since most of neodymium(III) absorption bands experience interference from the neighboring uranium(IV) bands. At present the intensity of the peak around 750 nm with the minimum overlap with uranium(IV) bands was selected to assess changes in Nd(III) concentration. Fig. 2 shows some examples of the time dependencies of uranium(IV) and neodymium(III) concentrations obtained after analyzing the sets of EAS recorded during bubbling oxygen through the melts. The results of this series of experiments are summarized in Table III.

Bubbling oxygen through the melt containing uranium and neodymium chlorides first resulted in oxidation of uranium(IV) to uranyl ions, Fig. 2. Increasing temperature (Fig. 2 (a–c)) resulted in increasing rate of oxidation. Increasing mean radius of the solvent salt cation, i.e. changing from LiCl–KCl to NaCl–CsCl melts at a constant temperature (Fig. 2 (c and d)) led to decreasing reaction rates. Continued oxygen bubbling then resulted in precipitation of neodymium. However uranium could also be partially precipitated. In some cases (LiCl–KCl melts, 450 and 550 ^{o}C, Table III) up to 20 % neodymium could be precipitated with all uranium remaining in the soluble form in the melt. Similar to the results obtained in the melts without neodymium chloride, increasing temperature and amount of oxygen passed through the melt resulted in an increased degree of uranium precipitation.

TABLE III. Reaction of oxygen a with alkali chloride melts containing mixture of uranium(IV) and neodymium(III) chlorides.

t / °C	Initial Concentration / wt. %		Molar Ratio			Fraction Remained in the Melt / %	
	U	Nd	O_2 : U(IV)	O_2 : Nd(III)	O_2 : (U(IV)+Nd(III))	U	Nd
LiCl–KCl based melts							
450	1.562	0.713	781	1036	445	100	83
550	1.567	0.715	903	1198	515	100	79
550	3.701	1.690	222	295	127	93	91
650	1.535	0.701	513	681	293	34	9
650	3.680	1.680	173	229	98	90	51
550*	1.480	0.675	6	8	3	100	100
NaCl–CsCl based melts							
650	1.504	0.536	534	892	330	67	61

* Ar–O_2 (0.966 %) gas mixture was used instead of pure oxygen.

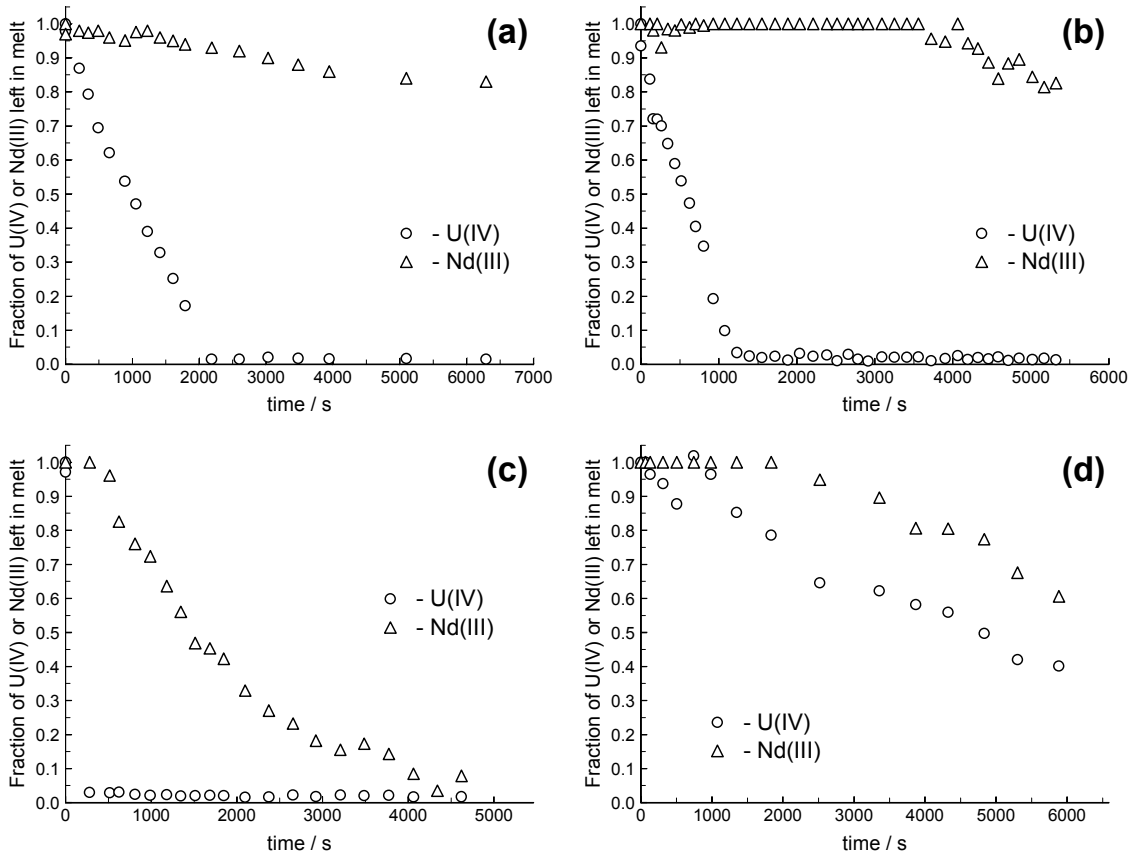

Figure 2. Change of fraction of U(IV) and Nd(III) remaining in the melt in the course of reaction of oxygen with LiCl–KCl–UCl_4–$NdCl_3$ (a–c) and NaCl–CsCl–UCl_4–$NdCl_3$ (d) melts at 450 °C (a), 550 °C (b) and 650 °C (c, d). Initial uranium concentration, wt. %: 1.562 (a); 1.567 (b); 1.535 (c); 1.504 (d). For other experimental conditions cf. Table III.

Since oxygen was taken in the large excess, the rate of reaction [1] in respect to uranium(IV) chloride could be determined. The results obtained are listed in Table IV. Expectedly the reaction rate increased with temperature and, in agreement with previous

observations, decreased with increasing the mean radius of the alkali metal cation of the solvent salt. The reaction rate constants were calculated assuming the first order of reaction [1] in respect to uranium(IV) chloride concentration.

TABLE IV. Kinetic parameters of reaction [1] in MCl– UCl_4–$NdCl_3$ melts.

Melt	t / °C	Gas Composition	Initial U(IV) Conc. / mol/l	Reaction Rate / mol/(l s)	Reaction Rate Constant / s^{-1}
LiCl–KCl	450	O_2	0.0976	$4.31 \cdot 10^{-5}$	$4.42 \cdot 10^{-4}$
	550	O_2	0.0959	$7.12 \cdot 10^{-5}$	$7.42 \cdot 10^{-4}$
	550	Ar–O_2 (0.966 %)	0.0906	$6.37 \cdot 10^{-5}$	$7.03 \cdot 10^{-4}$
	650	O_2	0.0920	$3.12 \cdot 10^{-4}$	$3.39 \cdot 10^{-3}$
NaCl–CsCl	650	O_2	0.1557	$1.64 \cdot 10^{-5}$	$1.05 \cdot 10^{-4}$

The activation energy of reaction [1] could be estimated using Arrhenius plot. For LiCl–KCl–UCl_4–$NdCl_3$ melt the activation energy value thus found was ca. 54 kJ/mol.

Conclusions

The reaction of solutions of uranium tetrachloride in alkali chloride melts with oxygen and argon–oxygen mixtures results in oxidation of uranium(IV) ions to uranyl ions and possible partial precipitation of uranium in form of U_3O_8. Uranium(IV) ions react with oxygen much more readily than rare earth (neodymium) chloro-ions.

Kinetic parameters of U(IV) oxidation reaction were determined. The rate of the reaction increases with temperature or decreasing the mean radius of the solvent salt cations.

References

1. Y.-J. Cho, H.-C. Yang, H.-C. Eun, E.-H. Kim and I.-T. Kim, *J. Nucl. Sci. Techn*., **43**, 1280 (2006).
2. Y.-J. Cho, H.-C. Yang, H.-C. Eun, E.-H. Kim and J.-H. Kim, *J. Ind. Eng. Chem.*, **11**, 707 (2005).
3. H.C. Eun, Y.Z. Cho, H.S. Park, T.K. Lee, I.T. Kim, K.I. Park and H.S. Lee, *J. Nucl. Mat.*, **408**, 110 (2011).
4. A. V. Shchetinskiy, A. S. Dedyukhin, V. A. Volkovich, R. Yu. Kaychenkova, D. S. Maltsev, I. B. Polovov and A. V. Chukin, *ECS Trans.*, **86**(14), 341 (2018).
5. J.-F. Vigier, A. Laplace, C. Renard, M. Miguirditchian and F. Abraham, *J. Nucl. Mat.*, **474**, 19 (2016).
6. J.-F. Vigier, A. Laplace, C. Renard, M. Miguirditchian and F. Abraham, *J. Nucl. Mat*., **499**, 394 (2018).
7. M. V. Smirnov and O. V. Skiba, M*emoirs Institute Electrochemistry UBAS USSR*, **4**, 3 (1963) (in Russian).
8. S. K. Vavilov, G. N. Kazantsev and T. I. Sabanova, *Kinetics of the Reaction of Oxidation of Uranium(IV) by Oxygen in NaCl–2CsCl Melt*. Technical Report NIIAR-35(394), p. 6, NIIAR, Dimitrovgrad (1976) (in Russian).

9. A. A. Kozlova, A. A. Ryzhov, A. B. Ivanov, D. S. Maltsev, A. V. Shchetinskiy, A. V. Novoselova and V. A. Volkovich, *AIP Conf. Proc.*, **2174**, 020034 (2019).
10. V. A. Volkovich, I. May, J. M. Charnock and B. Lewin, *Phys. Chem. Chem. Phys.*, **4**, 5753 (2002).

ECS Transactions, 98 (10) 373-381 (2020)
10.1149/09810.0373ecst ©The Electrochemical Society

Corrosion of Ceramic and Carbon-Based Materials in FLiNaK

I. B. Polovov[a], A. V. Abramov[b], R. R. Alimgulov[a], D. A. Zolotarev[a], A. F. Gibadullina[a], A. I. Trubcheninova[b], V. A. Volkovich[a], V. A. Khotinov[c], A. Y. Zhilyakov[c], and S. V. Belikov[c]

[a] Department of Rare Metals and Nanomaterials, Ural Federal University, Ekaterinburg, 620002, Russia
[b] Department of Physical and Chemical Methods of Analysis, Ural Federal University, Ekaterinburg, 620002, Russia
[c] Department of Heat Treatment and Physics of Metals, Ural Federal University, Ekaterinburg, 620002, Russia

Corrosion resistance of ceramic and carbon materials was studied in molten salt systems based on LiF–NaF–KF mixture in the temperature range 550–750 °C. The rates of corrosion of silicon nitride, boron nitride, carbon-carbon composites and high density graphite in the fluoride electrolyte were determined. The mechanisms of materials degradation after the contact with molten FLiNaK are proposed, and the effect of the salt media and the temperature on the mechanical properties of ceramic and carbon materials is considered.

Introduction

Molten salt nuclear fast neutron reactor (MSNFR) is one of the prospective designs in frame of Generation IV concept. This technology is also required for reprocessing of spent nuclear fuels (SNFs) in molten salts to extract valuable components. Recycling SNFs consists of extraction uranium and plutonium with the disposal of minor actinides and fission products. These stages need the materials that retain their corrosion and mechanical properties for prolonged time under the influence of high temperatures, radiation fields and contact with molten salts. Various steels and alloys were widely studied to assess their use under such extreme conditions. Alternative materials include ceramics, composite and carbon-based materials, which have high corrosion resistance in various media and can be used up to 1000 °C.

Oxygen-free ceramics (for example, SiC and Si_3N_4) and composites based on these materials are now widely used for high-temperature applications, including fluoride melts media (1–3). Such ceramics have the following advantages: excellent oxidation resistance, relatively high strength at temperatures up to 1400 °C, sufficient thermal shock resistance, and low density. In addition, these materials are corrosion resistant in many corrosive environments (1, 4). The main mechanism of degradation of oxygen-free ceramics in fluoride melts involves interaction of these materials with oxygen, that leads to the transformation of oxygen-free ceramics to oxide species with their subsequent dissolution in fluoride salts (5–7). For this reason, oxide-based ceramics are not promising material in terms of their application in contact with fluoride melts.

Carbon-based materials are widely used in fluoride melts as electrodes and construction materials (8–10). These materials perform well in these environments. Carbon-carbon composite materials are also widely employed. Carbon-carbon composite (C/C) consists of carbon fiber filled with a composite carbon matrix. C/C possesses high corrosion resistance in various aggressive media and retains high strength at temperatures up to 2000 °C. A slip coating saturated with pyrocarbon is formed on the surface of this type of material during its manufacture. This coating reduces the pore size and seals the surface of the samples, eliminating the permeability of the walls to various gaseous and liquid media. Carbon-carbon materials are chemically stable in molten salts, acids and alkalis. Their thermo-oxidative resistance is maintained up to 850–1000 °C which is higher than graphite (550–700 °C). Graphite has a crystalline structure that allows reagents in C/C to penetrate between hexagonal layers of graphite. This leads to a weakening of the cross C-C bonds and following separation of layers from the main body (4, 11). C/C has a turbostratic structure and does not form interstitial compounds; therefore, its chemical resistance is significantly higher than that of graphite.

Experimental

A number of oxygen-free materials were selected for the present study. They included silicon and boron nitrides, carbon-carbon composite materials and high purity graphite. Samples of silicon nitride Si_3N_4 were of cylindrical shape, 10 mm diameter and 10 mm height. Silicon nitride was produced by sintering under pressure in an inert atmosphere. The sintering additive was Al_2O_3. The density of the samples was 3.2–3.4 g/cm^3. The porosity of the material did not exceed 1 %; the samples had no open porosity. The grain size of Si_3N_4 was 1–15 μm. Boron nitride samples were prepared by hot pressing. Initially, boron nitride was pressed in a graphite mold with a pressure of 50 kg/cm^2 at the room temperature. Then, BN was hot pressed in a nitrogen flow at 1700 °C with a force of 50 kN and holding for 30 min. In addition to boron nitride, this ceramic contains 3 wt. % boron oxide.

Samples C/C were made of a cubic shape with a rib length of 10 mm. The open porosity of the samples did not exceed 6 %. High-density GS-1900 graphite is a fine-grained graphite obtained at high pressure and temperature by isostatic pressing. This material is characterized by low gas permeability, porosity and homogeneity, as well as high strength and heat resistance, which makes possible to use it at high temperatures in molten salts, acids, alkalis. Samples of high-density GS-1900 graphite had cylindrical shape with a diameter of 10 mm and a height of 8 mm. The open porosity of the samples did not exceed 10 %.

Anhydrous lithium, potassium and sodium fluorides (purity> 99 wt. %, Aldrich, ACS) were used for the corrosion tests. Potassium fluoride was dried in a vacuum drying oven for 20 h at 60 °C, then for 20 h at 200 °C and 20 h at 400 °C. Then, the salt was transferred to an inert box. Sodium fluoride and lithium fluoride were dried for 12 h at 400 °C in a vacuum drying oven. Then, each salt was melted at 950 °C and kept for 3 hours under vacuum. The prepared individual salts were fused in an inert box in a molar ratio LiF: NaF: KF = 46.5: 11.5: 42 (mass ratio LiF: NaF: KF = 29:12:59), then kept in a high purity argon atmosphere for 2 hours to homogenize the melt. The melt prepared in this way was cooled and stored in an inert box. The resulting FLiNaK salt was analyzed

by XRF (ARL Advant'X 4200) to determine the content of impurities and by CGHE (Horiba EMGA-620W/C) to determine the oxygen content.

The corrosion tests were carried out on an original complex for the study of corrosion (12). This equipment allows performing long-term corrosion tests in molten salts in a stream of various gases and gas mixtures. Corrosion experiments were carried out as follows. A glassy carbon crucible with three samples and salt was placed in a steel cell (the complex includes five such cells). Each cell was sealed, evacuated, filled with argon and placed in an furnace. The melt in the cell was under the atmosphere of high purity argon (argon content 99.9998 vol. %). Samples were held in the melts at 550, 650, and 750 °C. The duration of the corrosion tests was 100 h. After the experiment, the cells were cooled to the room temperature, and the crucibles with the ceramic samples were taken out. The samples were thoroughly washed and dried. After the experiment, the salt was transferred into an inert box, crushed, and analyzed to determine the content of the corrosion products. The corrosion rate of each sample was calculated from the mass loss and independently determined from the content of corrosion products in the salts. The surface of the corroded samples was examined by scanning electronic microscopy (JEOL JSM 6490), energy dispersive X-ray microanalysis (Oxford Inca) and XRD analysis (PANalytical X'PERT PRO MPD).

Results and Discussion

Corrosion rates of Ceramic and Carbon-Based Materials in FLiNaK

Gravimetric tests of oxygen-free ceramics and carbon-based materials were carried out in FLiNaK at 550, 650 and 750 °C. Table I shows the corrosion rates of samples of the test materials after 100 h of exposure in FLiNaK, depending on the test temperature.

TABLE I. Corrosion rate of samples of ceramic and carbon-based materials after 100 h in FLiNaK, mm/year.

Temperature, °C	550	650	750
C/C	0.09 ± 0.01	0.08 ± 0.02	0.09 ± 0.02
GS-1900	0.15 ± 0.03	0.14 ± 0.02	0.17 ± 0.02
Si_3N_4	0.8 ± 0.1	1.1 ± 0.1	2.5 ± 0.2
BN	1.0 ± 0.1	2.1 ± 0.2	5.3 ± 0.3

From all the investigated materials C/C samples had the lowest corrosion rates in FLiNaK (Table 1). The corrosion rate of samples of this material did not exceed 0.09 mm/year, that allows to declare C/C as a promising structural material for fluoride melts. The corrosion rate of C/C samples did not depend on the corrosion test temperature. C/C is resistant to oxygen up to 850-1000 °C (4). These facts indirectly indicate that C/C materials do not react chemically with molten fluorides (9, 10). The mechanism of their degradation has different nature.

The corrosion rate of the GS-1900 samples in FLiNaK was about 1.5 times higher than the corrosion rate of the C/C samples. GS-1900 samples can interact with residual oxygen from the gas phase or dissolved in molten salt. It is also known that porous carbon-based materials are prone to swelling in molten salt and can break mechanically during thermal cycling.

The corrosion rates of nitride ceramics in FLiNaK was extremely high (more than 1 mm/year) and increased with increasing temperature. This fact indicates that these materials chemically interact with fluoride melts, because the rate of the chemical reaction accelerates with temperature increase.

The Mechanism of the Ceramic and Carbon-Based Materials Degradation in FLiNaK

To determine the nature of the degradation of ceramic and carbon-based materials, their surface was examined after the exposure to fluoride melts by the SEM. Figs. 1 and 2 show the images of the surface and cross-sections of C/C and GS-1900 samples after exposure in FLiNaK at 550, 650 and 750 °C.

The structure of the C/C samples was porous, the pore shape was round and slit-like, the average linear pore size was about 50–150 μm. The porosity was lower on the surface of the samples compared to the bulk of the samples. The surface of the samples was uniform, did not have noticeable damage. The salt traces were found only on the surface of the samples. The surface of C/C samples after corrosion experiments was studied by XRD. No compounds other than carbon were found on the surface. These facts indicate that the rate of corrosion of C/C was not determined by the chemical interaction of carbon with FLiNaK melt. More probably the degradation was caused by mechanical destruction of the surface during the crystallization of salt and its subsequent separation from the samples (11).

The structure of GS-1900 samples was also porous, the pores were located mainly along the grain boundaries of graphite and had a chain structure. The average pore size was about 5–15 microns. The surface of the GS-1900 samples had no corrosion damage. The increase of the graphite GS-1900 corrosion rate in comparison with C/C was probably due to the oxidation of graphite by the residual amount of oxygen that could be present in the gaseous atmosphere and purified salt. The main product of this reaction was carbon dioxide. Therefore, corrosion products could not be detected on the sample surface or in the melt. Also, corrosion of this material could occur as a result of mechanical destruction of the surface during crystallization and exfoliation of salts (11).

Fig. 3 shows images of thin sections of boron nitride and silicon nitride samples after corrosion tests in FLiNaK at 550, 650 and 750 °C. Both materials had extremely low porosity because they were hot-pressed. However, the surface of the nitride ceramic samples was damaged. The nature of the destruction of the surface was uniform. The depth of corrosion penetration in boron nitride increased with increasing temperature from 8–10 to 15–20 microns. In silicon nitride, the penetration depth of corrosion increased from 10–12 to 25–30 microns.

The EDS analysis of the surface of the nitride ceramic samples showed that a significant amount of oxygen was present in the destroyed layers. Modeling of thermodynamically possible processes using the HSC 6.12 software indicated that the interaction of fluoride salts with nitride ceramics was unlikely in an inert atmosphere, but these processes were possible in the presence of oxygen. The investigated silicon nitride contained a sintering additive of aluminium oxide, and boron nitride contained boron oxide (3 %). Most likely, these oxide components interacted with fluoride salts and

dissolved forming silicates or fluorosilicates. This led to the destruction of the entire surface of the samples. Also, impurities in molten salt such as O and H_2O play an important role in the corrosion of BN and Si_3N_4. Oxygen and H_2O can react with BN and Si_3N_4 to form oxides:

$$4BN + 3O_2 \rightarrow 2B_2O_3 + 2N_2, \quad [1]$$
$$Si_3N_4 + 3O_2 \rightarrow 3SiO_2 + 2N_2. \quad [2]$$

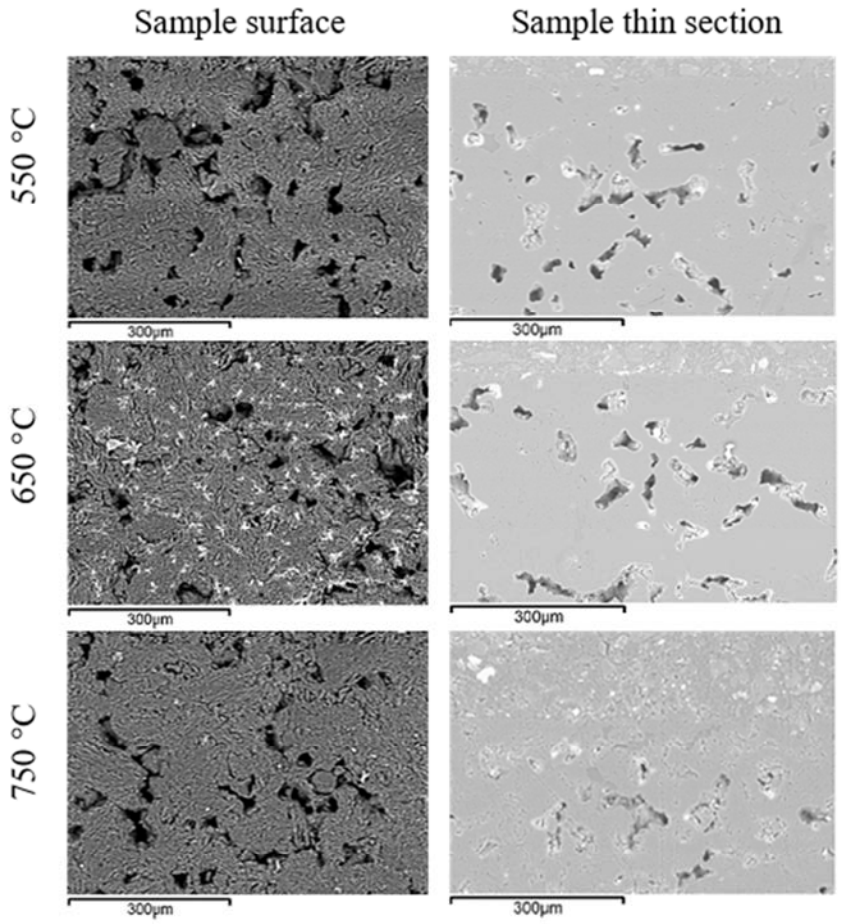

Figure 1. Surface and thin sections of C/C samples after 100 h in FLiNaK at 550, 650 and 750 °C.

Therefore, BN and Si_3N_4 can be etched by molten salt after oxidation (5). For example, oxides of silicon species may react with molten FLiNaK salt forming SiF_4, K_2SiF_6, Na_2SiF_6, $[SiO_4]^{4-}$, $[Si_2O_5]^{2-}$, $[SiO_3F]^{3-}$, $[SiO_2F_2]^{2-}$, and $Si_4O_7F_2$ (6, 7). Thus, it is extremely important that the nitride ceramics for fluoride molten salts are oxygen-free, that is, all sintering additives should also be free of oxygen.

The samples of ceramic and carbon-based materials were tested for compression in accordance with ISO 20504:2019 using the Instron 3382 tensile testing machine at a gripping speed of 2 mm/min. During the tests, two types of samples were used: cylindrical (height – 10 mm, diameter – 8 mm) and prismatic (height – 10 mm, side –

5 mm). Mechanical characteristics of ceramic and carbon-based materials before and after corrosion tests are given in Table II, compression curves are shown in Fig. 4.

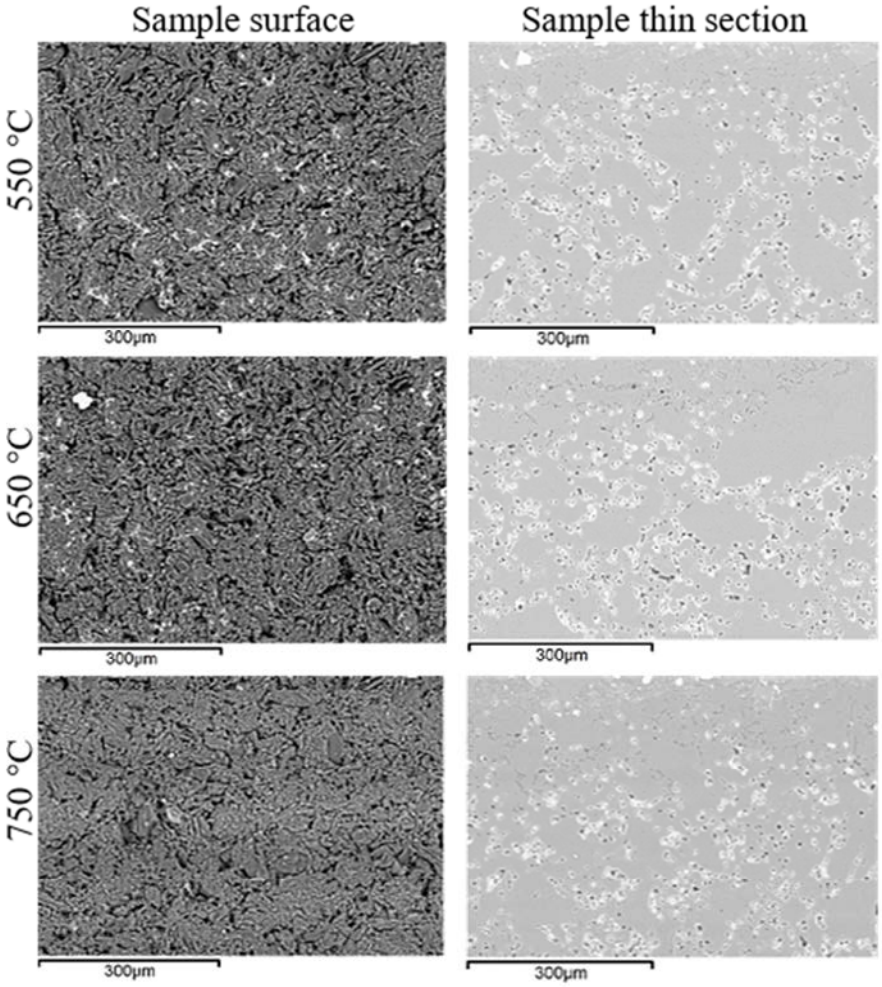

Figure 2. Surface and thin sections of graphite GS-1900 samples after 100 h in FLiNaK at 550, 650 and 750 °C.

The specimens after testing in corrosive environments (FLiNaK) showed a decrease in ultimate compressive strength (CS). Apparently, it was caused by the appearance of mechanical inhomogeneities (surface defects) on the surface of the samples after interaction with molten salts; such defects acting as microconcentrators of stresses. Also, these stresses can arise as a result of salt crystallization inside porous materials. These propositions allow explaining the decrease in plasticity after contact with melts; in the initial state, the compositions BN, GS-1900, and C–C showed little plasticity (ε = 0.6–2.2 %), and after contact with molten salt, it decreased by 30–50 %. GS-1900 has the best mechanical properties after exposure to molten salts among the materials studied. However one should see that the strength properties of most ceramic and carbon materials are significantly inferior to metallic materials. The exception is silicon nitride, which has a very high strength (Table II). However, Si_3N_4 is a completely non-plastic material.

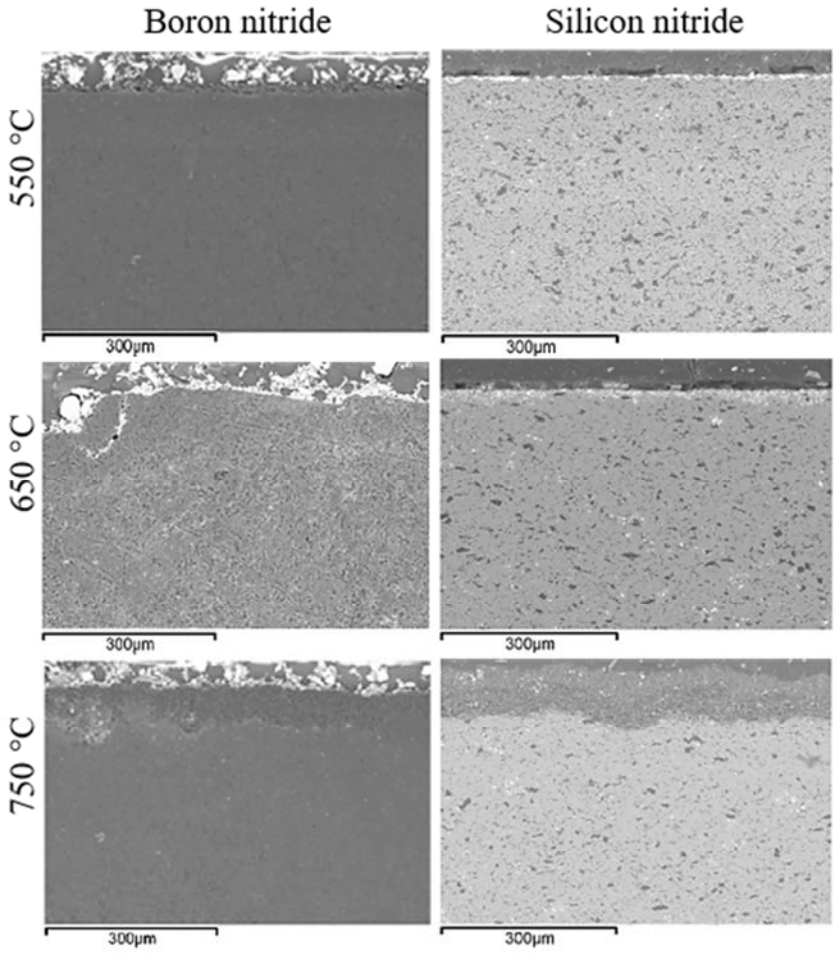

Figure 3. Thin sections of boron nitride and silicon nitride samples after 100 h in FLiNaK at 550, 650 and 750 °C.

TABLE II. Mechanical properties of ceramic and carbon materials after compression tests.

Material	YS, MPa	CS, MPa	ε, %
BN (the initial state)	34.5	37.0	0.6
BN (after FLiNaK)	24.0	25.0	0.3
GS-1900 (the initial state)	45.0	61.5	2.2
GS-1900 (after FLiNaK)	44.0	61.0	1.8
C/C (the initial state)	77.5	88.5	0.8
C/C (after FLiNaK)	38.0	43.0	1.1
Si_3N_4 (the initial state)	3184	3184	0
Si_3N_4 (after FLiNaK)	2161	2161	0

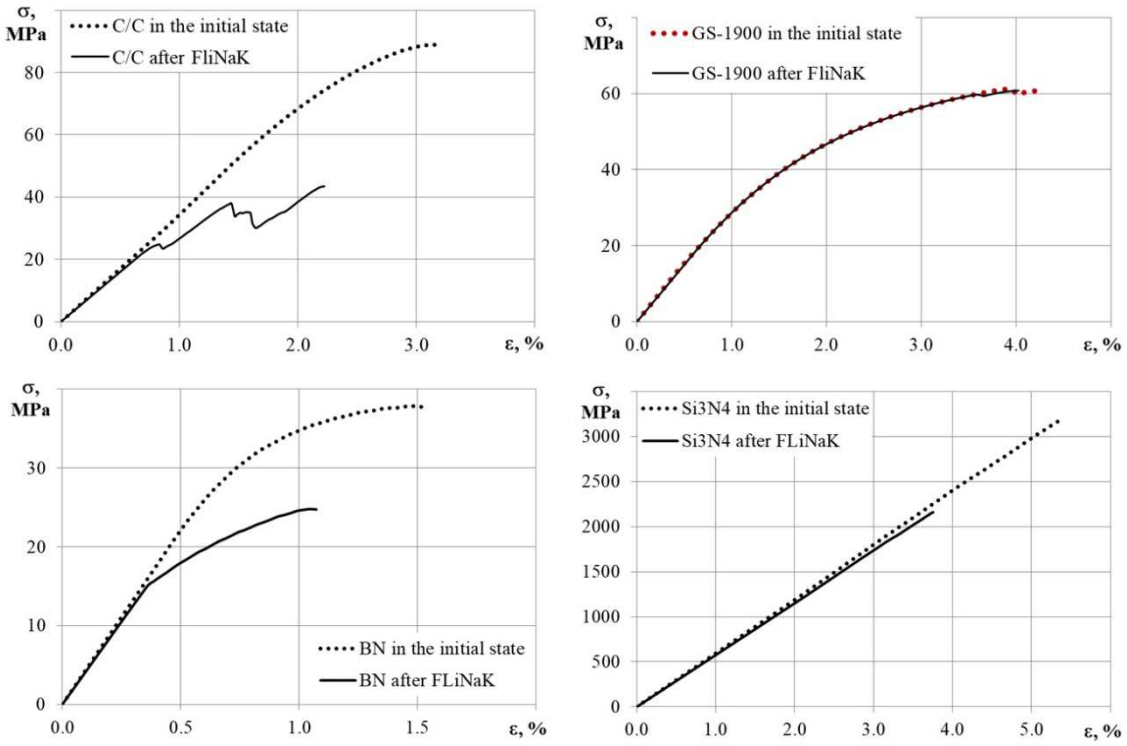

Figure 4. Diagrams of compression deformation of samples of the studied materials before and after interaction with FLiNaK.

Conclusions

Corrosion and mechanical properties of nitride ceramics (Si_3N_4 and BN) and carbon-based materials (carbon-carbon composite material (C/C) and high-density carbon) were studied in a molten mixture of lithium, sodium, and potassium fluorides (FLiNaK) in the temperature range of 550–750 °C under inert atmosphere.

It was found that carbon-containing materials (C/C and high-density carbon) showed high corrosion resistance in the melt. C/C samples had lower corrosion rates (less than 0.1 mm/year in the entire temperature range), while the high-density carbon showed better mechanical properties. The main disadvantage of these materials is their porosity, which leads to the impregnation of materials with molten salt and subsequent mechanical destruction during thermal cycling. However, C/C composite and high-density carbon could be the promising structural materials for the salt media based on FLiNaK in the selected temperature range.

The tested nitride ceramics (BN and Si_3N_4) demonstrated relatively low corrosion resistance in fluoride systems compare to carbon-containing and metallic materials. The corrosion rates of these materials in FLiNaK exceeded the value of 1 mm/year. It was found that for the effective use of nitride ceramics, the oxygen reduction in the composition of the ceramics and in a saline environment is required. The plastic properties of nitride ceramics were also poor. The possible application of such materials for MSNFR and SNF reprocessing is under further investigation.

Acknowledgements

This study was financially supported by the State Corporation "Rosatom" (Contract No. Н.4щ.241.09.20.1101).

References

1. N. S. Jacobson, J. L. Smialek, and D. S. Fox, *Molten salt corrosion of SiC and Si_3N_4*, NASA-TM-101346, p. 68, NASA, US (1988).
2. J. Schmidt, M. Scheiffele, M. Crippa, P. F. Peterson, E. Urquiza, K. Sridharan, L. C. Olson, M. H. Anderson, T. R. Allen and Y. Chen, *Int. J. Appl. Ceram. Technol.* **8**, 1073 (2011)
3. J. Xi, H. Jiang, C. Liu, D. Morgan and I. Szlufarska, *Corros. Sci.*, **146**, 1 (2019).
4. V. I. Kostikov and A. N. Varenkov, *Ultra-high temperature composite materials*, p. 560, Inzhiniring, Moscow, (2003) *(In Russian)*.
5. G. L. Harris, *Properties of silicon carbide*, p. 304, Institution of Electrical Engineers, London, (1995).
6. Yu. P. Zaykov, A. V. Isakov, I. D. Zakiryanova, O. G. Reznitskikh, O. V. Chemezov and A. A. Redkin, *J. Phys. Chem. B*, **118** (6), 1584 (2014).
7. B. O. Mysen and D. Virgo, *Phys. Chem. Miner.*, **12**, 77 (1985).
8. K. Grjotheim and M. Krohn, *Aluminium Electrolysis: Fundamentals of the Hall-Heroult Process*, p. 360, Aluminium Verlag Marketing & Kommunikation, Germany, (2002).
9. L. C. Olson, J.W. Ambrosek, K. Sridharan, M. H. Anderson and T. R. Allen, *J. Fluor. Chem.,* **130**(1), 67 (2009).
10. R. S. Sellers, W.-J. Cheng, B. C. Kelleher, M. H. Anderson, K. Sridharan, C.-J. Wang and T. R. Allen, *Nucl. Technol.*, **188(**2), 192 (2014).
11. A. R. Kamali and D. J. Fray, *Carbon*, **56**, 121 (2013).
12. I. B. Polovov, A. V. Abramov, A. F. Gibadullina, R. R. Alimgulov, V. V. Karpov, A. Yu. Zhilyakov, V.A. Khotinov and S. V. Belikov, *J. Alloys Compd.*, **810**, 151758 (2019).

Chapter 9

L02 – Tuesday Poster Session

ECS Transactions, 98 (10) 385-392 (2020)
10.1149/09810.0385ecst ©The Electrochemical Society

Influence of Physicochemical Properties on Gas Transport Properties of Silver-containing Ionic Liquid Mixtures for Olefin/Paraffin Membrane Separation

Sejoon Park, Benny Freeman, and Joan F. Brennecke

McKetta Department of Chemical Engineering, The University of Texas at Austin, Austin, Texas 78712, USA

Physicochemical properties, including viscosity and density, of silver salt-containing ionic liquids were measured and used to rationalize the permeability of ethane, ethylene, and helium through supported ionic liquid membranes (SILMs). Mixtures investigated included 1-hexyl-3-methylimidazolium bis(trifluoromethyl-sulfonyl)imide ([hmim][Tf_2N]) and 1-hexyl-3-methylimidazolium nitrate ([hmim][NO_3]) and their corresponding silver salts. The gas transport properties were very different for the two different ionic liquid/silver salt mixtures, consistent with very different behavior of viscosity and density upon silver salt dissolution. The distinctive dependence of both viscosity and density on temperature and silver salt concentration suggests different inter-ion interactions and molecular arrangements in the two ionic liquids. Free volume and physical/chemical interactions between the anion and the gas solutes are critical in determining gas permeabilities.

Introduction

Olefin/paraffin separation by cryogenic distillation is one of the most energy-intensive processes, not only within the chemical industry, but also among all human activities. Specifically, the purification of propylene and ethylene accounts for 0.3% of global energy use (1). Membrane separation is an attractive alternative, owing to its high energy-efficiency compared to conventional distillation processes. Many kinds of membrane materials, such as carbon (2-6), polymer composites (7, 8), and metal-organic frameworks (MOFs), have been utilized for olefin/paraffin membrane separation (9-11). Among them, liquid membranes that utilize gas transport through the liquid phase confined in the pore structures have shown promising performance due to faster transport than that of solid membrane materials (12-14). In liquid membranes, the liquid phase is physically held in membrane pores by capillary forces. In addition to physical stability, chemical and thermal stabilities of the liquid phase material are needed for stable long-term separation performance. In that sense, ionic liquids (ILs) are a suitable material because they have the potential to provide stable separation performance, owing to their extremely low vapor pressure, and good thermal/chemical stability. Moreover, the limitless tunability of ionic liquids can be manipulated to enhance molecular interaction with target gas molecules and thus yield better gas solubility. For olefin/paraffin separation, silver ions can be added to further improve olefin solubility (15-18). The silver ions can form complexes with olefin molecules via interaction between the double bonds of olefins and the orbitals of silver ions (19). Thus, understanding the interactions between ionic liquids and silver salts is essential for designing liquid membrane systems with improved separation performance.

Here, we report the physiochemical properties of silver ion-containing ionic liquid mixtures with two different anions and their gas transport properties when used in supported ionic liquid membranes (SILMs). Two ionic liquids, 1-hexyl-3-methylimidazolium bis(trifluoromethylsulfonyl)imide ([hmim][Tf_2N]) and 1-hexyl-3-methylimidazolium nitrate ([hmim][NO_3]), were studied, and their chemical structures are shown in Table 1. Silver bis(trifluoromethylsulfonyl)imide ($AgTf_2N$) and silver nitrate ($AgNO_3$), silver salts with the same anion as each ionic liquid, were added to the ILs to study the effect of the silver ion addition on IL mixtures. We measured densities and viscosities of silver-containing IL mixtures at five different silver ion concentrations for each IL. In addition, we determined pure gas permeabilities of ethane, ethylene, and helium in SILMs, using an Anopore disc as support, with pure ILs and 1M Ag^+ IL mixtures.

TABLE I. Chemical structures of ionic liquids in this study.

Abbreviation	Chemical Structure	Molecular Weight (g/mol)
[hmim][Tf_2N]	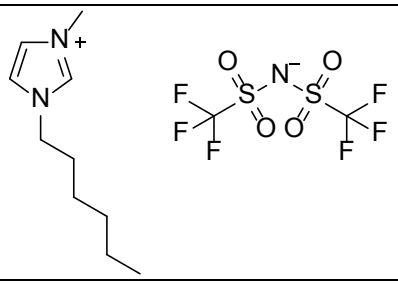	447.4
[hmim][NO_3]	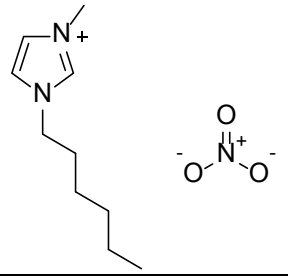	229.3

Experimental

Ionic Liquid Synthesis

Both ILs used in this work were synthesized in our laboratory. The synthesis method has been reported in previous work (23). Silver nitrate was purchased from Alfa Aesar. Silver bis(trifluoromethylsulfonyl)imide was synthesized in our laboratory.

Mixture Preparation

Five IL mixtures at five different Ag^+ concentrations were prepared for each anion by combining the salt and IL at a certain weight ratio. The weight ratios corresponding to the five molar concentrations considered were determined by dissolving 0.25 mmol, 0.5 mmol, 0.75 mmol and 1 mmol of silver salt with IL in separate 1-ml amber volumetric flasks. The determined weight ratios of silver salt to ionic liquid were used to prepare the mixtures on a larger scale to meet the volume required for the measurements. All mixtures were

prepared in amber vials to mitigate reduction of silver ions from Ag^+ to Ag^0 by ambient light. The vials were additionally wrapped with aluminum foil and stored in the desiccator.

Viscosity/Density Measurement

The density and the viscosity measurements were conducted using a DMA 4500 Anton Paar oscillating U-tube densitometer and a Lovis 2000 M/ME Anton Paar rolling-ball viscometer. The temperature was varied from 20 °C to 50 °C with an interval of 5 °C. The uncertainties in the measurements are estimated as ±0.0001 g/cm^3 for density and ± 0.5% for viscosity.

SILM Preparation and Gas Permeation

Two concentrations (0 M and 1 M Ag^+) for two anion conditions were used to prepare SILMs. Multiple droplets of the prepared mixtures were dropped on both sides of the porous supports (Whatman Anodisc inorganic filter membrane, dia. 13 mm, pore size 0.02 μm, thickness 60 μm). Full wetting was confirmed by checking the consistency of the weight difference before and after wetting. The wetted samples were attached to a brass disc with epoxy. A piece of porous polytetrafluoroethylene filter was placed on the underside of the SILM for mechanical support. The gas permeating area for gas permeation was imaged by a scanner and calculated using image-processing software.

Pure gas permeabilities of the SILMs were measured using a constant-volume, variable pressure gas permeator. Initially, the permeator was evacuated until the vacuum level of both upstream and downstream volumes was below 30 mTorr. After evacuation, a leak test on the downstream volume was performed for 1 hour to take into account the underlying leak rate of the instrument. All measurements were carried out at 35 °C, and the upstream pressure ranged between 10 and 30 psia. The rate of increase of the downstream pressure was measured at a given upstream pressure when steady-state was achieved. The gas permeabilities were calculated as follows (24):

$$P_{app} = \frac{V_d l}{p_1 ART}\left[\left(\frac{dp_2}{dt}\right)_{SS} - \left(\frac{dp_2}{dt}\right)_{leak}\right] \quad [1]$$

where P_{app} is the apparent permeability, V_d is the downstream volume, l is the membrane thickness, A is the gas permeating area, R is the gas constant, T is the temperature, p_1 is the upstream pressure, $(dp_2/dt)_{ss}$ is the steady-state rate of the downstream pressure rise, and $(dp_2/dt)_{leak}$ is the leak rate of the downstream volume. The estimated uncertainty in the permeability measurements is 2~4%.

Results and Discussion

Figure 1 presents the densities of silver-containing mixtures with five different silver ion molar concentrations. For ILs with both anions, addition of silver salt increased mixture density, due primarily to the presence of the heavier silver ions in the silver salts. The densities of both ILs and their mixtures with silver salts decreased linearly with increasing temperature, due to the thermal expansion of the mixtures. The densities of the IL and IL mixtures with Tf_2N^- anions are greater and increase more upon silver salt addition than do

the equivalent IL and IL mixtures with NO_3^- anions, due to the presence of the heavy fluorine atoms. The molar volumes of the mixtures were calculated by converting the density results using the weight ratios of IL and silver salt and the molecular weights. All the IL mixtures with Tf_2N^- anions have larger molar volumes than any of the IL mixtures with NO_3^- anions.

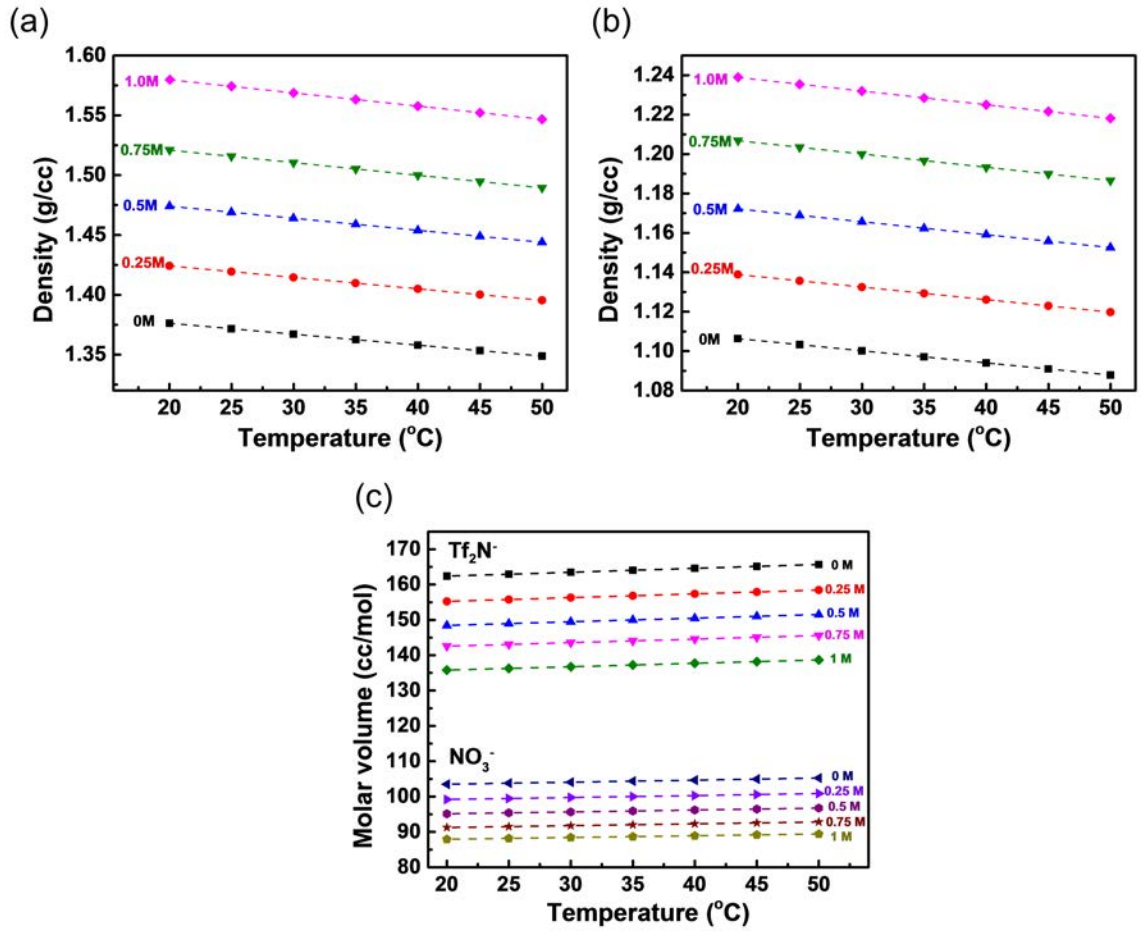

Figure 1. Densities of silver containing ionic liquid mixtures with (a) Tf_2N^- anions and (b) NO_3^- anions, as a function of silver salt concentration and temperature. (c) Calculated molar volumes of the silver-containing ionic liquid mixtures.

As shown in Figure 2, the viscosities of both ILs increased with increasing silver salt concentration. However, silver salt addition resulted in a significant increase in viscosity for the IL mixtures with Tf_2N^- anions, but only a very small increase in viscosity for the IL mixtures with NO_3^- anions. Based on this dramatic difference in viscosity behavior, the inter-ion interactions and molecular structure resulting from silver salt dissolution must be very different for the two ILs. As expected, the viscosities exponentially decrease with increasing temperature for both pure ILs and their mixtures. The temperature dependence of the viscosity becomes much more pronounced at higher silver ion concentration for the IL mixtures with Tf_2N^- anions. A change in the temperature dependence of liquid viscosity indicates a free volume change in the liquid (20). Clearly, the addition of $AgTf_2N$ to [hmim][Tf_2N] results in increased inter-ion interactions and increased ordering in the mixture. This does not occur when $AgNO_3$ is added to [hmim][NO_3]. We interpret this as the formation of molecular structures in the $AgTf_2N$/[hmim][Tf_2N] mixture. It is as if there

are strong interactions (reminiscent of hydrogen bonds), that form, resulting in increasing viscosity.

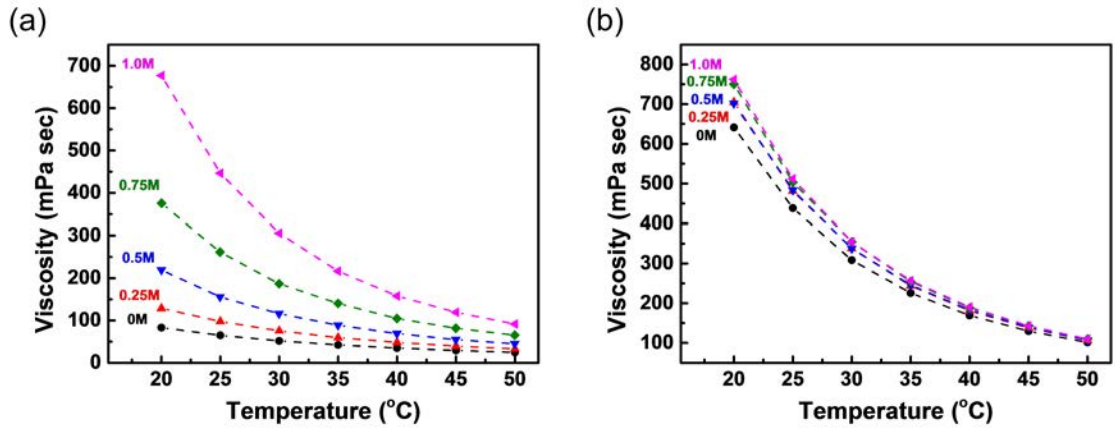

Figure 2. Viscosities of silver-containing IL mixtures with (a) Tf_2N^- anions and (b) NO_3^- anions, as a function of silver salt concentration and temperature.

Transport of gases through the IL and mixtures of IL and silver salts was examined by measuring gas permeation through supported IL membranes, where alumina oxide Anodiscs were used as the support. Two Ag^+ ion concentrations (i.e., 0 and 1 M) were investigated for each IL (cf. Figure 3). Three pure gases (helium, ethylene, and ethane) were permeated through the SILMs. The rate of increase in downstream pressure at steady-state was used to calculate the gas permeabilities.

As shown in Figure 3a and 3c, the permeability of all three gases in the pure ILs is independent of pressure. The permeability of ethylene and ethane is greater than that of helium. The ethylene/ethane selectivity in pure [hmim][Tf_2N] is about 1.5, whereas it is about 2.2 in pure [hmim][NO_3]. The addition of 1 M $AgTf_2N$ to [hmim][Tf_2N] (Figure 3b) substantially increases the ethylene permeability and decreases the ethane permeability, resulting in ethylene/ethane selectivities greater than 5.0. The addition of 1 M $AgNO_3$ to [hmim][NO_3] (cf. Figure 3d) did not increase the ethylene permeability, although it did decrease the ethane solubility, resulting in ethylene/ethane selectivities of about 3.0.

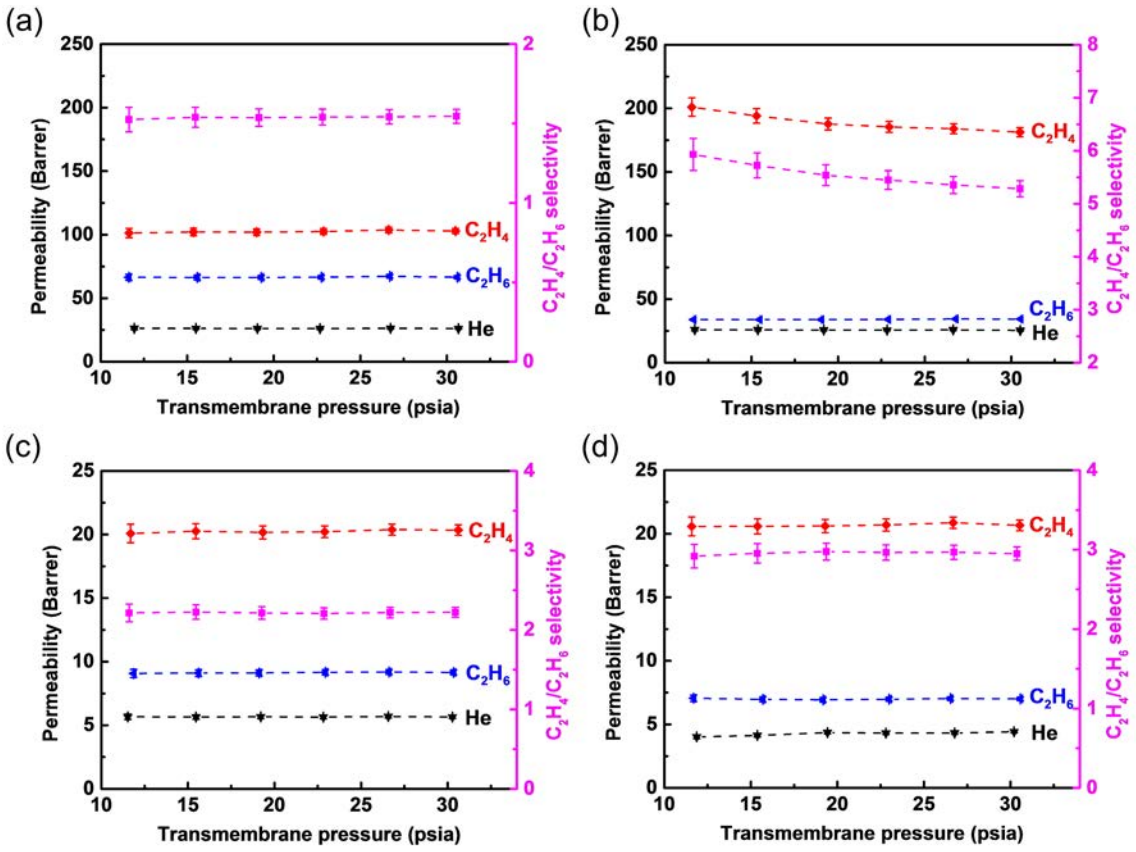

Figure 3. Gas permeabilities of ethane, ethylene, and helium in the SILM containing Tf_2N^- anions at (a) 0 M and (b) 1 M Ag^+ and NO_3^- anions at (c) 0 M and (d) 1 M Ag^+.

In general, one would expect the permeability (P) of a gas through the liquid in a SILM to be the product of solubility (S) and diffusivity (D): P = S x D. The Stokes-Einstein equation predicts that the diffusivity of a solute will be inversely proportional to the viscosity of the liquid. Since the viscosity of pure [hmim][Tf_2N] is significantly less than that of pure [hmim][NO_3] (cf. Figure 2), the diffusivities of gas solutes in [hmim][Tf_2N] should be higher than diffusivities in [hmim][NO_3]. This hypothesis is consistent with the permeabilities of all three gases being significantly higher in pure [hmim][Tf_2N] than in pure [hmim][NO_3], as shown in Figure 3a and 3c.

Using the measured values of the permeabilities and viscosities (to estimate diffusivity), one can compute the change in gas solubility due to addition of 1 M of silver salt to each of the ILs. The Stokes-Einstein equation predicts that diffusivity is inversely proportional to viscosity, but it was developed for large solute molecules diffusing through relatively small solvent molecules (22). A weaker viscosity dependence has been reported in the literature for the diffusivity of small gas molecules through large solvent molecules (21, 22). In this case, the diffusivity depends on the viscosity raised to the power of -0.7, instead of -1. To examine how the solubility changes upon addition of 1 M silver salt to both [hmim][Tf_2N] and [hmim][NO_3], the apparent ratios of the solubilities of ethane, ethylene, and helium in 1 M silver solutions to neat ILs were calculated using the -0.7-power relationship. As shown in Figure 4, the solubility of ethylene in both SILMs increases upon addition of 1 M silver salt, owing to chemisorption of ethylene by the silver ions. The ethylene solubility ratio in [hmim][Tf_2N] increases by a factor of ~6 upon silver salt addition, but it increases only slightly (~1.1) when the silver salt is added to [hmim][NO_3].

The increase in ethylene solubility in the 1 M Ag^+ SILM with Tf_2N^- anions is slightly greater in the low-transmembrane pressure range. We attribute this decrease in the solubility ratio with increasing transmembrane pressure to saturation of the olefin-silver complexation at the higher pressures.

The solubilities of both non-complexing gases (ethane and helium) decrease slightly upon addition of 1 M $AgNO_3$ to the [hmim][NO_3] (Figure 4b). We attribute this to the reduced free volume in the 1 M $AgNO_3$ in [hmim][NO_3] mixture (see Figure 1c). Moreover, the mixture contains a higher concentration of the high charge density NO_3^- anions, which would not interact favorably with non-polar solute molecules.

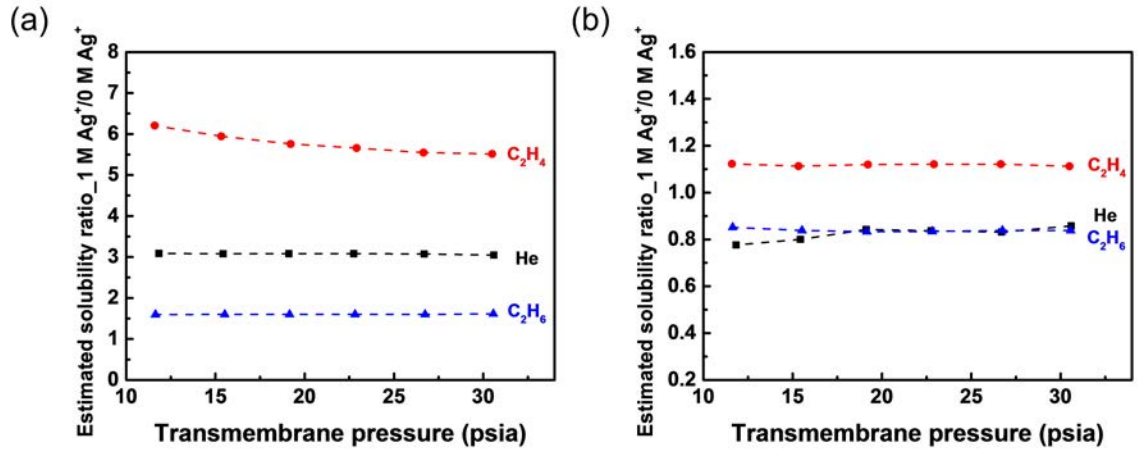

Figure 4. Calculated solubility ratios of SILMs with different anion conditions: (a) Tf_2N^- anion and (b) NO_3^- anion using -0.7 power relationship of diffusivity with viscosity.

By contrast, the solubility of both ethane and helium increase when 1 M $AgTf_2N$ is added to [hmim][Tf_2N]. Like [hmim][NO_3], the molar volume (and, subsequently, free volume) of [hmim][Tf_2N] decreases when $AgTf_2N$ is added. However, the absolute values of the molar volume in [hmim][Tf_2N] mixtures are always greater than those of the [hmim][NO_3] mixtures. In addition, the charge on the Tf_2N^- anion is highly dispersed, providing better opportunities for attractive van der Waals type interactions with nonpolar molecules like ethane and helium.

Conclusions

Neat 1-hexyl-3-methylimidazolium ILs and mixtures containing up to 1 M silver salt were studied using physicochemical property and gas permeation measurements. Upon salt dissolution, the density of both ILs increased significantly. Likewise, the viscosity of the [hmim][Tf_2N] increased dramatically upon silver salt addition, but the viscosity of the [hmim][NO_3] did not. Thus, the two mixtures likely have very different inter-ion interactions and molecular structure. The presence of silver in the [hmim][Tf_2N] significantly increased ethylene permeability through a supported ionic liquid membrane (SILM) using this mixture, greatly enhancing olefin/paraffin selectivity. However, this was not observed for [hmim][NO_3]. The macroscopic properties (viscosity and density) were used to rationalize the gas permeability results in terms of their effect on gas diffusivity and solubility.

Acknowledgments

This paper is based upon work supported in part by the National Science Foundation under Cooperative Agreement No. EEC-1647722. Any opinions, findings and conclusions or recommendations expressed in this material are those of the authors and do not necessarily reflect the views of the National Science Foundation. The research was also supported by the Robert A. Welch Foundation (grant No. F-1945-20180324) and the Cockrell School of Engineering at the University of Texas at Austin.

References

1. D. S. Sholl and R. P. Lively, *Nature*, **532**, 435 (2016).
2. L. Xu, M. Rungta, M. K. Brayden, M. V. Martinez, B. A. Stears, G. A. Barbay, and W. J. Koros, *J. Membr. Sci.*, **423-424**, 314 (2012).
3. M. Rungta, L. Xu, and W. J. Koros, *Carbon*, **50**, 1488 (2012).
4. L. Xu, M. Rungta, and W. J. Koros, *J. Membr. Sci*, **380**, 138 (2011).
5. O. Salinas, X. Ma, Y. Wang, Y. Han, and I. Pinnau, *RSC Adv.*, **7**, 3265 (2017).
6. O. Salinas, X. Ma, E. Litwiller, and I. Pinnau, *J. Membr. Sci.*, **504**, 133 (2016).
7. T. C. Merkel, R. Blanc, I. Ciobanu, B. Firat, A. Suwarlim, and J. Zeid, *J. Membr. Sci.*, **447**, 177 (2013).
8. M. Naghsh, M. Sadeghi, A. Moheb, M. P. Chenar, and M. Mohagheghian, *J. Membr. Sci.*, **423-424**, 97 (2012).
9. V. F. D. Martins, A. M. Ribeiro, A. Ferreira, U. H. Lee, Y. K. Hwang, J.-S. Chang, J. M. Loureiro, and A. E. Rodrigues, *Sep. Purif. Technol.*, **149**, 445 (2015).
10. J. Ploegmakers, S. Japip, and K. Nijmeijer, *J. Membr. Sci*, **428**, 445 (2013).
11. J. Ploegmakers, S. Japip, and K. Nijmeijer, *J. Membr. Sci*, **428**, 331 (2013).
12. C. M. Sanchez, T. Song, J. F. Brennecke and B. D. Freeman, *Ind. Eng. Chem. Res.*, **59**, 5362 (2020).
13. H. Dou, B. Jiang, M. Xu, J. Zhou, Y. Sun, and L. Zhang, *Chem. Eng. Sci.*, **193**, 27 (2019).
14. B. Jiang, H. Dou, L. Zhang, B. Wang, Y. Sun, H. Yang, Z. Huang, and H. Bi, *J. Membr. Sci*, **536**, 123 (2017).
15. L. M. Galán Sánchez, G. W. Meindersma, and A. B. Haan, *Ind. Eng. Chem. Res.*, **48**, 10650 (2009).
16. M. Fallanza, A. Ortiz, D. Gorri, and I. Ortiz, *J. Chem. Eng*, **58**, 2147 (2013).
17. S. W. Kang, K. Char, J. H. Kim, C. K. Kim, and Y. S. Kang, *Chem. Mater.*, **18**, 1789 (2006).
18. F. Agel, F. Pitsch, F. F. Krull, P. Schulz, M. Wessling, T. Melin, and P. Wasserscheid, *Phys. Chem. Chem. Phys.*, **13**, 725 (2011).
19. R. B. Eldridge, *Ind. Eng. Chem. Res.*, **32**, 2208 (1993).
20. A. A. Miller, *J. Phys. Chem.*, **67**, 1031 (1963).
21. D. Morgan, L. Ferguson, and P. Scovazzo, *Ind. Eng. Chem. Res.*, **44**, 4815 (2005).
22. E. L. Cussler, *Diffusion: Mass Transfer in Fluid Systems*, Cambridge University Press (2009).
23. S. N. V. K. Aki, B. R. Mellein, E. M. Saurer, and J. F. Brennecke, *J. Phys. Chem. B*, **108**, 20355 (2004).
24. Z. P. Smith, R. R. Tiwari, M. E. Dose, K. L. Gleason, T. M. Murphy, D. F. Sanders, G. Gunawan, L. M. Robeson, D. R. Paul, and B. D. Freeman, *Macromolecules*, **47**, 3170 (2014).

ECS Transactions, 98 (10) 393-400 (2020)
10.1149/09810.0393ecst ©The Electrochemical Society

Optimization of Electrolysis Conditions for Ti Film Electrodeposition from LiF–LiCl Eutectic Molten Salt

Makoto Unoki[a], Yutaro Norikawa[a], Kouji Yasuda[b,c,*], and Toshiyuki Nohira[a]

[a] Institute of Advanced Energy, Kyoto University, Uji 611-0011, Japan
[b] Agency for Health, Safety and Environment, Kyoto University, Kyoto 606-8501, Japan
[c] Graduate School of Energy Science, Kyoto University, Kyoto 606-8501, Japan
* Present address: Graduate School of Engineering, Kyoto University, Kyoto 606-8501, Japan

The optimum conditions for electrodepositing compact, smooth and adherent Ti films in LiF–LiCl–Li_3TiF_6 at 823 K were investigated. The Li_3TiF_6 was formed in-situ in the melt via comproportionation reaction between Li_2TiF_6 and Ti powder. The solubility of Li_3TiF_6 was confirmed to be higher than 7.1 mol% by cyclic voltammetry and ICP-AES measurement. Galvanostatic electrolysis was conducted on Ni plate substrates at various concentrations of Li_3TiF_6 (0.55, 2.6, 7.1 mol%) and cathodic current density (50–1200 mA cm^{-2}). Ti films with smoother surface were obtained at higher Li_3TiF_6 concentration and lower current density. In the present study, Ti films having the smoothest surface were obtained at 7.1 mol% of Li_3TiF_6 and 50 mA cm^{-2}.

Introduction

Titanium is a metal having excellent properties such as high specific strength, high corrosion resistance and high biocompatibility. Therefore, titanium is utilized for aircraft components, chemical plants, medical components, etc. Furthermore, titanium is attractive metal in terms of its abundant resources. However, widespread use of titanium is prevented due to the high smelting cost and the poor workability. As a method to solve these problems, titanium plating is an attractive technique because superior surface properties of titanium can be utilized. Among titanium plating methods, electrolytic plating is a promising candidate because of the advantages of higher deposition rate and shape flexibility. Electrodeposition of titanium has been studied using aqueous solutions (1,2), organic solvents (3,4), and high-temperature molten salts (5–13) as electrolytes. Nevertheless, pure titanium can be electrodeposited only from high-temperature molten salts.

In previous studies, chlorides (5–7), fluorides (8–10), and fluoride-chloride mixtures (11–13) have been mainly used as molten salt electrolytes. Generally, fluoride molten salts are advantageous for electrodepositing compact and smooth titanium films. Robin ***et al.*** obtained comparatively compact and smooth films in LiF–NaF–KF melts at 873–923 K (9). In the case of fluoride-chloride mixtures, several researchers reported that Ti films having better morphology can be obtained from the melts with sufficient fluoride concentrations. Takamura ***et al.*** reported that the morphology of deposits was improved by adding LiF to LiCl–KCl at 773 K (7). Song ***et al.*** reported that Ti metal with fine crystal grains was obtained when KF was added to NaCl–KCl at 1073 K (13). Based on these reports, we have focused on the electrodeposition of titanium in fluoride-chloride mixtures

consisting of single cations and having enough fluoride concentrations (14–17). We have already reported the electrochemical behaviors of Ti(III) ions and the electrodeposition of Ti in molten KF–KCl (45:55 mol%, 923 K) (14–16) and LiF–LiCl (45:55 mol%, 923 K) (17). We found that LiF–LiCl has an advantage for electrodepositing smooth Ti films due to its lower melting point (774 K at the eutectic composition (18)). In general, smoother Ti films are expected to be obtained at lower temperature by suppressing the growth of crystal grains. Thus, LiF–LiCl eutectic molten salt was selected to obtain Ti films with smooth surface.

In this study, we investigated the effect of Li_3TiF_6 concentration and current density on the morphology of electrodeposited Ti in LiF–LiCl eutectic molten salt at 823 K. First, the solubility of Li_3TiF_6 was investigated by cyclic voltammetry and inductive coupled plasma-atomic emission spectroscopy (ICP-AES) measurement. Second, galvanostatic electrolysis was conducted at various current densities at three different concentrations of Li_3TiF_6 (0.55, 2.6, 7.1 mol%). The optimum conditions to obtain compact and smooth Ti films were evaluated by scanning electron microscopy (SEM), surface roughness (S_a), and X-ray diffraction (XRD) measurement.

Experimental

Reagent-grade LiF (FUJIFILM Wako Pure Chemical Corp., >98.0%) and LiCl (FUJIFILM Wako Pure Chemical Corp., >99.0%) were separately dried under vacuum at 453 K for over 24 h. They are further dried under vacuum at 773 K for 24 h. The salts were mixed in the eutectic composition (molar ratio of LiF:LiCl = 30:70, melting point = 774 K (18), 300 g) and loaded in a graphite crucible (Toyo Tanso Co., Ltd., outer diameter: 90 mm, inner diameter: 80 mm, and height: 120 mm) or a Ni crucible (Chiyoda Industry Manufacturing Plant Co., Ltd., outer diameter: 98 mm, inner diameter: 96 mm, height: 102 mm). The mixture in the crucible was placed at the bottom of a stainless-steel vessel in an airtight Kanthal container. The electrochemical measurements were conducted in dry Ar atmosphere at 823 K in a glove box. After blank measurements in molten LiF–LiCl, 0.50–5.0 mol% of Li_2TiF_6 and 0.33–3.3 mol% of Ti powder (Kojundo Chemical Laboratory Co., Ltd., 99.9%) were added to the melt. Here, the synthetic method of Li_2TiF_6 was reported in our previous paper (17). The added amounts of Ti powder were approximately twice the amounts necessary to generate Ti(III) ions by comproportionation reaction between Ti(IV) ions and Ti(0) according to Eq. 1.

$$Ti(0) + 3Ti(IV) \rightarrow 4Ti(III) \quad [1]$$

This reaction is also described as:

$$6LiF + Ti + 3Li_2TiF_6 \rightarrow 4Li_3TiF_6 \quad [2]$$

Electrochemical measurements and galvanostatic electrolysis were conducted using a three-electrode method with an electrochemical measurement system (Hokuto Denko

Corp., HZ-7000). The working electrodes were Ni plate (Nilaco Corp., 10 mm × 10 mm, thickness: 0.1 mm, 99.95%), Mo flag (Nilaco Corp., diameter: 3.0 mm, thickness: 0.1 mm, 99.95%), Au flag (Nilaco Corp., diameter: 3.0 mm, thickness: 0.1 mm, 99.98%), and glass-like carbon rod (Tokai Carbon Co., Ltd., diameter: 3.0 mm) electrodes. The structure of the flag electrodes was reported in our previous paper (19). Ti rods (Nilaco Corp., diameter: 3.0 mm, 99.5%) were used as the counter and reference electrodes. In the blank measurement, a Pt wire (Nilaco Corp., diameter: 1.0 mm, 99.98%) was used as the quasi-reference electrode. The potential of reference electrodes was calibrated with respect to a dynamic Cl_2/Cl^- potential determined by cyclic voltammetry on a glass-like carbon rod electrode. The melt temperature was measured using a type-K thermocouple. The electrolyzed samples on the Ni plates were soaked in distilled water for 30 min and $Al(NO_3)_3$ aqueous solution (1.0 mol L^{-1}, obtained from FUJIFILM Wako Pure Chemical Co., Ltd., 98.0%) for 10 min at room temperature to remove the salt adhered on the deposits.

The surface and cross-section of the samples were observed by using scanning electron microscopy (SEM; Thermo Fisher Scientific Inc., Phenom Pro Generation 5). Before the observation of the cross section, the samples were cut at the center and embedded in acrylic resin. The samples were polished with emery papers, buffing compounds and a cross-section polisher (CP; Hitachi, Ltd., IM4000). The samples were then coated with Au using an ion-sputtering apparatus (Hitachi, Ltd., E-1010) to impart conductivity. The surface roughness (S_a) of the samples was also measured by SEM and calculated as the average of 5 points (the measurement conditions: shortest cut-off $\lambda_s = 20$ nm, longest cut-off $\lambda_c = 240$ μm, measured area $A = 1.2 \times 1.2$ mm). The samples were also characterized by energy-dispersive X-ray spectroscopy (EDX; Thermo Fisher Scientific Inc., Phenom Pro Generation 5) and X-ray diffraction (XRD; Rigaku Corp., Ultima IV, Cu-*K*α line). A small portion of the molten salt was sampled by the suction method using a borosilicate glass tube (Pyrex®, outer diameter: 6 mm, inner diameter: 4 mm) and dissolved in HNO_3 aqueous solution (pH 1, obtained from Tama Chemical Corp., AA-100 grade, 68 wt%). The solution was analyzed by using inductive coupled plasma-atomic emission spectroscopy (ICP-AES; Hitachi, Ltd., SPECTRO BLUE) to determine the concentration of Li_3TiF_6 in the sampled molten salt.

Result and Discussion

In-situ Preparation of Li_3TiF_6

Prior to electrodeposition, the solubility of Li_3TiF_6 was investigated with cyclic voltammetry and ICP-AES measurement. As described in Eq. 2, the Li_3TiF_6 are synthesized in the molten LiF–LiCl via the comproportionation reaction between Li_2TiF_6 and Ti powder.

Figure 1 (a) shows the cyclic voltammogram at a Au flag electrode in the positive potential region after the addition of Li_2TiF_6 (0.50–5.0 mol%) and Ti powder (0.33–3.3 mol%). The redox currents of Ti(III)/Ti(IV) were observed around −0.8 V vs. Cl_2/Cl^- at each added amount of Li_2TiF_6. Figure 1 (b) shows the plots of peak current densities of each cyclic voltammogram against the added amounts of Li_2TiF_6. The peak current densities increased almost linearly as the Li_2TiF_6 was added. This result indicates that the

added Li_2TiF_6 were almost completely dissolved up to 5.0 mol% to form Ti(III) ions by the comproportionation reaction.

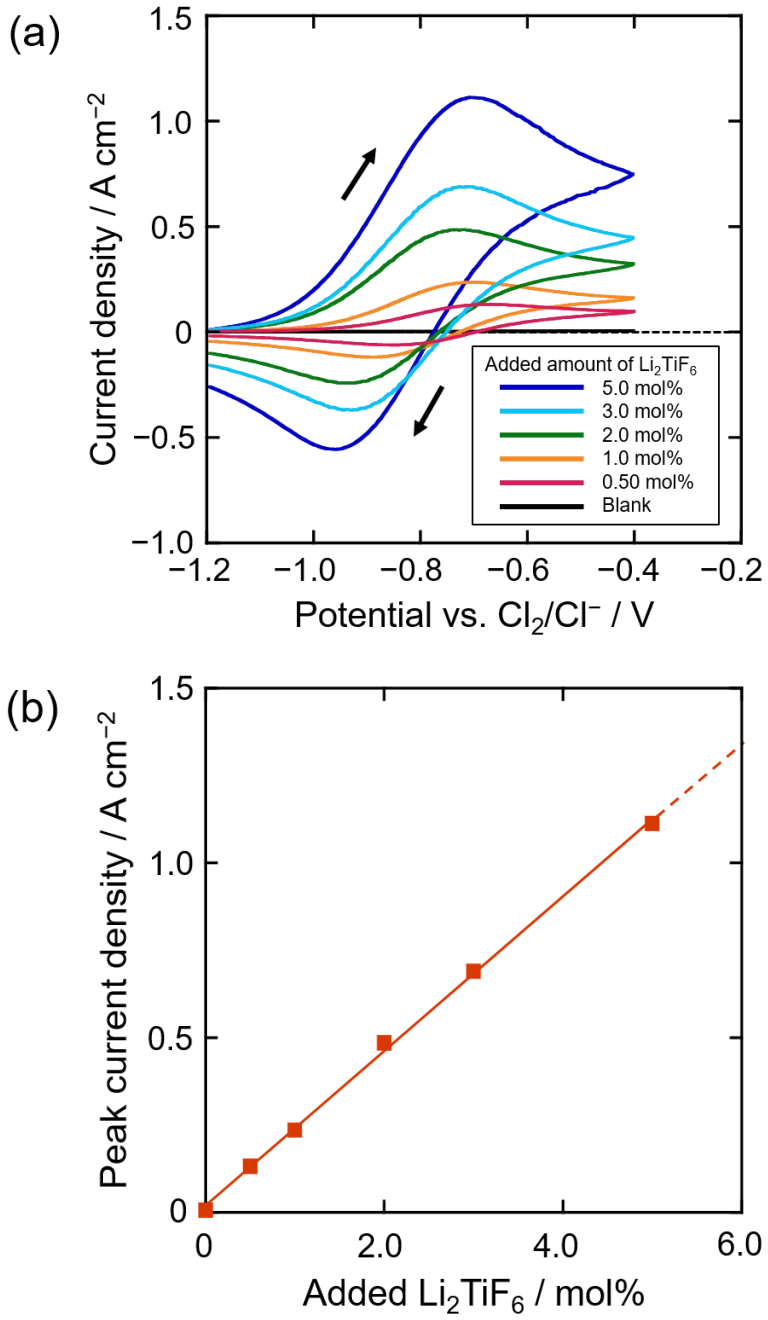

Figure 1. (a) Cyclic voltammograms at a Au flag electrode in molten LiF–LiCl after adding various amounts of Li_2TiF_6 (0–5.0 mol%) and Ti powder (0–3.3 mol%) at 823 K. Scan rate: 0.50 V s^{-1}. (b) Dependence of anodic peak current density on added amount of Li_2TiF_6.

Figure 2 shows the plots of the concentrations of Li_3TiF_6 determined by ICP-AES measurement against the added amounts of Li_2TiF_6. The black solid line indicates the theoretical value calculated from Eq. 2 and the red dots are the measured values. In this study, the concentration of Li_3TiF_6 is defined by the following equation.

$$[Li_3TiF_6] = n_{Li_3TiF_6} / (n_{LiF} + n_{LiCl} + n_{Li_3TiF_6}) \quad [3]$$

Here, $n_{Li_3TiF_6}$, n_{LiF} and n_{LiCl} indicate the molar amounts of Li_3TiF_6, LiF and LiCl in the molten salt, respectively. Since LiF is consumed in the comproportionation reaction of Eq. 2, the theoretical concentrations of Li_3TiF_6 are not simply four-thirds of the added amounts of Li_2TiF_6. Therefore, the theoretical value is not completely linear to the added amounts of Li_2TiF_6. As shown in Figure 2, the measured values were close to the theoretical ones up to 7.1 mol% of Li_3TiF_6. Thus, the solubility of Li_3TiF_6 is confirmed to be more than 7.1 mol%.

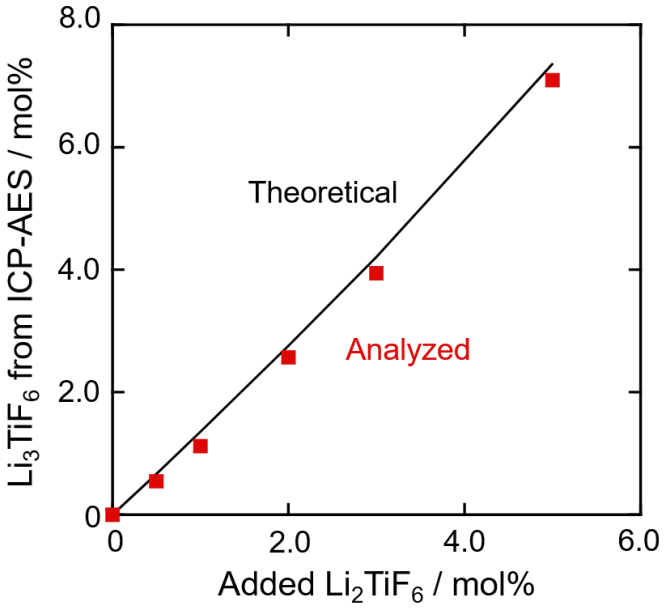

Figure 2. The concentration of Li_3TiF_6 determined by ICP-AES in molten LiF–LiCl after adding various amounts of Li_2TiF_6 (0–5.0 mol%) and Ti powder (0–3.3 mol%) at 823 K.

Electrodeposition of Ti Films

Galvanostatic electrolysis at Ni plate substrates was conducted under the conditions of various current densities (50–1200 mA cm^{-2}) and Li_3TiF_6 concentrations (0.55, 2.6, 7.1 mol%). Here, the reduction current is expressed as an absolute value. The electric charge density was fixed at 60 C cm^{-2} for all electrolysis. The theoretical thickness of electrodeposited Ti films at 60 C cm^{-2} is 22 μm. Figure 3 shows optical images of the electrodeposited samples after washing with distilled water and 1 mol L^{-1} $Al(NO_3)_3$ aqueous solution. XRD measurement confirmed that the electrodeposits were Ti. Compact and highly adherent Ti films were obtained at all Li_3TiF_6 concentrations at 50 mA cm^{-2}. When the concentration increases, Ti films can be obtained even at higher current densities; Ti films were obtained up to 200 mA cm^{-2} at 2.6 mol% of Li_2TiF_6 and up to 400 mA cm^{-2} at 7.1 mol%. On the other hand, the morphology of the deposits changed to powder-like as the current densities further increased; the powder-like deposits were obtained at higher current density than 400 mA cm^{-2} at 2.6 mol% and higher than 800 mA cm^{-2} at 7.1 mol%.

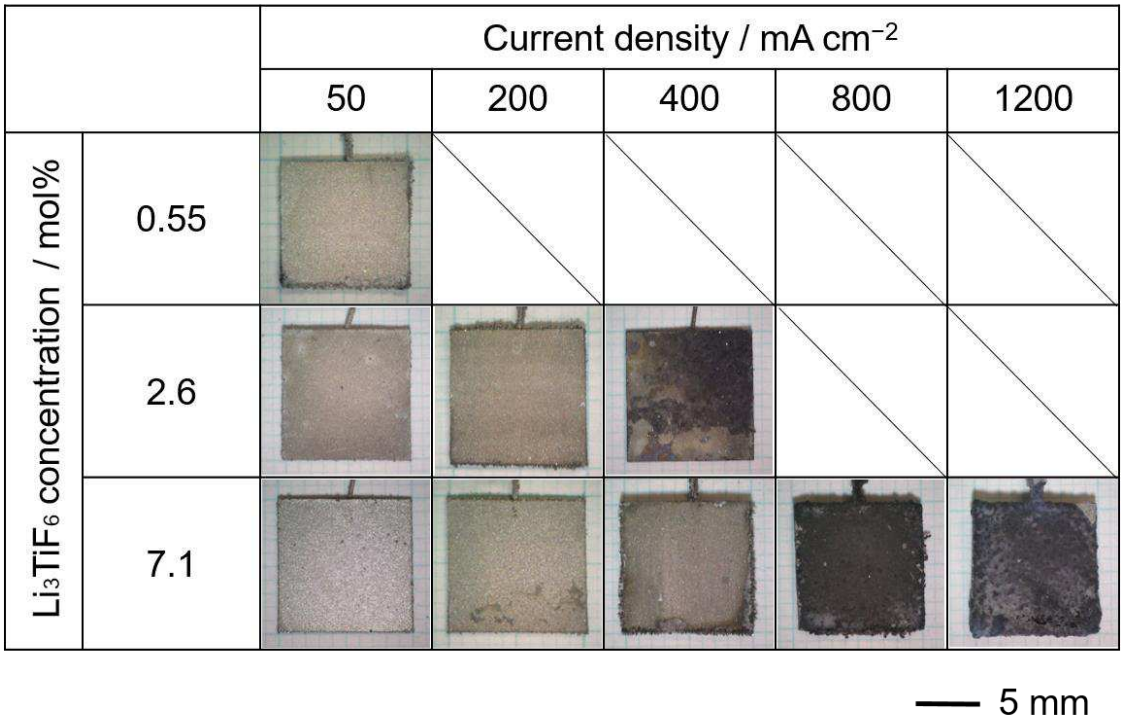

Figure 3. Optical images of the samples obtained by galvanostatic electrolysis at Ni plates in molten LiF–LiCl–Li_3TiF_6 at 823 K. Charge density: 60 C cm^{-2}.

Figure 4 compares the surface/cross-sectional SEM images and surface roughness (S_a) at the same current density (50 mA cm^{-2}) at various Li_3TiF_6 concentrations. The formation of compact and adherent Ti film was also confirmed by the SEM images. The smoothness of the deposits was improved as the Li_3TiF_6 concentration increased. The smallest S_a (1.32 μm), which means the smoothest surface, was obtained at 7.1 mol% of Li_3TiF_6.

Figure 5 shows the surface/cross-sectional SEM images and surface roughness (S_a) at the same Li_3TiF_6 concentration (7.1 mol%) at various current densities. In the case of at 400 mA cm^{-2}, the compactness and adhesion were almost the same as those of 50 mA cm^{-2}. However, the roughness was increased and nodule electrodeposits were partially observed. At a very high current density of 1200 mA cm^{-2}, the morphology of electrodeposits was powder-like and the adhesion was quite low.

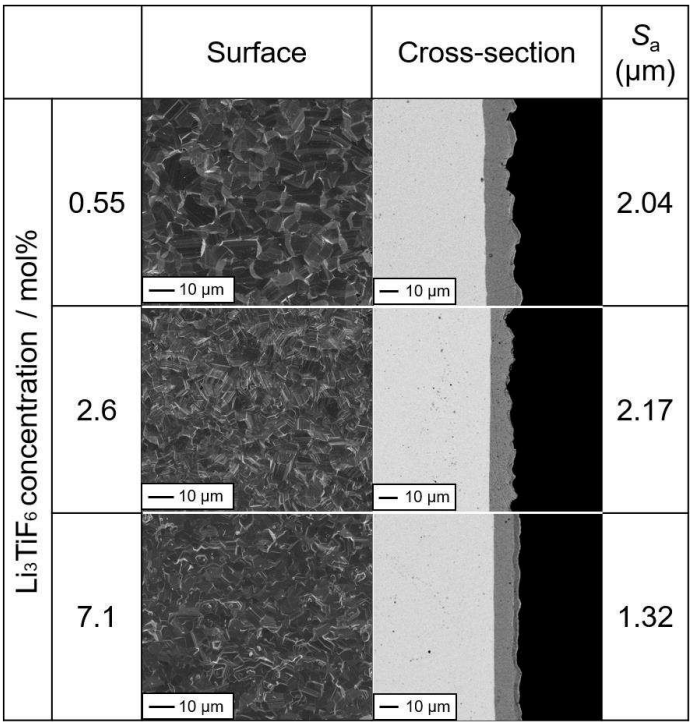

Figure 4. Surface and cross-sectional SEM images and surface roughness (S_a) of the samples obtained by galvanostatic electrolysis at Ni plates in LiF–LiCl–Li_3TiF_6 at 823 K. Charge density: 60 C cm^{-2}. Current density: 50 mA cm^{-2}.

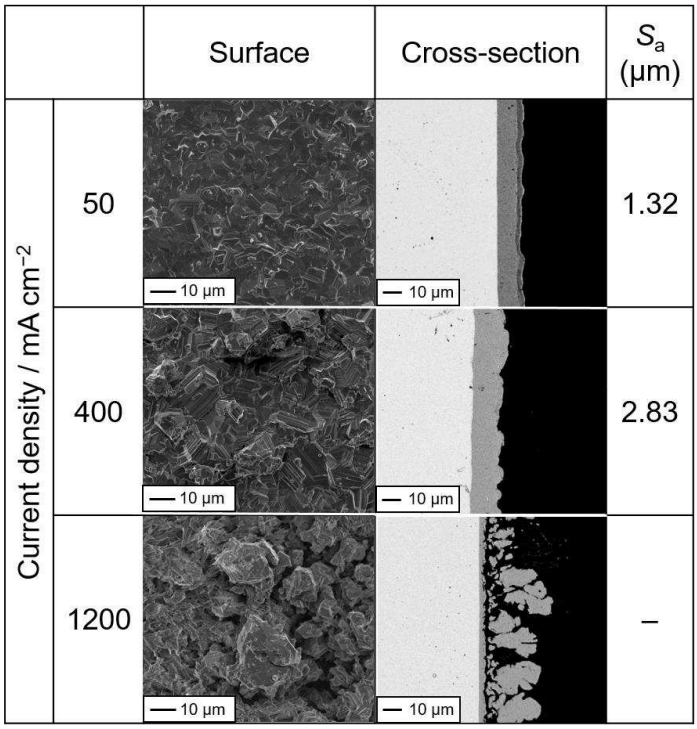

Figure 5. Surface and cross-sectional SEM images and surface roughness (S_a) of the samples obtained by galvanostatic electrolysis at Ni plates in LiF–LiCl–Li_3TiF_6 at 823 K. Charge density: 60 C cm^{-2}. Li_3TiF_6 concentration: 7.1 mol%.

Conclusion

The optimum conditions for electrodepositing compact, smooth and adherent Ti films were investigated in LiF–LiCl–Li_3TiF_6 at 823 K. The solubility of Li_3TiF_6 was confirmed to be more than 7.1 mol% by cyclic voltammetry and ICP-AES measurement. Galvanostatic electrolysis was conducted on Ni plate substrates at various Li_3TiF_6 concentrations (0.55, 2.6, 7.1 mol%) and current densities (50–1200 mA cm^{-2}). As a result, Ti films with smoother surface was obtained at higher Li_3TiF_6 concentration and lower current density. In the present electrolysis conditions, the smoothest surface Ti films were obtained at 7.1 mol% of Li_3TiF_6 and 50 mA cm^{-2}.

Acknowledgments

A part of this study was conducted as a collaborative research with Sumitomo Electric Industries, Ltd.

References

1. S. Morioka and A. Umezono, *J. Jpn. Inst. Metals*., **23**, 71 (1959).
2. S. Kazuo and A. Kitani, *Electrochemistry*, **52**, 302 (1984).
3. S. Biallozor and A. Lisowska, *Electrochim. Acta*, **25**, 1209 (1980).
4. A. Lisowska and S. Biallozor, *Electrochim. Acta*, **27**, 105 (1982).
5. M. B. Alpert, F. J. Schultz, and W. F. Sullivan, *J. Electrochem. Soc*., **104**, 555 (1957).
6. G. M. Haarberg, W. Rolland, A. Sterten, and J. Thonstad, *J. Appl. Electrochem*., **23**, 217 (1993).
7. H. Takamura, I. Ohno, and H. Numata, *J. Jpn. Inst. Metals*, **60**, 388 (1996).
8. J. De Lepinay, J. Bouteillon, S. Traore, D. Renaud, and M. J. Barbier, *J. Appl. Electrochem*., **17**, 294 (1987).
9. A. Robin, J. De Lepinay, and M. J. Barbier, *J. Electroanal. Chem*., **230**, 125 (1987).
10. M. E. Sibert and M. A. Steinberg, *J. Electrochem. Soc*., **102**, 641 (1955).
11. D. Wei, M. Okido, and T. Oki, *J. Appl. Electrochem*., **24**, 923 (1994).
12. V. V. Malyshev and D. B. Shakhnin, *Mater. Sci*., **50**, 80 (2014).
13. J. Song, Q. Wang, X. Zhu, J. Hou, S. Jiao, and H. Zhu, *Mater. Trans*., **55**, 1299 (2014).
14. Y. Norikawa, K. Yasuda, and T. Nohira, *Mater. Trans*., **58**, 390 (2017).
15. Y. Norikawa, K. Yasuda, and T. Nohira, *Electrochemistry*, **86**, 99 (2018).
16. Y. Norikawa, K. Yasuda, and T. Nohira, *J. Electrochem. Soc*., **166**, D755 (2019).
17. Y. Norikawa, K. Yasuda, and T. Nohira, *J. Electrochem. Soc*., **167**, 082502 (2020).
18. J. Sangster and A. D. Pelton, *J. Phys. Chem. Ref. Data*, **16**, 509 (1987).
19. K. Maeda, K. Yasuda, T. Nohira, R. Hagiwara, and T. Homma, *J. Electrochem. Soc*., **162**, D444 (2015).

ECS Transactions, 98 (10) 401-414 (2020)
10.1149/09810.0401ecst ©The Electrochemical Society

Charge Transport in Additive Modulated Aluminum Chloride Deep Eutectic Solvents (DES)

D. Paterno[a] and S. Suarez[a,b]

[a] Physics Department, Brooklyn College of the City University of New York, Brooklyn, New York 11210, USA
[b] Physics Department, The Graduate Center of the City University of New York, New York, New York 10016, USA

The effect of additives on the aluminum species transports in varying molar ratios of $AlCl_3$ deep eutectic solvents (DES) was studied using EIS conductivity measurements. The amides studied were acetamide, propionamide and butyramide and the molar ratios ranged from 1:1 - 1.7:1 for each $AlCl_3$:amide DES. The additives studied were propylene carbonate (PC) and fluoroethylene carbonate (FEC) in 5wt%. While FEC generally lowered the conductivities, PC appears to shift the reaction equilibrium towards lower $AlCl_3$ concentration. It is possible the fluorine atom on the FEC interacts with the $[AlCl_2(amide)_n]^+$ species, creating stronger interactions that lowers the conductivity. The data displayed non-Arrhenius behavior and were fitted using the Vogel-Fulcher-Tammann equation to reveal dynamic behaviors similar to some pure ILs where the effective inter-conversion between the *trans* and *cis* conformations of the anion facilitated faster ion dynamics. These results can be helpful in modifying DES and similar aluminum solvents for electrolyte applications.

Introduction

The need for safe, low cost, high energy and density storage devices is ubiquitous the world over. Similarly ubiquitous are lithium ion batteries (LIBs) (1-4), due to lithium's low molecular weight and small ionic diameter (1.80 Å) which allows it to deliver about 2.5 times the energy compared to others (lead-acid, nickel-metal hydride, nickel-cadmium) (3). These attributes have been especially fruitful for low temperature portable and selective automotive applications. Despite these advantages, issues such as cost, safety and lithium reserves location exist that make finding alternatives necessary (4-9). Additionally, markets such as commercial vehicles, large-scale storage of renewable energies, lightweight wearable electronics and batteries demand alternative energy sources. Together, these provide the need for implementation of more wide-scale competitive alternative electrochemical energy storage (EES) devices. However, due to the breadth of applications and their respective operational requirements, finding one EES to satisfy all is unrealistic. Instead, niche applications are more likely.

As alternatives to LIBs, researchers have turned to various multivalent ion batteries because of their multiple electron (> 1) transfer capability and one example of this is aluminum ion batteries (AIBs). Aluminum metal offers a three-electron redox property, favorable energy density

(theoretical 2980 mAh/gm compared to lithium's 3860 mAh/gm), low reactivity, easier handling, high cyclability and lower cost compared to lithium. It is also one of the earth's most abundant metal element. The Al-air battery - which is comprised of an Al anode, air cathode and suitable electrolyte - has a theoretical voltage of 2.7 V and energy density of 8.1 kWh/kg, and is being considered for future large-scale applications (10-12). Unfortunately, Al has a high open-circuit potential (-1.66 V vs. a standard Hg/HgO with a 4M NaOH electrolyte at 25^{o}C) (13), which prevents the use of highly conducting aqueous electrolytes due to the decomposition of water before deposition of Al. Additionally, Al has a strong affinity towards oxygen and hence cannot be electrolyzed from aqueous solutions (14). Most detrimental is the formation of protective oxide layers on the surface of Al which despite providing excellent corrosion resistance, also prevents the use of Al as an anode material. This oxide layer cannot be dissolved in most aqueous electrolyte solutions. However, high temperature molten salts have provided some aid with this problem (7), but due to their high working temperatures and cost, alternatives are needed.

The selection of the electrolyte is very important in batteries as they must allow the transports of ionic species between the electrodes while simultaneously blocking that of electrons. In the case of AIBs, chloroaluminate ILs have been used in aluminum electrodeposition (15-17) and because of their relatively high ionic conductivity, tunable acidity, and wide electrochemical window, to date they are the most used electrolytes in AIBs. Chloroaluminate ILs exhibit Lewis acid-base behavior with the solution pH, speciation and reactivity being determined by the chloride donor's concentration. They are mixtures of ionic liquids such as dialkylimidazolium chloride and metal halide salts of which the most used is aluminum chloride ($AlCl_3$) (18-25). The acidic $AlCl_3$/[EMIm]Cl system have received the most attention and depending on the molar ratio of $AlCl_3$ to the imidazolium chloride the electrolyte can be classified as basic (<1), acidic (>1) and neutral (=1). The different anionic species present in the basic melt are $AlCl_4^-$ and Cl^-, in acidic $Al_2Cl_7^-$, and $AlCl_4^-$ in neutral solution (18-29). The electrochemical reduction of $Al_2Cl_7^-$ ion in acidic solution proceeds as (26, 28, 30-32):

$$4\ Al_2Cl_7^- + 3e^- \rightarrow Al + 7\ AlCl_4^- \qquad [1]$$

Recently, deep eutectic solvents (DES) (33-40) have gained attention as electrolytes for energy storage devices (34-37). Fundamentally they are comprised of ionic and non-ionic moieties, with thermal and physical properties that are similar to room temperature ionic liquids. They are however generally cheaper and easier to prepare, and are also known to dissolve metal oxides (41) - which is one of the reasons for our interest. The reactions of DESs depend on several factors including the metal atom, the presence of chlorine coordinated cations or anions, and the hydrogen bond donor. In the case of metal halides, the eutectic formation rests with their asymmetric splitting whereby anions and donor-coordinated cations are formed (33). For $AlCl_3$, this process results in the formation of anionic and cationic structures such as $AlCl_4^-$, $Al_2Cl_7^-$, and $[AlCl_2(amide)_n]^+$ structures where n = 1 and 2 (33). Examples of possible equilibria are presented in Eqs. 2-4 (36) where L represents the amide.

$$2[AlCl_3L_n] \leftrightarrow [AlCl_2L_n]^+ + [AlCl_4]^- + nL \qquad [2]$$

$$2[AlCl_3L_n] + Al_2Cl_6 \leftrightarrow 2[AlCl_2L_n]^+ + 2[AlCl_4]^- \quad [3]$$

$$2[AlCl_4]^- + Al_2Cl_6 \leftrightarrow 2[Al_2Cl_7]^- \quad [4]$$

At low molar ratios, reaction 2 is favored. With increasing $AlCl_3$ concentration, the equilibrium shifts to reaction 3, and finally at higher molar ratios reaction 4 becomes the norm. Like ionic liquids, the transport properties of DESs can be tuned. Changing the hydrogen bond donor or the metal atom will change the resulting DES properties. Including additives can also change these properties. An example of this is the 1.3:1 molar ratio $AlCl_3$:Urea DES prepared by Yu et.al. (34) incorporating the 1,2-dichloroethane (DCE) additive. The pure DES ^{27}Al NMR spectrum was broad and extended between 95 and 105 ppm, while the additive DES gave individual peaks, possibly suggesting that either the additive reduced the electrostatic interactions between neighboring ions, or that it aided in moving the equilibrium reaction more in favor of ionic species.

In an effort to improve the ion transports in DES electrolytes, we have embarked on a series of studies that are focused on elucidating the various aluminum ion species and the interactions that govern their dynamics. Our initial study (42) delved into the local dynamics of the pure DES electrolytes comprised of varying molar ratios (1:1 – 1.7:1) of $AlCl_3$ mixed with acetamide (AA, AcA), butyramide (BA, BuA), or propionamide (PA, PrA). Our goal was to determine how the aluminum ion transport and speciation were affected by the amide type, relative concentration and temperature. We used ^1H and ^{27}Al Nuclear Magnetic Resonance (NMR) spin-lattice relaxation times, chemical shifts and linewidth measurements, complimented with electrochemical impedance spectroscopy (EIS) ionic conductivity measurements, both as a function of temperature. The amides were chosen because they differ in the alkyl chain length which may help in elucidating their electron donor capabilities and the resulting aluminum ion species formed. Our variable temperature conductivity results (42) showed a non-Arrhenius behavior which was fitted using the Vogel-Fulcher-Tammann (VFT) equation. Generally, VFT behavior indicates a 'fragile' state (43), where dynamics are the result of available free volume and disorder resulting from molecular fluctuations and reorganizations over a wide variety of different particle orientations and coordination states, almost independently of thermal aid. Unlike the case for the typical EMIM[Cl] ionic liquid, there was no monotonic decrease in the T_o value with increasing $AlCl_3$ concentration for any of the amides. Similarly, the pseudo activation energy did not display a monotonic increase with increasing $AlCl_3$ concentration. These indicate a significant difference between the ionic environments of the $AlCl_3$ DES analogues compared to the ionic liquid systems.

In this study we continue the characterization of the DES dynamics by focusing exclusively on the effect of the inclusion of additives such as propylene carbonate (PC) and fluoroethylene carbonate (FEC) on the transport of the aluminum species. Additives such as propylene carbonate (PC, dielectric constant 64.92 at 25°C, 132°C flash point, melting point -49°C) have been used in lithium ion battery electrolytes to reduce solution viscosity and enhance ion dynamics (44-47). FEC (48) has also been used but as a stabilizing additive for PC, thereby enhancing the electrolyte's cycling stability and solid electrolyte interface (SEI) formation capability. In our

efforts to not only improve the dynamics of the DES electrolytes for AIB applications, we incorporated each into the pure DESs. We expect their inclusion to provide additional hydrogen bonding pathways for the aluminum ion species, which can affect the resulting ion transport. Towards this, we report for the first time variable temperature ionic conductivity measurements of varying molar ratios (1:1 – 1.7:1) of $AlCl_3$:amide (acetamide, propionamide, and butyramide) with 5wt% PC, or FEC additives. Our future publications will include EIS measurements for additional additives and concentrations, and the comprehensive viscosity and NMR analyses of all DESs.

Experimental

Sample Preparation

The electrolytes studied were varying concentrations of the amides: acetamide (AA, AcA, CH_3CONH_2, Alfa Aesar, > 99%), butyramide (BA, BuA, $CH_3CH_2CH_2CONH_2$, Frontier Scientific, > 99%), and propionamide (PA, PrA, $CH_3CH_2CONH_2$, Frontier Scientific, 99%), with Aluminum chloride ($AlCl_3$, Alfa Aesar, > 99%). The additives used were 5wt% fluoroethylene carbonate (FEC, Sigma-Aldrich, anhydrous, 99%) and propylene carbonate (PC, Sigma-Aldrich, anhydrous, 99%). Chemical structures of these amides are shown in Figure 1. The amides were dried in a vacuum oven at 353K for 40 hours while the $AlCl_3$ was used as received. Both $AlCl_3$ and the amides were combined in their appropriate masses to create the required molar ratios of mixtures, which were mixed slowly with a magnetic stirrer to form the resulting liquid. The required amounts of additives were then added to the respective DES, after which the mixture was heated and magnetically stirred at 80°C for an additional 36 hours. The work was done in a glove box under constant flowing nitrogen atmosphere. The exothermic nature of the reaction eliminated the need for heating or vigorous mixing.

EIS Ionic Conductivity

Ionic liquid samples were packed in a dry nitrogen atmosphere into an airtight 3 mL (Biologic Brand) two-electrode sample cell, leaving 50% of the cell volume available for thermal expansion. The cells were temperature controlled from 303 to 363K using a silicone oil bath. The electrochemical impedance measurements were done using a Solartron 1260 Impedance Analyzer coupled with a Solartron 1287 Electrochemical Interface. Experimental parameters utilized a frequency sweep from 25 Hz to 2.5 MHz using a resolution of 20 data points per decade and the energization was set with AC amplitude of 10 mV with no DC offset. The resulting Nyquist plot of reactance versus resistance was inspected to determine the real electrical resistance. Using the corresponding cell constants and the electrical resistance, conductivity was calculated and plotted versus temperature. Data shown and discussed are the averages of three sets of measurements.

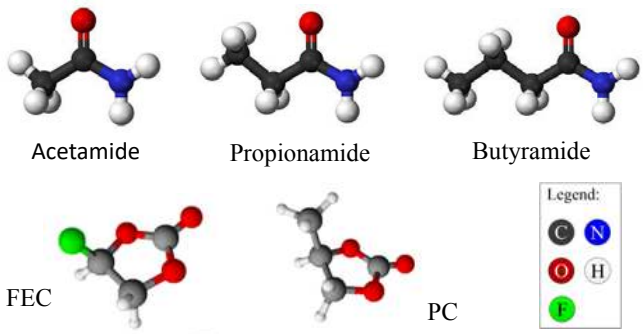

Figure 1. Chemical structures for the amides and additives.

Results

Variable temperature EIS ionic conductivity data were determined for $AlCl_3$:amide (acetamide, butyramide and propionamide) DESs with 5wt% propylene carbonate (PC) or fluoroethylene carbonate (FEC) additive. Conductivity (σ) values were obtained from corresponding Nyquist plots. The general behavior of the conductivity was a dependence on molar concentration, temperature, additive and amide types. Generally, several factors can contribute to σ but usually the biggest contributors are temperature, solution viscosity and the number of available charge carriers. We see the relationships between these parameters through the Nernst-Einstein (NE, left) and Stokes-Einstein (SE, right) equations (Eq. 5-6):

$$\sigma = \frac{Dq^2c}{k_BT} \quad [5]$$

$$D = \frac{k_BT}{4\pi r\eta} \quad [6]$$

where η, D, q, k_B, c, T and r are the solution viscosity, self-diffusion coefficient, charge of the carrier, Boltzmann constant, charge carrier concentration, temperature in Kelvin, and hydrodynamic radius respectively. Ideally, both equations are for application to very dilute solutions where the ions are depicted as hard non-interacting spheres, moving through a continuum of viscosity η. Correspondingly, the ions are expected to be single entities. Because of these, large errors are often obtained from the application of either equation to concentrated systems. The main sources of errors are usually due to concentration, relaxation or drag, and electrophoretic effects.

Temperature and Concentration Effects

As shown in Figure 2 for $AlCl_3$:PA (propionamide) with 5wt% FEC (left) and 5wt% PC (right), the conductivity increased with increasing temperature. This behavior was also observed for the $AlCl_3$:AA-additive and $AlCl_3$:BA-additive mixtures, as well as for the pure DESs (42). The increase in conductivity with temperature is expected since the greater thermal energies will cause

reduced electrostatic interactions resulting in faster ion dynamics. There was a maximum in σ for all DES-additive mixtures. For both the $AlCl_3$:PA and $AlCl_3$:BA, the maximum for the 5wt% PC mixtures occurred at the 1.1:1 molar ratio, while for the $AlCl_3$:AA mixture it occurred for the 1.5:1 molar ratio for all temperatures. In the case of the 5wt% FEC, the maxima occurred at the 1.3:1 molar ratio for all three amide mixtures. For comparison sake, the maxima for the pure $AlCl_3$:PA and $AlCl_3$:BA DES electrolytes occurred prominently at the 1.3:1 molar ratio (42) for all temperatures. The pure $AlCl_3$:AA DES had a broad plateau starting at the 1.1:1 molar ratio at lower temperatures which gave way to a more pronounced maximum at the 1.3:1 molar ratio at higher temperatures (42).

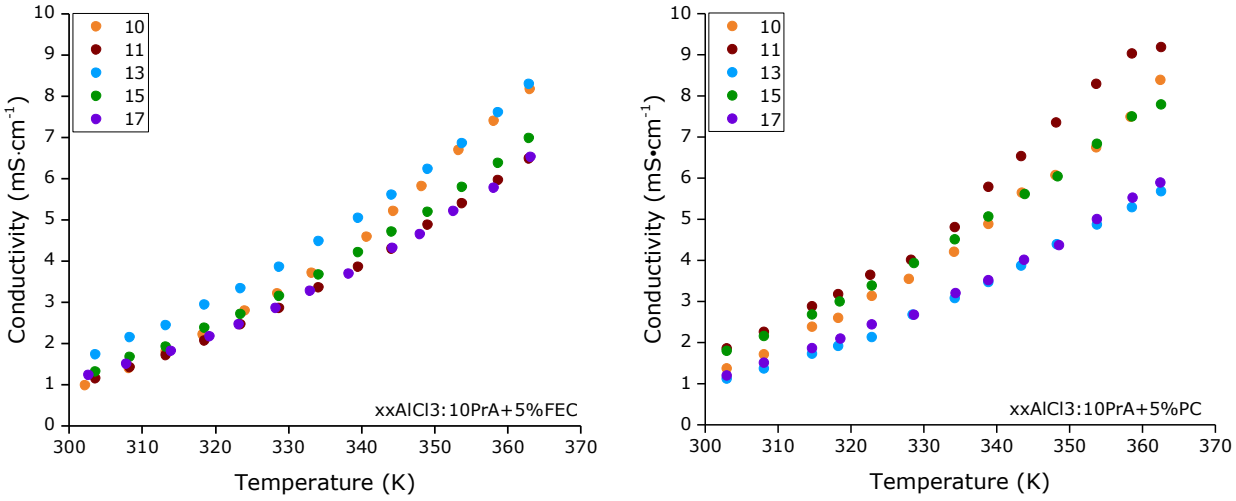

Figure 2. Variable temperature ionic conductivity data for varying molar ratios of $AlCl_3$:PA (propionamide) with 5wt% FEC (left) and 5wt% PC (right).

Like the pure DES, the maximum in conductivity may be due to a combination of factors. As shown in the NE equation, the increasing ionic species associated with greater $AlCl_3$ concentrations can increase the conductivity. Generally, an increase in charge concentration is accompanied by similar increases in viscosity. Unfortunately, we did not perform viscosity measurements on either the pure or additive mixtures but those measurements are a part of our future studies. We used the viscosity results of Liu et. al. (49) for the pure DESs - which for acetamide showed a linear decrease with increasing molar ratio, but for both the propionamide and butyramide DES electrolytes exhibited a broad minimum between 1.1:1 and 1.3:1 molar ratios. Since the minimum in η coincides with the maximum in σ for both the propionamide and butyramide additive mixtures, it suggests that viscosity is still influencing their aluminum ion transports. The additive dependent maximum in conductivity also supports the additive type being used as an additional tuning parameter for DES electrolytes and suggests differences in the interactions between the amides, the aluminum species and the additives.

Amide and Additive Type Effects

The effect of the additive type on the conductivity of the $AlCl_3$:amide-additive mixtures is illustrated more clearly in Figures 3 and 4 for the 1.1:1 (left) and 1.5:1 (right) molar ratios of $AlCl_3$:amide-additive mixtures. As shown in Figure 3, the 5wt% PC additive increased the conductivity for the 1.1:1 $AlCl_3$:PA, 1.1:1 $AlCl_3$:BA, 1.5:1 $AlCl_3$:AA and 1.5:1 $AlCl_3$:BA analogues compared to their pure forms. Similar enhancements were observed for the 1:1 $AlCl_3$:PA and 1.7:1 $AlCl_3$:AA analogues. As shown in Figure 4 for the 5wt% FEC mixtures, generally no enhancement was observed for the FEC mixtures and this was the trend for all molar ratios and amide types. Both FEC (78.4 at 25°C) (48) and PC (64.92 at 25°C) (44-47) have high dielectric constants and should offer additional screening for the aluminum species. Whereas the PC can serve as a solvent for LIB electrolytes and is often used in greater quantities than 5wt%, the FEC is used to enhance the electrolyte's SEI formation capability and cyclability and is used in similarly small quantities. Since the DES solvents are the potential electrolytes for AIBs, any additive incorporated is expected to be used in small quantities, therefore the 5wt% of both PC and FEC seems appropriate. Our future studies will include a variation on the additive concentration as well.

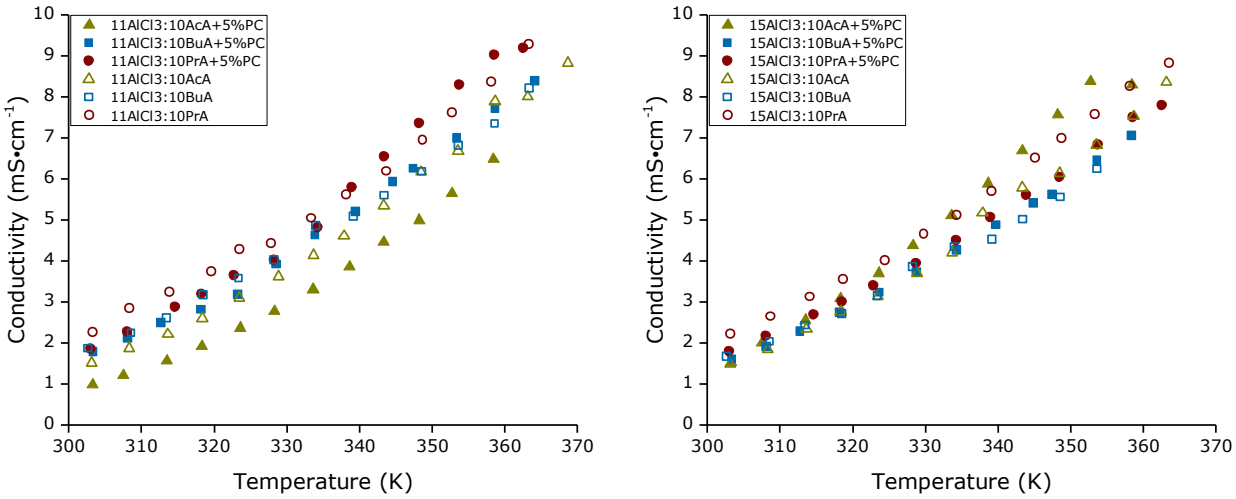

Figure 3. Variable temperature ionic conductivity data for 1.1:1 (left) and 1.5:1 (right) molar ratios of $AlCl_3$:amide-PC mixtures.

The difference between the effect of the two additives may be based upon their structures. As shown in Figure 1, the FEC additive has a terminating fluorine atom while PC has a methyl group. Unlike the methyl group, the terminal fluorine atom can interact electrostatically with the aluminum cationic $[AlCl_2(amide)_n]^+$ species. This has been shown in LIB electrolytes such as $LiPF_6$/EC/DEC/FEC where the FEC enhanced the formation of LiF (50) over Li_2CO_3. This interaction would result in stronger local interactions between the aluminum species and their solvation spheres thereby resulting in reduced transports and lower ionic conductivities. Unlike FEC, PC selectively enhances the mixtures ionic conductivity. Although preliminary, it appears PC shifts the reaction equilibrium to favor lower molar ratios for both propionamide and butyramide. In the case of acetamide, in spite of the concentration at which the conductivity maximum occurs remaining unchanged, the fact that the maximum encompassed the entire

temperature range - unlike for the pure DES - suggests PC reduced the electrostatic interactions between the aluminum species.

To determine the effect of the amide type on the conductivity we compared their structure. The size of the amide molecules is as follows: BA>PA>AA (see Figure 1). Compared to both propionamide and acetamide, butyramide is most bulky and because of this, its interaction with the various ionic species could be less effective. The effect of amide size seems to be temperature and concentration dependent. For PC additive mixtures, at molar ratios above 1.1:1 and temperatures below 343K, the acetamide mixtures have the lowest conductivity. Above this temperature the trend reversed. Additional revelations include propionamide mixtures at the 1:1 and 1.1:1 molar ratios being most conducting, while the butyramide were slightly more than the acetamide. This behavior was also observed for the pure DESs (42). For the FEC additive, generally acetamide mixtures have the lowest conductivities below 353K, while above they have the highest and also the largest thermal enhancements.

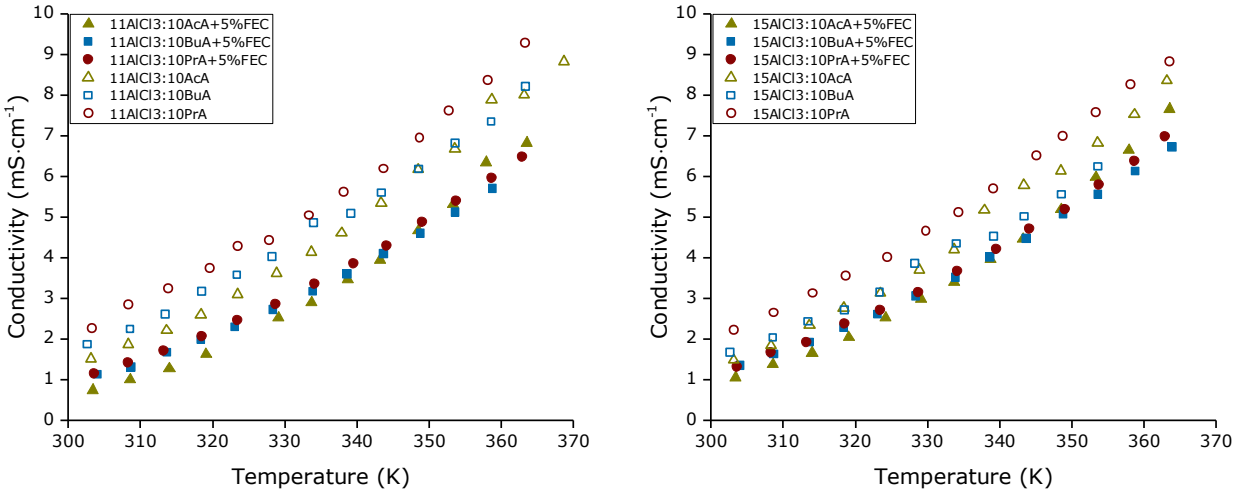

Figure 4. Variable temperature ionic conductivity data for 1.1:1 (left) and 1.5:1 (right) molar ratios of $AlCl_3$:amide-FEC mixtures.

The high-temperature thermal enhancements in conductivity experienced by the acetamide mixtures suggest the breaking of the hydrogen bonding network. Generally, hydrogen bonds lessen in strength and connectivity with increasing temperature. This can lead to faster ion dynamics as a result of the reduced interactions. Since the strength of the hydrogen bonding network as well as the local electrostatic interactions are modulated by the dielectric screening of the amide molecules, we tried to compare their dielectric constants. Unfortunately, at the time of writing only acetamide had a publicly available dielectric constant. Values were however available for their N-methyl analogues which at 30ºC are: 178.9, 164.3 and 124.7 respectively for N-methylacetamide (51-52), N-methylpropionamide (53-54) and N-methylbutyramide (55). N-methylacetamide having the highest dielectric constant could support the acetamide mixtures having lower conductivities. The N-methylbutyramide analogue having the lowest dielectric constant could support butyramide providing a weaker hydrogen bonding network. However, as previously stated, due to butyramide's bulky size, its solvating properties and the resulting ion dynamics in its

mixtures may be further impeded. Also, in the case of butyramide the inclusion of the PC molecules seems to provide additional screening for the aluminum species which allows for faster ion dynamics. This suggests that amide size is a determining factor as it affects the resulting electrostatic interactions between the ionic species, as well as their mobilities. Whereas the acetamide appears too small to provide effective screening for the aluminum species especially at lower temperatures, the butyramide appears too bulky to provide efficient translational dynamics at higher temperatures. The propionamide however appears to balance effectively the need for effective electrostatic screening and translational dynamics.

The inverse temperature behavior of the logarithmic conductivity was fitted to the VFT equation:

$$\sigma = \sigma_o \exp\left(\frac{-B}{T - T_o}\right) \quad [7]$$

where the adjustable parameters - B, T and T_o - are the pseudoactivation energy, current temperature, and 'pseudo' ideal glass transition temperature respectively in unit of Kelvin. The logarithmic form of the VFT was used instead of the exponential as it allows better fitting of data spanning orders of magnitude. Additionally, when compared to the Arrhenius fit, the VFT produced smaller errors and had R^2 values greater than 0.99 indicating the VFT was a more suitable model. As previously mentioned, the pure DESs also had curve-like inverse temperature behavior of their logarithmic conductivities and were fitted using the VFT equation (42). A representative plot for the variable molar ratios $AlCl_3$:AA DES with 5wt% FEC (left) and 5wt% PC (right) additives are shown in Figure 5. Similar behaviors were observed for the $AlCl_3$:PA-additive and $AlCl_3$:BA-additive mixtures (both not shown). There is no data for the 1:1 $AlCl_3$:AA and 1.7:1 $AlCl_3$:BA with 5wt% PC because the additive caused precipitation of the mixture.

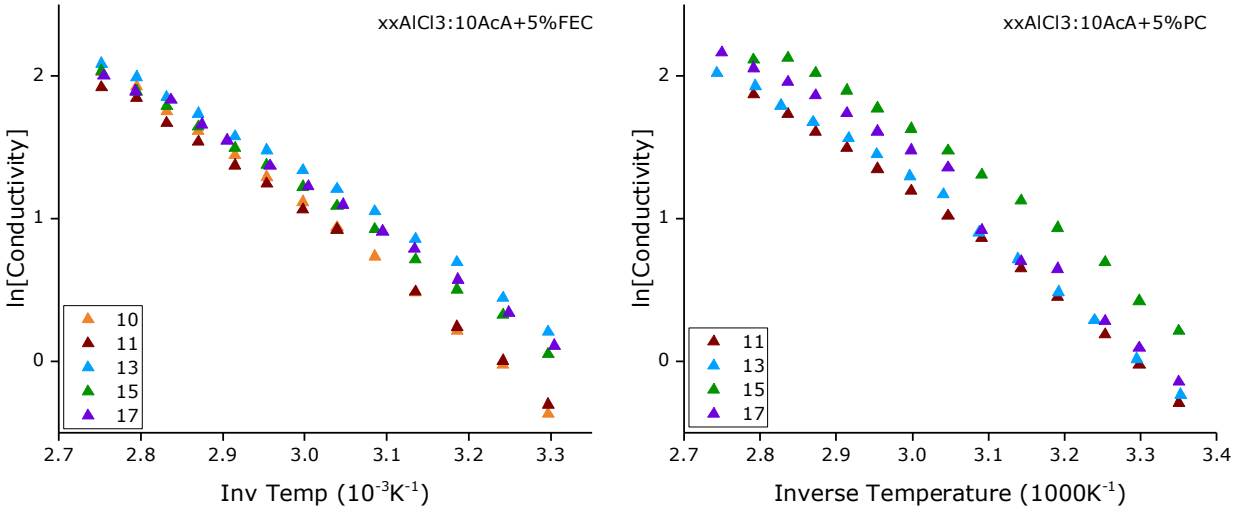

Figure 5. VFT plots of the ionic conductivity for 5wt % FEC (left) and 5wt % (right) $AlCl_3$:AA DES electrolytes.

As previously stated, liquids displaying VFT behaviors are dynamically disordered on the molecular level, whereby species reorganize over a wide variety of different particle orientations and coordination states, without thermal aid. The Fragility (*F*) value is generally accepted as an indicator of this dynamic behavior and values for both $AlCl_3$:amide-additive mixtures were determined from the relationship: B/T_o. *F* is used instead of *D* to differentiate the Fragility parameter from the self-diffusion coefficient (*D*) which is depicted in the SE equation and as is part of our future studies. As shown in Tables I and II, the Fragility values range from 3.7 to 9.4. Generally, fragility values for most ILs fall between 5 and 10. Those with values below 5 are considered 'most fragile.' This was demonstrated by Castner et.al. (56) in their study of the effect of the symmetry of fluorinated anions on dynamics in imidazolium based ILs. They obtained a value of 3.80 for the 1-ethyl-3-methylimidazolium bis(trifluoromethylsulfonyl)imide IL and attributed this to the effective inter-conversion between the *trans* and *cis* conformations of the anion that facilitated faster ion dynamics.

Table I. VFT fitting parameters for the 5wt% PC in varying molar ratio $AlCl_3$:amide DES electrolytes. Pseudo-activation energies (*B*) are given in Kelvin but can be represented in kJ/mol using the conversion factor 1kJ/mol = 120.31 K. Corresponding Arrhenius activation energies (E_A) and Fragility (*F*) are also included.

	T_0	*B*	*F*	E_A
Sample	(K)	(K)		($kJ \cdot mol^{-1}$)
10AlCl3:10AcA+5%PC				
11AlCl3:10AcA+5%PC	181 ± 4	743 ± 40	4.1 ± 0.1	6.2 ± 0.1
13AlCl3:10AcA+5%PC	227 ± 9	497 ± 78	2.2 ± 0.1	4.1 ± 0.1
15AlCl3:10AcA+5%PC	182 ± 19	666 ± 187	3.7 ± 0.2	5.5 ± 0.2
17AlCl3:10AcA+5%PC	158 ± 34	1037 ± 438	6.6 ± 0.4	8.6 ± 0.4
10AlCl3:10BuA+5%PC	192 ± 10	502 ± 76	2.6 ± 0.1	4.2 ± 0.1
11AlCl3:10BuA+5%PC	187 ± 16	546 ± 129	2.9 ± 0.1	4.5 ± 0.1
13AlCl3:10BuA+5%PC	191 ± 5	489 ± 33	2.6 ± 0.1	4.1 ± 0.1
15AlCl3:10BuA+5%PC	195 ± 5	477 ± 37	2.4 ± 0.1	4.0 ± 0.1
17AlCl3:10BuA+5%PC				
10AlCl3:10PrA+5%PC	207 ± 8	447 ± 59	2.2 ± 0.1	3.71 ± 0.06
11AlCl3:10PrA+5%PC	144 ± 31	961 ± 321	6.7 ± 0.1	8.0 ± 0.1
13AlCl3:10PrA+5%PC	164 ± 13	757 ± 118	4.6 ± 0.1	6.3 ± 0.1
15AlCl3:10PrA+5%PC	182 ± 5	544 ± 40	3.0 ± 0.0	4.53 ± 0.04
17AlCl3:10PrA+5%PC	171 ± 14	667 ± 119	3.9 ± 0.1	5.5 ± 0.1

Compared to the Fragility values of the pure DESs, those for the $AlCl_3$:amide-additive mixtures are larger. Depending on the molar concentration, the pure DES is expected to contain anionic ($AlCl_4^-$, $Al_2Cl_7^-$), cationic ($[AlCl_2(amide)_n]^+$) and neutral ($[AlCl_3(amide)]$ and $[AlCl_3(amide)_2]$) aluminum species. The inclusion of the PC additive is not expected to alter these species. However, the FEC can cause the formation of additional species including $[AlCl_2(amide)_n]$ [F]. In spite of this, the relatively small fragility factors support the existence of local conformational changes of the various species. In our future studies which includes ^{27}Al NMR measurements, one of the objectives will be to determine if additional aluminum ion species are formed from FEC and similar fluorinated additives.

Table II. VFT fitting parameters for the 5wt% FEC in varying molar ratio $AlCl_3$:amide DES electrolytes. Pseudo-activation energies (*B*) are given in Kelvin but can be represented in kJ/mol using the conversion factor 1kJ/mol = 120.31 K. Corresponding Arrhenius activation energies (E_A) and Fragility (*F*) are also included.

Sample	T_0 (K)	*B* (K)	*F*	E_A (kJ·mol^{-1})
10AlCl3:10AcA+5%FEC	195 ± 8	730 ± 83	3.7 ± 0.1	6.1 ± 0.1
11AlCl3:10AcA+5%FEC	193 ± 10	704 ± 104	3.7 ± 0.1	5.9 ± 0.1
13AlCl3:10AcA+5%FEC	180 ± 11	701 ± 106	3.9 ± 0.1	5.8 ± 0.1
15AlCl3:10AcA+5%FEC	162 ± 12	927 ± 135	5.7 ± 0.1	7.7 ± 0.1
17AlCl3:10AcA+5%FEC	161 ± 18	903 ± 190	5.6 ± 0.2	7.5 ± 0.2
10AlCl3:10BuA+5%FEC	163 ± 15	754 ± 139	4.6 ± 0.1	6.3 ± 0.1
11AlCl3:10BuA+5%FEC	197 ± 10	519 ± 76	2.6 ± 0.1	4.3 ± 0.1
13AlCl3:10BuA+5%FEC	150 ± 12	855 ± 118	5.7 ± 0.1	7.1 ± 0.1
15AlCl3:10BuA+5%FEC	187 ± 4	557 ± 34	3.0 ± 0.1	4.63 ± 0.03
17AlCl3:10BuA+5%FEC	126 ± 12	1126 ± 127	8.9 ± 0.1	9.4 ± 0.1
10AlCl3:10PrA+5%FEC	208 ± 6	503 ± 48	2.4 ± 0.1	4.2 ± 0.0
11AlCl3:10PrA+5%FEC	190 ± 3	576 ± 25	3.0 ± 0.1	4.8 ± 0.0
13AlCl3:10PrA+5%FEC	161 ± 13	746 ± 115	4.6 ± 0.1	6.2 ± 0.1
15AlCl3:10PrA+5%FEC	189 ± 10	550 ± 79	2.9 ± 0.1	4.6 ± 0.1
17AlCl3:10PrA+5%FEC	151 ± 7	887 ± 73	5.9 ± 0.1	7.4 ± 0.1

Summary

We determined the variable temperature ionic conductivities for mixtures comprised of varying molar ratios (1:1 – 1.7:1) of $AlCl_3$:amide (acetamide, propionamide, and butyramide) with 5wt% PC, or FEC additives. This was done in an effort to determine the effect of additives commonly

used to improve the performance and ion dynamics of lithium ion battery electrolytes on $AlCl_3$ deep eutectic solvents (DESs). Although the FEC has a larger dielectric constant compared to PC, compared to the pure DES electrolytes the conductivity of the mixtures was generally lowered by the FEC additive but selectively improved by the PC. The smaller conductivities of the FEC mixtures may be due to its terminating fluorine atom which may be interacting with the cationic species to create $[AlCl_2(amide)_n]^+$ [F]. Our future ^{27}Al NMR studies will investigate this possibility, as well as determine the changes in the local dynamics due to the incorporation of the additives. Similar to the pure DES, the $AlCl_3$:amide-additive mixtures show a maximum in conductivity that was amide dependent. In the case of PC, the maximum shifted from 1.3:1 in the pure DES to 1.1:1 molar ratio for both the propionamide and butyramide mixtures. This suggests that for both amides, it is possible to get effective ion transports at lower $AlCl_3$ concentration. Overall, these results show the use of additives can be used to improve and tune the ionic conductivity of deep eutectic solvents for aluminum electrolyte applications, and possibly extend to other multivalent ion electrolytes.

Acknowledgement

This work was supported by the National Science Foundation, Solid State and Materials Chemistry Program, Division of Materials Research, EAGER award # 1841398.

References

1. M. Armand and J.-M. Tarascon, *Nature*, **451**, 652 (2008).
2. H. Chen, M. Armand, M. Courty, M. Jiang, C.P. Grey, F. Dolhem, J.M. Tarascon, and P. Poizot, *J. Am. Chem. Soc*., **131**, 8984 (2009).
3. B. Dunn, H. Kamath, and J.M. Tarascon, *Science*, **334**, 928 (2011).
4. K. Hayamizu, S. Tsuzuki, S. Seki, K. Fujii, M. Suenaga, and Y. Umebayashi, *J. Chem. Phys*., **133**, 194505 (2010).
5. K. Ueno, J.-W. Park, A. Yamazaki, T. Mandai, N. Tachikawa, K. Dokko, and M. Watanabe, *J. Phys. Chem. C*., **117**, 20509 (2013).
6. B. Geĺinas, M. Natali, T. Bibienne, Q. P. Li, M. Dollé, and D. Rochefort, *J. Phys. Chem. C*., **120**, 5315 (2016).
7. H.-T. Kim, J. Kang, J. Mun, S. M. Oh, T. Yim, and Y. G. Kim, *ACS Sust. Chem. Eng*., **4**, 497 (2016).
8. M. L. Phung Le, F. Alloin, P. Strobel, J.-C. Lepretre, C. P. del Valle, and P. Judeinstein, *J. Phys. Chem. B*, **114**, 894 (2010).
9. F. Castiglione, E. Ragg, A. Mele, G.B. Appetecchi, M. Montanino, and S. Passerini, *J. Phys. Chem. Lett*., **2**, 153 (2011).
10. W. Gai and Z.Y. Deng, *J. Power Sources*, **245**, 721 (2014).
11. Q. Li and N. J. Bjerrum, *J. Power Sources*, **110**, 1 (2002).
12. D.R. Egan, C.P. Leon, R. J. K. Wood, R. L. Jones, K. R. Stokes, and F. C. Walsh, *J. Power Sources,* **236**, 293 (2013).
13. M.L. Douche, J.J. Rameau, R. Durand, and F. Novel-Cattin, *Corros. Sci*., **41**(4), 805 (1999).

14. M. Zhang, V. Kamavarum and R.G. Reddy, *JOM*, **55**, 54 (2003).
15. Y.G. Zhao, and T.J. VanderNoot, *Electrochim. Acta,* **42**, 3 (1997).
16. T. Jiang, M.J.C. Brym, G. Dube, A. Lasia, and G.M. Brisard, *Surf. Coat. Technol*., **201**, 1 (2006).
17. T. Jiang, M.J.C. Brym, G. Dube, A. Lasia, and G.M. Brisard, *Surf. Coat. Technol.,* **201**, 10 (2006).
18. J.J. Auborn and Y.L. Barberio, *J. Electrochem. Soc*., **132**, 598 (1985).
19. P.R. Gifford, *J. Electrochem. Soc.*,**135**, 650 (1988).
20. F.M. Donahue, S.E. Mancini, and L. Simonsen, *J. Appl. Electrochem*., **22**, 230 (1992).
21. C.J. Dymek, *J. Electrochem. Soc*., **131**, 2887 (1984).
22. P.R. Gifford, *J. Electrochem. Soc*.,**134**, 610 (1987).
23. R.T. Carlin, J. Fuller, W.K. Kuhn, M.J. Lysaght, and P.C. Trulove, *J. Appl. Electrochem.*, **26**, 1147 (1996).
24. G. Yue, S. Zhang and Y. Zhu, *AIChE Journal*, **55**, 783 (2009).
25. S.J. Ahn, K. Jeong, and J.J. Lee, *Bull. Korean Chem. Soc*., **30**, 233 (2009).
26. P. Rolland and G. Mamantov, *J. Electrochem. Soc*., **123**, 1299 (1976).
27. J. Robinson and R.A. Osteryoung, *J. Electrochem. Soc*., **127**, 122 (1980).
28. P.K. Lai and M. Skyllas-Kazacos, *J. Electroanal. Chem.*, **248**, 431 (1988).
29. T.J. Melton, J. Joyce, J.T. Maloy, J.A. Boon, and J.S. Wilkes, *J. Electrochem. Soc*., **137**, 3865 (1990).
30. R.T. Carlin, W. Crawford, and M. Bersch, *J. Electrochem. Soc*., **139**, 2720 (1992).
31. K.V. Kravchyk, S. Wang, L. Piveteau, and M.V. Kovalenko, *Chem. Mater*., **29**, 4484 (2017).
32. M. L. Agiorgousis, Y.Y. Sun, and S.B. Zhang, *ACS Energy Lett*., **2**, 689 (2017).
33. H.M.A. Abood, A.P. Abbott, A. D. Ballantyne, and K.S. Ryder, *Chem. Commun*., **47**, 3523 (2011).
34. W. Chu, X. Zhang, J. Wang, S. Zhao, S. Liu, and H. Yu, *Energy Storage Mater.*, **22**, 418 (2019).
35. B. Guchhait, S. Das, S. Daschakraborty, and R. Biswas, *J. Chem. Phys*., **140**, 104514 (2014).
36. P. Hu, R. Zhang, X. Meng, H. Liu, C. Xu, and Z. Liu, *Inorg. Chem.*, **55**, 2374 (2016).
37. M. Angell, C.-J. Pan, Y. Rong, C. Yuan, M.-C. Lin, B.-J. Hwang, and H. Dai, *PNAS*, **114**, 834 (2017).
38. A. P. Abbott, R. C. Harris, Y.-T. Hsieh, K. S. Ryder, and I.-W. Sun, *Phys. Chem. Chem. Phys.*, **16**, 14675 (2014).
39. F. Coleman, G. Srinivasan, and M. Swadźba-Kwasńy, *Angew. Chem., Int. Ed*., **52**, 12582 (2013).
40. J. Estager, P. Nockemann, K. R. Seddon, M. SwadzbaKwasny, and S. Tyrrell, *Inorg. Chem*., **50**, 5258 (2011).
41. A.P. Abbott, G. Capper, D.L. Davies, K.J. McKenzie, and S.U. Obi, *J. Chem. Eng. Data*, **51**, 1280 (2006).
42. D. Paterno, E. Rock, A. Forbes, N. Mohammad, and S. Suarez, *J. Molecular Liquids*, Accepted August 20, 2020. Publication pending.
43. C.A. Angell, *Science, New Series*, **267**, 1924 (1995).
44. B. Geĺinas, M. Natali, T. Bibienne, Q. P. Li, M. Dollé, and D. Rochefort, J. *Phys. Chem. C*., **120**, 5315 (2016).

45. P.M. Richardson, A.M. Voice, and I.M. Ward, *Polymer*, **97**, 69 (2016).
46. H. Shimizu, Y. Arioka, M. Ogawa, R. Wada, and M. Okabe, *Polymer*, **43**, 540 (2011).
47. W. Cui, Y. Lansac, H. Lee, S.-T. Hong, and Y. H. Jang, *Phys. Chem. Chem. Phys*., **18** 23607 (2016).
48. C.-K. Kim, K. Kim, K. Shin, J.-J. Woo, S. Kim, S.Y. Hong, and N.-S. Choi, *ACS Appl. Mater. Interfaces*, **9**, 44161 (2017).
49. C. Liu, W. Chen, Z. Wu, B. Gao, X. Hu, Z. Shi, and Z. Wang, *J. Molecular Liquids*, **247**, 57 (2017).
50. H. Shobukawa, J. Alvarado, Y. Yang, and Y.S. Meng, *J. Power Sources*, **359**, 173 (2017).
51. M. Yoshizawa, W. Xu, and C.A. Angell, *J. Am. Chem. Soc.,* **125**,15411 (2003).
52. J.P. Belieres and C.A. Angell, *J. Phys. Chem. B*, **111**, 4926 (2007).
53. S. J. Bass, W. I. Nathan, R. M. Meighan, and R. H. Cole, *J. Phys. Chem*., **68**, 509 (1964).
54. G.R. Leader and J.F. Gormley, *J. Am. Chem. Soc.,* **73**, 5731 (1951).
55. L.R. Dawson, R.H. Graves, and P.G. Sears, *J. Am. Chem. Soc.*, **79**, 298 (1957).
56. M. Zhao, B. Wu, S. I. Lall-Ramnarine, J.D. Ramdihal Papacostas, E. D. Fernandez, R.A. Sumner, C.J. Margulis, and E.W. Castner, *J. Chem. Phys*., **151**, 074504 (2019).

ECS Transactions, 98 (10) 415-424 (2020)
10.1149/09810.0415ecst ©The Electrochemical Society

Solubility of Rare Earth Oxides in Fused Alkali and Alkaline Earth Halides

V. A. Volkovich[a], A. B. Ivanov[a], A. V. Shchetinskiy[a], A. S. Mukhamadeev[a], A. A. Ryzhov[b], Yu. D. Afonin[a], I. B. Polovov[a], and A. I. Petrov[a]

[a] Department of Rare Metals and Nanomaterials, Ural Federal University, Yekaterinburg 620002, Russian Federation
[b] Department of Physical and Chemical Method of Analysis, Ural Federal University, Yekaterinburg 620002, Russian Federation

Solubility of rare earth oxides in mixtures of alkali or alkaline earth halides was determined by the method of isothermal saturation at the temperatures up to 1400 ^{o}C. The melts studied included $CaCl_2$–CaF_2 (20 or 75 mol. % CaF_2), $BaCl_2$–BaF_2 (15 or 73 mol. % BaF_2), equimolar CaF_2–BaF_2 and eutectic NaCl–NaF mixtures. Melting points of the salt mixtures were determined by differential thermal analysis and effect of added rare earth oxide on the melting point was considered. Solubility of yttrium, lanthanum, cerium, praseodymium, neodymium and samarium oxides was determined. The effect of temperature, melt composition and presence of a mixture of rare earth oxides on the solubility was assessed.

Introduction

Molten mixtures of alkali and alkaline earth halides can be used as working media for electrowinning rare earth metals (REMs). The fact that fluoride and mixed fluoride-chloride baths can be operated at high temperatures simplifies separation of the rare metals from the salt because the melting points of REMs are lower than the working temperatures and separation of two liquid phases (molten metal and liquid salt) is easier to organize. Possible formation of fluorine at the anode during electrowininng process is one of the problems in using fluoride melts. Similarly, chlorofluorocarbons can be produced at the anode in mixed fluoride-chloride melts. This problem can be solved by adding a rare earth oxide both as a source of REM and oxide ions. The latter will be oxidized at the anode to oxygen which will react with the anode material (commonly graphite) yielding carbon mono- or dioxide. From the other side, mixtures of halide salts can be employed as fluxes in melting rare earth metals, for example produced by metallothermic reduction of REM oxides, enabling additional purification from the oxide impurities.

One of the important parameters for organizing technological process is solubility of REM oxides in the salt phase. Solubility of most metal oxides, including REMs, in fused chlorides is low (1). The presence of fluoride ions increases oxide solubility. Solubility of REM oxides in molten salts was mostly studied with the aim of selecting a suitable oxide-fluoride electrolyte for electrowinning rare earth metals (2–9). Such electrolytes always contained fluoride of the corresponding REM as one of the components. As a result the number of works where the solubility of REM oxides was measured in the

melts not containing REM fluorides is relatively small. In one of the early works it was reported that the solubility of CeO_2 in CeF_3–BaF_2–LiF (63–16–21 wt. %) mixture at 800–850 ^oC was 1.7–2.1 wt. %, and the solubility of La_2O_3 in LiF–LaF_3 (16–84 wt. %) and LiF–LaF_3–BaF_2 (20–70–10 wt. %) melts at 950 ^oC was 2.3–2.6 wt. % (10). Subsequently a number of systems based on alkali and/or alkaline earth metal fluorides with added rare earth fluorides were considered. For example, the solubility of lanthanum and neodymium oxides in LiF–$REMF_3$ (40–60 mol. %) melts was reported below 1 wt. % (2). In LiF–BaF_2–$REMF_3$ melts at 900–1040 ^oC the solubility of REM oxides reached 2–4 wt. % (3). In the absence of rare earth fluorides the solubility of rare earth oxides was considerably lower. Electrochemical measurements showed that the solubility of neodymium oxide in fused LiF at 950 ^oC was below the detection limit (4). Contrary, the solubility of lanthanum oxide in molten LiF, NaF and KF was reported as sufficiently high (6). Solubility of REM oxides in fluoride melts noticeably increases in the presence of aluminum fluoride (11). Addition of zirconium fluoride to the melt also resulted in a certain increase of REM oxide solubility (8). For instance, the solubility of lanthanum, samarium and holmium oxides in LiF–ZrF_4, NaF–ZrF_4 and KF–ZrF_4 melts at 600–800 ^oC varied from 0.03 to 0.8 mol. %. A sufficiently full account of the results of studying rare earth oxides solubility in fluoride melts was given by Guo et al. (7).

The aim of the present work was measuring solubility of rare earth oxides in the melts not containing rare earth halides, and determining the effect of temperature and melt composition on REM oxides solubility in fused halides.

Experimental

The experiments were performed in molten CaF_2–BaF_2 (50 mol. % CaF_2); $CaCl_2$–CaF_2 (80 and 25 mol. % $CaCl_2$); $BaCl_2$–BaF_2 (85 and 27 mol. % $BaCl_2$) and NaCl–NaF (66 mol. % NaCl) mixtures. The melts will further be referred to as $0.5CaF_2$–$0.5BaF_2$; $0.8CaCl_2$–$0.2CaF_2$, $0.25CaCl_2$–$0.75CaF_2$; $0.85BaCl_2$–$0.15BaF_2$, $0.27BaCl_2$–$0.73BaF_2$ and 0.66NaCl–0.34NaF. The working temperature interval depended on the melting point and vapor pressure of the salts and was within 750–1400 ^oC range. Anhydrous calcium and barium chlorides (from AppliChem Panreac and Merck KGaA, respectively) were dried at 250 ^oC for 24 hours prior to use. Then dried salts were placed into silica cells and heated under vacuum to 500 ^oC. After reaching this temperature, the cells were filled with argon (99.998 %) and further heated to 850 ^oC for $CaCl_2$ or 1000 ^oC for $BaCl_2$. Molten salts were sparged with gaseous hydrogen chloride for two hours and then with argon for another hour to remove dissolved HCl. Liquid salts were poured into alumina crucibles, allowed to cool under argon and transferred into an argon filled glove box (Glovebox Systemtechnik, with oxygen and moisture content below 2 and 0.1 ppm, respectively) for further use. Calcium and barium fluorides and sodium halides were dried at 250 ^oC (24 h) and then calcined at 700 ^oC. Salt mixtures of the required composition were prepared by fusing required amounts of salts in glassy carbon crucibles under argon atmosphere.

Melting points of the prepared mixtures were determined using thermal gravimetric analysis (single pan differential thermal analysis (SDTA), TGA 851e instrument, Mettler Toledo). The instrument allows conducting the measurements at the temperatures up to 1600 ^oC. The error of the temperature determination is ±0.25 ^oC with the reproducibility of ±0.15 ^oC. Temperature resolution of the differential thermal analysis is 0.005 ^oC with

the root mean square value of 0.01 ^{o}C. The measurements were performed under nitrogen atmosphere and the samples were kept in platinum crucibles. To avoid the melt from getting on the temperature sensor, a small (70 µl) crucible containing the salt was placed into a large (150 µl) crucible. Each crucible was covered with its own platinum lid. The temperature of the beginning of the endothermic effect was taken as the melting point.

Solubility of REM oxides in molten salts can be determined using a variety of techniques including potentiometry, polarography and cyclic voltammetry (1, 4). Applicability of such methods to studying fluoride systems is limited by the absence of suitable material for limiting and controlling the surface area of the working electrode (to keep it constant) and the lack of commonly accepted reference electrode. Another technique for determining solubility of REM oxides in halide melts involves titrating the melt with alkali or alkaline earth oxide or carbonate. Such approach was used to determine the solubility of lanthanum and neodymium oxides in LiF–LaF_3 and LiF–NdF_3 melts, respectively (2). The most direct and universal method for measuring solubility of rare earth oxides in halide melts is isothermal saturation (5). It was reported that excess oxide added to the melt had no effect on the real solubility of REM oxides under equilibrium conditions, i.e. at a constant melt composition and temperature (10). Adding a large excess of the oxide increased the rate of the melt saturation due to increased surface area of the contact between the solid oxide and liquid melt. However, it was reported that in the presence of rare earth fluoride in the melt addition of excess oxide resulted in lowering total concentration of REM in the melt due to formation of sparingly soluble oxyfluorides MOF, where M = REM (12, 13). The method of isothermal saturation was employed in the present study. Time required for saturating the melt was determined in a preliminary series of experiments performed in 0.8$CaCl_2$–0.2CaF_2 melt at 800 ^{o}C. The melt was kept in contact with neodymium oxide for various time intervals (between 2 and 31 h). Analysis of the results showed no noticeable difference in neodymium concentration in the samples taken. This agrees with the observations reported previously where 30 minutes was given as the time required for equilibrating the melt with a REM oxide (10). In the present work the melt was saturated with the oxide for 4 hours before samples of the salt were taken for analysis. Experiments up to 1100 ^{o}C were performed in a vertical tube furnace positioned inside the glove box. The measurements at the higher temperatures (to 1400 ^{o}C) were conducted in a vertical tube furnace (LORA GLB 1800, HTM Reetz GmbH) equipped with a hermetic working chamber and a sampling device.

Samples of quenched salts (1.4–2.0 g) taken from the melts at the desired temperatures were first treated with concentrated sulfuric acid to expel hydrogen fluoride. Then residual alkaline earth sulfates were treated with water to extract rare earth sulfates. Concentration of the rare earths in solutions was determined by determined by ICP-MS analysis (PerkinElmer NexION 350x).

Results and Discussion

Melting Points of the Salt Mixtures

Melting temperatures were determined using SDTA method. Only one endothermic effect was observed on SDTA curves for all the samples except 0.25$CaCl_2$–0.75CaF_2.

The results obtained are summarized in Table I. The melting points obtained here agreed well with the corresponding binary phase diagrams. The effect around 730 ^{o}C in $0.25CaCl_2$–$0.75CaF_2$ system corresponds to the peritectic associated with the decomposition of $CaCl_2 \cdot CaF_2$ phase and 1070 ^{o}C is the temperature of the liquidus. Addition of a new component, e.g. rare earth oxide, into the system can change the melting temperature. To check this possibility, samples of salt mixtures containing neodymium oxide were also analyzed. The results obtained are included in Table I as samples with Nd_2O_3. Addition of neodymium oxide resulted in lowering melting temperatures, the effect was especially pronounced for $0.25CaCl_2$–$0.75CaF_2$ system where the temperature of the second endothermic effect decreased by over 130 degrees.

TABLE I. Temperatures of the beginning of endothermic effects on SDTA curves of salt mixtures.

Sample Composition	Pure Sample / ^{o}C	Sample with Nd_2O_3 / ^{o}C	Difference Between Pure Sample and Sample with Nd_2O_3 / ^{o}C
$0.5CaF_2$–$0.5BaF_2$	1034.0	1029.5	–4.5
$0.8CaCl_2$–$0.2CaF_2$	644.0*	634.6	–9.4*
	643.6*		–9.0*
$0.25CaCl_2$–$0.75CaF_2$	727.1* (1-st effect)	718.6 (1-st effect)	–8.5*
	729.9* (1-st effect)		–11.3*
	731.3* (1-st effect)		–12.7*
	1070.5 (2-nd effect)	936.4 (2-nd effect)	–134.1
$0.85BaCl_2$–$0.15BaF_2$	847.0	845.7	–1.3
$0.27BaCl_2$–$0.73BaF_2$	948.5	946.8	–1.7
0.66NaCl–0.34NaF	680.0	–	–

* Results obtained for different samples.

Effect of Temperature on Solubility of REM Oxides

In first set of experiments the solubility of yttrium, lanthanum, cerium, praseodymium, neodymium and samarium oxides was determined in $0.8CaCl_2$–$0.2CaF_2$ based melts at various temperatures. The results obtained are presented in Table II and summarized in Fig. 1.

Solubility of REM oxides in $0.8CaCl_2$–$0.2CaF_2$ melt varied from ca. 0.01 to 1.5 mol. %. These values are somewhat lower than 0.14–3.8 mol. % reported by Du et al. for solubility of rare earth oxides in LiF–MgF_2(CaF_2) and LiF–MgF_2–CaF_2(BaF_2) melts at 1000 ^{o}C (14). The solubility of La_2O_3 in the ternary LiF–NaF–KF eutectic at 447–995 ^{o}C was also higher and reached 1.5–6.0 mol. % (6). The reason for the low solubility of REM oxides in $0.8CaCl_2$–$0.2CaF_2$ melt might be high chloride content since solubility of rare earth oxides in fused chlorides is considerably lower than in fluorides.

Increasing temperature resulted in increased solubility of the oxides. Similar trend was observed for the solubility of REM oxides in all fluoride melts studied so far (7). Dissolution of REM oxides is an endothermic process and increasing temperature expectedly shifts the equilibrium of the dissolution reaction to the right leading to higher solubility (7). Temperature dependencies of REM concentration in the melts saturated with the corresponding oxides exhibited essentially linear behavior when the concentration was plotted in mol. % on the logarithmic scale vs. reciprocal temperature.

TABLE II. Experiment results of determining REM oxides solubility in melts based on $0.8CaCl_2$–$0.2CaF_2$ eutectic mixture.

REM	T / °C	Concentration in Saturated Melt		
		REM / wt. %	REM_2O_3 / wt. %	REM / mol. %
Y	761	0.012	0.015	0.014
		0.014	0.018	0.017
	822	0.016	0.020	0.018
		0.017	0.022	0.020
	914	0.036	0.046	0.042
		0.034	0.043	0.040
	996	0.068	0.087	0.080
	1007	0.087	0.110	0.102
	1090	0.214	0.272	0.252
La	744	0.023	0.027	0.017
	801	0.057	0.066	0.043
	898	0.139	0.163	0.105
	995	0.444	0.521	0.334
	1071	0.937	1.099	0.706
Ce	754	0.008	0.009	0.006
	803	0.040	0.047	0.030
	893	0.057	0.067	0.042
	986	0.165	0.193	0.123
	1079	0.440	0.516	0.328
Pr	753	0.027	0.031	0.020
		0.041	0.048	0.030
	816	0.057	0.067	0.042
	882	0.123	0.143	0.091
	981	0.383	0.448	0.283
	1070	0.885	1.035	0.657
Nd	700	0.009	0.010	0.006
	800	0.022	0.026	0.016
	900	0.050	0.058	0.036
	1013	0.251	0.293	0.182
	1103	0.557	0.650	0.404
	1200	2.062	2.405	1.501
Sm	804	0.055	0.064	0.038
	885	0.178	0.207	0.124
	980	0.271	0.314	0.188
	1075	0.749	0.896	0.521

No clear uniform dependence of the oxide solubility on the nature of the rare earth metal was observed. Data presented in Table II show that at comparable temperatures the solubility of yttrium oxide in most cases was the lowest. The solubility of cerium oxide was somewhat higher. Lanthanum oxide often (but not always) had the highest solubility and was followed by praseodymium, and then by samarium and neodymium. However, it would be difficult to position all six elements studied here in any strict order that would be correct for all the temperatures.

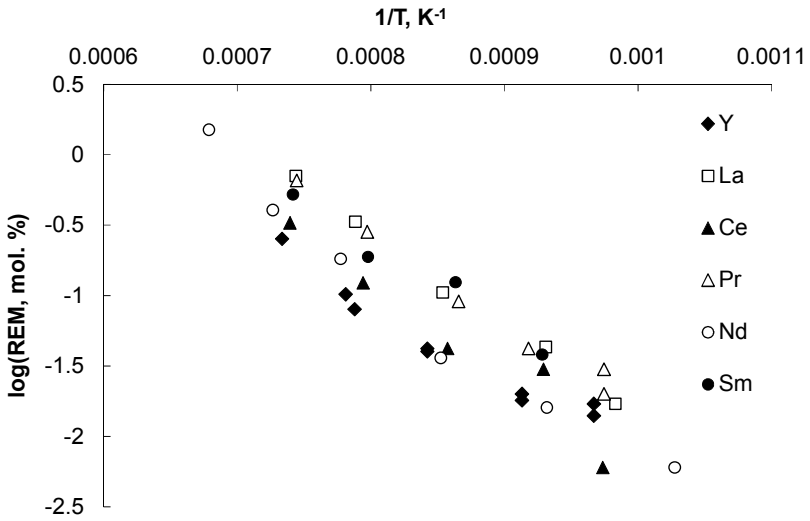

Figure 1. Concentration of REM in $0.8CaCl_2–0.2CaF_2$ based melts saturated with the corresponding oxides at different temperatures.

It was reported that the solubility of lanthanum, samarium and holmium oxides in molten mixtures of alkali metal (Li, Na and K) and zirconium fluorides decreased with increasing ionic radii of the rare earth element, i.e. in the order of holmium-samarium-lanthanum (15). In the present study this apparent effect of rare earth ionic radii was not fulfilled since yttrium oxide, with the smallest cationic radius amongst the elements used, generally showed the lowest solubility while lanthanum oxide, with the largest ionic radius, normally had the highest solubility. Analysis of data on solubility of rare earth oxides in fluoride melts irrespective of their cationic composition showed that the solubility decreased in the following order: $La_2O_3 > CeO_2 > Nd_2O_3 > Y_2O_3 > Ho_2O_3 > Sm_2O_3$, although scatter of the data for each individual oxide was very high (7). This trend somewhat agrees with the end members in our case, i.e. lanthanum (the highest solubility) and yttrium (the lowest solubility) but not for the intermediate oxides.

Effect of Melt Composition on Solubility of Neodymium Oxide

To assess the possible influence of the melt composition on the solubility of REM oxides, a series of experiments with neodymium oxide in various salt mixtures was performed. The results are presented in Table III and summarized in Fig. 2. Here again, solubility of REM oxides increased with temperature. Minimum solubility was observed in 0.66NaCl–0.34NaF, $0.85BaCl_2–0.15BaF_2$ and $0.27BaCl_2–0.73BaF_2$ melts, except for $0.27BaCl_2–0.73BaF_2$ melt at 1200 ^oC.

Analysis of the experimental data showed that the composition of $CaCl_2–CaF_2$ and $BaCl_2–BaF_2$ mixtures had a relatively weak effect on the solubility of neodymium oxide, Tables I and II. Solubility of Nd_2O_3 in $0.8CaCl_2–0.2CaF_2$ and $0.25CaCl_2–0.75CaF_2$ melts was very close, increasing fraction of calcium fluoride from 20 to 75 mol. % did not result in a drastic increase in the oxide solubility. Solubility of Nd_2O_3 in $0.27BaCl_2–0.73BaF_2$ melt was generally higher than in $0.85BaCl_2–0.15BaF_2$ melt, although the difference at 1000 and 1100 ^oC was less than an order of magnitude and only at 1200 ^oC it became significant. Interestingly, temperature dependencies of Nd_2O_3 solubility in

$BaCl_2$–BaF_2 mixtures deviated from linearity when plotted on logarithmic scale vs. reciprocal temperature, Fig. 2.

TABLE III. Experiment results of determining neodymium oxide solubility in melts based on alkali and alkaline earth halides.

Melt	T / °C	Concentration in Saturated Melt		
		Nd / wt. %	Nd_2O_3 / wt. %	Nd / mol. %
$0.5CaF_2$–$0.5BaF_2$	1100	0.65	0.76	0.57
	1200	0.87	1.01	0.77
	1300	1.69	1.97	1.49
	1400	2.47	2.88	2.18
$0.25CaCl_2$–$0.75CaF_2$	1100	0.46	0.54	0.277
	1200	2.70	3.15	1.63
	1300	5.57	4.50	3.41
	1400	8.36	9.75	5.18
$0.85BaCl_2$–$0.15BaF_2$	900	0.00084	0.0010	0.001
	1000	0.00079	0.0009	0.0012
	1100	0.0026	0.0030	0.0037
	1200	0.039	0.046	0.055
$0.27BaCl_2$–$0.73BaF_2$	1000	0.0026	0.0030	0.0033
	1100	0.0068	0.0079	0.0087
	1200	1.44	1.67	1.83
0.66NaCl–0.34NaF	751	0.0051	0.0059	0.0019
		0.0050	0.0058	0.0018
	795	0.0062	0.0072	0.0023
		0.0059	0.0069	0.0022
	845	0.0098	0.0114	0.0036
		0.0093	0.0108	0.0034
	886	0.0150	0.0174	0.0055
		0.0134	0.0156	0.0049
	928	0.0171	0.0200	0.0063
		0.0172	0.0201	0.0063

Surprisingly, solubility of neodymium oxide in purely fluoride melt ($0.5CaF_2$–$0.5BaF_2$) was not the highest, Fig. 2. Only at 1100 °C solubility of Nd_2O_3 in molten $0.5CaF_2$–$0.5BaF_2$ mixture was higher than in other melts studied. At the higher temperatures (1200–1400 °C) solubility of Nd_2O_3 in $0.25CaCl_2$–$0.75CaF_2$ melt was noticeably higher than in $0.5CaF_2$–$0.5BaF_2$. Dissolution of rare earth oxides in fluoride melts is considered either as a purely physical process (M_xO_y(solid)↔M_xO_y(dissolved)) or a chemical reaction leading to the formation of oxyfluoro-species, $MOF_x^{(x-1)-}$ or $M_2OF_x^{(x-4)-}$ (M = REM) (7). Therefore the effect that the melt composition can have on the solubility of REM oxides is not straightforward.

Comparison of calcium and barium chloride-fluoride mixtures showed that the solubility of neodymium oxide was higher in calcium halide based systems. This result agrees with the previously reported effect of cationic melt composition on solubility of rare earth oxides. Thus, solubility of rare earth oxides in MF–ZrF_4 melts (M = Li, Na, K) decreased with increasing alkali metal cation radii (15). Similarly, solubility of La_2O_3 in fused alkali fluorides (LiF, NaF, KF) decreased with increasing alkali cation radii (6). Therefore it seems likely that the solubility of REM oxides in the melts of similar

composition decreases with increasing radii of the solvent salt alkali or alkaline earth cations.

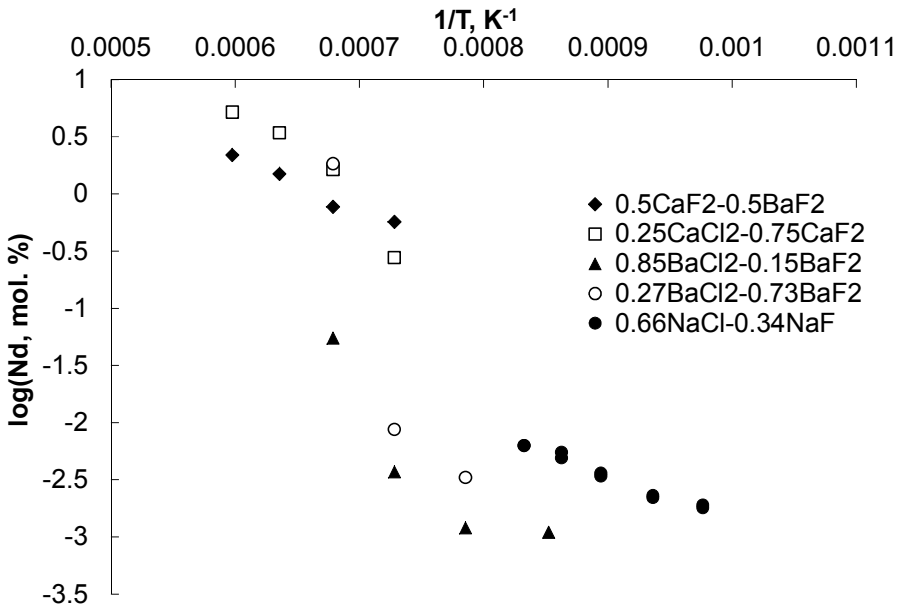

Figure 2. Concentration of neodymium in halide melts saturated with neodymium oxide oxides at various temperatures.

Sodium chloride-fluoride melt (0.66NaCl–0.34NaF) is somewhat different from other systems considered in the present work as being composed of alkali rather than alkaline earth halides. Due to high vapor pressure of alkali halides, the solubility of neodymium oxide in this melt was measured only to 930 ^{o}C and the data obtained showed good linear temperature dependence, Fig. 2. The solubility of neodymium oxide in NaCl–NaF melt was higher than in $BaCl_2$–BaF_2 mixture but lower than in $CaCl_2$–CaF_2 and CaF_2–BaF_2 melts. Nevertheless, the solubility of Nd_2O_3 in the NaCl–NaF eutectic was significantly lower than the solubility of La_2O_3 in the ternary LiF–NaF–KF eutectic mixture (6). The most likely reason for this difference is the lower fluoride content in the NaCl–NaF melt. The nature of the rare earth element can hardly account for the difference of almost three orders of magnitude and the mean cationic radii in LiF–NaF–KF and NaCl–NaF eutectic mixtures are very close, 1.034 and 0.98 Å, respectively.

Mutual Effect of Rare Earths on Solubility of Their Oxides

A separate series of experiments was performed to assess a possible effect that the rare earth elements can have on the solubility of their oxides if they are present together as a mixture. Here a mixture of yttrium, lanthanum, cerium, praseodymium, neodymium and samarium oxides was prepared and used in the experiments. The amount of each oxide added to the melt exceeded its solubility if taken individually. Samples of the salts were analyzed and concentration of each individual REM was determined. The results are presented in Table IV.

The results showed that there was a mutual effect of rare earths on solubility of their oxides. The solubility of each REM oxide in the mixture was lower than the solubility of

the same oxide taken individually, cf. Tables II and IV. The solubility of the sum of rare earths was of the same order as could be expected for individual oxides taken separately. Data presented in Table IV also show that in the melt saturated with the mixture of REM oxides concentration of yttrium often was the lowest and that of lanthanum the highest. Similar general trend was observed for the measurements performed with the individual oxides, Table II. Although again no uniform trend was found, in many cases solubility of rare earth oxides decreased in the following order: $La_2O_3 > Pr_6O_{11} > Sm_2O_3 > Nd_2O_3 > CeO_2 > Y_2O_3$.

TABLE IV. Solubility of a mixture of REM oxides in $0.8CaCl_2–0.2CaF_2$ melt.

REM	Concentration / wt. %		
	At 826 °C	At 920 °C	At 1007 °C
Y	0.0038±0.0004	0.008±0.001	0.0161±0.0007
La	0.0126±0.0006	0.045±0.009	0.076±0.005
Ce	0.0037±0.0002	0.019±0.004	0.029±0.002
Pr	0.0054±0.0003	0.027±0.006	0.049±0.004
Nd	0.0046±0.0003	0.021±0.005	0.042±0.003
Sm	0.0079±0.0004	0.022±0.002	0.040±0.003
ΣREM	0.038±0.001	0.14±0.03	0.25±0.02

Conclusions

Rare earth oxides have rather limited solubility in melts based on alkaline earth or alkali halides (chlorides and fluorides). Solubility in excess of 1 wt. % was observed at the temperatures exceeding 1100 °C. Highest solubility of REM oxides was observed in a fluoride melt ($CaF_2–BaF_2$) or mixed calcium chloride – calcium fluoride melts.

Acknowledgments

The study was supported by JSC “Proryv” (Moscow, Russia).

References

1. H. A. Laitinen and B. B. Bhatia, *J. Electrochem. Soc*., **107**, 705 (1960).
2. Z. Xiaoping, S. Shuchen, L. Chuan and T. Ganfeng, *Adv. Eng. Res.*, **125**, 466 (2017).
3. W. Wu and J. Zhang, *J. Nonfer. Mining Metall.*, **16**, 34 (2000).
4. A. Abbasalizadeh, S. Seetharaman, P. Venkatesan, J. Sietsma and Y. Yang, *Electrochim. Acta*, **310**, 146 (2019).
5. C. Liao, Q. Sun, X. Wang, Y. Jiao, B. Cai and J. Lin, *Zhongguo Xitu Xuebao (J. Chinese Rare Earth Soc.)*, **37**, 99 (2019).
6. M. Ambrová, J. Jurisová, V. Danielik and J. Gabcová, *J. Therm. Anal. Calorim.*, **91**, 569 (2008).
7. X. Guo, J. Sietsma and Y. Yang, in *Rare Earths Industry: Technological, Economic, and Environmental Implications*, I. B. De Lima and W. L. Filho, Editors, p. 223, Elsevier Inc., Amsterdam (2016).

8. R. N. Pshenichny and A. A. Omelchuk, *Russ. J. Inorg. Chem.*, **57**, 115 (2012).
9. R. G. Reddy and S. G. Kumar, *Metall. Material. Trans. B*, **25**, 91 (1994).
10. B. Porter and E. A. Brown, *Determination of Oxide Solubility in Molten Fluorides*, U.S. Dept. of the Interior, Bureau of Mines, Report 5878, p. 4, Washington, DC (1961).
11. , M. Ambrova and J. Jurisova, *Thermochim. Acta*, **443**, 105 (2006).
12. A.-L. Rollet, H. Matsuura and C. Bessada, *Dalton Trans.*, **44**, 522 (2015).
13. X. Zhu, S. Sun, S. Lu, X. Huang, K.Li, G. Tu, X. Huang and S. Huang, *Thermochim. Acta*, **636**, 42 (2016).
14. S. Du, M. Wu, F. Du and Y. Liu, *Chinese Rare Earths*, **8**(2), 59 (1987).
15. R. N. Pshenichny and A. A. Omelchuk, *Russ. J. Inorg. Chem*., **57**(1), 115 (2012).

ECS Transactions, 98 (10) 425-433 (2020)
10.1149/09810.0425ecst ©The Electrochemical Society

Electrochemical Behavior of SmF_3 in Alkali Chloride Melts

Yu. V. Stulov[a] and S. A. Kuznetsov[a]

[a] Tananaev Institute of Chemistry - Subdivision of the Federal Research Centre «Kola Science Centre of the Russian Academy of Sciences», 26a Akademgorodok, Apatity, 184209, Murmansk region, Russia

Electrochemical studies of the redox couple Sm(III)/Sm(II) were carried out in NaCl-KCl, KCl and CsCl melts in a temperature range of 973-1173 K by cyclic voltammetry. Diffusion coefficients (D) of Sm(III) in these melts were determined using the Randles–Sevcik equation. Diffusion coefficients decrease with a change in the composition of the second coordination sphere from sodium to cesium. It is associated with a decrease in the counter-polarizing effect during the transition from Na to Cs, which in turn causes a decrease the metal – ligand bond length in the complexes. The standard rate constants of charge transfer (k_s) of the redox couple Sm(III)/Sm(II) were determined by cyclic voltammetry in the all studied melts using the Nicholson equation, which is valid for quasi-reversible processes. The following series of the standard charge transfer constants was found k_s(CsCl)<k_s(KCl)<k_s(NaCl–KCl).

Introduction

A molten salt reactor in a closed nuclear fuel cycle can serve as an effective environmental barrier from pollution by long-lived radiotoxic nuclides. The design of such a reactor allows to add new of fuel and remove spent fuel without stopping the reactor. But for this it is advisable to reprocess spent nuclear fuel directly at power plants. The significant step of such processing is the effective separation of lanthanides and actinides. It can be carried out using electrochemical methods in molten salt mixtures. A necessary condition for the technology of electrochemical separation is a systematic study of the transport and electrochemical properties of lanthanides and actinides in different molten salts (1).

The electroreduction of samarium in different fluoride melts has been given a considerable attention (2-6). In (2) the two-steps mechanism of the samarium electroreduction was confirmed in LiF-CaF_2 melt by using cyclic voltammetry, chronopotentiometry and square wave voltammetry. Electrochemical behavior of samarium in LiF–BeF_2 on an inert molybdenum electrode was investigated in paper (3). A similar two steps–reduction mechanism of samarium was also identified in molten systems LiF–NaF-KF(eut.) (4) and in molten fluorozirconate (53ZrF_4-20BaF_2-2LaF_3-2YF_3-3AlF_3-20NaF) and fluoroaluminate (35AlF_3-10BaF_2-20CaF_2-10SrF_2-15YF_3-10MgF_2) melts (5). Alkali metal chlorides are not hygroscopic and less susceptible to high temperature hydrolysis and can be used as molten fluorides for separation of actinides and lanthanides (6). At the same time, no systematic studies of the influence of the second

coordination sphere on the electrochemical behavior of SmF_3 in chloride melts have been carried out in any work.

The aim of this study is the electrochemical investigation by cyclic voltammetry of the Sm(III)/Sm(II) redox couple in NaCl-KCl, KCl and CsCl melts containing SmF_3.

This work is a part of systematic study of the first and second coordination sphere compositions on the standard rate constants of charge transfer for the redox couples of rare earth metals, including samarium.

Experimental

Alkali chlorides (NaCl, KCl and CsCl) were purchased from Prolabo (99.5 % min.). They were dehydrated by continuous and progressive heating just above the melting point under gaseous HCl atmosphere in quartz ampoules. Excess HCl was removed from the melt by argon. Salts were handled in the glove box and stored in sealed glass ampoules. SmF_3 (99.5 % *Sigma* Aldrich) was used without any additional treatment. The total concentration of samarium was determined by inductively coupled plasma atomic emission spectroscopy (ICP-AES).

Chlorides of alkali metals were contained in an ampoule made of glassy carbon (SU-2000 type) and were transferred to a hermetically sealed stainless-steel retort. The latter was evacuated to a residual pressure of 0.66 Pa, first at room temperature and then at higher temperatures (473, 673 and 873 K). The retort was then filled with high purity argon and the electrolyte was melted. Experiments were performed under an argon (zero grade: less than 3 ppm H_2O and 2 ppm O_2) atmosphere. The cell was heated using a programmable furnace and temperatures were measured using the Pt-Pt10Rh thermocouple.

The electrochemical studies were performed using cyclic voltammetry, with the AUTOLAB PGSTAT 20 potentiostat and original software (GPES 4.4). The experiments were carried out over the temperature range 973-1123 K. A tungsten wire (99.95 % *Sigma* Aldrich) was used as a working electrode. Platinum wire was utilized as a quasi–reference electrode (7). A glassy carbon ampoule served as the auxiliary electrode. While the potential of this quasi-reference electrode does not constitute a thermodynamic reference, the use of this electrode was preferred to avoid any contact between the melt and oxygen-containing material as used in classical reference electrodes.

Results and Discussion

The cyclic voltammograms obtained at different scan rates (v) in NaCl-KCl-SmF_3 melt at a tungsten electrode are shown in Fig. 1. In studied melts one electroreduction peak R_1 and one electrooxidation peak O_1 was observed, which correspond to the redox process (2-6):

$$Sm(III) + e^- \leftrightarrow Sm(II) \qquad [1]$$

Similar voltammograms for the redox couple Sm(III)/Sm(II) were obtained in all studied melts.

The dependence of the peak current (I_p) on the square root of the potential sweep rate for the NaCl-KCl-SmF_3 melt is presented in Fig. 2. As seen in Fig. 2, the peak current of electroreduction [1] up to v = 1.0 V s^{-1} is directly proportional to $v^{1/2}$, while the peak potential (E_p) was independent on the sweep rate up to the values of v = 1.0 V s^{-1} (Fig. 3). The peak current depended linearly on the concentration of the SmF_3. Potentiostatic electrolysis at the potentials of the cathodic peak did not result in the formation of any solid phase on the electrode and the electrode underwent no noticeable changes. According to the cyclic voltammetry theory (8), the electrode process is controlled by the diffusion rate up to the polarization rate of v = 1.0 V s^{-1} resulting in the formation of a product soluble in the melt. At v > 1.0 V s^{-1}, a deviation of the experimental points is observed from the straight line passing through the origin of coordinates, which evidences a transition from a reversible process to a quasi-reversible process. To prove the quasi reversible nature of the process [1] at v > 1.0 V s^{-1}, additional diagnostic criteria were used. A nonlinear dependence of the peak potential *vs*. log v (Fig. 3) (a linear dependence is characteristic of an irreversible process in the given coordinates) and a higher difference between the potentials of the anodic and cathodic peaks as compared to the calculated value in the case of the reversible reaction point to quasi-reversibility of process.

It was found that in KCl-SmF_3 and CsCl-SmF_3 melts the redox process [1] was also reversible up to the scan rate 1.0 V s^{-1}. A transition from reversible to quasi-reversible process was found at v > 1.0 V s^{1} in KCl-SmF_3 and CsCl-SmF_3 melts.

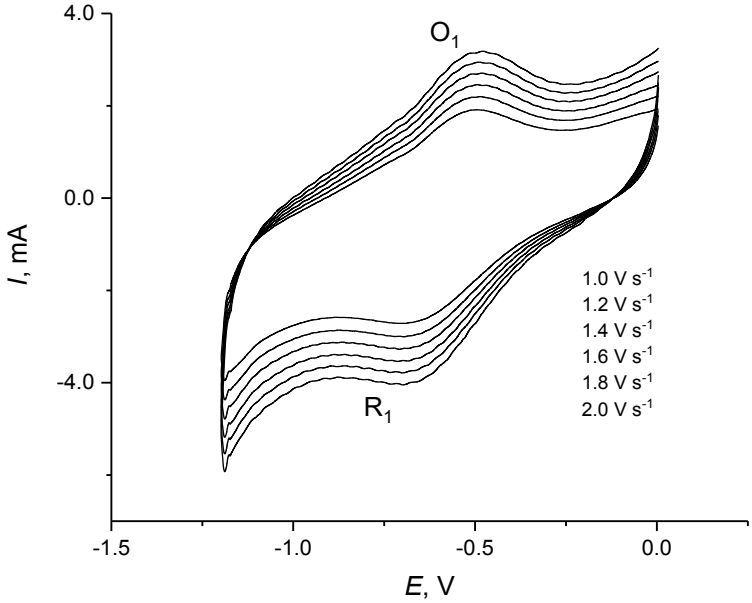

Figure 1. Cyclic voltammograms at a tungsten electrode in NaCl-KCl-SmF_3 melt. Sweep rate: 1.0 (inner curve); 1.2; 1.4; 1.6; 1.8; 2.0 V s^{-1}; temperature: 1073 K; concentration of SmF_3: 6.59 10^{-5} mol cm^{-3}; quasi-reference electrode: Pt wire.

As we have mentioned, based on the theory of cyclic voltammetry (8), there is a linear relationship between peak current and square root of potential scan rate for a reversible soluble/soluble system. This relationship was described by the Randles-Sevcik equation:

$$I_p = 0.446(nF)^{3/2}(RT)^{-1/2}AC(Dv)^{1/2} \quad [2]$$

where I_p is the peak current, A is the electrode area, C is the concentration of electroactive species, D is the diffusion coefficient of electroactive species, v is the potential scan rate, and n is the number of electrons involved in the reaction.

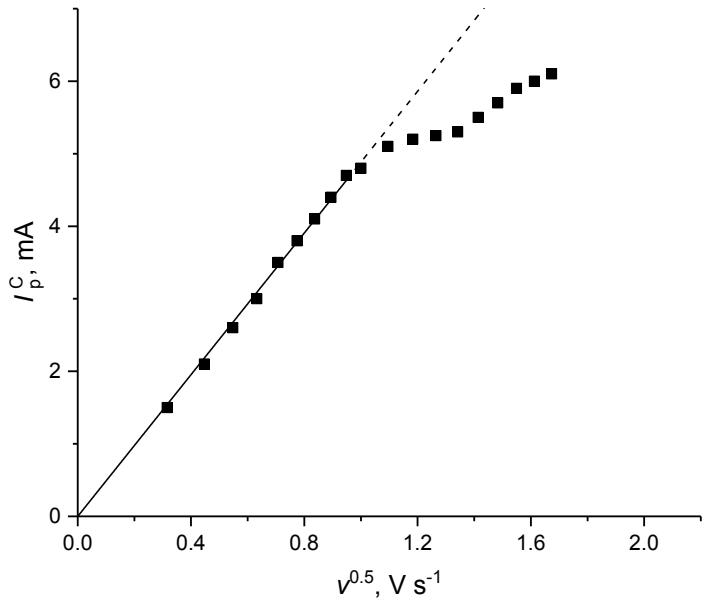

Figure 2. Dependence of the peak current on the potential sweep rate in NaCl-KCl-SmF_3 melt. Concentration of SmF_3: 6.59 10^{-5} mol cm^{-3}; temperature: 973 K.

Using the equation [2] the diffusion coefficients were determined in NaCl-KCl-SmF_3, KCl-SmF_3 and CsCl-SmF_3 melts. The temperature dependences of D are presented in Fig. 4.The activation energies for diffusion (ΔU) of SmF_3 in studied melts are also calculated from the equation:

$$-\Delta U/2.303R = \partial \log D/\partial(1/T) \quad [3]$$

The coefficients of the empirical equation for determining D are presented in Table I. The diffusion coefficients decrease with a change of the composition of the second coordination sphere from sodium to cesium. Similar dependencies for D values are well known (9, 10). It is associated with a decrease of the counter-polarizing effect during the transition from Na to Cs in second coordination sphere of the samarium complexes, which in turn causes a decrease of the metal – ligand bond length and increase the samarium complexes stability. Increasing of the complex stability leads to reducing the contribution of the "hopping" mechanism to the diffusion coefficients as discussed in literature (11-13).

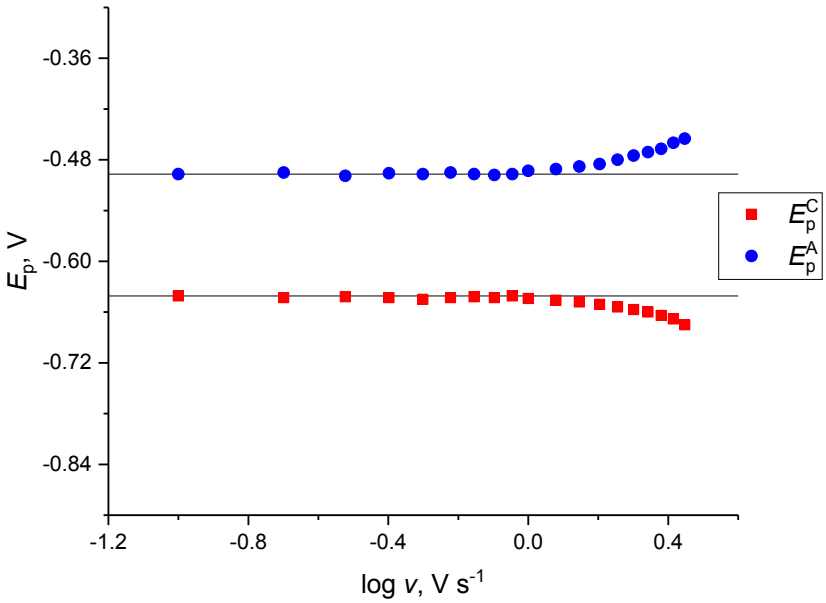

Figure 3. Dependence of the peak potential *vs*. decadic logarithm of the polarization rate in NaCl-KCl-SmF_3 melt. Concentration of SmF_3: 6.59 10^{-5} mol cm^{-3}, temperature: 973K.

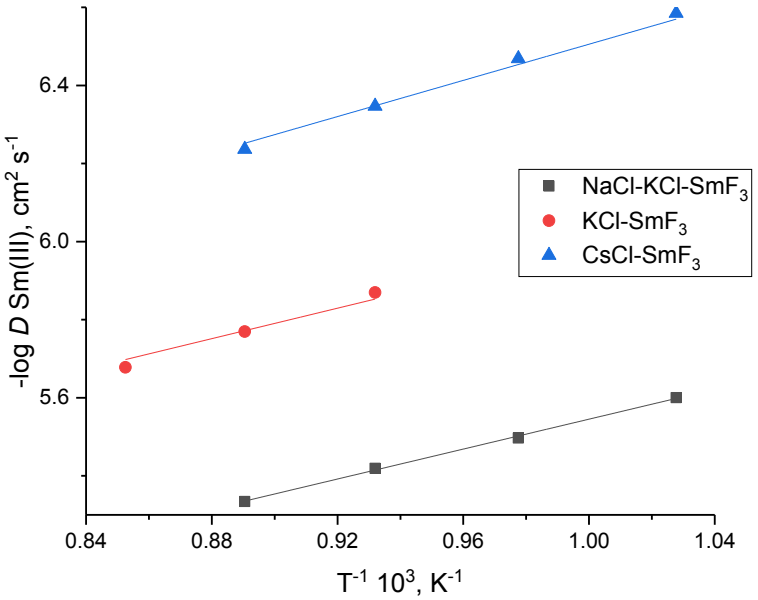

Figure 4. The dependences of the logarithm of Sm(III) diffusion coefficients *vs*. the reciprocal of the temperature in the alkali chloride melts. Concentration of SmF_3: 6.59 10^{5} mol cm^{-3}.

Table I. Diffusion coefficients of SmF_3 and ΔU in alkali chloride melts.

Melt	Temperature range, K	$\log D = - A - B / T \pm \Delta$, $cm^2 s^{-1}$		±Δ	ΔU, kJ mol^{-1}
		A	B 10^{-3}		
NaCl-KCl-SmF_3	973-1123	3.63	1.916	0.10	36.7±0.9
KCl-SmF_3	1073-1173	3.63	2.415	0.04	46.2±0.1
CsCl-SmF_3	973-1123	3.97	2.548	0.10	48.8±1.2

The theory for the determination of the standard rate constants of charge transfer for quasi-reversible redox processes without the formation of any insoluble product based on the method of cyclic voltammetry was developed in (14). In this work (14), the correlation was established between the function ψ related to the difference between potentials of the cathodic and anodic peaks (ΔE_p) and the standard rate constant of charge transfer:

$$\psi = \frac{k_s (D_{ox} / D_{red})^{\alpha/2}}{\sqrt{(\pi D_{ox} n F v) / RT}} \quad [4]$$

where α is the electrokinetic transfer coefficient.

The α = 0.5 value was used in equation [4] because it is for this a value that in the original work (14) a relationship between the ψ function and ΔE_p was established. Besides, for the ψ values, experimentally determined in this work, the ΔE_p values are practically independent of α, if α =0.3 - 0.7 (15).

Equation [4] can be simplified because usually $(D_{ox}/D_{red})^{\alpha/2} \approx 1$:

$$k_s = \Psi[\frac{\pi n F D_{ox} v}{RT}] \quad [5]$$

For determining of the standard rate constant of charge transfer, the data ΔE_p and ψ cited in work (14) for the 298 K should be recalculated for the working temperature. Recalculation was made by using equations (16):

$$(\Delta E_p)_{298} = (\Delta E_p)_T 298/T \quad [6]$$

$$\Psi_T = \Psi_{298} \sqrt{T/298} \quad [7]$$

The values of function Ψ_T obtained according to equations [6] and [7] allowed calculating the standard rate constants of charge transfer for the Sm(III)/Sm(II) redox couple using equation [5] and the values of diffusion coefficients of Sm(III).

The standard rate constants of charge transfer (k_s) of the redox couple Sm(III)/Sm(II) were determined by cyclic voltammetry in alkali chloride melts using the Nicholson's method (14). As expected, the values of k_s do not change with increasing of v in the range of quasi-reversibility of the redox process in all studied melts (Fig 5). In our opinion, this can be another proof of the quasi-reversible of the process [1]. The Fig. 6 shows, that k_s increase with increasing temperature. An increase in the k_s values with increasing

temperature is due to increase in the number of particles capable of overcoming the potential barrier for the electron transfer (17).

The temperature dependences of the standard rate constants of charge transfer in $\log k_s - T^{-1}$ coordinates for NaCl-KCl-SmF_3, KCl-SmF_3 and CsCl-SmF_3 melts are presented in Fig. 6. The values of k_s are described by these empirical equations:

for NaCl-KCl-SmF_3 melt:

$$\log k_s = - (3.91 \pm 0.45) - (6699 \pm 472) T^{-1} \quad [8]$$

for KCl-SmF_3 melt:

$$\log k_s = - (0.69 \pm 0.14) - (4194 \pm 158) T^{-1} \quad [9]$$

and for CsCl-SmF_3 melt:

$$\log k_s = - (2.35 \pm 0.19) - (6448 \pm 195) T^{-1} \quad [10]$$

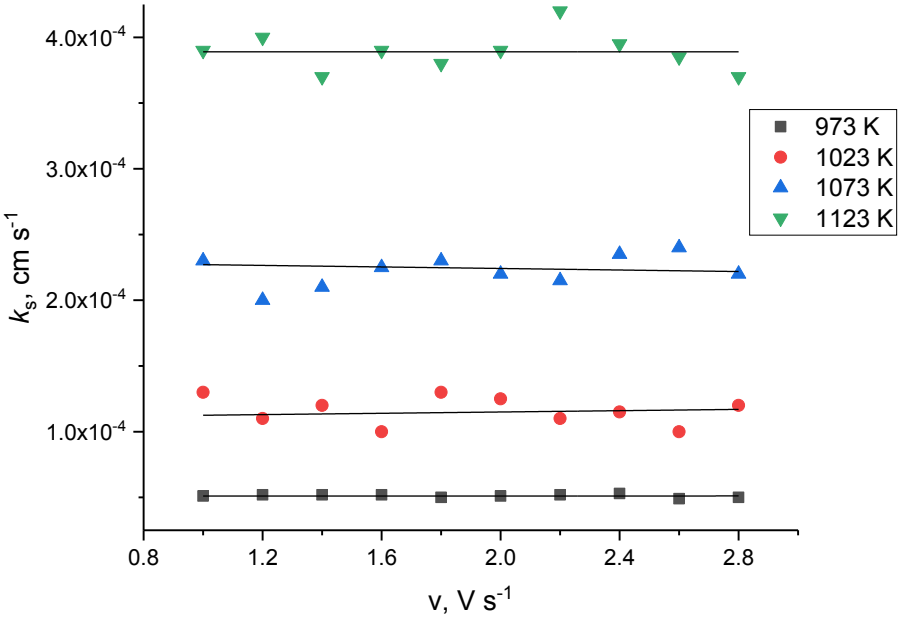

Figure 5. Dependences of the k_s *vs.* on the polarization rate in NaCl-KCl-SmF3 melt at different temperatures. Concentration of SmF_3: 6.59 10^{-5} mol cm^{-3}.

As can be seen from Fig. 5, the standard rate constants decreased from NaCl-KCl-SmF_3 to KCl-SmF_3 and CsCl-SmF_3 melts. Thus, the following series of the standard charge transfer constants was obtained k_s(CsCl)<k_s(KCl)<k_s(NaCl–KCl).

Activation energy (E_a) of the charge transfer for the Sm(III)/Sm(II) redox couple was 128.3±9.0 kJ mol^{-1}, 80.3±3.0 kJ mol^{-1} and 123.4±3.7 kJ mol^{-1} in NaCl-KCl-SmF_3, KCl-SmF_3 and CsCl-SmF_3 melts, respectively. In a general case, with a decrease the activation energy of charge transfer, the values of k_s increase. However, in our case, the following series of E_a was established: E_a(KCl)<E_a(CsCl)<E_a(NaCl-KCl). It should be noted that the activation energy depends on the structure complexes before and after charge transfer. Quantum chemical calculations are needed for explanation of this phenomenon (8, 9).

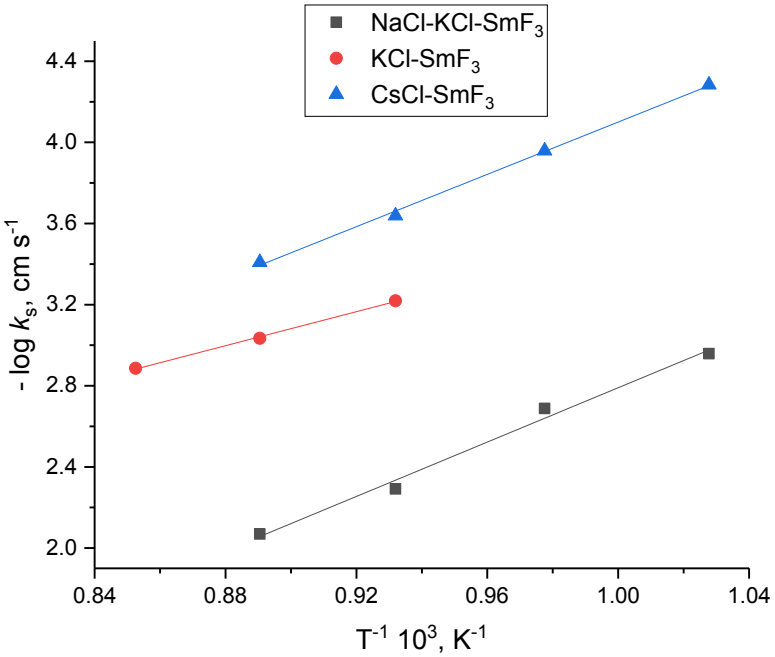

Figure 6. Dependences of k_s *vs.* reciprocal of the temperature in alkali chloride melts containing samarium. Concentration of SmF_3: 6.59 10^{-5} mol cm^{-3}.

Conclusions

Electrochemical behavior of the redox couple Sm(III)/Sm(II) was studied in NaCl-KCl-SmF_3, KCl-SmF_3 and CsCl-SmF_3 melts by cyclic voltammetry.

It was found that the redox process was reversible in NaCl-KCl-SmF_3, KCl-SmF_3 and CsCl-SmF_3 up to the scan rate 1.0 V s^{-1}. In this range of sweep rate, diffusion coefficients of Sm(III) were determined using the Randles–Sevcik equation. It was defined that the diffusion coefficients decreased and activation energies for diffusion increased with a change of the composition of the second coordination sphere from sodium to cesium.

A transition from reversible to quasi-reversible process was found at v > 1.0 V s^{-1} in NaCl-KCl-SmF_3, KCl-SmF_3 and CsCl-SmF_3 melts. The standard rate constants of charge transfer of the redox couple Sm(III)/Sm(II) were determined by cyclic voltammetry using the Nicholson's method. The following series of the standard charge transfer constants was found k_s(CsCl)<k_s(KCl)<k_s(NaCl–KCl).

References

1. B. J. Riley, J. McFarlane, G. D. DelCul, J. D. Vienna, C. I. Contescu, and C. W. Forsberg, *Nucl. Eng. Des.*, **345**, 94 (2019).
2. L. Massot, P. Chamelot, and P. Taxil, *Electrochim. Acta*, **50**, 5510 (2005).
3. M. Straka, M. Korenko, F. Lisý, and L. Szatmáry, *J. Rare Earth*, **29**, 798 (2011).
4. M. Korenko, M. Straka, F. Lisý, and J. Uhlíř, *Curr. Top. Electrochem.*, **16**, 25 (2011).
5. D. R MacFarlane, J Javorniczky, and P. J Newman, *J. Non-Cryst. Solids*, **256-257**, 36 (1999).
6. M. Korenko, Yu. V. Stulov, S. A. Kuznetsov, M. Ambrova, and B. Kubikova, *J. Radioanal. Nucl. Chem.*, **301**, 589 (2014).
7. Y. Berghoute, A. Salmi, and F. Lantelme, *J Electroanal. Chem.*, **65**, 171, (1994).
8. R. S. Nicholson and I. Shain, *Anal. Chem.*, **36**, 706 (1964).
9. A. V. Popova, V. G. Kremenetsky, and S. A. Kuznetsov, *J. Electrochem. Soc.*, **161**, H447 (2014).
10. A. V. Popova, V. G. Kremenetsky, and S. A. Kuznetsov, *ECS Trans.*, **75**, 379 (2016).
11. M. V. Smirnov and O. M. Shabanov*, Trans. Inst. Electrochem. Ural. Branch. Ac. Sci. USSR*, **8**, 55 (1966).
12. S. A. Kuznetsov and P.T. Stangrit, *Rasplavy*, **5**, 42 (1991).
13. S. A. Kuznetsov and M. Gaune-Escard, *J. Electroanal. Chem.*, **595**, 11 (2006).
14. R. S. Nicholson, *Anal. Chem.*, **37**, 1351 (1965).
15. Z. Galus, *Fundamentals of Electrochemical Analysis,* Ellis Horwood, London (1994).
16. S. A. Kuznetsov, S. V. Kuznetsova, and P. T. Stangrit, *Russ. J. Electrochem.*, **26**, 55 (1990).
17. L. I. Krishtalik, *Electrode Reactions. Mechanism of Elementary Act,* Nauka, Moscow (1982).

ECS Transactions, 98 (10) 435-441 (2020)
10.1149/09810.0435ecst ©The Electrochemical Society

Electrodeposition of Tantalum Coatings on Nitinol Stents

A. R. Dubrovskii[a], O. V. Makarova[a], A. I. Shamshurin[b], and S. A. Kuznetsov[a]

[a] Tananaev Institute of Chemistry of the Federal Research Centre "Kola Science Centre of the Russian Academy of Sciences", Akademgorodok 26a, Apatity, 184209 Russia
[b] St. Petersburg State Polytechnic University, ul. Politekhnicheskaya 29/1, St. Petersburg, 194064 Russia

The electrodeposition of tantalum from the NaCl-KCl-NaF (5 wt. %)-K_2TaF_7 (10 wt. %) melt onto nitinol stents was investigated. The formation of several intermediate layers between the coating and substrate was found and their chemical composition was determined.

Introduction

Nickel–titanium alloy (nitinol) is widely used as biomaterials for medical implants due to their unique properties, such as the shape memory and elasticity. However, the passive titanium oxide film providing the corrosion resistance of the alloy disintegrates in the course of time under the action of biological fluids and nickel ions dangerous to health and producing allergic, toxic, and carcinogenic effect find way into the organism (1). In turn, tantalum successfully used as wires or sheets in orthopedic and plastic surgery, has an exclusive corrosion resistance in aggressive media, and, at the same time, exerts absolutely no irritant influence on living tissues and does not interfere with the vital activities of an organism (2, 3). However, it is advisable to use tantalum coatings on various substrates, rather than the compact metal because of its high density. Thus, a topical task is to improve the corrosion resistance of nitinol, which can be done via deposition of protective tantalum coatings. Nitinol is corrosion protected by deposition of tantalum coatings by plasma assisted (4), electric spark (5), and magnetron (6) sputtering. However, these methods fail to produce poreless coatings on nitinol and cannot solve the problem of corrosion protection of nitinol implants in a human organism.

A promising method for obtaining tantalum coatings is electrodeposition of the metal from molten salts (7). The electrolytic technique makes it possible to obtain uniform poreless coatings on complex-shaped articles. This method has also other advantages: (a) electrolysis of melts enables easy control over the structure of deposits, the thickness, porosity, roughness, and texture of electrolytic coatings, and the grain size; (b) the electrodeposition parameters determined on laboratory scale can be extended to large-scale installations and adapted to processes with complex-shape substrates; (c) the resulting coatings are characterized by high purity even with poor-quality starting reagents because tantalum is refined in the course of electrolysis; (d) the operating costs are low and the electrochemical equipment is inexpensive. The most widely used electrolytes for deposition of tantalum coatings are halides of alkali metals, containing salts of tantalum ($TaCl_5$, K_2TaF_7) (7). However, chloride electrolytes are hardly used because of the high $TaCl_5$ vapor pressure and their instability and hygroscopicity. When

purely fluoride melts are used, there appears the problem of electrolyte removal by washing.

In the present study, we used chloride-fluoride melts because these electrolytes are easily removed from the coating surface and the vapor pressure of chloride-fluoride salt systems is substantially lower than that for chloride electrolytes.

The goal of our study was to investigate the mechanism and formation of transition phases during electrodeposition of tantalum onto nitinol stents.

Experimental

In this investigation we used a chloride-fluoride electrolyte of the composition NaCl-KCl-NaF(5 wt. %)-K_2TaF_7(10 wt. %). Sodium and potassium chlorides of analytically pure grade were recrystallized, calcined in a muffle furnace, and placed in quartz retort. The retort was evacuated to a residual pressure of 0.06 Pa, first at room temperature and then under stepwise heating to 200, 400, and 600 °C. After that the retort was filled with argon and the electrolyte was melted.

Sodium fluoride was purified by double recrystallization from a melt: NaF was dried at 400-500 °C in a vacuum and then heated to a temperature 50 °C higher than the melting point, kept at this temperature for several hours, and then slowly cooled at a rate of 3-4 deg min^{-1} to a temperature 50 °C lower than the melting point (8). On being solidified, the salt was transferred at 120 °C in a glove box with controlled atmosphere (O_2 and H_2O content less than 2 ppm) and contaminations were mechanically removed in the glove box.

Potassium heptafluorotantalate was prepared by recrystallization from solutions of a high-purity salt (manufactured at the pilot workshop of Institute of Chemistry and Technology of Rare Elements and Mineral Raw Materials, Kola Science Center, Russian Academy of Sciences) in hydrofluoric acid solutions (content of metallic impurities on the order of 10^{-3} wt. %), followed by washing with ethanol and drying in a vacuum box at 110-120 °C.

The salt mixtures prepared as described above were placed in a molybdenum crucible lined with tantalum and transferred to the retort of the electrolyzer, and the retort was evacuated to a residual pressure of 0.67 Pa at 200 °C and filled with argon of pure grade preliminarily passed through a titanium sponge heated to 800 °C, and the electrolyte was melted.

The microstructure was studied using a Thixomet image analysis system including a Carl Zeiss Observer.D1m optical microscope (OM) coupled to a video camera.

The coatings were also examined by scanning electron microscopy (SEM) on a Tescan MIRA 3 LMH electron microscope with a field-emission cathode. The phase contrast was determined with BSE (Back-Scattered Electrons) detector.

A microanalysis of the samples was made with an Oxford Instruments INCA Energy 450/X-max 80 X-ray energy-dispersive microanalyzer with a nitrogen-free detector.

The microhardness of the samples was measured by microhardness tester PMT-3M LOMO Microsystems including MMC-Microhardness software.

Results and Discussion

Previously, the electroreduction of tantalum complexes in the NaCl-KCl-NaF-K_2TaF_7 melt on a copper and tungsten electrodes has been investigated (9). Tantalum coatings were obtained on nitinol substrates and formation of some intermediate layers between the coating and substrate was observed, but their thickness was not enough for the determination of composition by microanalysis. To solve this problem, the conditions for electrodeposition of tantalum coatings were significantly changed. The electrolysis time was increased (from 10 or 30 min to 4 h.) and the cathodic current density decreased (from 100 mA cm^{-2} to 5 mA cm^{-2}), which made it possible to obtain intermediate layers of sufficient thickness for studying their composition.

Figure 1 (a, b) shows the microstructure of the coating/substrate composition, which consists of several zones. The first zone (outer extended layer) consists of two layers: an electrodeposited coating with a thickness of about 25 μm and an adjacent layer of Ta, Ni, and Ti. Based only on the concentration of elements in this layer, it can be concluded that this is an intermetallic compound or a mixture of phases, since the values of the concentration of elements are approximately the same. Nevertheless, taking into account three facts listed below, it follows that this zone consists of a supersaturated solid solution of nickel in a titanium-tantalum intermetallic compound.

- Figure 1 shows that two zones morphologically have a single base;
- According to the phase diagram (Figure 2a), titanium can dissolve in tantalum indefinitely;
- A synthesis method that creates conditions far from equilibrium realizes phases with a structure and chemical composition that are very different or do not exist at all in equilibrium conditions.

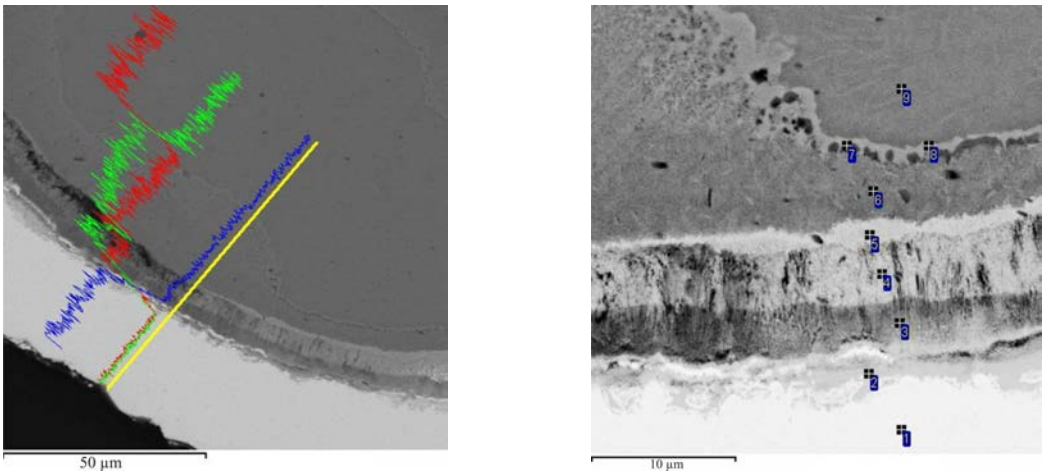

(a) (b)

Figure 1. Elemental distribution in the coating/substrate (Ta/TiNi) composition (red - Ti, green - Ni, blue - Ta), continuous scanning (a), discrete on the stent (b), stent diameter 10 mm, nitinol filament thickness 100 μm. Conditions: the melt – NaCl-KCl-NaF (5 wt. %)-K_2TaF_7 (10 wt. %), current density – 5 mA cm^{-2}, time of electrolysis – 4 h.

TABLE I. Parameters of the zones and transition layers of the TiNi/Ta composition.

Zone	Layer (No. of measurement in fig. 1b)	Length of zones, μm	Phase composition	Ti, wt.%	Ni, wt.%	Ta, wt.%
1	1 (1)	25	Ta	-	-	100
	2 (2)	5	Ta: Ni,Ti	18,27	19,66	62,07
2	1 (3)	~5	$TaNi_2$ +TiNi +$TiNi_3$	25,09	60,30	14,61
	2 (4)	~5	$TaNi_2$ +TiNi +$TiNi_3$	17,84	54,48	27,68
	3 (5)	2-5	$TiNi_{2.4}Ta_{0.06}$	23,87	70,98	5,15
3	1 (6)	5-25	$TiNi_3$ +TiNi	30,60	69,40	-
	2 (9)		TiNi	43,55	56,45	-

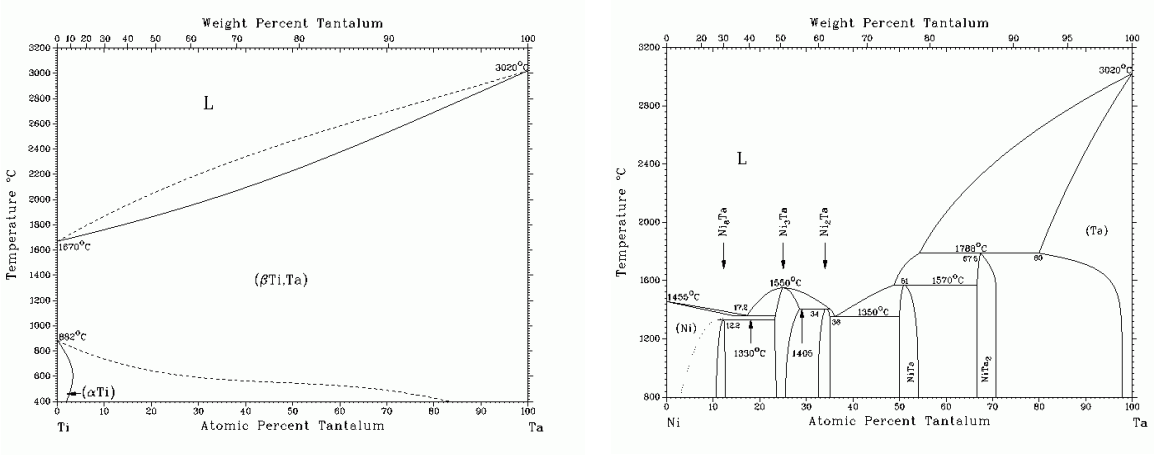

(a) (b)

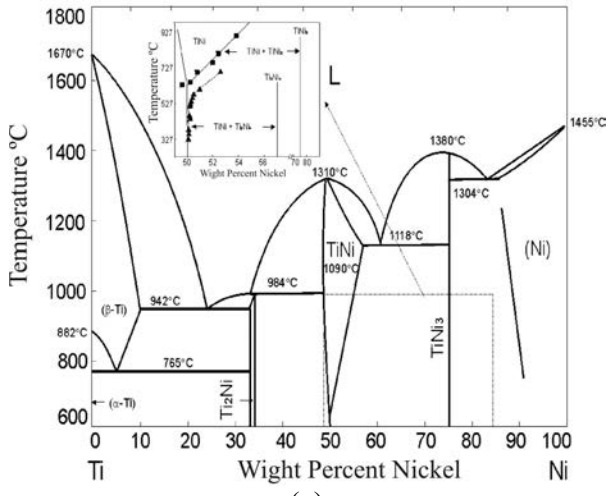

(c)

Figure 2. Equilibrium phase diagrams (a) Ti-Ta (10), (b) Ni-Ta (11), and (c) Ti-Ni (12).

The next zone (zone 2) consists of three layers, which differ slightly in morphology and chemical composition and in terms of atomic ratios and according to the phase diagram in Figure 3 the compositions of these layers are in the region of coexistence of three phases with different ratios between them: TiNi - $TiNi_3$ - $TaNi_2$. Common to these phases is the lower titanium concentration by 1.5-2.3 times less compared to TiNi.

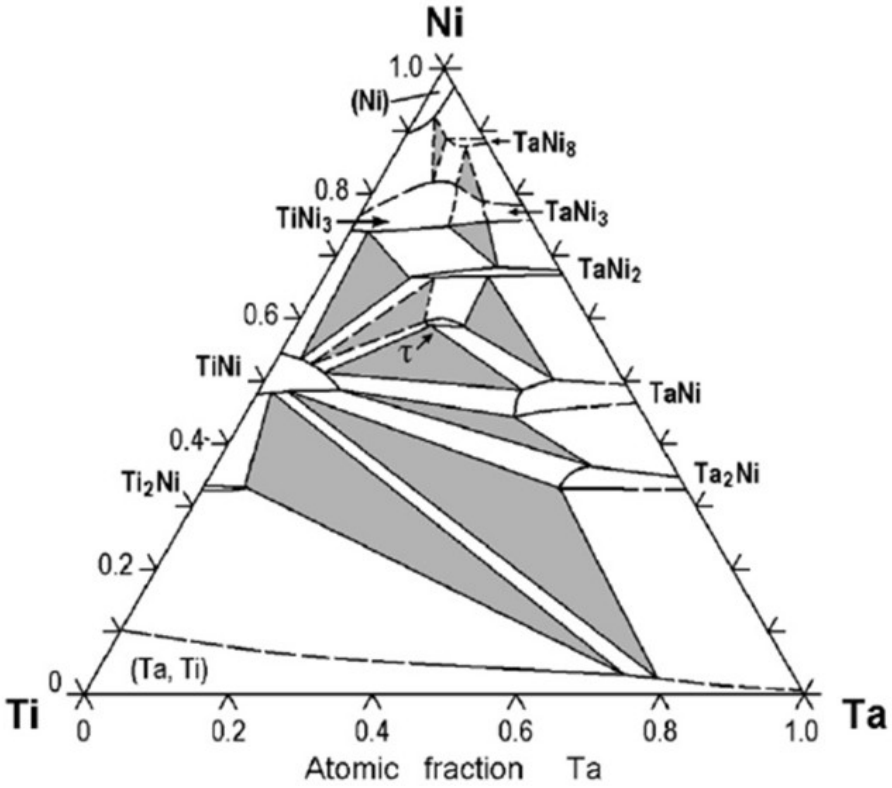

Figure 3. Ternary phase diagram of the Ti-Ni-Ta system (13).

The first layer has a width of two to five microns (Figure 1b). The thickness of the second layer is approximately five microns. The structures of the first two layers are morphologically similar but differ in color. The difference between the first and second layers is in the higher content of tantalum, which probably leads to a color change (Figure 1), i.e., these phases have different compositions but close in crystallographic structure. The third layer with a thickness of 1-3 microns is a barrier for the penetration of tantalum into titanium nickelide, since neither tantalum nor its traces have been recorded outside of it. According to its morphological form the layer is single-phase and taking into account the elemental composition this layer is an intermetallic compound.

The third zone is not inhomogeneous too; it consists of a titanium nickelide layer with a low titanium content (layer 1) and the base of the TiNi sample (layer 2). The width of layer 1 varies throughout the sample in the range from five to twenty-five microns (Figure 1). The reason most likely is the orientation of the boundary (edge) grains which either promotes or prevents the diffusion of titanium from the base material. The composition of this layer is in the two-phase region of the equilibrium Ti-Ni diagram (Figure 2c) and corresponds to the composition of $TiNi_3$ + TiNi.

The long duration of the experiment is not limited to the processes of relaxation of internal stresses and annihilation of defects without fundamental changes in the structure of the material but leads to polygonization (selective growth of grains) of the TiNi base (Figure 4), which worsens the mechanical characteristics of the tantalum-nitinol composition.

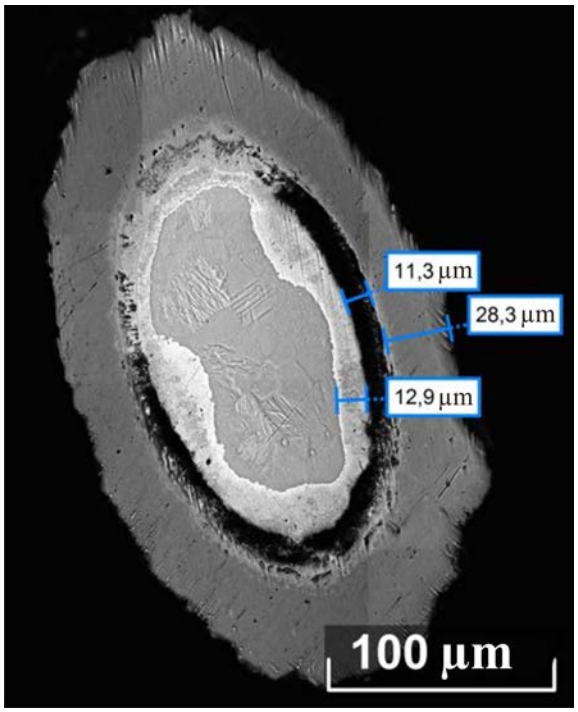

Figure 4. Microstructure of the coating/substrate (Ta/TiNi) composition on the stent, stent diameter 10 mm, thickness of titanium nickelide filament 100 µm. Conditions: the melt – NaCl-KCl-NaF(5 wt. %)-K_2TaF_7(10 wt. %), current density – 5 mA cm^{-2}, time of electrolysis – 4 h.

The microhardness of the substrate is on average 330 kg mm^{-2} and the tantalum coating 186 kg mm^{-2} which is typical for the cubic lattice of synthesized α-Ta (89-5152 ASTM card). An image of a sample with indentations from an indenter is shown in Figure 5.

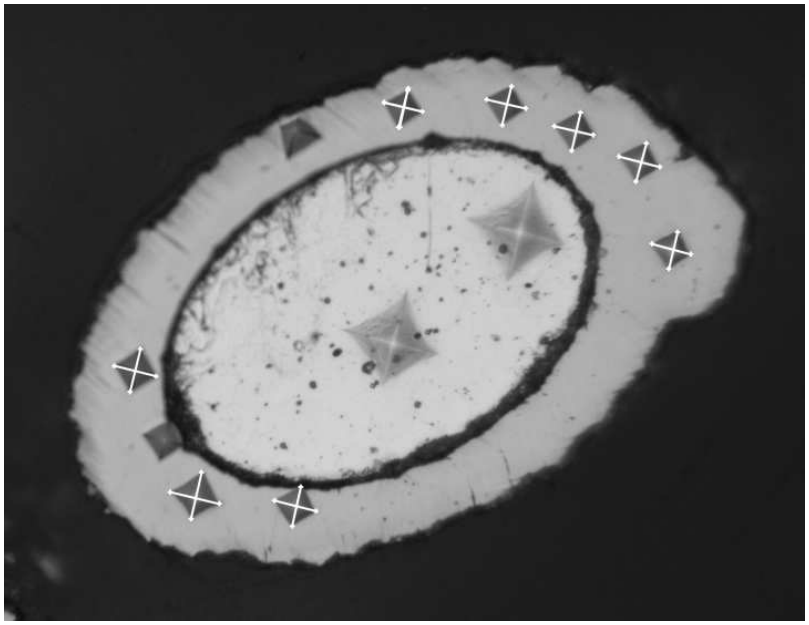

Figure 5. Vickers pyramid imprints for microhardness measurement. The load of 200 g per TiNi field and 20 g per the Ta coating field. Conditions of the synthesis are the same in figure 4.

Conclusions

It was determined that electrodeposition of tantalum on nitinol is accompanied by alloy formation.

The substrate transformation (nitinol), which appears itself during tantalum grain growth was detected. The surface layers of the substrate are depleted in titanium, which irreversibly leaves the nitinol due to corrosion in the melt.

During electrochemical synthesis, a barrier intermetallic layer $TiNi_{2.4}Ta_{0.6}$ is formed, which prevents the penetration of tantalum into the substrate, but does not prevent the diffusion of nickel and titanium from the substrate into the applied coating.

As the tantalum complexes are discharged on the "new" surface, the composition is enriched with tantalum and becomes two or three phase. Since the rate of electrocrystallization is higher than the diffusion of Ni, Ti, and Ta in the material, the newly formed layer does not form a three-phase structure, but a solid solution of nickel and titanium in tantalum and then the pure tantalum coating crystallizes. The length of the layers depends on the time and temperature of electrolysis - then higher the values of these parameters, so wider the layers due to the mutual diffusion.

References

1. S. Shabalovskaya, J. Anderegg and M. Van Humbeck, *Acta Biomater.*, 4, (2004).
2. A. N. Zelikman, B.G. Korshunov, A.V. Elyutin and A.M. Zakharov, *Niobii i tantal (Niobium and Tantalum)*, Moscow: Metallurgiya (1990).
3. R. W. Revie and H. H. Uhlig, *Corrosion and Corrosion Control: An Introduction to Corrosion Science and Engineering*, John Wiley & Sons (2008).
4. G. Wang, Y. Shen, Y. Cao and R. Guidoin, *IET Nanobiotech.*, 1, (2007).
5. Y. Cheng, W. Cai, H. T. Li and Y.F. Zheng, *J. Mater. Sci.*, 41, (2006).
6. A. A. Neiman, L. L. Meisner, A. I. Lotkov, V. P. Sergeev, K. P. Redlih, *Perspekt. Mater.*, 1, (2009).
7. V. I. Konstantinov, *Elektroliticheskoe poluchenie tantala, niobiya i ikh splavov (Electrolytic roduction of Tatalum, Niobium, and Alloys of These)*, Moscow: Metallurgiya (1977).
8. G.A. Bukatova, S.A. Kuznetsov and M. Gaune-Escard, *J. Min. Metall., Sect. B*, 39, (2003).
9. S. A. Kuznetsov, E. A. Papetova, *J. Phys.: Conf. Ser.*, 1281, 012042 (2019).
10. J. L. Murray. *Bulletin of Alloy Phase Diagrams*, 2, (1981).
11. I. I. Kornilov and Ya. N. Pylayeva, *Russ. J. Inorg. Chem.*, 7, (1962).
12. A. I. Lotkov, V. N. Khachin, V. N. Grishkov, L. L. Meysner, V. P. Sivoha, *Splavy s pamyatyu formy (Alloys with shape memory)*, Novosibirsk: Nauka (1995).
13. D. Yong, X. Honghui, Z. Yichun, O. Yifang, J. Zhanpeng, *Mater. Sci. Eng. A*, 448, (2007).

ECS Transactions, 98 (10) 443-451 (2020)
10.1149/09810.0443ecst ©The Electrochemical Society

Uranium Electrorefining in 3LiCl–2KCl Based Melts

D. I. Nikitin, D. A. Zolotarev, A. D. Mukhametdyanov,
V. A. Volkovich, and I. B. Polovov

Department of Rare Metals and Nanomaterials, Ural Federal University, Ekaterinburg, 620002, Russia.

The process of uranium electrorefining in 3LiCl–2KCl based melts was investigated. Dense and compact uranium deposits were obtained at low current densities, while application of relatively high current densities led to the formation of uranium dendrites. Cathodic current efficiency in the majority of experiments confirmed the three-electron scheme of uranium reduction. Cathodic current efficiency under certain conditions exceeded 95 %. The amount of salt retained in the cathodic deposit varied from 7 to 26 %, these values typical for dendrite electrolytic metals.

Introduction

Molten halides can be effectively employed for electrorefining refractory and radioactive metals with relatively negative reduction potentials and high melting temperatures. In the present study electrorefining of uranium was studied for developing pyrochemical reprocessing technology for metallic or metallized spent nuclear fuels (SNF). 3LiCl–2KCl eutectic based molten salt with relatively low melting point was chosen as a working electrolyte. Metallic uranium acted as a model of fissile materials. The main goal of the current investigation was the determination of the influence of galvanostatic electrolysis parameters on the morphology of uranium deposits and technological characteristics of uranium electrorefining procedure.

Investigation of uranium electrodeposition from molten salts was started in 1930s, when Driggs and Lilliendahl obtained first “tree-like” cathodic deposit of uranium in fused equimolar mixture of sodium and potassium chlorides containing UCl_4 и KUF_5 (1). Kolodney studied uranium deposition from NaCl–KCl–$BaCl_2$–UCl_3 melt, varied uranium concentration in the electrolyte and applied different cathodic current densities, and produced dendrite metal deposits on a tungsten cathode (2, 3). However, purity of the obtained uranium metal in the pioneering investigations was very poor.

First uranium electrorefining experiments in 3LiCl–2KCl based melts were performed by Marzano and Noland in Argonne National Laboratory (ANL) in the middle of 1950s (4). They obtained the current efficiency less than 61 % and reported the absence of other morphologies formation except dendrites. More expanded study of electrorefining processes was done by Niedrach and Glam (5). The experiments were carried out in 66 % $BaC1_2$–34 % UF_4, 24 % $CaC1_2$–76 % $UC1_3$, 62 % $CaC1_2$–38 % UCl_3, 75 % $CaC1_2$–25 % UCl_3, and 90 % $CaC1_2$–10 % $UC1_3$ melts at 900–1075 °C varying cathodic current densities from 0.1 to 1 A/cm^2. They found that liquid Ni–U alloy was formed on the nickel cathode.

Inman et al. noticed the formation of uranium dendrites on molybdenum or tungsten cathodes and calculated the number of electrons involved in cathodic reduction process (6). They demonstrated that process of uranium electrodeposition from 3LiCl–2KCl–UCl_3 melts at 440–550 °C and current densities below 0.1 A/cm^2 consisted of one three-electron step. They also indicated the dendrite morphology of the cathodic deposits when there was no interaction between deposited uranium and cathode material. Replacement of UCl_3 by UF_4 had no influence on the morphology of the cathodic deposits (7).

The most detailed investigation of uranium electrorefining in 3LiCl–2KCl-based melts under galvanostatic conditions was performed in Commissariat à l'énergie atomique (CEA), France (8–10). The following parameters were chosen for preliminary experiments concerning the electrodeposition of uranium on solid molybdenum cathode: uranium concentration in the melt – 30 mol. %, temperature – 450–500 °C, cathodic and anodic current densities – 0.1 A/cm^2 (8, 9). Uranium dendrites were the only product formed under the described conditions on molybdenum crucible acting as the cathode. Later French scientists described electrorefining experiments using industrial electrolytic bath allowed to produce 1000 kg uranium per year (10). Cathodic product was represented by dendrite deposits (length – from 2 to 100 mm, cross-section – from 0.01 to 10 mm^2) that were characterized by very high pyrophoricity. The cathodic current efficiency was equal to 65–70 %. The amount of metallic and non-metallic impurities in the refined product did not exceed their detection limit (5–20 ppm) but the crude material was very pure. However, the proposed regime allowed obtaining only dendritic uranium deposits with relatively low current efficiencies.

The next cycle of experiments in ANL was directed towards the production of non-dendritic electrorefined uranium (11). Uranium electrodeposition was performed in UCl_3-conaining chloride melts and UF_4-containing chloride-fluoride baths at 440–560 ºC. The authors also applied the impulse regimes to decrease the number of dendrites but obtained the coherent coatings of only 150 μm thickness.

Recently the large investigation on uranium electrorefining in molten salts was performed in Korea Atomic Energy Research Institute, KAERI in the frame of elaboration of new SNF pyrochemical reprocessing technology (12–14). All the experiments were performed in the argon-filled glove-box using 3LiCl–2KCl-based electrolyte at 500 °C with initial uranium trichloride concentration of 9 wt. %. The obtained cathodic deposits had the dendrite-type structure. However, their morphology varied depending on the applied current density. When a low current density was applied (less than 0.05 A/cm^2) a whisker like dendrite structure was observed. When the current density was within 0.1–0.3 A/cm^2, formation of a rhombic like dendrites was dominant, and the crystal size of the rhombic was decreased at a higher current densities (above 0.4 A/cm^2). Current efficiencies, however, were not reported (12). Further studies of Korean scientists were dedicated to application of different types of graphite as a cathode material. In these investigation the authors introduced the name of «sticking coefficient» that was equal to the ratio between mass of cathodic deposits and theoretically calculated mass of deposited uranium. In fact this is the same as the cathodic current efficiency (13, 14). This value was equal to 0.6 or 60 % when the applied current density was 0.03 A/cm^2, whereas it decreased to 6 % when current density was increased to 0.1 A/cm^2 (13).

One can see that that the presented data are incomplete and sometimes contradictive. The information about the influence of parameters of electrolysis on cathodic morphology is limited. The presented technological parameters are different (in terms of cathodic current efficiency) or absent (electrolyte retention by the cathodic deposit). The detailed analysis of the influence of electrolysis parameters (current densities, uranium concentration in the melt, and specific quantity of electricity) was not performed. The present work was aimed to fill these gaps.

Experimental

The experiments on uranium electrorefining were carried out in a semi-industrial water-cooled electrolyser made of 12Kh18N10T type stainless steel (15). A specially weaved molybdenum basket was made for performing elecrorefinig experiments. Metallic uranium bars were loaded in anodic basket to provide the required anodic current density (less than 0.1 A/cm^2). Individual alkali (lithium and potassium) chlorides were additionally purified as described previously (16). Binary 3LiCl–2KCl eutectic mixture (58 mol. % LiCl) was prepared by fusing individual salts in the required proportion at 650°C. Uranium containing electrolytes (3LiCl–2KCl+UCl_3, 7 wt. % uranium) was prepared by dissolving the necessary amount of uranium trichloride in the solvent melt. Uranium trichloride was synthesized by reducing uranium tetrachloride with excess zinc followed by vacuum distillation of the reaction product. The synthesis and purification procedure was described in detail previously (17).

After the electrolyser was heated and the electrolyte melted, a molybdenum cathode as a part of cathode assembly (Fig. 1) was lowered into the melt. The surface area of the cathode was constant and equal to 10 cm^2. Small BeO tubes were slipped on the cathodic supporting rod to guarantee the required surface and exclude the three-phase (solid cathode – liquid melt – gaseous atmosphere) contact, Fig. 1.

Figure 1. Cathode assembly (cathode is shown at the top).

To control the process samples of electrolyte were taken at beginning of electrolysis and at each stage of the refining procedure. Temperature of the process, electrolysis current and voltage on the bath were controlled during the experiments.

The obtained cathodic deposits were washed several times with 1 M solution of nitric acid until a transparent and colorless solution was obtained. The uranium deposit was separated from the captures quenched salt electrolyte during these procedures. At the next stage the precipitate was consequently washed by water and ethyl alcohol (95 wt. % solution). Then it was dried in a vacuum oven. Dried metal and electrolyte samples were stored in an MBraun Unilab inert box, where the content of oxygen and moisture impurities was maintained below 10 ppm.

Results and Discussion

The influence of different parameters on results of uranium electrorefining in 3LiCl–2KCl eutectic based melts under various conditions was determined. Current efficiently in terms of three-electron discharge scheme, morphology of obtained cathodic deposits, and the degree of capture of salt electrolyte by deposited uranium were chosen as response factors in the present study. Current density, uranium concentration and specific quantity of electricity were selected as variables. Variable parameters and their intervals were chosen on the basis of the preliminary experiments and the results of kinetics studies (18). The experimental results on various cathodic current densities during uranium electrorefining at 500 °C are presented in Table I.

TABLE I. Results of experiments on the electrorefining uranium performed using cathodes made of molybdenum (experiments 1, 2, 4, 6) and alloy KhN62M (experiments 3, 5) when the cathodic current density changed (uranium concentration 7.2±0.2 wt %, temperature 500±10 °C, specific quantity of electricity 1 A·h/cm^2).

Exp. No.	Cathodic Current Density, A/cm^2	Cathode Deposition, g	Morphology	Retention of Electrolyte, wt. %	Electrical Efficiency, %
1	0.05*	25.33	Coating + Splices	7.1	100.0
2	0.1**	25.84	Splices + Coating	14.4	86.7
3	0.2	27.01	Splices	17.2	90.6
4	0.4	29.58	Splices + Needles	7.5	99.3
5	0.6	22.98	Needles	18.5	77.1
6	0.8***	10.23	Needles	25.7	68.7

* – specific quantity of electricity was 0.85 A·h,
** – specific quantity of electricity was 0.93 A·h,
*** – specific quantity of electricity was 0.5 A·h.

Images of uranium deposits obtained at different cathodic current densities are presented in Fig. 2. The photos of the material washed from the electrolyte are shown in Fig. 3.

A dense uranium coating that could not be completely separated from the material of the cathode was formed at the current density of 0.05 A/cm^2. The adhesion of the obtained metal to the cathode material was higher in case of KhN62M compare to molybdenum cathode. The photo of coating remained on the cathode is presented in Fig. 4. In this case cathodic current efficiency was equal to 100 % taking into account the mass of separated metal and in assumption that dense coating represented only metallic

uranium. The capture of the electrolyte by the cathodic deposit was *ca.* 7 %. As the purpose of the current study was investigation of the cathodic deposit morphology and finding suitable parameters of electrorefining, we used relatively pure metallic uranium as a crude anode material. However, one can see (Table II) that purity of the cathodic metal correlates well with the chemical composition of the anodic uranium, we did not observe any noticeable contamination of the obtained material by components of the electrolyte or construction materials of electrolysis cell.

Figure 2. Cathodic deposits produced during uranium electrorefining in LiCl–KCl–UCl_3 melts at 500 ^{o}C and different cathodic current densities (shown on the graph for each sample).

The relatively compact deposits were formed at the current densities of 0.1–0.4 A/cm^2 when electrorefining was carried out at 500 ºC and uranium concentration in the electrolyte was close to 7.0 wt. %. The increase of electrolysis time led to formation of dendrite and lamellar structure that grew along the force lines of the electric field. The increase of current density within the indicated range made the separation of uranium metal from the electrolyte easier but caused the increase in electrolyte capture to 20 %.

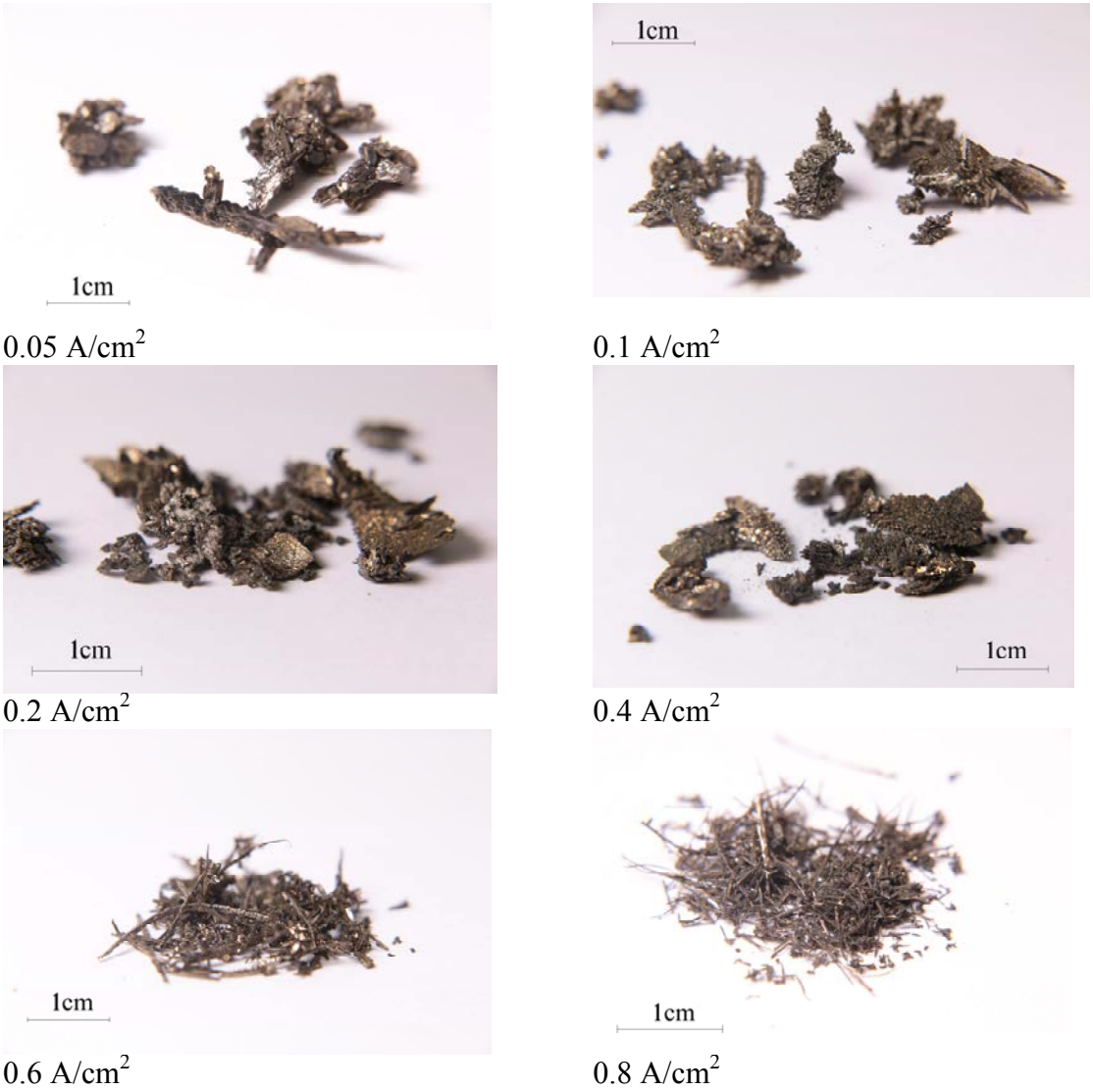

Figure 3. Cathodic deposits produced during uranium electrorefining at different cathodic current densities after being washed from the salt electrolyte.

Increasing cathodic current densities to 0.6–0.8 A/cm^2 led to noticeable changes in the cathodic deposit morphology when the electrorefining was performed at *ca.* 500 ºC and *ca.* 7 wt. % uranium in the electrolyte. The obtained cathodic metal had needle-type shape that tended to form a short circuit with the anodic basket. This shortening caused the decrease of current efficiency due to grown uranium needles when the passed quantity of electricity increased. The capture of electrolyte for the needle-type uranium cathodic deposits was higher than in the case of splices.

We also investigated the effect of concentration of uranium in the electrolyte on the parameters of the electrorefining process and the morphology of the resulting cathodic product. The comparative analysis of the obtained data is presented in Table III.

Figure 4. Uranium coating after hydrometallurgical treatment of uranium deposit produced at low cathode current densities (0.05 A/cm^2).

TABLE II. Results of chemical analysis (wt. %) anode crude material and electrorefinied uranium metal from the cathode.

Element	Anode Material	Electrorefined Deposit
Li	$5.2\cdot10^{-4}$	$4.8\cdot10^{-3}$
Be	$1.6\cdot10^{-5}$	$1.6\cdot10^{-3}$
Ti	$2.5\cdot10^{-4}$	–
Cr	$1.6\cdot10^{-3}$	$7.9\cdot10^{-3}$
Ni	$1.1\cdot10^{-3}$	$6.2\cdot10^{-3}$
Cu	$2.8\cdot10^{-4}$	–
Zr	$1.4\cdot10^{-4}$	–
Nb	$5.2\cdot10^{-6}$	$6.1\cdot10^{-6}$
Mo	$2.4\cdot10^{-3}$	$1.2\cdot10^{-4}$
Cs	$8.7\cdot10^{-6}$	$1.8\cdot10^{-5}$
La	$9.5\cdot10^{-6}$	$2.1\cdot10^{-5}$
Nd	$3.5\cdot10^{-7}$	$3.5\cdot10^{-7}$
W	$5.5\cdot10^{-5}$	$2.0\cdot10^{-5}$
Pb	$4.3\cdot10^{-3}$	–
K	–	$< 1.0\cdot10^{-3}$
Fe	$< 1.0\cdot10^{-3}$	$< 1.0\cdot10^{-3}$

TABLE III. Results of experiments on uranium electrorefining using cathodes made of molybdenum with different uranium concentration in the melt (cathodic current density of 0.4 A/cm^2, temperature 500±10 °C, specific quantity of electricity 0.5 A·h/cm^2).

Uranium Concentration	Mass of Deposit, g	Morphology	Capture of Electrolyte, wt. %	Cathode Efficiency, %
7.0	14.63	Splices	6.8	98.2
3.7	13.65	Needles	16.7	91.6

One can see that decrease of uranium concentration in the electrolyte to 3.7 wt. % led both to change of cathodic deposit morphology and small reduction of current efficiency. Also expected increase of electrolyte capture by the deposit was noticed. From technological point of view it is necessary to exclude the short circuit between the cathode and the anode in case of needle-type morphology of cathodic uranium deposits.

Conclusions

Dense and compact uranium deposits were obtained in 3LiCl–2KCl–UCl_3 melts at low current densities, while application of relatively high current densities led to the formation of uranium dendrites. Intermediate values of the current density allowed producing more coherent deposits that could be easily scraped off the cathode. Cathodic

current efficiency in the majority of experiments confirmed the three-electron scheme of uranium reduction.

The values of cathodic current efficiency in the most of experiments confirmed the three-electron scheme of uranium reduction. Cathodic current density under certain conditions exceeded 95 %. The amount of salt retained in the cathodic deposit varied from 7 to 26 %; these values are typical for dendrite electrolytic metals.

Acknowledgement

This work was financially supported by the JSC "Proryv" of the State Corporation "Rosatom".

References

1. F. H. Driggs and W. C. Lilliendahl, *Ind. and Eng. Chem*., **22**(5), 516 (1930).
2. M. Kolodney, *Production of Plutonium by Electrolysis*, Los Alamos National Laboratory Report, LA-148, (1944).
3. M. Kolodney, *J. Electrochem. Soc*., **129**, 2438 (1982).
4. C. Marzano and R. A. Noland, *The Electrolytic Refining of Uranium*, Argonne National Laboratory Report, ANL-5102, (1953).
5. L. W. Niedrach and A. C. Glamm, *J. Electrochem. Soc*., **103**(9) 521 (1956).
6. D. Inman, G. J. Hills, L. Young and J. O. M. Bockris, *Transactions of the Faraday Society*, **55**, 1904 (1959).
7. J. E Antill, D. S. Butler and E. Barnes, *Prog. in Nucl. En.*, **2**, 3 (1959).
8. G. Boisdie, G Chauvin, H. Coriou and J. Hure, *Electrochim. Acta*, **5**(1-2) 54 (1961).
9. G. Chauvin, H. Coriou and A. Simenauer, *Electrochim. Acta*, **8**(5) 323 (1963).
10. G. Chauvin, H. Coriou, P. Jabot and A. Laroche, *J. Nucl. Mat*., **11**(4) 2, 183 (1964).
11. S. L. Marshall, L. Redey, G. F. Vandegrift and D. R. Vissers, *Electroformation of Uranium Hemispherical Shells*, Argonne National Laboratory Report, ANL-89/26, (1989).
12. J. H. Lee, Y. H. Kang, S. C. Hwang, J. B. Shim, B. G. Ahn, E. H. Kim and S. W. Park, *J. Nucl. Sci. Technol*., **43**, 263, (2006).
13. Y. H. Kang, J. H. Lee, S. C. Hwang, J. B Shim, E. H. Kim and S. W. Park, *Carbon*, **44**, 3142 (2006).
14. J. H. Lee, Y. H. Kang, S. C. Hwang, J. B. Shim, E. H. Kim and S. W. Park, *Nucl. Tech*., **162**, 135 (2008).
15. I. B. Polovov, M. V. Chernyshov, V. A. Volkovich, O. I. Rebrin and A. N. Rylov, *ECS Trans.,* **86**(14) (2018).
16. I. B. Polovov, A. V. Abramov, A. F. Gibadullina, R. R. Alimgulov, V. V. Karpov, A. Yu. Zhilyakov, V.A. Khotinov and S. V. Belikov, *J. Alloys Compd*., **810**, 151758 (2019).
17. I. B. Polovov, A. V. Abramov, K. V. Dedov, V. V. Karpov, A. Yu. Zhilyakov, A. F. Gibadullina, S. V. Belikov, V. A. Volkovich and O. I. Rebrin, *ECS Trans*, **77**(11), 847 (2017).

18. D. A. Zolotarev, D. I. Nikitin and I. B. Polovov, *AIP Conf. Proc.*, **2174**(1), 020029 (2019).

ECS Transactions, 98 (10) 453-462 (2020)
10.1149/09810.0453ecst ©The Electrochemical Society

Corrosion of Metallic Materials in the Molten FLiNaK

I. B. Polovov[a], A. V. Abramov[b], R. R. Alimgulov[a], D. A. Zolotarev[a], A. I. Trubcheninova[b], A. F. Gibadullina[a], V. A. Volkovich[a], A. Y. Zhilyakov[c], V. A. Khotinov[c], and S. V. Belikov[c]

[a] Department of Rare Metals and Nanomaterials, Ural Federal University, Ekaterinburg, 620002, Russia.
[b] Department of Physical and Chemical Methods of Analysis, Ural Federal University, Ekaterinburg, 620002, Russia.
[c] Department of Heat Treatment and Physics of Metals, Ural Federal University, Ekaterinburg, 620002, Russia.

Corrosion resistance of molybdenum, tantalum and nickel-based alloys was studied in molten salt systems based on LiF–NaF–KF mixture in the temperature range 550–750 °C. The rates of corrosion of these materials were determined, the nature of the degradation of the surface of materials established, and the effect of the salt medium and temperature on the corrosive properties of metals and nickel-based alloys considered.

Introduction

Investigations of the corrosion resistance of structural materials in molten fluorides were carried out during the development of a molten salt reactor experiment (MSRE) with $LiF–BeF_2–ZrF_4–UF_4$ fuel (1, 2). During the implementation of this project, an INOR-8 nickel-based alloy was created with the following nominal composition, wt. %: Mo 15–17, Cr 7–8, Fe 4–6, C 0.04–0.08, which is currently known as Hastelloy® N (3–5). This alloy was chosen as the main construction material for MSRE.

Operation of MSRE has revealed two significant disadvantages of Hastelloy® N (6). First, the alloy at operating temperatures was embrittled by thermal neutrons. The creep resistance of the material did not deteriorate but the relative elongation of the alloy, which characterizes the plasticity of the material, decreased. Second, Hastelloy® N was prone to intergranular corrosion (IGC) and intergranular stress cracking. The depth of intergranular damage of the material in the melt was 0.1–0.25 mm. The phenomenon described above is called tellurium embrittlement, since tellurium formed during the fission of uranium interacts with nickel. As a result of this interaction, low-melting intermetallic compounds are formed at the grain boundaries of the alloy, which worsen the bond between the grains and lead to intergranular cracking of the material.

Based on the operating experience of the MSRE reactor, Oak Ridge National Laboratory (ORNL) had designed a molten salt breeder reactor (MSBR) by 1973. This reactor was to be made from Hastelloy N alloy modified with titanium and niobium. It was expected that the addition of titanium and niobium would reduce the embrittlement of the alloy due to radiation exposure and interaction with tellurium (1, 7–10). However, it turned out that niobium and titanium do not fit well with each other. For example,

Hastelloy® N alloy modified with 2 wt. % niobium, in the absence of titanium was resistant to tellurium embrittlement, but had a lower resistance to radiation damage compare to alloys alloyed with titanium only. On the other hand, alloying with titanium increased the resistance to radiation embrittlement, but noticeably worsened the resistance of the alloy to tellurium embrittlement. Nevertheless, Hastelloy N alloy with addition of 1–2 wt. % niobium was proposed as a candidate structural material for MSBR (6).

Studies carried out at ORNL showed that the interaction of steels and alloys with fluoride melts was accompanied by a predominant dissolution of chromium (1, 7–10). This was explained by the fact that chromium, as the most electronegative component of alloys and, according to electrochemical laws, was etched out of alloys and steels in the first place.

Currently, the corrosion processes in fluoride melts are being investigated by several scientific groups of the world community. The corrosion resistance of Hastelloy® N, Hastelloy® X, and Haynes® 230 alloys was investigated at 850 °C in a molten mixture of lithium, sodium and potassium fluorides (FLiNaK) for 500 hours in a graphite crucible container (11). After high-temperature tests in molten salts, chromium depletion and intergranular corrosion processes were found along the grain boundaries of the alloys. It was also noted that when a graphite crucible was used as a container, the corrosion rate increased due to formation of chromium carbide. Similar processes were found in the study of corrosion of AISI 316L steel in the LiF-BeF_2 melt (12). Metallographic analysis of corroded samples showed the presence of grain-boundary precipitates of Cr_7C_3 phase, which confirmed the phenomenon of diffusion of chromium and carbon in the samples in the direction of grain boundaries, which provoked the intergranular corrosion (IGC).

At present, there is no consensus on the choice of the optimal structural material stable in fluoride melts containing ions of fissile materials and breeder nuclides. This is largely due to the lack of a unified approach to obtaining and analyzing experimental data, as well as the lack of information on the mechanisms of corrosion in halide molten salts. In this work we investigated the corrosion of molybdenum, tantalum and nickel-based alloys (Hastelloy® G-35®, VDM® Alloy C-4, VDM® Alloy 59, VDM® Alloy 625, KhN62M) in FLiNaK melt in the temperature range of 550–750 °C.

Experimental

High purity metals were used for this work (Mo > 99.9 wt. %, Ta > 99.8 wt. %). The metal samples were cylindrical, 10 mm high, 6 and 4 mm in diameter for Mo and Ta, respectively. Samples of nickel-based alloys were cut from sheets 4–4.8 mm thick and had a rectangular shape. The composition of the alloys is shown in Table I.

Anhydrous lithium, potassium and sodium fluorides (purity > 99 wt. %, Aldrich, ACS) were used for the corrosion tests. Potassium fluoride was dried in a vacuum drying oven for 20 h at 60 °C, then for 20 h at 200 °C and 20 h at 400 °C. Then, the salt was transferred to an inert box. Sodium fluoride and lithium fluoride were dried for 12 h at 400 °C in a vacuum drying oven. Then, each salt was melted at 950 °C and kept for 3 hours under vacuum. The prepared individual salts were fused in an inert box in a molar

ratio LiF: NaF: KF = 46.5: 11.5: 42 (mass ratio LiF: NaF: KF = 29:12:59), then kept in a high purity argon atmosphere for 2 hours to homogenize the melt. The melt prepared in this way was cooled and stored in an inert atmosphere glove box. The resulting FLiNaK salt was analyzed by XRF (ARL Advant'X 4200) to determine the content of impurities and by CGHE (Horiba EMGA-620W/C) to determine the oxygen content.

Table I. Composition of the studied alloys according to the manufacturers' certificates, wt. %

	Ni	Cr	Mo	Fe	Mn	Ti	Al	Si	S	C	P	Nb	Cu	W
VDM Alloy C-4	base	16.1	15.6	0.84	0.02	0.01	—	0.016	0.002	0.003	0.002	—	—	—
Hastelloy G-35	base	33.12	8.22	0.78	0.22	<0.01	0.19	0.04	<0.002	0.012	0.003	—	0.03	0.11
KhN62M	base	23.21	12.78	0.47	0.03	0.08	0.11	0.06	0.003	0.005	0.004	0.03	—	—
VDM Alloy 59	base	22.6	15.4	0.9	0.19	—	0.23	0.02	<0.002	0.002	0.002	—	<0.01	—
VDM Alloy 625	base	21.15	8.6	4.5	0.08	0.21	0.16	0.18	0.003	0.021	0.006	3.35	0.09	—

The corrosion tests were carried out on an original complex for the study of corrosion phenomena (13). This equipment allows performing long-term corrosion tests in molten salts in a stream of various gases and gas mixtures. Corrosion experiments were carried out as follows. A glassy carbon crucible with three samples and salt was placed in a steel cell (the complex includes five such cells). Each cell was sealed, evacuated, filled with argon and placed in a furnace. The melt in the cell was under the atmosphere of high purity argon (argon content 99.9998 vol. %). Samples were held in the melts at 550, 650, and 750 °C. The duration of the corrosion tests was 100 h. After the experiment, the cells were cooled to the room temperature, and the crucibles with the ceramic samples were taken out. The samples were thoroughly washed and dried. The resulting salt was transferred into an inert box, crushed, and analyzed to determine the content of the corrosion products. The corrosion rate of each sample was calculated from the mass loss and independently determined from the content of corrosion products in the salts. The surface of the corroded samples was examined by scanning electronic microscopy (JEOL JSM 6490) and energy dispersive X-ray microanalysis (Oxford INCA).

Results and Discussion

Corrosion Rates of Individual Metals in FLiNaK

The corrosion rate of materials was determined by two independent methods: gravimetric and analytical. The gravimetric method consists of measuring the mass of samples before and after contact with a corrosive melt and further calculating the corrosion rate using the loss in mass of the samples. The analytical method involves determining the content of corrosion products in molten salts after testing and calculating the corrosion rate by mass of all the corrosion products. The content of corrosion products in FLiNaK after 100 hours of exposure of metal samples was determined by XRF.

The results of analysis of FLiNaK melts being held in contact with molybdenum and tantalum for 100 h are shown in Table II. Molybdenum content in FLiNaK remained extremely low and almost unchanged with an increase of the exposure temperature. The tantalum content in the salt increased with an increase in the temperature of the experiment, and the concentration of tantalum in the salt after the experiments was much

higher than the concentration of molybdenum under the same conditions. This indicates that the corrosion rate of tantalum in FLiNaK was higher than that of molybdenum.

TABLE II. The content of the corrosion products in FLiNaK (550, 650, 750 °C) after exposure of metallic samples for 100 h in the melt, wt. %

Analyte	Temperature, °C		
	550	650	750
Mo	0.005±0.001	0.009±0.002	0.009±0.001
Ta	0.016±0.003	0.051±0.004	0.20±0.02

Table III shows the rates of corrosion of samples of the studied metals determined after 100 h of exposure in FLiNaK at different temperatures. The corrosion rates were calculated by two independent methods, and the data obtained are in satisfactory agreement.

TABLE III. Corrosion rate of metallic samples after 100 h exposure in fluoride melts, mm/year

Temperature, °C	550		650		750	
Method of Determination	Gravi-metric	Analytical	Gravi-metric	Analytical	Gravi-metric	Analytical
Mo	0.012±0.002	0.008±0.001	0.038±0.004	0.037±0.003	0.071±0.006	0.041±0.003
Ta	0.18±0.02	0.13±0.01	0.34±0.4	0.36±0.2	1.7±0.2	1.3±0.1

The corrosion rate of molybdenum in FLiNaK up to 750 °C did not exceed 0.1 mm/year. This indicates a high corrosion resistance of molybdenum in this fluoride system and allows concluding that this metal can be classified as a promising construction material for this media. The corrosion rate of tantalum in this melt increased from 0.2 to 1.7 mm/year with rising temperature. The reason for the high corrosion rate of this metal is that tantalum in fluoride melts forms stable fluoride complexes $[TaF_7]^{2-}$; as a result the electrochemical stability of this metal was noticeably reduced (14). These results allowed to conclude that the use of tantalum is unpromising in FLiNaK-based melts.

Type of Metal Surface Degradation in FLiNaK

The surface of the samples of the studied metals after contact with fluoride melts was investigated using scanning electron microscopy. Fig. 1 shows images of the surface and metallographic sections of samples of the studied metals after exposure to FLiNaK. Molybdenum samples had a continuous uniform character of surface destruction after contact with FLiNaK for 100 h at 550–750 °C. A layer of 1–2 μm thick and poorly adhered to the surface of molybdenum samples appeared after the exposure in FLiNaK at 650 and 750 °C (Fig. 2). Taking into account EDS results (Fig. 2), we found that the layer was composed of molybdenum and oxygen. It was probably formed as a result of the interaction of the metal with residual oxygen from FLiNaK. According to the CGHE results, starting FLiNaK contained 0.04 wt. % oxygen, because it is extremely difficult to completely purify this salt from oxygen. Taking into account very low corrosion rate and uniform type of surface destruction, it can be concluded that molybdenum should be considered as a promising structural material for use in FLiNaK up to 750 °C.

Tantalum surface was significantly etched after contact with FLiNaK even at 650 °C. The type of surface destruction was continuous and uneven. The main reason for the low corrosion resistance of this metal is the high strength of complex tantalum ions with

fluoride ions. Tantalum is not very promising material for FLiNaK media at temperatures 550 °C and above.

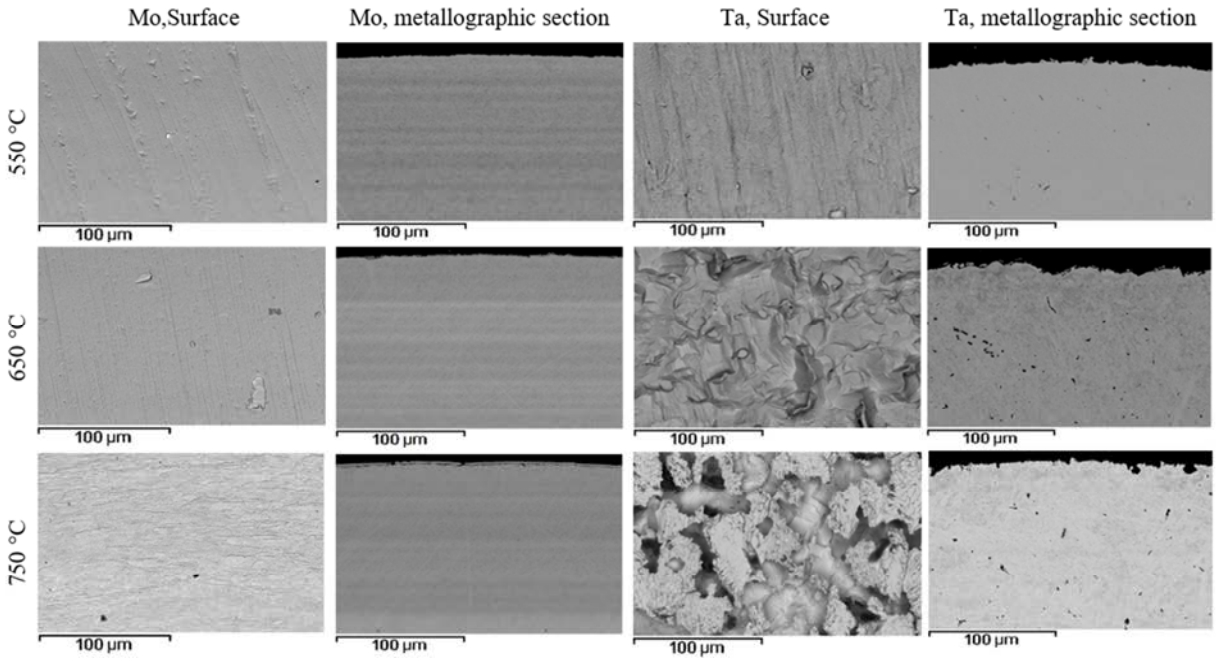

Figure 1. Surface and metallographic sections of metal samples after 100 h in FLiNaK at 550, 650 and 750 °C.

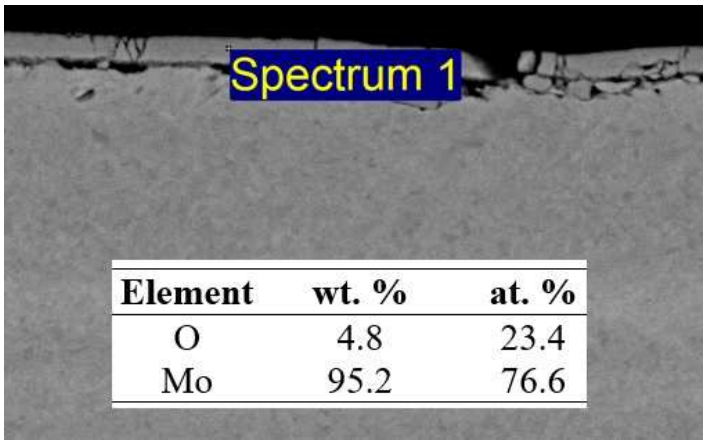

Figure 2. EDS analysis at the «Spectrum 1» point of the surface layer on a Mo sample after 100 h in FLiNaK at 750 °C.

Corrosion Rates of Alloys in FLiNaK

The content of corrosion products in FLiNaK after 100 hours of exposure of alloy samples was determined by XRF. The obtained results of spectral analysis are presented in Tables IV and V. Chromium was the main corrosion product in all fluoride systems in which alloys were tested. This fact confirms that selective etching of chromium occurs from the surface of the alloys as the most electronegative component of the alloys.

TABLE IV. The content of the corrosion products in FLiNaK (550, 650, 750 °C) after exposure of alloy samples for 100 h, wt. %

Hastelloy® G-35®				
Temperature, °C	**Cr**	**Ni**	**Mo**	**Fe**
550	0.005	<0.001	<0.001	<0.001
650	0.025	0.002	0.002	<0.001
750	0.105	0.008	<0.001	0.002
KhN62M				
Temperature, °C	**Cr**	**Ni**	**Mo**	**Fe**
550	0.005	<0.001	<0.001	<0.001
650	0.011	<0.001	<0.001	<0.001
750	0.062	0.002	0.001	0.001
VDM® Alloy 59				
Temperature, °C	**Cr**	**Ni**	**Mo**	**Fe**
550	0.003	<0.001	<0.001	<0.001
650	0.013	<0.001	<0.001	<0.001
750	0.033	<0.001	0.003	<0.001
VDM® Alloy C-4				
Temperature, °C	**Cr**	**Ni**	**Mo**	**Fe**
550	0.002	<0.001	0.002	<0.001
650	0.006	0.001	0.001	0.001
750	0.015	0.003	0.007	<0.001

TABLE V. The content of the corrosion products in FLiNaK (550, 650, 750 °C) after exposure of VDM® Alloy 625 samples for 100 h, wt. %

VDM® Alloy 625					
Temperature, °C	**Cr**	**Ni**	**Mo**	**Fe**	**Nb**
550	0.031	0.002	0.006	0.007	0.005
650	0.059	0.004	0.016	0.014	0.009
750	0.144	0.011	0.017	0.023	0.023

Table VI shows the rates of corrosion of samples of the studied alloys after 100 h of exposure in FLiNaK, depending on the temperature. Corrosion rates were calculated by two independent methods, the data of these methods are in satisfactory agreement. Corrosion rates for all alloys, with the exception of VDM® Alloy 625, at 550 °C in FLiNaK did not exceed 0.05 mm/year. The corrosion rate of alloys in FLiNaK at 650 °C, did not exceed 0.1 mm/year. The corrosion rate of alloys at 750 °C increased sharply and reached unacceptably high values.

TABLE VI. Corrosion rates of alloys samples after 100 h in fluoride melts, mm/years

Temperature, °C	**550**		**650**		**750**	
Method of Determination	**Gravi-metric**	**Analytical**	**Gravi-metric**	**Analytical**	**Gravi-metric**	**Analytical**
Hastelloy® G-35®	0.020	0.021	0.14	0.14	0.80	0.71
KhN62M	0.012	0.014	0.061	0.076	0.45	0.39
VDM® Alloy 59	0.011	0.008	0.041	0.048	0.18	0.19
VDM® Alloy C-4	0.010	0.016	0.017	0.025	0.11	0.11
VDM® Alloy 625	0.23	0.20	0.42	0.38	0.98	0.83

We conclude that Ni–Cr–Mo corrosion resistant alloys have similar corrosion rates in fluoride melts despite the differences in the content of main alloying components. High temperature and corrosion resistant Ni–Cr–Mo–Fe VDM® Alloy 625 has significantly higher corrosion rates than other alloys. A possible reason for the low corrosion resistance of this alloy is that it contains iron and also has structural differences from other alloys (small grain size, high proportion of phase inclusions) as a typical high

temperature material. Therefore all the investigated nickel alloys with the exception of VDM® Alloy 625 can be considered as promising construction materials in fluoride melts up to 650 °C. VDM® Alloy 59 and VDM® Alloy C-4 alloys can be classified as conditionally promising at 750 °C with corrosion rates of 0.18 and 0.11 mm/year at this temperature, respectively.

Type of Alloys Surface Destruction in FLiNaK

Surface of the samples of the studied alloys after contact with fluoride melts was investigated using scanning electron microscopy. Figs. 3–5 show images of the surface and metallographic sections of samples of the studied alloys after exposure to FLiNaK. A uniform spongy structure of surface destruction was observed for all the alloy samples, which indicate the localization of corrosion processes on their surface. This happens due to selective etching of chromium from the surface of the samples (Table VII, Fig. 6). Some differences in the spongy structure of different alloys were caused by various chromium content and different thermodynamic stability of the alloys.

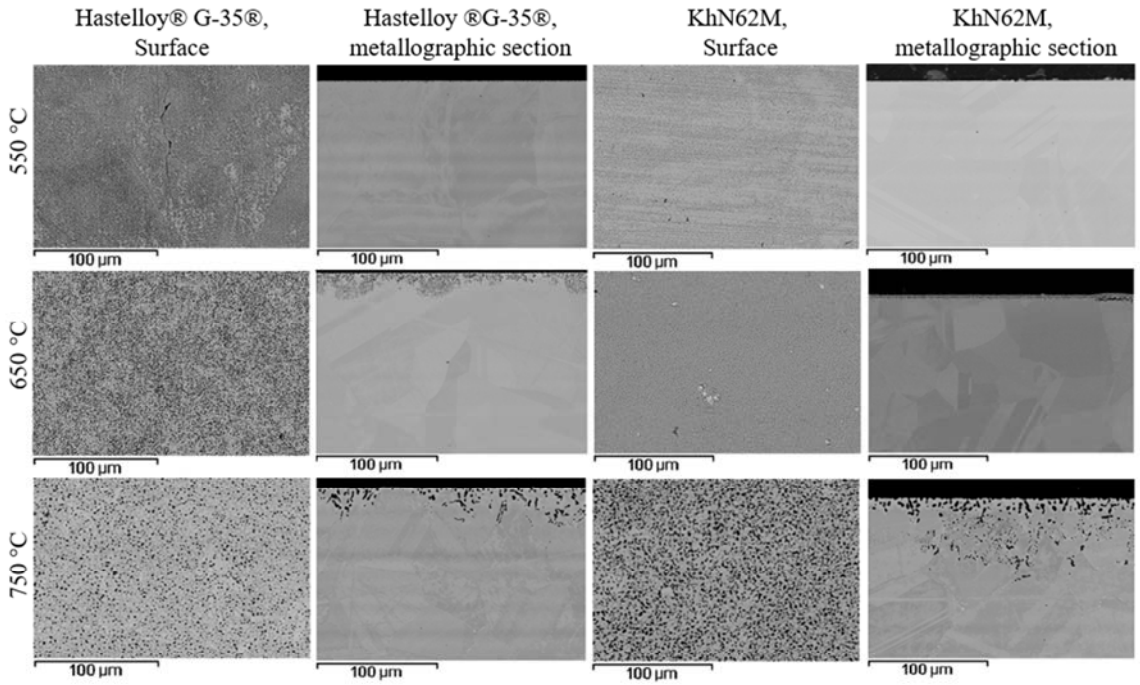

Figure 3. Surface and metallographic sections of samples of Hastelloy® G-35® and KhN62M alloys after 100 h in FLiNaK at 550, 650 and 750 °C.

TABLE VII. EDS at points on the surface of alloys after 100 h in FLiNaK at 750 °C.

Alloy	**KhN62M**	**VDM® Alloy C-4**
Point of Analysis	**Spectrum 4**	**Spectrum 5**
Element	**wt. %**	**wt. %**
Cr	0.6	1.8
Fe	0.6	1.5
Ni	86.8	77.7
Mo	12.0	19.0

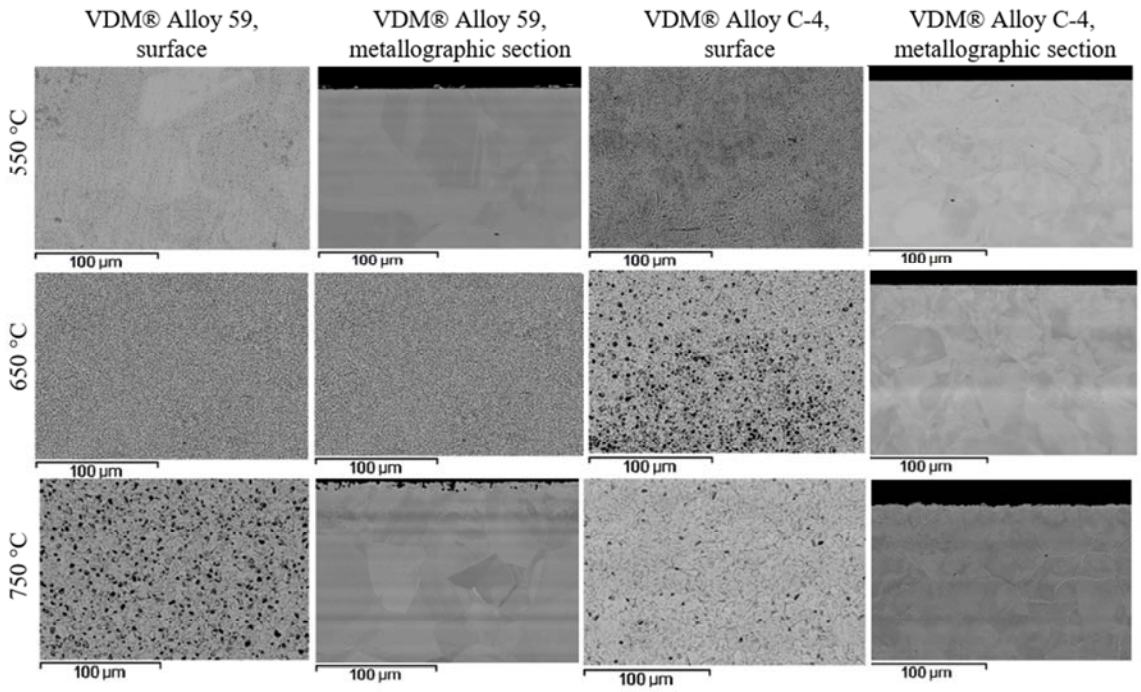

Figure 4. Surface and metallographic sections of samples of VDM® Alloy 59 and VDM® Alloy C-4 after 100 h in FLiNaK at 550, 650 and 750 °C.

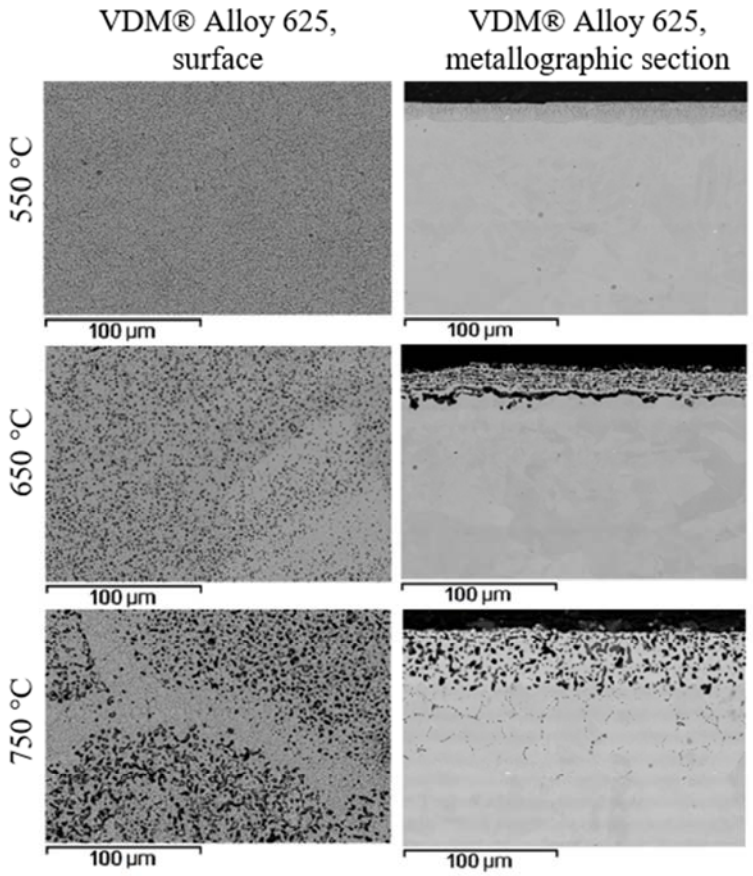

Figure 5. Surface and metallographic sections of samples of VDM® Alloy 625 after 100 h contact with FLiNaK at 550, 650 and 750 °C.

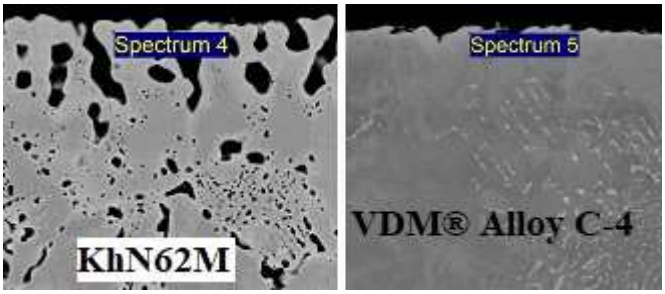

Figure 6. Points of elemental microanalysis of alloys after 100 h in FLiNaK at 750 °C.

The corrosion penetration depth was negligible at 550 and 650 °C for all the alloys except VDM® Alloy 625 and Hastelloy® G-35®. Character of the surface destruction and the depth of corrosion penetration changed significantly at 750 °C (Table VIII). The main reason for this effect is the intense precipitation of secondary phases along the grain boundaries of the alloys at 750 °C (15) that provokes an increase in the penetration depth and the development of intergranular corrosion. VDM® Alloy 625 is also destroyed under the influence of residual mechanical stresses along the rolling direction.

TABLE VIII. Depth of corrosion penetration into alloy samples after 100 h of exposure in FLiNaK, μm

Temperature, °C	**550**	**650**	**750**
Hastelloy® G-35®	1	10–20	12–38
KhN62M	<1	4–6	40–70
VDM® Alloy 59	<1	<1	3–5
VDM® Alloy C-4	<1	<1	1–2
VDM® Alloy 625	15–18	22–27	90–120

Conclusions

Corrosion properties of individual metals (Mo and Ta) and nickel-based alloys (KhN62M, Hastelloy® G-35®, VDM® Alloy C-4, VDM® Alloy 59, VDM® Alloy 625) were studied in a molten mixture of lithium, sodium, and potassium fluorides (FLiNaK) in the temperature range of 550–750 °C under inert atmosphere.

The results obtained showed that molybdenum should be considered as a promising structural material for use in FLiNaK up to 750 °C. Tantalum cannot be used FLiNaK media.

Nickel-based alloys are promising for operation in FLiNaK up to 650 °C. VDM® Alloy C-4 and VDM® Alloy 59 alloys can be considered as conditionally promising for operation in FLiNaK up to 750 °C.

Acknowledgements

This study was financially supported by the State Corporation “Rosatom” (Contact No. Н.4щ.241.09.20.1101).

References

1. V. L. Blinkin and V. M. Novikov, *Molten Salt Reactors*, p. 112, Atomizdat, Moscow (1978).
2. E. P. Velikhov, E. A. Azizov, P. N. Alekseev, M. I. Gurevich, S. A. Subbotin and A. L. Schimkevich, *Problems of Atomic Science and Technology, Series Thermonuclear Fusion,* **36** (1)**,** 5 **(**2013).
3. C. Madic, M. Lecomte, F. Testard, M. J. Hudson, J. O. Liljenzin, B. Satmark, M. Ferrano, A. Facchini, A. Geist, G. Modolo, A. G. Espartero and J. De Mendoza, in *Proceedings of the International Conference GLOBAL 2001*, Paris, France (2001).
4. C. Madic, F. Testard, M. J. Hudson, J. O. Liljenzin, B. Christiansen, M. Ferrano, A. Facchini, A. Geist, G. Modolo, G. A. Gonzales-Espartero and J. De Mendoza, *Partnew - New Solvent Extraction Processes for Minor Actinides - Final Report.* CEA-R–6066, CEA Valrho, Site de Marcoule, France (2004).
5. P. Masset, R. J. M. Konings, R. Malmbeck, J. Serp and J.-P. Glatz, *J. Nucl. Mater.*, **344**, 173 (2005).
6. H. E. McCoy Jr., *Status of materials development for Molten Salt Reactors*. ORNL/TM-5920, Oak Ridge National Lab., TN (1978).
7. H. F. McFarlane and M. J. Lineberry, *Progr. Nucl. Energ.,* **31**(1-2), 155 (1997).
8. J. Serp, M. Allibert, A. L. Terrier, R. Malmbeck, M. Ougier, J. Rebizant and J.-P. Glatz, *J. Electrochem. Soc.*, **152**, 167 (2005).
9. J. J. Laidler, J. E. Battles, W. E. Miller, J. P. Ackerman and E.L Carls, *Progr. Nucl. Energ.*, **31** (1-2), 131 (1997).
10. T. Inoue and H. Tanaka, in *Proc. on Future Nuclear Systems (GLOBAL'97)* p. 1588, Yokohama, Japan (1997).
11. L. C. Olson, J. W. Ambrosek, K. Sridharan, M. H. Anderson and T. R. Allen, *J. Fluor. Chem.,* **130** (1), 67 (2009).
12. G. Zheng, B. Kelleher, G. Cao, M. Anderson, T. Allen and K. Sridharan, *J. Nucl. Mater.,* **461**, 143 (2015).
13. I. B. Polovov, A. V. Abramov, A. F. Gibadullina, R. R. Alimgulov, V. V. Karpov, A. Yu. Zhilyakov, V.A. Khotinov and S. V. Belikov, *J. Alloys Compd.*, **810**, 151758 (2019).
14. L. P. Polyakova, E. G. Polyakov and N. J. Bjerrum, *Plasmas & Ions*. **2** (3–4), 117 (1999).
15. I. B. Polovov, A. V. Abramov, V. V. Karpov, A. F. Gibadullina, A. Yu. Zhilyakov, K. V. Dedov, S. V. Belikov, A. V. Shak, V. A. Volkovich and O. I. Rebrin, *ECS Trans.,* **77** (11), 753 (2017).

ECS Transactions, 98 (10) 463-470 (2020)
10.1149/09810.0463ecst ©The Electrochemical Society

Quantum-Chemical Study of the Electron Transfer in the $CaTiF_6$+12$CaCl_2$ Model System

Yu. V. Stulov[a], V. G. Kremenetsky[a], and S. A. Kuznetsov[a]

[a] Tananaev Institute of Chemistry - Subdivision of the Federal Research Centre «Kola Science Centre of the Russian Academy of Sciences», 26a Akademgorodok, Apatity, 184209, Murmansk region, Russia

The electron transfer mechanism in titanium containing model system was investigated by quantum-chemical methods. The calculations were performed using the Firefly quantum-chemical package by methods of the density functional theory (DFT). The method of frontier molecular orbitals (FMO) has shown a good applicability for studying electron transfer in the $CaTiF_6$+12$CaCl_2$ model system. Structures with a high probability of the electron transfer from the cathode to the titanium complex were found. The analysis of systems both with a high-ordered and a low-ordered boundary layer was considered. Such an approach made it possible to reveal the values of boundary ions shift and compression of the Ti–F bonds, which describe the transition state. It was shown that the structure of the transition state is disordered compared with the initial structures. The structure of transition state corresponds to the actual state of the boundary layer near the electrode surface. Using the FMO method made it possible with a small amount of computer time to determine the structure of the transition state of the TiF_6^{2-} complex near the electrode surface. The calculated activation energy of the electron transfer was in a good agreement with experimentally determined value.

Introduction

Today, quantum-chemical studies of the mechanism of electron transfer in molten salts based on a direct calculation of the transition state are faced with practically insurmountable computational difficulties. As our experience shows, model systems assigned to investigate the mechanism of charge transfer should include, in addition to the electroactive complex, two more of its coordination spheres. For electrolytes based on alkaline earth metal halides, this can be, for example, $MTiF_6$+12MX_2 type systems (M – Mg, Ca, Sr, Ba; X – F, Cl).

The search for a transition state by standard methods will require enormous computer time and is almost unrealistic. In this paper, we proposed another approach, which is based on the analysis of frontier molecular orbitals (FMO) under various deformations of the initial structure (1-3). Traditionally, this method was used to describe the reactivity of different molecules, but nothing prevents us from using it for the above purpose. Earlier, some possibilities of the FMO method were illustrated based on the analysis of the model system $MgTiF_6$+12$MgCl_2$ (2). In this work, the possibility of mixing closely lying

boundary molecular orbitals (MOs) was taken into account. When considering electron transfer in the $MgTiF_6$+12$MgCl_2$ system, it was found that for this system the structures most promising for charge transfer turned out to be structures in which the Ti–F bond lengths were compressed as a result of the completely symmetric vibration of the titanium complex. In addition to this parameter, the shift of the boundary calcium and chlorine ions from the reference state also varied in this paper (2). And then it was checked whether the type of the highest occupied molecular orbital (HOMO) of the system after electron transfer allows the localization of an additional electron on the complex in the process of complex relaxation during its diffusion into the depth of the system (2). In this regard, the use of the FMO method for searching for the transition state in other model systems is highly interest.

The aim of this work was to use the method of frontier molecular orbitals to search for the transition state during charge transfer in the $CaTiF_6$+12$CaCl_2$ model system.

Experimental

The geometry optimization of structures was performed with the Firefly program package (4), partially based on the source code of the GAMESS(US) program (5), by the density functional theory DFT/UHF method with the use of the B3LYP hybrid functional. For the F and Cl atoms quasi-relativistic basis set Stuttgart RLC ECP was used; for Ti and Ca – Stuttgart RSC 1997 ECP basis set (6-8).

In this work, we were interested in the state of the complex TiF_6^{2-} near the cathode surface. For this reason, on one side of the model system, a flat boundary layer consisting of 12-15 chlorine and calcium ions was formed. In the general case, boundary chlorine and calcium ions do not lie in the same plane. Mutual displacement of these ions was determined by calculation in the $C_{96}H_{24}$ + 7$CaCl_2$ model system, where $C_{96}H_{24}$ is the plane carbon cluster imitating the cathode surface, and hydrogen atoms close the dangling bond of carbon atoms to prevent artifacts. After optimization of this system, chlorine atoms turned out to be displaced by 0.5 Å with respect to calcium cations to the side opposite to the surface of a carbon cluster. The direction of this displacement corresponds to the action of an electric field on chlorine anions. The $CaTiF_6$+12$CaCl_2$ model system with such a displacement is the reference system. Note that the addition of a $C_{96}H_{24}$ cluster to our basic $CaTiF_6$+12$CaCl_2$ system would require a sharp increase in the calculation time. However, it is sufficient to analyze this $CaTiF_6$+12$CaCl_2$ system to draw qualitative conclusions. In further calculations, parameter of the boundary ions shift (Δd) and the compression of the Ti–F bond (Δr) was varied and the system was optimized for each value of Δd and Δr. Positive values of Δd correspond to a shift of boundary chlorine anions with respect to calcium cations toward the remaining part of the system, and its negative values point to the opposite displacement of boundary chlorine anions (toward cathode). An electric field of 10^9 V/m, which imitated the field of a cathode, was applied to all systems (9).

Results and Discussion

The probability of electron transfer from the electrode surface to the model system under study is determined primarily by the nature of the lowest unoccupied molecular orbital (LUMO) and neighboring unoccupied molecular orbitals (UMOs). The experimental data on the standard rate constants of charge transfer (k_s) (10) indicate the bridge mechanism of charge transfer, which means that the wave function of the LUMO (and the UMO lying close to it) should be delocalized between the boundary cations and the titanium complex. Only in this case, charge transfer to the complex is possible by a bridge mechanism. In addition, a linear dependence of k_s on the ionic potential of alkaline earth metal cations was established in (10), that is, the influence of the nature of the electrolyte cation on the value of k_s has no activation character (10).

The analysis of the $CaTiF_6$+12$CaCl_2$ system considered in this work has several differences from the analysis of electron transfer in the model system $MgTiF_6$+12$MgCl_2$ (2).

Firstly, for the quantum-chemical description of calcium cations in the present study, the Stuttgart 1997 ECP quasi-relativistic basis set was used, and the Crenbl ECP basis was used in (2). The Crenbl ECP basis for Mg has the 2-electron core of and a valence part consist of 10 electrons, while the core of the Stuttgart 1997 ECP includes 10 electrons and the valence part - 2. Therefore, the use of the Stuttgart 1997 ECP basis set for the description of cations Mg^{2+} led to a significant overstatement of energies. Nevertheless, our experience shows that the use of the Stuttgart family basis is preferable in comparison with the Crenbl basis since the Stuttgart basis describe the wave functions with sufficient reliability when considering electron transfer processes.

Secondly, important difference between the $CaTiF_6$+12$CaCl_2$ model system and the $MgTiF_6$+12$MgCl_2$ system is that calcium cations, in contrast to magnesium cations, has unoccupied 3*d* orbitals. Moreover, the 3*d* orbitals are separated by an energy gap of 3-4 kJ/mol from 3*s* orbitals. Consequently, these orbitals can mix, which in turn will have a strong effect on the electron transfer in the model system under consideration. In addition, the ionic radius of calcium is much larger than the ionic radius of magnesium, therefore, the structure of the boundary layer of ions and the transition state will have significant differences from that in the model system $MgTiF_6$+12$MgCl_2$.

The initial optimized model system has a rather trivial structure of molecular orbitals (MOs): several tens of the highest occupied MOs are mainly formed by the atomic *p* orbitals of chloride anions, while the five lowest unoccupied orbitals are localized on the Ti–F bonds of the complex, being a result of *d–p* interaction of titanium and fluorine atomic orbitals (AOs). However, the titanium complex is separated from the electrode surface by outer sphere calcium cations, which blocking the access of the ligands to the cathode surface. As a result, the electron transfer in such structures is impossible. Variation of the mutual arrangement of the boundary calcium cations and chloride anions has no noticeable effect on the MO structure: in all cases, the block of the highest occupied molecular orbitals is made of chloride ions orbitals, while in the region of the unoccupied MOs, two to five lowest orbitals are still localized on the Ti–F bonds. Fig. 1 shows LUMO for a similar structure.

The unoccupied MOs with a noticeable contribution of the AOs of calcium and chloride ions are separated from the above orbitals by an energy gap of about 150–200

kJ/mol, so that their mixing with the lower-lying unoccupied MOs is impossible. Thus, in this state, the electron transfer can occur only through fluoride ligands. However, the complex in this state is separated from the electrode surface by the outer sphere calcium cations, which block the access of the ligands to the cathode surface.

It was obvious to assume that the arrangement of the unoccupied MOs can change for some structure intermediate between the initial and final states of the system. However, calculations disprove this assumption. In this state, the LUMO nature does not change as compared with the initial state (see Fig. 1). In a structure that has arithmetic mean Ti–F bond lengths between those for the initial and final states, the LUMO, like the three orbitals lying above, is localized on Ti–F bonds. A noticeable contribution of the calcium and chlorine AOs is observed only for unoccupied MO that is 100 kJ/mol higher than the LUMO and cannot be mixed with the latter. Thus, the assumption is erroneous.

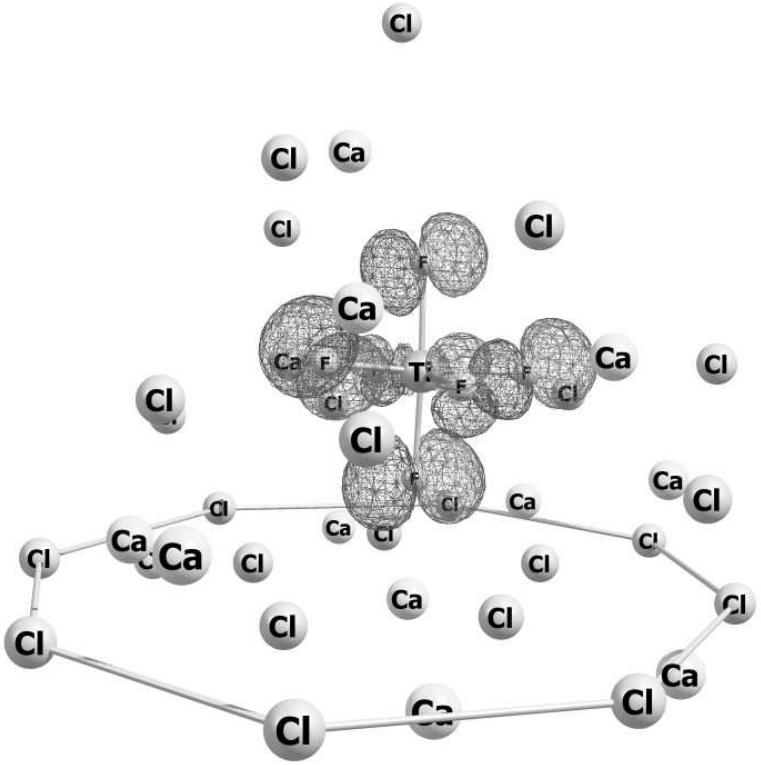

Figure 1. LUMO in the model system $CaTiF_6$+12$CaCl_2$.

The search for the optimal structure of the transition state for the $CaTiF_6$+12$CaCl_2$ model system was carried out by varying the compression of the Ti–F bonds and the shift of the boundary calcium and chlorine ions. However, in our case, the structure of the transition state was significantly different from the $MgTiF_6$+12$MgCl_2$ system. The Table I shows examples of some possible transition states of titanium-containing model systems. The transition state is characterized by the shift of the boundary ions (in brackets the shift is shown for chlorine anions distant from the bridging calcium cation) and the compression ratio of the Ti – F bond.

Electronic structure analysis of studied model systems was shown that shifting of the 4 boundary chlorine anions closest to the calcium cation destabilizes the unoccupied orbitals of the complex relative to the unoccupied orbitals of the bridge calcium cation (structures 1-3, 5-12 in Table I). LUMO also destabilizes upon compression of the bonds of the Ti–F complex (structure 4 in Table I). However, despite the delocalization of the LUMO wave function, electron transfer through structures 1 and 3 (Table I) is impossible due to the extremely high value of the activation energy. With a decreasing of the boundary ions total shift, the LUMO delocalization between the complex and the Ca^{2+} bridge cation practically disappears; however, the activation energy decreases significantly (structure 2, Table I). An analysis of the distribution of the LUMO wave functions in structures 4–7 in the Table I shows that the desired structure should has a mixed shift of chlorine anions (chlorine anions farthest from the bridge calcium cation have a lower shift values) and compression of Ti – F bonds.

The energy of structures (No. 8-12 in Table I) is close to the energy of the initial state, and the activation energy is in the range 16–36 kJ/mol, that is, close to the experimental value (10). Structure 10 is shown in Fig. 2. Here, the four boundary Cl^- anions closest to the bridge calcium cation have Δd =0.5 Å and the Δd for the rest anions is 0.3 Å.

Structures 8–12 have the same type of the LUMO (Fig. 2a), which is delocalized between the titanium complex and the bridged calcium cation. As noted above, this finding points to a high probability of the electron transfer from the cathode. The next (in energy) unoccupied orbital (LUMO + 1) is higher by 10-12 kJ/mol and has the same character as LUMO. The orbital LUMO+2 is higher than LUMO by 14–16 kJ/mol and belongs to the titanium complex. These three orbitals can mix with each other. The next orbital (LUMO+3) is separated from the LUMO by a gap of 80-83 kJ/mol and could not be mixed with the LUMO.

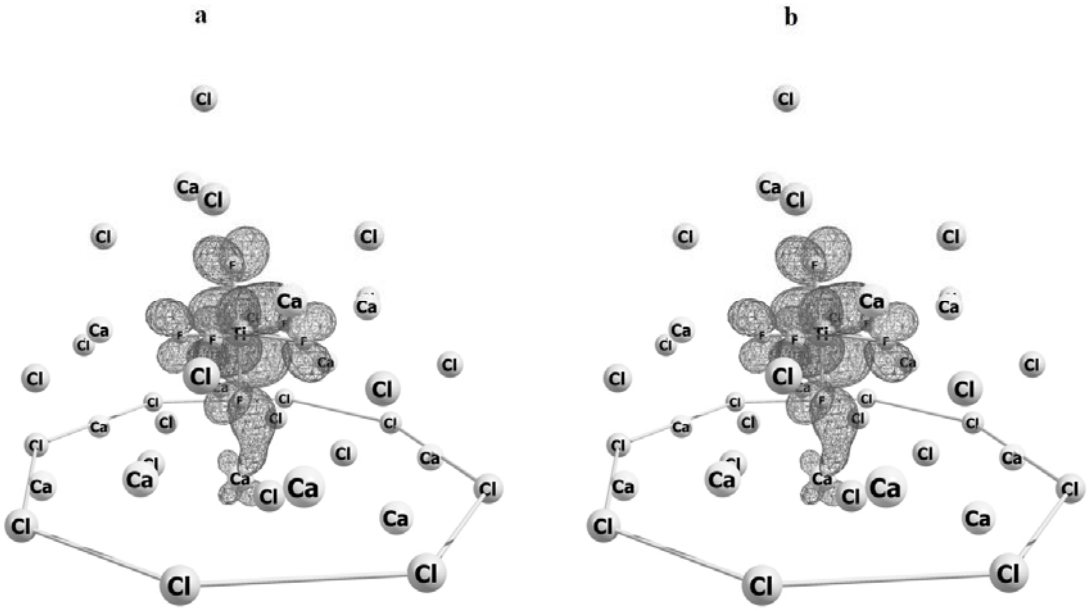

Figure 2. Frontier molecular orbitals of the structure 10 (Table I) Δd = 0.5 (0.2) Å ,Δr = 0.05 Å: LUMO before the charge transfer (a) and HOMO after the charge transfer (b). The activation energy is 24 kJ/mol.

Another, no less important, characteristic of the structure is the type of the highest occupied molecular orbital (HOMO) after electron transfer to the system (Fig. 2b). From a theoretical viewpoint, the following three basic types of HOMO can exist for our structures (11):

1. HOMO is fully localized on boundary ions;
2. HOMO is delocalized between boundary ions and the complex;
3. HOMO is fully localized on the complex.

In our calculations, we observed HOMO of all these types.

Table I. Characteristics of the transition state in the model system $CaTiF_6$+12$CaCl_2$

No	Δd, Å		Δr, Å	LUMO delocalization	E_a, kJ/mol	Electron transfer
	Ca^{2+}	Cl^-				
1	0	0.5	0	present	215	impossible
2	0.1	0.5	0	absent	30	impossible
3	0.1	0.5	0.05	present	100	impossible
4	0	0	0.05	present	53	impossible
5	0.5	0.3(0.5)	0.01	absent	1	impossible
6	0.5	0.3(0.5)	0.02	absent	2	impossible
7	0.5	0.3(0.5)	0.03	absent	4	impossible
8	0.5	0.3(0.5)	0.05	present	16	unlikely
9	0.5	0.5(0.3)	0.05	present	36	unlikely
10	0.5	0.5(0.2)	0.05	present	24	likely
11	0.5	0.5(0.2)	0.06	present	28	likely
12	0.5	0.5(0.1)	0.05	present	22	likely

The first type of HOMO was observed in the case of too low or too strong compression of Ti–F bonds. For example, if the $\Delta r \geq 0.1$Å the calculated activation energy is significantly higher than the experimental value, although HOMO before the charge transfer can have a delocalized character (with a predominant contribution of boundary cations to a wave function).

In the second case, there was a significant probability of electron transfer to the complex through the bridge calcium cation, and the probability of electron capture by the complex was close to 100%. The second type of HOMO always corresponds to the same type of LUMO before the charge transfer; therefore, in this case, the electron transfer to the complex by the bridge mechanism is quite real. Nevertheless, in this case, one should take into account the activation energy. If it has too high value, the electron transfer through such configurations is extremely unlikely.

The third case took place when HOMO before the charge transfer is almost fully localized on the complex. In this case, the electron transfer is impossible since the access of the complex to the electrode surface is blocked by outer shell cations.

The type of HOMO after electron transfer for structures No. 8 and 9 (see Table I) differs from structures 10-12 (Table I). In structures 8 and 9, HOMO is almost completely localized in the boundary calcium cation, and therefore, electron capture by the titanium complex is unlikely. Structures 10-12 have a HOMO delocalized between the boundary calcium cation and the complex (Fig. 2b). The type of this HOMO is the same as the type of LUMO before electron transfer. The spin density of the unpaired

electron is distributed between the complex and the bridge cation in a ratio of ~ 2:1, which also indicates a high probability of electron transfer to the complex.

Structure 10 after electron transfer and relaxation presents in Fig. 3. Structures 11 and 12 have a similar HOMO character after electron transfer and complex relaxation. As can be seen after relaxation, the spin density of the HOMO is completely localized on the complex of trivalent titanium. Thus, the probability of electron transfer in titanium containing systems through transition structures 10-12 (Table I) is very high.

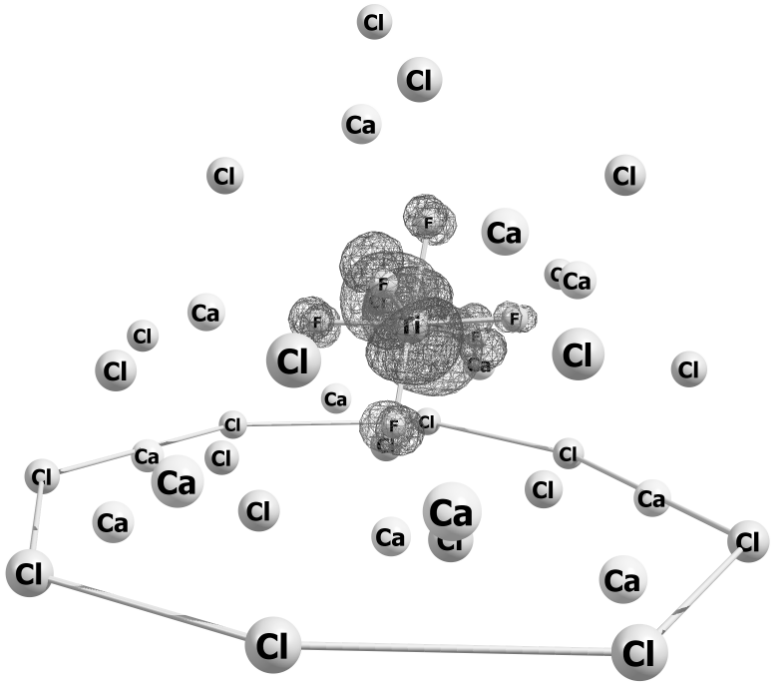

Figure 3. HOMO of the structure No 10 (Table I) of the $CaTiF_6$+12$CaCl_2$ model system after electron transfer and relaxation.

Conclusions

The frontier molecular orbitals method has shown a high information content for studying electron transfer in the $CaTiF_6$+12$CaCl_2$ model system. By varying the parameters of the transition state, structures were found with a high probability of the electron transfer from the cathode to the titanium complex.

Systems with a more ordered and a less ordered boundary layer are considered. This approach made it possible to reveal the ranges of the values of the boundary ions shift and the compression of the Ti–F bonds, which correspond to the transition state. In all studied model systems, it was found that the structure of the transition state is significantly disordered in comparison with the initial structures. This corresponds to the actual state of the boundary layer near the electrode surface.

Utilizing the frontier molecular orbital method, it was possible, with a small amount of computer time, to determine the structure of the transition state of the TiF_6^{2-}complex

particle near the electrode surface, using the matching of the calculated and experimental values of activation energy for electron transfer.

References

1. K. Fukui, T. Yonezawa, and H. Shingu, *J. Chem. Phys.,* **20**, 722 (1952).
2. V. G. Kremenetsky and S. A. Kuznetsov, *Russian Metallurgy (Metally)*, **2018**(2), 118 (2018)
3. A. A. Granovsky, http://classic.chem.msu.su/gran/gamess/index.html (accessed May 20, 2016).
4. M. W. Schmidt, K. K. Baldridge, J. A. Boatz, S. T. Elbert, M. S. Gordon, J. H. Jensen, S. Koseki, N. Matsunaga, K. A. Nguyen, S. Su, T. L. Windus, M. Dupuis, and J. A. Montgomery, *J. Comp. Chem.*, **14**, 1347 (1993).
5. D. J. Feller, *J. Comp. Chem.*, **17**, 1571 (1996).
6. K. L. Schuchardt, B. T. Didier, T. Elsethagen, L. Sun, V. Gurumoorthi, J. Chase, J. Li, and T. L. Windus, *J. Chem. Inf. Model*., **47**, 1045 (2007).
7. B. P. Pritchard, D. Altarawy, B. Didier, T. D. Gibson, L. Theresa, and A. Windus, *J. Chem. Inf. Model.*, **59(**11), 4814 (2019).
8. Z. Galus, *Fundamentals of Electrochemical Analysis,* Ellis Horwood, London (1994).
9. D. A. Vetrova and S. A. Kuznetsov, *Russian Metallurgy (Metally)*, **2017**(2), 100 (2017).
10. V. G. Kremenetsky, A. I. Nikolaev, and S. A. Kuznetsov, *Dokl. Phys. Chem*., **475**(1), 122 (2017).
11. V. G. Kremenetsky and S. A. Kuznetsov, *Russ. J. of Electrochem.*, **54**(9), 122 (2018).

ECS Transactions, 98 (10) 471-475 (2020)
10.1149/09810.0471ecst ©The Electrochemical Society

Ammonium·18-crown-6 bis(trifluoromethylsulfonyl)amide

Kio Kawata, Atsushi Kitada, Kazuhiro Fukami, and Kuniaki Murase

Department of Materials Science and Engineering, Kyoto University, Sakyo-ku, Kyoto 606-8501, Japan

We report synthesis and characterization of an ammonium-based molten salt, ammonium bis(trifluoromethylsulfonyl)amide-18-crown-6 (1/1), i.e. $[NH_4^+\cdot 18C6][Tf_2N^-]$ (Tf = SO_2CF_3). Raman spectra shows $[NH_4^+\cdot 18C6][Tf_2N^-]$ consists of NH_4^+ ion encapsulated by 18C6 and Tf_2N^- anion. The melting point of $[NH_4^+\cdot 18C6][Tf_2N^-]$ was around 100 °C. At 140 °C, the viscosity of $[NH_4^+\cdot 18C6][Tf_2N^-]$ was 14.7 mPa s, the conductivity was 8.0 mS cm^{-1}, and the density was 1.23 g cm^{-3}. These properties were comparable to those of common ionic liquids.

Introduction

Ammonium (NH_4^+) ion has some unique properties as a charge carrier, i.e., natural abundance and lightweight properties. Compared with metal cations (such as Li^+, Na^+, and K^+), NH_4^+ ion shows the highest intercalation potential and comparable cycling performance for Prussian blue-type positive electrode materials, K*M*[Fe(CN)$_6$] (*M* = Ni and Cu) (1). More recently, the first rocking-chair-type NH_4^+ ion battery has been proposed (2). The electrolytes for NH_4^+ ion batteries, however, have rarely been investigated except for aqueous solutions and solid state electrolytes (2, 3). Therefore, electrolytes which enable fast NH_4^+ ion transport at medium temperatures, i.e. 100–200 °C, have been of great interest.

Molten salts, especially ionic liquids (ILs), have received considerable attention as novel electrolyte materials for future electrochemical devices owing to their various characteristics such as negligible volatility, low flammability, high thermal/electrochemical stability, and high ionic conductivity (4–6). We have reported a hydronium (H_3O^+) solvate IL, which is described as $[H_3O^+\cdot 18C6][Tf_2N^-]$ (7–9). In $[H_3O^+\cdot 18C6][Tf_2N^-]$, protic H_3O^+ ion (i.e., solute) is solvated by 18C6 ligand (i.e., solvent) to form a $[H_3O^+\cdot 18C6]$ complex cation (i.e., solvate), and its physicochemical properties satisfy the criteria of solvate ILs (10).

It is well known that 18C6 features a six-oxygen cavity and matches well with NH_4^+ as well as H_3O^+ in a C_{3v} coordination, while the degree of off-center of $[NH_4^+\cdot 18C6]$ is larger than that of $[H_3O^+\cdot 18C6]$ (11). As far as we know, however, NH_4^+-based molten salts or ILs for electrolytes have never been reported, while alkyl ammonium-based ones have already been studied (12). Herein, we report synthesis and characterization of $[NH_4^+\cdot 18C6][Tf_2N^-]$ (Figure 1).

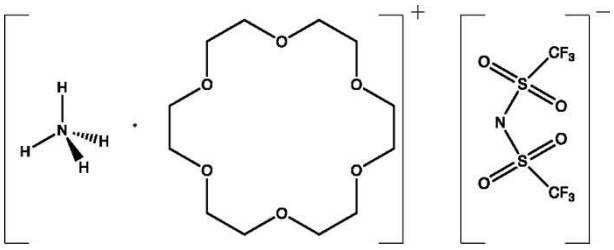

Figure 1. Schematic structure of 18C6, NH_4^+, and Tf_2N^-, of which $[NH_4^+ \cdot 18C6][Tf_2N^-]$ consists.

Experimental

18-crown-6 (18C6; Kanto Chemical, 99% purity), ammonia aqueous solution (Nakalai, 28%, 0.9 g cm^{-1}), and bis(trifluoromethylsulfonyl)imide (HTf_2N; Kanto Chemical, 99% purity) were used without further purification. Ultrapure water was prepared using a Merck Milli-Q Reference A system. First, NH_4Tf_2N was synthesized by neutralization of HTf_2N and NH_3 in water, followed by heating the precipitates at 100 °C for 24 h under Ar atmosphere, and the subsequent vacuum-drying at 80 °C for 24 h. Then, we added equimolar amount of NH_4Tf_2N to 18C6 and stirred at 500 rpm at 150 °C for 2.5 h to obtain $[NH_4^+ \cdot 18C6][Tf_2N^-]$.

The melting point of $[NH_4^+ \cdot 18C6][Tf_2N^-]$ was determined using a differential scanning calorimeter (DSC; Rigaku, DSC8231) with the heating rate of 5 °C min^{-1}. Raman spectra were obtained using an integrated Raman system (B&W Tek, InnoRam 785), consisting of a semiconductor laser light source (785 nm), an axial transmissive spectrograph, a holographic probe head, and a CCD detector. We conducted the thermogravimetric analysis (TGA) for $[NH_4^+ \cdot 18C6][Tf_2N^-]$, 18C6, and NH_4Tf_2N with the heating rate of 5 °C min^{-1}, using TG-DTA8122 (Rigaku) instrument in dry air. The conductivity at molten state was determined by electrochemical impedance spectroscopy (Bio-Logic Science Instruments SAS, VSP-300) using stainless steel electrodes. The cell constant was calibrated with 0.1 and 1 mol dm^{-3} KCl aqueous solutions. The measurement was carried out in a thermostatic chamber (Espec Co., SU-222) at 140 °C. Viscosity measurements were performed at the same temperature as conductivity measurements using a viscometer (Kyoto Electronics Manufacturing Co., Ltd., EMS-1000). The density was calculated using the measured values of weight and volume.

Results and discussion

A differential scanning calorimetry revealed that $[NH_4^+ \cdot 18C6][Tf_2N^-]$ melts at around 100 °C (Figure 2). Since no additional peaks were seen around the melting points of pure 18C6 (39–40 °C) and pure NH_4Tf_2N (165–168 °C), neither free ligands nor precursor NH_4Tf_2N were included.

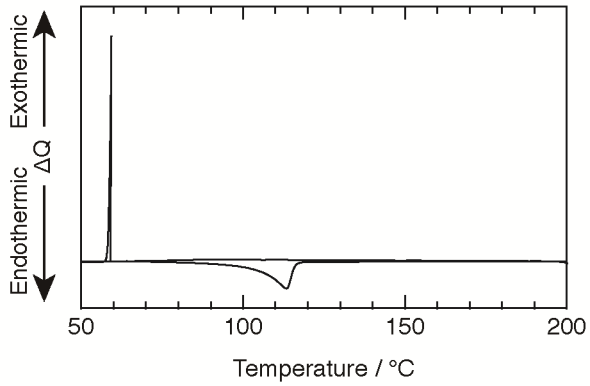

Figure 2. DSC curves for $[NH_4^+ \cdot 18C6][Tf_2N^-]$ with the heating rate of 5 °C min^{-1}.

Figure 3 shows a set of Raman spectra for $[NH_4^+ \cdot 18C6][Tf_2N^-]$ and 18C6. $[NH_4^+ \cdot 18C6][Tf_2N^-]$ displayed two sharp peaks at 870 and 830 cm^{-1} instead of the broad Raman bands assignable to pure 18C6, just like potassium–glyme complex in solid state (13). This indicates a change in the COC stretching and CH_2 rocking modes of 18C6 as a result of complexation. The Raman bands for Tf_2N^- anions emerged at around 745 cm^{-1}. Consequently, the mixture of NH_4Tf_2N and 18C6 consists of NH_4^+ ion (i.e., solute) solvated by 18C6 ligand (i.e., solvent) to form a $[NH_4^+ \cdot 18C6]$ complex cation (i.e., solvate), and Tf_2N^- anion.

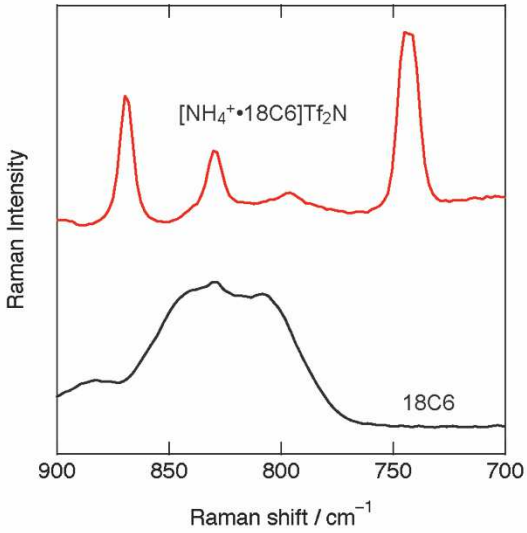

Figure 3. Raman spectra between 900–700 cm^{-1} of $[NH_4^+ \cdot 18C6][Tf_2N^-]$ and 18C6 at room temperature i.e., solid state.

As shown in Fig. 4, in TGA data obtained at 5 °C min^{-1} no mass loss was detected below 150 °C. Moreover, a 5 wt.% loss was detected at 212 °C, a temperature 100 °C higher than its melting point, indicating that neither free 18C6 and precursor NH_4Tf_2N were included.

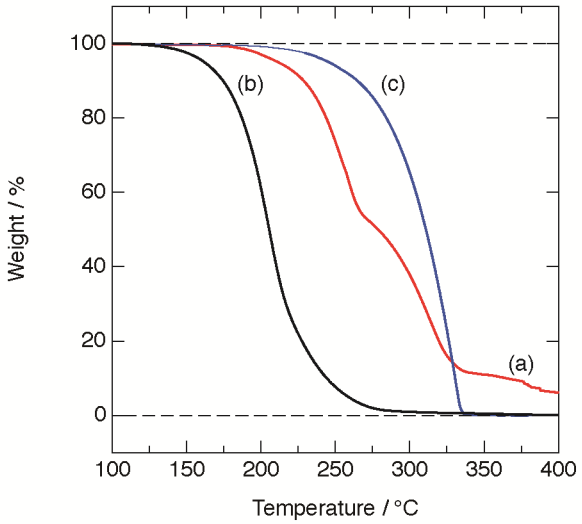

Figure 4. TGA data for (a) $[NH_4^+ \cdot 18C6][Tf_2N^-]$, (b) 18C6, and NH_4Tf_2N at 5 °C min^{-1}.

At 140 °C, the viscosity of $[NH_4^+ \cdot 18C6][Tf_2N^-]$ was 14.7 mPa s, the conductivity was 8.0 mS cm^{-1}, and the density was 1.23 g cm^{-3}. The bath properties of $[NH_4^+ \cdot 18C6][Tf_2N^-]$ were comparable to those of common ILs. Therefore, $[NH_4^+ \cdot 18C6][Tf_2N^-]$ has potential applications as electrolyte materials working at temperature higher than 100 °C.

Conclusions

In conclusion, we synthesized ether-coordinated ammonium amide, i.e. $[NH_4^+ \cdot 18C6][Tf_2N^-]$, of which melting point was around 100 °C. Raman spectroscopic measurement show that $[NH_4^+ \cdot 18C6][Tf_2N^-]$ consists NH_4^+ cation encapsulated by 18C6 and an amide anion. The ether-coordinated ammonium amide has potential applications as electrolyte materials toward a new class of ammonium ion batteries.

Acknowledgments

This work was supported financially by Grants-in-Aid for Scientific Research (B) (No.19H02490: A. K.) from the Japan Society for the Promotion of Science.

References

1. C. D. Wessells, S. V. Peddada, M. T. McDowell, R. A. Huggins, and Y. Cui, *J. Electrochem. Soc.*, **159** (2), A98 (2012).
2. X. Wu, Y. Qi, J. J. Hong, Z. Li, A. S. Hernandez, and X. Ji, *Angew. Chem. Int. Ed.*, **56**, 13026 (2017).
3. R. C. T. Slade, P. F. Fridd, and T. K. Halstead, *J. Solid State Chem.*, **32**, 87 (1980).

4. M. Armand, F. Endres, D. R. MacFarlane, H. Ohno, and B. Scrosati, *Nat. Matter*, **8**, 621 (2009).
5. G. A. Giffin, *J. Mater. Chem. A*, **4**, 13378 (2016).
6. M. Watanabe, M. L. Thomas, S. Zhang, K. Ueno, T. Yasuda, and K. Dokko, *Chem. Rev.*, **117**, 7190 (2017).
7. A. Kitada, S. Takeoka, K. Kintsu, K. Fukami, M. Saimura, T. Nagata, M. Katahira, and K. Murase, *J. Electrochem. Soc.*, **165** (3), H121 (2018).
8. A. Kitada, K. Kintsu, S. Takeoka, K. Fukami, M. Saimura, T. Nagata, M. Katahira, and K. Murase, *J. Electrochem. Soc.*, **165** (9), H496 (2018).
9. K. Kawata, A. Kitada, N. Tsuchida, M. Saimura, T. Nagata, M. Katahira, K. Fukami, and K. Murase, *J. Electrochem. Soc.*, **167**, 046508 (2020).
10. T. Mandai, K. Yoshida, K. Ueno, K. Dokko, and M. Watanabe, *Phys. Chem. Chem. Phys.*, **16**, 8761 (2014).
11. P. Hurtado, F. Gámez, S. Hamad, B. Martínez-Haya, J. D. Steill, and J. Oomens, *J. Phys. Chem. A*, **115**, 7275 (2011).
12. J. Qu, J. J. Truhan, S. Dai, H. Luo, and P. J. Blau, *Tribol. Lett.*, **22**, 207 (2006).
13. T. Mandai, K. Yoshida, S. Tsuzuki, R. Nozawa, H. Masu, K. Ueno, K. Dokko, and M. Watanabe, *J. Phys. Chem. B*, **119**, 1523 (2015).

ECS Transactions, 98 (10) 477-479 (2020)
10.1149/09810.0477ecst ©The Electrochemical Society

Author Index